Aloke Paul · Tomi Laurila
Vesa Vuorinen · Sergiy V. Divinski

Thermodynamics, Diffusion and the Kirkendall Effect in Solids

Springer

Thermodynamics, Diffusion and the Kirkendall Effect in Solids

Aloke Paul · Tomi Laurila
Vesa Vuorinen · Sergiy V. Divinski

Thermodynamics, Diffusion and the Kirkendall Effect in Solids

Springer

Aloke Paul
Department of Materials Engineering
Indian Institute of Science
Bangalore
India

Sergiy V. Divinski
Institute for Materials Physics
University of Münster
Münster
Germany

Tomi Laurila
Vesa Vuorinen
Department of Electrical Engineering
and Automation
School of Electrical Engineering
Aalto University
Aalto
Finland

ISBN 978-3-319-07460-3 ISBN 978-3-319-07461-0 (eBook)
DOI 10.1007/978-3-319-07461-0
Springer Cham Heidelberg New York Dordrecht London

Library of Congress Control Number: 2014940711

Printed on acid-free paper

Springer is part of Springer Science+Business Media (www.springer.com)

Prof. Frans J. J. van Loo

Aloke Paul dedicates this book to his Ph.D. guide

Prof. Frans J. J. van Loo, The Netherlands

Preface

Diffusion in solids plays an important role in many processes in Material Science and is the basis for numerous technological applications. In the nineteenth century, diffusion in a solid material was hard to imagine because of densely packed structure. In fact, the first systematic diffusion study in solid state was carried out only in the late nineteenth century.

Before the work of Ernst O. Kirkendall and Fredrick Seitz in the 1940s, it was a common belief that all the components diffuse at the same rate in solid materials. Based on this assumption, direct exchange and ring mechanisms were wrongly suggested to explain the diffusion of the components in crystalline solids. (Surprisingly, the ring mechanism was rediscovered in molecular dynamic simulation of grain boundary diffusion!) Kirkendall's work played an important role in formulating the basis of the theory of defect, i.e. vacancy-dependent diffusion mechanism. Following this thought-provoking concept many outstanding papers were published to further establish the relations to estimate the different diffusion parameters from experiments. In the mean time, based on Georg Karl von Hevesy's work, radiotracer technique to study diffusion was developed which sheds light on the fundamental aspect of the atomic nature of diffusion. In fact Seitz, based on the available tracer diffusion study on pure Cu and Kirkendall's experiment, proved beyond doubt that diffusion of substitutional atoms occurs by vacancy mechanism.

Looking back to the many books published on this subject by other researchers, it is evident that there exists no book with a special emphasis on interdiffusion and on the Kirkendall effect. Further, as thermodynamics plays an important role in interdiffusion, without a proper understanding of the subject, many fundamental aspects of interdiffusion may remain unclear. Therefore, we introduce the important aspects of thermodynamics from the solid-state diffusion perspective and then discuss the phenomenological process of interdiffusion extensively. Moreover, the understanding of the interdiffusion process is not complete without understanding the atomic mechanism of diffusion and different types of diffusion, such as lattice and grain boundary diffusion. Therefore, these topics are discussed in detail. Still, we are limiting the present consideration by metallic systems with uncharged defects.

Chapter 1 starts with very basic concepts of thermodynamics. The laws of thermodynamics are introduced and different extensive and intensive properties

and variables are briefly discussed. The chapter is focused on a short and concise description of the approaches to represent and utilize the thermodynamic data in a manner suitable for interdiffusion studies. Therefore, many different ways to represent the thermodynamic data of a given system graphically are introduced. Special emphasis is given to Gibbs energy diagrams, phase diagrams and different types of potential diagrams. Many of the relations developed and diagrams introduced in this chapter will be frequently used in subsequent chapters.

Chapter 2 introduces different aspects of the hierarchical structure of solids: atomic structure, unit cells, grain structure, defects, microstructure, etc., which are very essential for understanding of the material systems. Some aspects related to the defect structures in intermediate compounds, including the effect of atomic order, are also discussed.

Chapter 3 starts with the Fick's laws of diffusion. The second law is derived from the first law. Subsequently, several solutions for diffusion problems with different kinds of initial and boundary conditions are given. Limitations of the solutions obtained are discussed, too. This chapter is written in such a way that new students in the field or undergraduate students can understand the very basics of Fick's laws and their solutions, so that the formalism could directly be applied for processing of the experimental data.

Chapter 4 relates thermodynamics with interdiffusion of components. Different kinds of microstructures, which are expected to grow in the interdiffusion zone, depending on the given phase diagram and composition of the end members of the diffusion couples are explained in detail.

Chapter 5 discusses the atomic mechanisms of diffusion in detail. The main difference between the interstitial and substitutional diffusion mechanisms is discussed. Anisotropy of diffusion, effect of temperature, and the fundamental concept of a correlation factor are introduced in detail. The analytical and numerical approaches for calculation of the correlation factors are introduced. Diffusion in ordered phases is also disussed with a highlight on specific atomistic mechanisms and correlation effects.

Chapter 6 concentrates on interdiffusion in systems with a wide composition range. First, the limitations of the error function analysis are discussed based on the topics introduced in Chap. 3 After that, different approaches that are used to estimate the diffusion data are explained. The Kirkendall effect and the concept of intrinsic diffusion coefficients are introduced. The estimation of the tracer diffusion coefficients indirectly from a diffusion couple is also explained.

Chapter 7 discusses the estimation of the diffusion parameters in line compounds and phases with a narrow homogeneity range. Few practical examples are introduced to explain the steps needed for quantitative analysis.

Chapter 8 concentrates in the very recent developments in understanding the Kirkendall effect and the physicochemical approach. By using this approach, one can not only estimate the diffusion parameters, but also achieve more profound understanding of the microstructural evolution of an interdiffusion zone.

Chapter 9 concentrates on diffusion in multicomponent systems. The mathematical and experimental difficulties in estimating the diffusion parameters in

ternary or higher order systems are discussed. A pseudo-binary approach, which simplifies the conditions for the estimation of the diffusion parameter with much better efficiency, is introduced. The usefulness of the diffusion couple technique for the determination of phase diagrams is also discussed.

Chapter 10 concentrates mainly on short-circuit diffusion. Microstructures with a hierarchy of short-circuit paths are explained and the kinetic regimes of diffusion in such structures are introduced and discussed. Many practical examples are given in order to explain the practical estimation of the diffusion parameters. Finally, the effect of grain boundary diffusion on interdiffusion and Kirkendall effects are briefly discussed.

Chapter 11 introduces the complications arising from the growth of the phases as thin films. The roles of nucleation barriers, interfacial energies and elastic strains in reactive diffusion are discussed. Further, nucleation issues in solid-state amorphization are also discussed. Finally, it is shown that there is no fundamental difference between thin film and bulk diffusion couples and the complications in the former arise mainly from the structural features of thin films.

It should be noted that this book is biased towards experimental techniques. Important developments are going on simulation, which are not covered here. Three different groups have joined together to write on few important aspects such as thermodynamics, interdiffusion, atomic mechanism and short-circuit diffusion. In this also, few aspects are not covered extensively, which are beyond the requirements for the students or available in other books.

As usual, we don't expect it to be complete error-free. We would appreciate if you write us with your comments and feedback so that we can take care in the next edition.

Acknowledgment

Although four authors have written this book, the important contributions on different topics have come from several researchers over many decades. As one of the authors, I (Aloke Paul) dedicate this book to one of such researchers and my Ph.D. guide Prof. Frans J. J. van Loo, Eindhoven University of Technology, The Netherlands, for seminal contribution during his illustrious research career. At many places, especially in Chaps. 6–8, relations are derived based on his and coworker's work. He should have been the author of the book, which I expressed to him many times during my Ph.D. However, he was very clear that after my thesis, he would like to spend his retired life differently.

Dr. Alexander Kodentsov (Sasha) is another very important person influencing my research career. He taught me most of the experimental techniques and tricks leading to many successes. However, it was my inability that I could not improve my writing skill beyond a certain limit which is far behind his! He was always there, whenever I needed from personal to professional needs.

I am grateful to other co-workers, Dr. Mark van Dal, Dr. Csaba Cserháti, Dr. Pascal Oberndorff and Prof. Andrei Gusak for explaining many issues during my early stage of the career.

I am lucky to get very good research students and learnt many new aspects of diffusion through their work, questions and discussions. Additionally, they have done the most painful job of reading carefully, finding mistakes or drawing many figures. This book would be very difficult to complete without the help in the end, especially from Sangeeta Santra, Varun Baheti and Soumitra Roy on finalizing the chapters. I also thank my colleagues for their help during my difficult days.

I would like to acknowledge the financial support from Humboldt Foundation for my stay at Muenster University, Germany during which many chapters were written.

In the end, I thank two most important ladies in my life, wife Bhavna and daughter Pihu to make me get going through thick and thin.

We (Tomi Laurila and Vesa Vuorinen) would like to acknowledge our Ph.D. supervisor Professor (emeritus) Jorma Kivilahti for his contributions on the subject of thermodynamics. Many aspects of Chap. 1 are indebt to the textbook, which professor Kivilahti wrote in Finnish in the early 1980s. I (Tomi Laurila) would also like to pay my tribute to late Dr. Francois d'Heurle who I had the pleasure to know. He introduced to me the interesting fields of silicides and thin film reactions.

Also Dr. Kejun Zeng, Dr. Jyrki Molarius and Dr. Ilkka Suni are acknowledged for their contributions to the field of thermodynamic modelling and reactive phase formation in thin film diffusion couples as well as collaborating with me during my Ph.D. work. Finally, I want to thank the most important group of people in my life, my family, which consist of my wife Milla and our three children Miro, Mirella and Miko. Thanks for being there!

I (Vesa Vuorinen) would also like to express my gratitude to my family—my parents, my wife Maija and my children Viivi, Ville and Vili—for their love and support.

I (SergiyDivinski) acknowledge two outstanding persons who influence largely my scientific life—Prof. Leonid Nikandrovich Larikov, Institute of Metals Physics, National Academy of Science, Kiev, Ukraine, who was my Ph.D. supervisor, introduced me to the diffusion-based phenomena and whom I cannot overpay my late tribute, and Prof. Christian Herzig, Institute of Materials Physics, University of Münster, Germany, friendly and intensive collaboration and countless discussions with whom determined my current specialization. And, of course, my family—my wife Sveta and my daughters, Veronika and Alisa, they all together were and are on my side and not only support the viewpoint that "there is a life beyond science", but prove that this is the most important part of our life!

Contents

Chapter 1
Thermodynamics, Phases, and Phase Diagrams

In this chapter, we will briefly go through the basics of chemical thermodynamics. It is assumed that the reader is somewhat familiar with the fundamental concepts, and therefore, they are not discussed in great detail. The emphasis of the chapter is to build a thermodynamic foundation that can be utilized in the later chapters for diffusion kinetic analyses. We will put special emphasis on the use of different types of diagrams to represent thermodynamic data. Therefore, we introduce phase diagrams, potential diagrams, and Gibbs free energy diagrams in considerable detail. These "tools" are then used extensively in diffusion kinetic analysis later on in the book. We will conclude the chapter by introducing some commonly used thermodynamic conventions.

Classical thermodynamics is a phenomenological theory which deals with the physical properties of macroscopic systems under equilibrium conditions and the relations between them. The great importance of classical thermodynamics lies in its exactness as well as in its generality. It does not make any assumptions concerning the atomic structure of the system nor the interactions between the atoms. Even though this can be regarded as being beneficial in many applications, this can also be regarded as a weakness, especially in the case of solids and their solutions and compounds. Statistical thermodynamics, on the other hand, strives to obtain thermodynamic relationships based on the molecular behavior of matter. It provides additional information that cannot be achieved with classical thermodynamics. Firstly, statistical thermodynamics shows that the laws of thermodynamics are a direct consequence of the principles of quantum theory combined with one very general statistical postulate. Secondly, statistical thermodynamics provides general relations that cannot be derived from the laws of thermodynamics. Most importantly, by utilizing statistical thermodynamics, it is possible to obtain a physical understanding of the properties of solutions and about the reasons for their behavior. Thus, it is beneficial to utilize both of the approaches described above to obtain a more fundamental understanding of the behavior of different material combinations. The subject of thermodynamics is vast, and there are a large number of excellent books available [1–5]. The following seeks to summarize those parts of thermodynamics that are considered essential for a basic understanding of energetics in materials science. Further, the topics in Chap. 1 are

A. Paul et al., *Thermodynamics, Diffusion and the Kirkendall Effect in Solids*,
DOI: 10.1007/978-3-319-07461-0_1,

chosen in such a way to be closely correlated to the use of thermodynamics in the diffusion calculations from subsequent chapters. The treatment utilized in Chap. 1 partly follows the approach presented in the comprehensive textbook written by Kivilahti [6].

1.1 Thermodynamics System and Its State

The *system* is a clearly defined part of a macroscopic space, distinguished from the rest of the space by a physical boundary. The rest of the space (taking only the part that can be regarded to interact with the system) is defined as the *environment*. The system can be *isolated, closed,* or *open* depending on its interactions with the environment. An isolated system cannot exchange energy or matter, a closed system can exchange energy, but not matter, and an open system can exchange both energy and matter with the environment. A system can be homogeneous, thus thoroughly uniform, or heterogeneous. A homogeneous system is defined as a *phase*, which can be either a pure component (element or chemical compound) or a solution phase. A heterogeneous system, on the other hand, is a phase mixture. Thermodynamics aims to determine the state of the system under investigation. From experiment, it is known that when a certain number of macroscopic variables of the system have been fixed, the values of all other variables are also fixed and the state of the system becomes fully determined. In thermodynamics, the variables can be *extensive*, *intensive,* and *partial*. Extensive properties depend on the size of the system, whereas the intensive properties do not. Partial properties are the molar properties of a component. Those variables which are chosen to represent the system are called independent variables. A *macrostate* of the system is characterized, for example, by its temperature (T), pressure (p), and composition (n_i) or temperature (T), volume (V), and composition (n_i). A macrostate does not change over time if its observable properties do not change. The system can, however, go through changes in its state for a number of different reasons. These changes can be *reversible* or *irreversible*. A reversible change is a change that can be reversed by an infinitesimal modification of a variable, whereas irreversible processes have a definite direction which cannot be reversed. In a system, the energy of that system is constantly being redistributed among the particles of that system. The particles in liquids and gases are constantly redistributing in location as well as changing in quanta value (the individual amount of energy that each molecule has). Every specific arrangement of the energy of each molecule in the whole system at one instant is called a *microstate*. The nature of every microstate implicitly contains the important concept of *fluctuations* in it. It is evident that a given macrostate can be represented by number of different microstates.

1.2 The Laws of Thermodynamics

Thermodynamics is based on a few empirical generalizations, which are stated in the form of the following laws.

The zeroth law defines *temperature* such that if two systems are independently in equilibrium with a third system, they must also be in equilibrium with each other. Then, they have a common state variable—temperature.

The first law states the principle of conservation of energy such that the macrostate of a system can be characterized with an extensive variable, called internal energy E, which is constant in an isolated system. When the system interacts with the environment and transfers from one macrostate to another, the infinitesimal change in the internal energy can be stated as

$$E = dq + dw \tag{1.1}$$

where dq and dw are the heat and work transferred into the system during the change. When the system receives heat from the environment, $dq > 0$, and when the system gives up heat, $dq < 0$. The same is, of course, true for the work transferred. If the system does work, $dw < 0$, and if work is done on the system, $dw > 0$.If the external pressure acting on the systems' straight interface is p, then $dw = -pdV$, if the expansion work is the only form of work. The internal energy of the system is a state function. This means that dE is an *exact differential*. During a change, its value is, therefore, independent of the path between the initial and the final states. It is to be noted that dq and dw are not exact differentials, but infinitesimal quantities of heat and work, and thus, they are *path functions*. Their value, when integrated, depends on the path between the initial and final states.

The second law gives the criteria for the spontaneous change in nature that allows the macrostate in equilibrium to be characterized by a variable S, the entropy, which has the following properties

(i) Entropy, which is defined as

$$S = \left(\frac{dq}{T}\right)_{\text{rev}} \tag{1.2}$$

is a state function. In Eq. 1.2, the subscript rev refers to a reversible process. Entropy can be expressed as a function of the independent state variables of the system as $S = S(E, V_i, n_i)$. The infinitesimal entropy change of a closed system in an arbitrary reversible process can be thus written as

$$dS = \left(\frac{\partial S}{\partial E}\right) dE + \left(\frac{\partial S}{\partial V}\right) dV \tag{1.3}$$

By utilizing the first law $(dE)_{V,n_i} = dq$ and Eq. 1.2, we obtain

$$\left(\frac{\partial S}{\partial E}\right)_{V,n} = \frac{1}{T} \tag{1.4}$$

where T is the absolute temperature.

(ii) The entropy of the system is an extensive property.
(iii) The entropy of the system can change for one of two reasons, either as a result of the transfer of entropy between the system and the environment or by the creation of entropy within the system. The entropy change can be written as

$$dS = d_e S + d_i S \tag{1.5}$$

where $d_i S$ is the entropy created within the system. From the experiment, it is known that this quantity is *always positive*. During a totally reversible change, the entropy change can be zero. When the system is isolated, its entropy can never be decreased

$$dS = (dS)_{E,V} = d_i S \geq 0 \tag{1.6}$$

Hence, in real irreversible processes, the entropy of an isolated system always increases and reaches its maximum at the equilibrium state.

The third law states that the entropy of the system has a property that $S \to S_o$ when $T \to 0$, where S_o is a constant independent of the structure of the system. At absolute zero, the entropy of pure, defect-free, crystalline elements has the same value, S_o, which has been chosen to be zero.

Thus, the thermodynamics of closed and isolated systems is based on the following equations

$$\begin{aligned} dE &= dq + dw \quad \text{(for all changes)} \\ dS &= \frac{dq}{T} \quad \text{(for reversible changes)} \\ dS &\geq 0 \quad \text{(for changes in isolated systems)} \end{aligned}$$

These equations can be combined to give the fundamental equation for a closed homogeneous system

$$\begin{aligned} dE &= TdS + dw \quad \text{or} \\ dE &= TdS - pdV \end{aligned} \tag{1.7}$$

if only expansion work is considered.

Note The concept of entropy is highly ambiguous. Several interpretations have been given to entropy. The entropy law is a consequence of the fact that matter is composed of interacting particles that are in motion and which constantly show a tendency to muddle up and thereby to mix both matter and energy. Thus, it has been proposed that entropy is the measure of the systems mixed-upness (Gibbs), or the degree of disorder (Planck). According to Guggenheim, entropy is the measure of the spread of energy and matter. Shannon, on the other hand, has defined entropy as the lack of information or data [6].

The above equations are valid for closed systems with fixed composition. In order to extend the treatment to open heterogeneous systems, we need to choose a third variable, one that describes the composition and quantity of the system. This is the n_i being the number of moles of component i.

1.3 Heterogeneous Systems

A heterogeneous system is composed of several homogeneous subsystems, meaning phases which each have their own energy E^{ϕ}, entropy S^{ϕ}, and composition n_i^{ϕ} ($i = 1, 2, \ldots k$). Consequently, the energy, the entropy, and the number of moles of substance of the phase mixture are

$$E = \sum_{\phi} E^{\phi} \tag{1.8}$$

$$S = \sum_{\phi} S^{\phi} \tag{1.9}$$

$$n = \sum_{\phi} n^{\phi} = \sum_{\phi} \sum_{i} n_i^{\phi} \tag{1.10}$$

To exactly determine the state of the phase mixture requires that each phase that it contains must be described accurately. If we choose the variables (S, V, and n_i) to describe the state of a given phase, all other properties are then necessarily functions of the chosen variables. This means that especially the internal energy of a phase can be expressed as $E^{\phi}(S^{\phi}, V^{\phi}, n_i^{\phi})$. Its exact differential for an arbitrary change can be written as

$$dE = \left(\frac{\partial E}{\partial S}\right) dS + \left(\frac{\partial E}{\partial V}\right) dV + \sum_i \left(\frac{\partial E}{\partial n_i}\right) dn_i \tag{1.11}$$

When the composition of the phase does not change, Eq. 1.7 is valid and the first two partial derivatives in Eq. 1.11 are temperature of the phase (T) and its pressure (p). The last term is defined as the chemical potential of a component i. The chemical potential is defined formally in the following [1]: "If to any homogeneous mass we suppose an infinitesimal quantity of any substance to be added and its entropy and volume remaining unchanged, the increase of the energy of the mass divided by the quantity of the substance added is the (chemical) *potential* for that substance in the mass considered."

Consequently, we obtain an equation for the change in the phase internal energy

$$dE^{\phi} = T^{\phi} dS^{\phi} - p^{\phi} dV^{\phi} + \sum_i \mu_i^{\phi} dn_i^{\phi} \tag{1.12}$$

This equation is the fundamental equation for the independent variables S, V, and n_i. The internal energy E is their characteristic function, the thermodynamic potential of the phase. In a thermodynamic system, each phase has such a potential.

Next, a new thermodynamic function is defined with the help of internal energy and entropy

$$F = E - TS \tag{1.13}$$

By differentiating the function and by substituting Eq. 1.13 into the differential form of 1.12, we obtain

$$dF^{\phi} = -S^{\phi} dT^{\phi} - p^{\phi} dV^{\phi} + \sum_i \mu_i^{\phi} dn_i^{\phi} \tag{1.14}$$

This equation defines the Helmholtz free energy F, which is a function of the independent variables T, V, and n_i. The properties of this free energy function shall be discussed in more detail in Sect. 1.5.

Let us further examine the function E^{ϕ} with independent variables (S^{ϕ}, V^{ϕ}, and n_i^{ϕ}). Because T, p, and μ_i are intensive variables, they are not dependent on the amount of phase ϕ. From this, it follows that as the intensive variables remain constant, Eq. 1.12 can be integrated. This gives the thermodynamic potential of phase ϕ as

$$E^{\phi} = TS^{\phi} - pV^{\phi} + \sum_i \mu_i^{\phi} n_i^{\phi} \tag{1.15}$$

Next, we define two new functions, the enthalpy (H) and the Gibbs free energy (G)

$$H \equiv E + pV \tag{1.16}$$

$$G \equiv H - TS \tag{1.17}$$

By recalling the definition of Helmholtz free energy (1.13), Eq. 1.15 (together with 1.16 and 1.17) yields a function

$$G^{\phi} = \sum_i \mu_i^{\phi} n_i^{\phi} \tag{1.18}$$

This function (Gibbs free energy) is also a thermodynamic potential of a phase, and it is an extensive variable. Therefore, the Gibbs free energy of a phase mixture is given as

$$G = \sum_{\phi} \sum_i \mu_i^{\phi} n_i^{\phi} \tag{1.19}$$

When the Gibbs free energy function for a phase is known, all other thermodynamic properties of a given phase can be expressed with the help of this potential and its derivatives. The properties of the Gibbs free energy function are discussed in more detail in Sect. 1.5.

1.4 Commonly Used Terms and First Glance at Phase Diagrams

Thermodynamics is an exact discipline. Therefore, it is of great importance to define a few more key terms which will be frequently encountered later on in the text. *A component* refers to independent species in the system under investigation, giving the minimum number of substances which must be available in the laboratory in order to make up any chosen equilibrium mixture of the system in question. *A phase* is a region of uniformity in a system under investigation, as already stated. It is a region of uniform chemical composition and uniform physical properties. A phase is also distinguished from other dissimilar regions by an interface.

To illustrate the concepts of *compound* and a *phase,* we will consider a simple example H_2O. Ice, water, and water vapor are all different phases of the compound H_2O that exist in different temperature and pressure ranges, as shown in Fig. 1.1. The diagram shown in Fig. 1.1 is called a *unary phase diagram* and is shown for water in the figure. The point marked as C is called the critical point. When temperature rises above that critical point, the gas phase (water vapor) cannot be liquefied by increasing the pressure. The curve TC gives the equilibrium vapor pressure of the liquid as a function of temperature up to the critical point. At point *T* (called the triple point), all three phases of water are in equilibrium with each other.

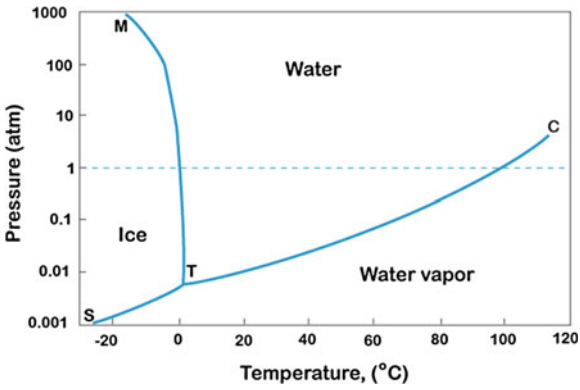

Fig. 1.1 The pressure–temperature diagram of H_2O

Based on the Gibbs phase rule (derived later on) at this point, the number of degrees of freedom is zero. The equilibrium can therefore be attained only at a specific temperature and pressure. The curve ST gives the equilibrium vapor pressure of the solid (ice) as a function of temperature. The curve TM gives the change in the melting point of ice as a function of pressure. It is to be noted here that the curve TM for the system H_2O is highly unusual as the TM curve here is descending, whereas in most of the systems, it is ascending. This is a result of the fact that the molar volume of solid water (ice) is larger than that of liquid water (in Sect. 1.7 is introduced the Clausius–Clapeyron equation that can be used to calculate this). In most systems, however, the opposite is true. Another unary system exhibiting this type of behavior (i.e., larger volume in solid than in liquid) is bismuth (Bi).

Different pure elements, for example, Cu or Ni, also have three different phases: solid, liquid, and gas. Similarly, two allotropic forms, solid gray tin and white tin, which have a different crystal structure and properties, are considered as distinct phases. To show the example of phases with two different components, we consider the Ag–Cu *binary phase diagram*, which is shown in Fig. 1.2. All phases are made of the two components, Ag and Cu. The different phases α, β, and liquid are stable within a certain *temperature* and *composition* (expressed here as weight percentage) range. Note that the phase diagram shown in Fig. 1.2 is determined at constant pressure. The α-phase is basically a solid solution Ag(Cu), that is, Ag (with its face-centered cubic (FCC) structure) with a limited amount of dissolved Cu, whereas the β-phase is a solid solution Cu(Ag), that is, Cu (with FCC structure) with a limited amount of dissolved Ag. Different notations (α and β) are used to differentiate solid solutions from pure elements. The *solvus* curve separates the single solid-phase region α from the solid two-phase region $\alpha + \beta$. Similarly, another solvus curve separates the one-phase solid region β from that of the solid two-phase region $\alpha + \beta$. The *solidus* curve separates the solid one-phase α-region from the two-phase region where the solid α and the liquid are in equilibrium. Similarly, another solidus curve separates the solid one-phase region β from the two-phase region β + liquid. The *liquidus* curve, on the other hand, separates the two-phase α + liquid and β + liquid areas from the liquid one-phase area L. In

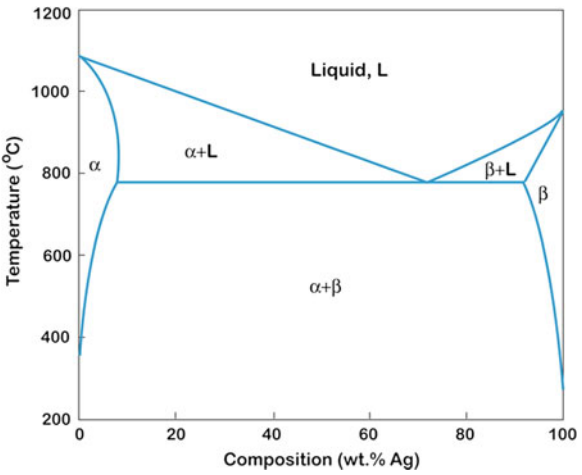

Fig. 1.2 Binary phase diagram of Ag–Cu

Fig. 1.2, there is a horizontal line of specific importance. It represents the so-called eutectic reaction, where liquid L reacts to form two new solid phases α and β. At the line, there are three phases L, α, and β which are in equilibrium with each other. According to the Gibbs phase rule (note that here the pressure is constant), such an equilibrium in a binary system can exist only at a specific temperature and only with specific compositions of the three phases participating in the equilibrium. It is common practice to show the stability of phases in a single-component system in different temperature and pressure ranges as shown in Fig. 1.1. In a binary system case, the stability of the phases is shown in a different temperature and composition range under constant pressure. Unless mentioned, a binary phase diagram (shown in Fig. 1.2) is commonly determined at atmospheric pressure. Note that at different pressure, the binary temperature–composition phase diagram will be different since the equilibrium transition temperature between different phases changes with pressure. It is also to be noted that typically, especially in the case of metals, the vapor region is not shown in the binary phase diagram as it typically exists at relatively high temperatures under atmospheric pressure. Finally, it is important to realize that one cannot obtain any information about kinetics or the morphology of the phase mixture from the phase diagram. The diagram only gives information about the phases that can be in equilibrium under certain composition–temperature combinations. Although there are three different species present in a system, there are times when the phase diagram is presented as a binary phase diagram. For example, as Fig. 1.3 shows, the $MgO–Al_2O_3$ phase diagram is presented as a binary phase diagram, where MgO and Al_2O_3 are considered as the components. The reason for this is clear. Even though there are three species (Mg, O, and Al) in the system, there are only two components (MgO and Al_2O_3). Only the amounts of these components can be changed *independently*. This is called a pseudobinary phase diagram.

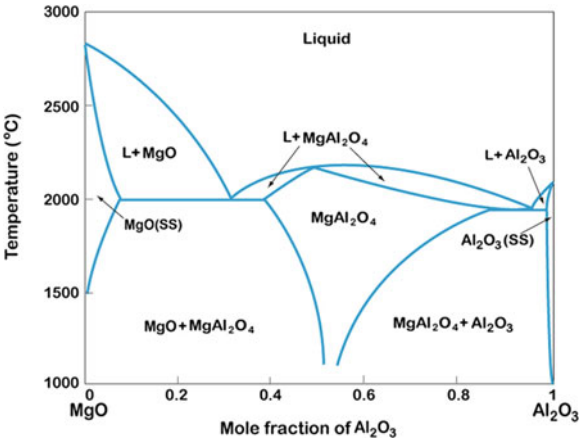

Fig. 1.3 Pseudobinary phase diagram of MgO and Al_2O

In a ternary system (Fig. 1.4), where three elements are mixed, the phase diagrams take the standard form of a prism which combines an equilateral triangular base (ABC) with three binary system "walls" (A–B, B–C, and C–A). This three-dimensional form allows the three independent variables to be specified (two-component concentrations and temperature). In practice, determining different sections of the diagram from these kinds of graphical models is difficult and, therefore, horizontal (isothermal) sections through the prism are used (Fig. 1.4b). The isothermal section is a triangle at a given temperature, where each corner represents the pure element, each side represents relevant binary systems, and areas of different phases can be determined inside the triangle. In addition to the isothermal section, also vertical sections (isopleths) can be taken from a space diagram of a given ternary system. We will return to these diagrams and their uses in Sects. 1.12 and 1.13.

Another commonly used term, as already mentioned, is *composition*. Composition can be expressed in terms of mole fraction, atomic fraction or atomic percentage, and weight fraction or weight percentage. It should be pointed out that in a binary (not pseudobinary) or multicomponent system, the mole fraction is equal to the atomic fraction. This can be shown very easily for a system of total 1 mol, where X_A and X_B are mole fractions of A and B, respectively. This can be written as

$$X_A + X_B = 1 \tag{1.21}$$

If n_A and n_B are the total number of atoms of A and B, respectively, we can write

$$X_A = n_A/N_o \quad \text{and} \quad X_B = n_B/N_o \tag{1.22}$$

where N_o (=6.022 $\times$ 10^{23} atoms/mole) is the Avogadro number.

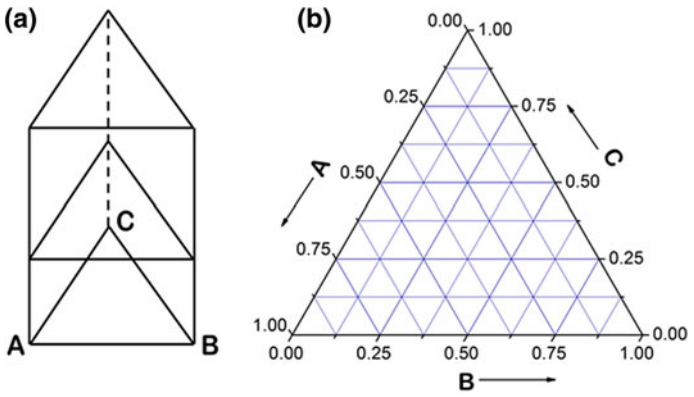

Fig. 1.4 **a** Ternary system, and **b** isothermal section at $T = x$ °C

This means that the atomic fraction of A (N_A) and B (N_B), with the help of Eq. 1.21, can be expressed as

$$N_A = \frac{n_A}{n_A + n_B} = \frac{X_A N_o}{X_A N_o + X_B N_o} = \frac{X_A}{X_A + X_B} = X_A \tag{1.23a}$$

$$N_B = \frac{n_B}{n_A + n_B} = \frac{X_B N_o}{X_A N_o + X_B N_o} = \frac{X_B}{X_A + X_B} = X_B \tag{1.23b}$$

Although in the previous example, we considered the one-mole system (which will be useful in the proceeding section), it can be shown that the mole fraction is always equal to the atom fraction, even if the system has a total more or less than one mole of atoms. For example, we consider the system of total x mole, where the mole of A and B are x_A and x_B, respectively. This can be written as

$$x_A + x_B = x \tag{1.24}$$

The mole fraction of A, X_A, can be expressed as

$$X_A = \frac{x_A}{x} = \frac{x_A}{x_A + x_B} \tag{1.25}$$

Consequently, the atomic fraction of A, N_A, can be expressed as

$$N_A = \frac{n_A}{n_A + n_B} = \frac{x_A N_o}{x_A N_o + x_B N_o} = \frac{x_A}{x_A + x_B} = x_A \tag{1.26}$$

A similar expression can be derived for B.

Concentration can be expressed as *molal concentration,* that is, c_i = number of moles (g-atoms, g-ions, etc.) of the solute i per 1,000 g of solution, or as *volume concentration,* that is, the number of moles per cubic meter (m^3). It is to be noted that the latter definition is valid only at constant temperature. When describing the composition of the liquid solution, for example, it is expedient to use as the two other independent variables (in addition to composition regardless of how it is expressed) temperature and pressure, so that differentiation with respect to temperature implies constant pressure. Thus, we have

$$\left(\frac{\partial C}{\partial T}\right) = -\alpha C_S$$

where α is the thermal expansivity and C_s is the concentration of the species of interest. The relation above shows that if C_s is chosen as a variable, it will not be an independent variable [2]. Further, when we consider the solid state, it becomes evident that in order to use volume concentrations, we should have knowledge about the molar volume as a function of composition of the phase under investigation. This is why volume concentrations are not always convenient variables and, for this reason, will not typically be used later on in the text.

1.5 Spontaneous Change

Entropy is the basic fundamental concept when the direction of natural change is considered as discussed in Sect. 1.2. Unfortunately, the use of entropy as the criteria for spontaneous change requires that changes in both the system and the environment are investigated. As the environment is not always easily defined, the entropy criterion is not convenient to use in many practical cases. However, if we concentrate on the system, we may lose some generality but gain a lot in the sense that the environment no longer needs to be considered. Next, we will look in greater detail how this can be achieved. Consider a system in thermal equilibrium with its surroundings at a temperature T. When a change in the system occurs, the second law of thermodynamics states (the Clausius inequality)

$$dS - \frac{dq}{T} \geq 0 \tag{1.27}$$

Depending on the conditions under which the process occurs, this inequality can be developed in two ways.

(i) Heat transfer at constant volume

In the absence of non-expansive work, it is possible to write $dq_V = dE$. This is because as volume is kept constant and only expansion work is considered, the work done by or to the system must be zero. Thus, we can write

$$dE = dq$$

and utilizing Eq. 1.27, the following is obtained

$$dS - \frac{dE}{T} \geq 0 \tag{1.28}$$

It is to be noted that here the criteria of spontaneity is expressed in terms of state functions only. Equation 1.28 can be rearranged as

$$TdS \geq dE \quad (V \text{ constant, no additional work}) \tag{1.29}$$

At either constant internal energy ($dE = 0$) or constant entropy ($dS = 0$), Eq. 1.29 can be expressed as

$$dS_{E,V} \geq 0 \quad \text{or} \quad dE_{S,V} \leq 0$$

The first inequality states that entropy increases in a spontaneous change in a system with constant volume and constant internal energy. The second inequality states that given the constant entropy and volume of a system, its internal energy decreases during spontaneous change. This is, in fact, a statement about entropy since it states that if the entropy of the system remains unchanged in the transformation, there must be an increase in the entropy of the environment caused by the outflow of heat from the system.

(ii) Heat transfer at constant pressure

Again, in the absence of non-expansive work, we may write $dq_p = dH$ and obtain

$$TdS \geq dH \quad (p \text{ constant, no additional work}) \tag{1.30}$$

At constant enthalpy or entropy, the following inequalities are obtained

$$dS_{H,p} \geq 0 \quad \text{or} \quad dH_{S,p} \leq 0$$

which can be interpreted in a similar fashion as inequalities concerning heat transfer at constant V.

Unfortunately, transformations where E and V, H and p, S and V, or S and p are constant are rare. Far more frequently, transformations take place under conditions where V and T, or even more typically, p and T, are constant.

Equations 1.29 and 1.30 can be written as

$$dE - TdS \leq 0 \quad \text{and} \quad dH - TdS \leq 0 \tag{1.31}$$

The Helmholtz and Gibbs free energy functions were defined as follows (Sect. 1.3)

$$F = E - TS \text{ and } G = H - TS \tag{1.32}$$

At constant temperature, the differentials of the functions F and G are

$$(dF)_{T,V} = dE - TdS \tag{1.33}$$

$$(dG)_{T,p} = dH - TdS \tag{1.34}$$

where the entropies of the phases have been replaced by the temperature of the system. We get two new inequalities for a spontaneous change with frequently observed variables

$$(dF)_{T,V} \leq 0 \tag{1.35}$$

$$(dG)_{T,p} \leq 0 \tag{1.36}$$

(iii) Expansion work is not the only form of work

How shall the above-derived conditions for spontaneity change if the expansion work is no longer the only form of work? The second law of thermodynamics states that $dE = dq + dw_{\text{tot}}$, where $dw_{\text{tot}} = dw' - pdV$ is the total work and dw' takes into account all other forms of work except expansion work. By solving dq, we get

$$dq = dE - dw' + pdV \tag{1.37}$$

and utilizing the fact that $dq - TdS \leq 0$, we obtain

$$dE - TdS - dw' + pdV \leq 0 \tag{1.38}$$

By utilizing the definition of the Helmholtz free energy, we obtain

$$(dF)_T \leq dw' - pdV = dw_{\text{tot}} \tag{1.39}$$

Thus, at constant T, change occurs spontaneously when the change in Helmholtz energy is smaller than the total amount of work. If the volume is constant $dV = 0$, then

$$(dF)_{T,V} \leq dw' \tag{1.40}$$

which is equal to Eq. 1.39 when the expansion work is the only form of work.

From the definition of enthalpy ($H = E + \text{pV}$) and from $dE = dq + dw' - pdV$ under constant pressure, it follows that

$$(dH)_p = dE + pdV = dq + dw' - pdV + pdV \tag{1.41}$$

which gives

$$dq_p = (dH)_p - dw' \tag{1.42}$$

Combining this with Eq. 1.31 results in

$$dH - TdS - dw' \leq 0 \text{ (constant pressure)} \tag{1.43}$$

and finally,

$$(dG)_{T,p} \leq dw' \tag{1.44}$$

At constants T and p, the change is spontaneous if the change in Gibbs energy is less than the additional work done. Equations 1.44 and 1.40 can be stated also as *$-\Delta G$is the maximum amount of work (other than expansion work) that the system can release during spontaneous change at constant temperature and pressure. The value $-\Delta F$is the maximum amount of total work that the system can release during spontaneous change at constant temperature.*

Given that $G = G(T, P, n_1, n_2, \ldots)$ in an open system, with n_i being the number of moles of component i, the derivative of the Gibbs energy function yields

$$dG = -SdT + Vdp + \sum_i \mu_i dn_i \tag{1.45}$$

where μ_i is the chemical potential of component i. At a constant value of the independent variables P, T, and $n_j (j \neq i)$, the chemical potential equals the partial molar Gibbs free energy, $(\partial G/\partial n_i)_{P,T,j\neq i}$. The chemical potential (partial Gibbs energy) has an important function analogous to temperature and pressure. A temperature difference determines the tendency of heat to flow from one body into another, while a pressure difference, on the other hand, determines the tendency toward a bodily movement. A chemical potential can be regarded as the cause of a chemical reaction or the tendency of a substance to *diffuse* from one phase to another.

As shown before in Eq. 1.17, the Gibbs free energy can be expressed as

$$G = H - TS$$

where H (J/mole) is the enthalpy, T (Kelvin, K) is the absolute temperature, and S (J/mole K) is the entropy of the system. Further, H, the total heat content or total energy of the system, was defined in Eq. 1.16 as

$$H = E + pV$$

where E is the internal energy, P is the pressure, and V is the volume of the system.

In general, the contribution of PV in Eq. 1.16 is very small in the solid and liquid states if the pressure is not exceptionally high. Therefore, while working with condensed phases (solid and liquid), the PV term can, in most cases, be neglected. Hence, the change in internal energy of the system can be approximated to be equal to its enthalpy

$$H = E \tag{1.46}$$

The internal energy of the system consists of the potential and kinetic energies of the atoms within the system. The kinetic energy of solids and liquids is caused by the vibration of atoms at their position. In liquids and gases, the translational and rotational movement of the atoms (or molecules), within the system, provides an additional contribution to the kinetic energy. Every atom vibrates with different energy at its position with degrees of freedom in x, y, and z directions with very high frequency that is temperature dependent. The frequency spectrum starts from 0 and goes up to a maximum value of v_D, which is called the Debye frequency. By utilizing the vibration frequencies, it is possible to calculate the heat capacity of a given solid. Above a certain temperature (θ_D, the Debye temperature), all atoms are essentially vibrating with their corresponding maximum Debye frequency. For metals at room temperature, they are typically above their Debye temperature, which makes it possible to use single (maximum) frequency values when considering the diffusion of atoms, for instance. The average total energy ($=3NkT$ where k is the Boltzmann constant and N is the number of atoms in a crystal) of atoms is fixed with respect to a particular temperature. Moreover, the vibration of any atom depends on the vibration of neighboring atoms because of inter-atomic bonding. This coupling produces an elastic wave with quantized energy. The quantum of energy in an elastic wave is called a phonon. For example, sound waves and thermal vibrations in crystals are phonons. The other part of internal energy in solids, the potential energy, depends on the inter-atomic bonding between the atoms. In a single-component system, the potential energy depends on one type of bonding, but, in a binary or multicomponent system, the potential energy depends on the type, number, and magnitude of the different bonds between the atoms within the system. This is explored further in Sect. 1.9 for binary systems cases. The entropy of a crystal is composed of two terms: *thermal entropy* and the *configurational entropy*. The first part is concerned with the distribution of energy over the available energy states in the crystal (system) and the latter part with the distribution of atoms or particles within the crystal (system).

Note By utilizing the Gibbs free energy, all forms of work (excluding expansion work) can be taken into account $\mathbf{-(\Delta G)_{p,T} \geq w' = \Sigma \mu_i n_i + \gamma A + zFU + \cdots}$, where the first term is the chemical part, the second is the surface energy contribution, the third is the electrical component, etc. Thus, Gibbs energy gives the amount of maximum additional (non-expansion) work that the system can perform. For all spontaneous processes, the change in Gibbs energy must be negative. It should also be noted that the temperature and pressure of the system do not have to be constant during the whole process. It is adequate that they are the same at the initial and final stages. An example is an exothermic reaction taking place at temperature T, where the reaction heat is transferred to the environment at the end of the reaction, thus making T_{initial} equal to T_{final}. This is, of course, a consequence of the fact that the Gibbs energy is a state function and its value is only dependent on the initial and final states, not the path between them.
The Helmholtz free energy of a closed system, on the other hand, is a function of *temperature* and *volume*. Helmholtz free energy (F) is maximum free energy, which can be used to do work at constant volume and temperature and can be expressed as

$$F = E - TS$$

where E is the internal energy. The main difference between Gibbs free energy (i.e., the change in energy at constant pressure and temperature) and Helmholtz free energy (i.e., the change in energy at constant volume and temperature) is "PV". This comes from the fact that there is need for extra work to accommodate the volume change. Thus, the Helmholtz free energy is the maximum amount of any kind of work the system can do and is, therefore, sometimes called the maximum work function. The change in Helmholtz free energy must also always be negative for a spontaneous change.

With the help of the Gibbs free energy function derived above, the equilibrium state of the system can be investigated. There is the relation between the chemical potential of components and the total Gibbs energy of the system, as expressed in Eq. 1.19 (Sect. 1.3) through

$$G_{\text{tot}} = \sum_{\phi} \sum_{i} \left(\mu_i^{\phi} n_i^{\phi} \right)$$

The Gibbs energy function can be utilized from the component level to the system level and back again. Hence, Eq. 1.19 provides the very important connection between component and system level properties.

Three stable equilibrium states to be considered here are (i) complete or global thermodynamic equilibrium, (ii) local thermodynamic equilibrium, and (iii) partial thermodynamic equilibrium. When the system is at *complete equilibrium,* its Gibbs free energy (G) function has reached its minimum value

$$dG = 0 \quad \text{or} \quad \mu_i^{\alpha} = \mu_i^{\beta} = \cdots = \mu_i^{\phi}, \quad (i = \mathrm{A}, \mathrm{B}, \mathrm{C}, \ldots) \tag{1.47}$$

and then, the system is in mechanical, thermal, and chemical equilibrium with its surroundings. Consequently, there are no gradients inside the individual phases and no changes in the macroscopic properties of the system are to be expected.

Local equilibrium, on the other hand, is defined in such a way that the equilibrium exists only at the interfaces between the different phases present in the system. This means that the thermodynamic functions are continuous across the interface and the compositions of the phases right at the interface are very close to those indicated by the equilibrium phase diagram. This also indicates that there are activity gradients in the adjoining phases. These gradients, together with the diffusivities, determine the diffusion of components in the various phases of a joint region.

Partial equilibrium means that the system is in equilibrium only with respect to certain components. It is generally found that some processes taking place in the system can be rapid, while others are relatively slow. If the rapid ones occur quickly enough to fulfill the requirements for stable equilibrium (within the limit of error) and the slow ones are slow enough that they can be ignored, then it is quite proper to treat the system as being in equilibrium with respect to the rapid processes alone [7].

It is also possible that the global energy minimum of the system is not accessible owing to different restrictions. In such cases, we are dealing with metastable equilibrium, which can be defined as a local minimum of the total Gibbs energy of the system. In order to obtain global stable equilibrium, some forms of activation (e.g., thermal energy) must be brought into the system. It is to be noted that metastable equilibrium can also be complete, local, or partial; the local metastable equilibrium concept, in any case, will be used frequently in the following sections. Very often, one or more interfacial compounds, which should be thermodynamically stable at a particular temperature, are not observed between two materials and, then, these interfaces are in local metastable equilibrium. Another situation commonly encountered occurs in solid/liquid reaction couples, where during the few first seconds, the solid material is in local metastable equilibrium with the liquid containing the dissolved atoms, before the intermetallic compound(s) is formed at the interface. In fact, a principle commonly known as *Ostwald's rule* states that, when a system undergoing reaction proceeds from a less stable state, the most stable state is not formed directly but rather the next more stable state is formed, and so on, step by step until (if ever) the most stable is formed. It is a fact that most materials used in everyday life have not been able to reach their absolute minimum energy state and are, therefore, in metastable equilibrium. It should be noted that a system at metastable equilibrium has thermodynamic properties, which are exactly determined, just as a system at stable equilibrium.

1.6 Free Energy and Phase Stability of Single-Component System

Different phases of a single element can be stable at a different temperature range under a particular pressure (we consider atmospheric pressure). For example, below the melting point, a solid phase is stable, whereas above the melting point, a liquid phase is stable. In general, at a particular temperature, the phase with the lowest Gibbs free energy will be the stable one. If at a particular temperature, the free energy of two phases is the same, then both phases are stable at that temperature. This takes place, for example, at the melting point where the solid and the liquid phases exist together. This also means that the system is in equilibrium and there is no driving force for change. To explain the stability of phases at different temperatures, we need to know the change in their free energies as a function of temperature. Consequently, (following Eq. 1.18) in order to determine free energy at a particular temperature, it is necessary to determine the enthalpy and the entropy at that particular temperature. Both properties can be determined from the knowledge of specific heat at constant pressure, C_P. The specific heat or specific heat capacity C_P (J/mole K) is defined as the amount of heat required to increase the temperature of a system by one Kelvin under constant pressure.

The absorption or release of heat, *dq,* in a reversible process, at constant pressure from the system to the surrounding area is equal to the enthalpy change, *dH,* of the system. We can write

$$dq = dH \tag{1.48}$$

Further, from the definition of C_p, the equation can be written

$$C_p = \frac{dq}{dT} \tag{1.49}$$

From Eqs. 1.48 and 1.49, follows

$$dH = C_p dT \tag{1.50}$$

By integrating Eq. 1.50, it can be expressed as

$$\begin{aligned} \int_o^H dH &= \int_o^T C_P dT \\ H_T &= H_o + \int_o^T C_P dT \end{aligned} \tag{1.51}$$

where H_T and H_o are enthalpy at temperature T and 0 K, respectively.

The enthalpy at room temperature 298 K is often known, and Eq. 1.51 can be written as

$$H_T = H_{298} + \int_{298}^{T} C_P dT \tag{1.52}$$

Further, from the definition of entropy for a reversible process, we know

$$dS = \frac{dq}{T} = \frac{C_P dT}{T} \tag{1.53}$$

By integrating Eq. 1.53, we get

$$S_T = S_o + \int_{o}^{T} \frac{C_P}{T} dT = \int_{o}^{T} \frac{C_p}{T} dT \tag{1.54}$$

where S_o is the entropy at 0 K. However at 0 K, the entropy of a defect-free pure element is, by definition, zero (according to the third law of thermodynamics). Moreover, if the entropy at 298 K is known, then Eq. 1.54 can be written as

$$S_T = S_{298} + \int_{298}^{T} \frac{C_P}{T} dT \tag{1.55}$$

Note We have considered above a pure element with a defect-free structure. However, it is to be emphasized that it is impossible to obtain a defect-free structure at temperatures above 0 K. There will always be a certain amount of point defects, such as vacancies and impurities present in the structure under the equilibrium condition. The free energy of a phase including the contribution from defects can be expressed as

$$G_m = G + \Delta G_d$$

G_m is the free energy of a single-component material with point defects; G is the free energy of the defect-free material, and ΔG_d is the free energy change because of the presence of defects. As will be shown later on, vacancies, for instance, are always present with a certain equilibrium concentration above 0 K. However, since the concentration of defects, in general, is small compared to the number of atoms, we can in many cases neglect the contribution from ΔG_d.

In general, the C_P values for different phases can be experimentally determined and are available in the literature. The way that C_P typically varies with temperature is shown in Fig. 1.5a. From the knowledge of C_P, it is possible to calculate H and S at a particular temperature T and consequently determine the variation of free energy G as a function of temperature. If there are phase transformations within the temperature range of interest, the enthalpies and entropies of the corresponding transformation must be added, at the appropriate T, and the integration must continue with the C_p value of the new phase, to obtain the correct H and S at the required temperature. The enthalpy of the formation of all pure elements under atmospheric pressure and with their most stable form at room temperature (298 K) has been defined to be zero at all temperatures. These are called the standard enthalpies of formation. And from these, the enthalpy change as a function of temperature can be determined as $H_T = \int_{298}^{T} C_P dT$. The typical change in enthalpy, entropy, and free energy is shown in Fig. 1.5b. There are a few important points that should be noted here. It is clear from Eq. 1.50 that the slope of the enthalpy curve dH/dT is equal to C_P. Since the value of C_P always increases with temperature, the slope of the enthalpy curve will also increase continuously with rising temperature. Further, from standard thermodynamic relation, we know that $dG = Vdp - SdT$. Since transformations at constant pressure are under consideration, we can write $dG = -SdT$. Hence, the slope of the free energy curve dG/dT is equal to $-S$. Since entropy always increases with temperature, the slope of the free energy, G, should always decrease with rising temperature.

Now, let us consider the stability of the solid and liquid phases of a metal. To do this, we will first need to determine the change in free energy with temperature for both solid and liquid phases separately. From Eqs. 1.17, 1.50, and 1.55, we can write the expressions for free energy for solid and liquid phases as

$$G^S = H_0^S + \int_0^T C_P^S dT - T\int_0^T \frac{C_P^S}{T} dT \tag{1.56a}$$

$$G^L = H_0^L + \int_0^T C_P^L dT - T\int_0^T \frac{C_P^L}{T} dT \tag{1.56b}$$

The superscripts "S" and "L" are denoted for solid and liquid phases, respectively. In general, the C_P of the liquid phase at a particular temperature is higher than that of the solid phase. The typical variation of C_P for solid and liquid phases is shown in Fig. 1.6a. The corresponding changes in enthalpy and free energy as a function of temperature of the phases are shown in Fig. 1.6b.

As already discussed, the pV term for both solid and liquid phases is very small and the enthalpy can be taken to be practically equal to E. Therefore, the Gibbs energy function can be written as $G = E - TS$, making the free energy low for a

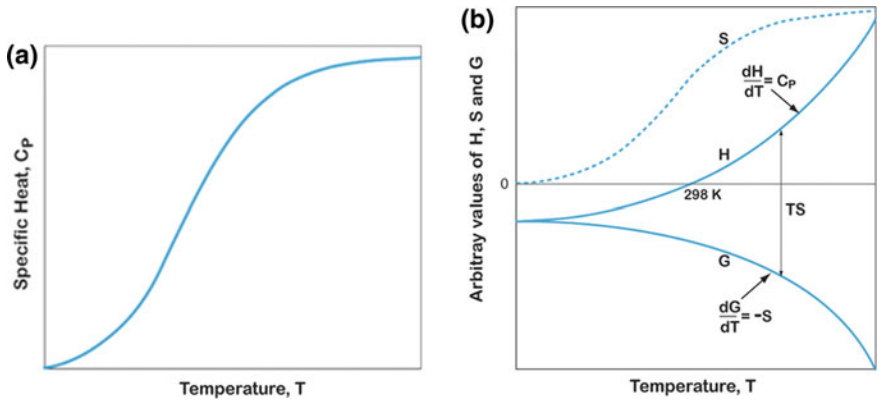

Fig. 1.5 **a** Typical change of C_P with temperature. **b** Arbitrary values of H, S, and G with temperature. Note that in many metals, the enthalpy is zero at room temperature, 298 K

phase with a low internal energy E and/or high entropy S. It is also apparent that at low temperature, the E term will dominate, whereas at higher temperature, the term becomes more and more significant. In general, the solid phases have higher bonding energies compared to those of liquid phases. So the internal energy, i.e., enthalpy, of the solid phase is lower than the liquid phase. Further, the entropies of liquids are typically larger than those of solids. Thus, at higher temperatures, the liquid phase becomes stable. From Fig. 1.6b, it can be seen, for instance, that below the melting point the solid phase is stable, whereas above the melting point the liquid phase is stable. At the melting point, their Gibbs energies are the same, as discussed in the beginning of this section.

Now, let us turn to consider solid-state transformation between gray tin to white tin. Gray tin has a diamond crystal structure which is very brittle. White tin, on the other hand, which is commercially available with a metallic luster has a BCT (body-centered tetragonal) structure. The Gibbs energy curves for both structures are shown in Fig. 1.7.

In Fig. 1.7, the molar Gibbs energy of the BCT-Sn has been set at zero for all temperatures. Thus, the BCT-Sn is the *reference state*. The Gibbs energies of different forms of Sn are then compared against this self-chosen reference value. As can be seen from Fig. 1.7, BCT-Sn should be stable between 13 and 232 °C. Below 13 °C, Sn with a diamond structure is the most stable form of tin, and above 232 °C, the liquid Sn is the most stable form of tin. It is to be noted that even though the transition temperature between the diamond and body-centered tetragonal structures is 13 °C, in practice the transformation requires undercooling to about −30 °C. This is because at 13 °C, the two crystal structures are in equilibrium and their Gibbs energies are the same. Thus, the driving force for the transformation is zero. As temperature decreases, the driving force for the transformation increases and the kinetics becomes slower. Thus, the optimum conditions for the transformation are found at −30 °C. This occurrence of the low

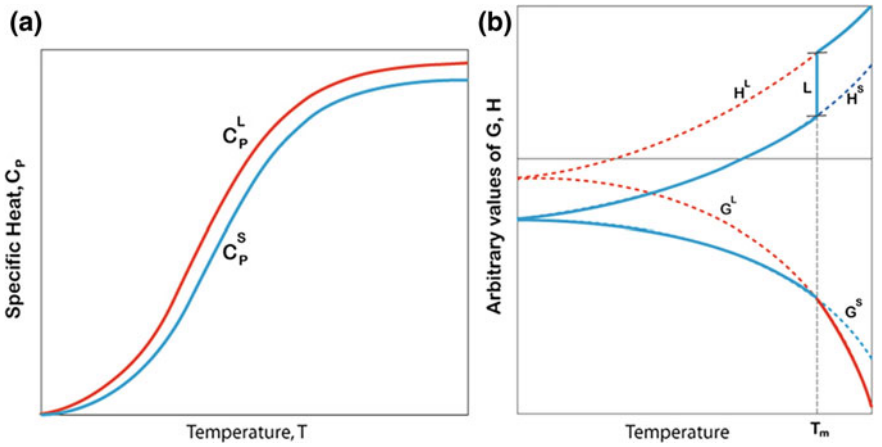

Fig. 1.6 **a** Arbitrary values of specific heat at constant pressure solid and liquid phase. **b** The change of enthalpy (H^S-enthalpy of solid phase, H^L-enthalpy of liquid phase) and free energy (G^S-free energy of solid phase, G^L-free energy of liquid phase) of solid and liquid phases with temperature. L is the latent heat of fusion. Solid line follows the change of enthalpy and free energy of the system with temperature

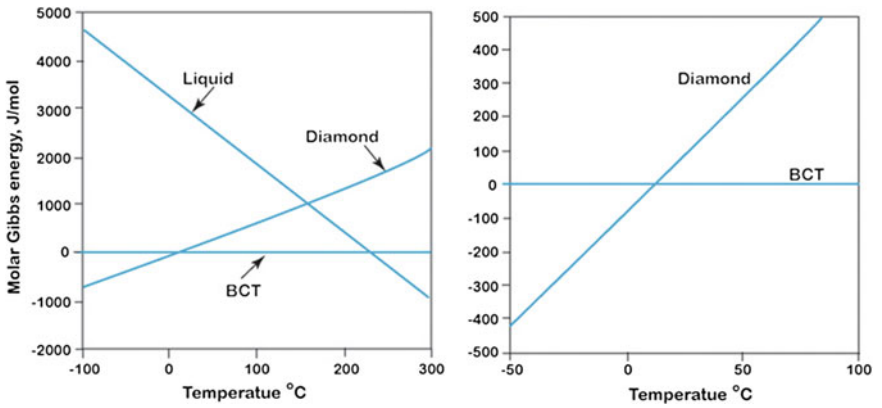

Fig. 1.7 The molar Gibbs energies of different phases of Sn as a function of temperature at 1 atm pressure. The figure on the right shows an enlarged part of the figure on the left

temperature diamond form of Sn should be avoided as it will lead to a phenomenon called tin pest. Owing to the much larger molar volume of Sn with the diamond structure (in comparison with the smaller BCT-Sn), the transition fractures (or even pulverizes) the tin objects going through the transition. One can also determine the hypothetical melting point of the diamond Sn from the intersection point of the metastable part of the diamond Gibbs energy curve with that of the liquid phase. It turns out to be about 160 °C.

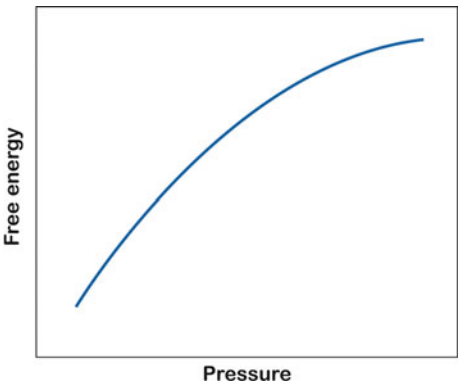

Fig. 1.8 The variation of molar Gibbs free energy g with increase in pressure

The increasing importance of the entropy term (−TS) is the reason why in many metals, we find the phase with a relatively closely packed structure is stable at a lower temperature, whereas a relatively loosely packed structure is stable at higher temperature. The reason for this lies in a more loosely packed structure where there is a higher degree of vibrational freedom. For instance, α-Ti with an HCP structure is stable at low temperature, whereas β-Ti with a BCC structure is stable at high temperature.

1.7 Pressure Effect of Single-Component Phase Diagram

Until now, as mentioned earlier, it has been assumed that all transformations occur under constant, typically atmospheric, pressure. If we consider the Gibbs free energy at constant temperature but under different pressure, for example, at higher pressure, then the freedom for vibration of atoms will be decreased in comparison with the normal pressure. This will result in an increase in free energy, as shown in Fig. 1.8. We know from the standard thermodynamic relation $dG = Vdp - SdT$ that the slope of the free energy versus pressure curve is equal to volume *V,* at constant temperature. Since the volume of matter generally decreases with increasing pressure, the slope of the free energy versus pressure curve will be positive, but it will decrease continuously with increasing pressure. Consequently, the equilibrium transition temperature from one phase to another will be different under different pressures and depending on the conditions, the transition temperature with increasing pressure might increase or decrease. This can be understood as being based on the Clausius–Clapeyron relation, which can be derived by considering the equilibrium transition temperature between the α- and γ-phases in an iron system. By using a standard thermodynamic relation, it is possible to write for the molar Gibbs energy

$$dg^{\alpha} = v_m^{\alpha} dP - s^{\alpha} dT \tag{1.57a}$$

$$dg^{\gamma} = v_m^{\gamma} dP - s^{\gamma} dT \tag{1.57b}$$

Since the equilibrium transition between these two phases is under consideration at equilibrium temperature, one has $g^{\alpha} = g^{\gamma}$ and further, $dg^{\alpha} = dg^{\gamma}$. By equating Eqs. 1.57a and 1.57b, the following is obtained

$$\left(\frac{\partial P}{\partial T}\right)_{eq} = \frac{s^{\gamma} - s^{\alpha}}{v_m^{\gamma} - v_m^{\alpha}} = \frac{\Delta s}{\Delta v_m} \tag{1.58}$$

From Eqs. 1.17, we can write

$$g^{\gamma} = h^{\gamma} - Ts^{\gamma} \tag{1.59a}$$

$$g^{\alpha} = h^{\alpha} - Ts^{\alpha} \tag{1.59b}$$

From Eqs. 1.59a and 1.59b and from the consideration of equilibrium transition, we can write

$$\Delta g = g^{\gamma} - g^{\alpha} = 0 = (h^{\gamma} - h^{\alpha}) - T(s^{\gamma} - s^{\alpha}) = \Delta h - T\Delta s \tag{1.60}$$

Further, we can write at the transition temperature (T_{tr})

$$\Delta s = \frac{\Delta h}{T} \tag{1.61}$$

By introducing Eq. 1.61 in Eq. 1.60, we arrive at the following

$$\left(\frac{dP}{dT}\right) = \frac{\Delta h}{T\Delta v_m} \tag{1.62}$$

Equation 1.62 is the Clausius–Clapeyron equation, which can be used to calculate, for example, the TM curve shown in Fig. 1.1. We know that the α-phase has a BCC structure and the γ-phase has an FCC structure. Since FCC is a more closely packed structure, we can write for the transition $\alpha \rightarrow \gamma$, $\Delta v = v_m^{\gamma} - v_m^{\alpha} < 0$. On the other hand, we have seen previously that the enthalpy of a phase which is stable at higher temperature is higher (less negative) than that of a phase which is stable at lower temperature. This becomes $\Delta h = h^{\gamma} - h^{\alpha} > 0$. From Eq. 1.63, it follows that $\left(\frac{dP}{dT}\right)_{\mathrm{eq}} < 0$ for the equilibrium transformation from the α-phase to the γ-phase. This is the reason why the equilibrium transition temperature decreases with increasing pressure. Let us consider the case of the equilibrium transition between the γ- to δ-phase. Since the γ-phase has an FCC structure, whereas the δ-phase has a BCC structure, it is possible to write for the transition $\gamma \rightarrow \delta$ $\Delta v = v_m^{\delta} - v_m^{\gamma} > 0$.

Further, from our previous explanation, we can write $\Delta h = h^{\delta} - h^{\gamma} > 0$. So $\left(\frac{dP}{dT}\right)_{\text{eq}} > 0$ for this transition and equilibrium transition temperature increases with increasing pressure.

1.8 Free Energy and Stability of Phases in a Binary System

In the previous sections, we have considered mainly single-component systems (i.e., pure elements). It is common knowledge that most materials in nature consist of several phases and that these phases themselves are never pure elements. In fact, based on the second law of thermodynamics, a pure substance exists only in our minds and represents a limiting state, which we may asymptotically approach but never actually obtain. Thus, the thermodynamic description of multicomponent systems is of great importance from the theoretical as well as from the practical point of view. In the treatment of multicomponent open systems, the most common process considered in defining the thermodynamic functions for a solution is called the mixing process, which Guggenheim defines as [2]:

> The mixing process is the change in state experienced by the system when appropriate amounts of the 'pure' components in their reference states are mixed together forming a homogeneous solution brought to the same temperature and pressure as the initial state.

It is to be noted that although the mixing process is strongly influenced by interaction forces between atoms and molecules (i.e., Δh), the fundamental cause behind mixing is the entropy (Δs) change of the system.

For our analysis, we shall consider a system with a total of one mole of atoms, where X_{A} is the mole fraction of element A and X_{B} is the mole fraction of element B. This translates into

$$X_{\text{A}} + X_{\text{B}} = 1 \tag{1.63}$$

We define the free energies of pure elements A as G_{A} and that of B as G_{B} at a particular temperature. The total molar free energy g_0 of a *purely mechanical mixture* can be written as

$$g_0 = X_{\text{A}} g_{\text{A}} + X_{\text{B}} g_{\text{B}} \tag{1.64}$$

Now, if we allow interdiffusion to taken place between the elements A and B, there will be change in the free energy because of mixing, g_{mix}. Consequently, the total free energy of the system after mixing can be written as

$$g = g_0 + \Delta g_{\text{mix}} \tag{1.65}$$

From Eqs. 1.17 and 1.65, we find the expression for the free energy change because of mixing as

$$\begin{aligned} \Delta G_{\text{mix}} &= g - g_0 = h - Ts - h_0 + Ts_0 = (h - h_0) - T(s - s_0) \\ \Delta g_{\text{mix}} &= \Delta h_{\text{mix}} - T\Delta s_{\text{mix}} \end{aligned} \tag{1.66}$$

where h_o and h are the total enthalpy of the system before and after mixing. The values s_o and s are the entropies of the system before and after mixing. The value $\Delta h_{\text{mix}} = (h - h_0)$ is the change in enthalpy, and $\Delta s_{\text{mix}} = (s - s_0)$ is the change in entropy due to mixing. The enthalpy of mixing can be zero, negative, or positive depending on the system; the entropy of mixing, on the other hand, is always positive. We shall first briefly discuss the mixing process in general and then look a little closer at where the different terms in Eq. 1.66 arise.

1.8.1 Change in Free Energy in an Ideal System

Note that in the case of an ideal solution, $\Delta h_{\text{mix}} = 0$ and the free energy of the system can be written as

$$g = g_0 + \Delta g_{\text{mix}} = g_0 - T\Delta s_{\text{mix}} \tag{1.67}$$

The change in free energy with composition is shown in Fig. 1.9a at one particular temperature T. The straight dotted line represents the total free energy $(g_0 = X_{\text{A}} g_{\text{A}} + X_{\text{B}} g_{\text{B}})$ of the elements A and B before any mixing (i.e., a purely mechanical mixture of A and B). The solid curved line represents the free energy of the system after mixing $(g = g_0 - T\Delta s_{\text{mix}})$. Further, the change in free energy with composition at higher temperature, T_1, is shown in Fig. 1.9b. The change in free energy caused by mixing in an ideal solution $\Delta g_{\text{mix}} = -T\Delta s_{\text{mix}}$ is naturally larger at the higher temperature.

Entropy of mixing (Δs_{mix})

The entropy of mixing originates from two different contributions, thermal and configurational. If we consider that there are no volume and enthalpy changes caused by mixing, then the only contribution to the entropy will configurational. Configurational entropy comes from the possibility of arranging the atoms A and B in different ways for a particular macrostate. Following statistical thermodynamics, the configurational entropy can be expressed as

$$S = k \ln w \tag{1.68}$$

where w is a thermodynamic probability, a kind of measure of randomness. This means that the molar entropy of mixing can be written as

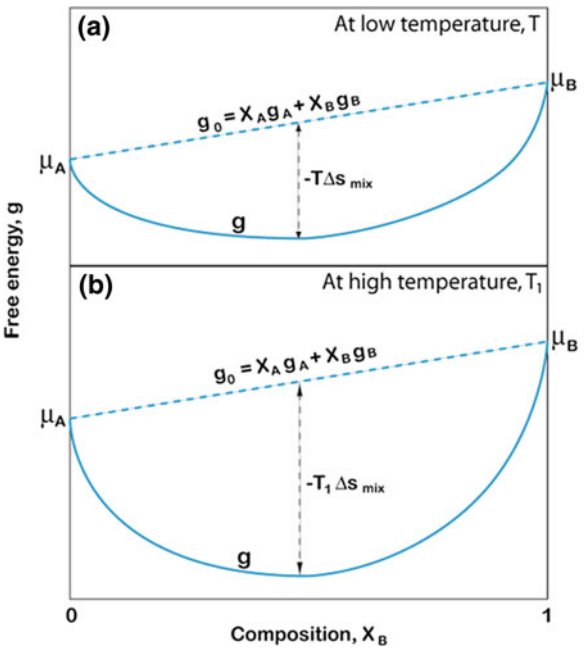

Fig. 1.9 Free energy versus composition diagram in an ideal case at **a** low temperature, T, and **b** high temperature, T_1

$$\Delta s_{\text{mix}} = s - s_0 = k \ln w - k \ln 1 = k \ln w \tag{1.69}$$

where, as explained before, s_0 is the entropy before mixing and s is the entropy after mixing. Since in the case of a pure element, there is only one way by which atoms can be arranged (if vacancies are neglected), we can write $w = 1$. If we consider the random solid solution, then the number of different ways by which atoms A and B can be arranged is

$$w = \frac{(n_{\text{A}} + n_{\text{B}})!}{n_{\text{A}}! n_{\text{B}}!} \tag{1.70}$$

where n_{A} and n_{B} are the total number of atoms of A and B, respectively.

According to Stirling's approximation,

$$\ln N! = N \ln N - N \tag{1.71}$$

Following Stirling's approximation, Eq. 1.69 can be written as

$$\begin{aligned} \Delta S_{\text{mix}} &= k \ln w \\ &= [(n_{\text{A}} + n_{\text{B}}) \ln(n_{\text{A}} + n_{\text{B}}) - (n_{\text{A}} + n_{\text{B}})] - [n_{\text{A}} \ln n_{\text{A}} - n_{\text{A}}] - [n_{\text{B}} \ln n_{\text{B}} - n_{\text{B}}] \end{aligned} \tag{1.72}$$

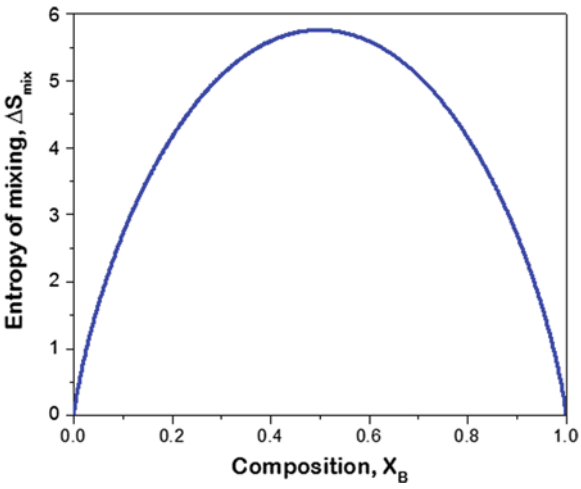

Fig. 1.10 The change in entropy of mixing with the change in composition

From the definition of the mole fraction, we can write

$$n_A = X_A N_0; \quad n_B = X_B N_0; \quad X_A + X_B = 1 \tag{1.73}$$

Substituting Eq. 1.73 in Eq. 1.72, we get

$$\begin{aligned} \Delta s_{mix} &= -kN_0[X_A \ln X_A + X_B \ln X_B] \\ &= -R[X_A \ln X_A + X_B \ln X_B] \end{aligned} \tag{1.74}$$

It is, therefore, clearly apparent from Eq. 1.74 that the entropy of mixing is always positive and will vary, as shown in Fig. 1.10. It can also be seen that the entropy of mixing reaches its maximum at $X_B = 0.5$. To find the slope at different compositions, we can differentiate Eq. 1.74 (note that $X_A + X_B = 1$).

$$\begin{aligned} \frac{d\Delta s_{mix}}{dX_B} &= -R\left[-\ln(1-X_B) - (1-X_B)\frac{1}{(1-X_B)} + \ln X_B + X_B \frac{1}{X_B}\right] \\ &= -R \ln \frac{X_B}{(1-X_B)} \end{aligned} \tag{1.75}$$

So the slope at $X_B = 0.5$ is equal to zero, whereas the slope at $X_B = 0$ or 1 is infinity. Thus, it is evident from the above discussion why a pure substance is just a limit which we can approach but never achieve—as stated at the beginning of this section. As the slope goes to infinity at $X_B = 0$, it states that in order to remove the last B impurity from A, an infinite amount of energy must be used.

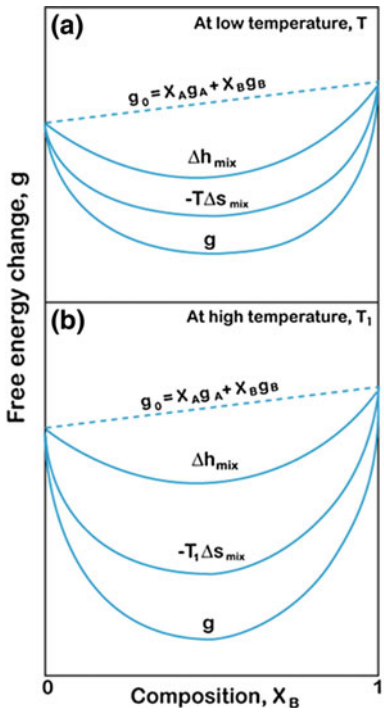

Fig. 1.11 Free energy versus composition diagram for a system with exothermic transformation at **a** low temperature, T, and **b** high temperature, T_1

1.8.2 Change in Free Energy in a System with Exothermic Transformation

As discussed above, the enthalpy of mixing in an exothermic transformation is negative. The free energy of mixing for such a case at different compositions at a particular temperature T is shown in Fig. 1.11a. The free energy curves at higher temperature T_1 are shown in Fig. 1.11b. At higher temperature, the $T\Delta s_{\text{mix}}$ term will be higher, making Δg_{mix} higher after mixing. In consequence, the total free energy of the system will change far more drastically with composition compared to at lower temperature.

1.8.3 Change in Free Energy in a System with Endothermic Transformation

In endothermic transformation, the enthalpy of mixing $\Delta h_{\text{mix}} > 0$. So, if the temperature under consideration is reasonably low, the negative contribution to the Gibbs energy of mixing from $T\Delta s_{\text{mix}}$ may be smaller than the positive contribution from the enthalpy of mixing Δh_{mix} within a certain composition range. In that case,

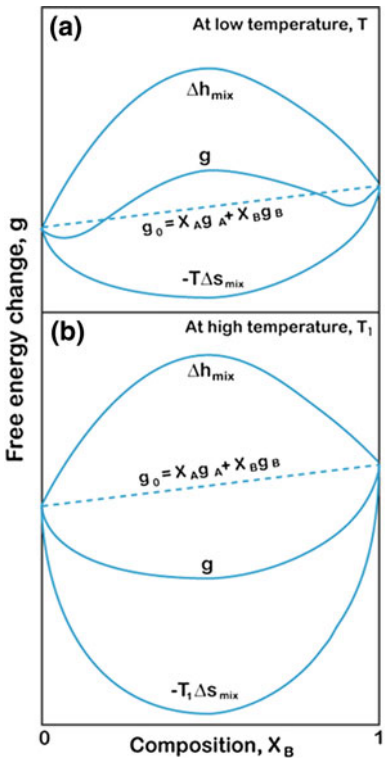

Fig. 1.12 Free energy versus composition diagram in a system with endothermic transformation at **a** low temperature, T, and **b** high temperature, T_1

the free energy of mixing will be positive at a certain composition range and the total free energy change can vary, for example, as shown in Fig. 1.12 resulting in a formation of a miscibility gap. However, at higher temperature, T_1 at all compositions Δh_{mix} will be smaller than $T\Delta s_{\text{mix}}$ and the free energy of mixing is always negative, as can be seen in Fig. 1.12b. The next section considers the origin of the enthalpy of mixing.

Note We have considered a very simplified model to establish the relation of free energy after mixing in a binary system. We have not considered the elastic strain that could play an important role. In some systems, where the size of the atoms is very similar, this factor can be disregarded. However, in some systems because of a large difference in atomic size, the elastic strain might play a significant role. Calculations, however, become extremely complicated if we are to consider the effect of elastic strain and so it is left outside the scope of this book. It must, nevertheless, be remembered that the elastic energy (as other forms of work) can be incorporated into the Gibbs free energy of the system.

1.9 Thermodynamics of Solutions and Phase Diagrams

In the following section, the thermodynamic background necessary for understanding the phase diagrams introduced briefly in Sect. 1.4 is discussed. After that the binary and ternary phase diagrams are discussed in greater detail.

1.9.1 The Chemical Potential and Activity in a Binary Solid Solution

For any heterogeneous system at equilibrium, the chemical potential of a component i has the same value in all phases of the system, where the component has accessibility. A general problem for dealing with solutions thermodynamically can be regarded as one of properly determining the chemical potentials of the components. Usually, the treatment utilizes the activity function introduced by Lewis and Randall [8]. The value of the treatment lies in its close relation to composition; with appropriate choice of reference state, the activity approaches the mole fraction as the mole fraction approaches unity. Most commonly in the thermodynamics of solutions, it is not the activity which is used, but rather the activity coefficient which is defined as the ratio of the activity a_i to the mole fraction X_i

$$\gamma_i = \frac{a_i}{X_i} \tag{1.76}$$

In terms of the chemical potential, the activity can be expressed

$$\mu_i^j - \mu_i^o = RT \ln a_i^j = RT \ln X_i^j + RT \ln \gamma_i^j \tag{1.77}$$

where μ_i^o is the chemical potential of pure i in the reference or standard state, μ_i^j the chemical potential of i in phase j, a_i^j the activity of component i in phase j, R the gas constant, T the temperature, and (i = A, B,…; $j = \alpha, \beta, \ldots$). In the limiting case of ideal solutions, where the enthalpy ($\Delta h = 0$) and volume change ($\Delta v = 0$) of mixing are zero and the only contribution to Gibbs free energy of mixing arises from the configurational entropy term

$$\Delta s_m = \sum_{i=\mathrm{A}} X_i \ln X_i \tag{1.78}$$

the activity coefficient in Eq. 1.77 is unity and the activity of the component equals its mole fraction (i.e., Raoultian behavior, see discussion below). If the equality is valid for all compositions, the solution is called perfect. Thus, the activity coefficient represents deviation of the real solutions from this limiting behavior. The use of activity coefficient instead of activity in Eq. 1.77 clearly indicates the

excess energy term $RT \ln \mu_i^j$ to be responsible for the non-ideal behavior. This issue is addressed in more detail in the next section.

As only relative values of thermodynamic functions can be determined, an agreed reference state has to be established for each element or species in order to make thermodynamic treatment quantitative (see Fig. 1.7 and related discussion). In principle, the choice of the reference state is arbitrary as long as the chosen state is used consequently throughout the analysis. The chosen state is then defined to be zero and all other possible states of the element are compared against the reference state to obtain their relative stabilities. It should be noted that there are some uncertainties related to the usage of reference states in the literature.

1.9.2 Free Energy of Solutions

In Sect. 1.9, we briefly discussed the so-called mixing process as well as the binary solution phases. In the beginning of this section, we also introduced the concept of activity, which describes the deviation of the behavior of a solution from ideal behavior. A statistical approach can be used to provide more insight into the properties of the phases. The simplest model is one in which the total energy of the solution is given by a summation of interactions between the nearest neighbor atoms. If we have a binary system with two types of atoms (A and B), there will be three interaction energy terms. These are the energy of the A–A pairs, that of the B–B pairs, and that of the A–B pairs. Here, we assume that the total energy of the solution arises from the interactions between the nearest neighbors. The binding energy may be defined by considering that the change in energy as the distance between a pair of atoms is decreased from infinity to an equilibrium separation. The change in energy during this process is the binding energy, which for a pair of A atoms is given as $-2\varepsilon_{\mathrm{AA}}$, for B atoms as $-2\varepsilon_{\mathrm{BB}}$, and so forth. Thus, the bond energies are negative quantities.

The simplest model for real solution phases based on the above-defined nearest neighbor interaction approach is the so-called regular solution model. It is based on the following assumptions: (i) Mixing among accessible lattice spaces is completely random $p_i = \frac{N_i}{N} = X_i$, (ii) atoms interact only with their nearest neighbors, (iii) the bond energy between dissimilar atoms ε_{ij} is independent of composition and temperature, and (iv) there is no change in volume upon mixing.

Let us examine a solution which is formed by two metals (A and B) with an identical crystal structure. Let us further assume that the system as defined above is in equilibrium with its surroundings. We will presume that metal A has N_{A} atoms and metal B has N_{B} atoms and that $\varepsilon_{\mathrm{AA}}$ and $\varepsilon_{\mathrm{BB}}$ are the bond energies of the AA and BB atom pairs according to the assumptions (ii) and (iii). Then, the configuration energies of pure metals, with the coordination number z, are $E_{\mathrm{A}}^0 = zN_{\mathrm{A}}^0\varepsilon_{\mathrm{AA}}/2$ and $E_{\mathrm{B}}^0 = zN_{\mathrm{B}}^0\varepsilon_{\mathrm{BB}}/2$, when the atoms are at rest at their equilibrium lattice points. The number two in the nominator in the above equations is

introduced in order to prevent calculating the A–A and B–B interactions twice. The formation of the solution phase starts by removing one atom from each metal and transferring them to an infinite distance from the metal (and each other). The work associated with this process is $-z(\varepsilon_{AA} + \varepsilon_{BB})$. By returning an atom A to metal B and an atom B to metal A, the pure metals are transformed into solutions with infinite dilution. The total number of A–B bonds with bond energy ε_{AB} in these solutions is $2z$. The energy associated with this mixing process (per interchange) can be described as

$$dE = 2z\left[\varepsilon_{AB} - \frac{1}{2}(\varepsilon_{AA} + \varepsilon_{BB})\right] = -2zI_{AB} \tag{1.79}$$

where I_{AB} (per bond) is the interchange energy.

As the energy change associated with the formation of a mixture with a number of N_{AB} bonds is $\Delta E = N_{AB}I_{AB}$, the internal energy of the solution phase is

$$E = \left(\frac{z}{2}\right)N_A(\varepsilon_{AA}) + \left(\frac{z}{2}\right)N_B(\varepsilon_{BB}) + N_{AB}I_{AB} \tag{1.80}$$

The next step is to identify what the most probable number of AB bonds (N_{AB}) is with the nominal composition of X_B^o. This problem can be resolved by utilizing the first assumption of the regular solution model, i.e., that the mixing among the lattice sites is completely random. This means that the probability that an atom A is in position 1 equals $p_{A(1)} = (N_A/N)$ and that atom B is in position 2 equals $p_{B(2)} = (N_B/N)$. However, since $p_{A(1)}p_{B(2)} = (N_A N_B/N^2)$ and because $p_{A(1)}p_{B(2)} = p_{A(2)}p_{B(1)}$, we get

$$p_{AB}^{(1,2)} = \frac{2N_A N_B}{N^2} \tag{1.81}$$

In the solution phase, we have total of $0.5zN$ adjacent lattice site pairs and therefore,

$$\bar{p}_{AB} = p_{AB}^{(1,2)} = \frac{2N_A N_B}{N^2}\left(\frac{zN}{2}\right) = z\left(\frac{N_A N_B}{N_A + N_B}\right) \tag{1.82}$$

Thus, the internal energy of the solution phase can be written as

$$E = \left(\frac{z}{2}\right)N_A(\varepsilon_{AA}) + \left(\frac{z}{2}\right)N_B(\varepsilon_{BB}) + z\left(\frac{N_A N_B}{N_A + N_B}\right)I_{AB} \tag{1.83}$$

By assuming that the chemical potentials of pure metals A and B can be approximated as $\mu_A^0 \cong \frac{1}{2}Z(\varepsilon_{AA})$ and $\mu_B^0 \cong \frac{1}{2}Z(\varepsilon_{BB})$ and utilizing the definition of the chemical potential, the Gibbs energy of the regular solution phase becomes

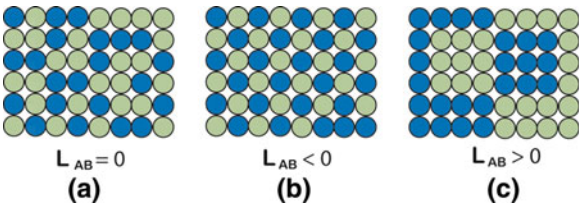

Fig. 1.13 Schematic presentation of the effect of the sign of the enthalpy of mixing and that of the interaction parameter on the formation of a solution phase

$$G = N_A\mu_A^o + N_B\mu_B^o + kT\sum_i N_i \ln\left(\frac{N_i}{N_A + N_B}\right) + z\left(\frac{N_A N_B}{N_A + N_B}\right)I_{AB} \tag{1.84}$$

from which the molar Gibbs energy is obtained as

$$g = X_A^o\mu_A + X_B^o\mu_B + RT\sum_i X_i \ln X_i + L_{AB}X_A X_B \tag{1.85}$$

where L_{AB} ($=zNI_{AB}$) is the molar interaction energy, i.e., the *interaction parameter*.

The relationship between activity and the interaction parameter can be written as

$$a_i = \gamma_i X_i = X_i \exp\left[\frac{L_{ij}(1 - X_i)^2}{RT}\right] \tag{1.86}$$

Consequently, the sign of the interaction parameter determines whether the formation of mixture is favored or hindered. When $|\varepsilon_{AA} + \varepsilon_{BB}| < |2\varepsilon_{AB}|$ and the interaction parameter is negative (remember that the bonding energies are negative), the solution will have a larger than random probability of bonds between unlike atoms, and thus, mixing or compound formation is favored, as in Fig. 1.13. The converse is true when the interaction parameter is positive ($|\varepsilon_{AA} + \varepsilon_{BB}| > |2\varepsilon_{AB}|$) since atoms then prefer to be neighbors to their own kind and form clusters. From Eq. 1.86, it is also seen how the activity coefficient depends on both the sign and magnitude of the interaction parameter. Activity is eventually determined by the interactions between different types of atoms in the solution phase. It is also helpful to notice that the excess term in Eq. 1.86 $L_{AB}X_A X_B$ can be identified with the enthalpy of mixing in Eq. 1.66.

Justification of Eq. 1.86
Deviations from ideal behavior are commonly expressed in the form of excess functions. The excess Gibbs energy of mixing can be expressed as $\Delta g_{mix}^{xs} = \Delta h_{mix}^{xs} - T\Delta s_{mix}^{xs}$. This is the extra energy of mixing resulting from the formation of a real instead of an ideal solution. In a regular solution model, the entropy of mixing is defined to be the same as that of an ideal solution.

Thus, the excess entropy of mixing $\Delta s^{xs}_{\text{mix}}$ is zero and $\Delta g^{xs}_{\text{mix}} = \Delta h^{xs}_{\text{mix}}$ in the case of regular solutions. Therefore, the expression $L_{\text{AB}}X_{\text{A}}X_{\text{B}}$ in Eq. 1.86 can be equated to the excess enthalpy of mixing. It is to be noted that the expression $L_{\text{AB}}X_{\text{A}}X_{\text{B}}$ is also the simplest possible expression for the excess energy of mixing, as it is required that the excess energy of mixing goes to zero when $X_{\text{A}} = 0$ or $X_{\text{A}} = 1$. There is a standard relation between the partial molar properties of a component and the total properties of a phase that can be expressed for the excess enthalpy of mixing and the partial excess enthalpy of the mixing of component B as

$$\Delta h^{xs}_{\text{B,mix}} = \Delta h^{xs}_{\text{mix}} + X_{\text{A}} \frac{d\Delta h^{xs}_{\text{mix}}}{dX_{\text{B}}}$$

We have the above-defined $\Delta h^{xs}_{\text{mix}} = L_{\text{AB}}X_{\text{A}}X_{\text{B}} = L_{\text{AB}}(1 - X_{\text{B}})X_{\text{B}} = L_{\text{AB}}(X_{\text{B}} - X_{\text{B}}^2)$
Thus,

$$\frac{d\Delta h^{xs}_{\text{mix}}}{dX_{\text{B}}} = L_{\text{AB}}(1 - 2X_{\text{B}})$$

and we obtain

$$\begin{aligned}\Delta h^{xs}_{\text{B,mix}} &= L_{\text{AB}}X_{\text{A}}X_{\text{B}} + X_{\text{A}}L_{\text{AB}}(1 - 2X_{\text{B}}) \\ &= X_{\text{A}}L_{\text{AB}}(X_{\text{B}} + 1 - 2X_{\text{B}}) = X_{\text{A}}L_{\text{AB}}(1 - X_{\text{B}}) = L_{\text{AB}}X_{\text{A}}^2\end{aligned}$$

The excess enthalpy of the mixing of component B can also be equated (in the case of regular solution model) to $RT \ln \gamma_{\text{B}}$ as discussed above.
Thus, we can write as follows:

$$\begin{aligned}RT \ln \gamma_{\text{B}} &= L_{\text{AB}}X_{\text{A}}^2 \\ \gamma_{\text{B}} &= \exp\left[\frac{L_{\text{AB}}(1 - X_{\text{B}})^2}{RT}\right]\end{aligned}$$

As $a_{\text{B}} = X_{\text{B}}\gamma_{\text{B}}$, we finally obtain

$$a_{\text{B}} = X_{\text{B}}\gamma_{\text{B}} = X_{\text{B}} \exp\left[\frac{L_{\text{AB}}(1 - X_{\text{B}})^2}{RT}\right]$$

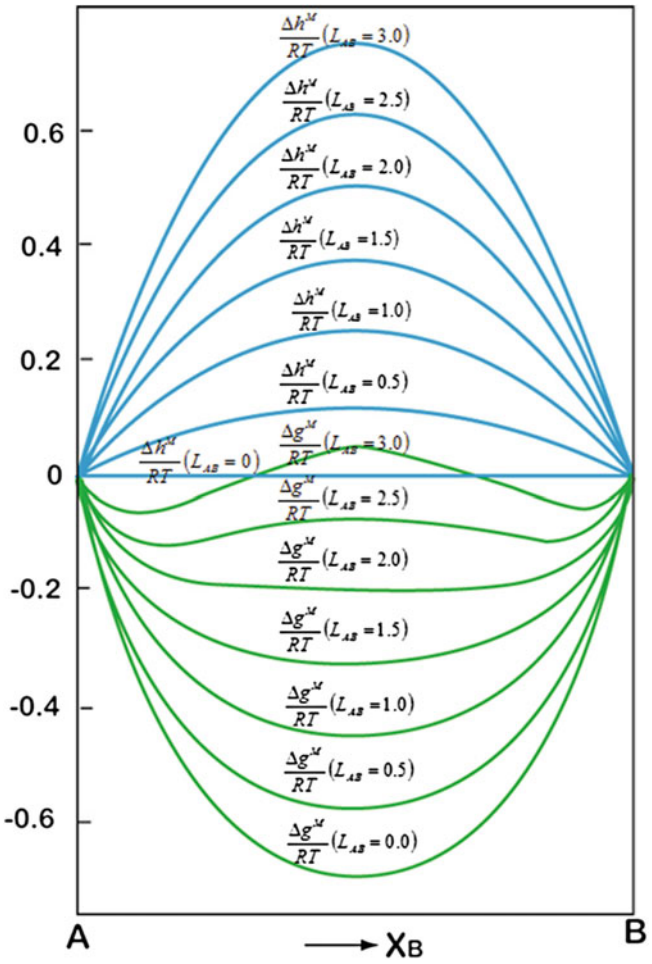

Fig. 1.14 The effect of interaction parameter on the stability of a solution phase [9]

In Fig. 1.14, the effect of the sign and magnitude of the interaction parameter on the formation of a solution phase is shown [9]. When there is no preferred interaction between the atoms in the system, the interaction parameter $L_{AB} = 0$ ($\varepsilon_{AA} + \varepsilon_{BB} = 2\varepsilon_{AB}$), the integral heat of mixing is zero, and the free energy of mixing is given by curve I. As the interaction parameter is made more positive, it can be seen how the enthalpy of mixing becomes more positive and the free energy of mixing becomes less negative. When a certain magnitude of positive interaction is reached, it can be seen that the system is about to enter the state where the solution phase becomes unstable. When L_{AB} is increased to even more positive values, one can see how the Gibbs energy curve changes its sign of curvature at the middle region and the so-called miscibility gap is formed. This is associated with the formation of two separate phase regions—one rich in A and another rich in B.

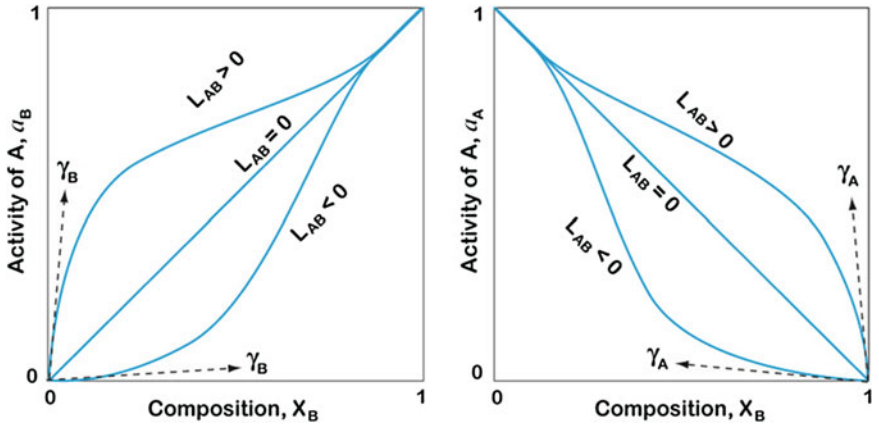

Fig. 1.15 Raoult's and Henry's laws in a binary solution

It was shown that one may find a situation where the interaction parameter is zero and there is no net interaction between A and B (i.e., $\varepsilon_{AA} + \varepsilon_{BB} = 2\varepsilon_{AB}$). This type of behavior is associated with the above-defined ideal systems and is described by Raoult's law. The Raoultian solution was shown above to be the one where the activity coefficient (Eq. 1.76) is unity and the activity of the component equals its mole fraction. Such behavior is shown in Fig. 1.15. If Raoult's law is obeyed by the solution phase through the whole composition range, the solution is called perfect. This type of solution does not exist in reality, but it does provide a convenient reference state to which the behavior of real solutions can be compared. In Fig. 1.15, another limiting law (Henry's law) is also shown. This limiting law can be understood by utilizing the regular solution model and Eq. 1.86. When one approaches the limit where $X_i \to 0$, i.e., the solution becomes dilute, it can be seen from Eq. 1.87 that the activity coefficient becomes concentration independent as

$$^{\infty}\gamma_i = \exp\left[\frac{L_{ij}}{RT}\right] \tag{1.87}$$

This defines the Henry's law line seen in Fig. 1.15. The limiting laws shown in Fig. 1.15 provide the reference states to which real solutions can be compared. As we approach pure substance ($X_i \to 1$), the solution behavior necessarily approaches Raoultian behavior no matter how "non-ideally" it otherwise behaves. This is true also for Henry's law, as all solutions approach it as the solution becomes dilute enough. It is also to be noted that if the solute follows Henry's law, then the solvent necessarily follows Raoult's law. Furthermore, whereas perfect solutions do not exist, ideal solution behavior is commonly encountered in practice within restricted composition limits.

Historically, activity measurements have been carried out mainly by measuring the changes in the partial pressure of a given substance upon alloying with respect to the values of the pure component. As this type of approach also gives an easily accessible alternative route to derive the above-defined limiting laws, we shall briefly consider Raoult's and Henry's laws from this point of view. Consider a pure liquid A in a closed vessel (initially evacuated) at temperature T. It will spontaneously evaporate until the pressure in the vessel is equal to the saturated vapor pressure of liquid A (p^o_{A}) at temperature T. At this point, the rate of evaporation $r_{\mathrm{e(A)}}$ and the rate of condensation $r_{c(\mathrm{A})}$ are equal. In order for an atom to escape the surface of the liquid and enter the gas phase, it must overcome the attractive forces exerted on it by its neighbors (i.e., overcome the activation energy E^* barrier). The magnitude of E^* determines the intrinsic evaporation rate. The condensation rate is proportional to the number of A atoms in the vapor phase, which strike (and stick) the liquid surface in unit time. For a fixed temperature, the condensation rate is proportional to the pressure of the vapor $r_{c(\mathrm{A})} = kp^o_{\mathrm{A}}$ which is equal to $r_{e(\mathrm{A})}$ at equilibrium. A similar situation holds for a liquid B. If we now add a small amount of liquid B to liquid A, what happens? If the mole fraction of A in the resulting binary mixture is X_{A} and assuming that the atomic diameters of A and B are comparable and there is no surface excess, the fraction of the surface area occupied by A atoms is X_{A}. It is a natural assumption that atom A can evaporate only from a site where it is present and, therefore, $r_{e(\mathrm{A})}$ is decreased by a factor of X_{A} and the equilibrium pressure exerted by A is decreased from p^o_{A} to p_{A}

$$r_{e(\mathrm{A})}X_{\mathrm{A}} = kp_{\mathrm{A}} \tag{1.88}$$

and by utilizing the above-defined equality between evaporation rate and equilibrium pressure, we obtain

$$p_{\mathrm{A}} = X_{\mathrm{A}}p^o_{\mathrm{A}} \tag{1.89}$$

which is Raoult's law. A similar equation holds for component B. The law states that the vapor pressure exerted by a component i in a solution is equal to the product of the mole fraction of i in the solution and the vapor pressure of i at the temperature of the solution.

While deriving Raoult's law, it was assumed that there is no change in the intrinsic evaporation rates. This requires that the magnitudes of the A–A, B–B, and A–B interactions are balanced so that the depth of the potential energy well of an atom at the surface site is independent of the types of atoms surrounding it (see discussion below). If we take that the A–B interaction is much stronger than that between identical atoms and consider a solution of A in B which is sufficiently dilute in such a way that every A atom is surrounded only by B atoms, in this case, the activation energy for an A atom to evaporate from the surface is higher than without B and thus, the intrinsic evaporation rate will be smaller ($r'_{e(\mathrm{A})} < r_{e(\mathrm{A})}$) and equilibrium occurs when

$$r'_{e(\mathrm{A})} X_{\mathrm{A}} = k p_{\mathrm{A}} \tag{1.90}$$

which results in

$$p_{\mathrm{A}} = \frac{r'_{e(\mathrm{A})}}{r_{e(\mathrm{A})}} X_{\mathrm{A}} p^{o}_{\mathrm{A}} \tag{1.91}$$

and as $\left(r'_{e(\mathrm{A})} < r_{e(\mathrm{A})}\right)$, p_{A} is a smaller quantity than that in Eqs. 1.88, 1.91 can be written as

$$p_{\mathrm{A}} = k'_{\mathrm{A}} X_{\mathrm{A}} \tag{1.92}$$

If the X_{A} of the solution is increased, it becomes more probable that not all of the A atoms at the surface are surrounded only by the B atoms. This will have an effect on the activation energy (depth of the potential energy well), and thus, after a certain critical value of X_{A}, the intrinsic evaporation rate becomes composition dependent and Eq. 1.93 no longer holds. Equation 1.93 is, of course, Henry's law (a similar equation holds for B atoms also). Note also that Raoultian and Henrian activity coefficients have different reference states. More information about the use of these standard states as well as changing between them can be found, for example, from Refs. [10, 11].

1.10 Lever Rule and the Common Tangent Construction

When two materials, especially metals, are mixed together, they either form a homogeneous solution or separate into a mixture of phases, as already discussed. Let us consider an alloy X in Fig. 1.16 in the binary system A–B to separate into a mixture of two phases α and β (under a particular temperature and pressure).

We shall assume that there are N atoms of alloy X and that the fraction of atoms in the α-phase is $(1-x)$ and in the β-phase is x. The number of B atoms in alloy X is n^{X}_{B}, the number of B atoms in the α-phase is n^{α}_{B}, and the number of B atoms in the β-phase is n^{β}_{B}. We can change these to atomic fractions by dividing by the total number of atoms N to get

$$\begin{aligned} X_{\mathrm{B}} &= \frac{n^{x}_{\mathrm{B}}}{N} \\ X^{\alpha}_{\mathrm{B}} &= \frac{n^{\alpha}_{\mathrm{B}}}{N(1-x)} \\ X^{\beta}_{\mathrm{B}} &= \frac{n^{\beta}_{\mathrm{B}}}{Nx} \end{aligned} \tag{1.93}$$

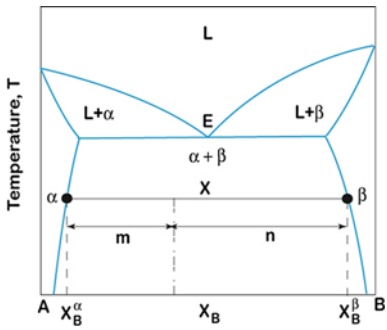

Fig. 1.16 The lever rule

Since $n_B^X = n_B^\alpha + n_B^\beta$, then

$$NX_B = NX_B^\alpha(1-x) + NX_B^\beta x \tag{1.94}$$

where

$$x = \frac{X_B - X_B^\alpha}{X_B^\beta - X_B^\alpha} = \frac{m}{m+n} \tag{1.95}$$

and

$$1 - x = \frac{X_B^\beta - X_B}{X_B^\beta - X_B^\alpha} = \frac{n}{m+n} \tag{1.96}$$

and

$$\frac{x}{1-x} = \frac{m}{n} \tag{1.97}$$

Equation 1.97 is called the lever rule, which enables us to calculate the relative amounts of phases in a phase mixture in terms of the alloy composition and the phases into which it separates. The free energy of a phase mixture can also be determined by using the lever rule. If alloy X separates into phases α and β, the free energy of an alloy will be unchanged by the separation. The free energy of alloy X is, therefore, equal to the sum of the free energies of the α- and β-phases. Since alloy X consists of an amount of the α-phase equal to $\left(\frac{X_B^\beta - X_B}{X_B^\beta - X_B^\alpha}\right)$ and similarly $\left(\frac{X_B - X_B^\alpha}{X_B^\beta - X_B^\alpha}\right)$ of the β-phase, the molar free energy of alloy X will be

$$g = a\left(\frac{X_B^\beta - X_B}{X_B^\beta - X_B^\alpha}\right) + b\left(\frac{X_B - X_B^\alpha}{X_B^\beta - X_B^\alpha}\right) \tag{1.98}$$

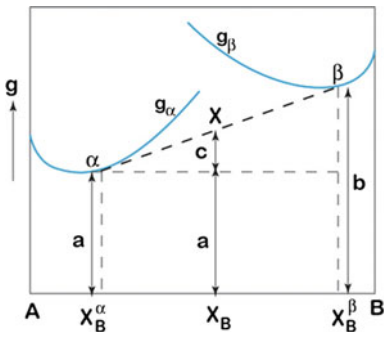

Fig. 1.17 The common tangent construction

where a and b represent the free energies of the α- and β-phases at the given temperature and pressure, as seen from Fig. 1.17. We can further rearrange Eq. 1.98 in order to obtain the free energy of alloy X

$$\begin{aligned} g &= a\left[\frac{(X_B^\beta - X_B^\alpha) - (X_B - X_B^\alpha)}{X_B^\beta - X_B^\alpha}\right] + b\left(\frac{X_B - X_B^\alpha}{X_B^\beta - X_B^\alpha}\right) \\ &= a + (b-a)\left(\frac{X_B - X_B^\alpha}{X_B^\beta - X_B^\alpha}\right) \\ &= a + c \end{aligned} \tag{1.99}$$

Hence, alloy X which separates into two phases of composition X_B^α and X_B^β with the free energies a and b has a free energy given by the point x on the straight line connecting α and β (the common tangent). This is depicted in Fig. 1.17.

As an example of the use of common tangent construction, the calculation of two-phase equilibrium is presented in Fig. 1.18. The condition for chemical equilibrium is that the chemical potentials of the components are equal in the phases that are in equilibrium. In the beginning, the α-phase with composition α1 is contacted with the β-phase with a composition β1. As seen from Fig. 1.18 (at the moment in question), the chemical potential (partial molar Gibbs energy) of component A in the α-phase is $\mu_A^{\alpha 1}$ and in the β-phase $\mu_A^{\beta 1}$, whereas that of component B in the α-phase is $\mu_A^{\alpha 1}$ and in the β-phase it is $\mu_A^{\beta 1}$, which are hardly equal. Thus, there is a driving force $\Delta^1\mu_B(\mu_B^{\alpha 1} - \mu_B^{\beta 1})$ which drives the diffusion of the B atoms to the α-phase (from composition β1 to α1) and $\Delta^1\mu_A(\mu_A^{\beta 1} - \mu_A^{\alpha 1})$ driving the A atoms in the opposite direction. As the diffusion proceeds, the driving force for diffusion gradually decreases ($\Delta^2\mu_B$ and $\Delta^2\mu_A$) and vanishes when the chemical potentials of the components (A and B) become equal in both phases. This takes place when the two Gibbs energy curves for the α- and β-phases have a common tangent and the equilibrium has been established.

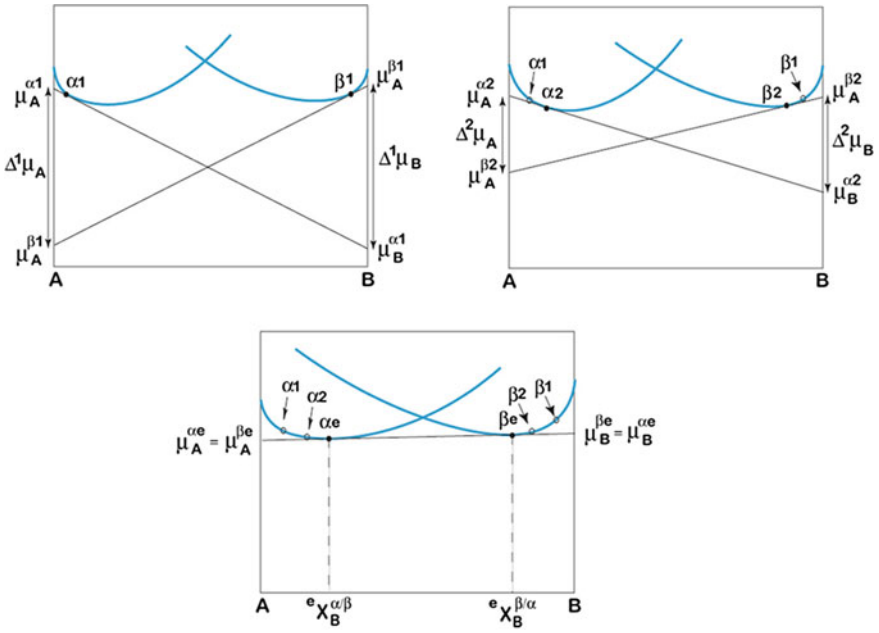

Fig. 1.18 Use of the common tangent construction to determine the phase equilibria

1.11 The Gibbs Phase Rule

The Gibbs phase rule explains the number of phases that will be present in a system in equilibrium and is expressed as

$$F + P = C + N \tag{1.100}$$

where F is the number of degrees of freedom (always ≥ 0), P is the number of phases (liquid phase, α-phase, β-phase), C is the number of components, and N corresponds to the non-compositional variable. In our case, there are two non-compositional variables present, temperature and pressure. This means that Eq. 1.100 can be written as

$$F + P = C + 2 \tag{1.101}$$

Now for the purpose of explaining the stability of the phases in equilibrium, a single-component system that is presented in Fig. 1.19a is considered. First, let us examine the single-phase, solid, liquid or gas phase, region which can be written in this region $C = 1$, $P = 1$. Also from Eq. 1.101, we can write $F = 2$. This means that in this region, there are two degrees of freedom, temperature and pressure. Accordingly, temperature and pressure can be varied independently within the region. Consequently, to determine the state of the phase in a single-phase region,

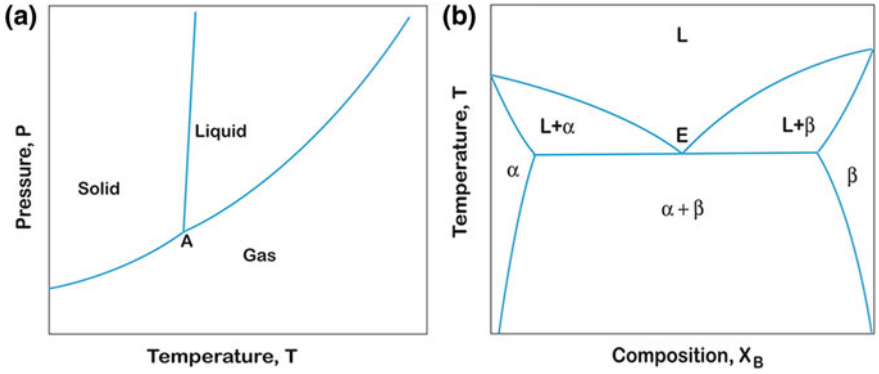

Fig. 1.19 **a** single-component phase diagram **b** binary phase diagram

both temperature and pressure must be fixed. Next, we consider the phase boundary, along which the two phases are in equilibrium. For this can be written $C = 1$, $P = 2$. Further, from Eq. 1.100, we can write $F = 1$, meaning that there is only one degree of freedom and only temperature or pressure can be varied along that tie-line. The other variable is automatically fixed for a particular temperature or pressure. Let us further consider the invariant point A, where all three phases can exist together. At this point, $C = 1$, $P = 3$. Therefore, following Eq. 1.100, $F = 0$, meaning that there are no degrees of freedom at that point and all three phases can exist only at one particular pressure and temperature.

Let us further consider the binary phase diagram shown in Fig. 1.19b. Since binary phase diagrams are measured at constant (in general, atmospheric) pressure, there is only one non-compositional variable present, which is temperature. Equation 1.100 can thus be written as

$$F + P = C + 1 \tag{1.102}$$

Now, if we consider the single-phase region, then we can write $C = 2$, $P = 1$. Following Eq. 1.102, we find $F = 2$ in the single-phase α-region. This means that to determine the state of an alloy inside a single-phase region, both temperature and composition must be fixed. Further, if we consider a two-phase region such as $(L + \alpha)$, then we can write $P = 2$, $C = 2$. So following Eq. 1.102, we find the number of degrees of freedom $F = 1$. To determine the state of an alloy inside this region, we need to fix only one variable, either T, X_A, or X_B. Since, if we fix any one of these variables, other variables will be fixed automatically. Take, for instance, T_2 where the composition of liquid and α-phases have fixed values. Next, if we consider the eutectic point E, where the three phases, α, β, and liquid exist together, we can write $P = 2$, $C = 2$. Following Eq. 1.103, we find $F = 0$, meaning that there are no degrees of freedom and T, X_A, and X_B are all fixed at this point.

The phase rule is a convenient tool to check that experimentally determined phase diagrams are correct. With its help, it is possible to point out anomalies in phase diagrams and to offer corrections.

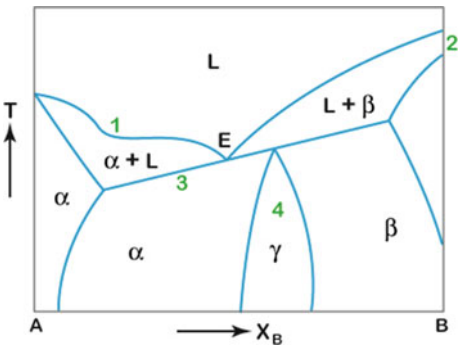

Fig. 1.20 A hypothetical erroneous phase diagram

Let us briefly look at one example. In Fig. 1.20, there is a hypothetical binary A–B phase diagram. It contains four errors. Let us next look what they are and produce two versions of the corrected diagram.

Error 1 Two-phase region in a binary diagram, thus $F = 1$ (pressure is fixed). If the temperature is fixed, the compositions are unambiguously determined. In the diagram, this is not so. If we choose temperature conveniently, the tie-line enters the single-phase region and returns back to the two-phase region. *Correction* remove the bend from the liquidus.

Error 2 Pure element, thus one component $F = 1 + 1 - P = 2 - P$. At the melting point, there are two phases in equilibrium $F = 2 - 2 = 0$. Hence, phase transformation for a pure element takes place at one particular temperature. *Correction*: Liquidus and solidus curves must meet at the same point.

Error 3 Eutectic line represents three-phase equilibrium, thus $F = 0$. Temperature must be constant. *Correction* Eutectic line must be horizontal.

Error 4 There are four phases in equilibrium at the eutectic isotherm, and thus, $F = -1$. The number of degrees of freedom must not be negative and, therefore, four-phase equilibrium in a binary system, with constant pressure, is not possible. *Correction 1* γ-phase must be removed to obtain the necessary degree of freedom to make $F = 0$. *Correction 2* If there is first a two-phase $\alpha + \beta$ region below the eutectic isotherm and after that a peritectoid reaction takes place, we can preserve the γ-phase.

The two versions of the corrected phase diagrams are shown in Fig. 1.21.

1.12 Correlation of Free Energy and Phase Diagram in Binary Systems

We shall first start with the simplest possible binary system, where elements A and B are completely miscible in both solid and liquid state. This requires that the elements A and B have (i) the same crystal structure, (ii) their size difference is less than 15 %, and (iii) their electronegativities have similar values. These are

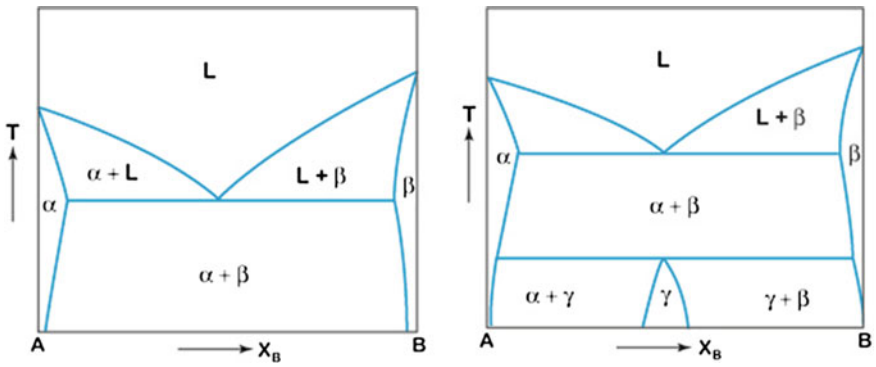

Fig. 1.21 The two correct versions of the diagram shown in Fig. 1.20

known as the Hume-Rothery rules. An example of such a system is Cu–Ni above 355 °C (i.e., above the solid state, miscibility gap caused at least partly by the ferromagnetism of Ni). Thus, the A–B system shown in Fig. 1.22 exhibits ideal behavior and atoms will not have any preference to select neighboring atoms. To give a mental picture of what complete miscibility in solid state means, we can trace the following line of thought. If one begins with pure A, with its own crystal structure, and starts to replace A atoms with B atoms, then, in the case of complete solubility, one can eventually replace all A atoms with B atoms without any change in crystal structure or formation of new phases and reach pure element B, with its own crystal structure (which has to be, by definition, the same as A's). To illustrate this behavior, we have to consider the change in free energy with composition for two different phases, solid (g^s) and liquid (g_L), to find the stability of the phases at different temperatures and compositions. Here, we assume that the melting point of element A (T_m^{A}) is higher than the melting point of element B (T_m^B). First, if we consider a relatively high temperature, as shown in Fig. 1.22a, we know from our previous discussion that the liquid phase will be stable because of a high contribution of entropy. Now, if we start to decrease the temperature to a certain extent, two factors shall be mainly noticed, which shall change in the free energy diagram. We have seen before that the free energy of a liquid phase decreases faster than that of a solid phase. So with the decrease in temperature, the difference in free energy of both liquid and solid phases will decrease. Further, because of the decrease in temperature, the contribution of $\Delta g_{\mathrm{mix}} \approx -T\Delta s_{\mathrm{mix}}$ will decrease, which means that the curvature of both curves will recede. If we decrease the temperature up to the melting point of element A (T_m^A), then we shall find, as shown in Fig. 1.22b, that g^L and g^S will intersect at $X_{\mathrm{B}} = 0$. If the temperature is decreased further, then the curves are found to intersect somewhere in the middle, as shown in Fig. 1.22c. The diagram can be separated into three different composition range of $\left(0 - X_{\mathrm{B}}^S\right)$, $\left(X_{\mathrm{B}}^S - X_{\mathrm{B}}^L\right)$, and $\left(X_{\mathrm{B}}^L - 1\right)$. Here, especially the composition range of $\left(X_{\mathrm{B}}^S - X_{\mathrm{B}}^L\right)$ draws attention for further discussion.

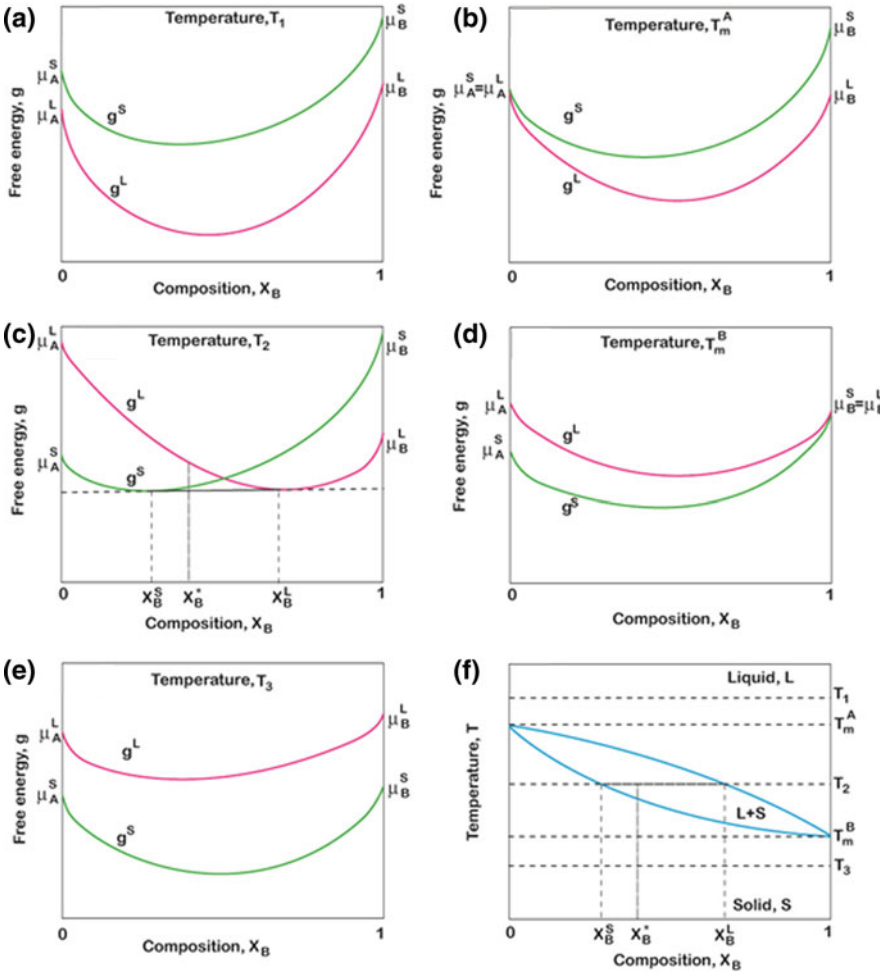

Fig. 1.22 Free energy versus composition diagram at different temperatures **a**–**e** for an isomorphous system and **f** the corresponding phase diagram

For the sake of discussion, if we consider the nominal composition X_B^* in this composition range, then it is apparent that the liquid phase (with this composition) cannot be stable at this temperature, since it does not correspond to the minimum free energy of the system. At the first instance, the solid phase with this composition seems to be the stable one. However, the system always tries to minimize its free energy if possible. In this case, there is a possibility to further minimize the free energy, if both solid and liquid phases exist together, the Gibbs energy value then sits on the common tangent as defined in Sect. 1.10. It is clear from Fig. 1.22c that the system will have minimum free energy when the solid phase with the composition of X_B^S exists with the liquid phase having the composition of X_B^L.

Since X_B^* is the average composition of the alloy, the mole fraction of the solid phase, following the lever rule (defined in Sect. 1.8), will be $(X_B^L - X_B^*)/(X_B^L - X_B^S)$ and the mole fraction of the liquid phase will be $(X_B^* - X_B^S)/(X_B^L - X_B^S)$. It should be noted that with the change in average composition within the range of $(X_B^L - X_B^S)$, the composition of the solid and liquid phases will not change, but, only the relative amount of the phases will change. It can also be understood from Fig. 1.22c that in this range, the liquid and solid phases with the composition X_B^S and X_B^L will exist together, since the chemical potential or activity of elements A and B in both the phases must be the same ($\mu_A^S = \mu_A^L$ and $\mu_B^S = \mu_B^L$). In other words, once solid and liquid phases reach their stable composition, there is no further driving force for change. It is also clear that in the composition range of $\left(0 - X_B^S\right)$, the solid phase will be stable since it has minimum free energy in that composition range, whereas in the composition range of $\left(X_B^L - 1\right)$, only the liquid phase will be stable since it has minimum free energy in that composition range. If we decrease the temperature to T_m^B, the free energy curves of the phases, as depicted in Fig. 1.22d, will intersect at $X_B = 1$. If we decrease the free energy of the system even further, the free energy of the solid phase, as shown in Fig. 1.22e, will be lower than the free energy of the liquid phase in all compositions and the solid phase will be stable. The corresponding phase diagram can be seen from Fig. 1.22f.

Next, let us consider a solution with a positive heat of mixing (endothermic behavior), which means that there is a miscibility gap in the system. Further, it is assumed that the miscibility gap occurs only in the solid state but not in the liquid phase. Thus, at low temperatures, the free energy of the mixing of the solid phase will be positive because of the positive heat of mixing. At higher temperature, however, the free energy of mixing becomes negative, because of the growing importance of the entropy term $(-T\Delta s_{mix})$. At a reasonably high temperature, the free energy of the solid and liquid phases might vary with composition, as shown in Fig. 1.23a.

With a further decrease in temperature to T_m^A, the free energy curves of solid (g^S) and liquid (g^L) phases will intersect, as is presented in Fig. 1.23b. Any further decrease in temperature down to T_2, because of the difference in curvature, g^L intersects g^S at two points, so there are five-phase regions stable at a different composition range, as given in Fig. 1.23c. With a further decrease in temperature to T_3, we shall find that g^S is lower than g^L at all compositions so that only the solid phase is stable at this temperature, as shown in Fig. 1.23d. It also should be noted that because of the endothermic nature of transformation, with the decrease in temperature, the curvature of g^S is decreased very rapidly and with the further decrease in temperature to T_4, the free energy of mixing becomes positive and the curvature of the free energy curve will become positive in a certain composition range in the middle.

This is the reason why in this composition range, the solid cannot be present as a single stable phase but will spontaneously dissociate into two different phases with compositions α_1 and α_2, as can be seen from Fig. 1.23e. The area between compositions α_1 and α_2 in Fig. 1.23e is called the spinodal region. It is to be noted that

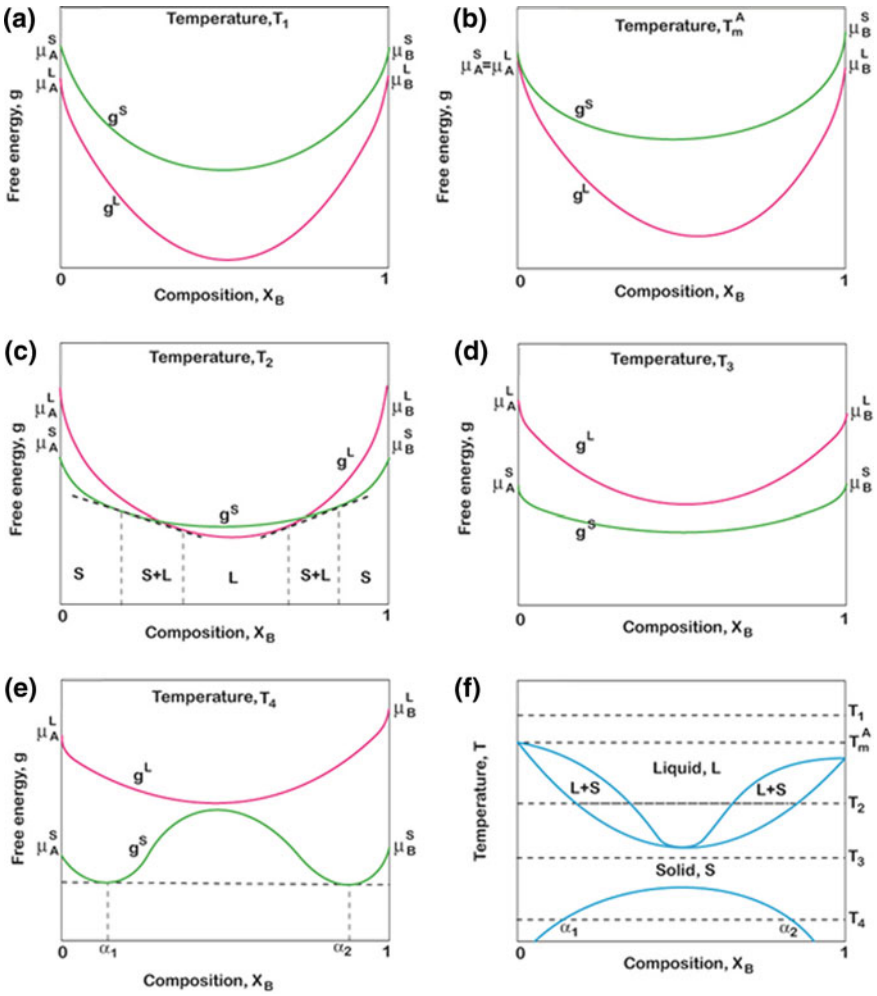

Fig. 1.23 Free energy versus composition diagram of a system which goes through endothermic transformation because of mixing and corresponding phase diagram

decomposition of the phase inside the spinodal does not require nucleation. Only after reaching the inflection points of the Gibbs energy curve, must nucleation precede the formation of a new phase. Figure 1.23f presents the corresponding phase diagram.

There are systems in which the enthalpy of mixing is positive and of such a high magnitude that the free energy curve will have positive curvature within a certain composition range up to a reasonably high temperature. In such cases, the free energy curves of the phases will change as a function of temperature in a way shown in Fig. 1.24a–e. The corresponding phase diagram is presented in Fig. 1.24f. Here, the main difference will be that at temperature T_E and at a particular

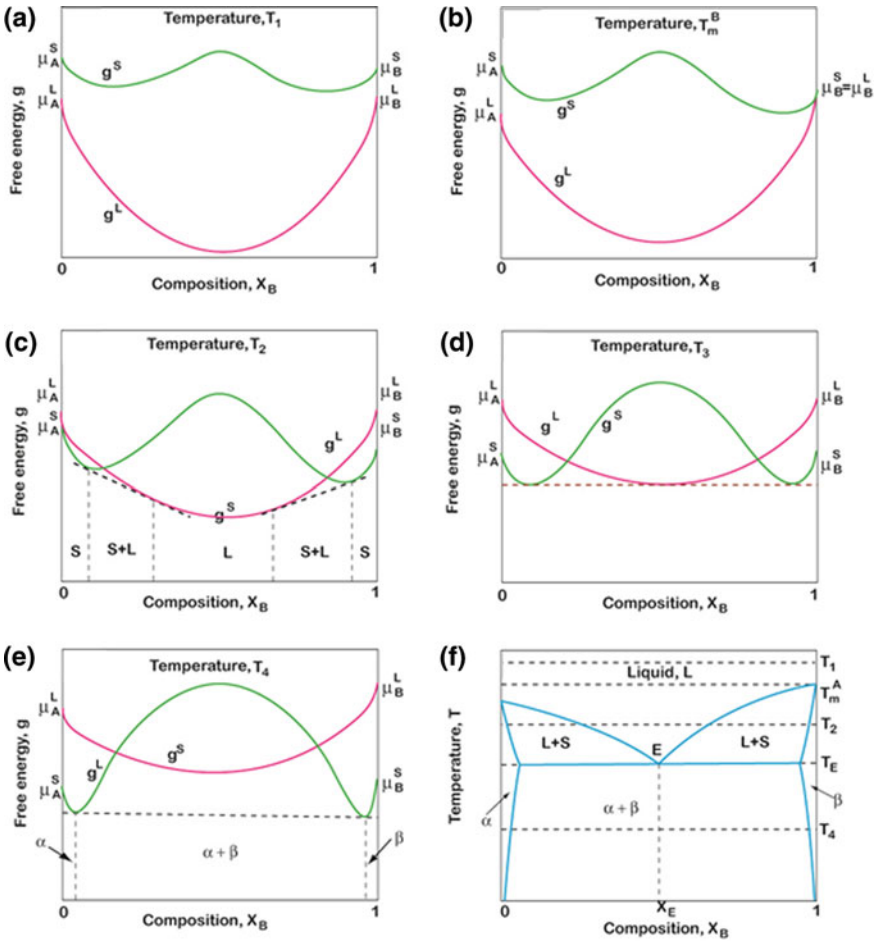

Fig. 1.24 Free energy versus composition diagram of a system which goes through endothermic transformation with very high enthalpy of mixing and corresponding phase diagram

composition X_E, the three phases, α, β, and L, can all exist together. Point E, plotted in Fig. 1.24f, corresponds to eutectic transformation. At the eutectic isotherm, the number of degrees of freedom is zero and thus, the equilibrium can occur only at a specific temperature and with fixed compositions of α, β, and L.

In all the above cases, we have considered systems where the crystal structure of elements A and B were similar and thus, there has been only one free energy curve for the solid phase. However, in a system where the elements have different crystal structure, we need to consider different free energy curves for different elements, as shown in Fig. 1.25. Let us designate, A(B), i.e., element A with a particular crystal structure, alloyed with some B as the α-phase. Similarly, B(A) is

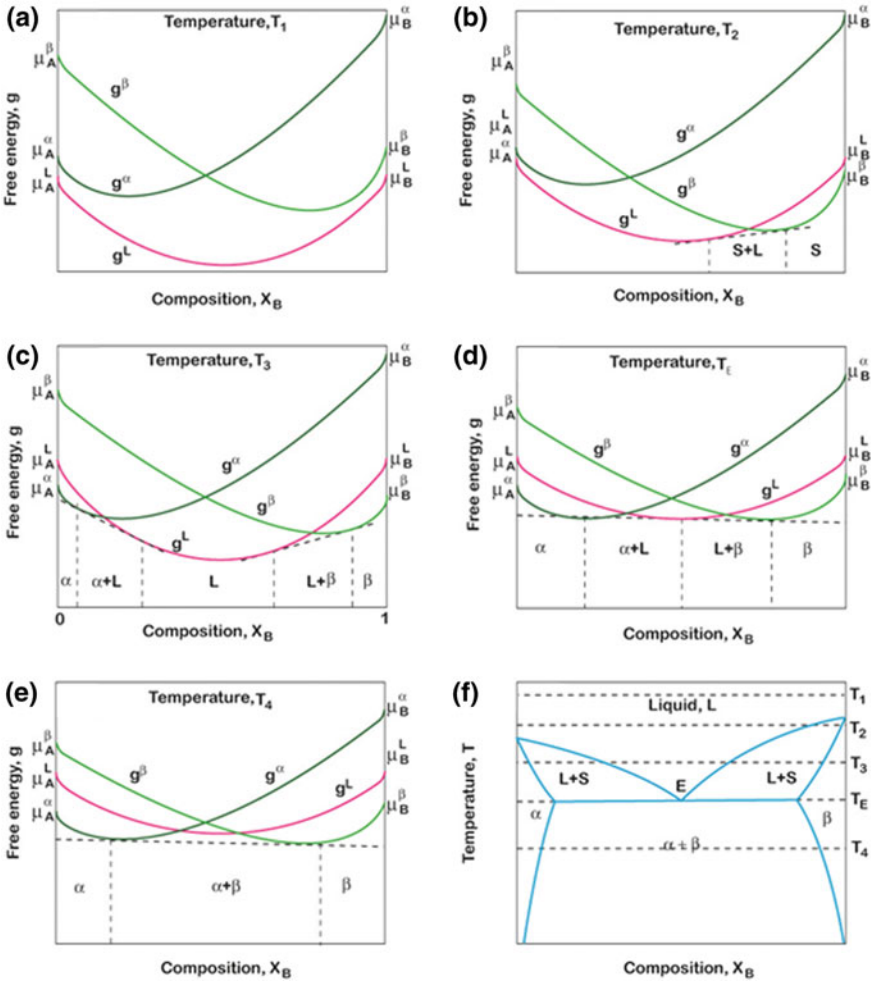

Fig. 1.25 Free energy versus composition diagram of a system where elements have different crystal structures and corresponding phase diagram

designated as the β-phase. Note in Fig. 1.25a that element A with the crystal structure of element B (g_B^{α}) will have a much higher free energy than its stable free energy (g_A^{α}); thus, it is a metastable crystal structure of A. Similarly, g_B^{α} is much higher than g_B^{α}. This system, under our consideration, also has an eutectic transformation as in the previous example.

Let us next consider the case, where the formation of the γ-phase in the system is associated with strong exothermic transformation, as can be noted from Fig. 1.26a. This implies that there is considerable difference in the electronegativities of the elements A and B. Note also that with only a slight change in

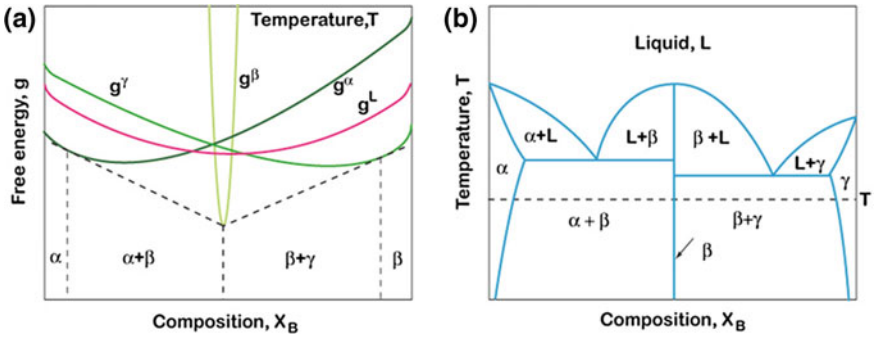

Fig. 1.26 Free energy versus composition diagram and the corresponding phase diagram where the phase (ordered γ-phase) goes through strong exothermic transformation

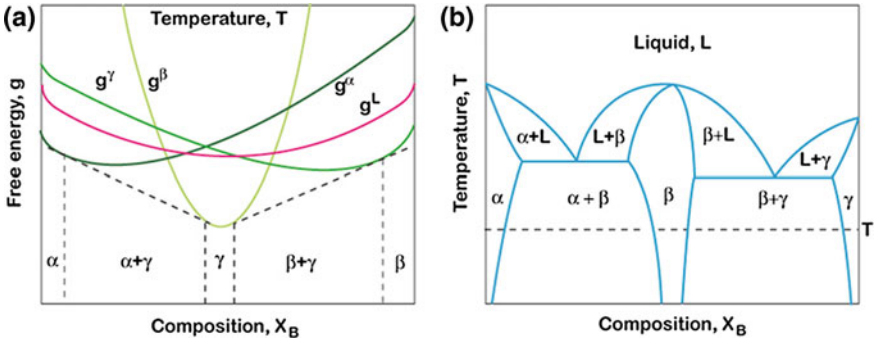

Fig. 1.27 Free energy versus composition diagram and the corresponding phase diagram where the ordered γ-phase has a wide homogeneity range

composition, the free energy of this phase increases very rapidly. Thus, the composition limits of the stability region of this phase are strictly limited. The corresponding phase diagram at a particular temperature T is given in Fig. 1.26b. As will be discussed in Sect. 2.6, different atoms in the ordered phase try to occupy particular lattice positions in the crystal to maximize the number of A–B bonds depending on the average composition of the phase. These ordered phases are known as *intermetallic compound* or *intermediate phases,* and in general, these phases have a different crystal structure than the crystal structure of the pure element. In the example shown in Fig. 1.26, it is to be observed that the γ-phase has a very narrow homogeneity range. However, in some cases, as presented in Fig. 1.27, the ordered phase can, in fact, have a wide homogeneity range, where the change in free energy (because of the small change in composition) is not very striking, unlike as in the previous example. These phases can deviate from their stoichiometric composition because of the presence of defects, as discussed in Sect. 1.11.

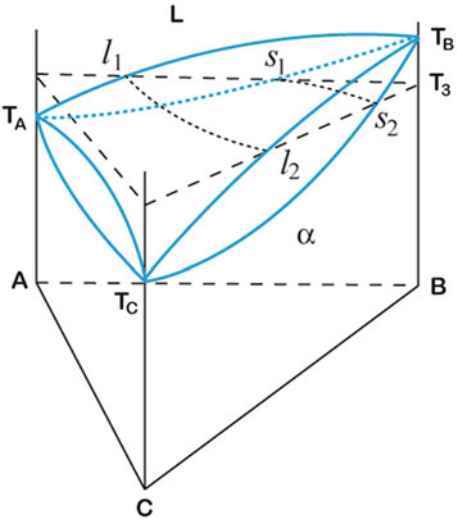

Fig. 1.28 Ternary space diagram with complete solid and liquid solubilities in all three binary systems

1.13 Ternary Phase Diagrams

According to the Gibbs phase rule, the number of degrees of freedom in a homogeneous ternary phase under constant pressure is three. Thus, we need to specify three independent variables (two-component mole fractions and temperature) in order to fix an equilibrium in a ternary solution phase. This leads to a three dimensional (T, X_A, X_B) presentation. As already discussed, it is of common practice to utilize an equilateral triangular (the Gibbs triangle) base (ABC) with three binary system "walls" (A–B, B–C, C–A) and temperature as the vertical axis. Next, we will briefly discuss ternary space diagrams as well as the isothermal and vertical sections taken from those diagrams.

Figure 1.28 shows the simplest possible ternary system, where there is complete solid and liquid solubility in the system (ABC). This ternary space model is very simple and easy to interpret, but as the systems become more complex, the space model becomes harder and harder to use. Therefore, it is common practice to utilize different sections and projections from the space model to yield more easily accessible information. As an example, the liquidus and solidus projections from the ABC system are shown in Fig. 1.29.

These types of projections are typically made with constant temperature intervals and can therefore be interpreted similarly as the contour lines in a map. Accordingly, the closer the spacing of the projection lines, the steeper is the projected surface. Isothermal sections are the most commonly used types of presentation of ternary equilibria. Figure 1.30 shows the isothermal section at temperature T_3 from the ABC system given in Fig. 1.28.

The plane intersects the liquidus surface at T_3 along the curve l_1l_2 and the solidus surface along the curve s_1s_2. On the left-hand side of the curve l_1l_2, there is

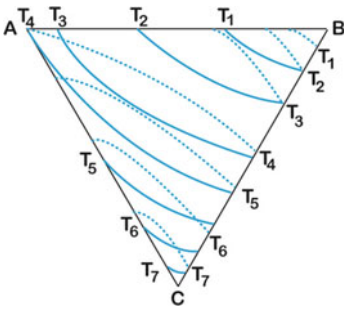

Fig. 1.29 Solidus and liquidus projections from the space diagram in Fig. 1.28

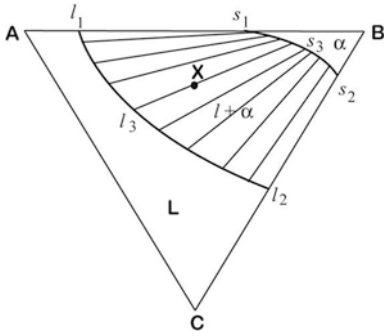

Fig. 1.30 Isothermal section at temperature T from the diagram seen in Fig. 1.28

a single-phase liquid region and on the right-hand side of the curve s_1s_2, there is a single-phase solid region. Between these two curves, there is a two-phase liquid and a solid region. The compositions of the phases in two-phase equilibrium are obtained at the end points of the tie-line and the amounts by the lever rule, as in binary phase diagrams. The directions of the tie-lines lying within the figure vary fan-like, so that there is a gradual transition from the direction of one bounding tie-line to that of the other. No two tie-lines at the same temperature may ever cross. This is a direct result of the Gibbs phase rule. Beyond these considerations, nothing can be said about the direction of tie-lines, except that they must run from liquidus to solidus. Other than those tie-lines on the edges of the diagram, none of them point toward a corner of the diagram unless by mere coincidence or due to a complete lack of solubility with the element at the given corner. Therefore, it is necessary to determine the position and direction of the tie-lines experimentally. It should be noted that the activity of a given component has the same value at each end of a tie-line.

Vertical sections (isopleths) from ternary space diagrams can also be taken. Figure 1.31 presents some ways in which this can be achieved. Afterward, these isopleths are shown in Fig. 1.32.

Even though the isopleths appear quite like binary phase diagrams, they must not be confused with them. In general, tie-lines cannot be used with isopleths and they only show the temperature composition regions of the different phases.

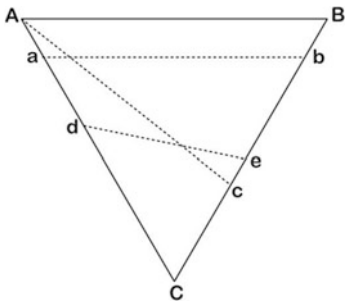

Fig. 1.31 Different ways one can take an isopleth

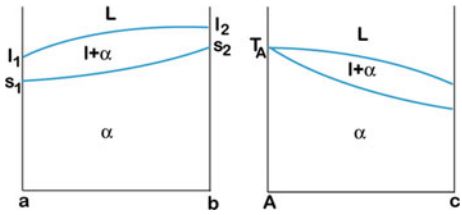

Fig. 1.32 Two isopleths taken along the lines ab and Ac

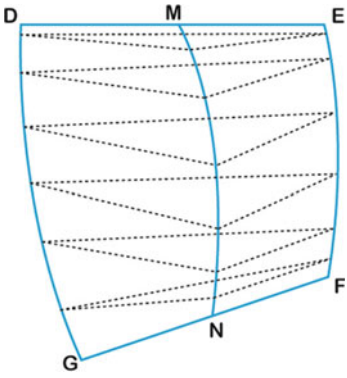

Fig. 1.33 Stack of tie-traingles

When there are three phases in equilibrium in a ternary system under constant pressure, there is still one degree of freedom left. Thus, three-phase equilibrium in a ternary system exists within a certain temperature range and not at a single temperature as in binary systems under constant pressure. Three-phase equilibrium in a ternary phase diagram is represented by a tie-triangle and as the temperature changes these tie-triangles form a "stack" of tie-triangles (Fig. 1.33). The composition of phases participating in the three-phase equilibrium can be found from the corners of the tie-triangle and the amount by applying the lever rule three times.

In this hypothetical ternary system in AC, there is complete solid and liquid solubility, whereas AB and BC are eutectic systems. Point M is the eutectic point of system AB, which is at a higher temperature than *N*, which is the eutectic point of the system BC. Thus, in both binary systems (AB and BC), an eutectic reaction $l \Leftrightarrow \alpha + \beta$ takes place. In Fig. 1.34, the surfaces AMNC ja MNB are the liquidus

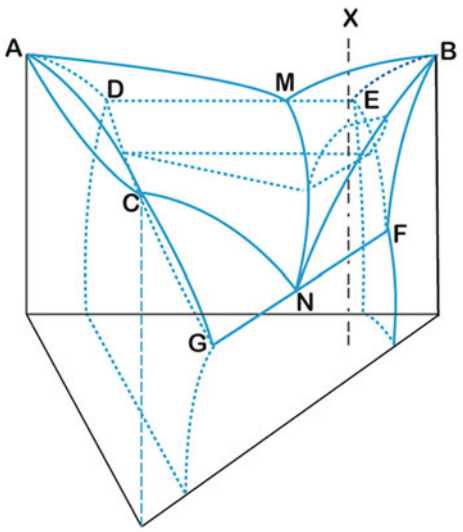

Fig. 1.34 ABC ternary system, where binary system AC has complete solid solubility and binary systems AB and BC are eutectic ones

surfaces and thus determine the solubilities of α and β to liquid. These surfaces meet at the eutectic valley MN. DG and EF are curves joining the points representing the respective compositions of the α and β phases formed in the eutectic reactions in the binary systems. DME and GNF are horizontal lines that represent these eutectic reactions. The surfaces ADGC and BEF are the solidus surfaces. The three curves MN, DG, and EF do not lie in the same plane. The curve MN lies above the surface DEFG, in such a way that there are three curved surfaces DMNG, MEFN, and DEFG, which enclose a three-phase space where α, β, and the liquid are in equilibrium. Each of these surfaces is made up of tie-lines representing $l + \alpha$, $l + \beta$, and $\alpha + \beta$ equilibria. The surfaces DMNG, MEFN, and DEFG separate the three-phase space from the liquid + α, liquid + β , and $\alpha + \beta$ regions, respectively. Where the three-phase region terminates in the binary systems AB and BC, it shrinks to the binary eutectic lines. In a ternary system, the eutectic reaction $l \rightarrow \alpha + \beta$ occurs over a range of temperature. If we have an alloy with nominal composition of X, as in Fig. 1.34, the solidification takes place as follows. During the solidification, the first solid phase to form is primary β, when the liquidus surface is first met. The composition of the liquid then changes along a path on the liquidus surface and that of the solid β along a path on the solidus surface as the temperature decreases. Then, at a certain temperature T_1, before solidification is completed, the liquid composition reaches a point on the curve MN and solid composition a point on the curve EF. The situation at T_1 is given in Fig. 1.35a where a tie-triangle is drawn. At this temperature, the nominal composition is seen to lie on the $l\beta$ tie-line. When the temperature is decreased to T_2, the three-phase equilibrium is established, as the nominal composition now lies inside the tie-triangle Fig. 1.35b. The compositions of the liquid, α, and β are given by the points l_2, α_2, and β_2, and their respective amounts can be obtained by applying the lever rule three times

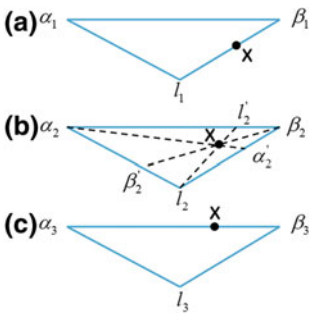

Fig. 1.35 The process of solidification of an alloy with nominal composition X in the system shown in Fig. 1.34 is exemplified in this figure as a function of temperature. **a** Temperature at which liquid composition reaches a point on the curve MN and solid composition a point on the curve EF, **b** temperature where three-phase equilibrium is established, and **c** temperature when solidification ends

$$\%\,\text{liquid}(l_2) = \frac{Xl_2'}{l_2l_2'} \times 100, \quad \%\,\beta_2 = \frac{X\beta_2'}{\beta_2\beta_2'} \times 100 \quad \text{and} \quad \%\,\alpha_2 = \frac{X\alpha_2'}{\alpha_2\alpha_2'} \times 100$$

Solidification ends at T_3 when the $\alpha_3\beta_3$ tie-line is encountered.

As the ternary systems become more complicated, the analysis shown above becomes increasingly difficult. Thus, it is of common practice to utilize different sections taken from the space model to provide information in a more accessible form. Next, we shall consider isothermal sections a little more, as they, in general, provide the most useful information on the ternary system. When working with the isothermal section and naming the phase regions, it is helpful to remember that the sides of the three-phase triangles must always face the two-phase regions, and at the corners of the tie-triangle, single-phase regions exist. These rules are based on the more general Palatnik-Landau theorem. Figure 1.36 contains an example of the AuPbSn system at 200 °C with all the phase regions clearly marked in the figure. It is to be noted that in the case of systems with stoichiometric compounds, the two-phase regions between three-phase regions may be reduced to just a single tie-line.

As an example of utilization of isothermal sections, we shall consider the following case. An interesting behavior has been observed in the Cu/SnBi eutectic system during soldering at temperatures above 200 °C. In particular, when the solder volume is small, reactions can result in drastic changes to the microstructure when soldering times are increased. Since bismuth does not react with Cu, only tin is consumed during the reactions. This will eventually lead to a shift in the liquid solder composition toward the Bi-rich corner. When the isothermal section of the SnBiCu equilibrium phase diagram is investigated, it is to be noted that when the enrichment of liquid with bismuth increases and the composition of the solder is around 60 at-% bismuth, the local equilibrium condition changes, as shown in Fig. 1.37.

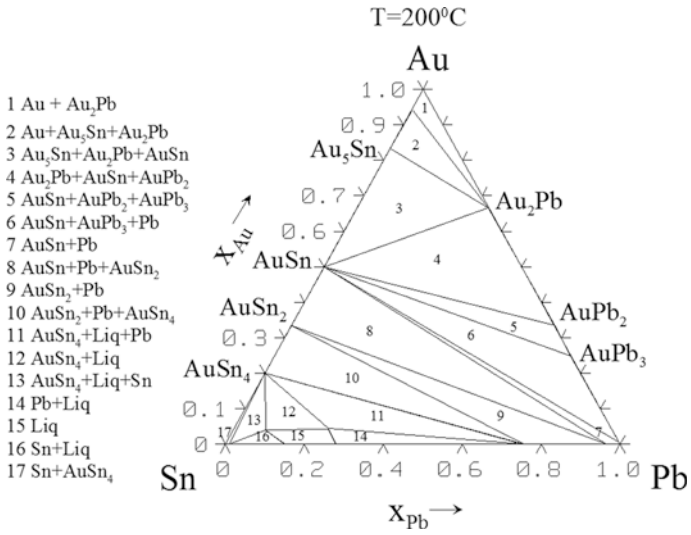

Fig. 1.36 Isothermal section from the Au–Pb–Sn ternary system at 200 °C

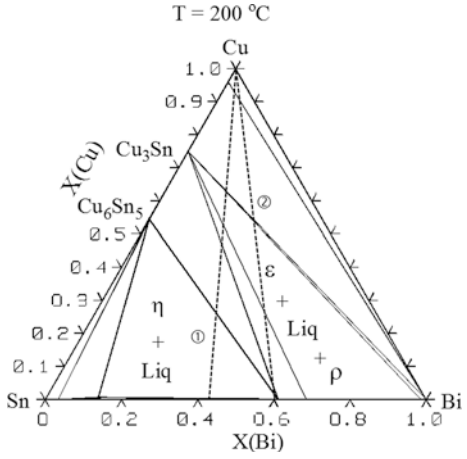

Fig. 1.37 Isothermal section from the Bi–Cu–Sn phase diagram at 200 °C

Cu_6Sn_5 cannot exist in local equilibrium with solder enriched with Bi at this temperature ($\sim$200 °C, shown as contact line 2). Cu_3Sn can, however, exist in local equilibrium even with pure Bi. Therefore, the Cu_6Sn_5 should transform into the Cu_3Sn layer. This has indeed been experimentally verified to take place [12]. The thing of special interest was that the Cu_3Sn layer maintained the original Cu_6Sn_5 morphology that it replaced [12].

From the thermodynamic data, one can also calculate the so-called phase fraction diagram (NP)-diagrams, which can be utilized to investigate, for example,

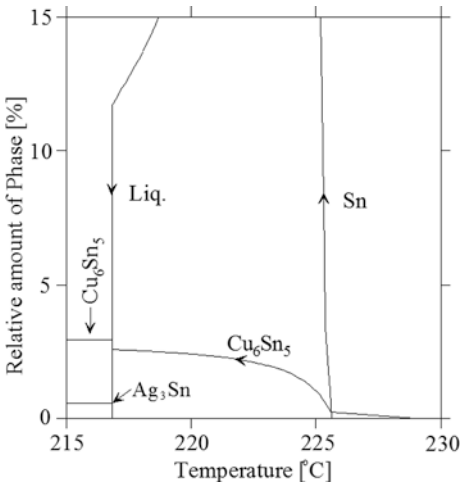

Fig. 1.38 NP-diagram of the phase formation during solidification of a SnAgCu solder, when Cu/(OSP) metallization is used. Note that owing to the high fraction of Sn, the diagram has been enlarged and therefore relative amount of phases goes only up to 15 %

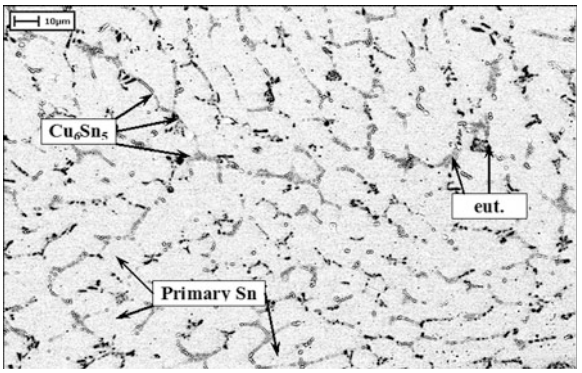

Fig. 1.39 Solder microstructure after reflow when Ni(P) metallization is used [13]

solidification. They show, as a function of temperature, the changes in the fractions of phase with a given nominal composition. An example is shown in Fig. 1.38.

As an example of the use of phase fraction diagrams, let us consider the next case, where identical SnAgCu solder alloy is used to solder components on two types of printed wiring boards (PWB's)—one with an Ni(P)/Au and one with a Cu(OSP) surface finish. Under the reflow conditions typically used in lead-free soldering, the solidification structure is generally cellular, where the small Cu_6Sn_5 and Ag_3Sn phases are dispersed between the large primary Sn grains [13]. If protective Au surface finishes are used, some small needle-like $AuSn_4$ can also be found inside the solder matrix at the high-angle boundaries. An example of the microstructure formed in the interconnections soldered with the Sn0.5Ag0.5Cu alloy on electrochemical Ni(P) with a thin flash Au on top (denoted Ni(P)|Au in the following) is shown in Fig. 1.39.

Both the Cu_6Sn_5 and the Ag_3Sn particles are uniformly distributed around the relatively large Sn grains. Figure 1.40 shows a micrograph taken from a sample

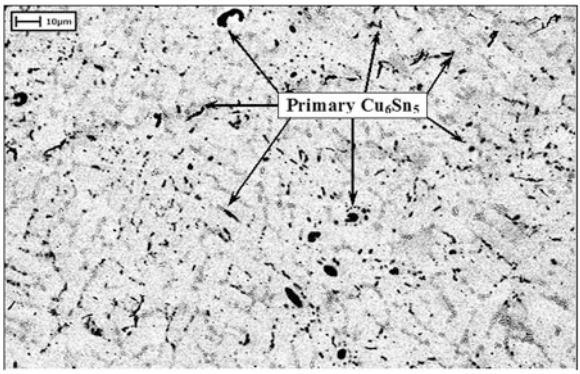

Fig. 1.40 Solder microstructure after reflow when Cu(OSP) metallization is used [13]

soldered with the same solder alloy but this time on the boards with organic solderability preservative (OSP) on the Cu pads (noted Cu|OSP). The resulting microstructure seems to be different even though the same solder alloy was used relative to Ni(P)|Au, interconnections formed on the Cu|OSP contain more and larger Cu_6Sn_5 intermetallic particles dispersed inside the solder.

What is the reason behind these differences observed experimentally? Let us take a closer look at what takes place during soldering. The thin layer of Au on top of Ni(P) dissolves instantly and completely into the molten solder, and the Ni starts dissolving next into the melt. The OSP coating partially evaporates and the rest dissolves into the solder flux during soldering. In the case of the Cu|OSP boards, it is the Cu pad that starts dissolving into the solder alloy. The dissolution rate of Cu in Sn0.5Ag0.5Cu (wt%) is about 0.07 μm/s. Based on this, the amount of Cu dissolution at the entire area of the soldering pad during the typical 40–45 s time above 217 °C is enough to lift the Cu concentration in the soldered interconnections close to 1 wt%, even when taking the amount of Cu bonded into the intermetallic layers on both sides of the interconnections into account. The dissolution rate of Ni is about 50 times smaller than that of Cu and thus, the dissolution of Ni to the solder is insignificant. All Ni that is dissolved at the interface is bonded to the $(Cu, Ni)_6Sn_5$ layer. Taking into account the amount of Cu bonded to the intermetallic layers on both sides of the interconnections, the nominal composition of the interconnections soldered on the Ni(P)|Au-coated pads will result in about Sn0.5Ag0.3Cu, whereas the final composition on the interconnection on Cu was about Sn0.5Ag1.0Cu.

An important consequence of higher Cu content is that solidification process is different in interconnections soldered on Ni from those soldered on Cu. Figures 1.38 and 1.41 present the phase fraction diagrams, where the amount of different phases in the relative number of moles can be presented as a function of temperature. The interconnections soldered on Ni(P)|Au PWB have the Sn0.5Ag0.3Cu composition, whereas the interconnections soldered on Cu|OSP have the Sn0.5Ag1.0Cu.

As can be seen from Fig. 1.41, the solidification of the liquid interconnections soldered on Ni(P)|Au boards starts with the formation of the primary Sn phase when

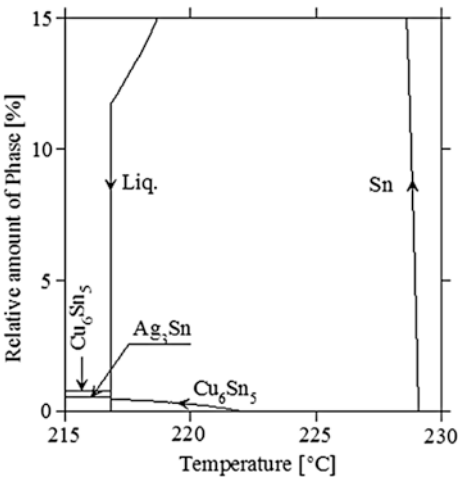

Fig. 1.41 NP-diagram of the phase formation during solidification when Ni(P)/Au metallization is used [13]

the interconnections are cooled down from the peak reflow temperature to below the liquidus temperature of 229 °C. The Cu_6Sn_5 phase does not nucleate until below 222 °C, where the composition of the liquid reaches the eutectic valley. Figure 1.38 presents the phase fraction diagram of the liquid interconnections soldered on Cu|OSP boards. In this case, the solidification begins with the formation of primary Cu_6Sn_5 below 229 °C. However, the nominal composition of the liquid soon meets the curve of two-fold saturation, after which the solidification of the interconnections proceeds by the binary eutectic reaction $L \rightarrow (Sn)eut + (Cu_6Sn_5)eut$. Below the four-phase invariant temperature, there is more than three times as much Cu_6Sn_5 in the Cu|OSP interconnections as in those on the Ni(P)|Au substrate. It is to be noted that the above analysis of solidification has been carried out by considering that the system is in complete equilibrium. As this is not typically the case in practical applications, the above-presented discussion must be taken to represent the ideal situation where kinetics plays no role in the process.

1.14 Stability Diagrams (Activity Diagrams, etc.)

The activity diagram shown in the right-hand side of Fig. 1.42 is one form of many different types of stability diagrams. In such a diagram, the thermodynamic potential of one of the components is plotted as a function of the relative atomic fractions of the other two components. The activity values which are needed in the construction of such a diagram can be calculated from the assessed thermodynamic data. When calculating the activities of the components, the activities of the stoichiometric compounds at equilibrium are regarded to be one. It should be noted that the precision of the calculations is very much dependent on the accuracy and

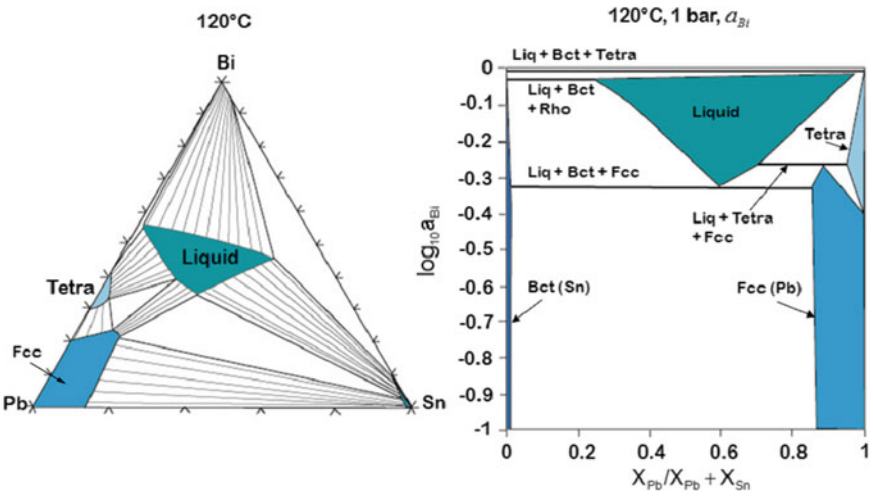

Fig. 1.42 Isothermal section from the Bi–Pb–Sn phase diagram at 120 °C and the corresponding activity diagram at the same temperature

consistence of the thermodynamic data used. Therefore, great care should be exercised when using data from different sources.

The edges of the diagram shown in Fig. 1.42 represent the binary systems (Sn–Bi, Sn–Pb, and Pb–Bi). The ternary phase relations are represented by the inside of the diagram. The stoichiometric single-phase regions are represented as vertical lines, two-phase regions as areas, and three-phase fields as horizontal lines. The vertical left- and right-hand axes represent the binary edge systems. In Fig. 1.42, the identical phase regions in the ternary isotherm and in the activity diagram at the same temperature are identified with the same color. The three-phase equilibria are shown as red triangles in the isothermal Section and as red horizontal lines in the activity diagram. In Fig. 1.43, the activity diagrams for all three species of the C–Si–Ta system are shown. Figure 1.44 shows the corresponding isothermal section.

The activity diagrams provide useful information about the formation of the reaction layer sequence when used together with the isothermal sections as follows. The example is from the Si/TaC/Cu diffusion barrier structure where the Si/TaC interface is studied. From the phase diagram, it is evident that the Si/TaC interface is not in equilibrium and a driving force for the formation of additional phases between the substrate and the TaC layer therefore exists (Fig. 1.44). Although there exists a TaC + $TaSi_2$ two-phase region in the phase diagram (Fig. 1.44), SiC must be formed to incorporate the carbon released after the formation of $TaSi_2$ in the reaction between Si and TaC, because of the mass balance requirement. The formation of SiC and $TaSi_2$ was confirmed with TEM investigations and therefore gives support to the assessed phase diagram. The reacted structure consisted of layers of SiC and $TaSi_2$ on top of the silicon substrate.

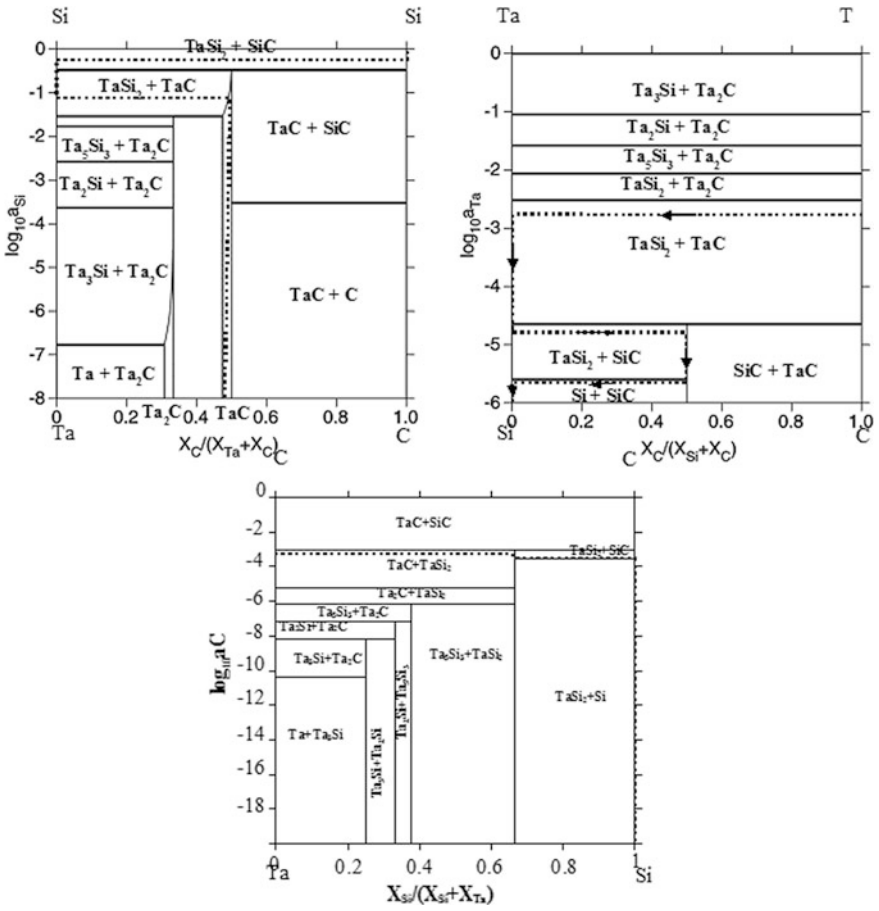

Fig. 1.43 Activity diagrams for C, Si, and Ta at 800 °C [14]

The original TaC was completely consumed during the reaction, since no traces of it could be found at 800 °C. The reaction sequence seemed to be Si/SiC/$TaSi_2$/TaC, in which the TaC was used completely to yield the final structure Si/SiC/$TaSi_2$. Silicon is expected to be the first species moving at this interface owing to the following reasons. Firstly, Si has been found to be the mobile species during the formation of $TaSi_2$ that occurs around 650 °C in the binary Ta–Si system by Si in diffusion, whereas the movement of Ta has not been observed under similar conditions. Secondly, chemical bonding between Ta and C in the TaC compound is expected to be strong, and breaking of these bonds, which is required for the release and subsequent diffusion of Ta, would require large amounts of energy. Owing to the facts stated above, the diffusion of tantalum or carbon in this system is not considered to be highly probable. Consequently, Si is anticipated to be the main diffusing species at the Si/TaC interface around 800 °C.

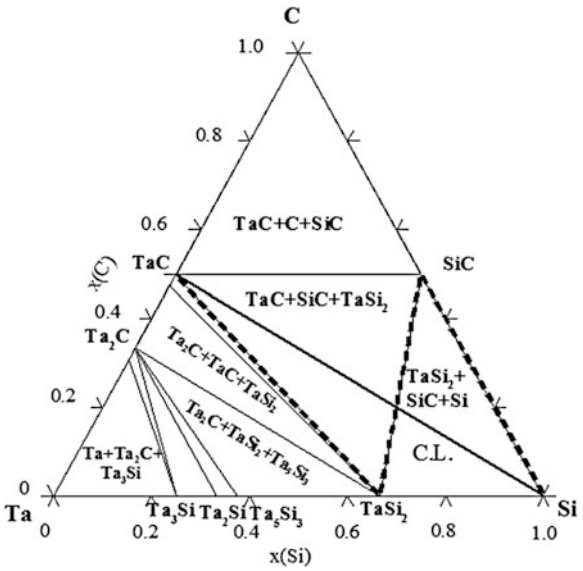

Fig. 1.44 Isothermal section at 800 °C from the C–Si–Ta system [14]

Whether the above-presented phase formation sequence is thermodynamically possible can be investigated with the help of Fig. 1.43. As can be seen from the calculated activity diagram, Si can move along its lowering activity in the proposed reaction sequence and therefore, diffusion of Si in this particular reaction sequence is allowed on thermodynamic grounds. The examination of the calculated activity diagrams for carbon and tantalum does not restrict the diffusion of these elements in the suggested reaction sequence either (Fig. 1.43). However, as already discussed, carbon and tantalum are strongly bonded to each other in the TaC compound and are not expected to move easily. Therefore, the reaction most likely starts by Si in diffusion into TaC (most probably via grain boundaries). This is followed by the formation of $TaSi_2$, which then leads to the accompanied dissociation of TaC. The released carbon is then available for the formation of SiC in the reaction with Si. This mechanism will finally yield the experimentally observed structure $Si/SiC/TaSi_2$.

1.15 The Use of Gibbs Energy Diagrams

In the following examples, the use of Gibbs energy diagrams is presented. The discussion follows largely that presented in the classical treatments of the subject by Hillert [10, 15].

In Fig. 1.45, a typical molar property diagram at a given temperature T_0 is shown. The diagram shows some of the basic properties of a molar property diagram. From Fig. 1.45, one can see, for example, how a Gibbs energy of a phase is defined ($g^{\alpha} = X_A^{\alpha}\mu_A^{\alpha} + X_B^{\alpha}\mu_B^{\alpha}$) with the help of chemical potentials, how the

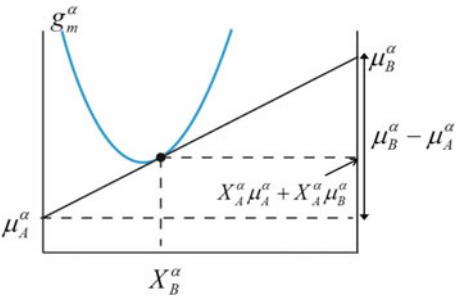

Fig. 1.45 Typical molar property diagram

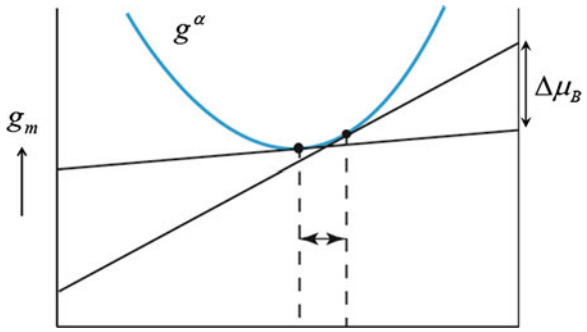

Fig. 1.46 Determination of the driving force for diffusion within a solution phase

chemical potentials for a species in a given phase are defined (from the end points of the tangent), that the slope of a tangent equals the chemical potential difference of B and A in the alpha phase $\left(\frac{dg^\alpha}{dX_\mathrm{B}} = \mu_\mathrm{B}^\alpha - \mu_\mathrm{A}^\alpha\right)$, and so on. These simple geometrical features of the molar diagrams can be used for a wide variety of applications [15].

The positive curvature of the Gibbs energy curve makes the phase stable against fluctuations in composition. The same feature of the curve also provides the driving force for the elimination of differences in composition within the phase (Fig. 1.46). Thus, this is the driving force for diffusion. Let us consider the situation where B atoms diffuse from a region of high concentration (more precisely activity) to a region of low concentration. Each individual region may be regarded as a reservoir of B with its own value of g_B, and the difference in g_B is identical to the decrease in Gibbs free energy when one mole of B is transferred. We make an assumption that the rate of transfer is proportional to the decrease in Gibbs free energy and the number of B atoms per volume $\frac{X_\mathrm{B}}{v_m}$ and inversely proportional to the transport distance Δy. With these assumptions, the expression for the flux of B atoms may be written as

$$J_\mathrm{B} = -\frac{M_\mathrm{B} X_\mathrm{B}}{v_m}\frac{\Delta g_\mathrm{B}}{v_m} = -\frac{M_\mathrm{B}}{v_m} X_\mathrm{B} \frac{dg_\mathrm{B}}{dX_\mathrm{B}}\frac{\Delta X_\mathrm{B}}{\Delta y} \tag{1.103}$$

The constant of proportionality, M_B, may be regarded as the mobility of the B atoms. By introducing the curvature of the g curve, we obtain

$$J_B = -\frac{M_B}{v_m} X_A X_B \frac{d^2 g}{dX^2} \frac{\Delta X_B}{\Delta v_m} \tag{1.104}$$

By considering the Fick's first law (see Chap. 3), the diffusion constant for B is recognized as

$$D_B = M_B X_A X_B \frac{d^2 g}{dX_B^2} \tag{1.105}$$

The mobility is thus multiplied by the thermodynamic factor. By using the activity or activity coefficient for B, the thermodynamic factor can be transformed to the shape as used in Chap. 3

$$X_A X_B \frac{d^2 g}{dX_B^2} = X_B \frac{dg_B}{dX_B} = \frac{dg_B}{d \ln X_B} = RT \frac{d \ln a_B}{d \ln X_B} = RT \left(1 + \frac{d \ln \gamma_B}{d \ln X_B}\right) \tag{1.106}$$

A similar derivation can be carried out also for component A, and the same factor is obtained

$$D_A = M_A X_A X_B \frac{d^2 g}{dX_B^2} \tag{1.107}$$

It is to be noted that in ternary systems, there are more than one thermodynamic factor. In a binary system, the Gibbs–Duhem equation (will be derived in Sect. 1.16) gives

$$X_A d\mu_A + X_B d\mu_B = 0$$

and

$$X_A d\mu_A = RT(dX_A + X_A d \ln \gamma_A)$$
$$X_B d\mu_B = RT(dX_B + X_B d \ln \gamma_B)$$

In a binary system, $X_A + X_B = 1$ and thus, $dX_A + dX_B = 0$ which finally gives

$$X_A \left(\frac{d \ln \gamma_A}{dX_A}\right) = X_B \left(\frac{d \ln \gamma_B}{dX_B}\right)$$

or

$$\frac{d\ln a_A}{d\ln X_A} = \frac{d\ln a_B}{d\ln X_B}$$

In a ternary system, Gibbs–Duhem equation is written as

$$X_A d\mu_A + X_B d\mu_B + X_C d\mu_C = 0$$

and it is immediately seen there must be more than one thermodynamic factor in a given ternary system. In fact, there are four factors of which three are independent.

van Loo et al. have derived [16] equations for the four thermodynamic factors in a ternary system as well as the relation between the three independent ones and the fourth which depends on the other three as follows.

$$\Theta_{11} = \left(\frac{d\ln a_1}{d\ln X_1}\right)_{p,T,X_2} \quad \Theta_{12} = \left(\frac{d\ln a_1}{d\ln X_2}\right)_{p,T,X_1}$$

$$\Theta_{21} = \left(\frac{d\ln a_2}{d\ln X_1}\right)_{p,T,X_2} \quad \Theta_{22} = \left(\frac{d\ln a_2}{d\ln X_2}\right)_{p,T,X_1}$$

$$\Theta_{21} = \frac{X_1}{(1-X_1)}\left[\frac{(1-X_2)}{X_2}\Theta_{12} + \Theta_{22} - \Theta_{11}\right]$$

By noting that the so-called phenomenological constant is related to the mobility by $L_B = M_B C_B$ and by remembering the relation between the chemical potential and the activity, the fluxes of elements A and B can be expressed as

$$\begin{aligned} J_A &= -L_A \frac{d\mu_A}{dx} \\ J_B &= -L_B \frac{d\mu_B}{dx} \end{aligned} \tag{1.108}$$

This equation will be utilized in Chap. 4.

One can also use Gibbs energy diagrams to obtain the driving force for diffusion of a particular species over a growing phase.

In Fig. 1.47, the common tangent construction defined above is used to determine the driving forces for diffusion of Cu through Cu_3Sn and Sn through Cu_6Sn_5. $\Delta\mu^{\varepsilon}_{Cu}$ is the chemical potential difference of Cu between interfaces Cu_3Sn/Cu and Cu_6Sn_5/Cu_3Sn, which drives the diffusion of Cu through Cu_3Sn and $\Delta\mu^{\eta}_{Sn}$ is the chemical potential difference of Sn between the interfaces Sn/Cu_6Sn_5 and Cu_6Sn_5/Cu_3Sn, which drives the diffusion of Sn through the Cu_6Sn_5 layer. It is easy to realize from Fig. 1.47 that changes in the stabilities of the η- and ε-phases

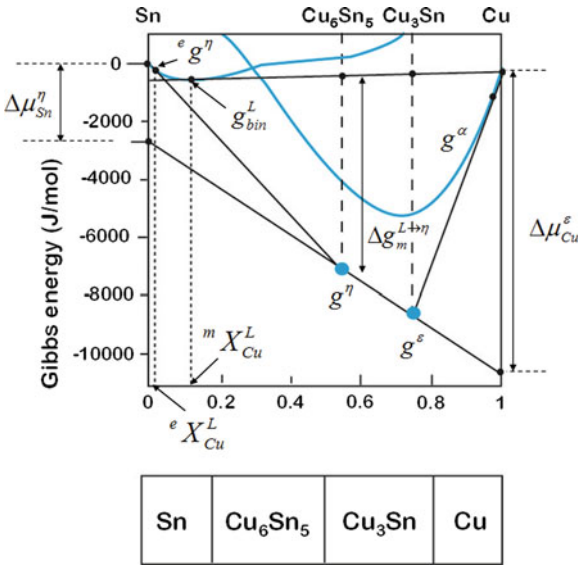

Fig. 1.47 Gibbs energy diagram from the Cu–Sn system at 235 °C

(in their Gibbs free energy) will change the values of $\Delta\mu^{\eta}_{\mathrm{Sn}}$ and $\Delta\mu^{\varepsilon}_{\mathrm{Cu}}$ and thus increase or decrease the driving forces for diffusion of components in the system.

From Fig. 1.47, other important features can also be extracted. For instance, the common tangent between the curves g^{L}_{bin} and g^{η} gives the equilibrium solubility of Cu to a liquid solder (L), which is given as ${}^{e}X^{L}_{\mathrm{Cu}}$. The equilibrium solubility is the amount of Cu that can be dissolved infinitely slowly to liquid solder before the η-phase comes into equilibrium with the liquid. The formation of the η-phase does not, however, occur with this composition, as the driving force is zero at this point (no supersaturation). In real cases, the dissolution of Cu does not take place infinitely slow and, therefore, the equilibrium solubility is generally exceeded. The solubility of Cu does not increase infinitely, but there is an upper limit for its value and this can also be determined from Fig. 1.47. When more and more Cu dissolves into liquid, eventually, a situation is faced where the dissolution of more Cu would lead to the precipitation of pure metallic Cu out of the supersaturated solder. This corresponds to the common tangent construction between the solder and pure Cu. The tangent point in the liquid curve at this metastable equilibrium gives the upper value of Cu that can be dissolved into liquid solder at any rate, i.e., the metastable solubility ${}^{m}X^{L}_{\mathrm{Cu}}$. When this value has been reached, also the driving force for the formation of the η-phase has reached its maximum (shown in the diagram as $\Delta g^{L\rightarrow\eta}$ in Fig. 1.47). Since the metastable solubility is directly related to the dissolution rate of a given metal to a solder in question, it provides important information about the formation of intermetallic compounds between different metals and solders. In many cases, its value is about 2–3 times larger than the equilibrium solubility [17–19].

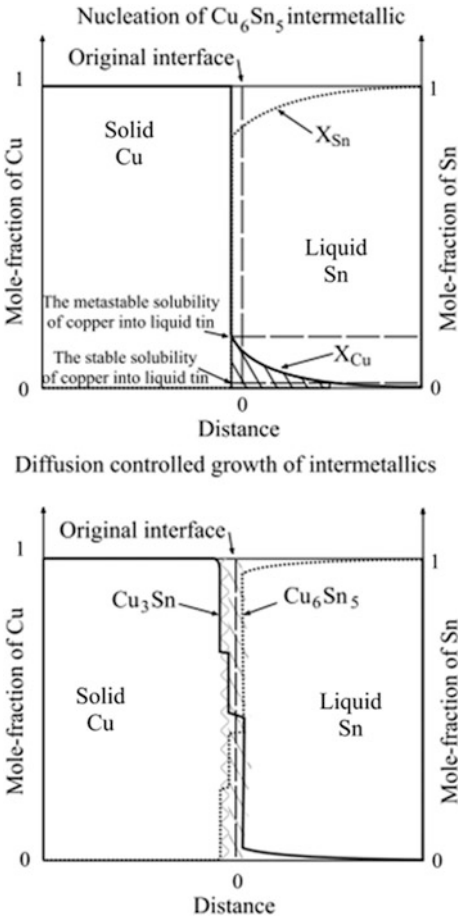

Fig. 1.48 Schematic presentation of the solid Cu/liquid Sn reaction couple after about 1 s (*upper figure*) and after several minutes (*lower figure*)

To get an idea about the relation between the above discussion and the actual phase formation in reaction couple where solid Cu is in contact with liquid Sn, it is helpful to consider the schematic presentation of the situation in Fig. 1.48. As Cu comes into contact with liquid Sn, it starts to dissolve rapidly. The equilibrium solubility of Cu_6Sn_5 to liquid Sn ($^eX_L^{Cu}$) is achieved quickly (in fractions of second). Owing to the reasons explained above, the dissolution does not stop at this value but the dissolution of Cu continues until the ultimate limit, the metastable solubility ($^mX_L^{Cu}$), is reached. At this point, the equilibrium between pure Cu and supersaturated liquid is achieved (equal chemical potential of Cu in both phases). This means that the dissolution of Cu must stop as there is no driving force for that anymore. At the same point, the maximum driving force for the formation of Cu_6Sn_5 is established (see Fig. 1.47). The composition profile of Cu is during these initial stages are shown by the hatched area in Fig. 1.49. As can be seen,

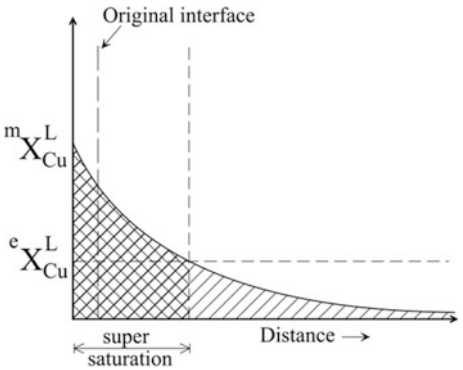

Fig. 1.49 Enlarged part of the solubility curves of the upper figure in Fig. 1.48

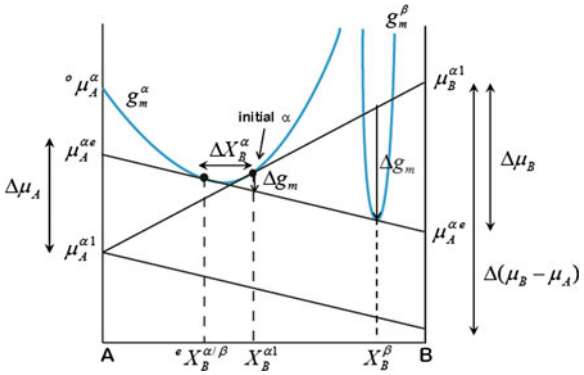

Fig. 1.50 Determination of a driving force for the nucleation of a new phase from supersaturated solid solution

there is a certain amount of Cu, the double hatched area, which exceeds the equilibrium solubility of Cu_6Sn_5 to liquid Sn. This is the extra amount of Cu that can be used to form Cu_6Sn_5 isothermally. It is evident from Fig. 1.49 that at the interface between Cu_6Sn_5 and the liquid Sn, the equilibrium solubility is established (where the second vertical dashed line from the left crosses the composition curve in Fig. 1.49).

The driving force for the precipitation can also be evaluated from the Gibbs phase diagram (Fig. 1.50). In Fig. 1.50, an alloy, α_1, which is inside the two-phase region $\alpha + \beta$ is shown. The Gibbs free energy of the system would decrease by precipitation of β, and the total driving force for the complete reaction in one mole of the alloy is given by the short arrow Δg The driving force for the formation of a very small quantity of β from a large quantity of α_1 is obtained by considering the tangent representing the supersaturated α-phase. The magnitude of the driving force (in nucleation stage) is given by the separation of the points at the two tangents as

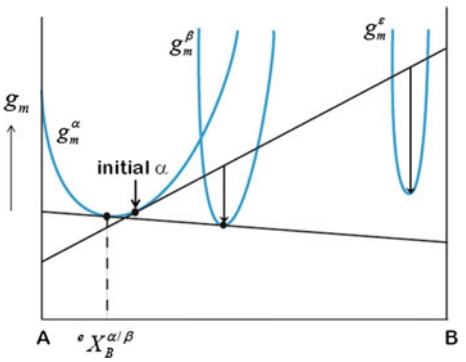

Fig. 1.51 Formation of a metastable phase

$$\begin{aligned}\Delta g &= X_A^\beta \mu_A^{\alpha 1} + X_B^\beta \mu_B^{\alpha 1} - g^\beta \\ g^\beta &= X_A^\beta \mu_A^{\alpha e} + X_B^\beta \mu_B^{\alpha e} \\ \Delta g &= X_A^\beta (\mu_A^{\alpha 1} - \mu_A^{\alpha e}) + X_B^\beta (\mu_B^{\alpha 1} - \mu_B^{\alpha e})\end{aligned} \tag{1.109}$$

For low supersaturations, one can introduce the curvature of the g^α curve. By comparing the triangles in Fig. 1.50, one obtains

$$\frac{\Delta g}{X_B^\beta - X_B^\alpha} = \frac{(\mu_B - \mu_A)}{1} \tag{1.110}$$

This can be further modified to obtain

$$\Delta g = \left(X_B^\beta - X_B^\alpha\right)\Delta(\mu_B - \mu_A) = \left(X_B^\beta - X_B^\alpha\right)\Delta\left(\frac{dg^\alpha}{dX_B}\right) \tag{1.111}$$

$$\Delta g = \frac{d^2 g^\alpha}{dX_B^2}\left(X_B^\beta - X_B^\alpha\right)\Delta X_B^\alpha \tag{1.112}$$

The last expression contains a factor $\left(x_B^\beta - x_B^\alpha\right)$ which is the difference in composition between the two phases. At the start of the precipitation, a new phase may be favored (higher driving force) if it differs much in composition even when it cannot be in stable equilibrium with the matrix phase. Thus, formation of a metastable phase (here ε) is favored (Fig. 1.51) according to the Ostwald rule.

One can also obtain quantitative numerical data about energy changes in a given system, by utilizing the simple geometric constructions shown above together with some simplified assumptions. Let us take one example from the important Cu–Sn system (Fig. 1.52). Consider the nucleation and growth of the η-phase, with $X_{Cu}^\eta = a$ and $X_{Sn}^\eta = b$ $(a + b = 1)$, out of supersaturated solder $^m X_{Cu}^L = c$. The driving force for the nucleation of the η-phase is given by $\Delta g^\eta = g_{tg}^L - g_{tg}^L$ (per mole of η). The two terms can be expanded as

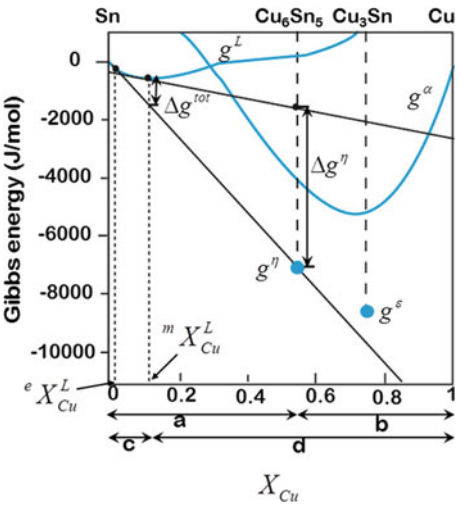

Fig. 1.52 Gibbs energy diagram from the Cu–Sn system at 235 °C

$$g^L_{tg} = X^\eta_{\mathrm{Cu}}\,{}^m\mu^L_{\mathrm{Cu}} + (1 - X^\eta_{\mathrm{Cu}})^m\mu^L_{\mathrm{Sn}} \tag{1.113}$$

and

$$g^L_{tg} = X^\eta_{\mathrm{Cu}}\,{}^e\mu^L_{\mathrm{Cu}} + (1 - X^\eta_{\mathrm{Cu}})^e\mu^L_{\mathrm{Sn}} \tag{1.114}$$

which gives

$$\Rightarrow \Delta g^\eta = X^\eta_{\mathrm{Cu}}\,{}^m\mu^L_{\mathrm{Cu}} + \left(1 - X^\eta_{\mathrm{Cu}}\right)^m\mu^L_{\mathrm{Sn}} - \left[X^\eta_{\mathrm{Cu}}\,{}^e\mu^L_{\mathrm{Cu}} + \left(1 - X^\eta_{\mathrm{Cu}}\right)^e\mu^L_{\mathrm{Sn}}\right] \tag{1.115}$$

and by using the definition of the chemical potential of a component, this gives

$$= RT\left[X^\eta_{\mathrm{Cu}} \ln\left(\frac{{}^m a^L_{\mathrm{Cu}}}{{}^e a^L_{\mathrm{Cu}}}\right) + X^\eta_{\mathrm{Sn}} \ln\left(\frac{{}^m a^L_{\mathrm{Sn}}}{{}^e a^L_{\mathrm{Sn}}}\right)\right] \tag{1.115}$$

If we simplify the treatment by assuming that the liquid behaves as a perfect solution, the activity values can be replaced by compositions, which give

$$\begin{aligned}
&\cong RT\left[X^\eta_{\mathrm{Cu}} \ln\left(\frac{{}^m X^L_{\mathrm{Cu}}}{{}^e X^L_{\mathrm{Cu}}}\right) + (1 - X^\eta_{\mathrm{Cu}}) \ln\left(\frac{1 - {}^m X^L_{\mathrm{Cu}}}{1 - {}^e X^L_{\mathrm{Cu}}}\right)\right] \\
&\cong 8.3145\ \mathrm{J/Kmol} \cdot 508\ \mathrm{K}\left[0.545 \ln\left(\frac{0.06}{0.018}\right) + (1 - 0.545) \ln\left(\frac{1 - 0.06}{1 - 0.018}\right)\right] \\
&= 2687.5\ \mathrm{J/mol}
\end{aligned} \tag{1.116}$$

Similarly, the change in Gibbs energy of the system owing to the precipitation of Cu_6Sn_5 can be expressed as

$$\Delta g^{\text{tot}} = g_{tg}^{L} - {}^{e}g_{tg}^{L} (= \Delta g^{L \to L+\eta}) \tag{1.117}$$

This can be written as

$$= RT \left[{}^{m}X_{\text{Cu}}^{L} \ln \left(\frac{{}^{m}a_{\text{Cu}}^{L}}{{}^{e}a_{\text{Cu}}^{L}} \right) + {}^{m}X_{\text{Sn}}^{L} \ln \left(\frac{{}^{m}a_{\text{Sn}}^{L}}{{}^{e}a_{\text{Sn}}^{L}} \right) \right] \tag{1.118}$$

and by again assuming perfect behavior

$$\begin{aligned} &\cong RT \left[{}^{m}X_{\text{Cu}}^{L} \ln \left(\frac{{}^{m}X_{\text{Cu}}^{L}}{{}^{e}X_{\text{Cu}}^{L}} \right) + \left(1 - {}^{m}X_{\text{Cu}}^{L}\right) \ln \left(\frac{1 - {}^{m}X_{\text{Cu}}^{L}}{1 - {}^{e}X_{\text{Cu}}^{L}} \right) \right] \\ &\cong 8.3145\,\text{J/Kmol} \cdot 508\,\text{K} \left[0.06 \ln \left(\frac{0.06}{0.018} \right) + (1 - 0.06) \ln \left(\frac{1 - 0.06}{1 - 0.018} \right) \right] \\ &= 131.6\,\text{J/mol} \end{aligned} \tag{1.119}$$

Hence, it can be concluded that these simple molar diagrams (Gibbs free energy diagrams) give an extensive amount of important information in an easily visualized form.

1.15.1 Effect of Pressure on the Phase Equilibrium

Related to the effects of pressure on the phase equilibrium, we shall consider two equations, the Laplace and the Kelvin equations. If a fluid interface is curved between two phases, then it turns out that the pressures on either side must be different. When the system is in equilibrium, every part of the surface must be in mechanical equilibrium (also in thermal and chemical). For a curved surface, the forces of surface tension are exactly balanced by the difference in pressure on the two sides of the interface. This is expressed by the Laplace equation

$$p^{\alpha} - p^{\beta} = \gamma \left(\frac{1}{r'} + \frac{1}{r''} \right) \tag{1.120}$$

where P stands for the pressure, γ is the surface tension, and r' and r'' are the radii of curvatures. By convention, positive values are assigned for the radii of curvature if they lie in phase α (see Fig. 1.53).

An important consequence of the Laplace equation concerns the effect of surface curvature on the vapor pressure of a liquid. This relationship is known as the Kelvin equation

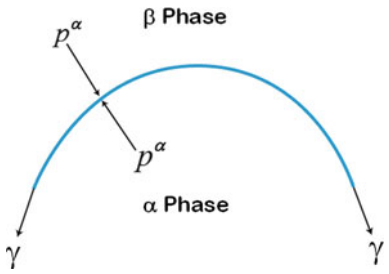

Fig. 1.53 Pressure difference across a curved surface

$$\ln\left(\frac{p^{c}}{p^{\infty}}\right) = \left(\frac{\gamma v_m^L}{RT}\right)\left(\frac{2}{r_m}\right) \tag{1.121}$$

where p^{c} and p^{∞} are the vapor pressures over the curved surface of mean curvature $r_m\left(\frac{1}{r_m} = \frac{1}{2}\left(\frac{1}{r'} + \frac{1}{r''}\right)\right.$ and a flat surface ($r = \infty$) and v_m^L is the molar volume of the liquid. There is a convention to assign a positive sign to r_m when it lies in the liquid phase and a negative sign when it lies in the vapor phase. Equation 1.121 can be used, for example, to rationalize capillary condensation or in the treatment of nucleation (Chap. 11). Condensation occurs when the actual vapor pressure exceeds the equilibrium vapor pressure. If the surface is curved, the Kelvin Eq. 1.121 shows that the actual pressure can be significantly lower than equilibrium pressure and thus, condensation in pores in the solid (if the liquid wets the solid) or between closed spaced solid particles may occur.

The effect pressure on the phase equilibrium can be investigated with Gibbs energy diagrams. According to the definition, the Gibbs free energy of a phase depends upon the pressure according to $g = g(0) + pv_m$ where 0 denotes the atmospheric pressure. As discussed above, for condensed phases, the pv_m term can often be neglected if the pressure is not exceptionally high. However, it plays an important role if the two phases in equilibrium are under different pressures. This occurs, as shown above, when the interface is curved and is caused by the surface tension (or energy) of the curved interfaces. Next, we shall briefly discuss how the equilibrium between two phases is changed by the introduction of increased pressure. The two g curves are displaced upward by the amounts $p^{\alpha}v_m^{\alpha}$ and $p^{\alpha}v_m^{\beta}$, respectively. This takes place even with phase compositions so well defined that they will not change (Fig. 1.54a). The change in g_B, for instance, can be evaluated as follows. By comparing the triangles in Fig. 1.54b, one obtains

$$\frac{g_B - p^{\beta}v_m^{\beta}}{g_B - p^{\alpha}v_m^{\alpha}} = \frac{X_A^{\beta}}{X_A^{\alpha}} \tag{1.122}$$

where ΔG_B equals $g_B(p^{\alpha}, p^{\beta}) - g_B(0)$. The above equation can be rearranged to give

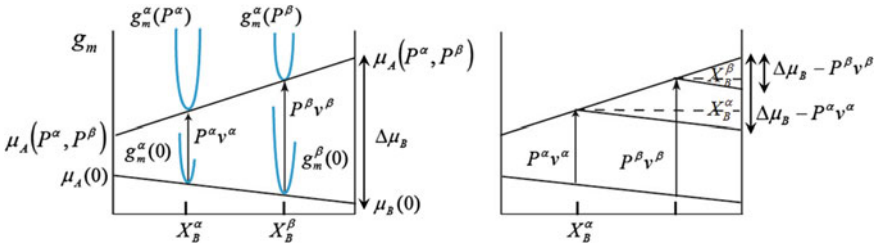

Fig. 1.54 Effect of pressure on phase equilibrium between two stoichiometric phases

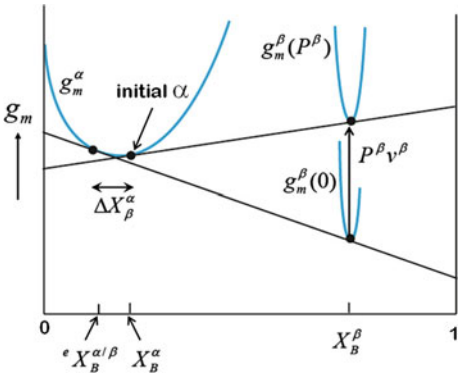

Fig. 1.55 Nucleation of β phase from α-matrix

$$g_{\mathrm{B}}(p^\alpha, p^\beta) - g_{\mathrm{B}}(0) = \frac{X_{\mathrm{A}}^\alpha p^\beta v_m^\beta - X_{\mathrm{A}}^\beta p^\alpha v_m^\alpha}{X_{\mathrm{A}}^\alpha - X_{\mathrm{A}}^\beta} \tag{1.123}$$

A similar equation can be derived also for g_{A}. When considering a spherical β particle in an α matrix, it is usually assumed that the matrix is under atmospheric pressure and one can therefore use $p^\alpha = 0$. One then obtains a diagram shown in Fig. 1.55. The compositional change, $\Delta X_{\mathrm{B}}^\alpha$ (for small values), can be written as

$$\Delta X_{\mathrm{B}}^\alpha = \frac{p^\beta v_m^\beta}{d^2 g^\alpha / dX_{\mathrm{B}}^2 \cdot \left(X_{\mathrm{B}}^\beta - X_{\mathrm{B}}^\alpha\right)} \tag{1.124}$$

By inserting $p^\beta = \frac{2\gamma}{r}$ and utilizing the regular solution model, one obtains

$$\Delta X_{\mathrm{B}}^\alpha = \frac{2\gamma v_m^\beta X_{\mathrm{A}}^\alpha X_{\mathrm{B}}^\alpha}{r\left(RT - 2L_{AB}^\alpha X_{\mathrm{A}}^\alpha X_{\mathrm{B}}^\alpha\right)\left(X_{\mathrm{B}}^\beta - X_{\mathrm{B}}^\alpha\right)} \tag{1.125}$$

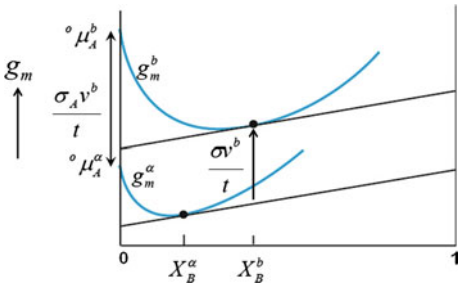

Fig. 1.56 Parallel tangent construction to investigate segregation

If both phases can vary in composition, the calculations become much more complicated.

It is also possible to use Gibbs energy diagrams to investigate the segregation of a given impurity to grain boundaries (Fig. 1.56). This involves a so-called constant volume condition. If we assume that the interface can be approximated as a thin layer of a homogeneous phase with constant thickness and its own Gibbs energy function as well as that the partial molar volumes of all the phases (including the interfacial phase) are independent of composition, we can use parallel tangent construction to find the interfacial composition. In this case, we consider exchange of atoms (A and B) between the interface and the bulk. The number of atoms at the interface is considered to be constant. Thus, if atom A leaves the interface and enters the bulk and atom B moves into opposite direction at the same time, the Gibbs free energy should not change

$$\mu_{\mathrm{A}}^{\alpha} - \mu_{\mathrm{A}}^{b} = \mu_{\mathrm{B}}^{\alpha} - \mu_{\mathrm{B}}^{b} \tag{1.127}$$

where α refers to the bulk phase and b to interface. This can be rewritten as

$$\mu_{\mathrm{B}}^{b} - \mu_{\mathrm{A}}^{b} = \mu_{\mathrm{B}}^{\alpha} - \mu_{\mathrm{A}}^{\alpha} \tag{1.128}$$

which gives the slopes for the interfacial phase and for the bulk phase

$$\frac{dg^{b}}{X_{\mathrm{B}}} = \frac{dg^{\alpha}}{X_{\mathrm{B}}} \tag{1.129}$$

For interphase segregation, where the volume is not necessarily fixed other approaches, like that of Gibbs surface excess model, must be utilized. Any change of γ due to an appreciable addition of B can be obtained directly from the molar Gibbs energy diagram. For instance, if one wants to estimate the maximum segregation to a grain boundary (which can possibly occur), the construction shown in Fig. 1.57 can be used. This is based on the fact that the maximum amount to segregate must certainly be less than the segregation needed in order to make the surface tension

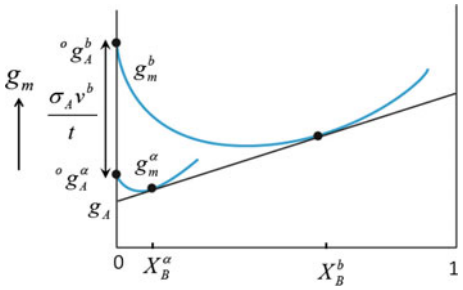

Fig. 1.57 The determination of the upper limit for segregation

to disappear, as this has never been observed experimentally. The surface tension will vanish when the two parallel tangents coincide as shown in Fig. 1.57. This gives the hypothetical upper limit for interfacial segregation. Several more advanced treatments of intergranular segregation have been published during recent decades [20–22].

1.15.2 Ternary Molar Gibbs Energy Diagrams

The molar Gibbs free energy diagrams for ternary systems can also be conveniently drawn, as shown in Fig. 1.58. In this case, the molar Gibbs energies of solution phases are represented by surfaces instead of curves and the common tangent construction is replaced by a common tangent plane. In Fig. 1.58, the ternary equivalent of the process shown in Fig. 1.18 is presented. As mentioned above, the chemical equilibrium condition of the equal value of the chemical potential of each component leads to the common tangent construction in a binary system and to the *common tangent plane* construction in a ternary system. In the latter case, the values for the chemical potentials are read from the intersections of the tangent plane with the three edges of the diagram. As shown in Fig. 1.58, the tangent plane is allowed to roll under the given Gibbs energy surfaces until a common tangent plane for the curves is established. Figure 1.58a shows the starting point of the process. The initial compositions of the phases are given by the points where the tangent plane touches the free energy surface of the given phase. The values for the chemical potentials for each component in a given phase are obtained for the intersection points of the corresponding tangent planes. As can be seen, the chemical potentials for components A, B, and C are hardly equal in the two phases to start with. Thus, there is driving force for diffusion of the components. The tangent plane drawn with green color belongs to the β-phase (blue curve) and that with red to the α-phase (red curve). The plane drawn with black lines shows the Gibbs energy for a purely mechanical mixture of A, B, and C. From the composition profile in Fig. 1.58a, it can be seen that no interdiffusion

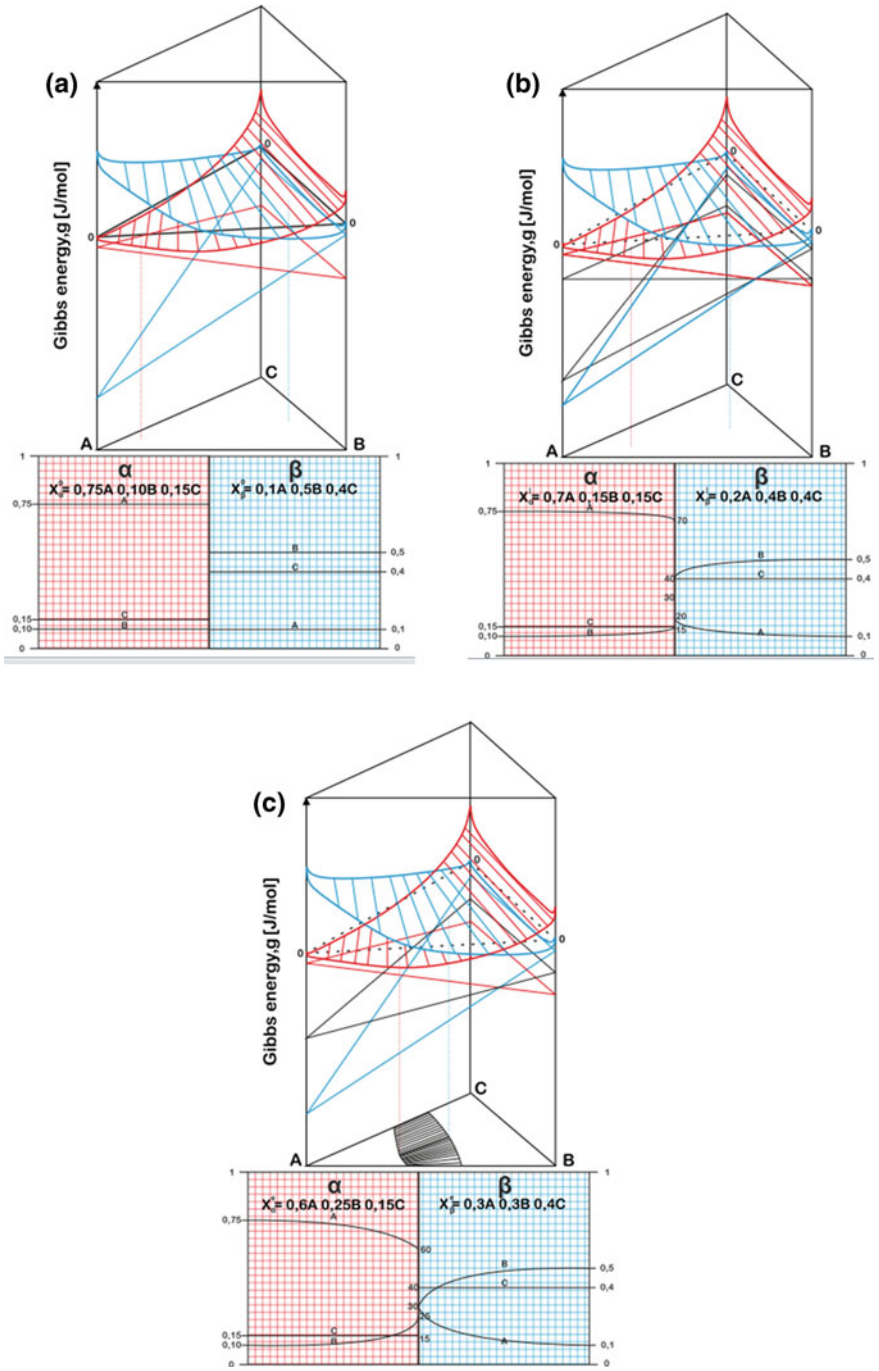

Fig. 1.58 **a** Ternary Gibbs energy diagram with composition profile showing the initial situation for the diffusion couple α/β. **b** Ternary Gibbs energy diagram with composition profile showing the situation for the diffusion couple α/β after some interdiffusion has taken place, but the equilibrium has not been reached. **c** Ternary Gibbs energy diagram with composition profile showing the final equilibrium situation for the diffusion couple α/β

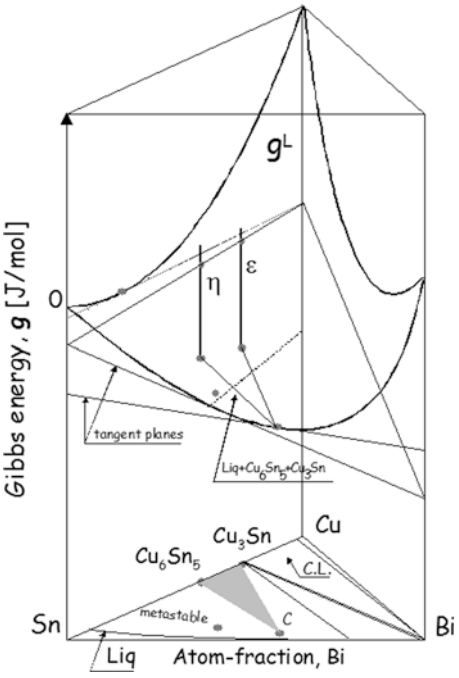

Fig. 1.59 Ternary molar Gibbs energy diagram from the BiCuSn system at 235 °C [17]

has taken place. As can be seen from Fig. 1.58b, the tangent planes start to roll under the Gibbs free energy surfaces and, consequently, the chemical potentials of the components start to change. It is evident that Fig. 1.58b represents an intermediate stage in the process as the chemical potentials for components A, B, and C are not yet equal in both phases. From the composition profile of the α/β-diffusion couple in Fig. 1.58b, it can be seen that the compositions at the interface have been changed. Further, it is noticed that only components A and B diffuses in this case and component *C* is immobile. The end-member compositions are unaffected by the diffusion process as required (See Chap. 3 for further discussion). The final equilibrium situation is given in Fig. 1.58c, in which the common tangent plane is shown. As can be seen, the chemical potentials for the components are now equal at each phase and thus, the chemical equilibrium condition is fulfilled.

Another example from a ternary Gibbs energy diagram is shown in Fig. 1.59 which represents the stability of phases in the BiCuSn system at 235 °C. There are two intermetallic compounds, (Cu_6Sn_5 (η) and Cu_3Sn (ε)), which enter the stable equilibrium at this temperature. A vertical section ($SnBi_{eut} \rightarrow Cu$) through this diagram is shown in Fig. 1.60. As can be seen, the section resembles the Gibbs energy diagram of the binary Cu-Sn system, but it is not exactly the same. The "tangent lines" drawn in the diagram (Fig. 1.60) are not identical to the tangent lines in Fig. 1.52, but are 2D sections through the corresponding tangent planes.

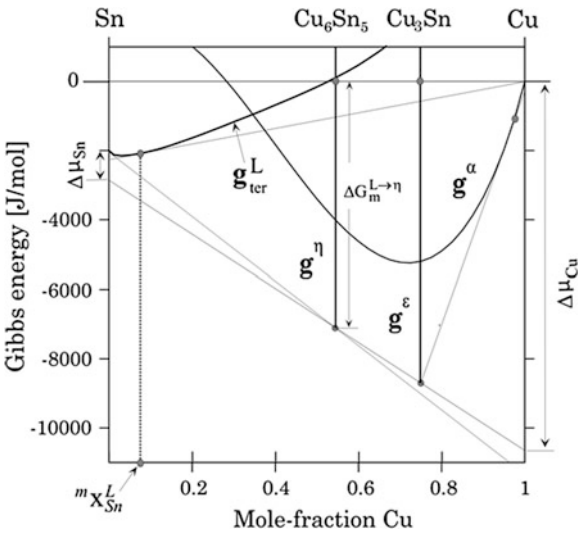

Fig. 1.60 A vertical section through the Gibbs energy diagram shown in Fig. 1.59 [17]

1.16 Interdependence of Chemical Potentials: Gibbs–Duhem Equation

In this section, we shall derive the Gibbs–Duhem relation, which will be useful in proceeding chapters to find the relation between diffusion under chemical potential gradient with the diffusion in the absence chemical potential gradient as the driving force. From our point of view, the application of Gibbs–Duhem equation to obtain the change in the chemical potential because of the change in composition of an alloy is the most important use of the general relation. For the sake of explanation, let us consider the free energy versus composition diagram, as shown in Fig. 1.61. First, we consider the point P and from the slope at that we can determine the chemical potential of elements A and B at that point as μ_A^P and μ_B^P, respectively. Now suppose we make a small change in the composition and move to the point Q. Again from the slope of the free energy at that point, we can find the chemical potential of elements as μ_A^Q and μ_B^Q. So it is apparent that the change in chemical potential of elements, A and B, because of the change in composition is $-d\mu_A = \left(\mu_A^Q - \mu_A^P\right)$ and $-d\mu_B = (\mu_B^Q - \mu_B^P)$, respectively. Further, from any point P or Q, it can be written that

$$-\frac{d\mu_A}{X_B} = \frac{d\mu_B}{X_A} = \frac{d(\mu_B - \mu_A)}{1} \tag{1.130}$$

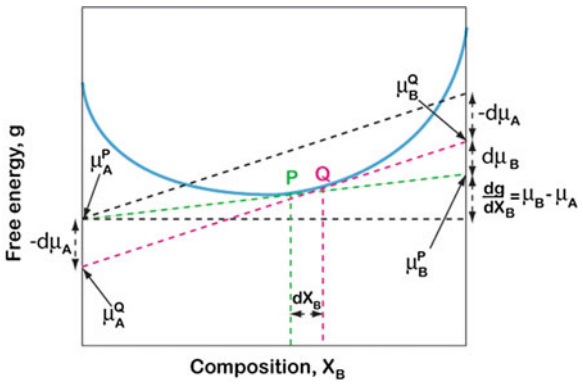

Fig. 1.61 The change in chemical potential because of the change in composition is shown to derive the Gibbs–Duhem equation

Further, from the slope, we can write

$$\frac{dg}{dX_B} = \frac{\mu_B - \mu_A}{1} \tag{1.131}$$

Combining Eqs. 1.130 and 1.131 and multiplying $X_A X_B$, the expression becomes

$$-X_A d\mu_A = X_B d\mu_B = X_A X_B \frac{d^2 g}{dX_B^2} dX_B \tag{1.132}$$

Further, it can be shown that

$$\frac{d^2 g}{dX_B^2} = \frac{d^2 g}{dX_A^2} \tag{1.133}$$

It follows that

$$X_A d\mu_A + X_B d\mu_B = 0 \tag{1.134}$$

Equation 1.134 is known as Gibbs Duhem equation. It illustrates clearly that chemical potentials, or any other partial thermodynamic properties [5], cannot be changed independently. On the contrary, for example, in a binary system considered here, when the one chemical potential is changed, the other one must change also. This is evident also in ternary systems as shown in Fig. 1.58a–c. Further, we can derive one another useful relation from Eq. 1.134. From Eqs. 1.132 and 1.133 follows

$$-X_A \frac{d\mu_A}{dX_B} = X_B \frac{d\mu_B}{dX_B} = X_A X_B \frac{d^2 g}{dX_B^2} = X_A X_B \frac{d^2 g}{dX_A^2} \tag{1.135}$$

and consequently,

$$\mu_B =^{\circ} \mu_B + RT \ln a_B =^{\circ} \mu_B + RT \ln \gamma_B X_B \tag{1.136a}$$

$$\mu_A =^{\circ} \mu_A + RT \ln a_A =^{\circ} \mu_A + RT \ln \gamma_A X_A \tag{1.136b}$$

From Eq. 1.136, the following expression can be obtained

$$\begin{aligned} &\frac{d\mu_B}{dX_B} = RT\left[\frac{d\ln\gamma_B}{dX_B} + \frac{d\ln X_B}{dX_B}\right] = RT\left[\frac{1}{\gamma_B}\frac{d\gamma_B}{dX_B} + \frac{1}{X_B}\right] = \frac{RT}{X_B}\left[1 + \frac{d\ln\gamma_B}{d\ln\gamma_B}\right] \\ &\frac{d\mu_B}{dX_B} = \frac{RT}{X_B}\frac{d\ln a_B}{d\ln X_B} \end{aligned} \tag{1.137}$$

Similarly from Eq. 1.137, since $X_A + X_B = 1$, follows

$$\begin{aligned} &\frac{d\mu_A}{dX_B} = -RT\left[\frac{d\ln\gamma_A}{dX_A} + \frac{d\ln X_A}{dX_A}\right] = -RT\left[\frac{1}{\gamma_A}\frac{d\gamma_A}{dX_A} + \frac{1}{X_A}\right] = \frac{RT}{X_B}\left[1 + \frac{d\ln\gamma_A}{d\ln\gamma_A}\right] \\ &\frac{d\mu_A}{dX_B} = \frac{RT}{X_B}\frac{d\ln a_A}{d\ln X_A} \end{aligned} \tag{1.138}$$

Using Eq. 1.137 in Eq. 1.138, we obtain

$$\frac{d\ln a_A}{d\ln X_A} = \frac{d\ln a_B}{d\ln X_B} = \frac{X_A X_B}{RT}\frac{d^2 g}{dX_A^2} = \frac{X_A X_B}{RT}\frac{d^2 g}{dX_B^2} \tag{1.139}$$

This is again the thermodynamic factor discussed in Sect. 1.15.

1.17 Molar Volume of a Phase and Partial Molar Volumes of the Species

Many times it is important to determine the molar volume of the phases and partial molar volume of the species. By definition, the molar volume, v_m, of a phase can be determined from

$$v_m = \frac{v_{\text{cell}}}{n_a} N_{\text{Avo}} \tag{1.140}$$

where $v_{\text{cell}}(m^3)$ is the volume of the unit cell determined from the known data on the lattice parameters available in the literature, N_0 is the Avogadro number (6.023×10^{23} mol^{-1}), and n_a is the number of atoms in the unit cell.

When virtually no structural vacancies are present in a unit cell, the number of atoms, n_a, in the last equation can be replaced by the number of lattice sites, n_s.

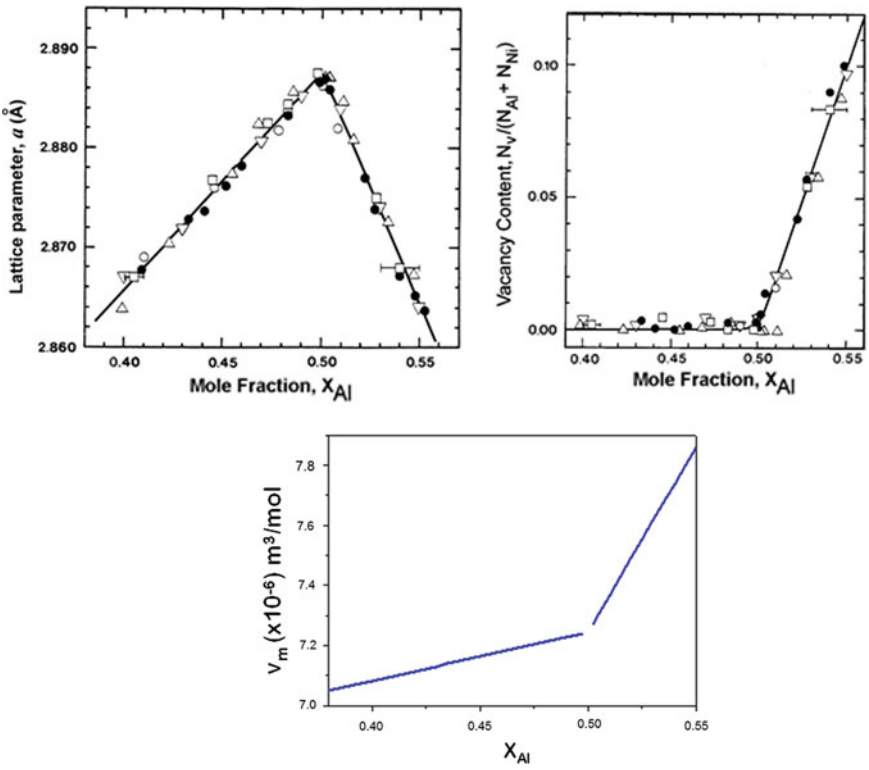

Fig. 1.62 The change in **a** lattice parameter and **b** vacancy concentration of NiAl phase and **c** molar volume of the phase (**a** and **b** are from [23])

We can neglect the amount of thermal vacancies, since this number is very small. On the other hand, when constitutional vacancies are created in the structure and if the number is appreciable, we should consider this for the calculation of molar volumes. In this case, we can write $n_a = n_s - n_V$, with n_V being the number of vacancies present in the unit cell.

So, when there are no structural vacancies present in the structure, the calculation of molar volume is rather straightforward. However, for further clarification, we like to extend our discussion to the calculation which contains structural vacancies. For this purpose, we consider the B2 NiAl phase in an Ni–Al system. The homogeneity range of the B2 phase is shown in Fig. 1.62. It can be seen that there is a wide homogeneity range on both sides of the stoichiometry. As will be discussed in Chap. 2, deviation from the homogeneity in the Ni-rich side is achieved by the Ni-antisite defects (Ni_{Al} that is Ni atom occupying the sublattice belongs to Al atom), whereas deviation in the Al-rich side is achieved by the presence of triple defect ($2V_{Ni} + Ni_{Al}$ composed of two vacancies in sublattice belonging to Ni atoms and one Ni atom occupying a site in a sublattice belonging to Al atoms).

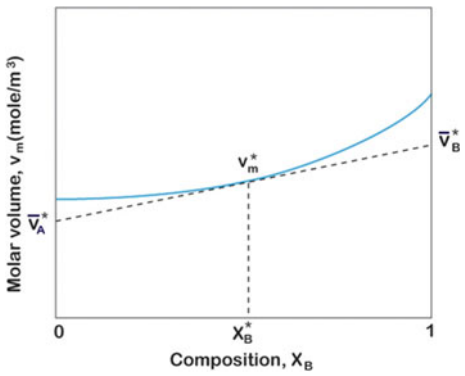

Fig. 1.63 The determination of partial molar volume of the species, *A* and *B* in a binary system is shown

So to calculate the molar volume in the Ni-rich side is straightforward and the number of lattice positions can be used to count the number of atoms. However, in the Al-rich side, we need to consider the number of antisites for the calculation of molar volume. The molar volume of the phase at different compositions can be calculated from the available data on the lattice parameter and vacancy concentration, as shown in Fig. 1.62a and b, respectively. The calculated molar volume of the phase is shown in Fig. 1.62c.

The partial molar volume of the species can be defined as the change in molar volume because of the addition of a very small amount of the species. The partial molar volume of the species A$(\bar{v}_A)$ and B$(\bar{v}_B)$ is related with the molar volume of a phase, or an alloy (v_m) is related by

$$v_m = X_A \bar{v}_A + X_B \bar{v}_B \tag{1.141}$$

Thus, the partial molar volume of the species at a particular composition, X_B^*, can be calculated by taking slope at v^* from the molar volume versus composition diagram, as shown in Fig. 1.63. The values $\bar{v}_A^*$ and $\bar{v}_B^*$ are the partial molar volumes of the species A and B, respectively, at X_B^*. This is a property diagram similar to that which was extensively used in Sect. 1.15 (the molar Gibbs energy diagram).

1.18 Few Standard Thermodynamic Relations

Derivations for a few relations can be found in [24]. We have previously shown that the mole fraction and the atomic fraction are the same in the systems we have considered. We commonly present the diffusion data with respect to atomic fraction or atomic percentage, and we shall use them for further derivations.

$$N_A + N_B = 1 \tag{1.142}$$

where N_A and N_B are the atomic fractions of A and B.

$$\begin{aligned} C_A &= \frac{X_A}{v_m} = \frac{N_A}{v_m} \\ C_B &= \frac{X_B}{v_m} = \frac{N_B}{v_m} \end{aligned} \tag{1.143}$$

where C_i is the concentration of species i and v_m is the molar volume at the composition of interest.

$$N_A \bar{v}_A + N_B \bar{v}_B = v_m \tag{1.144}$$

where ν_i is the partial molar volume of the species i. By utilizing (1.142 and 1.143), we get

$$C_A + C_B = \frac{N_A}{v_m} + \frac{N_B}{v_m} = \frac{(N_A + N_B)}{v_m} = \frac{1}{v_m} \tag{1.145}$$

On the other hand by substituting $N_i = C_i v_m$ from (1.143) to (1.144), we obtain

$$\begin{aligned} C_A v_m \bar{v}_A + C_B v_m \bar{v}_B &= v_m \\ v_m (C_A \bar{v}_A + C_B \bar{v}_B) &= v_m \\ C_A \bar{v}_A + C_B \bar{v}_B &= 1 \end{aligned} \tag{1.146}$$

Since the molar volumes also follow Gibbs–Duhem relation, which was presented in Sect. 1.16, we can write

$$X_A d\bar{v}_A + X_B d\bar{v}_B = 0 \quad \text{or} \quad N_A d\bar{v}_A + N_B d\bar{v}_B = 0 \tag{1.147}$$

By multiplying this with total concentration C, one gets $C(N_A d\bar{v}_A + N_B d\bar{v}_B) = 0$ $(C_A + C_B)(N_A d\bar{v}_A + N_B d\bar{v}_B) = 0$, and from (1.145), we see that $\left(\frac{1}{v_m}\right)(N_A d\bar{v}_A + N_B d\bar{v}_B) = 0$, which based on (1.143) reduces to

$$C_A d\bar{v}_A + C_B d\bar{v}_B = 0 \tag{1.148}$$

When taking total differential from (1.146), we get

$$C_A d\bar{v}_A + C_B d\bar{v}_B + \bar{v}_A dC_A + \bar{v}_B dC_B = 0$$

According to (1.148), the first two terms are zero and, thus,

$$\bar{v}_A dC_A + \bar{v}_B dC_B = 0 \tag{1.149}$$

When we consider that molar volume is not constant

$$dC_{\mathrm{A}} = \left(\frac{\bar{v}_{\mathrm{B}}}{v_m^2}\right) dN_{\mathrm{A}}$$
$$dC_{\mathrm{B}} = \left(\frac{\bar{v}_{\mathrm{A}}}{v_m^2}\right) dN_{\mathrm{B}} \tag{1.150}$$

References

1. K. Denbigh, The Principles of chemical equilibrium, 3rd ed., Cambridge University Press, Cambridge, U.K, 1978.
2. E.A. Guggenheim, Thermodynamics, Elsevier Science, The Netherlands, 1967.
3. D. Kondepudi and I. Prigogine, Modern Thermodynamics From Heat Engines to Dissipative Structures, Wiley, 1998.
4. P. Atkins and J. DePaula, Physical Chemistry, Macmillan Higher Education, 2009.
5. N. A. Gokcen, Thermodynamics, Techscience incorporated, 1975.
6. J.K. Kivilahti, Theory of metallic solutions, Otakustantamo, 1982, (in Finnish).
7. L. Darken and R. Gurry, Physical Chemistry of Metals, McGraw-Hill, (1953).
8. G.N. Lewis and M. Randall, Thermodynamics, revised by K. Pitzer and L. Brewer, McGraw-Hill, 1961.
9. D. Gaskell, Introduction to Metallurgical Thermodynamics, McGraw-Hill, Tokyo, 1973.
10. M. Hillert, Phase Equilibria, Phase Diagrams and Phase Transformations: Their Thermodynamic Basis, Cambridge Univ. Press, 1998.
11. H. Lukas, S. Fries, and B. Sundman (2007) Computational Thermodynamics- The Calphad Method, Cambridge University Press (2007).
12. Rönkä K., van Loo F.J.J. and. Kivilahti J.K, Metal. Mater. Trans. A, 29A (1998) 2951.
13. T. Mattila, V. Vuorinen and J.K. Kivilahti, J. of Mater. Res. 19 (2004) 3214.
14. Laurila T., Zeng K., Molarius J., Suni I., and Kivilahti J.K., Journal of Applied Physics 91 (2002) 5391.
15. Hillert M., "The Uses of Gibbs Free Energy-Composition Diagrams", in Lectures on the Theory of Phase Transformations, (Ed. H.I. Aaronson, The Metallurgical Society of the AIME, (1975)).
16. C. Cserhati, U. Ugaste, M. van Dal, N. Lousberg, A. Kodentsov, and F.J.J. van Loo, Defect and Diffusion Forum 194-199 (2001) 189.
17. T. Laurila, V. Vuorinen and J.K Kivilahti, Materials Science and Engineering – R, R49, (1-2), pp. 1-60, (2005).
18. Laurila T, Vuorinen V. and Paulasto-Kröckel M, Materials Science and Engineering – R, R68 (2010) 1-38.
19. R. Wang and Y. Kim, Metall Trans 5 (1974) 1973.
20. E. Hondros and M. Seah, Metall. Trans. A, 8A (1977) 1363.
21. M. Guttmann, Metall. Trans. A 8A (1977) 1383.
22. E. Guggenheim, Trans. Faraday Soc, 36 (1940) 397.
23. Y.A. Chang and J.P. Neumann, Prog. Solid State Chem. 14 (1982) 221.
24. L. Trimble, D. Finn and A. Cosgarea, Acta Metallurgica 13 (1965) 501.

Chapter 2
Structure of Materials

In this chapter, we will briefly go through the hierarchical structure of materials. First, the atomic bonding and crystal structures are covered briefly. Then, the emphasis is placed on the presence of different types of defects and imperfections. Since point defects provide the fundamental basis for understanding the atomic mechanisms of diffusion, they are discussed in detail. In addition, the crystal structures including also the defect structures of intermediate phases and ordered binary intermetallics are quantitatively presented.

2.1 Hierarchical Structure of Materials

Most properties are actually highly structure sensitive. Therefore, it is of utmost importance to understand the basis for the structure of materials to be able to control the properties and reliability of engineering materials. Microstructure is a general term used to cover a wide range of structural features, ranging from those visible to the naked eye (for instance, macrostructure) to those corresponding to the inter-atomic distances in the crystal lattice (for instance, nanostructure). In other words, the size scale of the structural features ranges about 10 orders of magnitude. Therefore, in order to observe the structural features at these different scales, as shown in Fig. 2.1 [1], adequate resolving power is required.

Frequently, a large variety of structural features on different levels is noteworthy. Therefore, in the following chapters, the hierarchical structure of materials is presented.

2.2 Atomic Bonding

An atom can exist in different energy states according to the kind of interaction it has with neighboring atoms. The nature of this interaction is defined by the type of atomic bonding. The bonds can be categorized into two classes according to the bond energy. The primary bonds (>100 kJ/mol) are ionic, covalent, and metallic.

A. Paul et al., *Thermodynamics, Diffusion and the Kirkendall Effect in Solids*,
DOI: 10.1007/978-3-319-07461-0_2,

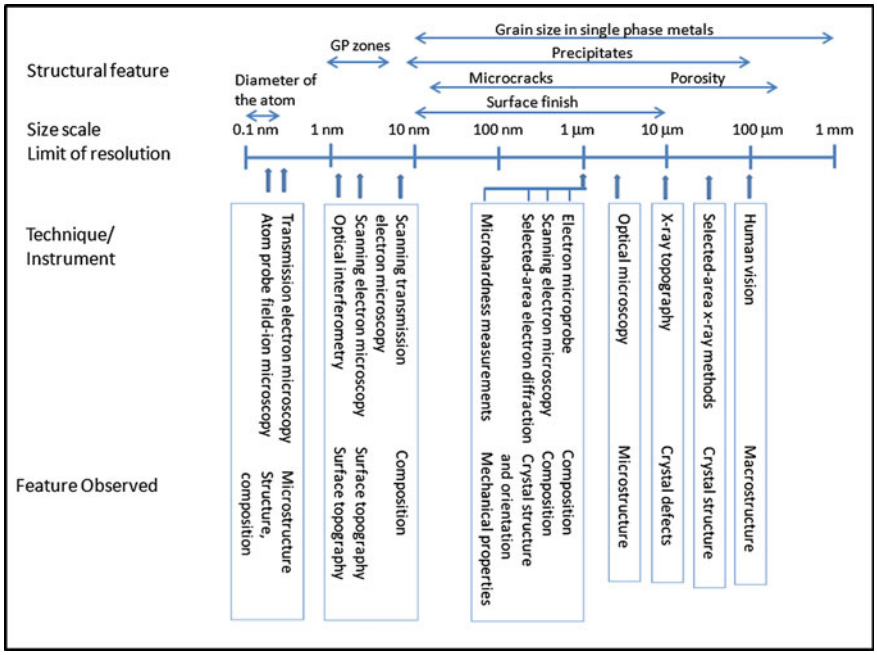

Fig. 2.1 Size scale relating structural features of metals to techniques of observation (redrawn from [1])

It is to be emphasized that in many materials, the bonding falls between these distinct categories. For example, the Si–O bond in silica is approximately half ionic and half covalent. The secondary bonds are of the van der Waals, or hydrogen, type. Many of the material properties, such as Young's modulus, the melting point, and the coefficient of thermal expansion (CTE) (as seen from Table 2.1), are related to the bond energy.

Ionically bonded crystals that possess high binding energies are generally considered to be hard, brittle, insulating, and thermally stable. The bond is based on the equilibrium between attractive and repulsive coulombic (electrostatic) forces. The ions are ordered in the crystal in such a non-directional manner that a macroscopically neutral material is generated. The structures typically have simple stoichiometry such as AB, AB_2, and A_2B.

Covalent crystals and molecules are based on bonds that share the pair of electrons in the direct line between the atoms. The directional bonding is caused by the concentrated electron density between the nuclei. Covalent bonding includes many types of interactions such as σ-bonding and π-bonding. These bonds can be either saturated, as in gas molecules H_2, N_2, O_2 …, or unsaturated, as in polymer's or covalent crystals C, Si, SiC …. Materials that possess bonds of a covalent nature are either insulators or semiconductors.

The nature of the atomic bond in metallic crystals differs from those of ionically and covalently bonded materials. The fundamentals of ionic and covalent bonds are

Table 2.1 Atomic bonding types, bonding energies, and respective melting temperatures for various substances

Bonding type	Substance	Bonding energy (kJ/mol)	Young's modulus (GPa)	CTE (10^{-6})	Melting temperature (°C)
Ionic	NaCl	640	39.98	44	801
	MgO	1,000	249	10.8	2,800
Covalent	Si	450	129	2.8	1,410
	C (diamond)	713	1,220	1.1	>3,550
Metallic	Hg	68		182	−39
	Al	324	69	23	660
	Fe	406	196	12	1,538
	W	849	344	4.5	3,410
Van der Waals	Ar	7.7			−189
	Cl_2	31			−101
Hydrogen	NH_3	35			−78
	H_2O	51	8.6–12 (ice)	51 (ice)	0

based on chemical valence. However, in metallic bonding, the theory enables the rationalization–typical metallic properties in addition to the aspect of the linking of atoms. By releasing the valence electrons the metal atoms in crystal can lower their energy state compared to individual atom. In this case the electrons are always close to nucleus (low potential energy region) but are not localized (i.e. cannot be associated with specific atom) so the kinetic energy is not increased too much. When summarized over the crystal this leadsto a stable structure. The bonds act between identical and different metallic atoms, as is revealed by the formation of numerous element and alloy structures. Typically, metallic atoms have either 8 or 12 neighboring atoms between which the bonds act. These resonating bonds usually permit plastic deformation and easy electron transfer throughout the structure.

2.3 Crystal Lattice

The formation of a crystal structure occurs as a result of bonding between atoms. Strong non-directional bonding typically allows atoms to pack efficiently, exhibiting planes of high atomic density containing close-packed directions. Crystals are thus solids in which all of the atoms occupy well-defined locations, being ordered across the whole material. These locations are defined by a crystal lattice, which is an infinite pattern of points, each of which having the same surroundings in the same orientation. Therefore, lattice is a mathematical concept out of which any point can be used as the origin for defining any other lattice points. There are only 14 possible three-dimensional lattices, called Bravais lattices, from which all crystal structures can be built as shown in Fig. 2.2.

It is to be noted that the crystal structure of a simple pure metal and that of a complex protein may both be described in terms of the same lattice, but the

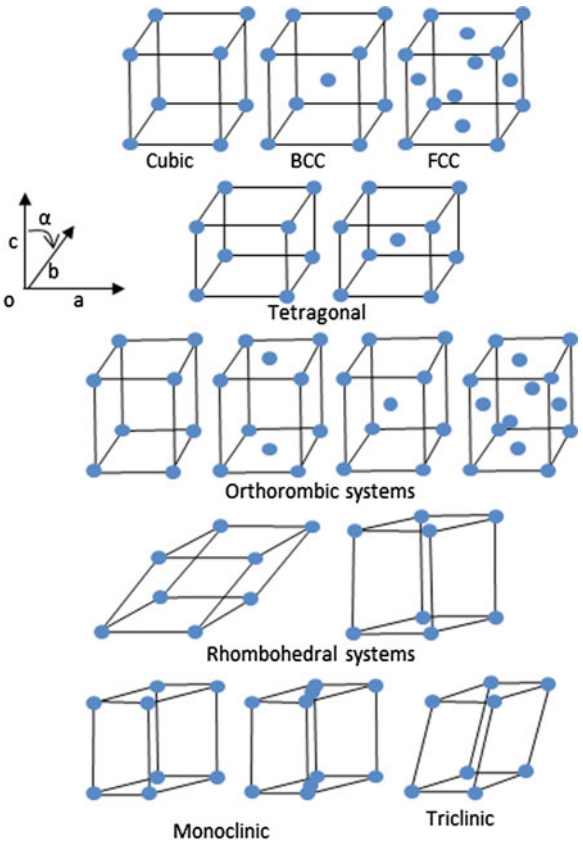

Fig. 2.2 Bravais lattices

number of atoms allocated to each lattice point (i.e., motifs) can vary from one to few thousands. Thus, a crystal structure is composed of a lattice plus a motif. The unit cells can be either simply primitive, body centered, face centered, or base centered. A primitive unit cell contains only a single lattice point, whereas a base-centered and body-centered cell contains two lattice points and a face-centered cell contains four lattice points.

The fundamentals of the crystal symmetry, planes, and directions as well as their indexing and nomenclature can be found from many excellent textbooks, for instance [2, 3]. Therefore, only the most common crystal types for pure metals and alloys, i.e., the close-packed face-centered cubic (FCC), body-centered cubic (BCC), and hexagonal close-packed (HCP) crystals, are presented in brief here. The atomic arrangement of the FCC and HCP crystals are shown in Fig. 2.3, where the location of the atom in the third layer defines whether the structure becomes hexagonal close packed (left, ABAB… arrangement) or FCC (right, ABCABC… arrangement). BCC crystals are not closely packed, and therefore, they contain more empty spaces (tetrahedral and octahedral interstitial sites) as can be seen from Fig. 2.4 and Table 2.2.

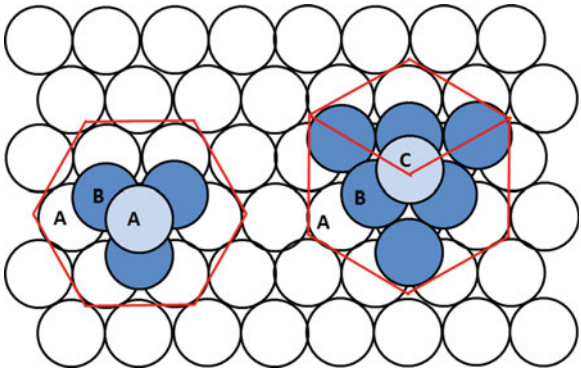

Fig. 2.3 Close-packed arrangements

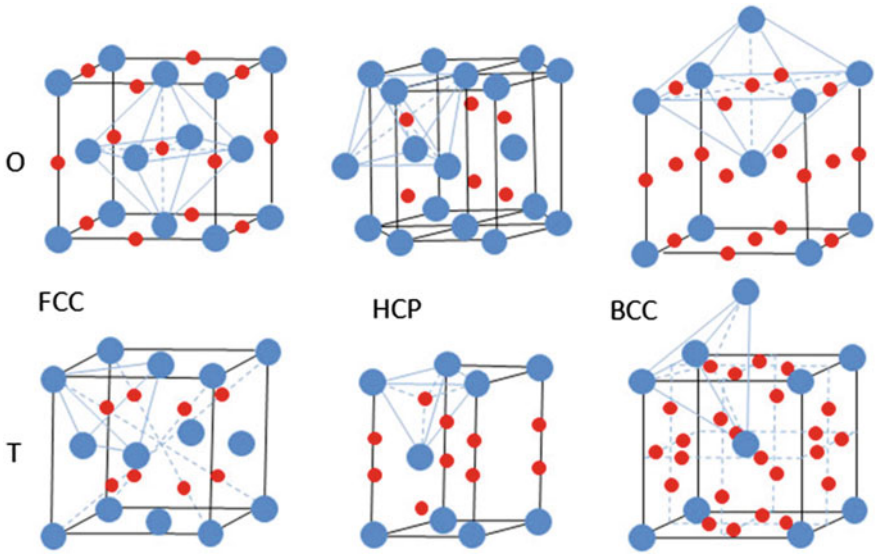

Fig. 2.4 Octahedral (*O*) and tetrahedral (*T*) interstitial sites in FCC-, HCP-, and BCC-type metals

2.4 Grain Structure

Grain structure is composed of small crystals that form a three-dimensional aggregate. The main characteristics are grain size, shape, and grain shape anisotropy. An impingement grain structure forms when grains grow until they meet or impinge, for example, during secondary recrystallization, producing characteristic ragged interfaces. A columnar grain structure is produced by unidirectional growth

Table 2.2 Number, location, and size of octahedral and tetrahedral sites in FCC, BCC, and HCP crystals [4]

Crystal structures	FCC	BCC	HCP
Number of atoms per unit cell	4	2	2
Coordination number of substitute atoms	12	8	12
Fraction of empty space	26.1 %	31.9 %	26.1 %
Octahedral sites	4	6	2
	0.414	155	0.414
	(1/2,0,0)	((1/2,0,0)	(1/3,2/3,1/4)
		(1/2,1/2,0)	
Number per unit cell	(1/2,1/2,1/2)		
Largest atom that fits in the site relative to the size of parent atom			
Coordinates that are reproduced by the symmetry			
Number of octahedral sites per parent atom	1	3	1
Coordination number of octahedral sites	12	8	12
Tetrahedral sites			
Number per unit cell			
Largest atom that fits in the site relative to the size of parent atom	8	12	4
Coordinates that are reproduced by the symmetry	0.225	0.291	0.225
	(1/4,1/4,1/4)	(1/2,1/4,0)	(1/3,2/3,1/8)
Number of tetrahedral sites per parent atom	2	6	2
Coordination number of tetrahedral sites	6	2	1
Closest packed planes and directions	{111}	{110}	{0001}
	<110>	<111>	<2110>
Typical metals having this structure	Al, Ni,	β-Ti,V,Cr	Mg, Zn, Cd,
	Cu, Ag,	Nb,	α-Ti, Zr,
	Au, Pb,γ-Fe,	Mo,W,	α-Co, Hf
	β-Co	α-Fe,Ta	

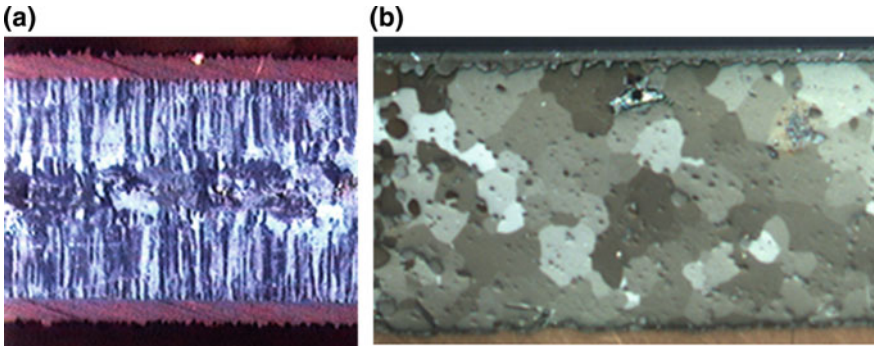

Fig. 2.5 Cross-polarized optical images from **a** columnar electrochemically plated Sn crystals between Cu equiaxed SnBi alloy and **b** recrystallized SAC solder interconnection after 3,000 cycles during a −40 °C ⟺ +125 °C thermal cycling test

such as in solidification or electrochemical plating (See Fig. 2.5a). Equiaxed grains can be formed by several processes such as recrystallization (See Fig. 2.5b) or solidification.

2.5 Defects

Many physical (especially mechanical) properties of solid materials are primarily based on the presence of different types of defects and imperfections. In other words, often specific material characteristics are deliberately fashioned by introducing a controlled amount of particular defect. The classification of crystalline imperfections is generally made according to either the geometry or dimensionality of the defect. Thus, the defects are typically divided into (i) point defects, which are related to a single or a few atomic positions, (ii) linear (or one-dimensional) defects, (iii) two-dimensional defects such as surfaces, interfaces, and different types of boundaries, and (iv) volume defects including inclusions, cracks, voids, and pores.

2.5.1 Point Defects

Point defects are central to gain an understanding of the atomic mechanisms of diffusion, and therefore, they are discussed in detail. There can be a few types of point defects present in the structure in an equilibrium condition (e.g., vacancies, impurities, and antistructure). Typically, in "pure" elements, vacancies and impurities are present in the structure. First, let us discuss the defects present in the pure elements and then turn to consider the defects present in the ordered phases.

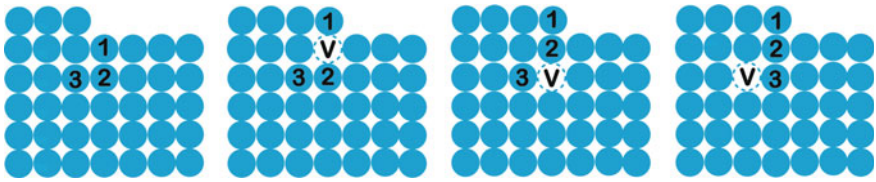

Fig. 2.6 Movement of atoms to create a vacancy at the interior

2.5.1.1 Equilibrium Vacancy Concentration in Pure Elements

The presence of vacancies in a pure element can be estimated using the same kind of treatment as was followed to find the free energy in a binary system, as explained previously in Sect. 1.8. The formation of vacancies can be explained, as shown in Fig. 2.6, where one atom diffuses from the interior of the crystal to the surface leaving a vacant site (the Schottky defect). There is another type of point defect, called the Frenkel defect, which is formed when an atom from a lattice site moves into an interstitial site thus leaving an empty space (vacancy) behind. For the sake of analysis, the presence of vacancies (V) in the element A can be visualized as a binary system of A and V. Now, the creation of vacancies is associated with the increase in internal energy because of broken bonds around the vacancies. In general, the equilibrium number of vacancies is so small that we can neglect the interaction between them. Thus, if we consider that the number of vacancies to be very small, then the increase in enthalpy resulting from the formation of vacancies can be written as

$$\Delta h \approx X_v \Delta h_v \tag{2.1}$$

Here, ΔX_v is the mole fraction of the vacancy and Δh_v is the increase in enthalpy caused by one mole of vacancies.

Factors contributing to Δh_v in metals are as follows:

1. Change in the volume. When an atom is removed from the center of the lattice and is placed at the surface, there is no change in the surface area, but rather an increase in the volume. This decreases the average energy of the electrons, giving a negative change in energy.
2. The removal of an atom leaves behind one atomic volume devoid of charge. Free electrons around the site tend to flow into this vacancy. Since there in no positive charge in the vacant site, the electrostatic energy is increased. To minimize this effect, there will be a sharp change in the electron density, which imposes in the end a higher kinetic energy for the electrons and an increase in the energy of the lattice.
3. When an atom is removed, the surrounding ions will relax into the vacancy decreasing slightly the energy of the final lattice.

If we now consider the total effect of all the above-mentioned three contributions, it is to be found that the sum is positive Δh_v; thus, it costs energy to form a vacancy.

The entropy can be divided into two parts, namely thermal entropy and configurational entropy (Sect. 1.5). Now, if we consider the change in entropy resulting from the mixing of vacancies with the pure element, there will be two types of contributions. First, there will be the change in the vibration pattern of the atoms next to vacancies because of extra free space. The increase in entropy caused by the extra freedom of vibration can be written as $X_v \Delta s_v$. Here, Δs_v is the increase in entropy for one mole of vacancies. Furthermore, there will be a change in configurational entropy considering the mixing of A and V and this can be expressed as (Note that we are considering $X_A + X_v = 1$)

$$\Delta s_{\text{mix}} = -R[X_v \ln X_v + (1 - X_v) \ln(1 - X_v)] \tag{2.2}$$

So the total change in entropy can be written as

$$\Delta s = \Delta s_v X_v - R[X_v \ln X_v + (1 - X_v) \ln(1 - X_v)] \tag{2.3}$$

Thus, the total free energy of the system containing vacancies can be written as

$$G = G_A + \Delta G \tag{2.4}$$

where G_A is the free energy of the defect free system of pure element A. ΔG is the change in free energy and can be expressed as (Sect. 1.3)

$$\Delta G = \Delta H - T\Delta S \tag{2.5}$$

From Eqs. 2.2 to 2.5, the total free energy of the system can be written as

$$G = G_A + X_v \Delta H_v - T\{\Delta S_v - R[X_v \ln X_v + (1 - X_v) \ln(1 - X_v)]\} \tag{2.6}$$

The change in enthalpy, entropy, and free energy due to an increasing number of vacancies can be seen in Fig. 2.7. It is apparent that ΔH increases linearly with the increase in vacancies, whereas $-T\Delta S$ decreases very rapidly in the beginning, but the rate of change decreases drastically. So it should be clear that in the beginning, the total free energy of the system will decrease with the creation of vacancies, but after a certain range, the free energy will start to increase because ΔH will start dominating. The system will therefore go through a minimum. We have seen before in Sect. 1.2 that a system will stay in equilibrium when it has minimum free energy. So we can state that the system will remain in equilibrium with free energy G_e. Further, we know that in the equilibrium condition,

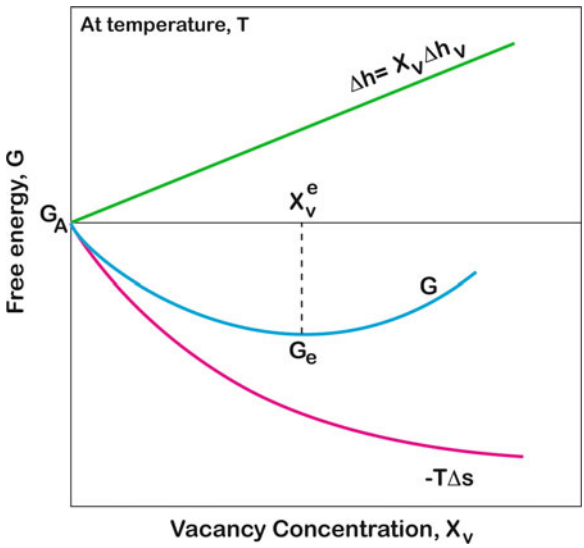

Fig. 2.7 The change in free energy of element A with the increase in vacancy concentration

$$\frac{dG}{dX_v} = 0 \tag{2.7}$$

So from the differentiation of G (Eq. 2.6) with respect to X_v and then by equaling it to zero, we can write

$$\Delta H_v - T\Delta S_v + RT\left[\ln X_v + X_v \cdot \frac{1}{X_v} - \ln(1 - X_v) - (1 - X) \cdot \frac{1}{(1 - X_v)}\right] = 0 \tag{2.8}$$

Since the number of vacancies that can be present in the system is very small, we can write $1 - X_v \approx 1$. Thus, Eq. 2.8 can be written as

$$\Delta H_v - T\Delta S_v + RT \ln X_v = 0 \tag{2.9}$$

So the relation for the equilibrium concentration of vacancies can be written as

$$X_v^e = X_v = \exp\left(-\frac{\Delta H_v - T\Delta S_v}{RT}\right) = \exp\left(-\frac{\Delta G_v}{RT}\right) \tag{2.10}$$

Here, X_v^e is the equilibrium concentration of vacancies at a particular temperature T, and ΔG_v is the activation energy for the formation of one mole of vacancies. Equation 2.10 can further be written as

$$X_v^e = X_v^0 \exp\left(-\frac{\Delta H_v}{RT}\right) \tag{2.11}$$

where ΔH_v is the activation enthalpy for the formation of vacancies and X_v^0 is the pre-exponential factor and is equal to

$$\exp\left(\frac{\Delta S_v}{R}\right) \tag{2.12}$$

It is to be noted here that if the vacancies are not present in their equilibrium fraction in a binary system, their chemical potential is not zero, and thus, it will transform the system essentially into a ternary one where, for instance, there is now more than one thermodynamic factor (Sect. 1.15).

2.5.1.2 Equilibrium Concentration of Impurities in Pure Elements

In many metals, especially in transition metals, interstitial atoms such as carbon, nitrogen, oxygen, and hydrogen can be present depending, to a large extent, on the metal. The presence of these impurities can change the properties of the material drastically. The maximum concentration of interstitial atoms that can be present depends on different factors such as the crystal structure of the metal and the size of the interstitial atoms. There are mainly two types of interstitial sites present in the structure: tetrahedral (surrounded by four solvent atoms) and octahedral (surrounded by six solvent atoms). However, since it has been observed that interstitial atoms typically prefer to occupy octahedral interstices (hydrogen is a known exception), we shall mainly consider this type of sites. The treatment to calculate the maximum solubility of interstitial atoms is slightly different to the treatment that was followed in the previous section to calculate vacancy concentration. This is because these atoms will occupy interstitial positions without displacing metal atoms which occupy normal lattice positions. To explain the treatment, let us first consider an element A, which has a BCC crystal structure and the presence of interstitial atoms, I, as shown in Fig. 2.8a. Possible octahedral interstitial positions in the BCC lattice are shown by black dots. In general, the size of the interstitial atoms is larger than the size of the interstitial site and furthermore, it cannot be smaller. So if any interstitial atom is present, the surrounding lattice will be strained. This means that the enthalpy of the system will be increased. If the increase in enthalpy resulting from the addition of one mole of interstitial atoms is Δh_I, then the total enthalpy increment of the system is expressed by

$$\Delta h = X_I \Delta h_I \tag{2.13}$$

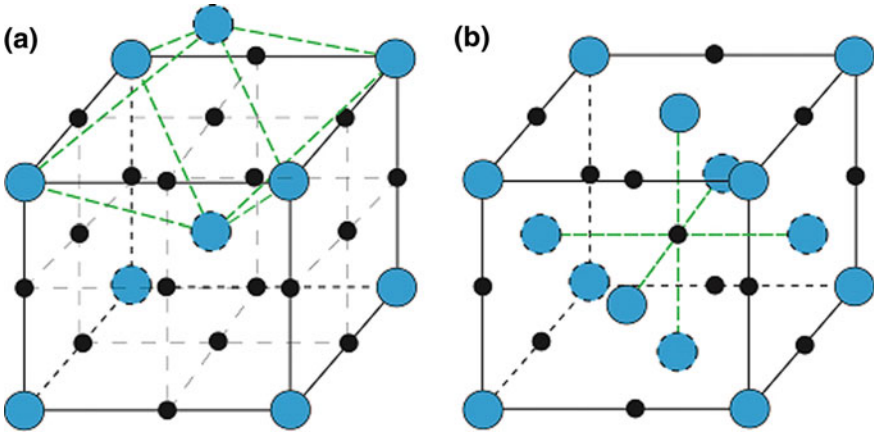

Fig. 2.8 Octahedral interstitial positions are shown by black dots in **a** BCC unit cell and **b** FCC unit cell

where $X_I = \frac{n_I}{N_0}$ is the mole fraction of the interstitial atoms present in the system and n_I is the total number of interstitial atoms. Again, there will be two different types of contribution to entropy. The first contribution comes from the fact that the vibration of atoms A next to the interstitial atoms will change from a normal mode of vibration and will be more random and irregular because of the distortion of the lattice. If we consider that the change of the entropy due to the change of vibration pattern is ΔS_I for one mole of interstitial atoms, then for X_I mole of interstitial atoms the change in entropy will be $X_\mathrm{I}\Delta S_\mathrm{I}$. Further, there will also be an increase in entropy because of the mixing of the solvent and interstitial atoms. Now, from the crystal structure, as shown in Fig. 2.8a for two solvent atoms, there are six sites for interstitial atoms. Additionally, we can write that for each A atom, there are three sites for interstitial atoms. So if we consider that there are N_0 numbers of A atoms, then there will be $3N_0$ numbers of sites available for interstitial atoms. In another sense, we can say that n_I atoms will randomly occupy n_I sites from $3N_0$ sites. Following statistical thermodynamics, the entropy of mixing can be written as

$$\Delta S_\mathrm{mix} = S - S_0 = k \ln w - k \ln 1 = k \ln w \tag{2.14}$$

where w is roughly the measure of randomness, S_0 is the entropy before mixing, and S is the entropy after mixing. Since in the case of a pure element, there is only one way by which atoms can be arranged, we can write $w = 1$. If we consider that interstitial atoms will choose their sites completely randomly, then we can write

$$w = \frac{3N_0!}{n_\mathrm{I}!(3N_0 - n_\mathrm{I})!} \tag{2.15}$$

According to Stirling's approximation,

$$\ln N! = N\ \ln N - N$$

Following Stirling's approximation, Eq. 2.15 can be derived as

$$\Delta S_{\text{mix}} = k[3N_0\ \ln 3N_0 - n_{\text{I}}\ \ln n_{\text{I}} - (3N_0 - n_{\text{I}})\ \ln(3N_0 - n_{\text{I}})] \tag{2.16}$$

Furthermore, Eq. 2.16 can be written as

$$\begin{aligned} \Delta S_{\text{mix}} &= R\left[3\ln 3N_0 - \frac{n_{\text{I}}}{N_0}\ln n_{\text{I}} - \frac{3N_0 - n_{\text{I}}}{N_0}\ln(3N_0 - n_{\text{I}})\right] \\ \Delta S_{\text{mix}} &= R\left[3\ln\frac{3N_0}{3N_0 - n_{\text{I}}} - \frac{n_{\text{I}}}{N_0}\ln\frac{n_{\text{I}}}{3N_0 - n_{\text{I}}}\right] \end{aligned} \tag{2.17}$$

Further, replacing $X_{\text{I}} = n_{\text{I}}/N_0$, Eq. 2.17 can be written as

$$\Delta S_{\text{mix}} = R\left[3\ln\frac{3}{3 - X_{\text{I}}} - X_{\text{I}}\ln\frac{X_{\text{I}}}{3 - X_{\text{I}}}\right] \tag{2.18}$$

So the total free entropy change can be written as

$$\Delta S = X_{\text{I}}\Delta S_{\text{I}} + R\left[3\ln\frac{3}{3 - X_{\text{I}}} - X_{\text{I}}\ln\frac{X_{\text{I}}}{3 - X_{\text{I}}}\right] \tag{2.19}$$

Moreover, the total free energy of the system after the addition of interstitial atoms can be written as

$$\begin{aligned} G &= G_A + \Delta G = G_A + \Delta H - T\Delta S_{\text{I}} \\ G &= G_A + X_{\text{I}}\Delta H_{\text{I}} - TX_{\text{I}}\Delta S_{\text{I}} - RT\left[3\ln\frac{3}{3 - X_{\text{I}}} - X_{\text{I}}\ln\frac{X_{\text{I}}}{3 - X_{\text{I}}}\right] \end{aligned} \tag{2.20}$$

As we have seen in the previous section that the equilibrium concentration of interstitial atoms can be found from $\frac{dG}{dX_{\text{I}}} = 0$. Thus,

$$\begin{aligned} &\Delta H_{\text{I}} - T\Delta S_{\text{I}} - RT\left[-\frac{3}{3 - X_{\text{I}}} - \frac{X_{\text{I}}}{X_{\text{I}}} - \ln X_{\text{I}} + \ln(3 - X_{\text{I}}) - \frac{X_{\text{I}}}{3 - X_{\text{I}}}\right] = 0 \\ &\Delta H_{\text{I}} - T\Delta S_{\text{I}} + RT\ \ln\frac{X_{\text{I}}}{3 - X_{\text{I}}} = 0 \end{aligned} \tag{2.21}$$

Further, the activation energy for the interstitial atom additions can be written as $\Delta g_{\text{I}} = \Delta H_{\text{I}} - T\Delta S_{\text{I}}$. Since we have considered that the concentration of impurities is much less, we can write $3 - X_{\text{I}} \approx 3$. So Eq. 2.21 can be written as

$$X_I = 3\exp\left(-\frac{\Delta g_I}{RT}\right) \tag{2.22}$$

Similarly, if we consider the FCC crystal, as shown in Fig. 2.8b, then the number of octahedral sites available for interstitial atoms is four. Further, in an FCC unit cell, the total number of atoms per unit cell is likewise four. So we can say that for N_0 solvent atoms, there will be N_0 sites available for interstitial atoms. As in the previous example, if we consider n_I interstitial atoms which will occupy randomly N_0 sites, then we can show that

$$X_I = \exp\left(-\frac{\Delta g_I}{RT}\right) \tag{2.23}$$

So in general, we can write that the equilibrium concentration of interstitial impurities present is

$$X_I = B\exp\left(-\frac{\Delta g_I}{RT}\right) \tag{2.24}$$

Here, factor B depends on the crystal structure.

Furthermore, Eq. 2.24 for any kind of crystal structures can be written as

$$X_I = X_I^0\exp\left(-\frac{\Delta h_I}{RT}\right) \tag{2.25}$$

where ΔH_I is the activation enthalpy for interstitial impurities and X_I^0 is the pre-exponential factor which is defined as

$$X_1^\circ = B\exp\left(\frac{\Delta s}{R}\right). \tag{2.26}$$

In above examples, we have seen that a BCC crystal has a higher number of octahedral sites than an FCC crystal. However, the size of these interstitial sites in an FCC crystal is d = 0.414D (d is the interstitial void size and D is the diameter of the solvent atom), whereas the corresponding size in a BCC crystal is d = 0.155D. In general, the size of the interstitial atoms is greater than the interstitial site size. So the addition of interstitial atoms always creates a strain in the lattice. Since the size of the interstitial sites in an FCC crystal is larger than that in a BCC crystal, the concentration of impurities (except hydrogen) in an FCC crystal is typically higher than in a BCC crystal. This is the reason why the carbon concentration in an α-iron (BCC structure) is much less than in a γ-iron (FCC structure).

Another important difference between BCC and FCC lattices in terms of interstitial atoms is that in a BCC lattice, the occupation of the octahedral lattice site (Fig. 2.8) leads to distortion (due to the asymmetry of the octahedral site) and, consequently, to formation of a shear stress field around the interstitial. This enables the screw component (see Sect. 2.5.2) of the

dislocations (which possesses only the shear stress component) to interact with the stress field created. As in iron, for instance, at low temperatures, the majority of dislocations are of the screw type (or have the majority of the screw component), and this leads to differences in the mechanical properties of the BCC and FCC forms of iron.

2.5.2 Linear Defects

Dislocations, which are the most typical linear (or one-dimensional) defects, and their ability to move define the ductility (plasticity) of metals and explain why the strength of a metal crystal is far less than the theoretical strength calculated on the basis of the bond strength between the metal atoms. During typical plastic deformation, dislocations are formed by the Frank-Read source with the rate of $\sim 10^6$/s. Due to the force (stress), the dislocations glide along the close-packed crystal planes. When the dislocation density of a material is increased, also the internal energy is increased more than the entropy. Therefore, the dislocations are not stable and tend to annihilate or escape from the crystal. The decrease in ductility and increase in strength are related to the interactions between the dislocations as well as between the dislocations and other obstacles to movement such as precipitations or grain boundaries. At high homologous temperatures ($T > 0.45\ T_m$), dislocations can also climb, which increases the degrees of freedom of movement, leading to lower strength and higher ductility. In addition, many different types of crystals react at increased rates at the points where dislocations intersect the surface.

Even though the plastic deformation occurring via dislocation movement is qualitatively fully comprehended in macro- and microcrystalline materials, the quantitative analyses still remain incomplete [5]. This is due to the difficulties in averaging the interactions between dislocations and the other mechanisms contributing to the plastic flow on the plastic flow on the nanoscale, such as grain rotation, twinning, etc. [5]. It is also to be noted that, from an atomistic point of view, the length of dislocation becomes increasingly important as the grain size of the material approaches the nanoscale.

Although there are many different types of dislocations, they all can be considered as combinations of the two fundamental types (i.e., the edge dislocations and screw dislocations shown in Fig. 2.9).

Summary of dislocations:

1. Dislocations are formed during deformation.
2. Dislocations glide due to a stress (force) along close-packed planes running in a close-packed direction.

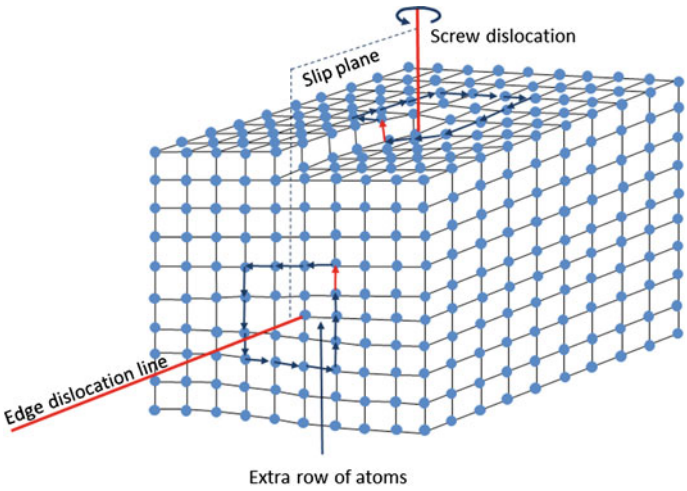

Fig. 2.9 Edge dislocation and screw dislocation

3. As dislocation density increases, the internal energy of the material increases more than its entropy. Therefore, dislocations are not stable and try to annihilate.
4. Dislocations interact with each other, and thus, gliding becomes more difficult. This, in turn, increases the strength of the material, yet the ductility is decreased. Other obstacles, such as grain boundaries and precipitates, have a similar effect.
5. At increased temperatures ($T > 0.45\ T_m$), dislocations can climb, which increases the degrees of freedom for their movement. This causes decrease in strength and increase in ductility.

2.5.3 Two-Dimensional Defects

The two-dimensional defects (i.e., planar defects, especially surfaces and interfaces) have a significant effect not only on the mechanical properties of materials but also on their chemical reactivity. For example, the reaction rates during corrosion are typically determined by the amount of exposed surface area. In addition, these defects, such as grain boundaries between crystallites in a polycrystalline alloy, provide lower activation energy short circuit paths for atomic diffusion and impurities tend to segregate there. Since the surface and interfacial diffusion can be orders of magnitude faster than that of bulk diffusion, see Fig. 10.2 in Chap. 10

Table 2.3 Lattice, grain boundary, and surface interdiffusion coefficients of Cu, Al, and $(SnPb)_{eut}$ at 100 °C [6]

Material	Temp. ratio $373/T_m$	Diffusivities at 100 °C (m^2/s)
Cu	0.275	Lattice $D_l = 7 \times 10^{-24}$ Grain $D_{gb} = 3 \times 10^{-11}$ Surface $D_s = 10^{-8}$
Al	0.4	$D_l = 1.5 \times 10^{-15}$ $D_{gb} = 6 \times 10^{-7}$
$(SnPb)_{eut}$	0.82	$D_l = 2 \times 10^{-5 \text{ to } -6}$

these short circuit paths may have significant technological impacts, for example, in the electromigration reliability of electronic circuits, as can be seen from Table 2.3. In addition, the two-dimensional defects interact with other defects, such as dislocations, as discussed in Sect. 2.5.2.

It is also to be noted that these defects have their own energy, surface energy, which quantifies the disruption of intermolecular bonds that occur when a surface is created. The minimization of surface energy provides a driving force for many important phenomena such as sintering, wetting, and grain coarsening. Other types of planar defects are low- and high-angle grain boundaries, in which adjacent grains can be distinguished depending on the misalignments of atomic planes, twin boundaries, and antiphase boundaries.

2.5.4 Volume Defects

Volume defects (bulk defects, 3D defects) like precipitates, inclusions, cracks, voids, and pores also have important effects on the mechanical, thermal, electronic, and optical properties of solids. These defects are typically introduced into the material during manufacturing and fabrication steps. Furthermore, these defects are capable of increasing mechanical stress locally and are thus especially deleterious to the mechanical reliability of the metal. However, in dispersion hardening, foreign particles or additional elements that form precipitates are added to strengthen the parent material by forming obstacles to movement of dislocations facilitating plastic deformation. The good high-temperature strength of many super-alloys is due to the second-phase particles. Nonetheless, pores, cracks, and voids that act as stress concentration sites are typically detrimental for mechanical strength.

2.6 Some Examples of Intermediate Phases and Their Crystal Structure

There are numerous different kinds of ordered phases that are present with many differing crystal structures varying from being relatively simple to extremely complicated. There are basically two types that intermediate phases can form,

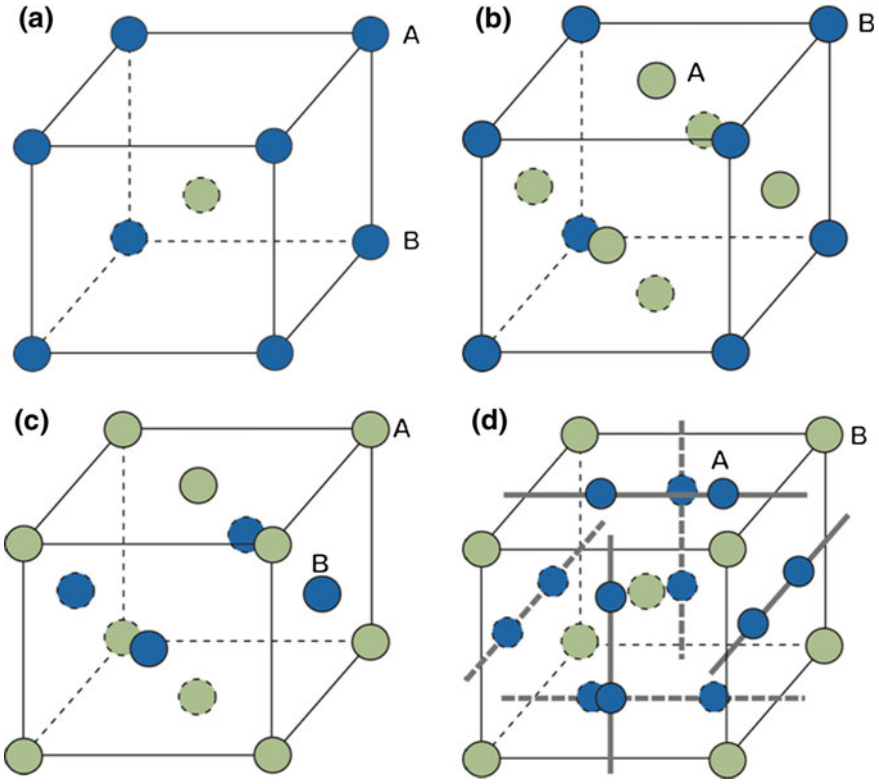

Fig. 2.10 Crystal structure of substitutional ordered phases: **a** B2 (AB)-NiAl, CoAl, CuZn, AuZn; **b** $L1_2$ (A_3B)-Ni_3Al, Ni_3Ga, Ni_3Ge; **c** $L1_o$ (AB) −CuAu, CoPt, FePt; **d** A15 (A_3B)- Nb_3Sn, Nb_3Ge, V_3Si

being interstitial and substitutional compounds. The precise type of phase that will form depends on the relative atomic size, valency, and electronegativity as was discussed earlier (Sect. 1.12). When one type of atom is much smaller than another, then the smaller atoms are able to occupy the interstitial positions in the crystal of the other atom. For example, different kinds of metal carbides are interstitial intermetallic compounds. Some of the examples are shown in Fig. 2.10. When atom sizes differ by a factor of 1.1–1.6, Laves phase might form (see Fig. 2.11). The other type are substitutional compounds where one type of atom occupies one particular sublattice and another type of atom occupies the other sublattice.

The main difference with these kinds of substitutional alloys and the case of random alloys is that there is an equal probability for both atoms to occupy a particular position. A few different examples of these kinds of compounds are shown in Fig. 2.10. Note that we have shown relatively simple examples which will be considered for discussion in forthcoming chapters. Some systems, for example, Cu_3Au, CuAu, and CuZn, transform to disordered phases at high temperature, because of the dominating role of entropy compared to enthalpy in these systems.

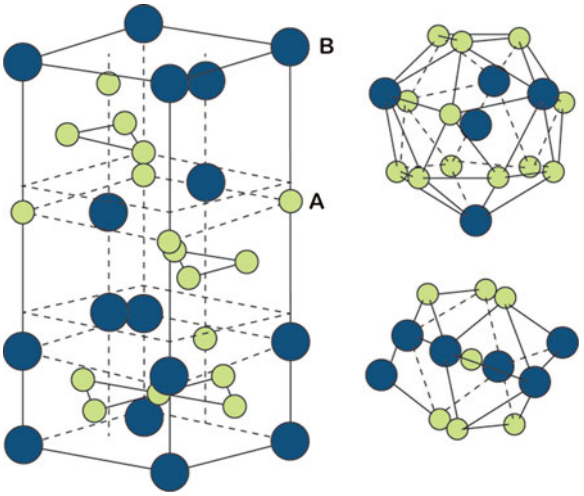

Fig. 2.11 C15 Laves phase A_2B type

2.6.1 Defects in Intermediate Phases

The composition range of the intermediate phases in binary systems can vary from a very narrow homogeneity range, as shown in Fig. 1.26, to a reasonably wide homogeneity range, as shown in Fig. 1.27. There is no ordered phase present which is a perfect line compound that is with stoichiometric composition without any deviation. The deviation from stoichiometric composition is achieved by the presence of constitutional defects in the structure. Mainly two types of defects are found in these structures. One type is structural vacancies. Note that structural vacancies found because of deviation from the stoichiometric composition are different from the thermal vacancies which are always present at a specific temperature with a certain equilibrium concentration. Another type of defect which is typically found is an antisite (or an antistructure) defect that is created when an atom occupies a position belonging to the other type of atom.

To clarify what has been stated above, let us consider one of the most studied ordered structures, the B2 phase. Let us see the crystal structure a little differently, as shown in Fig. 2.12a. The lattice positions can be divided into two types, the α- and β-sublattices. If A atoms, in a binary A–B alloy, occupy the α-sublattice ([0,0,0] positions), then the B atoms will occupy the β-sublattice ($[\frac{1}{2}, \frac{1}{2}, \frac{1}{2}]$ positions). It can be seen that two simple cubes of the α-sublattice and the β-sublattice interpenetrate each other forming the B2 structure. At stoichiometric composition and in a perfect crystal, we expect this condition to occur. However, when composition deviates from the stoichiometric composition, defects will be present in the structure and the number of defects depends on the extent of deviation in the composition.

There can be two types of B2 intermediate phases. One type is in the A-rich side where antisite defects are present, whereas in the B-rich side, triple defects are present, as shown in Fig. 2.12. A triple defect is so named because it comprises a total

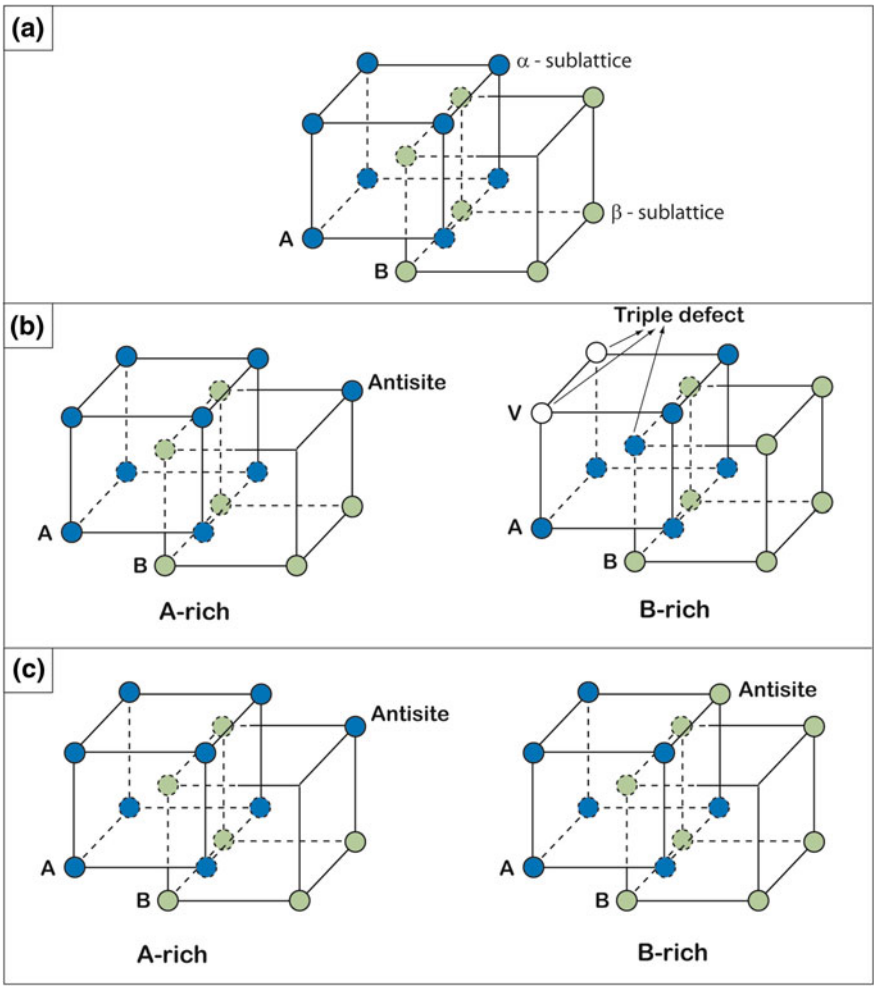

Fig. 2.12 Defect structure in B2 phases. **a** Perfect crystal. **b** Phases where on one side of the stoichiometric composition, there is the presence of triple defects, whereas on the other side, antisite defects are present. **c** Phases where on both sides of the stoichiometric compositions, antisite defects are present

of three defects, namely two vacancies in the α-sublattice and one antisite defect in the β-sublattice. It is important to keep in mind that the triple defects are not necessary bounded defects, i.e. the vacancies and antisite do not necessary occupy nearest neighboring positions. The triple defect disorder refers the *total* defect concentrations when there are two vacancies for each antisite atom, see Sect. 2.6.3 for more details. These kinds of defects are found, for example, in the B2 NiAl, CoAl, NiGa, and CoGa phases. There is another kind of B2 phase, where in both sides of the stoichiometry, only antisite defects are present, as shown in Fig. 2.12c. This kind of defect is found in the B2 AuZn, CuZn, AgZn, and AgMg phases, for instance.

However, it should be pointed out that a triple defect is not a common defect in phases other than the B2 structure. Instead, simple vacancies are typically present. Moreover, in most of the ordered phases in both sides of the stoichiometry, only antistructure defects are present. We have seen earlier that at above 0 K, there will always be some vacancies present (their number depending on the temperature) due to the fact that they are thermodynamic equilibrium defects. Similarly, in ordered phases, even at stoichiometric composition vacancies and antistructure, defects will be present and the number of defects increases with increasing temperature. However, calculation of point defects in ordered phases is not very straightforward as shown next.

2.6.2 *Crystal Structures and Point Defects in Ordered Binary Intermetallics on an Example of Ni-, Ti-, and Fe-Aluminides*

The ordered Ni-, Ti-, and Fe-aluminides reveal different crystalline structures. The most important are the following: B2 (NiAl and FeAl, see Fig. 2.10a), $L1_2$ (Ni_3Al, see Fig. 2.10b), $L1_0$ (TiAl, see Fig. 2.10c), $D0_{19}$ (Ti_3Al, see Fig. 2.13a), and $D0_3$ (Fe_3Al, see Fig. 2.13b). Here, the ideally ordered crystalline structures of Ni-, Ti-, and Fe-aluminides are schematically presented, i.e., the structures at zero temperature and at perfect stoichiometric compositions. As the temperature increases and/or the composition deviates from stoichiometry, substitutional point defects are inevitably generated. Four types of substitutional point defects can generally be introduced in a two-atomic intermetallic compound AB, namely the vacancies on both sublattices, V_A and V_B, and the atoms on the differing sublattices, A_B and B_A (the antistructure or antisite atoms). One may differentiate between *structural* (constitutional) and *thermal* point defects which could be created in an off-stoichiometric intermetallic compound. In a strict definition, the structural defects are those defects which remaining thermal equilibrium in the intermetallic compound even at $T = 0$ in its maximally ordered state in order to accommodate the deviation from the stoichiometric composition. The difference between the real concentration of defects at $T \neq 0$ and the concentration of the structural defects presents the concentration of the thermal defects.

In a strict sense, nature does not "mark" the defects as constitutional or thermal ones. Such subdivision is helpful only from an educational point of view in order to refer to different sources of defects in a given compound. In such a definition, the concentration of thermal defects can even be *negative*. The Al-rich phase NiAl seems to present such an example. A further difference between the structural and thermal defects stems from the fact that one type of structural point defects is generally sufficient to accommodate the deviation from the stoichiometry, whereas at least two types of thermal point defects have to be simultaneously created to satisfy the mass-balance conditions (to preserve the given composition, i.e., the given ratio between the constitutional elements).

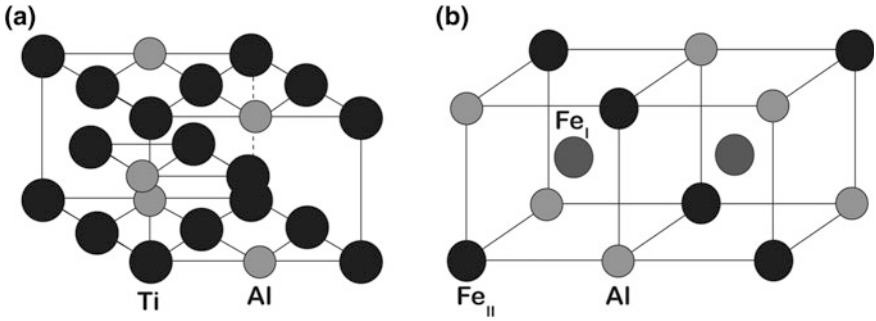

Fig. 2.13 Lattice structures of Ti_3Al **a** and Fe_3Al **b** aluminides. The Ti and Al atoms are represented by *black* and *gray* spheres. Fe has two sublattices indicated by Fe_I and Fe_{II}

Moreover, the point defects have not to be uniformly distributed over the different sublattices in an ordered intermetallic compound.

In Fig. 2.14, the concentrations of different defects in the intermetallic compounds under consideration are compared at $T = 0.75T_m$. This temperature corresponds to $T = 1{,}252$ K for Ni_3Al, 1,434 K for NiAl, 1,457 K for Ti_3Al, 1,294 K for TiAl, and 1,195 K for FeAl. T_m is the melting temperature of the stoichiometric composition of the given compound. The defect concentrations on different sublattices can be calculated according to the chemical reaction approach described below. Since in an intermetallic compound, point defects are created in a correlated manner in order to preserve the given composition, the concentration of point defects depends on the formation energies of all four types of defect. The literature data were here used for numerical estimates. It is important to note that the formation entropy effects were neglected.

The chemical reaction approach is outlined below for the example of NiAl. The vibrational energy contribution is neglected.

2.6.3 Calculation of Point Defect Formation Energies

The calculation of defect energies in pure metals is quite straightforward and was presented in Sect. 2.5 in detail. In the case of intermetallic compounds, however, the defect energies have to be calculated in a modified way. The energy difference between a block of perfect unit cells and that containing a given defect yields the values which may be called the "raw" formation energy of the defect. The "raw" values of single defects together with the cohesive energy per atom, ε_0, used in the presented estimates, are listed in Table 2.4. The B2 NiAl phase is exemplified here as a binary AB compound (A = Ni and B = Al). Since introduction of a single defect generally violates the composition of the compound, these "raw" values by themselves cannot represent the thermodynamical quantities. The effective formation energies, which correspond to the Arrhenius approximations of the temperature dependence of the defect concentrations, can be used with this aim.

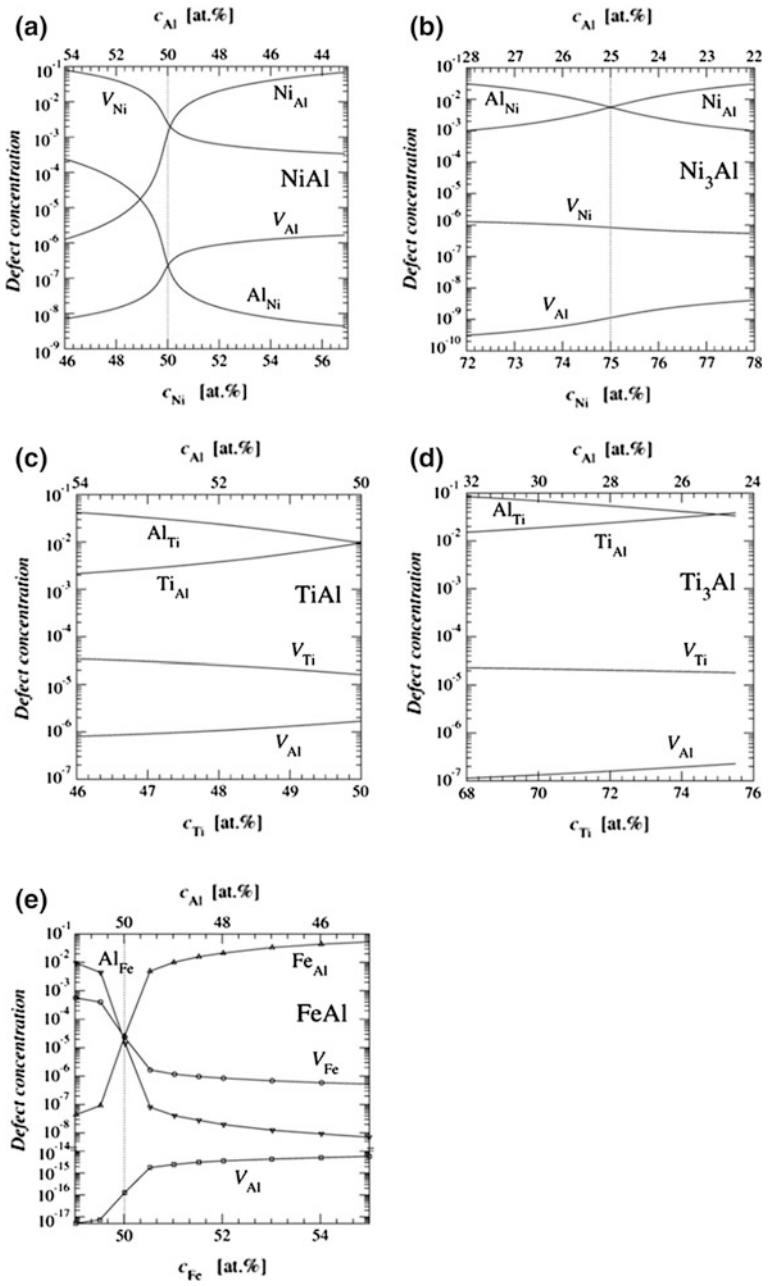

Fig. 2.14 Concentrations of vacancy and antistructure atoms on transition metal and aluminum sublattices in NiAl, Ni_3Al, TiAl, Ti_3Al, and FeAl as a function of composition at $T = 0.75\ T_m$ (T_m is the melting point of the compound)

Table 2.4 The "raw" formation energies of single point defects in NiAl where V is the vacancy, the bottom subscript denotes the sublattice, and ε_0 is the cohesive energy of the alloy

	$\varepsilon_{V\mathrm{Ni}}$	$\varepsilon_{V\mathrm{Al}}$	$\varepsilon_{\mathrm{Ni\_Al}}$	$\varepsilon_{\mathrm{Al\_Ni}}$	ε_0
"Raw" formation energy, eV/atom	5.978	5.471	−0.920	3.457	−4.494

The equilibrium defect concentrations in an intermetallic compound can be calculated using either canonical or grand canonical ensemble formalism. Of course, both methods will give the same result, so the choice of approach is a matter of convenience. Alternatively, the point defects can be treated as individual species and different point defect reactions can be considered as chemical reactions in a multicomponent lattice gas [7]. This approach is sketched here and, of course, it gives the same results as the previous two, yet in a slightly more elegant way.

Till the end of this section, we will use a special notation for the defect concentrations in view of a specific structure of an ordered compound. We will introducing the occupation probabilities of a defect P on a given sublattice denoted as Y_P instead of concentration variables, which are determined in mole fractions. This approach simplifies significantly the analysis for ordered compounds.

The point defect concentrations are assumed to be small, so that the defect interactions are neglected. Formally, each type P of point defects is described by a chemical potential

$$\mu_P = \varepsilon_P + kT \ln Y_P \tag{2.27}$$

Here, ε_P is the "raw" formation energy of a single defect and Y_P is the occupation probability of the defect P per unit site in its own sublattice. The commonly used defect concentrations, X_P, see Sect. 2.5, expressed as the site fractions of the number of defects are related to Y_P by the obvious relation for the B2 structures: $2X_P = Y_P$.

The four unknown equilibrium point defect concentrations $\{Y_P\}$ in a B2 compound, i.e., the vacancy concentrations on the two sublattices and the concentrations of the two types of antisite atoms, can be determined from the kinetic equilibrium conditions with respect to the three point defect reactions, supplemented by the conservation law for a fixed alloy composition. The latter can be written in the form

$$\xi(1 - 2Y_{V_\mathrm{A}} - 2Y_{V_\mathrm{B}}) = \frac{1}{4}(Y_{V_\mathrm{B}} - Y_{V_\mathrm{A}}) + \frac{1}{2}(Y_{\mathrm{A_B}} - Y_{\mathrm{B_A}}) \tag{2.28}$$

where

$$\xi = X_\mathrm{A} - \frac{1}{2} \tag{2.29}$$

is the deviation of the alloy composition (mole fraction of A, $\mathrm{X_A}$) from the ideal stoichiometric composition ($X_\mathrm{A} = 0.5$). Neglecting the terms such as ξ^2 in

Eq. 2.28 for small deviations from the stoichiometric composition and small concentrations of the point defects, the above equation can be presented as

$$\xi = \frac{1}{4}(Y_{V_B} - Y_{V_A}) + \frac{1}{2}(Y_{A_B} - Y_{B_A}) \tag{2.30}$$

The choice of three point defect reaction is a matter of convenience and depends on whether we deal with a triple-defect or antisite disorder compound. For the NiAl alloy, for instance, a convenient set of reactions is

$$2V_A + A_B + AB \leftrightarrow 0 \tag{2.31}$$

$$A_B + B_A \leftrightarrow 0 \tag{2.32}$$

$$2V_B + AB \leftrightarrow A_B \tag{2.33}$$

Equation 2.31 represents the triple-defect equilibrium in the system. It simply shows that a triple defect can be cancelled by adding a structural unit AB to the system. Similarly, Eq. 2.32 represents an antisite equilibrium and shows that a pair of antistructure atoms can be created or cancelled. Finally, Eq. 2.33 shows that, if we initially have two B vacancies and add a structural unit NiAl, then Al will cancel one of the vacancies, while Ni will turn the other vacancy into an Ni_{Al}-antistructure atom.

The dynamic equilibrium in the above defect reactions, Eqs. 2.31–2.33, can be reached by the equality of corresponding chemical potentials. The structural unit, NiAl, will be presented by $2\varepsilon_0$. This will give

$$\varepsilon_t d + kT \ln Y_{V_A}^2 Y_{A_B} = 0 \tag{2.34}$$

$$\varepsilon_{A_B} + \varepsilon_{B_A} + kT \ln Y_{A_B} Y_{B_A} = 0 \tag{2.35}$$

$$2\varepsilon_{V_B} - \varepsilon_{A_B} + 2\varepsilon_0 + kT \ln\left(\frac{Y_{V_B}^2}{Y_{A_B}}\right) = 0 \tag{2.36}$$

Here, $\varepsilon_{td} = 2\varepsilon_0 + 2\varepsilon_{V_A} + \varepsilon_{A_B}$ is the so-called triple-defect energy.

Equations 2.30 and 2.34–2.36 could be solved numerically for the four defect concentrations in dependence on the composition of the alloy. Then, the effective activation energies can be estimated by linear fitting in the logarithm concentration against the inverse temperature coordinates within the given temperature interval. The analysis shows that the temperature dependence of the point defect concentrations can be adequately treated with a single formation energy. The specific results for NiAl are given in Fig. 2.15.

Besides that, Eqs. 2.30 and 2.34–2.36 can be solved analytically in an approximate manner by using the fact that in NiAl, Y_{V_A} and Y_{A_B} are much greater than the other two concentrations. Then, Eq. 2.30 can be rewritten in the form

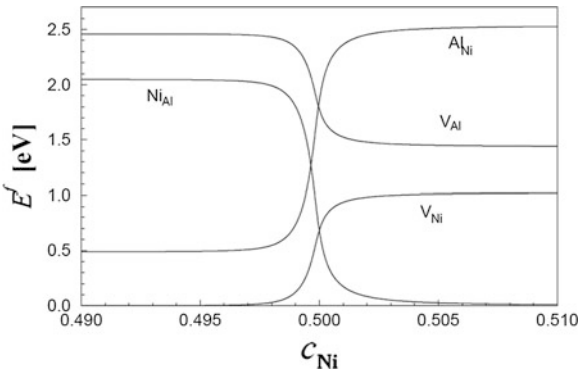

Fig. 2.15 Effective formation energies E^f of the point defects as function of composition c_{Ni}

$$\xi = \frac{1}{2} Y_{A_B} - \frac{1}{4} Y_{V_A} \tag{2.37}$$

From Eq. 2.37, we have $Y_{V_A} = 2Y_{A_B}$ for the stoichiometric composition, $\xi = 0$. For the A-rich compositions $\xi > 0$, the A antistructure atoms are the main defects $(Y_{V_A} \ll Y_{A_B})$ and Eq. 2.37 transforms into $Y_{A_B} = 2\xi$. On the other hand, for the B-rich compositions $\xi < 0$, the A vacancies are mainly formed $(Y_{V_A} \gg Y_{A_B})$ and Eq. 1.174 will be read as $Y_{V_A} = -4\xi$. These relations make it possible to solve analytically the system of Eqs. 2.34–2.36 and to find the concentrations of all four point defects under the given approximations. The analytical expressions for the effective formation energies are given in Table 2.5. The comparison with Fig. 2.15 suggests that these results correspond well to the numerical data at the stoichiometric composition and far from the stoichiometry.

The calculations suggest that the Ni vacancies and the Ni antistructure atoms are the main defects in NiAl and the concentration of Al vacancies is by a few orders of magnitude lower than the concentration of Ni vacancies in accordance with the experimental observations.

A similar form of analytic solution can be used for other compounds, and the results are presented in Fig. 2.14. Figure 2.14a–e demonstrate a few important features of defect behavior. It is obvious that both the Ti-aluminides (Fig. 2.14c, d) and Ni_3Al (Fig. 2.14b) belong to the antistructure defect type of intermetallic compounds, since antistructure atoms are predominantly generated to accommodate the deviation from the stoichiometry. In contrast, NiAl reveals a triple-defect type of point defect disorder and constitutional Ni vacancies exist in NiAl on the Al-rich side, as in Fig. 2.14a. Moreover, the Ni vacancy concentration is very large also on the Ni-rich side, for example, $X_{V_A} \sim 10^{-4}$ at $T = 0.75T_m$. In the other intermetallics under consideration, the vacancies are also mainly concentrated on the transition metal sublattice and their concentration amounts to about 10^{-6} to 10^{-5} at $T = 0.75T_m$. These are also the typical vacancy concentrations in close-packed pure metals at the same reduced temperature. The vacancy concentration on the Al sublattice is remarkably smaller, especially in B2–FeAl, see Fig. 2.14e.

Table 2.5 Analytical expressions of the effective formation energies Q_P^f of the point defects P, $P = V_{Ni}$, V_{Al}, Ni_{Al}, and Al_{Ni} (in eV/Atom) in NiAl in dependence on composition $\xi = X_{Ni} - ½$

	$\xi < 0$	$\xi = 0$	$\xi > 0$
$Q^f_{V_{Ni}}$	0	$\varepsilon_{td}/3$	$\varepsilon_{td}/2$
	0	0.683	1.024
$Q^f_{V_{Al}}$	$2\varepsilon_0 + \varepsilon_{V_{Al}} + \varepsilon_{V_{Ni}}$	$(4\varepsilon_0 + 3\varepsilon_{V_{Al}} + \varepsilon_{V_{Ni}} - \varepsilon_{Ni_{Al}})/3$	$\varepsilon_0 + \varepsilon_{V_{Al}} - \frac{1}{2}\varepsilon_{Ni_{Al}}$
	2.461	1.778	1.437
$Q^f_{Ni_{Al}}$	ε_{td}	$\varepsilon_{td}/3$	0
	2.048	0.683	0
$Q^f_{Al_{Ni}}$	$\varepsilon_{Al_{Ni}} - 2\varepsilon_0 - 2\varepsilon_{V_{Ni}}$	$(-2\varepsilon_0 - 2\varepsilon_{V_{Ni}} + 3\varepsilon_{Al_{Ni}} + 2\varepsilon_{Ni_{Al}})/3$	$\varepsilon_{Al_{Ni}} + \varepsilon_{Ni_{Al}}$
	0.489	1.854	2.537

B2–FeAl is neither a compound with a pure antisite disorder nor a compound with a pure triple-defect disorder. FeAl demonstrates a hybrid behavior in which the relation between the Fe vacancy concentration and that of the antistructure atoms depends crucially on temperature.

The concentration of the Ti antistructure atoms in the Ti-aluminides is generally larger than that of the Ni antistructure atoms in the Ni-aluminides of the same composition, as in Fig. 2.14. This fact corresponds to a higher degree of thermal disorder inherent in Ti-aluminides at similar reduced temperatures. These features play a decisive role in the analysis of the respective self-diffusion behavior.

An important question now arises as to how the particular crystal structure of the given intermetallic compound can affect the self-diffusion properties. It is generally accepted that self-diffusion in close-packed structures occurs via nearest-neighbor jumps of vacancies. Since random vacancy jumps between different sublattices would generally produce disorder (and since there is a strong tendency to accomplish the reverse), ordering jump after a given disordering jump, the correlated jumps of vacancies will clearly play a decisive role in the long-range diffusion process. These problems will be considered in Chap. 5.

2.7 Microstructure and Phase Structure

The structural details at different levels that create the microstructure of a given material are shown in Fig. 2.16. On the other hand, microstructures can be divided, based on the formation mechanism, into three major types namely solidification structures, solid-state transformation structures, and annealing structures. Figure 2.17 shows, as an example, an eutectic solidification structure of AuSn-alloy and the same material after annealing at 150 °C for 6,600 h. A profound discussion on different types of microstructures can be found, for example, from the ASM handbook, and therefore, it is not included here [1] (Fig. 2.16).

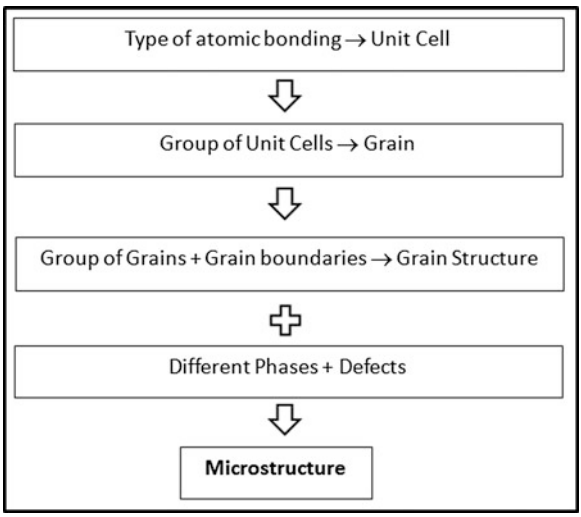

Fig. 2.16 Structural details at different levels creating the microstructure of a material

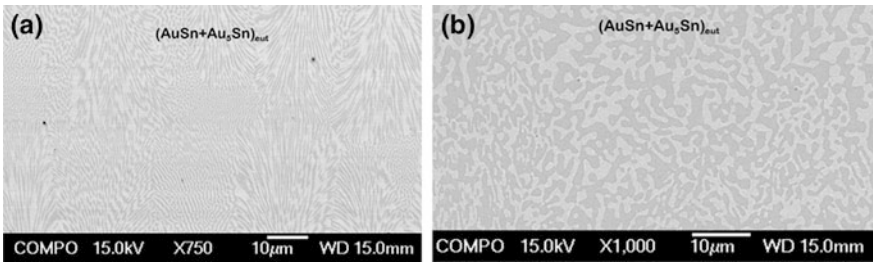

Fig. 2.17 **a** Eutectic solidification structure of Au80Sn20 (wt %) alloy and, **b** the same structure after annealing at 150 °C for 6,600 h

References

1. ASM Handbook, vol 9, Metallography and Microstructures, ASM International Materials Park Ohio, USA 2004.
2. W. D. Callister, Jr., D. G. Rethwisch, Materials Science and Engineering: An Introduction,John Wiley & Sons, Canada 2009.
3. R. Tilley, Understanding Solids-The Science of Materials, John Wiley & Sons, Chichester West Sussex, England 2006.
4. J. K. Kivilahti, Metalliseosten teoria: Tasapaino-ominaisuudet ja rakenne, Otakustantamo, 1982.
5. K.S. Kumar, H. Van Swygenhoven, S. Suresh, Mechanical behavior of nanocrystalline metals and alloys, Acta Materialia 51 (2003) 5743–5774.
6. K.-N. Tu, Solder Joint Technology: Materials, Properties, and Reliability, Springer, 2007.
7. Y. Mishin, C. Herzig, Diffusion in the Ti-Al system, Acta Materialia 48 (2000) 589–623.

Chapter 3
Fick's Laws of Diffusion

In this chapter, Fick's laws of diffusion are introduced. The second law is derived using the first law and the mass conservation. Solutions for the second law considering a constant diffusion coefficient for different conditions are given. Few examples are also introduced to show the estimation procedure.

3.1 Fick's First and Second Laws of Diffusion

Adolf Fick [1] was the first man to propose the phenomenological relation for diffusion. His reasoning being the following: when considering the flux of particles (atoms, molecules, ions etc.) in a one-dimensional system caused by a concentration gradient, the flux can be expressed as

$$J = \frac{dm}{dtA} = -D\frac{\partial C}{\partial x} \tag{3.1a}$$

where J (mol/m^2 s) is the flux, dm (mol) is the change in the amount of matter in small time dt (seconds), A (m^2) is the area, D (m^2/s) is the diffusion coefficient, C (mol/m^3) is the concentration of the particles, and x (m) is the position parameter. The negative sign stems from the fact that diffusion occurs in the direction opposite to the increasing concentration gradient.

It should be noted immediately that the Fick's first law can be directly applied only in a steady-state condition, as shown in Fig. 3.1, where the composition does not change with time. In addition, there should not be any external driving forces present other than the concentration gradient. Let us consider a square pipe of iron and pass carburizing gas inside and decarburizing gas outside of the pipe. If the wall is reasonably thin, a steady state might prevail in the system. Suppose further that the concentrations at the inner and the outer surfaces are C_i and C_o, respectively. Then, the concentration gradient can be written as $\frac{dC}{dx} = \frac{C_o - C_i}{x_o - x_i} = -\frac{C_i - C_o}{x_o - x_i} = -\frac{C_i - C_o}{d}$. Here, d is the wall thickness. The diffusion coefficient, D in this system, can be

A. Paul et al., *Thermodynamics, Diffusion and the Kirkendall Effect in Solids*,
DOI: 10.1007/978-3-319-07461-0_3,

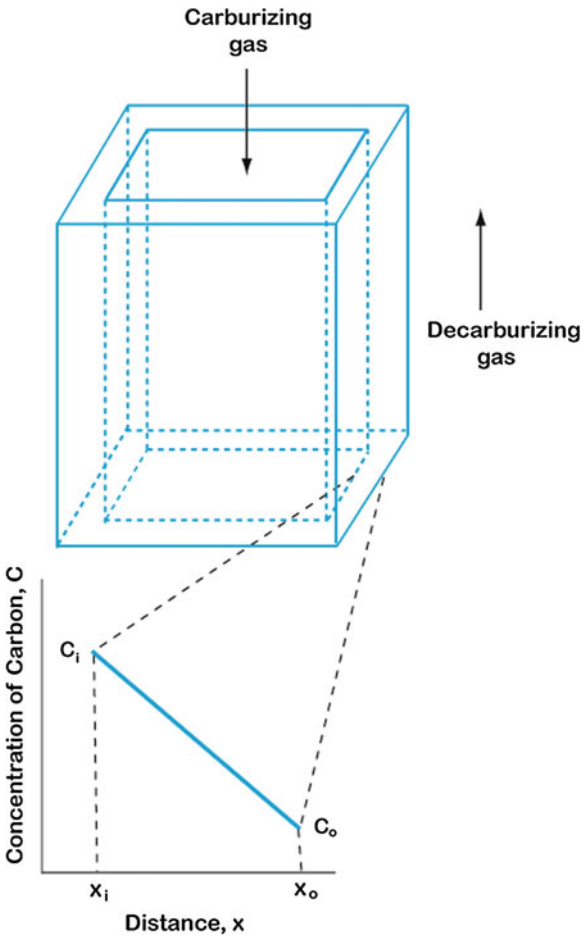

Fig. 3.1 Steady-state diffusion and the composition profile

estimated from what we know about the flux in the system. The flux can be estimated from the transferred material per unit time, that is, $\frac{dm}{dt}$ (mol/s) $= \frac{\Delta m}{\Delta t}$ divided by the area. If the pipe is cylindrical with an average radius of r and length of l, then the concentration gradient is $\frac{dC}{dr}$ and material transferred in mol/s through the area $A = 2\pi rl$ is $\frac{\Delta m}{\Delta t}$. Therefore, we can write

$$J = \frac{\Delta m}{\Delta t\,(2\pi rl)} = -D\frac{\partial C}{\partial r}$$
$$\frac{\Delta m}{\Delta t} = -D(2\pi l)\frac{\partial C}{\partial \ln r} \tag{3.1b}$$

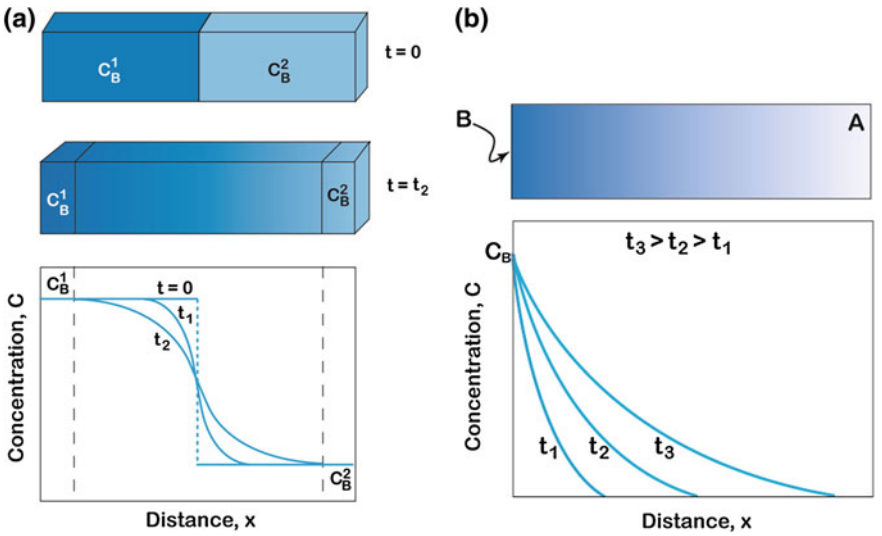

Fig. 3.2 Change in non-steady-state composition profile with time (**a**) in a diffusion couple of C_B^1 and C_B^2 (**b**) for diffusion of B in A

Note here that if a steady state prevails, then concentration profile, which is $\frac{\partial C}{\partial x}$ or $\frac{\partial C}{\partial \ln r}$, will not change with time. However, under most experimental conditions, the concentration at a particular position changes with time at any location. For example, consider two blocks of alloys A–B with average concentrations of $C_B{}^1$ and $C_B{}^2$ which are coupled and annealed at an increased temperature. The change in the concentration with the annealing time is shown in Fig. 3.2a. Similarly, we can consider the diffusion of element B in a block of material A, as shown in Fig. 3.2b. Any possible changes in the composition profiles with time are shown. In this condition, Fick's first law cannot be used to estimate the diffusion coefficient of the components because of the absence of a time parameter. What is needed, therefore, is a relation which is able to explain the non-steady-state diffusion process, that is, the change in concentration at a particular position with increasing annealing time.

For this purpose, Fick's second law is derived from the consideration of mass conservation and Fick's first law. For the sake of explanation, let us consider a very thin slab $\Delta x\,(= x_2 - x_1)$ in the diffused block of A from the example, as shown in Fig. 3.2b. The flux of element B in this thin slab, as shown in Fig. 3.3. The block with a unit cross-sectional area is the one under consideration. If the flux coming in through the plane x_1 is J_B^1, then the total amount of element B coming through this plane in a short time δt can be written as $J_B^1 \delta t$. Similarly, the total amount of material out through the plane x_2 can be written as $J_B^2 \delta t$. If we consider $J_B^1 > J_B^2$, the increase in concentration of B in the small thickness of Δx can be written as

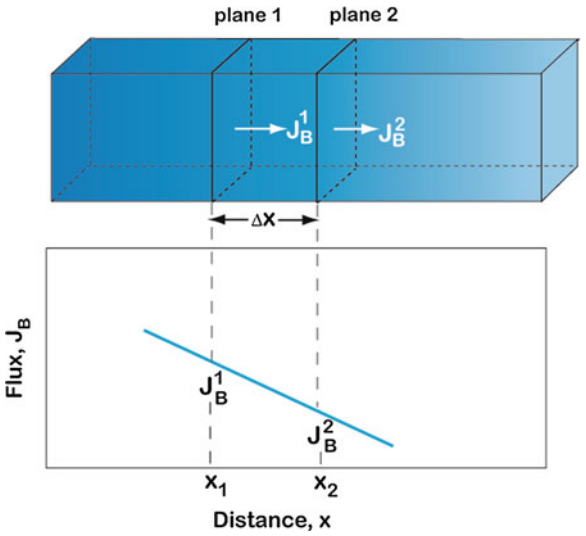

Fig. 3.3 Change in flux with distance in a very thin slab

$$\delta C_B = \frac{(J_B^1 - J_B^2)\delta t}{\Delta x} \tag{3.2}$$

Furthermore, since only a very small thickness Δx is being considered, the variation of flux in this region can be considered linear so that

$$\frac{\partial J_B}{\partial x} = \frac{J_B^2 - J_B^1}{\Delta x} = -\frac{J_B^1 - J_B^2}{\Delta x} \tag{3.3}$$

Using Eq. 3.2 in Eq. 3.3 and considering very small time, we can write

$$\frac{\partial C_B}{\partial t} = -\frac{\partial J_B}{\partial x} \tag{3.4}$$

Following Fick's first law, shown above in Eqs. 3.1a, 3.4 can be written as

$$\frac{\partial C_B}{\partial t} = \frac{\partial}{\partial x}\left(D_B \frac{\partial C_B}{\partial x}\right) \tag{3.5a}$$

For a constant diffusion coefficient, we can write

$$\frac{\partial C_B}{\partial t} = D_B \frac{\partial^2 C_B}{\partial x^2} \tag{3.5b}$$

Equation 3.5a is better known as Fick's second law. One important point, however, should be noted here that it is not possible to use Fick's first law to estimate the distribution of components over the whole interaction zone in a

non-steady-state condition. Nevertheless, it can be applied at any particular point since the flux is proportional to the concentration gradient at every location in a profile developed by a diffusion-controlled process.

3.2 Solution of Fick's Second Law to Estimate the Diffusion Coefficient

In the majority of systems in practical applications, the diffusion coefficient is not constant, but is rather a function of concentration. However, solving Fick's second law for such cases is not as straightforward as it may first appear. It is achieved with the help of the Boltzmann parameter as explained in Chap. 6. However, in some cases, the variation in the diffusion coefficient with composition is negligible. Moreover, an element will have a constant diffusion coefficient in a homogeneous material with constant concentration. Different solutions can be found for different situations considering D as constant (as in Eq. 3.5b above). In the sections that follow, three such solutions are introduced and explained in greater detail.

3.2.1 Solution for a Thin-Film Condition

The first case to consider is that where a very small amount of material B as thin film is sandwiched between two rods of pure material A, as shown in Fig. 3.4. By small, we mean that, after diffusion, B will become mixed in A as an impurity, without significantly changing the concentration of A. If this system is annealed for time t at a particular temperature of interest, then the concentration profile of element B in A can be expressed as

$$C_B(x) = \frac{C_0}{t^{1/2}} \exp\left(-\frac{x^2}{4D_B t}\right) \tag{3.6}$$

where $C_B(x)$ is the concentration of material B at x, C_0 is the constant, and D_B is the diffusion coefficient of component B. This relation is developed based on the exponential decay in the composition profile that is found in practical examples, as shown in the C_B versus x plot. The correctness of the solution can be examined after differentiating Eq. 3.6 with respect to t and x and then replacing them in Eq. 3.5b. It can be seen that the distribution of element B is symmetrical to the plane $x = 0$ and the positive side of the distribution is just a reflection of the negative side. Additionally, the total amount of material B, M_B, sandwiched between A can be expressed as

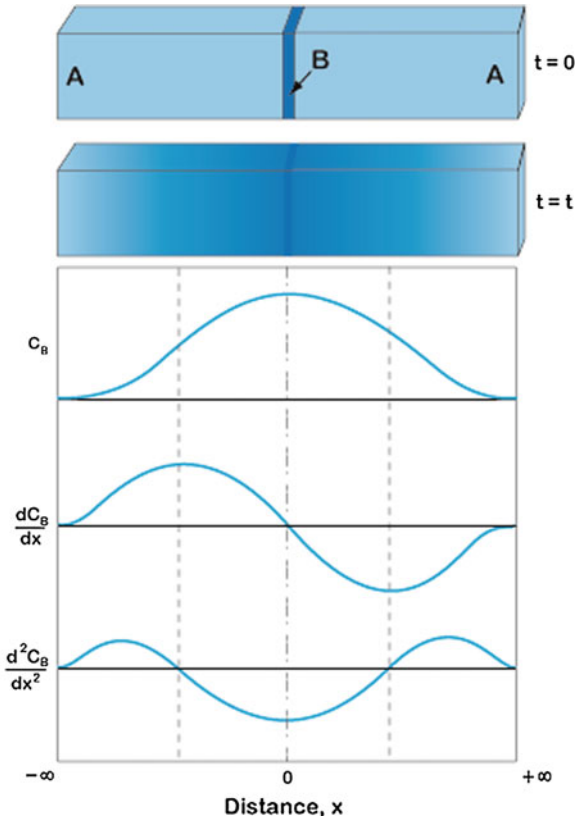

Fig. 3.4 Material B is sandwiched between blocks of material A. The change in C_B, $\frac{dC_B}{dx}$, and $\frac{d^2C_B}{dx^2}$ with x is shown after annealing for time, t

$$M_B = \int_{-\infty}^{+\infty} C_B dx \tag{3.7}$$

Thus, M_B can be found by replacing Eq. 3.6 in Eq. 3.7 as

$$M_B = \int_{-\infty}^{+\infty} \frac{C_0}{t^{1/2}} \exp\left(-\frac{x^2}{4D_B t}\right) dx \tag{3.8}$$

We consider $\lambda = \frac{x}{2\sqrt{D_B t}}$ so that $dx = \left(2\sqrt{D_B t}\right) d\lambda$. Since C_0 is a constant term, we can write

$$M_B = 2C_0\sqrt{D_B} \int_{-\infty}^{+\infty} \exp\left(-\lambda^2\right) d\lambda = 2C_0\sqrt{\pi D_B} \tag{3.9}$$

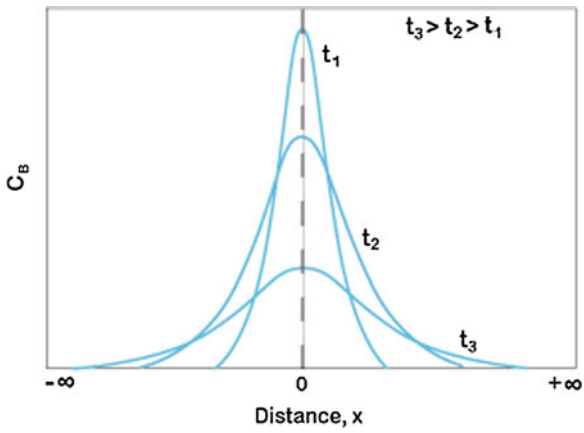

Fig. 3.5 Change in concentration with time in a thin-film sandwiched couple

Since $\int_{-\infty}^{+\infty} \exp(-\lambda^2)\, d\lambda = \sqrt{\pi}$

For a particular annealing time, t is constant and using Eq. 3.9 in Eq. 3.6, we can write

$$C_B(x) = \frac{M_B}{2\sqrt{\pi D_B t}} \exp\left(-\frac{x^2}{4D_B t}\right) \tag{3.10}$$

From the C_B versus x plot, one can find $\frac{dC_B}{dx}$ versus x as shown in Fig. 3.4. Since the constant diffusion coefficient is under consideration, $\frac{dC}{dx}$ versus x reflects the flux at different planes after a certain annealing time t that can be understood from the Fick's first law. It is apparent from the profile that there is no diffusion at $x = 0$, $+\infty$, and $-\infty$. The infinite distance represents the ends of the sample, which are not affected by the diffusion of components. Moreover, the fact that the flux is zero at $x = 0$ demonstrates that both positive and negative sides of the system do not influence each other. In another sense, it seems as if the two different parts are joined together at $x = 0$. Further, the $\frac{d^2C}{dx^2}$ versus x profile gives an overall idea about the region where the system is losing the diffusing element (i.e., where $\left(\frac{\partial^2 C_B}{\partial x^2}\right) < 0$) and in which part it is gaining (i.e., where $\left(\frac{\partial^2 C_B}{\partial x^2}\right) > 0$). However, it should be noted that the region where the system is losing or gaining flux changes with time, since the concentration profile changes with time, as shown in Fig. 3.5.

As already mentioned, the system considered for the above discussion acts as if two different parts are joined together. If material B is joined or deposited on the surface of material A, as shown in Fig. 3.6, then Eq. 3.10 must be written as

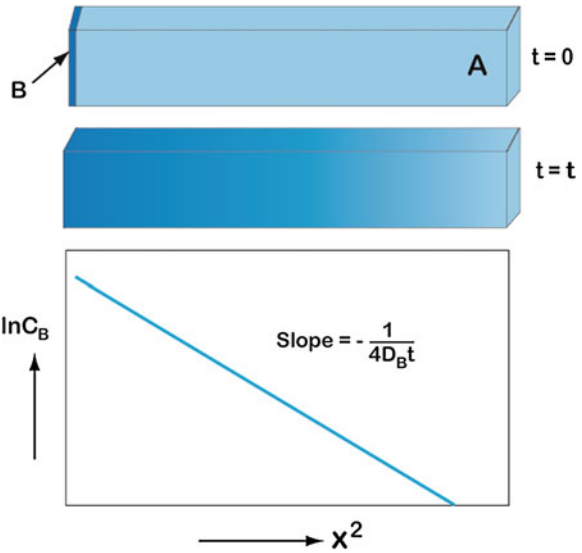

Fig. 3.6 Determination of the diffusion coefficient is shown from the slope of the ln C_B versus x^2 plot

$$C_B = \frac{M_B}{\sqrt{\pi D_B t}} \exp\left(-\frac{x^2}{4D_B t}\right) \tag{3.11}$$

Note here that the factor 2 from the denominator in Eq. 3.10 is removed since the material diffuses in one direction only. Equation 3.11 can be written as

$$\ln C_B = \ln \frac{M_B}{\sqrt{\pi D_B t}} - \frac{x^2}{4D_B t} \tag{3.12}$$

As shown in Fig. 3.6, the diffusion coefficient D_B can be estimated from the slope $\left(= -\frac{1}{4D_B t}\right)$ of the $\ln C_B$ versus x^2 plot.

3.2.1.1 Solution for a Semi-infinite Diffusion Couple (Error Function Analysis)

When two blocks with different concentrations are joined and annealed at an increased temperature for diffusion, this is called a diffusion couple. A diffusion couple is one of the important techniques to study diffusion with an added advantage that often it resembles the actual reaction layer structure in many applications. The treatment to estimate the diffusion parameters is similar when a piece of material is exposed to the gaseous medium, for example, as in carburization of steel having a situation as shown in Fig. 3.2b. With the change in time, the penetration length and the concentration at a particular position will be changed. A semi-infinite system is one where the ends of the couple are not affected by the

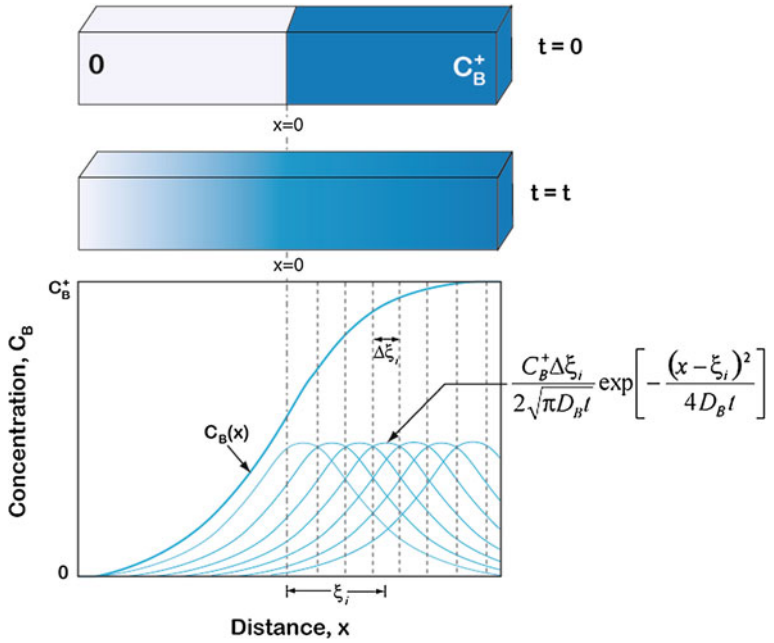

Fig. 3.7 Concentration profile in a diffusion couple based on the consideration of many thin slices

diffusion of components. The relations developed here will be applicable only in a semi-infinite diffusion couple case, which will be explained in greater detail. In general, the lengths of the blocks are considered to be semi-infinite when the following relation for the length is valid $> 10\sqrt{Dt}$. It can be immediately seen that this length actually depends on the system under study. For our analysis, we first consider a diffusion couple of pure A ($C_B = 0$) and an alloy of A–B ($C_B = C_B^+$), as shown in Fig. 3.7. The initial boundary conditions are

$C_B = 0$ at $x < 0$ before annealing, that is, for time $t = 0$ and
$C_B = C_B^+$ at $x > 0$ before annealing, that is, for time $t = 0$.

The solution to this can be found with the help of the solution developed for the thin-film condition. We assume that the block with the concentration C_B^+ is built from n numbers of very thin slices of thickness $\Delta\xi$. Now, we can see this problem similar to the thin-film condition, given above in Eq. 3.10. In a particular thin slice $\Delta\xi_i$, the total concentration of element B is $M_B = C_B^+\Delta\xi_i$. Therefore, this can be written as

$$C_B(x) = \frac{C_B^+\Delta\xi_i}{2\sqrt{\pi D_B t}}\exp\left[-\frac{(x-\xi_i)^2}{4D_B t}\right] \tag{3.13}$$

Here, x is replaced by $(x-\xi_i)$, since the slice $\Delta\xi_i$ is located at a distance ξ_i from the initial contact plane, $x=0$. Similarly, we consider all other thin slices and from the assumption that different slices do not affect each other, the concentration at any position x after superposition can be written as

$$C_B(x) = \frac{C_B^+}{2\sqrt{\pi D_B t}} \sum_{i=1}^{n} \exp\left[-\frac{(x-\xi_i)^2}{4D_B t}\right] \Delta\xi_i \tag{3.14}$$

The first slice $\Delta\xi_1$ is at the distance of $\xi_1 = 0$ and the nth slice $\Delta\xi_n$ is at the distance of $\xi_n = +\infty$ from the initial contact plane, $x=0$. The concentration at any position x, following Eq. 3.14, can be written in the integral form as

$$C_B(x) = \frac{C_B^+}{2\sqrt{\pi D_B t}} \int_0^{\infty} \exp\left[-\frac{(x-\xi)^2}{4D_B t}\right] d\xi \tag{3.15}$$

Let us consider

$$\eta = \frac{x-\xi}{2\sqrt{D_B t}} \tag{3.16}$$

Differentiating Eq. 3.16,

$$d\eta = -\frac{d\xi}{2\sqrt{D_B t}} \tag{3.17}$$

For $\xi = 0$, $\eta = \frac{x}{2\sqrt{D_B t}}$, and for $\xi = \infty$, $\eta = -\infty$. So Eq. 3.15 can be written as

$$C_B(x) = -\frac{C_B^+}{\sqrt{\pi}} \int_{x/\left(2\sqrt{D_B t}\right)}^{-\infty} \exp\left(-\eta^2\right) d\eta = \frac{C_B^+}{\sqrt{\pi}} \int_{-\infty}^{x/\left(2\sqrt{D_B t}\right)} \exp\left(-\eta^2\right) d\eta \tag{3.18}$$

The value of the integral in Eq. 3.18 is not straightforward to estimate. So for the sake of convenience, Eq. 3.18 is converted in terms of error function. The error function of z, which is basically the value of the integral from 0 to z, expressed as

$$\mathrm{erf}(z) = \frac{2}{\sqrt{\pi}} \int_0^{z} \exp\left(-\eta^2\right) d\eta \tag{3.19}$$

In general, the values of erf(z) as a function of z is available in the literature and the positive values of z are listed in Table 3.1. The variation is shown in Fig. 3.8 for both positive and negative values of z. From Eq. 3.18,

Table 3.1 erf(z) values are listed for z, which can be obtained from $\mathrm{erf}(z) = \frac{2}{\sqrt{\pi}} \sum_{n=0}^{\infty} \frac{(-1)^n z^{2n+1}}{n!(2n+1)} = \frac{2}{\sqrt{\pi}} \left(z - \frac{z^3}{1! \times 3} + \frac{z^5}{2! \times 5} - \frac{z^7}{3! \times 7} \cdot \ldots \ldots \ldots \ldots \right)$

	Second digit after decimal of z									
z	0	1	2	3	4	5	6	7	8	9
0.0	0.00000	0.01128	0.02256	0.03384	0.04511	0.05637	0.06762	0.07886	0.09008	0.10128
0.1	0.11246	0.12362	0.13476	0.14587	0.15695	0.16800	0.17901	0.18999	0.20094	0.21184
0.2	0.22270	0.23352	0.24430	0.25502	0.26570	0.27633	0.28690	0.29742	0.30788	0.31828
0.3	0.32863	0.33891	0.34913	0.35928	0.36936	0.37938	0.38933	0.39921	0.40901	0.41874
0.4	0.42839	0.43797	0.44747	0.45689	0.46623	0.47548	0.48466	0.49375	0.50275	0.51167
0.5	0.52050	0.52924	0.53790	0.54646	0.55494	0.56332	0.57162	0.57982	0.58792	0.59594
0.6	0.60386	0.61168	0.61941	0.62705	0.63459	0.64203	0.64938	0.65663	0.66378	0.67084
0.7	0.67780	0.68467	0.69143	0.69810	0.70468	0.71116	0.71754	0.72382	0.73001	0.73610
0.8	0.74210	0.74800	0.75381	0.75952	0.76514	0.77067	0.77610	0.78144	0.78669	0.79184
0.9	0.79691	0.80188	0.80677	0.81156	0.81627	0.82089	0.82542	0.82987	0.83423	0.83851
1.0	0.84270	0.84681	0.85084	0.85478	0.85865	0.86244	0.86614	0.86977	0.87333	0.87680
1.1	0.88021	0.88353	0.88679	0.88997	0.89308	0.89612	0.89910	0.90200	0.90484	0.90761
1.2	0.91031	0.91296	0.91553	0.91805	0.92051	0.92290	0.92524	0.92751	0.92973	0.93190
1.3	0.93401	0.93606	0.93807	0.94002	0.94191	0.94376	0.94556	0.94731	0.94902	0.95067
1.4	0.95229	0.95385	0.95538	0.95686	0.95830	0.95970	0.96105	0.96237	0.96365	0.96490
1.5	0.96611	0.96728	0.96841	0.96952	0.97059	0.97162	0.97263	0.97360	0.97455	0.97546
1.6	0.97635	0.97721	0.97804	0.97884	0.97962	0.98038	0.98110	0.98181	0.98249	0.98315
1.7	0.98379	0.98441	0.98500	0.98558	0.98613	0.98667	0.98719	0.98769	0.98817	0.98864
1.8	0.98909	0.98952	0.98994	0.99035	0.99074	0.99111	0.99147	0.99182	0.99216	0.99248
1.9	0.99279	0.99309	0.99338	0.99366	0.99392	0.99418	0.99443	0.99466	0.99489	0.99511

(continued)

Table 3.1 (continued)

	Second digit after decimal of z									
z	0	1	2	3	4	5	6	7	8	9
2.0	0.99532	0.99552	0.99572	0.99591	0.99609	0.99626	0.99642	0.99658	0.99673	0.99688
2.1	0.99702	0.99715	0.99728	0.99741	0.99753	0.99764	0.99775	0.99785	0.99795	0.99805
2.2	0.99814	0.99822	0.99831	0.99839	0.99846	0.99854	0.99861	0.99867	0.99874	0.99880
2.3	0.99886	0.99891	0.99897	0.99902	0.99906	0.99911	0.99915	0.99920	0.99924	0.99928
2.4	0.99931	0.99935	0.99938	0.99941	0.99944	0.99947	0.99950	0.99952	0.99955	0.99957
2.5	0.99959	0.99961	0.99963	0.99965	0.99967	0.99969	0.99971	0.99972	0.99974	0.99975
2.6	0.99976	0.99978	0.99979	0.99980	0.99981	0.99982	0.99983	0.99984	0.99985	0.99986
2.7	0.99987	0.99987	0.99988	0.99989	0.99989	0.99990	0.99991	0.99991	0.99992	0.99992
2.8	0.99992	0.99993	0.99993	0.99994	0.99994	0.99994	0.99995	0.99995	0.99995	0.99996
2.9	0.99996	0.99996	0.99996	0.99997	0.99997	0.99997	0.99997	0.99997	0.99997	0.99998
3.0	0.99998	0.99998	0.99998	0.99998	0.99998	0.99998	0.99998	0.99999	0.99999	0.99999
3.1	0.99999	0.99999	0.99999	0.99999	0.99999	0.99999	0.99999	0.99999	0.99999	0.99999
3.2	0.99999	0.99999	0.99999	1.00000	1.00000	1.00000	1.00000	1.00000	1.00000	1.00000

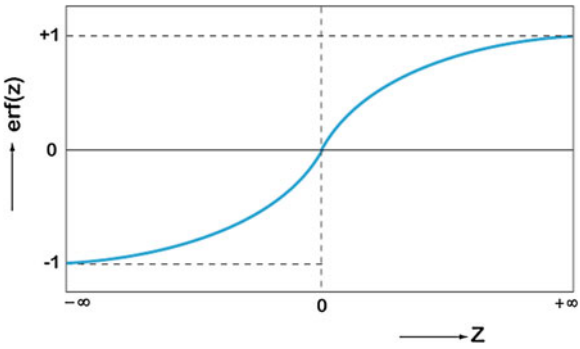

Fig. 3.8 Variation of erf(z) with z

$$C_B(x) = \frac{C_B^+}{\sqrt{\pi}}\left[\int_{-\infty}^{0} \exp\left(-\eta^2\right) d\eta + \int_{0}^{x/\left(2\sqrt{D_B t}\right)} \exp\left(-\eta^2\right) d\eta\right]$$

$$C_B(x) = \frac{C_B^+}{\sqrt{\pi}}\left[-\int_{0}^{-\infty} \exp\left(-\eta^2\right) d\eta + \int_{0}^{x/\left(2\sqrt{D_B t}\right)} \exp\left(-\eta^2\right) d\eta\right] \tag{3.20}$$

$$C_B(x) = \frac{C_B^+}{2}\left[-\text{erf}(-\infty) + \text{erf}\left(\frac{x}{2\sqrt{D_B t}}\right)\right]$$

It can be seen from Fig. 3.8 that

$$\text{erf}(-z) = -\text{erf}(z); \qquad \text{erf}(-\infty) = -1 \tag{3.21}$$

Therefore, Eq. 3.20 can be written as

$$C_B(x) = \frac{C_B^+}{2}\left[1 + \text{erf}\left(\frac{x}{2\sqrt{D_B t}}\right)\right] \tag{3.22a}$$

$$\frac{C_B(x)}{C_B^+} = \frac{1}{2}\left[1 + \text{erf}\left(\frac{x}{2\sqrt{D_B t}}\right)\right] \tag{3.22b}$$

It should be noted here that position x is the distance from $x = 0$. For the negative side, the sign inside the bracket will be negative. Thus, it is mandatory to find the location of $x = 0$ after measuring the concentration profile for the calculation of the diffusion coefficient. For $x = 0$, $C_B(x) = \frac{C_B^+}{2}[1 + 0] = \frac{C_B^+}{2}$. Therefore, the location of the initial contact plane is $\frac{C_B^+}{2}$ that is exactly at the middle of the concentration profile. This is to be expected, since we are considering here a constant diffusion coefficient at all possible concentrations.

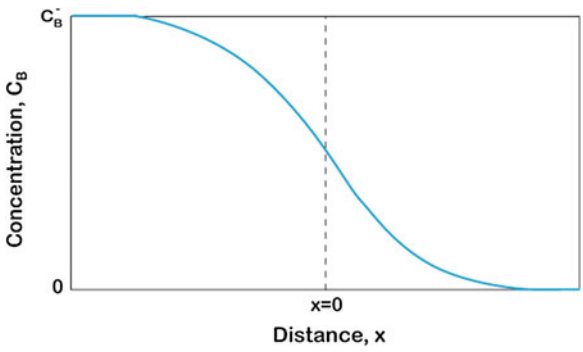

Fig. 3.9 Composition profile in a diffusion couple of $C_B = C_B^-$ and $C_B = 0$

When the concentration profile is opposite to that in Fig. 3.7, as shown in Fig. 3.9, the concentration profile is expressed as

$$C_B(x) = \frac{C_B^-}{2}\left[1 - \text{erf}\left(\frac{x}{2\sqrt{D_B t}}\right)\right] = \frac{C_B^-}{2}\text{erfc}\left(\frac{x}{2\sqrt{D_B t}}\right) \tag{3.23a}$$

$$\frac{C_B(x)}{C_B^-} = \frac{1}{2}\left[1 - \text{erf}\left(\frac{x}{2\sqrt{D_B t}}\right)\right] = \frac{1}{2}\text{erfc}\left(\frac{x}{2\sqrt{D_B t}}\right) \tag{3.23b}$$

where erfc(z) is the error function complement.

So the only difference between Eqs. 3.22a and 3.23a is the negative sign inside the brackets, which originates from the difference in the concentration profiles that are considered in these systems. By denoting "−" and "+" in C_B^- and C_B^+, respectively, we define the concentrations of the left- and right-hand unaffected side of the couple halves.

In the above examples, the concentration in one end member was considered to be $C_B = 0$. Now, let us consider the diffusion couple of C_B^- and C_B^+, where the concentration of element B is not zero. First, by considering that $C_B^+ > C_B^-$ and the profile shown in Fig. 3.10a and by following Eq. 3.22b, the relation can be written as

$$\frac{C_B(x) - C_B^-}{C_B^+ - C_B^-} = \frac{1}{2}\left[1 + \text{erf}\left(\frac{x}{2\sqrt{D_B t}}\right)\right] \tag{3.24a}$$

Here, the concentration is normalized with respect to the concentration difference of the end members. Note that when $C_B^- = 0$, Eq. 3.24a reduces to Eq. 3.22b. Moreover, the sign of the x should be considered properly. The left-hand side of the couple from $x = 0$ should have a negative sign.

After rearranging, Eq. 3.24a can be written as

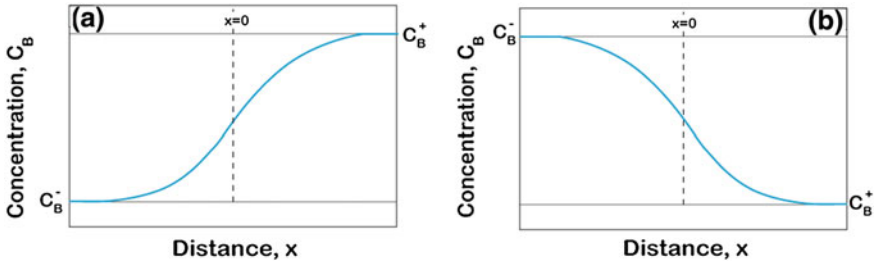

Fig. 3.10 Concentration profile in diffusion couples of C_B^- and C_B^+, where in **a** $C_B^+ > C_B^-$, and **b** $C_B^- > C_B^+$

$$C_B(x) = \frac{C_B^+ + C_B^-}{2} + \frac{C_B^+ - C_B^-}{2}\text{erf}\left(\frac{x}{2\sqrt{D_B t}}\right) \tag{3.24b}$$

Similarly, if we consider that $C_B^- > C_B^+$ and the profile shown in Fig. 3.10b, then Eq. 3.23b should be rewritten as

$$\frac{C_B(x) - C_B^+}{C_B^- - C_B^+} = \frac{1}{2}\left[1 - \text{erf}\left(\frac{x}{2\sqrt{D_B t}}\right)\right] \tag{3.25a}$$

Rearranging Eq. 3.25a, we can write

$$C_B(x) = \frac{C_B^- + C_B^+}{2} - \frac{C_B^- - C_B^+}{2}\text{erf}\left(\frac{x}{2\sqrt{D_B t}}\right) \tag{3.25b}$$

that coincides exactly with Eq. 3.24b. The specific way to represent the solution, i.e., expressions (3.24a) or (3.25a), remains an arbitrary choice which may be dictated by a demand of "elegancy" to have positive numbers in equations. This is explained below.

Please note that the error function is antisymmetric just by definition, Eq. 3.21. Thus, on the negative side from $x = 0$, i.e., at $x < 0$, minus sign inside the bracket in Eq. 3.25a changes to a plus sign with a positive argument of the error function. Therefore, it should be noted from Eqs. 3.24a and 3.25a that any combination of these equations can be considered if the signs inside the brackets are taken properly. A positive sign might be used for the part of the concentration profile where the concentration increases when we move toward the end of the couple from the initial contact plane. A negative sign might be used for the part of the concentration profile where the concentration decreases when we move toward the end of the couple from the initial contact plane. Any choice is allowed and they are equivalent as the direct comparison of Eqs. 3.24b and 3.25b reveals.

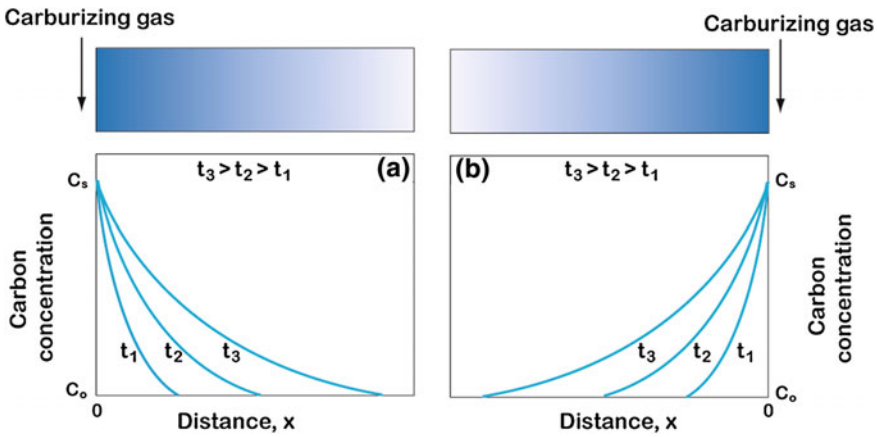

Fig. 3.11 Change in concentration profile with annealing time during carburization of steel in which **a** C diffuse from *left* to *right*, and **b** C diffuse from *right* to *left*

Note that here it is also necessary to find the location of the initial contact plane ($x = 0$) for the calculation of the diffusion coefficient from the concentration profile. For $x = 0$, Eq. 3.24b or 3.25b will reduce to

$$C_B(x = 0) = \frac{C_B^- + C_B^+}{2} \tag{3.26}$$

This suggests that the average concentration will indicate the location of the initial contact plane.

Now, let us turn to consider the carburization of steel, where the carbon concentration of steel from the surface is increased by diffusion. In this process, steel is kept in a gas mixture of CH_4 and CO at the temperature of interest. Depending on the ratio of the gases supplied, the carbon concentration at the surface is kept constant by a constant supply of gases. Thus, with the increase in annealing time, the concentration profile of the carbon changes, as shown in Fig. 3.11a. If we consider that the initial carbon concentration of the steel is C_o and the carbon concentration at the surface is C_s, following Eq. 3.25a (since C diffuses from left to right), the concentration of C, $C(x)$, comparing Fig. 3.10b can be written as

$$\frac{C(x) - C_o}{C_S - C_o} = 1 - \text{erf}\left(\frac{x}{2\sqrt{Dt}}\right) \tag{3.27a}$$

Furthermore, Eq. 3.27a can be rearranged as

$$C(x) = C_S - (C_S - C_0)\,\text{erf}\left(\frac{x}{2\sqrt{Dt}}\right) \tag{3.27b}$$

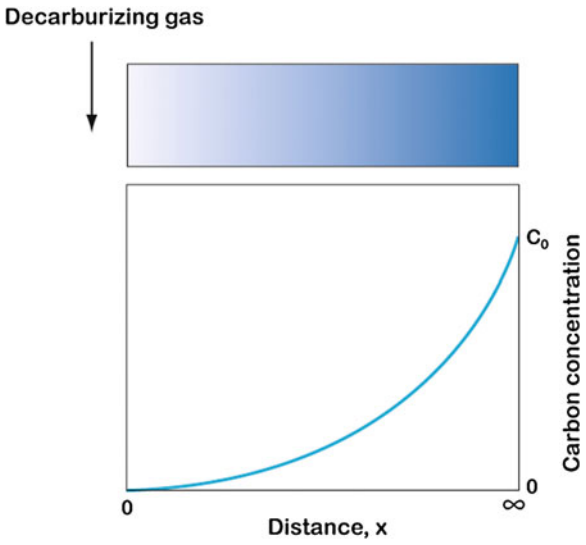

Fig. 3.12 Concentration profile for a decarburization treatment

Here, the main difference between Eqs. 3.25a and 3.27a is that the numerical factor ½ is missing. The numerical factor is removed since here we have only one side of the profile from $x = 0$ compared to the two sides in the previous diffusion couple example. It is also important to note that if we consider that the carbon is diffusing in the opposite direction, as shown in Fig. 3.11b, we shall find the same relation as in Eq. 3.27a. In this case, as C is diffusing from right to left, Eq. 3.24a should be written comparing Fig. 3.10a as

$$\frac{C(x) - C_o}{C_S - C_o} = 1 + \text{erf}\left(-\frac{x}{2\sqrt{Dt}}\right) = 1 - \text{erf}\left(\frac{x}{2\sqrt{Dt}}\right) = \text{erfc}\left(\frac{x}{2\sqrt{Dt}}\right) \tag{3.28}$$

If we consider the carburization treatment of a material with no carbon present before the carburization treatment, that is, $C_o = 0$, the above relation will reduce to

$$C(x) = C_S\left[1 - \text{erf}\left(\frac{x}{2\sqrt{Dt}}\right)\right] = C_S\,\text{erfc}\left(\frac{x}{2\sqrt{Dt}}\right) \tag{3.29}$$

When considering decarburization, as shown in Fig. 3.12 where the carbon concentration at the surface $C_s = 0$ for the whole time, then from Eq. 3.28, the relation for decarburization can be written

$$C(x) = \text{C}_0\,\text{erf}\left(\frac{x}{2\sqrt{Dt}}\right) \tag{3.30}$$

Yet another important relation can be obtained from the above discussion. Let us consider the carburization experiment once again. We know that the diffusion coefficient depends on temperature; it is considered to be D_1 at T_1 and D_2 at T_2. Suppose we wish to know what is the time difference needed to achieve a particular concentration, let us say $C(x) = C_1$ at a particular distance, x_1 at two different temperatures. We can write $\frac{C(x)-C_o}{C_S-C_o} = \frac{C_1-C_o}{C_S-C_o}$ in Eq. 3.28 and

$$\frac{x_1^2}{D_1 t_1} = \frac{x_1^2}{D_2 t_2} \tag{3.31}$$

Next follows a discussion of the calculation of the diffusion coefficient in a diffusion couple. Suppose that under consideration, we have a diffusion couple of two different blocks with composition $C_B^- = C_B^1$ and $C_B^+ = C_B^2$ such that $C_B^2 > C_B^1$. Therefore, the concentration profile shown in Fig. 3.10a can be expected and it can be expressed as

$$C_B(x) = \left(\frac{C_B^2 + C_B^1}{2}\right) + \left(\frac{C_B^2 - C_B^1}{2}\right)\text{erf}\left(\frac{x}{2\sqrt{Dt}}\right) \tag{3.32}$$

If the system has a constant molar volume, Eq. 3.32 reduces to

$$N_B(x) = \frac{N_B^2 + N_B^1}{2} + \left(\frac{N_B^2 - N_B^1}{2}\right)\text{erf}\left(\frac{x}{2\sqrt{Dt}}\right) \tag{3.33}$$

since $C_B = \frac{N_B}{V_m} = \frac{X_B}{V_m}$, where N_B is the atomic fraction, X_B is the mole fraction of element B, and V_m is the molar volume. Suppose these compositions are $N_B^1 = 0.3$ and $N_B^2 = 0.7$, as shown in Fig. 3.13. This couple is annealed for 25 h. A composition profile might built up such that the atomic fraction of B at the distance of 2.5 μm from x = 0 would be $N_B = 0.6$. Using the relation in Eq. 3.33, it is possible to estimate the diffusion coefficient in this system. From the description above, we know that $N_B = 0.6$, $N_B^1 = 0.3$, $N_B^2 = 0.7$, $t = 25$ h $= 25 \times 60 \times 60 = 90{,}000$ s, and $x = 2.5$ μm $= 2.5 \times 10^{-6}$ m. Substituting these values in Eq. 3.33, we get

$$\text{erf}\left(\frac{2.5 \times 10^{-6}}{2\sqrt{D \times 90{,}000}}\right) = 0.5 \tag{3.34}$$

From the values listed in Table 3.1, we see that there is no value exactly for erf(z) = 0.5. We have the values erf(z) = 0.49375 for z = 0.47 and erf(z) = 0.50275 for $z = 0.48$. Since these values are very close, we can consider linear variation and find the value of z for erf(z) = 0.5 following

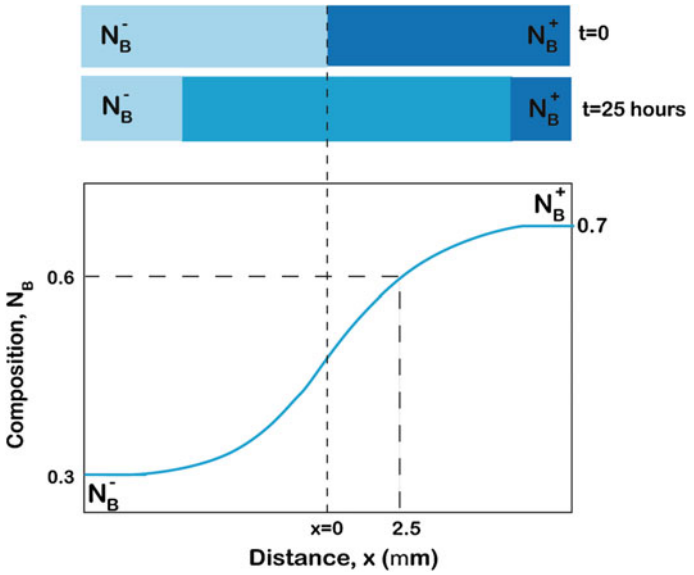

Fig. 3.13 Composition profile developed in a diffusion couple

$$\frac{z - 0.47}{0.48 - 0.47} = \frac{0.5 - 0.49375}{0.50275 - 0.49375}$$
$$z = 0.477$$

So we get

$$\text{erf}(0.477) \approx 0.5 \tag{3.35}$$

Comparing Eqs. 3.34 and 3.35, we can write

$$\frac{2.5 \times 10^{-6}}{2\sqrt{90{,}000 \times D}} = 0.477$$

This gives the diffusion coefficient $D = 7.6 \times 10^{-17}$ m^2/s.

Now, suppose that we are interested in annealing the couple at a higher temperature where diffusion is faster and the diffusion coefficient is $D = 1.05 \times 10^{-16}$ m^2/s. We would like to find how much time it will take to develop a similar concentration profile, i.e., $N_B = 0.6$ at the position $x = 2.5$ μm. Since the compositions are the same, we can use Eq. 3.31 for this calculation, where $D_1 = 7.6 \times 10^{-17}$ m^2/s, $t_1 = 25$ h, $x_1 = x_2 = 2.5$ μm, and $D_2 = 1.05 \times 10^{-16}$ m^2/s. Thus, we find that the system needs $t_2 = \frac{D_1 t_1}{D_2} = 18.1$ h.

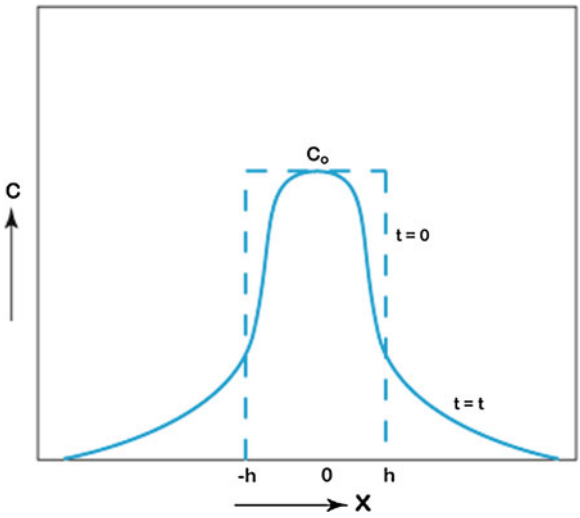

Fig. 3.14 Diffusion profile developed from a thick film

The relations used above are strictly applicable only in the case of semi-infinite diffusion couples. This means that annealing time must be short enough such that the end parts of the material are not affected by the diffusion of components. We have stated previously that the length of each block in a couple should be greater than $10\sqrt{Dt}$. However, in practice, even if one atomic layer in the end is found to be unaffected, the couple can be considered as semi-infinite. It must be apparent that the values for the length of the blocks can be considered as semi-infinite depend on diffusion coefficient, temperature, and desired annealing time. If the system is not semi-infinite, the analysis will lead to an inaccurate results.

Let us consider a situation shown in Fig. 3.14. At time $t = 0$, that is, the time before annealing, the concentration in the position ranges from $-h$ to h is $C = C_o$. Outside this range, the concentration is $C = 0$. Therefore, this can be seen as a block/film with the thickness of 2 h having concentration of C_o sandwiched between the materials with the concentration of zero. The initial profile at $t = 0$ is indicated by the dotted line. The concentration profile, after time $t = t$, is indicated by the solid curve. It should be noted here that this condition is different from the condition discussed in Sect. 3.2.1, where the diffusing element from a very thin layer mixes in the impurity level without significantly altering the concentration of the bulk material into which the component is diffusing. In this example, we consider a relatively thick film or block with a finite thickness such that the diffusing components from this relatively thick film/block will change the overall concentration of the material in between which this layer is sandwiched. In the

thin-film solution as shown Sect. 3.2.1, we considered the concentration of the diffusing element only. In this example, however, we consider the concentration profile of an alloy.

Following a procedure similar to that used to develop the error function analysis, the diffusion profile can be expressed as

$$C(x) = \frac{1}{2}C_o\left[\text{erf}\frac{h-x}{2\sqrt{Dt}} + \text{erf}\frac{h+x}{2\sqrt{Dt}}\right] \tag{3.36}$$

It can be seen that the diffusion profile has a reflection at $x = 0$. The book written by J. Crank can be consulted for a more detailed treatment on this [2].

3.2.2 Solution for Homogenization (Separation of Variables)

Now, let us consider a system that ultimately reaches homogenization, meaning that we must turn to consider relatively long annealing times. In any system, the concentration varies with respect to two variables time t and position x. Hence, we can write

$$C(x,t) = X(x)T(t) \tag{3.37}$$

Partial differentiation with respect to x and t gives

$$\frac{dC}{dt} = X\frac{dT}{dt} \tag{3.38a}$$

$$\frac{d^2C}{dx^2} = T\frac{d^2X}{dx^2} \tag{3.38b}$$

Replacing Eqs. 3.38a and 3.38b in Fick's second law expressed in Eq. 3.5b, we obtain

$$X\frac{dT}{dt} = \text{DT}\frac{d^2X}{dx^2} \tag{3.39a}$$

$$\frac{1}{\text{DT}}\frac{dT}{dt} = \frac{1}{X}\frac{d^2X}{dx^2} \tag{3.39b}$$

From Eq. 3.39a, it can be observed that the relation is divided with respect to t and x. Both sides should be equal to the same constant value. For the sake of convenience, let us consider the constant as $-\lambda^2$. There is an advantage in considering the constant like this, which will become clearer to the reader during the derivation that follows. We can write

$$\begin{aligned} \frac{1}{\mathrm{DT}}\frac{dT}{dt} &= -\lambda^2 \\ \frac{dT}{T} &= -\lambda^2 D dt \end{aligned} \tag{3.40}$$

By integration, it yields

$$\begin{aligned} \int_{T_o}^{T}\frac{dT}{T} &= -\lambda^2 D\int_{o}^{t} dt \\ \ln\frac{T}{T_o} &= -\lambda^2 Dt \\ T(t) &= T_o \exp\left(-\lambda^2 Dt\right), \end{aligned} \tag{3.41a}$$

where T_o is the value at time $t = 0$. This relation indicates the reason for considering the negative sign in the constant value. It shows that T decreases exponentially with increasing annealing time. Additionally, we can write

$$\begin{aligned} \frac{1}{X}\frac{d^2X}{dx^2} &= -\lambda^2 \\ \frac{d^2X}{dx^2} + \lambda^2 X &= 0 \end{aligned}$$

Integration gives

$$X(x) \;=\; (A'\sin\lambda x + B'\cos\lambda x), \tag{3.41b}$$

where A' and B' are the constant.

Replacing T and X (from Eq. 3.41a) in Eq. 3.36, we get

$$\begin{aligned} C(x,t) &= (A'\sin\lambda x + B'\cos\lambda x)T_o\exp\left(-\lambda^2 Dt\right) \\ &= (A\sin\lambda x + B\cos\lambda x)\exp\left(-\lambda^2 Dt\right) \end{aligned}$$

where $A = A'T_o$ and $B = B'T_o$

This solution is valid for any values of λ. If there are different values of λ, then the solution will be the sum of all the values

$$C(x,t) \;=\; \sum_{m=1}^{\infty}(A_m\sin\lambda_m x + B_m\cos\lambda_m x)\exp\left(-\lambda_m^2 Dt\right) \tag{3.42}$$

The values of A_m, B_m and λ_m should be determined depending on the system under investigation. We consider a thin sheet, with thickness h, where the concentration of the diffusing substance is kept uniformly before the start of the

diffusion process. Further, the concentration at the surfaces of the sheet is always kept at zero. Thus, the boundary conditions can be written as

$$C = C_o, \quad \text{for } 0 < x < h, \quad \text{at} \quad t = 0$$
$$C = 0, \quad \text{for } x = 0 \quad \text{and } x = h, \quad \text{at} \quad t > 0$$

From the second boundary condition, C is zero at $x = 0$ at any time only if $B_m = 0$. Moreover, C is zero at $x = h$ at any time only if $\lambda_m = m\pi/\mathrm{h}$, where m is a positive integer. Replacing these values in Eq. 3.42, we get

$$C(x,t) = \sum_{m=1}^{\infty} \left(A_m \sin \frac{m\pi}{h} x \right) \exp\left(-\frac{m^2\pi^2}{h^2} Dt \right) \tag{3.43}$$

From the first boundary condition for $t = 0$, we get

$$C_o = \sum_{m=1}^{\infty} \left(A_m \sin \frac{m\pi}{h} x \right) \tag{3.44}$$

Now, we need to find the value of A_m. We multiply both sides by $\sin \frac{n\pi}{h} x dx$ and integrate in the range of 0 to h.

$$\int_o^h C_o \sin\left(\frac{n\pi}{h} x\right) dx = \sum_{m=1}^{\infty} \left(A_m \int_o^h \sin \frac{n\pi}{h} x \sin \frac{m\pi}{h} x dx \right) \tag{3.45}$$

On the right-hand side, all integrals will be zero except for only one value $n = m$. When $n = m$, the value of the integral is $h/2$. So we can write

$$A_m = \frac{2}{h} \int_o^h C_o \sin\left(\frac{m\pi}{h} x\right) dx \tag{3.46}$$

Integration of this shows the value of 0 for even values of m and $4C_o/m\pi$ for any odd values of m. The summation of the integer values can be changed so that we can use this relation for every integer, with the result that it will give odd m values for every integer. This can be written as

$$A_m = \frac{4C_o}{m\pi} = A_j = \frac{4C}{(2j+1)\pi} \qquad j = 0,\ 1,\ 2. \ldots \ldots \ldots$$

So Eq. 3.43 can be written as

$$C(x,t) = \frac{4C_o}{\pi} \sum_{j=0}^{\infty} \frac{1}{2j+1} \sin \frac{(2j+1)\pi x}{h} \exp\left(-\frac{(2j+1)^2\pi^2}{h^2} Dt \right) \tag{3.47}$$

This solution is the summation of all the terms for j equal from zero to infinity. However, it must be clear from the relation that the value for every successive j decreases exponentially (note the negative sign inside the exponent). It should, therefore, be possible to represent the concentration with the first few values of j. Let us estimate the value for $j = 0$ and 1 after time t.

$$C_{j=0}(x,t) = \frac{4C_o}{\pi}\sin\frac{\pi x}{h}\exp\left(-\frac{\pi^2}{h^2}Dt\right) \quad \text{for } j = 0.$$

$$C_{j=1}(x,t) = \frac{4C_o}{\pi}\frac{1}{3}\sin\frac{3\pi x}{h}\exp\left(-\frac{9\pi^2}{h^2}Dt\right) \quad \text{for } j = 1.$$

Taking ratio of these two values, we get

$$\frac{C_{j=0}(x,t)}{C_{j=1}(x,t)} = 3\exp\left(\frac{8\pi^2}{h^2}Dt\right)$$

As explained earlier, this solution can be used where the thickness of the system is relatively small so that it can reach homogeneity in a reasonable time frame. This thickness again depends on the diffusion coefficient at that particular temperature of interest. Let us consider $h = 4\sqrt{Dt}$, where the ratio given above is 419. This means that if we neglect even the second term, the error is only 0.2 %. On the other hand, if we have $h = 10\sqrt{Dt}$, the ratio is 6.6. If we neglect the second term, an error of around 15 % is to be expected. Thus, the number of terms that should be considered depends on the system and the temperature, since D varies differently in different systems at a particular temperature.

Note There is widespread confusion as to the usefulness or the applicability of Fick's fist law. Many even think that this law cannot be used in any realistic situation. It should be noted here that there is no fundamental problem in Fick's first law. It is true that it cannot be used directly to study the time-dependent mass distribution in a non-steady case. However, at one particular composition after a fixed annealing time, Fick's first law is still applicable to relate the flux and the concentration gradient at any particular concentration. This will be shown in Chap. 6 in which the relations for the calculation of different diffusion parameters are developed.

It is also stated many times that the chemical potential gradient is the real driving force for the diffusion process and not the concentration gradient. As will be discussed in Chap. 4, it is correct that the chemical potential gradient always indicates the direction of diffusing components correctly, since components always diffuse down the chemical potential gradient. It is rather common to find the diffusion of components also down the concentration gradient in the majority of systems. However, there are also several examples of uphill diffusion (especially in multicomponent systems), where the direction of the diffusing components is against the concentration gradient

because of a favorable chemical potential gradient. In this case also, Fick's laws are applicable and the uphill diffusion is indicated by a negative sign in the diffusion coefficient compared to a positive sign for the downhill diffusion. For further clarification, see Chap. 9 on multicomponent diffusion analysis.

References

1. A. Fick, Annalen der Physik 170 (1855) 59
2. J. Crank, The Mathematics of Diffusion, Oxford University Press, New York, 1956

Chapter 4
Development of Interdiffusion Zone in Different Systems

In this chapter, the microstructural evolution in the interdiffusion zone in a diffusion couple is explained based on thermodynamics. A two-phase mixture cannot develop in a binary system, whereas this is possible to find in a ternary system. Condition for finding an uphill diffusion is explained.

As discussed in the previous chapter, when two different blocks are joined for diffusion, it is called a diffusion couple. For example, two alloys of *A*-*B* binary system are coupled, as shown in Fig. 4.1. The concentration (or composition) of the left-hand side of the couple is C_B^- (or N_B^-) and the concentration (or composition) of the right-hand side of the couple is C_B^+ (or N_B^+). We consider $C_B^- < C_B^+$ (or $N_B^- < N_B^+$). In general (meaning not in uphill diffusion), as will be discussed later in this chapter, *A* will diffuse from left to right and *B* will diffuse from right to left. In uphill diffusion, the direction of diffusing component is just the opposite. As the atoms interdiffuse with each other, the overall process is known as interdiffusion. The definition and details of the diffusion parameters are discussed at greater length in Chaps. 5–8. In this chapter, the discussion is on the growth of the phases in an interdiffusion zone in different systems.

4.1 Chemical Potential as the Driving Force for Diffusion and Phase Layer Growth in an Interdiffusion Zone

In most practical examples, diffusion occurs under the presence of driving forces. A chemical driving force that is the diffusion caused by differences in the chemical potential or activity of the components is common to the majority of systems. Additionally, a few other types of forces might influence the diffusion process. For example, in the electronic industry, the flow of electrons also drives the diffusion process because of the presence of current. The presence of driving forces makes the jump rate of atoms higher in one particular direction. Let us consider the isomorphous phase diagram that is presented in Fig. 4.2a. The free energy curve of the solid solution phase at temperature, *T*, is shown in Fig. 4.2b. At any

A. Paul et al., *Thermodynamics, Diffusion and the Kirkendall Effect in Solids*,
DOI: 10.1007/978-3-319-07461-0_4,

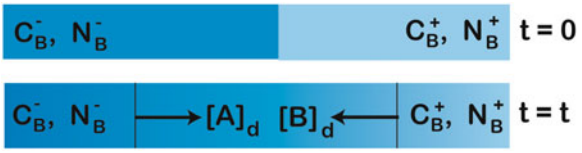

Fig. 4.1 Interdiffusion of components A and B in a diffusion couple

composition, let us say, X_B^*, we can determine the chemical potentials of the components by taking a slope and then extending it to $X_B = 0$ and 1. Following on from this, the activity of the components can be estimated from the relation $\mu_i - \mu_i^o = RT \ln a_i$, where μ_i^o is the chemical potential of component i at the standard state (25 °C and 1 atmospheric pressure). As discussed in Chap. 1, we know that the activity of component B, represented by the value a_B, increases from 0 to 1 with an increase in composition from $X_B = 0$ to 1. In an (almost) ideal system, the activity coefficient γ_B is almost equal to 1 and $a_B \approx X_B$. The variation of the chemical potential is also similar. For instance, the chemical potential of B increases from a negligible value to μ_B with an increase in $X_B = 0 - 1$. The variation in the activity and chemical potential of A with an increase in X_B is just the opposite. Suppose, at temperature T, two alloys P (composition X_B^P) and R (composition X_B^R) are coupled. P is a relatively A-rich alloy and R is a B-rich alloy. The free energies of P and R are g_P and g_R. The compositions of the alloys are such that the average composition considering the total amounts of P and R is X_B^Q, meaning that the couple has an average free energy of g'_Q before mixing by interdiffusion. However, it is higher than the free energy at equilibrium g_Q when they form an alloy after mixing. Since the blocks are coupled below the melting point, the equilibrium composition can only be realized using a solid-state interdiffusion process. Therefore, the driving force comes from the drive to decrease the free energy of the system. It can be seen in Fig. 4.2c that $\mu_A^P > \mu_A^R$ and $\mu_B^R > \mu_B^P$. These values will change to the chemical potentials of the components in the homogenized alloy Q that is μ_A^Q and μ_B^Q. Therefore, the A-rich alloy should lose A and add B. Conversely, the B-rich alloy should lose B and add A. This process indicates that atom A should diffuse from P to R and atom B should diffuse from R to P. The change in the concentration profile with increasing annealing time is shown in Fig. 4.2d. After infinite time, the block will reach to a single equilibrium composition of X_B^Q. Here, infinite time is symbolic, which is basically the time required for complete homogenization to occur. It will vary from system to system depending on the diffusion coefficients at the temperature of interest and thickness of the blocks.

Since atoms diffuse down the chemical potential gradient, the flux of element A can be written based on a phenomenological point of view as

$$J_A \alpha \frac{\mu_A^R - \mu_A^P}{\Delta x} \alpha - \frac{\mu_A^P - \mu_A^R}{\Delta x}$$
$$J_A = -L_A \frac{d\mu_A}{dx}, \tag{4.1a}$$

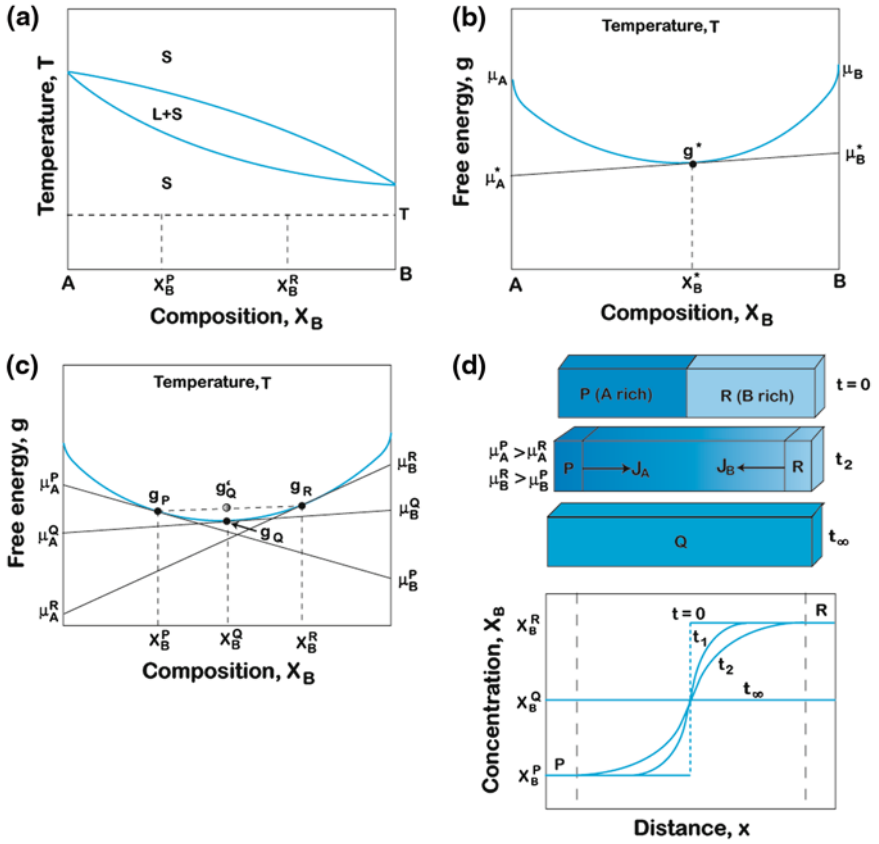

Fig. 4.2 Interdiffusion in a complete solid solution is explained in **a** phase diagram, **b***g* versus composition diagram, **c** chemical potentials of components, and **d** the diffusion couple and composition profiles

where the proportionality constant L_A is called the phenomenological constant of component A.

Similarly for component B, it can be written as

$$J_B \alpha \frac{\mu_B^P - \mu_B^R}{\Delta x} \alpha - \frac{\mu_B^R - \mu_B^P}{\Delta x}$$
$$J_B = -L_B \frac{d\mu_B}{dx}, \tag{4.1b}$$

where L_B is the phenomenological constant for element B. These relations were developed previously in Chap. 1 (Sect. 1.15).

In terms of the concentration gradient, we can write

$$J_A \alpha \frac{C_A^R - C_A^P}{\Delta x} \alpha - \frac{C_A^P - C_A^R}{\Delta x}$$
$$J_A = -D_A \frac{dC_A}{dx} \tag{4.1c}$$

Similarly, we can write

$$J_B \alpha \frac{C_B^P - C_B^R}{\Delta x} \alpha - \frac{C_B^R - C_B^P}{\Delta x}$$
$$J_B = -D_B \frac{dC_B}{dx} \tag{4.1d}$$

D_A and D_B are the intrinsic diffusion coefficients, i.e., the diffusion coefficients of the components A and B.

Therefore, it can be seen in this system that the components diffuse down the chemical potential and concentration gradient. This is indeed the case for most systems. However, in uphill diffusion, it is different—as will be explained at the end of this section. Since composition changes with time at one particular location, driving force and flux of components also change accordingly. It is a fact that the diffusion coefficient depends on a few other factors such as crystal structure and defects, which will be covered in the next few chapters. For now, we consider a hypothetical phase diagram, the one shown in Fig. 4.3a. A diffusion couple is made of the pure components A and B, at temperature T, as presented in Fig. 4.3a. At this temperature of interest, there are three regions between A and B: the phase mixture of A and β, the single-phase β, and the phase mixture of β and B. Following the Gibbs phase rule, $F = C - P + 2$, where F is the degrees of freedom, C is the number of the components, and P is the number of the phases. As the experiments are conducted at constant temperature and pressure, this relation can be written as $F = C - P$. In a binary system ($C = 2$), it becomes $F + P = 2$. Therefore, in binary diffusion couple, the total number of phases and the degrees of freedom can be two. Since composition is one of the degrees of freedom already present, only one phase can be present in the interdiffusion zone. This further indicates that at any position to the diffusion direction, a phase mixture cannot grow in a binary system. Therefore, only the β phase will grow in the interdiffusion zone. We can observe from Figs. 4.3b and c that at the interface I, A and β are in equilibrium, and at the interface II, β and B are in equilibrium. Although local equilibrium exists at these interfaces, the diffusion of the components will occur since there is a difference in the chemical potential of the components between interfaces I and II. We witness a continuous change in the chemical potential across the interdiffusion zone. For example, it changes from μ_A^{I} to μ_A^{II} for the element A. In fact, this is true in any interdiffusion zone, where there will be a continuous variation in chemical potential during the entire interdiffusion process. In this particular case, since the phase has a very narrow homogeneity range, the chemical potential changes very sharply.

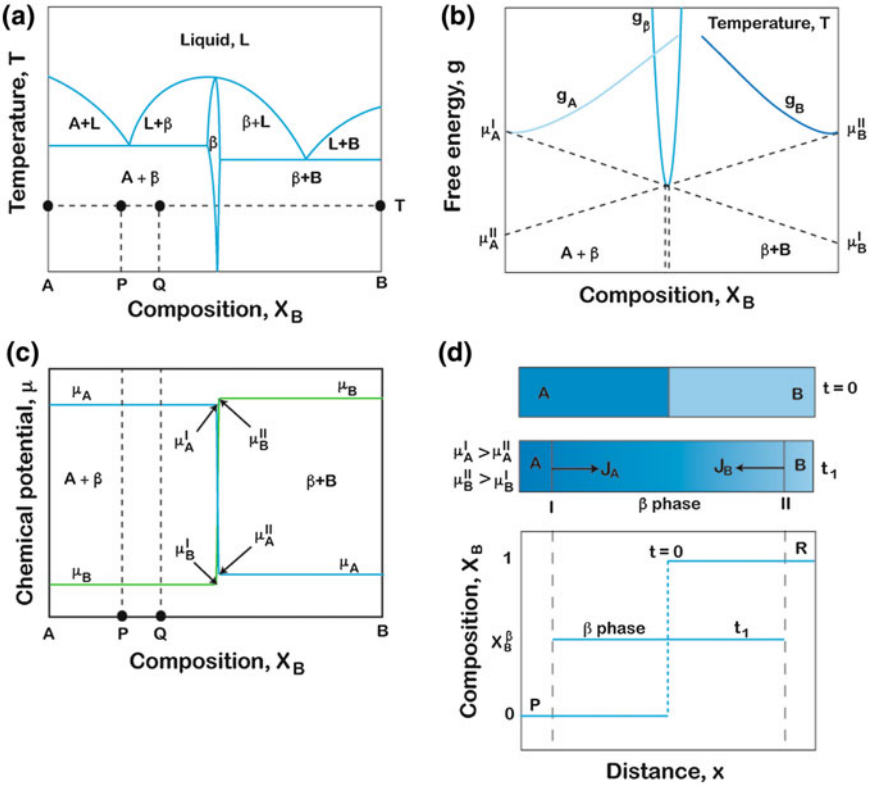

Fig. 4.3 Growth of a phase with narrow composition range is explained in **a** the hypothetical phase diagram, **b** free energy versus composition diagram, **c** the variation of the chemical potential of components, and **d** the interdiffusion zone and composition profile

From the above discussion, it must be clear that if we couple the alloys *P* and *Q*, as shown in Fig. 4.3a, there will be no interdiffusion because there is no difference in the chemical potential of the components even though a composition difference exists. This indicates that the composition or concentration differences between the couples do not explain the interdiffusion of the components. It is necessary to examine the interdiffusion process based on the difference in the chemical potentials. What we are actually saying is that there will be no interdiffusion between the alloys *P* and *Q*. Self-diffusion of the components in the respective alloys still can occur. All these are covered to in greater detail in the next chapter as a part of the discussion on the atomic mechanism of diffusion. Even the size of the phases increases in the alloys to minimize the interfacial energy since these are two-phase mixtures.

Let us consider another phase diagram, as shown in Fig. 4.4a. At the temperature of our interest *T*, we have a solid solution α, an intermetallic compound β, and a solid solution γ. The free energy diagram is shown in Fig. 4.4b and the

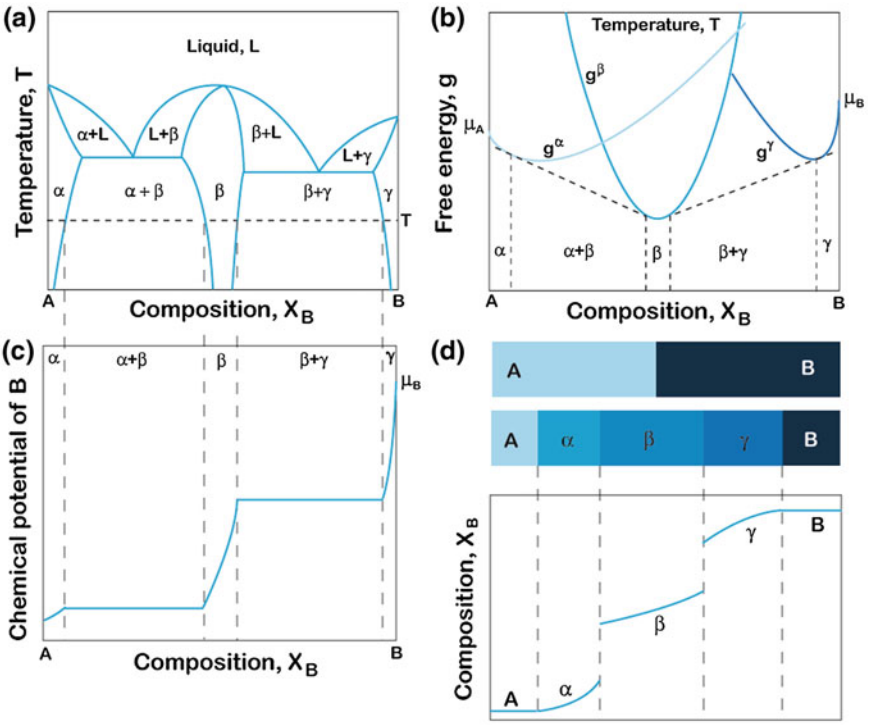

Fig. 4.4 Interdiffusion in a system where the solid solution phases are present along with an intermetallic compound with a wide homogeneity range is explained. **a** Hypothetical phase diagram, **b** g versus X_B diagram, **c** the change in chemical potential with composition, and **d** the diffusion couple and composition profile

change in the chemical potential of element B is shown in Fig. 4.4c. Following the explanations above, it can be understood that the α, β, and γ phases will grow in the interdiffusion zone and the likely composition profile is shown in Fig. 4.4d. It can be seen that the two-phase mixture, where the chemical potentials of the components are constant, will not develop in the interdiffusion zone. Therefore, as expected, the continuous change in the chemical potential is present in the interdiffusion zone.

Now we turn to consider a phase diagram, shown in Fig. 4.5a, which has a complete solid solution in the high temperature range and a miscibility gap in the low temperature range. Therefore, when A and B are coupled in these temperature ranges, different composition profiles will develop in the interdiffusion zone. As shown in Fig. 4.5b, interdiffusion zone will show continuous change in the composition profile at T_1, whereas at T_2, it will exhibit a composition jump.

The whole diffusion process is completely different, if we couple two alloys P and Q inside the miscibility gap, as presented in Fig. 4.6a. The process is explained with respect to the chemical potential of the components, as can be

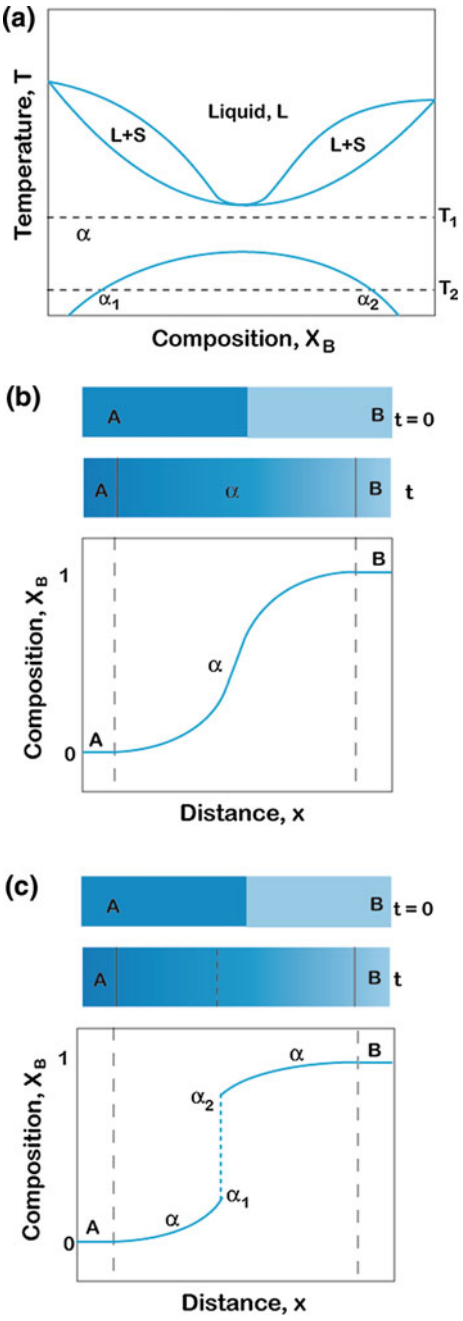

Fig. 4.5 Interdiffusion at two different temperatures is explained in a system where there is a miscibility gap at the lower temperature. **a** Hypothetical phase diagram, **b** composition profile at higher temperature, where it has a complete solid solution, and **c** composition profile at lower temperature, where it has a miscibility gap

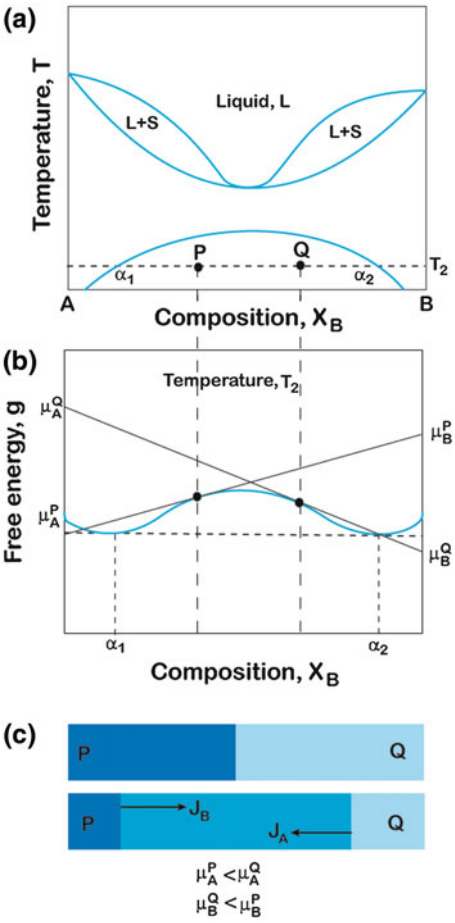

Fig. 4.6 Interdiffusion in a diffusion couple of two alloys inside the miscibility gap is explained in **a** a hypothetical phase diagram, **b** g versus X_B diagram, and **c** the direction of the diffusing components in a diffusion couple

observed in Fig. 4.6b. The alloy P is relatively A-rich and the alloy Q is B-rich. However, it can be seen that in Fig. 4.6b, $\mu_A^P < \mu_A^Q$ and $\mu_B^Q < \mu_B^P$. Therefore, element A will diffuse from the A-lean alloy Q to the A-rich alloy P, whereas B will diffuse from the B-lean alloy P to the B-rich alloy Q.

With respect to the chemical potential gradient, the flux of the atoms can be expressed as

$$J_A \alpha \frac{\mu_A^P - \mu_A^Q}{\Delta x} \alpha - \frac{\mu_A^Q - \mu_A^P}{\Delta x}$$
$$J_A = -L_A \frac{d\mu_A}{dx}, \tag{4.2a}$$

Similarly,

$$J_B \alpha \frac{\mu_B^Q - \mu_B^P}{\Delta x} \alpha - \frac{\mu_B^P - \mu_B^Q}{\Delta x}$$
$$J_B = -L_B \frac{d\mu_B}{dx}, \tag{4.2b}$$

In terms of concentration gradient, we can write

$$J_A \alpha \frac{C_A^P - C_A^Q}{\Delta x}$$
$$J_A = D_A \frac{dC_A}{dx}. \tag{4.2c}$$

Similarly,

$$J_B = D_B \frac{C_B^Q - C_B^P}{\Delta x} = D_B \frac{dC_B}{dx}. \tag{4.2d}$$

Therefore, the minus sign of Fick's first law is not there in the relations expressed in Eqs. 4.2c and 4.2d. This would suggest that the components diffuse up the concentration gradient rather than down the concentration gradient and, for this simple reason, it is called uphill diffusion. It should be noted here that the relations for the calculation of the diffusion coefficients from the composition profiles are derived considering the minus sign in Fick's first law. The same relations can be used to determine the diffusion coefficients even if the system goes through uphill diffusion. Nonetheless, the diffusion coefficient will have a negative sign.

4.2 Few Practical Examples

In this section, we shall provide a few examples that are based upon real working systems. From Fig. 4.7a [1], it can be seen that in the high temperature range, the Au–Cu system has a complete solid solution. Thus, after coupling Au and Cu at 850 °C for 9 h [1], a continuous change in the composition is to be found, as depicted in Fig. 4.7b. It needs to be pointed out here that, below 410 °C, a continuous change in the composition profile will not develop because of the presence of the intermediate phases, as was discussed above based on the hypothetical diffusion couples in Figs. 4.3 and 4.4.

It can be seen in the Au–Sb phase diagram in Fig. 4.8a [2], that below 633 K, there is only one compound $AuSb_2$ that is present. The solubility of Sb in Au is very low and the solubility of Au in Sb is negligible. In the diffusion couple of Au and Sb at 607 K (330 °C) annealed for 225 h, it is mainly the $AuSb_2$ phase that is

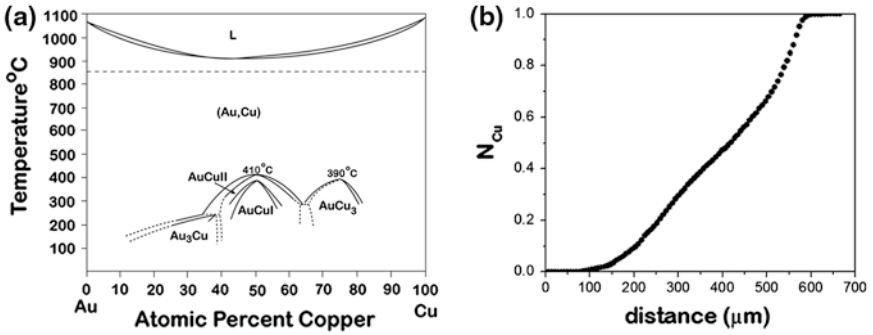

Fig. 4.7 **a** Au–Cu phase diagram. **b** The composition profile developed at 850 °C in the Au–Cu system [1]

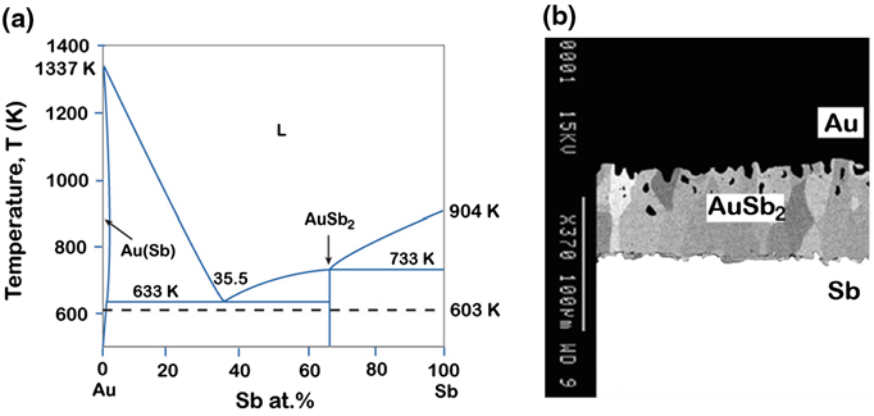

Fig. 4.8 **a** Au–Sb phase diagram [2]. **b** Growth of the $AuSb_2$ phase in the Au–Sb diffusion couple annealed for 225 h at 330 °C [3]

noted to have grown [3]. Both the solid solubility phases do not grow with any reasonable thickness.

Next we consider the diffusion couple in a Co–W system [4]. At 1,200 °C, the three phases, the Co(W) solid solution, Co_7W_6, and the W(Co) solid solution, are expected to grow according to the phase diagram presented in Fig. 4.9a [5, 6]. It can be seen from the micrograph in Fig. 4.9b and the composition profile in Fig. 4.9c that mainly the Co(W) solid solution, denoted as Co(ss), and the Co_7W_6 phase grows with reasonable thickness in the interdiffusion zone [6]. We should also note here that thermodynamics explains the existence of the phases; however, the growth of the phase layer with reasonable thickness depends on the kinetics that is the interdiffusion rate. The W(Co) solid solution must be present as a very thin layer because of its very low interdiffusion rate.

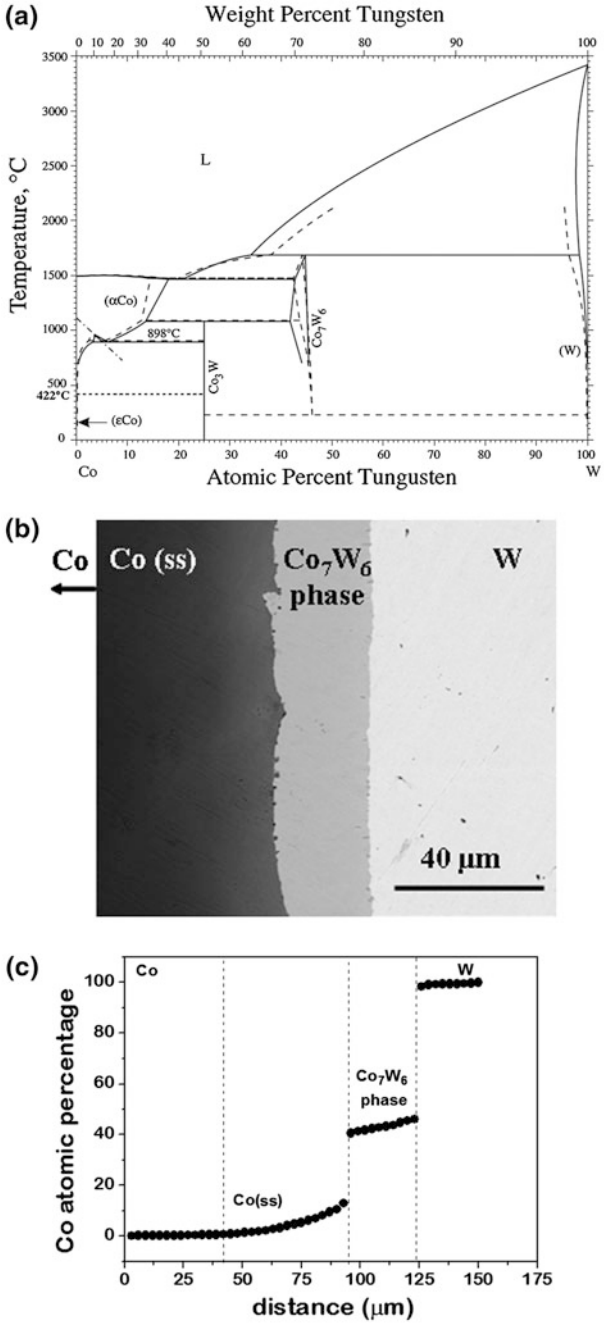

Fig. 4.9 **a** Co–W phase diagram [4], **b** diffusion couple of Co/W annealed at 1,200 °C for 25 h [6], and **c** the measured composition profile [6]

Next, we consider the Ag–Zn system [7] that is presented in Fig. 4.10a. From this figure, it can be seen that the Ag(Zn) solid solution has a much wider homogeneity range compared to the Zn(Ag) solid solution. Moreover, the three intermediate phases, β-AgZn, γ-Ag_5Zn_8 and ε-$AgZn_3$ are present. In the Ag/Zn diffusion couple that was annealed at 370 °C for 5 h, all three intermediate phases grow, as shown in Fig. 4.10b [8]. Although Ag(Zn) has a very wide composition range in the phase diagram, it does not develop because of slow kinetics. The presence of a relatively thin Zn(Ag) solid solution is evident from the composition profile, which can be seen from Fig. 4.10c. ThO_2 particles were used to detect the position of the Kirkendall marker planes K_1 and K_2, which will be discussed in greater depth later in Chaps. 6 and 7.

We consider an incremental diffusion couple in the Ni–Al system [9]. By incremental diffusion couple, we mean that the end-member compositions are not made from pure components. Two alloys $Ni_{0.65}Al_{0.35}$ and $Ni_{0.845}Al_{0.155}$, as represented by dots in Fig. 4.11a used in a diffusion couple annealed at 1,000 °C for 24 h [10]. The $Ni_{0.65}Al_{0.35}$ alloy has two phases, β-NiAl and γ′-Ni_3Al. The $Ni_{0.845}Al_{0.155}$ alloy consists of γ′-Ni_3Al and γ-Ni(Al). Since the two-phase regions cannot grow, only the γ′-Ni_3Al grows in the interdiffusion zone. This is the reason that we find a jump in the composition profile on either side of the product phase.

As we have discussed till now, all the phases present in the phase diagram should grow simultaneously in the interdiffusion zone. This is generally true when speaking about bulk diffusion couples. On the other hand, the sequential growth of the phase layers is very common during the growth of the phases in thin-film conditions [11], something that will be discussed later on in Chap. 11. Now we shall show a few examples on the growth of silicides in bulk diffusion couples. For example, we consider first Nb–Si system [12]. Figure 4.12a shows that the two silicides, $NbSi_2$ and Nb_5Si_3, are present at 1,250 °C, the temperature of interdiffusion [13]. These two phases are indeed found in the interdiffusion zone, as shown in Fig. 4.12b. The growth rate of the Nb_5Si_3 phase is lower than that of the $NbSi_2$ phase, so we find it only as a thin layer.

Next we move on to consider the W–Si system [14], in which two phases, WSi_2 and W_5Si_3, are present, as shown in Fig. 4.13a. It can be seen that the interdiffusion zone in Fig. 4.13b contains mainly the WSi_2 phase [15]. This W_5Si_3 phase is actually present (not visible in the micrograph), however, with the thickness of less than a micron, indicating that the W_5Si_3 phase has a much lower growth rate compared to the WSi_2 phase. As shown in Fig. 4.13c, after removing Si from one side of the couple, an incremental diffusion couple of W/WSi_2 was prepared and annealed at a higher temperature of 1,350 °C in order to achieve a higher growth rate in which the W_5Si_3 phase can be very clearly seen.

In the V–Si system [16], as the phase diagram in Fig. 4.14a shows, four phases should grow in the interdiffusion zone at 1,200 °C [17]. It can, however, be seen in Fig. 4.14b that only two phases, V_5Si_3 and VSi_2, grow with reasonable thickness and the V_3Si phase grows only as a thin layer. The presence of the V_6Si_5 phase is not clearly visible in this microstructure; however, under a higher magnification

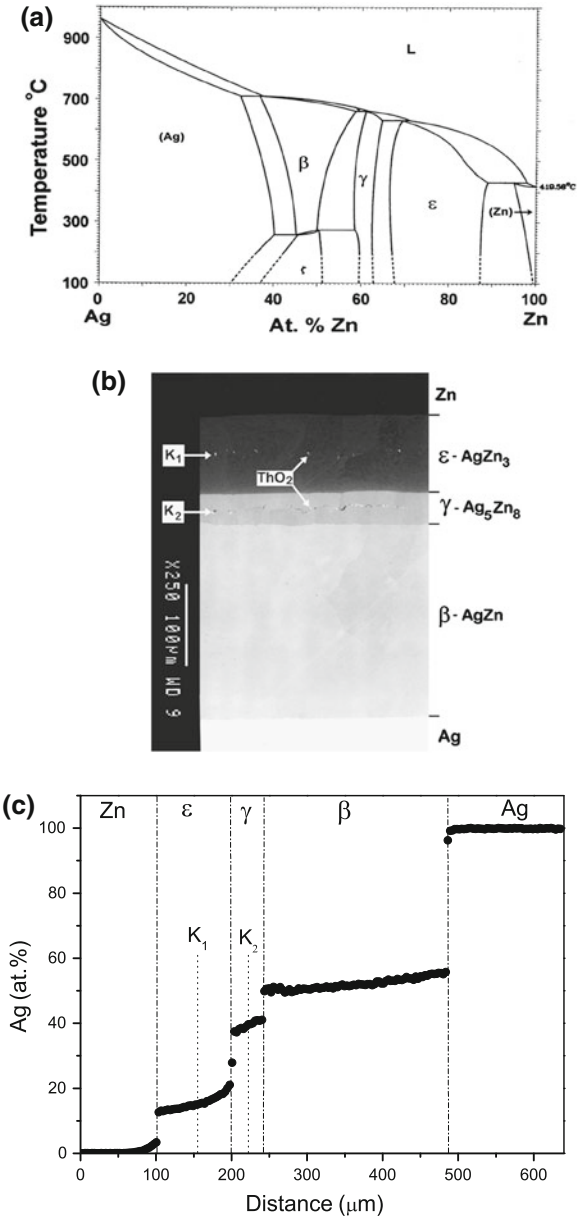

Fig. 4.10 **a** Ag–Zn phase diagram [7], **b** diffusion couple of Ag/Zn annealed at 370 °C for 5 h [8], and **c** the measured composition profile [8]

micrograph, the presence of this phase is very clearly seen, as Fig. 4.14c demonstrates.

Similarly, in the Ta–Si system four phases are present, as shown in Fig. 4.15a [18]. However, in the interdiffusion zone, only two phases, $TaSi_2$ and Ta_5Si_3, were detected in the scanning electron microscope image that is reproduced in

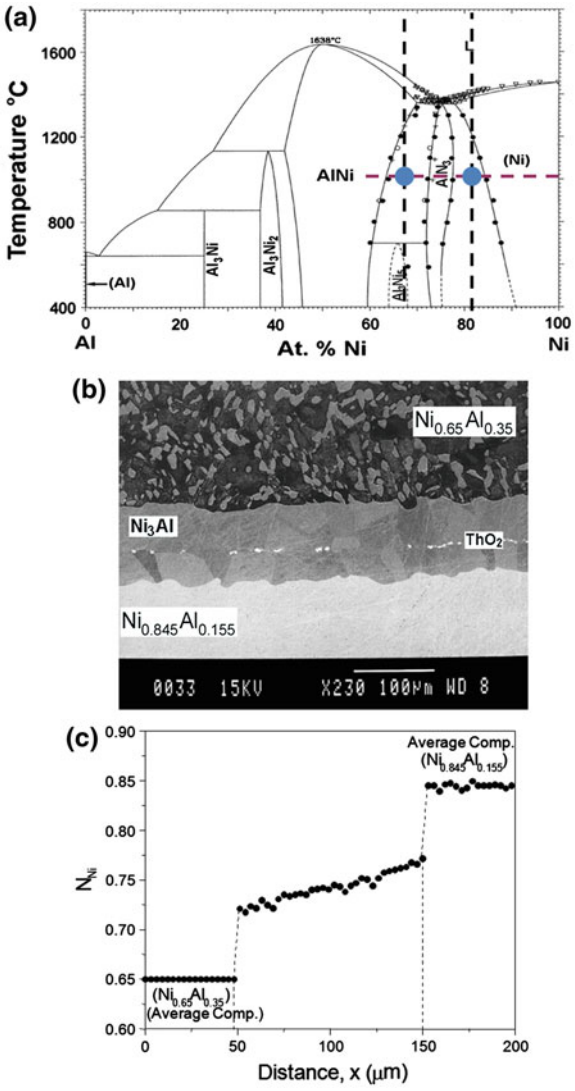

Fig. 4.11 **a** Ni–Al phase diagram is shown [9]. *Dots* indicate the compositions of end members of the incremental diffusion couple. **b** the diffusion couple annealed at 1,000 °C for 24 h, and **c** the measured composition profile [10]

Fig. 4.15b [19]. The Ta_5Si_3 phase was grown as a very thin layer. When Si was removed from one side of the diffusion couple to study the growth of the Ta_5Si_3 phase, as shown in Fig. 4.15c, another phase, Ta_2Si, was found at the interface, suggesting that the other phase, the Ta_3Si phase, must have an even lower growth rate that makes the presence of this phase difficult to detect under a scanning electron microscope.

In the Mo–Si system that is shown in Fig. 4.16a [20], three phases, Mo_3Si, Mo_5Si_3, and $MoSi_2$, are present. In the interdiffusion zone [21], as Fig. 4.16b demonstrates, there were two phases, Mo_5Si_3 and $MoSi_2$, detected in the

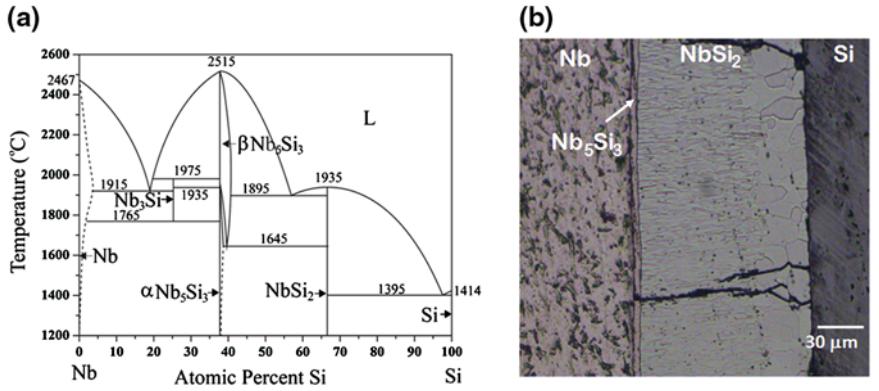

Fig. 4.12 **a** Nb–Si phase diagram [12] and **b** the interdiffusion zone developed in between the diffusion couple of Nb/Si annealed at 1,250 °C for 24 h [13]

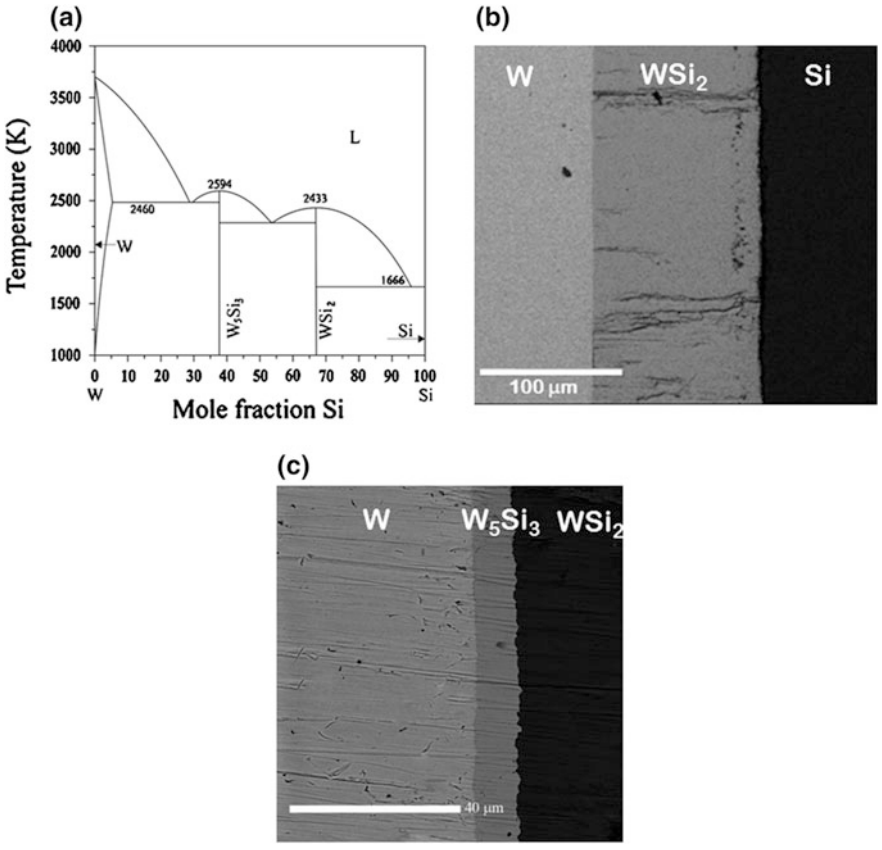

Fig. 4.13 **a** W–Si phase diagram [14], **b** the interdiffusion zone of the W/Si diffusion couple annealed at 1,225 °C for 9 h, and **c** the interdiffusion zone of the incremental diffusion couple W/WSi_2 annealed at 1,350 °C for 16 h [15]

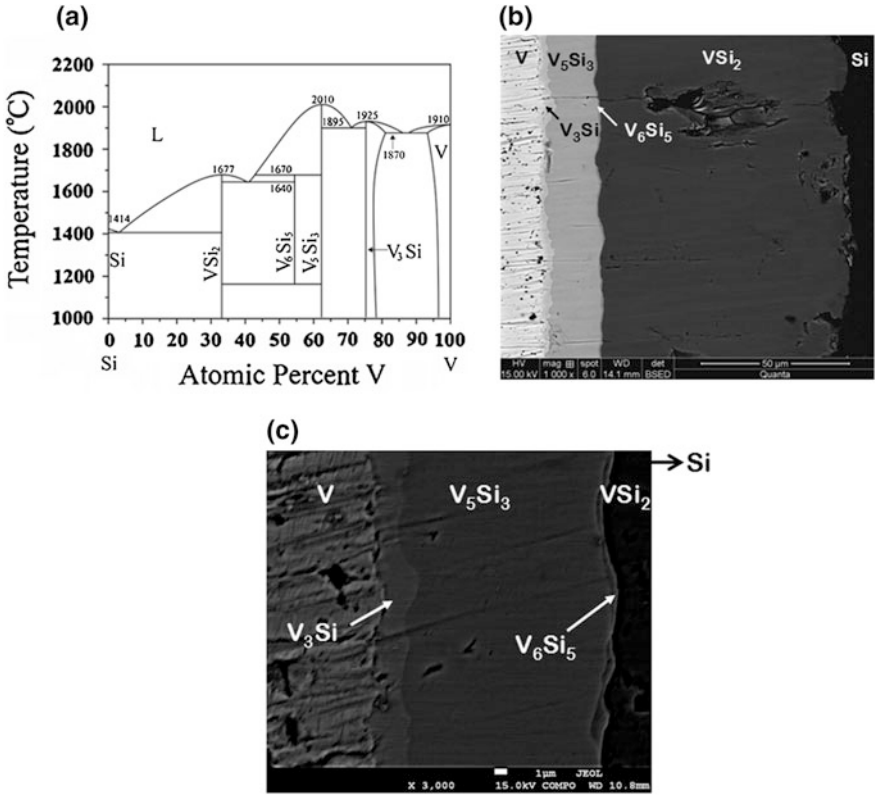

Fig. 4.14 **a** V–Si phase diagram [16], **b** interdiffusion zone of the V/Si diffusion couple annealed at 1,200 °C for16 h, and **c** V-rich phases of the same diffusion couple [17]

interdiffusion zone. The transmission electron microscope image [22] shows the presence of the Mo_3Si phase, which was not possible to detect under the scanning electron microscope. This would strongly suggest that the growth rate of the Mo_3Si phase is much lower compared to the other phases. In fact, in the Ti/Al diffusion couple, only the $TiAl_3$ phase was found in the interdiffusion zone [23]. All the other phases present in the phase diagram, the $TiAl_2$, TiAl, and Ti_3Al phases, were not to be found. These three phases appeared in an incremental couple of $TiAl_3$/Ti, which is suggestive of a much lower growth rate compared to that of $TiAl_3$ in the Ti/Al diffusion couple.

Sometimes, changing annealing temperature or time plays an important role on finding the phases differently in the interdiffusion zone. In the Co–Ta system, as presented in Fig. 4.17 [24], we found that only the Co_2Ta phase grows in the interdiffusion zone at 1,050 °C. However, when the couple is annealed at 1,150 °C, the other two phases, $CoTa_2$ and CoTa, which were not visible (but must be present as very thin layer) at 1,050 °C, were found to form. This indicates that the growth rate of these two phases increased at 1,150 °C making it possible to

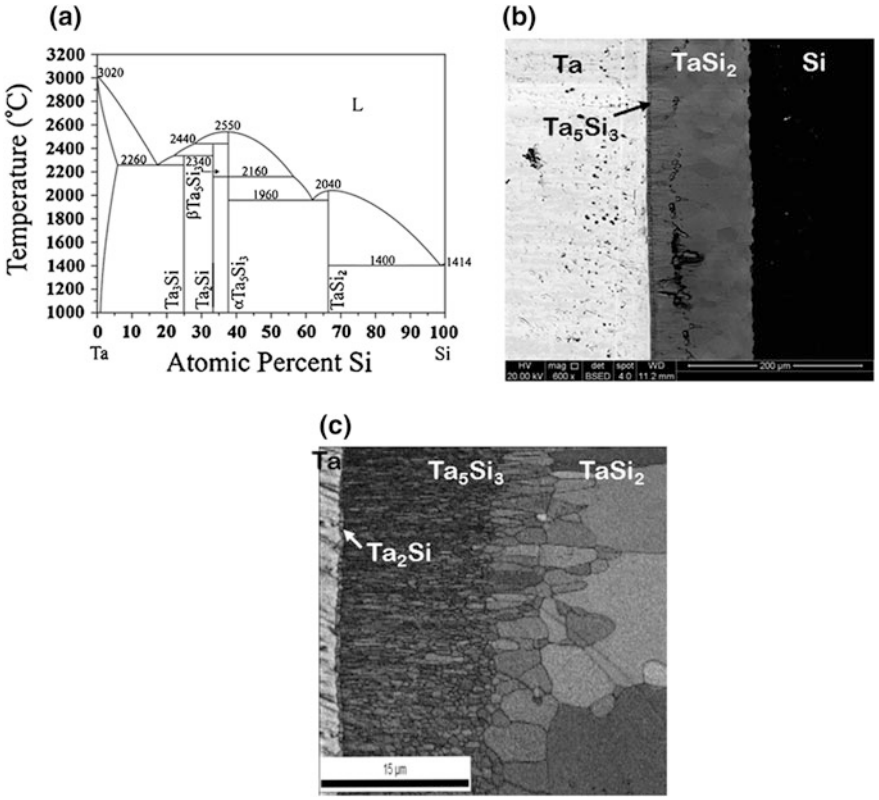

Fig. 4.15 **a** Ta–Si phase diagram [18], **b** interdiffusion zone of the Ta/Si diffusion couple annealed at 1,250 °C for 9 h, and **c** incremental diffusion couple of Ta/$TaSi_2$ annealed at 1,350 °C for 9 h [19]

find them along with the Co_2Ta phase. In the Pd−Sn phase diagram [25], eight intermetallic compounds are present. When the Pd/Sn diffusion couple was annealed at 175 °C for 9 h, only the $PdSn_4$ phase layer was found with higher thickness, as Fig. 4.18a makes clear of its presence [26]. However, upon closer examination—at the $PdSn_4$/Pd interface as the location is marked by (b) in Fig. 4.18a and shown in Fig. 4.18b—another two phases, $PdSn_3$ and $PdSn_2$, were detected. Similar behavior was noticed at 150 °C for the same annealing time of 9 h at 150 °C. However, when the couple was annealed for a longer period of 36 h, the other two phases were also to be found with higher thickness, as shown in Fig. 4.18c. All these further indicate that the growth rate of the other missing phases must be even lower.

Therefore, as expected, all the phases might grow simultaneously especially in bulk diffusion couples. Yet all the phases might not grow with a reasonable thickness to be detectable by the scanning electron microscope. A much higher resolution image from a transmission electron microscope might show the

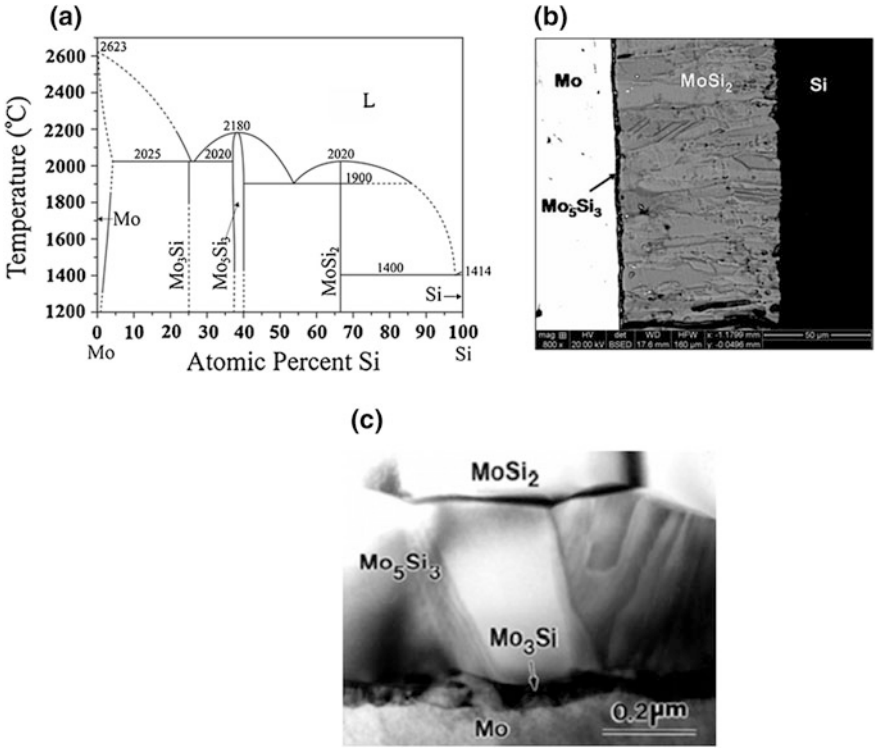

Fig. 4.16 **a** Mo–Si phase diagram [20], **b** interdiffusion zone of the Mo/Si diffusion couple annealed at 1,300 °C for 16 h [21], and **c** interdiffusion zone of the Mo/$MoSi_2$ couple showing the presence of the Mo_3Si phase [22]

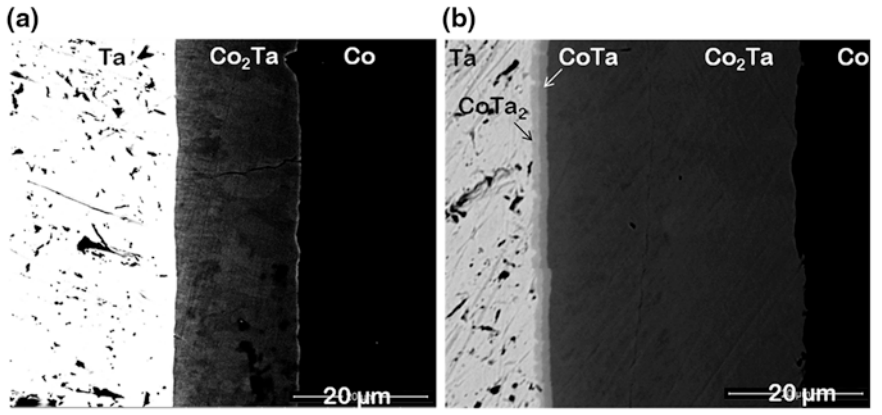

Fig. 4.17 Interdiffusion zone of the Ta/Co diffusion couple annealed at **a** 1,050 °C for 16 h and **b** 1,150 °C for 16 h [24]

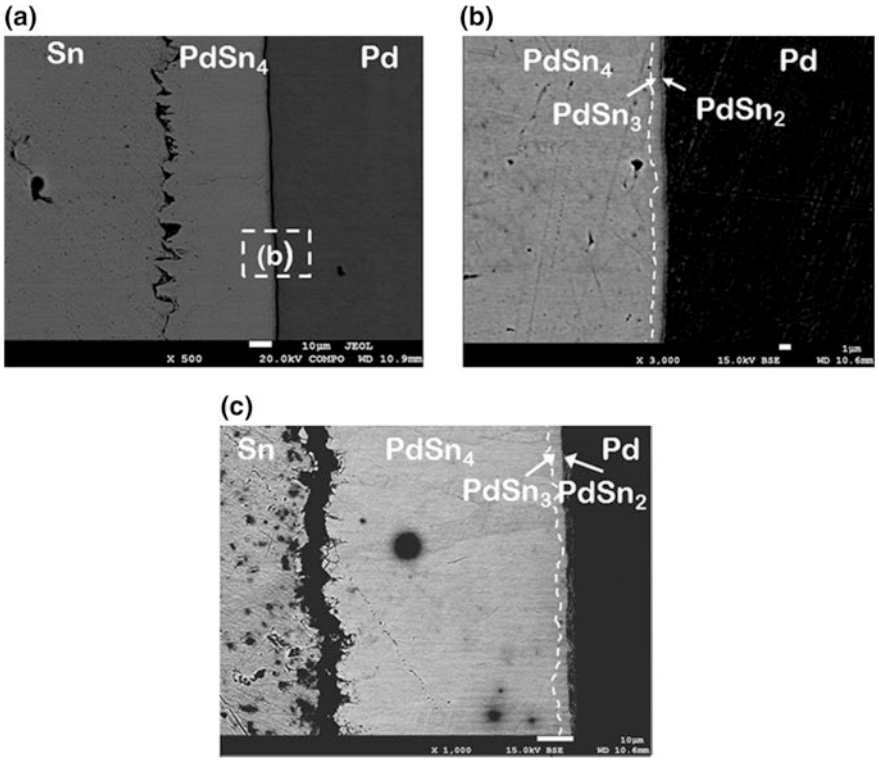

Fig. 4.18 **a** Interdiffusion zone of the Pd/Sn diffusion couple annealed at 175 °C for 9 h, **b** Pd-rich phases in the same diffusion couple, and **c** interdiffusion zone of the Pd/Sn diffusion couple annealed at 150 °C for 36 h [26]

presence of these phase layers as very thin layers. However, it might not be always true. In the Cu–Sn diffusion couple [27], it is suspected that the Cu_3Sn phase does not grow in the beginning along with the Cu_6Sn_5 phase. As will be discussed much later in Chap. 11, sequential growth is rather commonplace in thin-film conditions.

Sometimes, the phases developed in the interdiffusion zone suggest that the problem lies in the phase diagram. As the Ti–Si phase diagram in Fig. 4.19a shows, the Ti_3Si phase does not exist at above 1,170 °C [28]. However, when the experiment was conducted at 1,200 °C, this phase was found along with the other phases as shown in Fig. 4.19b. The same was to be found at 1,225 °C; however, it was not found at 1,250 °C, as shown in Fig. 4.19c and d, hinting strongly that this phase exists up to the temperature somewhere between the temperatures 1,225–1,250 °C [29]. Similarly, the diffusion couple experiments were used to detect problems in a few other phase diagrams [10, 24, 30].

In a ternary system, unlike in a binary system, a phase mixture can evolve in the interdiffusion zone. This could be understood with the help of the Gibbs phase rule, $F = C - P + 2$. Again, since the experiments are conducted at constant

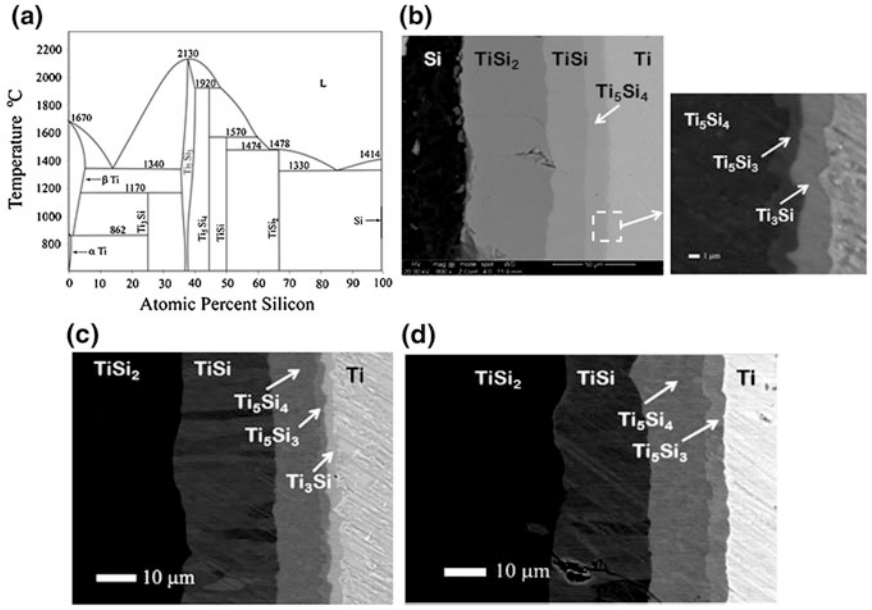

Fig. 4.19 **a** Ti–Si phase diagram [28], **b** Ti/Si couple annealed at 1,200 °C for 16 h, and **c** and **d** Ti-rich phases in the interdiffusion zone annealed at 1,225 and 1,250 °C annealed for 16 h [29], respectively

temperature and pressure, this relation can be written as $F = C - P$. In a ternary system ($C = 3$), it becomes $F = 3 - P$. Therefore, in the ternary diffusion couple, the total of number of phases and the degrees of freedom can be three. Since the composition is one of the degrees of freedom, a mixture of the two phases could develop in the interdiffusion zone. It can, for instance, be seen in the Au(20Cu)/Sn diffusion couple presented in Fig. 4.20a [31] that two layers with phase mixtures have developed: one layer with (Au,Cu)Sn_4 and (Au,Cu)Sn and another layer with (Au,Cu)Sn_2 and (Au,Cu)Sn. This does not necessarily mean that layers always will grow with the phase mixture in a ternary system, as found in the Co(50Ni)/Mo diffusion couple, which can be seen in Fig. 4.20b. This will be discussed further in Chap. 9 (Sect. 9.5).

4.3 Making Products by a Diffusion Process

The study of diffusion is important to gain a full understanding on many physical and mechanical properties of materials. Most of the phase transformations in the solid state occur by some kind of a diffusion-controlled process. It is a common assumption that the study of diffusion is important in order to generate data for further understanding of the related processes. However, there are many products

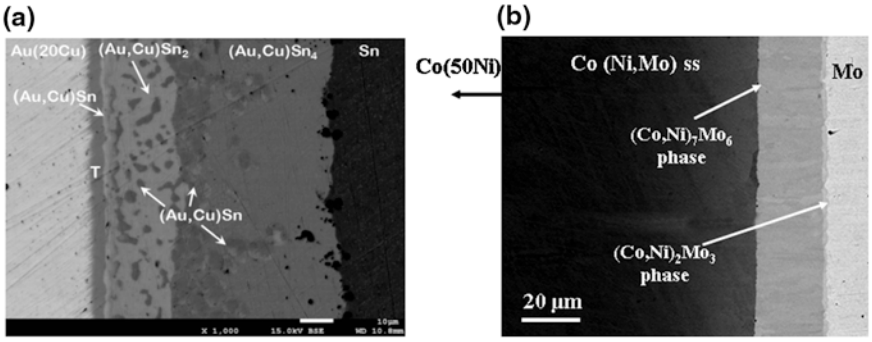

Fig. 4.20 **a** Interdiffusion zone of an Au(20Cu)/Sn diffusion couple annealed at 200 °C for 9 h [31]. *T* is a ternary phase, **b** Interdiffusion zone of a Co(50Ni)/Mo diffusion couple annealed at 1,200 °C for 25 h [6]

on the marketplace that are actually produced by harnessing the diffusion process. Time and time again, the diffusion-controlled growth of the phase layers at the interface determines the overall performance of the structures. In this section, a few technologically important systems are discussed briefly to give an idea of how diffusion can work in practice.

Take, for instance, the turbine blades used in land- and air-based gas turbines. These are required to maintain their high strength at the highest possible temperatures while working in extreme harsh environmental conditions. One single material cannot possess the required mechanical properties along with superior oxidation and corrosion resistance. Superalloys are considered at present as the suitable materials for these demanding applications because of their ability to retain high mechanical strength at very high temperatures. Regrettably, these superalloys do not have enough oxidation resistance. Furthermore, there is a demand to increase the operating temperature for higher efficiency and low emission of unwanted gases. Therefore, two different layers of coatings are used on the superalloy, β Ni(Pt)Al or MCrAlY (M = Ni, Co, Fe) as a bond coat and yittria-stabilized zirconia (*YSZ*) as a thermal barrier top coat. A cross section of the turbine blade is shown in Fig. 4.21a [32]. The material β Ni(Pt)Al is called the diffusion coating, since it is produced by harnessing a diffusion process. First, Pt is electroplated on the superalloy, and following this, Al is deposited by pack cementation process as gas phase at an elevated temperature. After reaction diffusion, a layer of β Ni(Pt)Al forms on the surface. Finally, *YSZ* is deposited on top of it. During deposition and service, an Al_2O_3 layer forms between the bond and top coat that protects the superalloy from oxidation because of very low diffusion rate of oxygen. Moreover, an interdiffusion zone is formed between the superalloy and the bond coat because of composition difference, as shown in Fig. 4.21b [33]. A high concentration of brittle topological closely packed compounds grows in this interdiffusion zone and could be a potential source of failure. The loss of Al in this interdiffusion zone from the bond coat is unwanted since a continuous supply is required for the self-healing that is the continuous growth of the Al_2O_3 layer on

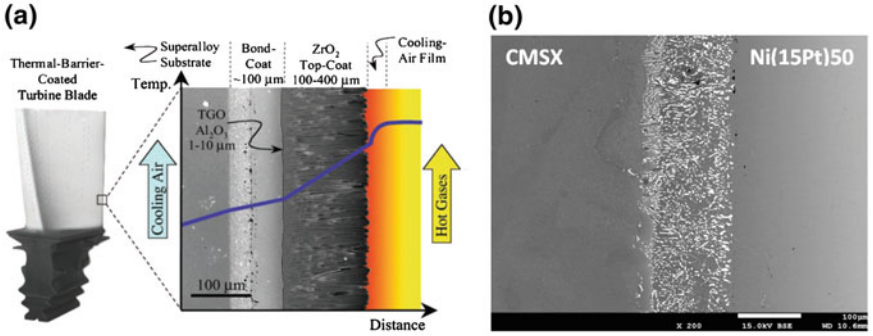

Fig. 4.21 **a** Cross section of a turbine blade [32] **b** Diffusion couple of CMX 4 superalloy with Ni(15Pt)Al bond coat at 1,200 °C, annealed for 25 h [33]

top of the bond coat, i.e., in the middle of bond coat and top coat. Self-healing is important to cover the surface where spallation of Al_2O_3 occurs. Since Al diffuses out from the bond coat, it is important to study the role of different factors that determine the diffusion of components [34–36]. One of the beneficial roles of Pt in the bond coat is an increase in the Al diffusion rate [37]. This ensures that the service life of a turbine blade is increased threefold. Another type of bond coat, MCrAlY, is called an overlay coating since it is deposited directly on the superalloy—unlike the β Ni(Pt)Al coating. Again, similar studies are important to understand or enhance the performance. Studies not only on the bond coat, but also extensive diffusion studies in the superalloys, themselves conducted to understand many properties such as homogenization and creep.

Nb_3Sn is one of the A15 intermetallic superconductors used in many applications where the need is beyond the ability of NbTi (greater than a magnetic field of 8 *T*). Since this is a brittle intermetallic compound, it cannot be drawn as wire. Different manufacturing techniques are used to circumvent this problem, such as the bronze technique, the internal tin process, the powder-in-tube process, the jelly roll process, as well as infiltration, to name but a few. Diffusion plays an important role in the vast majority of production processes. To make our point, we shall now discuss only the bronze technique, which is one of the most favored routes. In this technique, Nb rods are inserted into Cu(Sn) bronze alloys. Next, this block is drawn as wire. The cross-sectional view is given in Fig. 4.22a [38]. Following this, the composite wire is annealed in the temperature range of 700–850 °C such that Nb_3Sn grows at the Nb/Cu(Sn) interface, as shown in Fig. 4.22b, which was annealed at 850 °C for 4 h. It has already been shown that the growth rate of the intermetallic compound changes drastically because of a small change in Sn content in the Cu(Sn) bronze alloy, which changes the Sn diffusion rate through the product phase [39, 40]. Even the addition of small amounts of different components such as Ti, Zr, or Hf also increases the growth rate [41]. Similarly, the manufacturing procedure of V_3Ga is being researched, a process which may replace Nb_3Sn because of better properties.

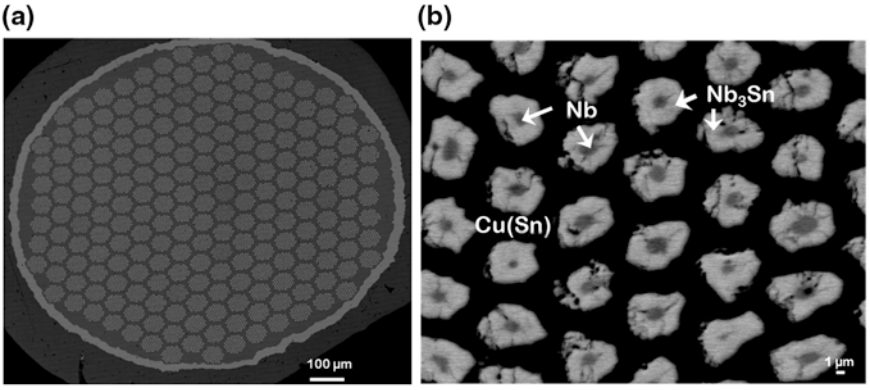

Fig. 4.22 **a** Cross-sectional view of Nb/Cu(Sn) composite wire and **b** growth of Nb_3Sn at 800 °C, annealed for 4 h [38]

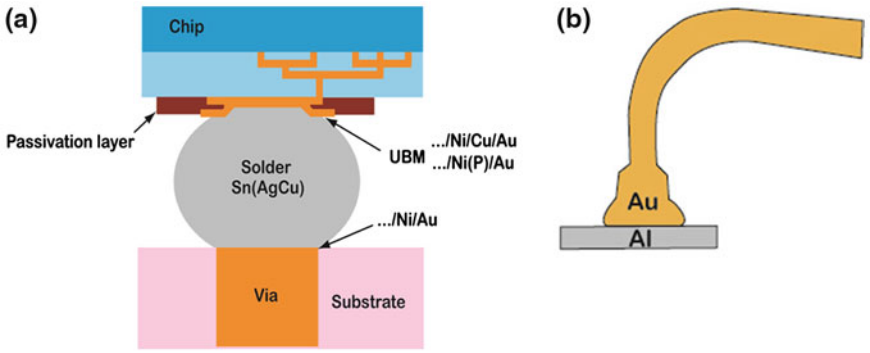

Fig. 4.23 Schematic diagram of cross-sectional view where **a** flip-chip and **b** wire bonds are shown

Flip-chip and wire bonding are the two techniques to join chip–chip and chip–substrate. As shown in the schematic diagram presented in Fig. 4.23a, different underbump metallizations (UBM) are used for different purposes to make the bonding by using an Sn-based solder alloy in flip-chip bonding. Cu is used for good bonding, Ni is used as a barrier layer, and Au is used for corrosion protection. During soldering, Sn-based intermetallic compounds form by reaction between the UBM layers in the solid state and the solder in the liquid state. Further, during the service, these compounds grow by a solid-state diffusion-controlled process. As already explained, the chemical potential difference acts as the driving force for the growth of the phases. Additionally, an electrical current with a very high density due to the small dimensions also plays an important role in the growth of the phases. The growth of the phase layers in the Cu–Sn system is explained in Fig. 4.24b [42]. In the absence of any current, the two-phase layers, Cu_3Sn and

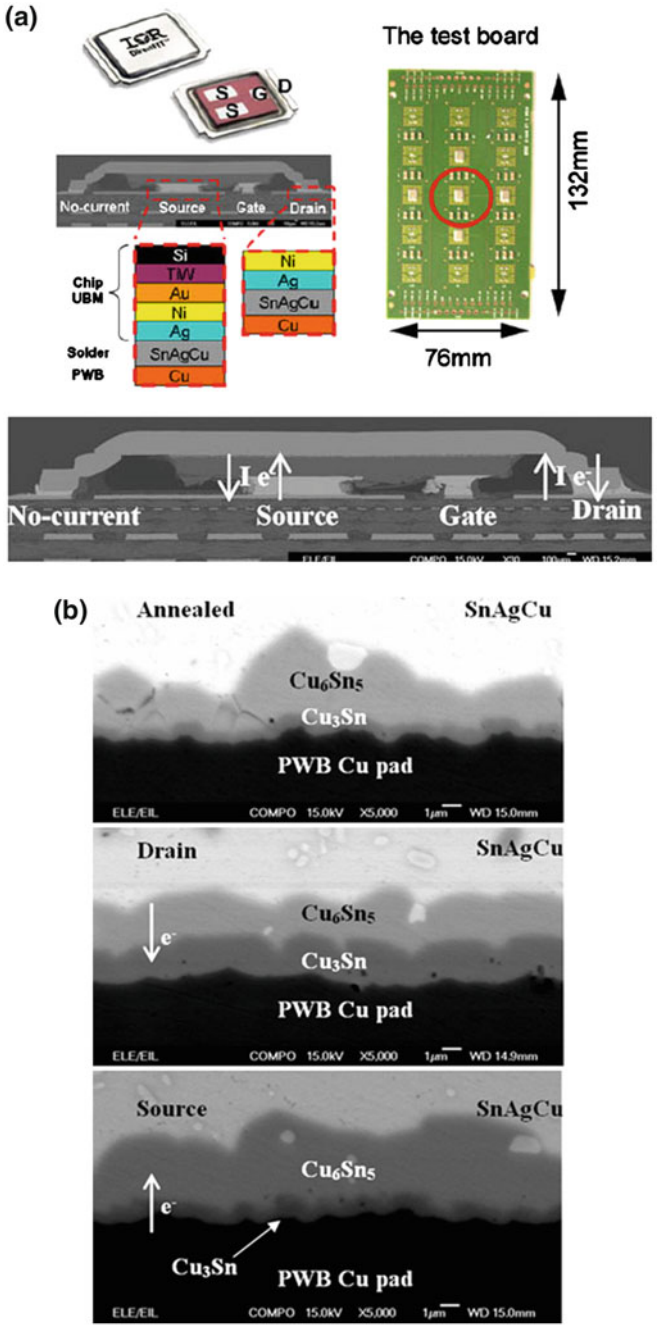

Fig. 4.24 **a** The IRF6716MPbF component package and the test board. **b** The growth of the phase layers of the three interconnections investigated is shown for no current (*NC*) drain and source. Phase layers are grown in the middle of printed wire board (*PWB*) Cu and SnAgCu (*SAC*) solder [42]

Cu_6Sn_5, grow in the interdiffusion zone. It must be clear that Cu diffuses from the Cu end member toward the solder, whereas Sn diffuses from the solder alloy toward the Cu. Depending on the direction of the electron flow, the diffusion of these components is affected. When there is no current, the thickness of the Cu_3Sn phase is less than the thickness of the Cu_6Sn_5 phase. The thicknesses of these layers become comparable when the electrons flow in the direction of the solder to the Cu. On the other hand, the thickness of Cu_6Sn_5 increases without changing the thickness of Cu_3Sn, when the electrons flow from the Cu to the solder. This phenomenological process is discussed in further detail in Chap. 8.

Similarly in wire bonding, as shown in Fig. 4.23b, Au wires are connected with Al pad. During service, several phases grow at the interface, being affected by chemical and electrical driving forces.

Often, in order to achieve a property balance, dissimilar materials such as metal–metal, metal–ceramic and ceramic–ceramic are joined by a solid-state diffusion bonding process. This process is being exploited to produce a seamless bond between two different types of superalloys. Metal–metal bondings are produced by this method when these are difficult to join properly by welding. In many applications, however, ceramics are preferred as the top layer and a metal or alloy as the substrate. In this case, the materials are bonded directly or joined using an inter-layer. Even two different ceramic layers are also bonded using a metal interlayer. Multilayer laminate structures are also produced following a similar method. To achieve this, alternate layers are deposited using various techniques or rolled after stacking before annealing to create a good bond by a diffusion-controlled process.

References

1. R. Ravi and A. Paul, Journal of Materials Science: Materials in Electronics, 23 (2012) 2152
2. H. Okamoto, Journal of Phase Equilibria 17 (1996) 78
3. A. Paul, A.A. Kodentsov, G. de With, F.J.J. van Loo, Intermetallics 11 (2003) 1195
4. H. Okamoto, Journal of Phase Equilibria and Diffusion 29 (2008) 119
5. R. Ravi and A. Paul, Intermetallics 19 (2011) 426
6. V.D. Divya, U. Ramamurty and A. Paul, Metallurgical and Materials Transactions 43 (2012) 1564
7. B. Predel, Landolt-Börnstein, Group IV Physical Chemistry 12A (2006) 1
8. A.A. Kodentsov, Aloke Paul, Frans J.J. van Loo, Zeitschrift für Metallkunde 95 (2004) 258
9. K.J. Lee, P. Nash, Journal of Phase Equilibria 12 (1991) 551
10. C. Cserháti, A. Paul, A.A. Kodentsov, M.J.H. van Dal, F.J.J. van Loo, Intermetallics 11 (2003) 291
11. U. Gösele and K. N. Tu, Journal of Applied Physics 53 (1982) 3252
12. M.E. Schlesinger, H. Okamoto, A.B. Gokhale and R. Abbaschian, Journal of Phase Equilibria 14(1993) 502
13. S. Prasad and A. Paul, Acta Materialia 59 (2011) 1577
14. Z. Guo, W. Yuan, Y. Sun, Z. Cai and Z. Qiao, Journal of Phase Equilibria and Diffusion 30 (2009) 564
15. S. Roy and A. Paul, Intermetallics 37 (2013) 83

16. J. F. Smith, Bulletin of Alloy Phase Diagrams 6 (1985) 266
17. S. Prasad and A. Paul, Journal of Phase Equilibria and Diffusion 32 (2011) 212
18. M.E. Schlesinger Journal of Phase Equilibria 15 (1994) 90
19. S. Roy and A. Paul, Philosophical Magazine, 92 (2012) 4215
20. A.B. Gokhale and G.J. Abbaschian, Journal of Phase Equilibria 12 (1991) 493
21. S. Prasad and A. Paul, Intermetallics 19 (2011) 1191
22. J.K. Yoon, J.Y. Byun, G.H. Kim, J.S. Kim, C.S. Choi, Thin Solid Films 405 (2002) 170
23. F.J.J van Loo and G.D Rieck, Acta Metallurgica 21 (1971) 61
24. V. Baheti, S. Roy, R. Ravi and A. Paul, Intermetallics, 33 (2013) 87
25. H. Okamoto, Journal of Phase Equilibria and Diffusion 33 (2012) 253
26. R. Ravi and A. Paul, Journal of Materials Science: Materials in Electronics,23 (2012) 2306
27. A. Paul, C. Ghosh and W.J. Boettinger, Metallurgical and Materials Transactions A 42A (2011) 952
28. H.J. Seifert, H.L. Lukas and G. Petzow, Zeitschrift für Metallkunde 87 (1996) 2
29. S. Roy, S. Divinski and A. Paul, Philosophical Magazine 94 (2014) 683
30. V.D. Divya, U. Ramamurty and A. Paul, Intermetallics 18 (2010) 259
31. S. Santra, S. Islam, R. Ravi, V. Vuorinen, T. Laurila and A. Paul, Phase evolutions in AuCu/Sn system by solid state reactive diffusion. Journal of Electronic Materials (2014). doi:10.1007/s11664-014-3241-z
32. Nitin P. Padture, Maurice Gell, Eric H. Jordan, Science 296 (2002) 280
33. P. Kiruthika and A. Paul, Private communication.
34. A. Paul, A.A. Kodentsov and F.J.J. van Loo, Acta Materialia 52 (2004) 404
35. A. Paul, A.A. Kodentsov and F.J.J. van Loo, Journal of Alloys and Compounds 403 (2005) 147
36. V.D. Divya, U. Ramamurty and A. Paul, Philosophical Magazine 92 (2012) 2187
37. Kristen A. Marino, Berit Hinnemann, and Emily A. Carter, Proceedings of the National Academy of the Sciences of the United States of America 5 (2011) 5480
38. S. Santra and A. Paul, Private communication
39. A.K. Kumar and A. Paul, Journal of Electronic Materials, 38 (2009) 700
40. T. Laurila, V. Vuorinen A.K. Kumar and A. Paul, Applied Physics Letters, 96 (2010) 2319101
41. M. Suenaga, D.O. Welch, R.L. Sabatini, O.F. Kammere and S. Okuda, Journal of Applied Physics 59 (1986) 840
42. T. Laurila, J. Karppinen, V.Vuorinen, A. Paul and M. Paulasto-Kröckel, Journal of Electronic Materials 40 (2011) 1517

Chapter 5
Atomic Mechanism of Diffusion

In this chapter, we analyze the diffusion mechanisms in metals from an atomistic point of view. It is shown that the defects of crystalline structure, mainly vacancies and interstitial atoms, mediate diffusion. The fundamental difference between self-diffusion and tracer (self- or impurity) diffusion is introduced, and the basic concept of correlation factors is discussed. Further, the temperature and orientation dependence of diffusion according to both substitutional and interstitial mechanisms are examined. The complications related to specific structure of compounds, including the effect of ordering, are introduced.

In the previous chapter, we discussed diffusion without considering the atomistic mechanisms of diffusion. For example, we considered a diffusion couple where two different materials are fixed together. In another example, we considered a thin film sandwiched between different materials. Further, diffusion during carburization and decarburization was discussed. It is important to note here that different atomistic mechanisms of diffusion are involved in these different cases.

5.1 Different Types of Diffusion

On atomistic scale, diffusion of atoms is mediated by defects of the crystalline state. In this respect, the diffusion mechanisms can mainly be divided into two categories: substitutional and interstitial. Interstitialcy diffusion (of importance in the case of semiconductors), which is not so common, is not considered for discussion here. As shown in Fig. 5.1a, host atoms exchange positions with vacancies in substitutional diffusion. Therefore, the presence of vacancies is the primary requirement for substitutional diffusion and an atom can jump on the condition that vacancy is present at the nearest neighbor position. Impurities such as C, H, N, and O occupy the interstitial sites, as shown in Fig. 5.1b. When these atoms jump to another vacant interstitial position, it is called interstitial diffusion. We have seen in Chap. 2 that the equilibrium concentrations of vacancies or impurities are very small. Therefore, the jump of atom in substitutional diffusion is restricted, which depends on the availability of a vacancy. On the other hand, since concentration of

A. Paul et al., *Thermodynamics, Diffusion and the Kirkendall Effect in Solids*,
DOI: 10.1007/978-3-319-07461-0_5,

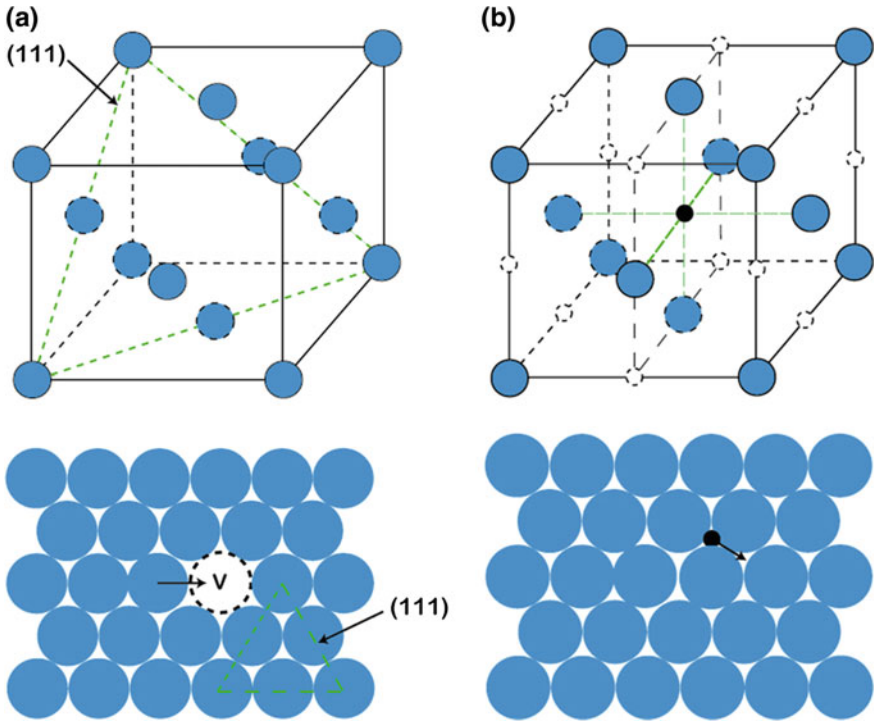

Fig. 5.1 **a** Substitutional diffusion is explained based on atomic arrangement on (111) plane in a FCC crystal. "v" denotes a vacancy. **b** Interstitial diffusion is explained in a FCC crystal. *Filled black dot* is the impurity atom, and *open small circles* indicate the free interstitial positions

impurities is typically very low, most of the nearest neighbor interstitial positions are free for the atom to jump. This is one of the reasons to find much higher rate of interstitial diffusion compared to that of substitutional diffusion. As it will be discussed later in this chapter, substitutional diffusion is even more complicated in an ordered phase compared to a solid solution phase.

As discussed in Chap. 2, in a polycrystalline material, different kinds of defects might be present. When diffusion occurs through the lattice inside a grain by point defects, it is called lattice diffusion or volume diffusion. It is denoted as D_l or D_v. Edge dislocations are one of the line defects present in the structure. When diffusion occurs via these dislocations, it is called pipe diffusion, since it resembles like flow of atoms through a pipe, as shown in Fig. 5.2. In polycrystalline materials, grain boundaries are always present, as shown by arrows in Fig. 5.3. In general, these are more open (compared to the lattice inside the grain). Therefore, atoms can diffuse at much faster rate and it is called the grain boundary diffusion. As it will be discussed in Chap. 10, grain boundary diffusion coefficient, D_{gb}, depends on the type of the particular interface, mainly on the misorientation of the grains and the interface inclination. Generally, diffusion along low-angle grain

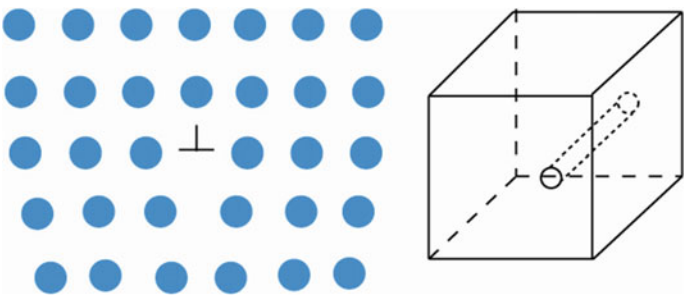

Fig. 5.2 Diffusion through an edge dislocation is explained

Fig. 5.3 Grain boundaries in a polycrystalline material

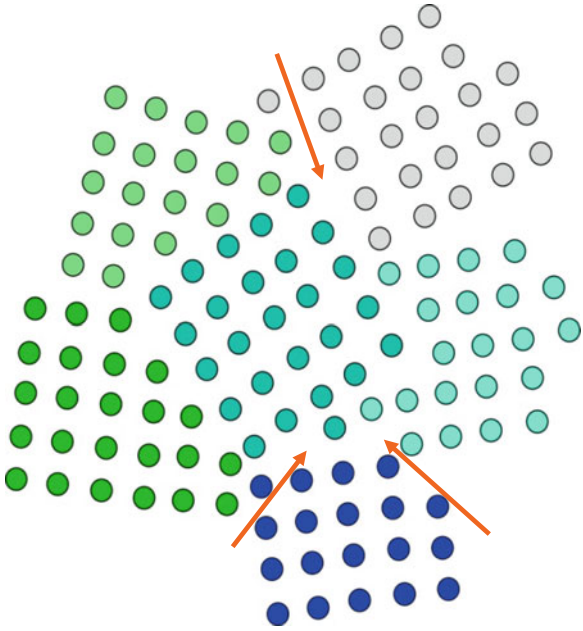

boundaries (with the misorientation angle θ taken conventionally to be less than 15°) is slower with respect to that along the high-angle grain boundaries (i.e., with $\theta > 15°$). For further details, the reader is referred to Chap. 10. When diffusion occurs over the surface, as shown in Fig. 5.4, it is called surface diffusion. This type of diffusion is also found through the cracks or pores in the material.

As already discussed, in substitutional lattice diffusion, first condition is that vacancy is available at the next neighbor position where an atom could jump. We have seen in Chap. 2 that it has its own activation energy barrier for the formation of vacancies. Moreover, the jumping atom has to displace the neighboring atoms

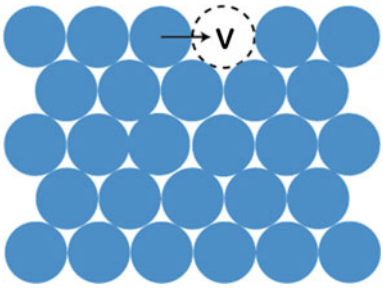

Fig. 5.4 Surface diffusion is explained

from their equilibrium positions temporarily to create enough space to exchange the position with vacancies. Energy is required to spend for this elastic deformation, which is called the activation energy for migration. Therefore, as it will be seen during the derivation for Arrhenius equation, the activation energy for substitutional lattice diffusion comes from activation energy for vacancy formation and migration. In the case of pipe and grain boundary diffusion, the activation energy for migration is less (compared to the lattice diffusion) because of extra free space available. This is the reason that with the increase in misorientation of grains, grain boundary diffusion rate generally increases (still this diffusion enhancement can remain relatively small for "compact" interfaces such as a coherent twin boundary). In surface diffusion, the activation energy barrier is even less since atoms are missing above the jumping atom. Further, the activation energy barrier for interstitial diffusion is less than the substitutional diffusion since vacancies are not required. Even the activation energy for migration is also less because of smaller size of diffusing atom. With the decrease in the size of the interstitial atoms, the activation energy is expected to decrease in a particular material.

A diffusion couple of alloys C_B^- and C_B^+ in the A–B system is shown in Fig. 5.5. The interdiffusion zone is grown because of diffusion of elements A and B. The diffusion of these elements is called intrinsic diffusion, and diffusion coefficients are called the intrinsic diffusion coefficients, denoted by D_A and D_B. Since, overall, the atoms interdiffuse to each other, it is called interdiffusion and the diffusion coefficient is called the interdiffusion coefficient, $\tilde{D}$. It should be noted here that the interdiffusion coefficient is a kind of average of the intrinsic diffusion coefficients and expressed as $\tilde{D} = C_A V_A D_B + C_B V_B D_A$. V_i is the partial molar volume of element i. When the variation of the molar volume with composition in the interdiffusion zone can be neglected, it is expressed as $\tilde{D} = N_A D_B + N_B D_A$. Therefore, it is not a direct average of the intrinsic diffusion coefficients. It should be noted here that following the error function analysis as discussed in Chap. 3, we calculate the interdiffusion coefficient. More accurate approaches to calculate the interdiffusion coefficients and the intrinsic diffusion coefficients will be discussed in Chap. 6.

In the example above, we discussed interdiffusion that occurs in the presence of chemical driving force. Electric current could also be present in some systems used especially in the electronics industry. In fact, diffusion also occurs in the absence

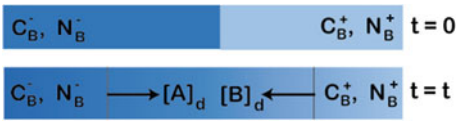

Fig. 5.5 Interdiffusion of elements A and B in a diffusion couple

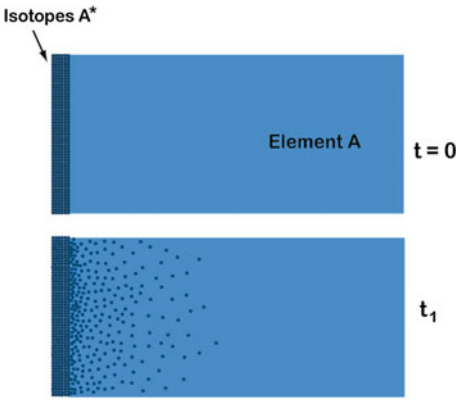

Fig. 5.6 Tracer diffusion of element A is shown

of any external driving forces, as shown in the example in Fig. 5.6. If radioisotope of element A (A*) is deposited on the surface of the same element A, by measuring the intensity of isotope decays, we know that A* diffuses inside A. Note that the difference between A* and A is only in the atomic mass and there is no difference in chemical potential. So except the very little gain in configurational entropy in this particular example, there is no other driving force present. Radioisotopes are actually used to trace the diffusion of elements. It indicates that in a piece of pure element A, jump, that is, the diffusion of atoms, is always happening just because of thermal vibration.

Let us consider the defects which mediate diffusion, i.e., vacancies or interstitial atoms. The corresponding diffusion coefficients (of vacancies, D_v, or interstitials, D_i) are defined as the self-diffusion coefficient D_S (to be not mixed with the tracer self-diffusion coefficient, D^*, see below). Since self-diffusion of elements cannot be traced or measured, if it proceeds via vacancies since there is no marker for a vacancy. On the other hand, (radio) tracer atoms are used to monitor movements of atoms and to measure the diffusion coefficient. The corresponding phenomenon is called tracer diffusion (or tracer self-diffusion), and tracer self-diffusion coefficient is denoted as D^*. Note that although radioisotopes are used to trace the diffusion, the tracer self-diffusion coefficient is not necessarily equal to D_S. These are related by $D^* = fD_S$, where f is the correlation factor and it is less than one in substitutional diffusion. In the case of diffusion via vacancy mechanism, the above relationship is written as $D^* = fD_v$ and f is a just geometric factor specific to the given lattice in the case of *tracer self-diffusion*.

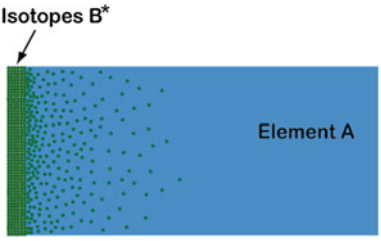

Fig. 5.7 Measurement of impurity diffusion coefficient is shown

In the interstitial diffusion, the correlation factor is just unity, $f = 1$, which means $D^* = D_S$. This will be explained in detail in this chapter. Note here that thin-film solution of the Fick's second law, as explained in Chap. 3 (Sect. 3.2), is used to determine the tracer diffusion coefficients. Then, from the calculated/known value of f, one can estimate the self-diffusion coefficient. Note that the so-called perturbed angular correlation method [54] might provide D_v directly.

If the diffusion rate of element B using the radioisotope (B*) is measured in element A, it is called impurity (or solute) tracer diffusion of B in A and the diffusion coefficient is expressed as $D^*_{B(A)}$. This is shown in Fig. 5.7. Note here that the amount of B* should be so small that it can mix in A in the impurity level without forming a solid solution or a compound. Otherwise, the relation, developed based on thin-film solution, cannot be used to determine the diffusion coefficient. If the concentration is high, interdiffusion coefficient should be calculated following the relation developed by error function analysis or the relations developed in Chaps. 6 and 7.

In previous chapters, we have discussed diffusion in general and the development of concentration profiles. There are two approaches to study diffusion in solids, namely a continuum approach and a consideration of the atomic mechanism. Following the continuum approach, we study the development of concentration profiles and calculate diffusion parameters without going into the details of the atomic level of diffusion. That means we deal with mainly the kinetics of diffusion. This is followed in previous two chapters. On the other hand, the atomic mechanism of diffusion is important to understand the diffusion mechanism. Depending on the types of diffusion and the phase or materials, diffusion mechanism could be very different in different systems.

We know from our discussion in the first chapter that atoms vibrate with the Debye frequency of about 10^{13} s^{-1} and the average energy of $3kT$ (k is the Boltzmann constant and T is the absolute temperature). With increasing temperature, the average energy of atoms increases without changing much in the frequency. In general, the size of atoms is higher than the size of the voids or the passage through which the atom should jump. Therefore, sufficient energy is required to displace the neighboring atoms elastically or temporarily from their equilibrium positions. The actual barrier in three dimensions will be explained later. The energy required for this migration is called the activation energy for migration. This is the same as the activation energy for diffusion in the case of interstitial diffusion. However, in substitutional diffusion, as explained earlier, the presence of a vacancy is must for a successful jump. We have explained in Chap. 2 that there is always equilibrium

concentration of vacancies present. However, the system has to spend energy to create vacancies, which is called the activation energy for the formation of vacancies. These will be discussed in detail in the following sections. Therefore, the activation energy for substitution diffusion is the sum of activation energy for migration and the activation energy for vacancy formation. On the other hand, activation energy for interstitial diffusion is equal to the energy required for migration.

It should be noted here that we do not have any technique to see how really the atoms jump. The diffusion mechanism also could be very complicated because of various factors involved. However, it is possible to visualize diffusion based on very simplified theories, as explained for interstitial and substitutional diffusion separately.

5.2 Interstitial Atomic Mechanism of Diffusion

5.2.1 Relation Between Jump Frequency and the Diffusion Coefficient

As already mentioned, atoms vibrate at their equilibrium positions and might gain sufficient energy to jump to another position. This jump is possible just because of thermal vibration even if there are no other internal (chemical potential difference) or external (flow of electrons) forces present. Diffusion of atoms increases to a particular direction because of the presence of driving forces. Otherwise, the jump is truly random. It means that the successive jump does not depend on the previous jump and it has equal probability to jump to all the neighboring free sites available. That means it might go back to its previous position.

In the beginning, we shall discuss the random jump of atoms. The jump rate or frequency of atoms can be related to the diffusion coefficient following very simplified discussion. We consider a FCC unit cell, as shown in Fig. 5.8. Depending on equilibrium concentration, there could be one interstitial atom at the center of the unit cell. The equilibrium concentration of impurities, in general, is so small that we neglect the presence of another interstitial atom very close to it. Three adjacent planes, denoted by P, Q, and R, are shown. Out of these three planes, let us consider first the exchange of atoms between planes Q and R. Following, we shall discuss it considering jump to any directions in three dimensions. Suppose the number of interstitial atoms on plane Q is n_Q per unit area and plane R is n_R per unit area. For the sake of discussion, we assume that $n_Q > n_R$. If we consider the jump frequency, that is, the number of jumps of atoms per unit time from plane Q, as Γ_Q, then the flux of atoms can be written as

$$J_Q = \frac{1}{2} n_Q \Gamma_Q \tag{5.1a}$$

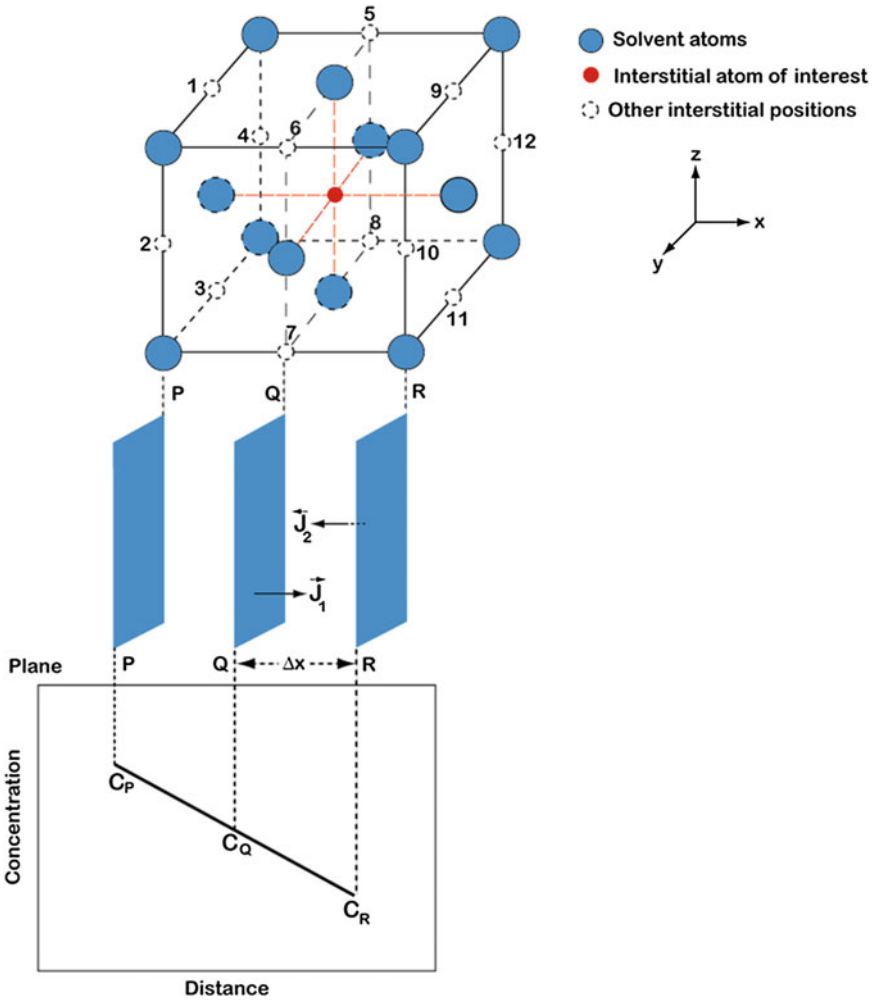

Fig. 5.8 Diffusion of interstitial atoms between different planes is shown

Factor ½ comes from the fact that there is an equal probability that atoms will jump from plane Q to P or R. Note here that the unit of flux is number/(unit area × unit time). If number is converted to moles, unit area in m^2 and time in s, the unit for flux will be $mol/m^2 \cdot s$, which is considered in Chap. 3 for the discussion of Fick's laws of diffusion. If the jump frequency of atoms from plane R is Γ_R, then the flux of atoms from R to Q can be written as

$$J_R = \frac{1}{2} n_R \Gamma_R \tag{5.1b}$$

Since $n_Q > n_R$, the net flux of atoms from R to Q can be written as

$$J = J_Q - J_R = \frac{1}{2}(n_Q\Gamma_Q - n_R\Gamma_R) \tag{5.2}$$

Note here that we have considered random jump of atoms in the absence of any driving forces. In an isotropic or cubic system (as explained in Sect. 5.2.5),

$$\Gamma_Q = \Gamma_R = \Gamma \tag{5.3}$$

It indicates that the resultant flux is because of the difference in number of atoms in different planes only.

Therefore, Eq. 5.2 can be written as

$$J = \frac{1}{2}(n_Q - n_R)\Gamma \tag{5.4}$$

We consider the distance between planes Q and R is very small and equal to Δx. So the concentration of interstitial atoms on plane Q is $C_Q = n_Q/\Delta x$ and that of plane R is $C_R = n_R/\Delta x$. Note here that the number of atoms is divided by a length parameter to get the unit of number/unit volume for concentration.

Therefore, Eq. 5.4 can be written as

$$J = \frac{1}{2}(C_Q - C_R)\Delta x\Gamma \tag{5.5}$$

Further, since we have considered very small inter-planar spacing, the concentration gradient can be written as

$$\frac{(C_R - C_Q)}{\Delta x} = -\frac{(C_Q - C_R)}{\Delta x} = -\frac{dC}{dx} \tag{5.6}$$

We could assume the linear change in the concentration profile, since Δx is very small.

By replacing Eq. 5.6 in Eq. 5.5, we get

$$J = -\frac{1}{2}\Delta x^2\Gamma\frac{dC}{dx} \tag{5.7}$$

After comparing with Fick's first law $\left(J = -D\frac{dC}{dx}\right)$, the diffusion coefficient can be expressed as

$$D = \frac{1}{2}\Gamma\Delta x^2 \tag{5.8}$$

Note here that Δx is related to the lattice parameter. For a known crystal structure, the average jump frequency can be calculated from the measured diffusion coefficients. One important fact here should be noted here that the factor ½ comes from our consideration of jumps between two planes. Jump to forward or backward direction is considered for easy explanation. However, in actual case, in a crystal in three dimensions, every atom can jump to any of the Z positions. Z is the coordination number, that is, the number of nearest neighbors.

Therefore, the diffusion coefficient is related to the jump frequency by

$$D = \frac{1}{Z}\Gamma(\Delta x)^2 \tag{5.9}$$

Similarly, if we consider the jump of an atom to a particular position i only, Eq. 5.9 can be written as

$$D = \Gamma_i(\Delta x_i)^2 \tag{5.10}$$

Here, Γ_i is the jump frequency to a particular position. Therefore, the overall jump frequency, Γ, can be related to Γ_i by

$$\Gamma = Z\Gamma_i \tag{5.11}$$

Atoms are free to jump to any of the nearest neighbor positions. That means atom can jump to any of the interstitial sites numbered as 1–12 in a FCC crystal, as shown in Fig. 5.8. We have considered n_Q atoms on plane Q. Different atoms on that plane could jump randomly to any of the positions. If the structure is not isotropic, as discussed in Sect. 5.2.5, jump frequency could be different to different positions. Since we calculate the diffusion coefficient from the average of jumps of many atoms, we can write

$$D = \frac{1}{Z}\sum_{i=0}^{Z}\Gamma_i\Delta x_i^2 \tag{5.12}$$

In an isotropic FCC crystal, the average diffusion coefficient with equal jump frequency to all the positions can be written as

$$D = \frac{1}{12}\sum_{i=0}^{i=12}\Gamma\Delta x_i^2 \tag{5.13}$$

Let us determine the diffusion coefficient in x direction in a FCC lattice, as shown in Fig. 5.8. The effective jump lengths to positions 1, 2, 3, and 4 are $\Delta x = -\frac{a}{2}$, to positions 5, 6, 7, and 8 are $\Delta x = 0$, and to positions 9, 10, 11, and 12 are $\Delta x = \frac{a}{2}$. Further jump frequencies to any of the sites are the same, since it is an isotropic system and there should not be any difference in the activation energy for migration. Following Eq. 5.13, we can write

$$\begin{aligned} D &= \frac{1}{12}\left(\sum_{i=1}^{4}\Gamma\Delta x_i^2 + \sum_{i=5}^{8}\Gamma\Delta x_i^2 + \sum_{i=9}^{12}\Gamma\Delta x_i^2\right) \\ &= \frac{1}{12}\left[4\Gamma(\Delta x)^2 + 4\Gamma(0) + 4\Gamma(\Delta x)^2\right] \\ &= \frac{2}{3}\Gamma\Delta x^2 = \frac{1}{6}\Gamma a^2 \end{aligned} \tag{5.14}$$

The possibilities of different jump frequencies and anisotropy of diffusion are discussed in Sect. 5.2.5. The main difference in the relation derived in Eqs. 5.8 and 5.14 for the diffusion coefficient calculated from the same crystal structure stems from the fact that in the latter case, we have considered the jump of atoms to both negative and positive directions along the x-axis. So it is apparent that the numerical factor depends on our consideration and also on the crystal structure. In a broader sense, diffusion coefficient in any system can be written as

$$D \propto \Gamma a^2 = g\,\Gamma a^2 \tag{5.15}$$

Here, the proportionality constant, g, in some literatures is called geometric constant.

Fick's first law is the center relation in physics of diffusion. How far does it remain to be valid if one goes to the atomistic scale and do consider gradients between successive atomistic layers? Very recently, Adda et al. [1] have demonstrated by an atomistic study that Fick's first law is valid also for a "strongest possible" concentration gradient. The authors used numerical simulations as a tool to check the linearity between the flux and the concentration gradient for vacancy-mediated diffusion of atoms in a solid and for atom diffusion in a model liquid. It was proven that Fick's law is valid in both systems even in the presence of the strongest possible tracer concentration gradients, provided that the diffusion time is enough for tracer jumps over *several nearest neighbor distances*.

From the relations derived above, we find an interesting fact. From the measured values, we know that the diffusion coefficient of carbon in γ-iron with FCC structure at 1,100 °C is in the order of 10^{-10} m^2/s. The jump distance can approximately be considered as $\Delta x \approx 1$ Å $= 10^{-10}$ m. This gives the jump frequency Γ in the order of 10^{10} s^{-1}. This means that atoms change their position in the order of 10^{10} times per second at 1,100 °C! This number looks very large. However, it should be noted that atoms make successful jump one out of 10^3 only, since Debye vibration frequency is in the order of 10^{13} s^{-1}. Now, just for the sake of discussion, we consider that one particular atom moves only in one direction following the straight line. Then, it would cover a distance of 10^{10} (m) × 10^{-10} (s^{-1}) × 3,600 (s) =

3,600 m = 3.6 km in 1 h! However, measured composition profiles in an experiment indicate that the actual penetration length is less than a millimeter. That means atoms do not follow a straight path. In fact, in the absence of any driving forces, atoms move completely randomly, which is explained in the next section.

5.2.1.1 Jumps in the Presence of External Force

If an external force is applied, the effective energy barriers for atom jumps will be modified. Correspondingly, the jump frequencies depend on the external force that in turn modifies the resulting flux of atoms.

Let us consider an external force F caused by an external potential field, $F = -\nabla V(x)$, as shown in Fig. 5.9. If the potential field $V(x)$ is applied, the energy landscape for atom jumps is modified as shown in Fig. 5.9—while without external field all sites were equivalent and all barriers are considered to be equal to ε, the energy barriers of jumps along and opposite to the direction of potential gradient become to be different. This difference is designated by Δ in Fig. 5.9.

Let n_1 and n_2 be the numbers of interstitial atoms at planes 1 and 2, respectively. The planes are considered to be located at $x - a/2$ and $x + a/2$, and a is the distance between the planes. Let the jump frequencies of atoms from site 1 to site 2 be Γ_{12}, and Γ_{21} is the frequency of a reverse jump. The number of atoms in the layer at the middle of the planes 1 and 2 is $n(x)$ and $n(x) = a \cdot C(x)$, respectively, where $C(x)$ is the atomic concentration at the position x. Then, considering the planes 1 and 2 as atomic positions with a very small distance in between and assuming that the atom concentration practically does not vary on such distances, we can write

$$n_1 = n(x) - \frac{a}{2}\frac{\partial n}{\partial x} \tag{5.16a}$$

and

$$n_2 = n(x) + \frac{a}{2}\frac{\partial n}{\partial x}. \tag{5.16b}$$

Then, the flux of atoms between the planes 1 and 2 is

$$J = n_1\Gamma_{12} - n_2\Gamma_{21}, \tag{5.17}$$

and substituting Eqs. 5.16a and 5.17, we arrive at

$$\begin{aligned} J &= -a\frac{\Gamma_{12} + \Gamma_{21}}{2}\frac{\partial n}{\partial x} + n(\Gamma_{12} - \Gamma_{21}) \\ &= -a^2\frac{\Gamma_{12} + \Gamma_{21}}{2}\frac{\partial C}{\partial x} + aC(\Gamma_{12} - \Gamma_{21}). \end{aligned} \tag{5.18}$$

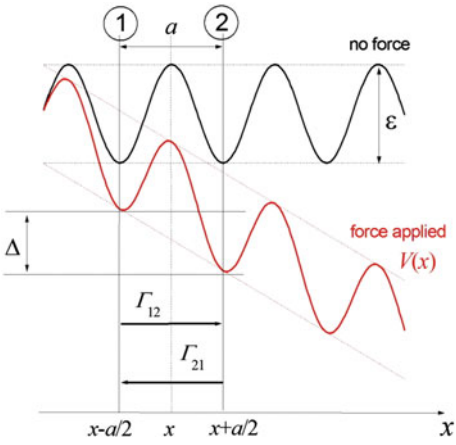

Fig. 5.9 Effect of external potential field $V(x)$ on the energy landscape of jumping atom. Γ_1 and Γ_2 are the jump frequencies between planes 1 and 2, separated by the distance a, and the energy barrier is ε in the absence of external potential field. In the presence of the external field, the site energies are modified and they are shifted by Δ for the neighboring planes (sites)

Note that in the absence of external force, $\Gamma_{12} = \Gamma_{21} = \Gamma/2$, Eq. 5.18 is reduced to

$$J = -\frac{a^2}{2}\Gamma\frac{\partial C}{\partial x}, \tag{5.19}$$

that coincides with Eq. 5.7 derived previously. Here, Γ is the total frequency of atomic jumps from plane 1, and these jumps are equally distributed between those to the right, i.e., to plane 2, and to the left.

Since the atomic jumps are thermally activated, we can write

$$\Gamma_{12} = \Gamma^* \exp\left(-\frac{\varepsilon_{12}}{RT}\right), \tag{5.20a}$$

and

$$\Gamma_{21} = \Gamma^* \exp\left(-\frac{\varepsilon_{21}}{RT}\right). \tag{5.20b}$$

Here, Γ^* is the corresponding pre-exponential factor. The activation barriers are modified by the applied external force (external potential field) and see Fig. 5.9

$$\varepsilon_{12} = \varepsilon - \frac{\Delta}{2}, \tag{5.21a}$$

and

$$\varepsilon_{21} = \varepsilon + \frac{\Delta}{2}. \tag{5.21b}$$

As it was stated above, the case $\Delta/2 \ll \varepsilon$ is considered. Then,

$$\Gamma_{12} = \Gamma^* \exp\left(-\frac{\varepsilon - \Delta/2}{RT}\right) = \Gamma^* \exp\left(-\frac{\varepsilon}{RT}\right) \exp\left(\frac{\Delta}{2RT}\right) \approx \frac{1}{2}\Gamma\left(1 + \frac{\Delta}{2RT}\right), \tag{5.22a}$$

and

$$\Gamma_{12} = \Gamma^* \exp\left(-\frac{\varepsilon + \Delta/2}{RT}\right) = \Gamma^* \exp\left(-\frac{\varepsilon}{RT}\right) \exp\left(-\frac{\Delta}{2RT}\right) \approx \frac{1}{2}\Gamma\left(1 - \frac{\Delta}{2RT}\right). \tag{5.22b}$$

Now, substituting these equations into relation (5.18), the flux of atoms between planes 1 and 2 is

$$J = -\frac{a^2}{2}\Gamma\frac{\partial C}{\partial x} + \frac{a\Delta\Gamma}{2RT}C = -D\frac{\partial C}{\partial x} + vC. \tag{5.23}$$

Here, the diffusion coefficient defined by Eq. 5.8 is used ($\Delta x = a$ is the present case), and an additional term to Fick's first law, vc, is appeared in the presence of the driving force. We see that if an external potential field is applied, the net flux of atoms is determined by a sum of two terms, diffusional one, $-D\frac{\partial c}{\partial x}$, and convective one, vc. The convection velocity, v, is given by

$$v = \frac{a\Delta\Gamma}{2RT} = \frac{a^2}{2}\Gamma\frac{\Delta/a}{RT} = D\frac{\Delta/a}{RT} = \frac{D}{RT}F, \tag{5.24}$$

which is the well-known Nernst–Einstein equation. We used an obvious relation, $F = -\frac{\partial V}{\partial x} = \frac{\Delta}{a}$, and see Fig. 5.9. Within the given approximation, i.e., linear terms, the convection velocity is proportional to the external force F and mobility M is determined by the diffusion coefficient D, $M = D/RT$.

The effect of other driving force (e.g., temperature gradient or electric force) can be treated quite similarly. The driving force F induces inequality of the jump frequencies Γ_{12} and Γ_{21}, and to the first-order expansion, we may write

$$\Gamma_{12} = \frac{1}{2}\Gamma(1 + \xi) \tag{5.25a}$$

and

$$\Gamma_{12} = \frac{1}{2}\Gamma(1 - \xi). \tag{5.25b}$$

These equations can be considered as a definition of the term ξ. Substituting these expressions to Eq. 5.18, we arrive to Eq. 5.23 with the following expression for the convection velocity,

$$v = a\xi\ \Gamma. \tag{5.26}$$

The thermal energy RT per net jump of one mole of interstitial atoms in the direction of the applied force is equal to the work done by the force over the jump distance a,

$$RT\frac{\Gamma_{12} - \Gamma_{21}}{\Gamma/2} = Fa, \tag{5.27}$$

and using expressions (5.25a) and (5.25b),

$$\xi = \frac{a}{2}\frac{F}{RT}\ . \tag{5.28}$$

Thus, the convection velocity is

$$v = \frac{a^2\Gamma_0}{2}\frac{F}{RT}\ = \frac{D}{RT}F. \tag{5.29}$$

Again, we arrived to the Nernst–Einstein equation, expression (5.24), which is valid if the driving force is small when the expansions (5.25a) and (5.25b) can be used (Fig. 5.9).

5.2.2 Random Walk of Atoms

As explained already, atoms vibrate at their equilibrium position and might gain sufficient energy to jump to any of the neighboring available positions. Further, after making a successful jump, it might jump again to any of the sites. Two successive jumps are not related. If the atom does not come back to the previous position, then we can say that the atom is diffused. For the sake of explanation, let us consider a two-dimensional array of solvent atoms as shown in Fig. 5.10. Following, the jump in a three-dimensional lattice will be considered. Suppose initially one interstitial atom is located at position P. After many jumps, this atom reaches, let say, to Q. Now question is that how many jumps it will make to reach Q.

One can easily count that there are few short routes available, as shown by green dotted arrows, which need 14 jumps to reach Q from P. However, chance of taking any of the short routes by making all necessary jump is least expected. It might take a torturous route as shown by black solid arrows. Note that the steps in the middle are not shown. At first glance, it seems impossible to make any prediction on the average number of jumps or time necessary for considering random walk of atoms.

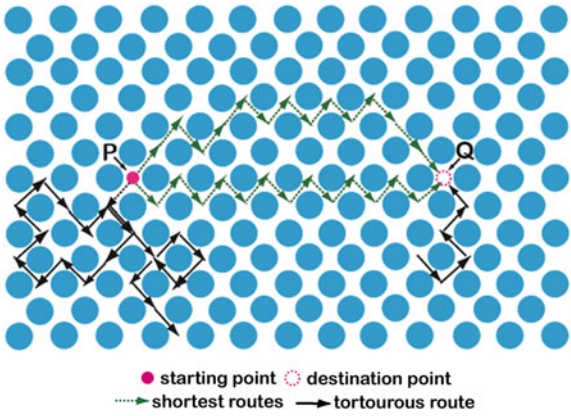

Fig. 5.10 Jump of an interstitial atom through different routes from the position P to the position Q

However, following a simplified approach, we can roughly estimate it. We assume that the atom makes n jumps to reach from P to Q. The jump vector L_n connecting the points P and Q can be written as

$$L_n = l_1 + l_2 + l_3 + \cdots + l_n = \sum_{i=1}^{n} l_i, \tag{5.30}$$

where l_i is the jump vector of the ith jump. To calculate the magnitude, we need to take dot product.

$$\begin{aligned} L_n \cdot L_n = L_n^2 = {} & l_1 \cdot l_1 + l_1 \cdot l_2 + l_1 \cdot l_3 + \cdots + l_1 \cdot l_n \\ & + l_2 \cdot l_1 + l_2 \cdot l_2 + l_2 \cdot l_3 + \cdots + l_2 \cdot l_n \\ & + l_3 \cdot l_1 + l_3 \cdot l_2 + l_3 \cdot l_3 + \cdots + l_3 \cdot l_n \\ & \cdots \\ & \cdots \\ & + l_n \cdot l_1 + l_n \cdot l_2 + l_n \cdot l_3 + \cdots + l_n \cdot l_n \end{aligned} \tag{5.31}$$

Equation 5.31 can be arranged as

$$L_n^2 = \sum_{i=1}^{n} l_i \cdot l_i + 2\sum_{i=1}^{n-1} l_i \cdot l_{i+1} + 2\sum_{i=1}^{n-2} l_i \cdot l_{i+2} \ldots \tag{5.32}$$

The first sum includes all diagonal terms $l_i \cdot l_i$, the second sum consists all $l_i \cdot l_{i+1}$ and $l_{i+1} \cdot l_i$ terms (according to dot product of vectors, these are the same), the third sum consists all $l_i \cdot l_{i+2}$ and $l_{i+2} \cdot l_i$ terms, and so on. Equation 5.32 can be rewritten as

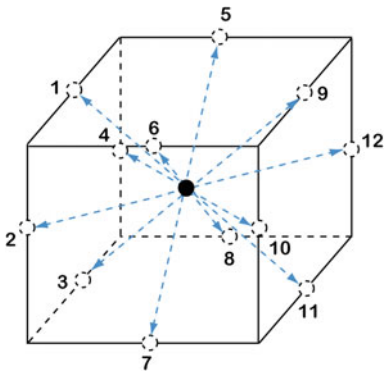

Fig. 5.11 Jump vectors of an interstitial atom are shown

$$\begin{aligned} L_n^2 &= \sum_{i=1}^{n} l_i \cdot l_i + 2\sum_{j=1}^{n-1}\sum_{i=1}^{n-j} l_i \cdot l_{i+j} \\ &= \sum_{i=1}^{n} l_i^2 + 2\sum_{j=1}^{n-1}\sum_{i=1}^{n-j} |l_i||l_{i+j}| \cos\theta_{i,i+j} \end{aligned} \tag{5.33}$$

Here, $\cos\theta_{i,i+j}$ is the angle between jump vectors l_i and l_{i+j}.

Note that we are considering diffusion in crystalline solids. If we consider the diffusion in cubic system, magnitude of the jump vectors are equal since direct jump is possible only to the nearest neighbor positions. Therefore, Eq. 5.33 can be written as

$$L_n^2 = nl^2 + 2l^2 \sum_{j=1}^{n-1}\sum_{i=1}^{n-j} \cos\theta_{i,i+j} \tag{5.34}$$

Till now, we have considered jumps of one particular atom only. However, to find the average jump distance, we should consider many atoms together and take average of jumps of all the atoms. The first term in Eq. 5.34, that is, nl^2, will be the same for all the atoms. The differences in total jump distance because of choosing different path by different atoms are counted in the second term. Therefore, Eq. 5.34 can be written, after taking average from many atoms, as

$$\bar{L}_n^2 = nl^2 \left(1 + \frac{2}{n}\overline{\sum_{j=1}^{n-1}\sum_{i=1}^{n-j} \cos\theta_{i,i+j}}\right) \tag{5.35}$$

Further, since we have considered the random walk of many atoms together, for every positive value of $\cos\theta_{i,i+j}$ from an atom, there will be an equal chance of a negative value from the jump of another atom. It is explained with the help of interstitial atoms sitting in an octahedral void in a FCC crystal, as shown in Fig. 5.11. There are 12 jump vectors l_1 to l_{12}. It must be clear that for every jump vector, there is an equal but negative jump vector; for example, $l_2 = -l_{12}$. Further

because of random nature of jump, atoms have equal probability to jump to any of the locations. If one atom has jump sequence of $l_1 \cdot l_2$, then there is an equal probability that another atom has jump sequence of $l_1 \cdot l_{12}$. So we can write, for example, $l_i \cdot l_2 - l_i \cdot l_{12} = 0$. This will lead the double summation of Eq. 5.35 to zero. Therefore, it is safe to write that $\left(\overline{\sum_{j=1}^{n-1} \sum_{i=1}^{n-j} \cos \theta_{i,i+j}}\right) = 0$ in a cubic isotropic crystal, and Eq. 5.35 can then be rewritten as

$$\bar{L}_n^2 = nl^2 \tag{5.36}$$

Therefore, the average magnitude of jumps of many atoms after n number of jumps can be written as

$$\bar{L}_n = \sqrt{\bar{L}_n^2} = \sqrt{n}\, l \tag{5.37}$$

Note that we are considering the average taken from many atoms. There can be huge difference in the distance that different atoms will travel after a particular diffusion time. Equation 5.37 indicates that atoms will make an average $(14)^2 = 386$ jumps to reach from P to Q, where 14 jumps are required following the shorter routes. We reconsider the example what we have discussed already in the previous section. With average jump frequency of $10^{10}\ \mathrm{s}^{-1}$ of carbon at 1,100 °C in Γ-iron, the average effective jump length in 1 h is $\bar{L}_n = \sqrt{n}\, l = \sqrt{10^{10} \times 3{,}600} \times 10^{-10}\ \mathrm{m} = 0.6\ \mathrm{mm} = 600\ \mu\mathrm{m}$. Further, note here that this is an average from many atoms. Different atoms will actually jump different distances and the difference in jump length could be very large.

This concept of random walk is actually developed based on Einstein's mathematical analysis of Brownian motion. He developed the relation for diffusivity as $D = \langle \bar{L}_n^2 \rangle / 6t$, considering the jump of atoms in three dimensions.

5.2.3 *Effect of Temperature on the Interstitial Diffusion Coefficient*

We have already discussed that atoms vibrate at their positions with an average energy of $3kT$. With the increase in temperature, thermal energy of the system increases so that atoms vibrate even more violently. That means the jump frequency will increase with increasing temperature. However, the atoms cannot jump freely, since the void between the host atoms, through which atoms should jump, is smaller than the size of the atom. Therefore, the host atoms should be

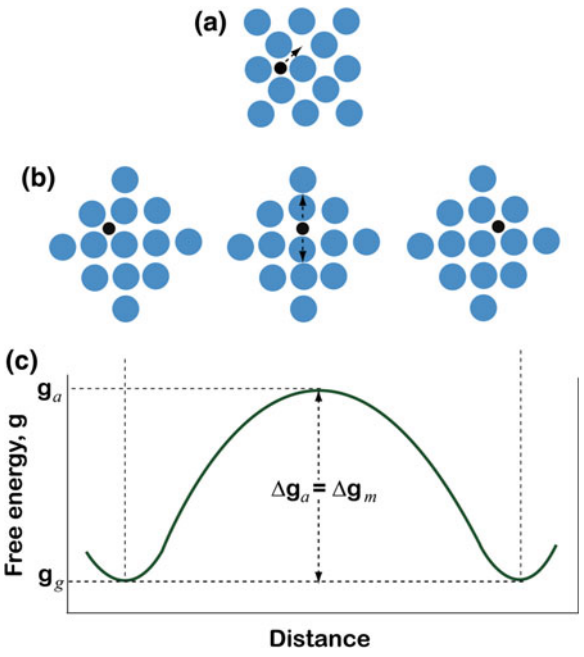

Fig. 5.12 **a** The jump of atom from one equilibrium position to another equilibrium position. **b** The movement of interstitial atom and the neighboring solvent atoms is shown. For the sake of explanation, we have rotated the atomic structure by 45°. **c** The associated free energy change with the movement of the interstitial atom is shown

moved elastically as explained in Fig. 5.12. The change in local free energy with the movement of the atom is shown. In the beginning, the atoms are at their equilibrium positions and the energy at this ground state is g_g per mol of atoms. The free energy is the highest in the middle, where it needs maximum energy to move the host atoms elastically. This is called an activated state, and the free energy is g_a per mol of atoms. Following, atoms reach to another ground state. So an extra energy of $\Delta g_a = g_a - g_g$ per mole of atoms is required to cross the barrier. This is the activation energy for interstitial diffusion and is equal to the energy required for the migration Δg_m. Atoms jump with Debye frequency, ν, and the probability of the successful jump to a new position is $\exp(-\Delta g_m/RT)$. Therefore, the jump frequency to a particular position can be written as

$$\Gamma_i = \nu \exp\left(-\frac{\Delta g_a}{RT}\right) \tag{5.38}$$

From Eq. 5.10, Eq. 5.38 can be written as

$$D = \nu \Delta x^2 \exp\left(-\frac{\Delta g_a}{RT}\right) = D'_0 \exp\left(-\frac{\Delta g_a}{RT}\right), \tag{5.39}$$

where D'_0 is the temperature-independent pre-exponential factor. This temperature-dependent relation for the diffusion coefficient relation is the Arrhenius equation.

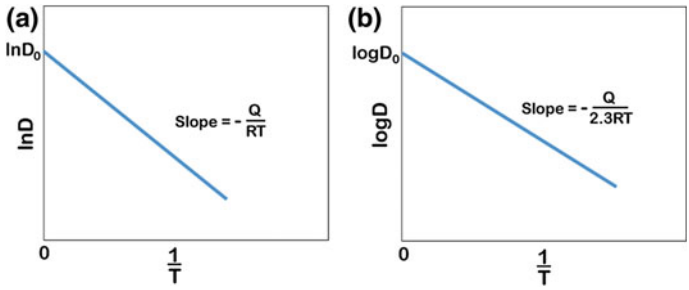

Fig. 5.13 **a** ln D versus $1/T$ plot and **b** log D versus $1/T$ plot to calculate the activation energy and the pre-exponential factor

Further, $\Delta g_a = \Delta h_a - T\Delta s_a$. With the help of this relation, many times Eq. 5.39 is expressed as

$$D = v\,\Delta x^2 \exp\left(\frac{\Delta s_a}{\mathrm{R}}\right) \exp\left(-\frac{\Delta h_a}{RT}\right) = D_0 \exp\left(-\frac{\Delta h_a}{RT}\right) \tag{5.40}$$

In this equation, $D_0 = v\,\Delta x^2 \exp\left(\frac{\Delta s_a}{\mathrm{R}}\right) = D_0' \exp\left(\frac{\Delta s_a}{RT}\right)$ is the pre-exponential factor and Δh_a is the activation enthalpy for diffusion. Note here that at a particular temperature, the change in entropy because of migration is more or less fixed in a system. This accounts for the change in entropy because of the change in vibration pattern of neighboring atoms where the elastic displacement of the host atoms is greatest.

Equation 5.40 can be written as

$$\ln D = \ln D_0 - \frac{\mathrm{Q}}{RT} \tag{5.41a}$$

$$\log D = \log D_0 - \frac{\mathrm{Q}}{2.3RT} \tag{5.41b}$$

Therefore, the activation energy and the pre-exponential factor can be determined from the plots shown in Fig. 5.13.

It must be clear from the discussion above that the pre-exponential factor and the activation energy depend on a number of factors, such as size of the interstitial atoms, elastic modulus of the material, lattice parameter and the crystal structure. Because of this size factor, e.g., the diffusion rates of small elements in Fe have to decrease generally in the order of H, O, N, and C. Some available data are listed in Table 5.1. It is clearly seen that solely the size factor has a limited applicability, though it is very useful in the analysis of the diffusion trends. One has to mention that the atomic radii depend strongly on the environment and the charge state and any tabulated data have to be used with cautions.

Table 5.1 The tracer impurity diffusion coefficients, D^* (m^2/s), and the corresponding activation enthalpies, Q (kJ/mol), for diffusion of small atoms in FCC and BCC iron [2–8]

Impurity	Atomic radius (pm)	BCC Fe			FCC Fe		
		Q (kJ/mol)	D* at 300 K (m^2/s)	References	Q (kJ/mol)	D* at 1,400 K (m^2/s)	References
H	25	6	7×10^{-9}	[2]	43	2×10^{-8}	[3]
O	60	92	4×10^{-23}	[4]	166	9×10^{-11}	[5]
N	65	73	2×10^{-20}	[6]	169	5×10^{-11}	[7]
C	70	84	5×10^{-21}	[6]	148	7×10^{-11}	[8]

The atomic radii after [9] are listed. For comparison, the atomic radius of Fe is 140 pm

Similar dependencies for these small elements were found for their diffusion in α-Ti with the HCP lattice, too. However, one recognizes immediately that the electronic effects are also important in explaining the atomic diffusion rates. Most prominent example is the diffusion of transition metal atoms, such as Co, Fe, and Ni, in α-Ti, see below in the chapter—they are even faster than C or N!

5.2.4 *Tracer Method of Measuring the Interstitial Diffusion Coefficient*

Since the concentration of the diffusing impurity element is very small, tracer method is followed to calculate the impurity diffusion coefficient utilizing radioisotopes, which are easy to detect. This is explained in Fig. 5.14. Radioisotopes of impurity element A are deposited on the substrate B, in which the impurity diffusion coefficient would be measured. At the temperature of the experiment, radioisotope impurity elements diffuse inside the substrate. Different atoms diffuse different lengths because of random walk of atoms. With the increase in annealing time, the penetration distance increases. After the experiment for certain time at a desired temperature, the specimen is sliced at different known distances along the x direction and the concentration of the radioisotopes is measured by measuring intensities of the emitted rays. Following the solution for thin film from Fick's second law, we can write

$$I_R(x) = \frac{1}{\sqrt{\pi D_A^* t}} \exp\left(-\frac{x^2}{4D_A^* t}\right) \tag{5.42}$$

$$\ln I_R = \ln\left(\frac{1}{\sqrt{\pi D_A^* t}}\right) - \frac{x^2}{4D_A^* t} \tag{5.43}$$

where I_R is the specific or relative intensity measured and D_A^* is the impurity diffusion coefficient of element A.

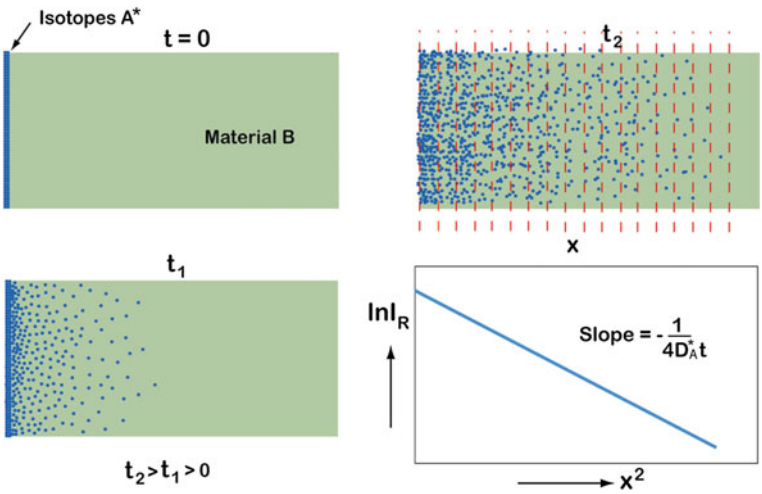

Fig. 5.14 Tracer method to determine impurity tracer diffusion coefficient is shown

From the slope $-\frac{1}{4D_A^* t}$ of $\ln I_R$ versus x^2 plot, as shown in Fig. 5.14, D_A^* can be calculated using the known annealing time.

5.2.5 *Orientation Dependence of Interstitial Diffusion Coefficient*

In Sect. 5.2.2, we considered a cubic crystal to simplify the derivation for average jump length calculation during random walk in which the magnitudes of all jump vectors are equal. Following, we were able to derive a simple relation to explain the random walk of atoms. However, in some structures such as hexagonal, tetragonal, or orthorhombic, the jump vectors in different directions could be different. Even the void size through which the atoms jump could also be different to find different jump frequencies and the activation energy for diffusion.

For comparison, we consider face-centered cubic and orthorhombic structures, as shown in Fig. 5.15. We consider again the presence of an interstitial atom in an octahedral site in the middle. Other octahedral sites are shown by open dotted circle to which the interstitial atom could jump. We have discussed earlier that diffusion coefficient is calculated from the average jumps of many atoms. In a FCC crystal, the diffusion coefficient can be written as

$$D = \frac{1}{12}\sum_{i=0}^{12} \Gamma_i \Delta x_i^2 \tag{5.44}$$

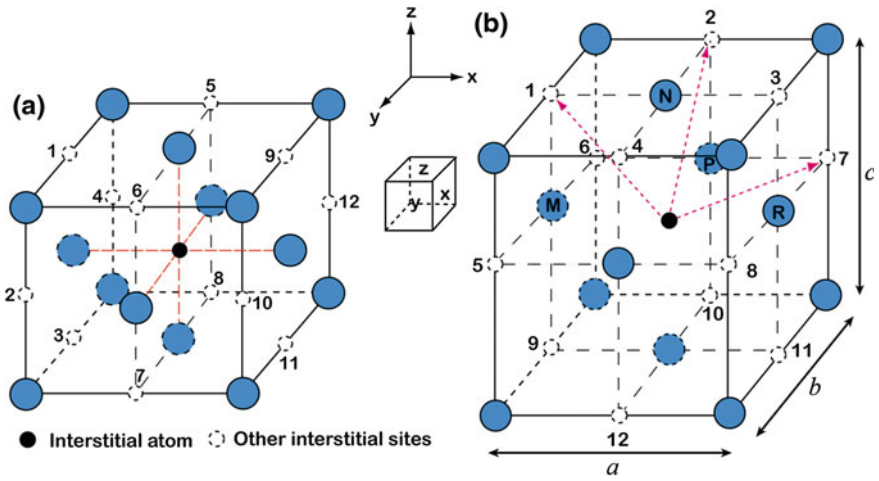

Fig. 5.15 Interstitial sites are shown in **a** face-centered cubic and **b** orthorhombic face-centered cubic crystal structures to explain the anisotropy in diffusion

In a cubic crystal because of symmetry, as shown in Fig. 5.15a, there is equal probability of jump frequency to any of the positions and Eq. 5.44 can be written as

$$D = \frac{1}{12}\Gamma \sum_{i=0}^{12} \Delta x_i^2 \tag{5.45}$$

We consider the diffusion along the x-axis. All the nearest neighbor interstitial sites have equal distances. Considering positive and negative sides on the x-axis, the effective jump length for the positions 1, 2, 3 and 4 is $-a/2$, where a is the lattice parameter. This is zero for positions 5, 6, 7 and 8. Although atoms jump to these positions, the effective length is zero considering the jump along the x-axis. This is $a/2$ for positions 9, 10, 11 and 12. Therefore, the diffusion coefficient along the x-axis can be written as

$$D_x = \frac{1}{12}\Gamma\left[4\left(-\frac{a}{2}\right)^2 + 4(0) + 4\left(\frac{a}{2}\right)^2\right] = \frac{1}{6}\Gamma a^2 \tag{5.46}$$

We consider the diffusion along the y-axis. The effective jump length to the positions 2, 6, 7, and 10 is equal to $-a/2$. This is zero for positions 1, 3, 9, and 11 and $a/2$ for positions 4, 5, 8, and 12. Therefore, the diffusion coefficient along the y-axis can be written as

$$D_y = \frac{1}{12}\Gamma\sum_{i=0}^{12}\Delta y_i^2 = \frac{1}{12}\Gamma\left[4\left(-\frac{a}{2}\right)^2 + 4(0) + 4\left(\frac{a}{2}\right)^2\right] = \frac{1}{6}\Gamma a^2 \tag{5.47}$$

where Δy_i is the effective jump length along the y-axis.

Similarly, it can be shown that the diffusion coefficient along the z-axis is also equal to $\frac{1}{6}\Gamma a^2$. Hence, the diffusion coefficients in a cubic crystal along all the axes are the same. In other words, the diffusion coefficient in a cubic crystal is orientation independent.

Now let us consider the diffusion in a face-centered orthorhombic structure, as shown in Fig. 5.15b. Lattice parameters along the x-, y-, and z-axes are a, b, and c, respectively, which are different in length. Further, we denote the planes perpendicular to the x, y, and z directions as x, y, and z, respectively. In this case, it is apparent that the effective jump length will be different, when we consider diffusion at different directions. Even the activation energy and the jump frequency also could be different depending on the site to which the atom jumps. To explain this, we consider the jump to three different positions at 1, 2, and 7. Although the actual barrier is because of four atoms around the void through which the atom jumps, it can be explained based on two atoms inside the same unit cell. For example, for the jump to position 1, the barrier will be from the atoms M and N. Similarly, when it jumps to positions 2 and 7, the main barrier comes from N–P and P–R, respectively. Note that M–N, N–P, and P–R barrier atoms are sitting on the planes y, x, and z, respectively. The areas inside the unit cell of these planes are ac, bc and ab, respectively, which are different. Therefore, the void size through which the atoms jump are different. This will lead to different activation energy barrier and jump frequency.

We denote the jump frequencies to different positions as

Γ_1 for the positions 2, 4, 10, and 12
Γ_2 for the positions 1, 3, 9, and 11
Γ_3 for the positions 5, 6, 7, and 8

Following the same line of discussion as above for the cubic crystal, the diffusion coefficients along the x-axis can be written as

$$D = \frac{1}{12}\sum_{i=0}^{12}\Gamma_i\Delta x_i^2 = \frac{1}{12}\left[\Gamma_1\Delta x_1^2 + \Gamma_2\Delta x_2^2 \ldots \Gamma_{12}\Delta x_{12}^2\right]$$

$$D_x = \frac{1}{12}\left[\begin{array}{l}\Gamma_2\left(-\frac{a}{2}\right)^2 + \Gamma_1(0)^2 + \Gamma_2\left(\frac{a}{2}\right)^2 + \Gamma_1(0)^2 + \Gamma_3\left(-\frac{a}{2}\right)^2 + \Gamma_3\left(-\frac{a}{2}\right)^2 \\ \quad + \Gamma_3\left(\frac{a}{2}\right)^2 + \Gamma_3\left(\frac{a}{2}\right)^2 + \Gamma_2\left(-\frac{a}{2}\right)^2 + \Gamma_1(0)^2 + \Gamma_2\left(\frac{a}{2}\right)^2 + \Gamma_1(0)^2\end{array}\right]$$

$$= \frac{a^2}{12}\left[\Gamma_2 + \Gamma_3\right]$$

Similarly, we find

$$D_y = \frac{b^2}{12}[\Gamma_1 + \Gamma_3]$$
$$D_z = \frac{c^2}{12}[\Gamma_1 + \Gamma_2]$$

Therefore, we get $D_x \neq D_y \neq D_z$. From the above discussion, we can say that if tracer diffusion experiments with impurity elements are conducted on a cubic crystal, the diffusion coefficient will be the same irrespective of the orientation of the substrate. On the other hand, the diffusion coefficient in a substrate with orthorhombic structure will be different in different directions. This can be found from experiments by selecting a single crystal substrate with different orientations and then by doing tracer diffusion experiments, as explained in the previous section. It can be easily understood that even if the jump frequency is the same and there is a difference in lattice parameters in a non-cubic crystal structure, such that the total jump length for atoms will be different in different directions to find different diffusion coefficients.

There exist experimental evidences on the anisotropic nature of the interstitial diffusion. Typically, this kind of diffusion anisotropy is not as large as that found in some cases of substitutional diffusion. What is a reason for such behavior? In order to answer this non-trivial question, at least semiqualitatively, one has to consider these diffusion mechanisms in details. We will limit us to the case of metallic system in which one should not deal with the charge state of the point defects. The key point is the magnitude of the corresponding energy barriers. The migration barriers are typically smaller in the case of interstitial diffusion, which are typically of the order of 0.2–0.5 eV, and they are larger for substitutional diffusion (1 eV and more). Correspondingly, the *differences* in the barriers for the diffusion jumps in different directions are typically larger for substitutional diffusion in comparison with those for interstitial one. Therefore, the diffusion anisotropy is more prominent. The effect is still moderate for pure metals, e.g., in HCP α-Ti or Zn, in which the diffusion anisotropy for self-diffusion is within a factor of 2 or 3 (Fig. 5.16), but it can reach the orders of magnitude in intermetallic compounds due to the *anisotropy* of sublattices (see the discussion in Sect. 5.3.6).

5.3 Diffusion in Substitutional Alloys

In the second chapter, we have discussed the formation of equilibrium concentration of vacancies. This concentration is, in general, in the order of 10^{-3}–10^{-4} near the melting point. That means one vacancy is present in a cube of 10–14 atoms in each direction. Because of this low concentration, we can neglect the vacancy–vacancy interactions. Although vacancy is just a vacant lattice site, it is considered as one of the entities to mediate discussion. Therefore, exchanging

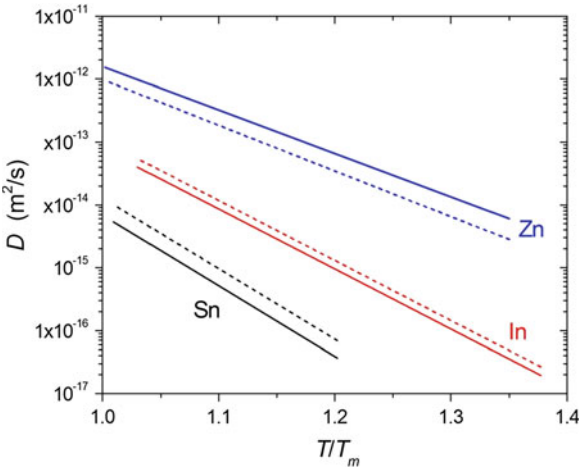

Fig. 5.16 Self-diffusion in single crystals of Zn, In, and Sn parallel (*solid lines*) and perpendicular (*dashed lines*) to the *c*-axis of the HCP structure. The data from the collection [11] are used

position of a vacancy with an atom can be seen as diffusion of atom, as well as the diffusion of the vacancy. One interesting fact should be noted here that if we are looking at one particular atom, the diffusion of that atom will depend on the availability of a vacancy to its neighboring position. On the other hand, for a vacancy, this restriction is not there and it can exchange position with any of the atoms. In other words, one particular atom cannot go through a random jump process; however, a vacancy can go through it. This is the reason that in substitutional diffusion, tracer and self-diffusion coefficients are different, although radioisotopes are used to study the self-diffusion of elements. These two are related by a correlation factor. To explain this in detail, first we need to explain the tracer diffusion method in substitutional diffusion.

5.3.1 Measurement of Tracer Diffusion Coefficient

As stated earlier, even in a pure material, diffusion of atoms is always happening just because of thermal vibration. Since there is no driving force present, atoms go through a random jump. The diffusion rate depends on the homologous temperature, that is, the temperature relative to its melting point. Since the atoms are very small and at relatively high temperature these might change place too many times per second, we cannot study the diffusion directly. For this sake, the tracer technique is developed, in which the diffusion of radioisotopes is quantified from the measurement of intensities of emitted rays at different depths after certain annealing time. This is similar to the procedure already explained for the calculation of impurity diffusion coefficient in Sect. 5.2.4. To study the self-diffusion coefficient of element B, radioisotopes of B* are deposited as very thin layer on a block of material B, as shown in Fig. 5.17. After certain annealing time, the

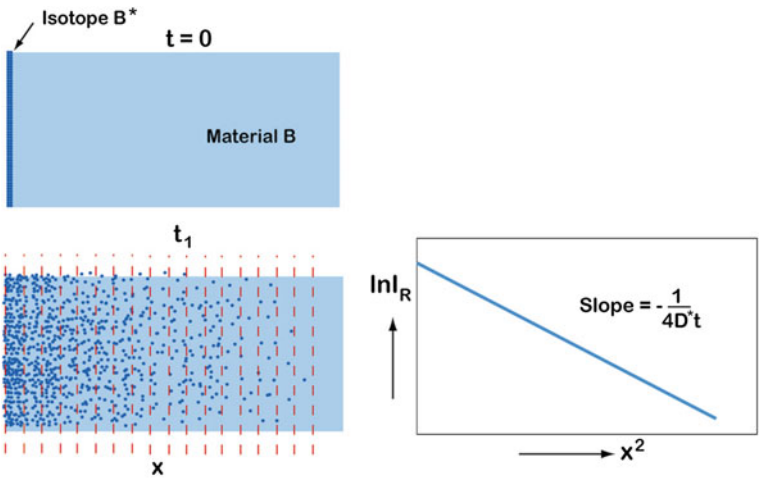

Fig. 5.17 Tracer method to determine tracer diffusion coefficient is shown

specific intensity of the emitted ray is measured at different depths after serial sectioning. In this case, Eq. 5.44 can be rewritten as

$$\ln I_R = \ln\left(\frac{1}{\sqrt{\pi D_B^* t}}\right) - \frac{x^2}{4D_B^* t} \tag{5.48}$$

Following the tracer diffusion coefficient, D_B^* could be calculated from the slope, $-\frac{1}{4D_B^* t}$, of the plot $\ln I_R$ versus x^2. However, as mentioned earlier, the measured tracer diffusion coefficient is not exactly the same as the self-diffusion coefficient. They are related by a correlation factor, f. Sometimes, the tracer self-diffusion coefficient is stated as the same as self-diffusion coefficient, which is not really correct. In the next section, we have explained the concept of the correlation factor.

5.3.2 *Concept of the Correlation Factor*

For the sake of discussion, we consider the tracer diffusion experiment as explained above in a FCC metal structure with [111] orientation. Atomic arrangement on the (111) plane is shown in Fig. 5.18. For the ease of explanation, we consider two-dimensional arrangements, although the argument is valid in three dimensions also. Suppose we have a situation that a vacancy, V, is surrounded by five B and one B^*, as shown in Fig. 5.18a. Now suppose B^* and V exchange their position and come to the situation, as shown in Fig. 5.18b. Since

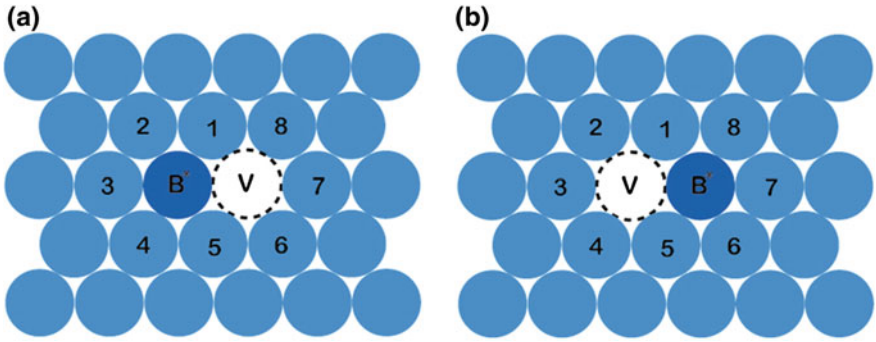

Fig. 5.18 Exchanging position between radioisotope B^* and vacancy is shown

the fraction of vacancies present in the structure is rather small, there is no guarantee that the tracer atom will find another vacancy to exchange its position immediately again to move forward. As explained before, there could be one vacancy present in a cube of 10 to 14 atoms each side only at melting point. At lower temperatures the vacancy concentration is significantly smaller and the imaginary size of the corresponding cube is considerably larger. So the next probable jump of B^* is back to the previous position after exchanging position with the vacancy. Then, there will be no diffusion. However, from the previous example, we have seen that the tracer atoms indeed move forward. Therefore, if this move forwards, the next probable jump is to position 1 or 5, on the condition that vacancy already exchanged position with the atoms located at these positions. To move even further, the next probability of jump of the tracer atom is to any of the positions 8 or 6. However, the probability is even lower than that of the previous jump, since after two successive jumps, vacancy has to reach to these positions of interest before the tracer atom could exchange position. Note that in the middle of these two successive jumps, also vacancy might deviate to other direction because of random nature. The probability of tracer atom to reach to the position 7 is the least, since before this exchange; the vacancy first has to reach to that position after making few successful jumps. Therefore, vacancy can go through a completely random jump process. However, the jump of the tracer atom is related to other jumps.

From the arguments developed in Sect. 5.2.2, we can write

$$\bar{L}_{\mathrm{v}}^2 = nl^2 \tag{5.49}$$

Since tracer atoms go through correlated jumps, the second term in Eq. 5.43, that is, double summation, is not zero and can be expressed as

$$\bar{L}_t^2 = nl^2\left(1 + \frac{2}{n}\overline{\sum_{j=1}^{n-1}\sum_{i=1}^{n-j}\cos\theta_{i,i+j}}\right) \tag{5.50}$$

where $\bar{L}_t^2$ is the square of average jump distance of tracer atoms after n jumps.

The correlation factor considering very large number of atoms and averaging over large number of trajectories is expressed as

$$f = \lim_{n\to\infty} \frac{\bar{L}_t^2}{\bar{L}_v^2} = \lim_{n\to\infty} \left(1 + \frac{2}{n} \overline{\sum_{j=1}^{n-1} \sum_{i=1}^{n-j} \langle \cos\theta_{i,i+j} \rangle} \right) \tag{5.51}$$

Looking at Eq. 5.51, it can be understood that the correlation factor actually measures the fraction of total jumps that give the diffusion or movement of tracer atoms. Since vacancies go through a random jump and it makes possible the diffusion of many atoms, the diffusion coefficient of vacancies, D_v, is actually equal to the self-diffusion coefficient, D_s. Therefore, it is necessary to calculate the correlation factor theoretically before determining the self-diffusion coefficient from the experimentally measured tracer self-diffusion coefficients. The correlation factor depends on the crystal structure, and the strict calculation is explained in the next section. However, before that, we can get further insights from a rough estimation.

Following previous line of discussion, we can say that the probability of exchanging positions between the vacancy and the tracer atom is $1/Z$ (Z is the coordination number). From Fig. 5.18b, we understand that the next probable jump for the tracer atom is back to the previous position; however, it is not necessary that the vacancy will definitely exchange position with the tracer atom again, since vacancy can exchange position with any other atoms. Therefore, the probability of the second jump again is $1/Z$. Two successive change of positions, as explained, will not result any successful jump, and we can say roughly that the fraction of jumps that will give successful diffusion for the tracer atom is

$$f = 1 - \frac{2}{Z} \tag{5.52}$$

Note here that we add the probabilities since these two steps are separate events. This is very rough estimation since we have not considered the possibilities of coming back of the tracer atom to its initial position after few or many jumps, which also should be added with the factor $2/Z$. However, these numbers are much smaller than $2/Z$. If all other possibilities are also considered, the difference between the actual correlation factor and roughly estimated value using Eq. 5.52 is small, which can be found from the values listed in Table 5.2. Note here that the difference increases with increasing coordination number because of increase in the number of possible ways to exchange positions.

Since the square of average jump length is proportional to the diffusion coefficient, we can write from Eq. 5.51 as

$$D^* = fD_s \tag{5.53}$$

Table 5.2 Actual and roughly estimated values $(1 - 2/Z)$ depending on the crystal structure

Crystal structure	Z	$1 - \frac{2}{Z}$	f
Simple cubic	6	0.6667	0.65549
Body-centered cubic	8	0.75	0.72149
Face-centered cubic	12	0.8333	0.78145

5.3.3 Calculation of the Correlation Factor

The calculation of the correlation factor represents generally an involved task, and the result depends on the diffusion mechanism, crystalline lattice, and type of diffuser. It is just a number for self-diffusion in pure metal via vacancy mechanism, but could be temperature dependent already for solute diffusion in pure metals or for diffusion in ordered compounds.

In this book, we will follow the general method of Howard [10] which could be applied for such involved situation as, e.g., calculations of the correlation factors for grain boundary diffusion.

First, we will outline the calculation of the correlation factor for cubic metals and then will introduce a generalization for arbitrary lattices. Thus, we will start from Eq. 5.51.

The corresponding summations can be performed analytically in very special cases, which are though general enough to be broadly applied at least for cubic metals, namely in situations where

(i) the crystal is isotropic;
(ii) all jump vectors of the diffusing atom are axes of twofold or threefold symmetry, and
(iii) all jumps are equivalent, i.e., jump lengths are the same.

Then, the series expression for the correlation factor reduces to the simple expression

$$f = \frac{1 + \langle \cos \theta_{12} \rangle}{1 - \langle \cos \theta_{12} \rangle} \tag{5.54}$$

where $\langle \cos \theta_{12} \rangle$ is the average value of the cosine of the angle between any two consecutive jumps of the diffusing atom in view of the conditions (i)–(iii). The quantity $\langle \cos \theta_{12} \rangle$ may be calculated numerically (see below).

In the case when the conditions (i)–(iii) are not fulfilled, Eq. 5.54 cannot be applied. Instead, one may either use the numerical method directly or, after a careful analysis of the lattice and possible diffusion jumps, apply the concept of partial correlation factors which will be shortly outlined in that follows.

The starting point again is the expression for the correlation factor f_x which is defined for the principle x-axis as

$$f_x = 1 + 2\frac{\sum_{i=1}^{\infty}\sum_{j=1}^{\infty}\langle x_i x_{i+j}\rangle}{\sum_{i=1}^{\infty}\langle x_i^2\rangle} \tag{5.55}$$

Here, x_i is the x projection of the ith jump, which could be now different for different jumps. It is clear that the summation has to be done over the jumps with nonzero x component. Only such jumps will be considered and counted in the summations. The consideration is general with no limitations on jump lengths and symmetry. Thus, it is applicable for short-circuit diffusion, too, or in the case of diffusion in non-cubic lattices.

The critical point is the classification of all jumps in different *types*. Since the lattice is periodic, the number of all types N is finite and let the subscript α label these types as $\alpha = 1, 2, 3, \ldots N$. The types are defined such as for all x_i of the same type, the sum $\sum_{j=1}^{\infty}\langle x_i x_{i+j}\rangle$ could be rewritten as

$$\sum_{j=1}^{\infty}\langle x_i x_{i+j}\rangle = \sum_{j=1}^{\infty}\langle x_\alpha x_{\alpha,j}\rangle \tag{5.56}$$

and it does not depend on i. Here, the subscript α, j refers to the jth jump after a jump of the type α. Then, one can show that Eq. 5.55 could be written in matrix notation as

$$f_x = \mathbf{c}\cdot\mathbf{f} \tag{5.57}$$

where $\mathbf{c} = (c_1,\ldots,c_N)$ is the vector with components c_α which represent the fraction of jumps of the type α in any very long sequence of atom jumps and $\mathbf{f} = (f_1,\ldots,f_N)$ is the vector of the partial correlation factors representing the contributions of the given types of jumps. The latter is defined by the expression

$$\mathbf{f} = \mathbf{I} + 2\mathbf{Z}\cdot\mathbf{T}(\mathbf{E}-\mathbf{T})^{-1}\cdot\mathbf{d}. \tag{5.58}$$

Here, $\mathbf{I}$ is the N-component unit column vector, $\mathbf{E}$ is the $N \times N$ unit matrix, $\mathbf{d} = (|z_1|,\ldots, |z_N|)$ is the column vector of the jump distances of type α jumps, $\mathbf{Z}$ is the $N \times N$ matrix which diagonal elements are equal to $\left|z_\alpha^{-1}\right|$, $\alpha = 1,\ldots, N$, and $\mathbf{T}$ is a $N \times N$ matrix with the elements

$$t_{\alpha\beta} = P_{\alpha\beta}^{+} - P_{\alpha\beta}^{-}, \quad \alpha,\beta = 1,\ldots,N.$$

Here, $P_{\alpha\beta}^{+}\left(P_{\alpha\beta}^{-}\right)$ is the probability that a tracer jump of type α is immediately followed by a tracer jump of type β in the same (+) or opposite (−) direction. The main point is the determination of these probabilities which may be evaluated using numerical methods. The advantage is a low cost of the numerical calculations in which the jump history of a given tracer is enough to follow over 10^6 individual jumps. If the numerical method will be applied directly to Eq. 5.54, the

atom jumps have to be followed up to 10^9 individual jumps to have a reasonable accuracy in sophisticated cases of non-cubic crystals. The application of the concept will be demonstrated for the case of diffusion in $MoSi_2$ below.

Generally, the correlation factors can directly be calculated using numerical methods. The starting point is the determination of all jump frequencies which are involved in diffusion of a tracer atom over the lattice. Having calculated the transition probabilities for all possible vacancy jumps, the correlation factor can be calculated by the Monte Carlo approach. In simulations, a box of the size of, let us say, $100 \times 100 \times 100$ with the given structure is first generated. A vacancy is created at the center of the block, and the vacancy is allowed to perform the given types of jumps. The probabilities p_i of these jumps can be calculated according to the transition frequencies v_i estimated before:

$$p_i = \frac{v_i}{\sum_{j=1}^{z} v_j}, \tag{5.59}$$

where z is the coordination number of the given lattice. The time-residence algorithm is typically applied. Each jump of the vacancy is successful, and the time variable is increased by

$$\tau = \frac{1}{\sum_{j=1}^{z} v_j}. \tag{5.60}$$

The atomic correlation factors for species k, several species belong to the lattice under consideration, are calculated from the equation:

$$f_k = \frac{\sum_{i=1}^{n_k} R_i^2}{m_k a_k^2}, \tag{5.61}$$

where R_i is the net displacement of the ith atom of type k, n_k is the total number of atoms of type k, m_k is the total number of vacancy exchanges with atoms of type k, and a_k is the elementary jump length.

5.3.4 The Relation Between the Jump Frequency and the Diffusion Coefficient in Substitutional Diffusion

For the sake of explanation, let us consider (111) planes of a pure element B with FCC crystal, as shown in Fig. 5.19. We consider that there is a radioisotope, B^*, present on the plane Q which is surrounded by six B, numbered as 4–9, respectively. Based on the crystal structure, we can say that if three nearest neighbor sites, numbered as 1–3, respectively, are actually on the plane P below Q, then

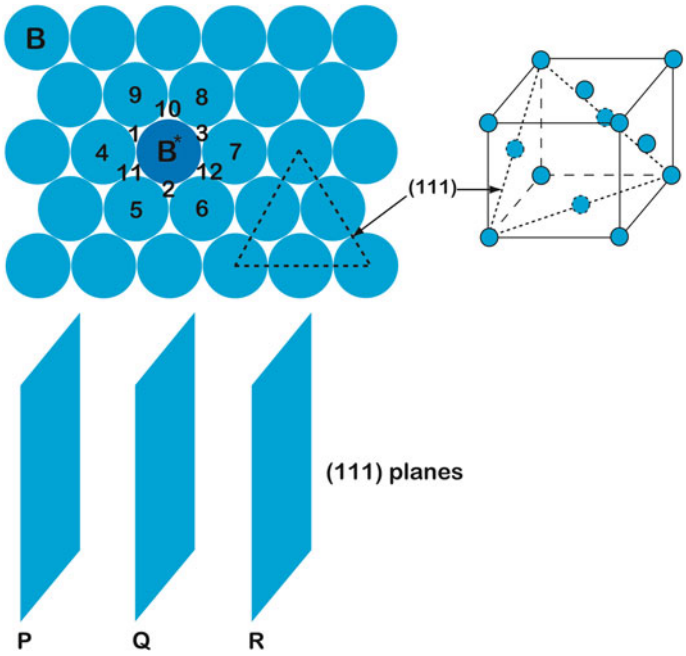

Fig. 5.19 The jump of the radiotracer B^* between (111) planes of B with FCC crystal structure is discussed

other three nearest neighbor sites, numbered as 10–12, respectively, are on the plane R above the plane P. Since we are considering random jump process, we can say that the tracer atom can jump to any of these 12 positions, on the condition that vacancy is present on that site. To derive the relation, as we did in the case of interstitial diffusion, we first consider the jump of atoms between planes Q and R. Following, we shall develop the general relation that can be used without any restrictions.

Now, we follow the previous line of discussion as considered to relate the jump frequency with the diffusion coefficient in Sect. 5.2.1. We consider the exchange of vacancies and the tracer atom between planes Q and R. B^* can jump to any of the sites 10–12, on the condition that vacancy is available at the site of interest. Therefore, the flux of the tracer atom can be expressed as

$$\vec{J}_{\mathrm{Q}}^{*} = \frac{3}{12} n_{\mathrm{Q}} f\, p_{\mathrm{V}} \Gamma_{\mathrm{Q}} = \frac{1}{4} n_{\mathrm{Q}} f\, p_{\mathrm{V}} \Gamma_{\mathrm{Q}} \tag{5.62}$$

The numerical factor comes from the fact that a tracer atom exchanges position with vacancy in one of the 3 sites (10–12) on the plane R out of total 12 nearest neighbors. n_{Q} is the total number of tracer atoms present on the plane Q. p_{V} is the probability to find a vacancy, f is the correlation factor, and Γ_{Q} is the jump

frequency of the tracer atom from plane Q to R. Similarly, the flux of tracer atoms from R to Q can be written as

$$\overleftarrow{J}_{\mathrm{R}}^{*} = \frac{3}{12} n_{\mathrm{R}} f\, p_{\mathrm{V}} \Gamma_{\mathrm{R}} = \frac{1}{4} n_{\mathrm{R}} f\, p_{\mathrm{V}} \Gamma_{\mathrm{R}} \tag{5.63}$$

where n_{R} is the total number of tracer atoms present on the plane R and Γ_{R} is the jump frequency of tracer atom from plane R to plane Q.

Since we are considering isotropic FCC crystal, we have $\Gamma_{\mathrm{Q}} = \Gamma_{\mathrm{R}} = \Gamma$. If we consider, $n_{\mathrm{Q}} > n_{\mathrm{R}}$, then the resultant flux from plane Q to R can be written as

$$J^{*} = \frac{1}{4} f\, p_{\mathrm{V}} \Gamma (n_{\mathrm{Q}} - n_{\mathrm{R}}) \tag{5.64}$$

Following similar arguments as discussed for interstitial diffusion in Sect. 5.2.1, we get

$$J^{*} = -\frac{1}{4} f\, p_{\mathrm{V}} \Gamma \Delta x^{2} \frac{dC}{dx} \tag{5.65}$$

Here, Δx is the effective jump length or the inter-planar spacing. Comparing with Fick's first law $\left(J^{*} = -D^{*} \frac{dC}{dx}\right)$, we can write the tracer diffusion coefficient of element B as

$$D^{*} = \frac{1}{4} f p_{\mathrm{V}} \Gamma \Delta x^{2} \tag{5.66}$$

Since the concentration of vacancy is very small, the probability of finding a vacancy for the successful jump is equal to the mole fraction of the vacancies, X_{V}. Therefore, Eq. 5.66 can be written as

$$D^{*} = \frac{1}{4} f\, X_{\mathrm{V}} \Gamma \Delta x^{2} \tag{5.67}$$

The above equation is derived based on the jump between the planes Q and R. However, as such, atoms are free to jump to any of the neighboring atoms depending on the availability of vacancy. There are many atoms present on the same plane, and there is a probability that different atoms will jump to different positions, so the average tracer diffusion coefficients can be written as

$$D^{*} = f X_{\mathrm{V}} \frac{1}{Z} \sum_{Z=1}^{Z} \Gamma \Delta x_{i}^{2} \tag{5.68}$$

The tracer diffusion to a particular position i can be expressed as

$$D_i^* = f X_V \Gamma_i \Delta x_i^2 \tag{5.69}$$

where $\Gamma = Z\Gamma_i$.

If the crystal is not isotropic and the jump frequency is different to different positions, then the tracer diffusion coefficient from the average of different kinds of jumps can be written as

$$D^* = f X_V \frac{1}{Z} \sum_{Z=1}^{Z} \Gamma_i \Delta x_i^2 \tag{5.70}$$

From the relation between the tracer self-diffusion and self-diffusion coefficients (Eq. 5.53), the self-diffusion coefficient, that is, the vacancy diffusion coefficient, can be expressed as

$$D_s = X_V \frac{1}{Z} \sum_{Z=1}^{Z} \Gamma_i \Delta x_i^2 \tag{5.71}$$

5.3.5 *Effect of Temperature on Substitutional Diffusion*

As it is discussed, in substitutional diffusion, atoms exchange position with the vacancies. However, the atom has to move the neighboring atoms elastically for a successful jump, as shown in Fig. 5.20. Just for the sake of explanation, two-dimensional atomic arrangements are shown instead of actual three dimensions. The probability with which atoms will make a successful jump at a particular temperature T is expressed as $\exp\left(-\frac{\Delta g_m}{RT}\right)$. Here, Δg_m is the activation energy for migration per mol of atoms. Since atoms make ν (Debye frequency) attempts per second, the jump frequency can be written as $\Gamma_i = v \exp\left(-\frac{\Delta g_m}{RT}\right)$ and the self-diffusion coefficient can be expressed as

$$D = v X_V \Delta x^2 \exp\left(-\frac{\Delta g_m}{RT}\right) \tag{5.72}$$

Therefore, the only difference in the relation between temperature-dependent self-diffusion coefficient and the interstitial diffusion coefficient (Eq. 5.39) is the extra term X_V. From the discussion in Chap. 2, we know that the equilibrium vacancy concentration at a particular temperature, T, is expressed as

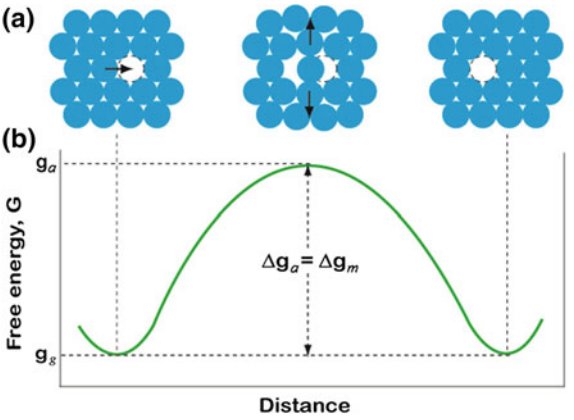

Fig. 5.20 Activation energy barrier for substitutional diffusion is explained with the **a** atomic movement and **b** change in free energy during movement

$$X_V = \exp\left(-\frac{\Delta g_V}{RT}\right) \tag{5.73}$$

By replacing Eq. 5.73 in Eq. 5.72, we get

$$D = v\,\Delta x^2 \exp\left(-\frac{\Delta g_m + \Delta g_V}{RT}\right) = D_0 \exp\left(-\frac{\Delta g_a}{RT}\right) \tag{5.74}$$

D_0 is the temperature-independent pre-exponential factor. The activation energy barrier for the self-diffusion comes from two different contributions, one from the activation energy for the formation of vacancies and another is from the activation energy barrier for migration. So it must be apparent that the interstitial diffusion in general is much easier than substitutional diffusion. Sometimes, anomalies are found, as shown in Fig. 5.21. Further, Eq. 5.74 can be written as

$$\ln D = \ln D_0 - \frac{Q}{RT}$$
$$\log D = \log D_0 - \frac{Q}{2.3RT}$$

So it is apparent that one can determine the activation energy for diffusion from the plot of ln D versus $\frac{1}{T}$ or log D versus $\frac{1}{T}$, where the slope is equal to −Q/R or −Q/2.3R, respectively.

Interstitial diffusion and substitutional diffusion of C and Fe are compared for the case of Fe in Sect. 5.3.7. The hexagonal lattices of α-Ti, α-Zr, and α-Hf represent other interesting cases featuring fast diffusion rates of small nonmetallic atoms, such as C or O, and even "ultrafast" diffusion rates of transition metals—Fe, Ni, Co, and Mn (see Fig. 5.21). The corresponding diffusion rates are faster than those of self-diffusion by five (C in α-Ti) or seven (Ni in α-Ti) orders of

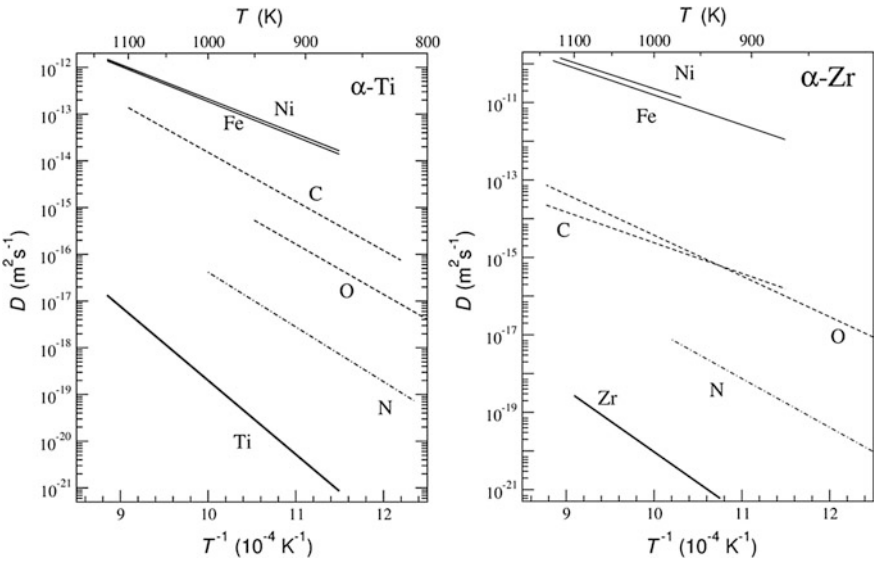

Fig. 5.21 Ultrafast diffusion of transition metal atoms (Fe and Ni) and fast diffusion of nonmetallic solutes (C, O, and N) in α-Ti (*left*) and α-Zr (*right*) in comparison with self-diffusion (*thick solid lines*). Only the diffusivities perpendicular to the *c*-axis are presented. The data for α-Ti are from (Ti) [12], (Fe) [13], (Ni) [14], (C) [15], (O) [16], and (N) [17], and for α-Zr, they are taken from (Zr) [18], (Fe) [19], (Ni) [20], (C) [21], (O) [22], and (N) [23]

magnitude! The diffusion enhancement of, e.g., Ni in α-Zr approaches 10 orders of magnitude at 1,000 K. These ultrafast diffusion rates are explained by interstitial diffusion mechanism of the transition metal atoms and are related to the specific electronic effects owing to their unfilled *d*-states. Only, hydrogen reveals even faster diffusion rates in these hexagonal structures.

Note that the diffusion rates of transition metal atoms become "normal" in bcc beta phases, i.e., β-Ti, β-Zr, or β-Hf, and in fact, these atoms diffuse via a common vacancy mechanism. As an example, diffusion of small nonmetallic atoms, transition metals, and Ti is shown in Fig. 5.22. At first glance, the diffusion behavior of Fe and Ni at the $\alpha \rightarrow \beta$ transition in Ti does not follow common rules (see Sect. 5.3.7 for the $\alpha \rightarrow \gamma$ transition in Fe)—although the bcc lattice (β-Ti) is more open, the diffusion rates of Ni and Fe either continue to follow the low-temperature Arrhenius line established in the more dense phase (Ni) or even drop with increasing temperature (Fe). The reason is the basic change of the underlying diffusion mechanism—from interstitial one for Ni and Fe in α-Ti to substitutional one in β-Ti.

Figure 5.22 features several important issues on self- and solute diffusion in crystalline solids:

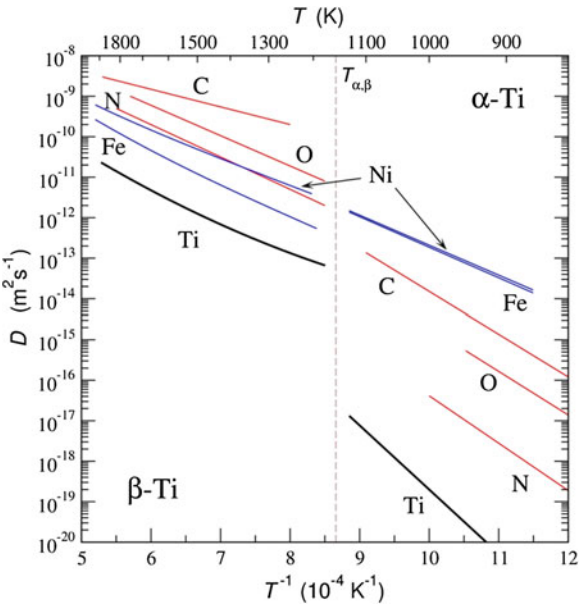

Fig. 5.22 Comparison between the diffusion rates of small nonmetallic atoms (C, O, and N) and transition metals (Ni and Fe) in the α- and β-phases of Ti. The data are taken from Refs. [15, 24] (C), [16, 25] (O), [17, 26] (N), [14, 27] (Ni), [13, 27] (Fe), and [12, 28] (Ti) for α- and β-phases, respectively

- Diffusion mechanism (interstitial vs. vacancy mediated) has a strong effect on diffusion rates, and small nonmetallic atoms diffuse typically much faster in metals in comparison with the self-diffusion rates.
- The diffusion rate depends strongly on the type of lattice. In fact, self-diffusion of Ti is significantly enhanced in more open bcc structure of β-Ti comparing to that of very dense hcp structure of α-Ti. This is true for vacancy-mediated diffusion hopping mechanism, and the enhancement is less pronounced for species diffusing via interstitial mechanism.
- Strongly curved temperature dependences in the Arrhenius coordinates could be measured, e.g., for Ti self- or Fe solute diffusion in β-Ti, as shown in Fig. 5.22.

The latter point required a special consideration. Generally, two different mechanisms can be suggested to explain the observed behavior:

(a) A change of basic properties of the lattice with approaching the critical temperature, as phonon softening in β-Ti near melting point [28] or a decrease of magnetization in ferromagnetic Fe at the ferro-para-magnetic transition temperature;
(b) Existence of two different diffusion mechanisms with different activation energies.

The existence of fast diffusing solutes with strong binding to vacancies or (potentially) a tendency to form a solute—self-interstitial pairs could significantly

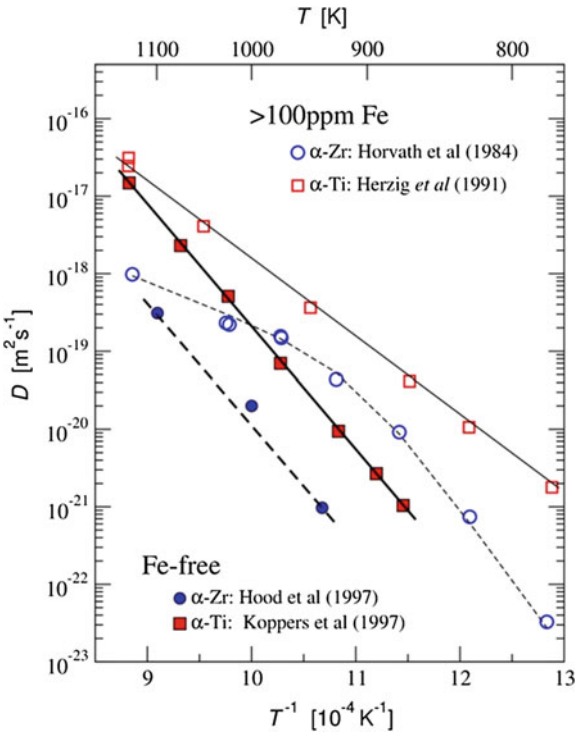

Fig. 5.23 Impurity effect on self-diffusion in α-Ti and α-Zr substantiated as the influence of Fe content. Zr and Ti diffusion rates were measured in Fe-doped [29, 30] and "Fe-free" [12, 31] materials, respectively

affect self-diffusion. In fact, such behavior was observed in α-phases of Ti and Zr and it is featured in Fig. 5.23.

The enhancement of Zr and Ti self-diffusion rates in less pure materials is due to the strong interaction between Fe interstitial atoms, which are ultrafast diffusers in α-Zr or α-Ti, with host vacancies. The formation of very mobile vacancy–interstitial impurity complexes causes in this way "extrinsic" diffusion behavior. This strong attractive interaction between interstitially dissolved Fe atoms and metallic vacancies results in an increased vacancy concentration. Generally, the vacancy concentration c_v in the presence of strongly interacting impurities is increased by the amount of vacancy–impurity pairs, the concentration (in terms of mol fraction) of which can be presented as $X_v = X_v^0 \cdot \exp\{-(\Delta H^f + \Delta H^b)/\mathrm{RT}\}$. Here ΔH^f and ΔH^b are the vacancy formation enthalpy and vacancy–impurity binding enthalpy, respectively, and $X_v^0 = \exp\{(\Delta S^f + \Delta S^b)/\mathrm{R}\}$ with corresponding contributions of formation, ΔS^f, and binding, ΔS^b, entropies. If $\Delta H^b < 0$ (attraction), the overall concentration of vacancies will be increased, and if the vacancy–impurity complexes are highly mobile, this effect will give rise to an enhanced self-diffusion. Note that the total effect from all fast diffusing impurities available in the material should be taken into account.

We have explained the activation barrier with the help of two-dimensional arrays of atoms. However, to understand the actual barrier, we need to consider the atomic arrangements in three dimensions as shown in Fig. 5.24. We consider the atomic arrangement on a (111) plane of a FCC crystal. We further consider that

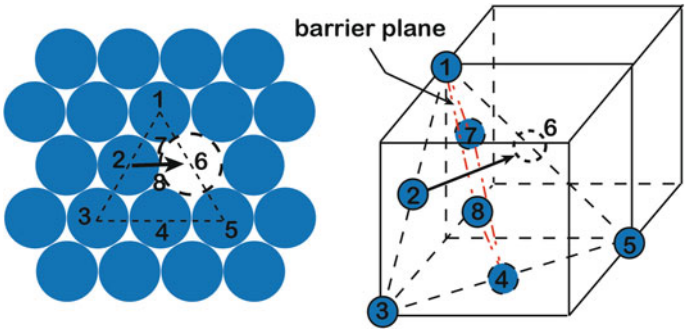

Fig. 5.24 Activation barrier plane is shown in a FCC structure

atom 2 jumps to vacancy at 6. Therefore, the jumping atom has to displace atoms 1 and 4 on the same plane and 7 below and 8 above this plane, respectively. Therefore, the actual barrier plane has atoms 1, 8, 4, and 7.

Now, we consider a material with BCC structure, as shown in Fig. 5.25. Two-dimensional atomic arrangement is shown for (110) plane. The activation barrier is not clear, when, for example, atom 2 jumps to a vacant lattice site at the center. If we consider just one unit cell, it seems that the activation barrier is mainly because of the atoms 1, 7, and 6. However, to understand the actual barrier, we need to consider another unit cell, keeping atom 2 at the body center position. It must be apparent that actually, the atom has to cross another barrier plane also with atoms 9, 10, and 11. That means it has to cross two barrier planes in total to make a successful jump. This is the reason that the free energy versus distance curve in BCC crystal may have two humps.

In Fig. 5.26, the results of real calculations are presented for α-Fe and β-Zr. Although such shallow minima are sometimes observed in other cases, too, one has to be careful with corresponding interpretation in view of approximate nature of the used inter-atomic potentials.

5.3.6 Orientation Dependence in Substitutional Diffusion

We start our discussion with a BCC lattice, which has coordination number $Z = 8$. For the ease of explanation, we consider the presence of a vacancy at the body center position, as shown in Fig. 5.27.

This is an isotropic system. That means all the jump lengths are equal. Even the activation energy for all the jumps also should be the same to consider $\Gamma_i = \Gamma$. We consider diffusion along the x-axis ($\langle 100 \rangle$ direction). Suppose atoms 1, 2, 5, and 6 are on one plane, V is on the next plane, and atoms 3, 4, 7, and 8 are on another plane. So vacancy has equal probability to exchange position with any of the

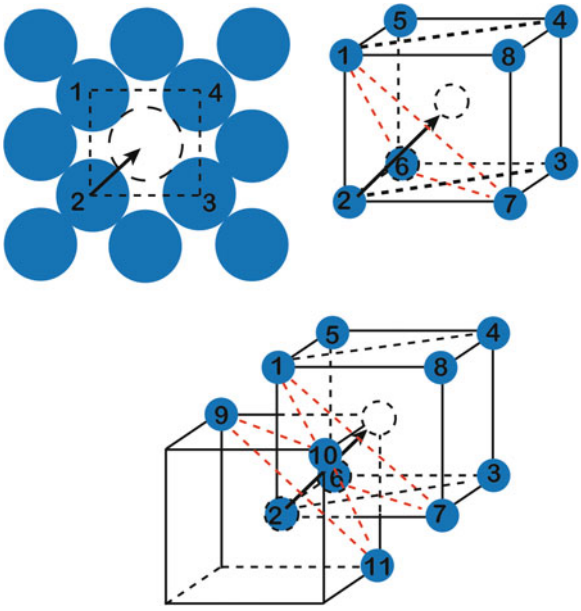

Fig. 5.25 Activation barrier planes are shown in a BCC structure

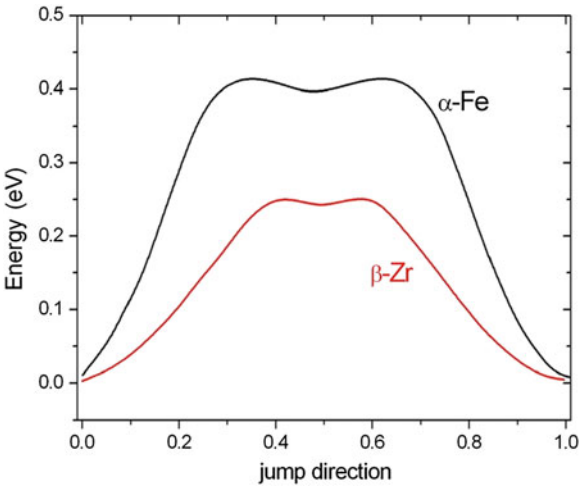

Fig. 5.26 Energy barrier as a function of the position of the jumping atom normalized to the jump distance for α-Fe and β-Zr after Chirkov and Nazarov [32]. Two humps in the energy landscape are clearly seen

atoms. Further, different vacancies will exchange position with different atoms. Therefore, the diffusion coefficient from Eq. 5.71 can be written as

$$D_{\mathrm{s}}^{x} = D_{\mathrm{s}}^{\langle 100\rangle} = X_{\mathrm{v}} \frac{1}{Z} \sum_{Z=1}^{Z} \Gamma_i \Delta x_i^2 = X_{\mathrm{v}} \Gamma \frac{1}{8} \left[4\left(-\frac{a}{2}\right)^2 + 4\left(\frac{a}{2}\right)^2 \right] = \frac{1}{4} X_{\mathrm{v}} \Gamma a^2 \quad (5.75)$$

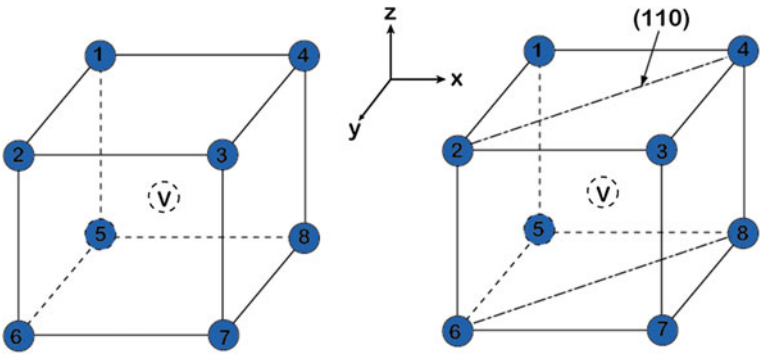

Fig. 5.27 BCC unit cell is shown with the presence of a vacancy at the center

where $\pm\, a/2$ are the effective jump lengths.

Similarly, we can show that $D_s^y = D_s^{\langle 010\rangle} = \frac{1}{4}X_v\Gamma a^2$ and $D_s^z = D_s^{\langle 001\rangle} = \frac{1}{4}X_v\Gamma a^2$.

Now, we consider diffusion along the $\langle 110\rangle$ direction that is perpendicular to the plane (110). The effective jump length is equal to the inter-planar spacing $\pm a/\sqrt{2}$. It can be seen easily that atoms 2, 4, 6, and 8 are located on the same plane (110) with the vacancy. So the exchange of the vacancy with these atoms will not contribute to diffusion distance along the $\langle 110\rangle$ direction. The exchange of vacancy to any of the atoms 1, 5, 3, and 7 will only contribute to the diffusion. So the diffusion coefficient in this direction can be written as

$$D_{\langle 110\rangle}^s = X_v\Gamma\frac{1}{8}\left[4(0) + 4\left(\pm\frac{a}{\sqrt{2}}\right)^2\right] = \frac{1}{4}X_v\Gamma a^2 \tag{5.76}$$

From the above discussions, we can see that the diffusion coefficient is insensitive to the direction in a BCC structure.

Let us now consider a FCC structure, as shown in Fig. 5.28a. Again, we can consider $\Gamma_i = \Gamma$, since it is an isotropic system. It has a coordination number of 12. That means different vacancies on the same plane will exchange position with any of the 12 atoms with an equal probability. When we consider the diffusion along the x-axis, the effective jump length is $\Delta x = -a/2$ for the exchange with atoms 5, 6, 7, and 8 and $a/2$ for the exchange with atoms 10, 11, 12, and 13. On the other hand, the effective jump length is zero for the exchange with atoms 1, 2, 3, and 4. So the diffusion coefficient along the x-axis can be written as

$$D_s^x = X_v\Gamma\frac{1}{12}\left[4\left(-\frac{a}{2}\right)^2 + 4(0) + 4\left(\frac{a}{2}\right)^2\right] = \frac{1}{6}X_v\Gamma a^2 \tag{5.77}$$

The same value will be found, when we consider diffusion along the y- or z-axis.

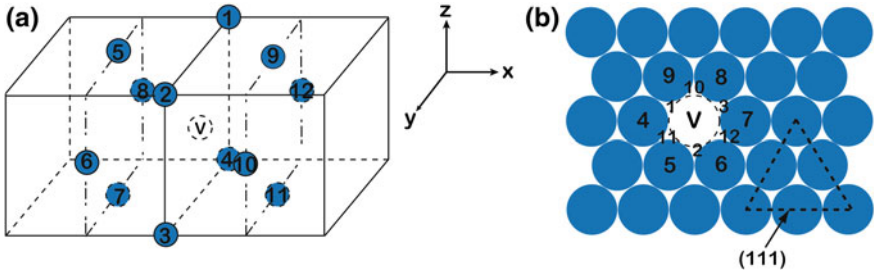

Fig. 5.28 **a** FCC unit cell and **b** atomic arrangement on plane (111) are shown with the presence of a vacancy in the middle

Now, we consider the diffusion along the $\langle 111 \rangle$ direction that is perpendicular to the plane (111), as shown in Fig. 5.28b. Note that the numbers used to denote the atoms in figures (a) and (b) are not related. Vacancy is surrounded by 6 atoms 4–9 on the same plane and will not contribute to the diffusion perpendicular to this plane. If atoms 1–3 are located below the plane with the vacancy, then atoms 10–12 are located above the plane. The effective jump lengths for the exchange of vacancies with any of these atoms are equal to the inter-planar spacing $\Delta x = \pm \frac{a}{\sqrt{3}}$. Therefore, the coefficient along the $\langle 111 \rangle$ direction can be written as

$$D_{\mathrm{s}}^{\langle 111 \rangle} = X_{\mathrm{v}} \Gamma \frac{1}{12} \left[3 \left(-\frac{a}{\sqrt{3}} \right)^2 + 6(0) + 3 \left(\frac{a}{\sqrt{3}} \right)^2 \right] = \frac{1}{6} X_{\mathrm{v}} \Gamma a^2 \tag{5.78}$$

So we can say that the diffusion coefficient to any directions in a FCC lattice will be the same.

Now, we extend our discussion to body-centered tetragonal structures, as shown in Fig. 5.29a. It has the same lattice parameter a along the x- and y-axes. Along the z-axis, it has different lattice parameter c. So the effective jump lengths along the x- and y-axes for exchanging position between atoms and the vacancies are $\pm a/2$, and along the z-axis, it is $\pm c/2$. However, if we consider the vacancy at the center, it must be clear that the actual distance (not the effective jump length) and the size of the void through which the atoms jump are the same for any jumps. Therefore, we can write $\Gamma_i = \Gamma$. The diffusion coefficients along different axes can be written as

$$D_{\mathrm{s}}^{x} = D_{s}^{y} = X_{\mathrm{v}} \Gamma \frac{1}{8} \left[4 \left(-\frac{a}{2} \right)^2 + 4 \left(\frac{a}{2} \right)^2 \right] = \frac{1}{4} X_{\mathrm{v}} \Gamma a^2 \tag{5.79}$$

$$D_{z}^{\mathrm{s}} = X_{\mathrm{v}} \Gamma \frac{1}{8} \left[4 \left(-\frac{c}{2} \right)^2 + 4 \left(\frac{c}{2} \right)^2 \right] = \frac{1}{4} X_{\mathrm{v}} \Gamma c^2 \tag{5.80}$$

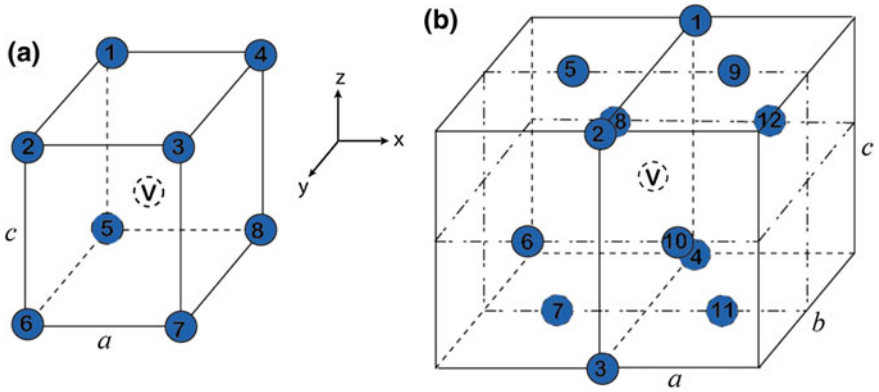

Fig. 5.29 **a** Body-centered tetragonal and **b** face-centered orthorhombic structures are shown with the presence of a vacancy in the middle

Further, we consider the face-centered orthorhombic structure with lattice parameters a, b, and c along the x-, y-, and z-axes, respectively, as shown in Fig. 5.29b. Note here that (similar to the discussion on interstitial diffusion in the same crystal structure in Sect. 5.2.5) atoms 1, 2, 3, and 4 are on the x plane with the area of bc, atoms 5, 7, 9, and 11 are on the y plane with the area of ac, and atoms 6, 8, 10, and 12 are on the z plane with the area of ab. So the jump frequencies will be different when vacancies exchange position with the atoms on different planes. These are denoted as Γ_1, Γ_2, and Γ_3 for the atoms on x, y, and z planes, respectively. Further, the effective jump lengths along the x, y, and z directions are $\pm a/2$, $\pm b/2$ and $\pm c/2$. Therefore, the diffusion coefficients can be expressed as

$$D_s = \frac{1}{12} X_V \sum_{i=0}^{12} \Gamma_i \Delta x_i^2 = \frac{1}{12}\left[\Gamma_1 \Delta x_1^2 + \Gamma_2 \Delta x_2^2 \cdots + \Gamma_{12} \Delta x_{12}^2\right]$$

$$D_s^x = X_v \frac{1}{12}\left[\begin{array}{l}\Gamma_1(0)^2+\Gamma_1(0)^2+\Gamma_1(0)^2+\Gamma_1(0)^2+\Gamma_2(-a/2)^2+\Gamma_3(-a/2)^2 \\ \quad +\Gamma_2(-a/2)^2+\Gamma_3(-a/2)^2+\Gamma_2(a/2)^2+\Gamma_3(a/2)^2+\Gamma_2(a/2)^2+\Gamma_3(a/2)^2\end{array}\right]$$

$$= \tfrac{1}{12} X_v(\Gamma_2 + \Gamma_3)a^2 \tag{5.81a}$$

$$D_s^y = X_v \frac{1}{12}\left[\begin{array}{l}\Gamma_1(-b/2)^2+\Gamma_1(b/2)^2+\Gamma_1(b/2)^2+\Gamma_1(-b/2)^2+\Gamma_2(0)^2+\Gamma_3(b/2)^2 \\ \quad +\Gamma_2(0)^2+\Gamma_3(-b/2)^2+\Gamma_2(0)^2+\Gamma_3(b/2)^2+\Gamma_2(0)^2+\Gamma_3(-b/2)^2\end{array}\right]$$

$$= \frac{1}{12} X_v(\Gamma_1 + \Gamma_3)b^2 \tag{5.81b}$$

$$D_s^z = X_v \frac{1}{12}\begin{bmatrix}\Gamma_1(c/2)^2+\Gamma_1(-c/2)^2+\Gamma_1(c/2)^2+\Gamma_1(-c/2)^2+\Gamma_2(c/2)^2+\Gamma_3(0)^2 \\ +\Gamma_2(-c/2)^2+\Gamma_3(0)^2+\Gamma_2(c/2)^2+\Gamma_3(0)^2+\Gamma_2(-c/2)^2+\Gamma_3(0)^2\end{bmatrix}$$
$$= \frac{1}{12}X_v(\Gamma_1+\Gamma_2)c^2 \tag{5.81c}$$

Therefore, from Eqs. 3.58a, 3.58b, and 3.58c, we can write in an orthorhombic structure

$$D_x^s \neq D_y^s \neq D_z^s \tag{5.82}$$

Now, we discuss hexagonal close packed structure. Lattice parameters are a and c, as shown in Fig. 5.30. If we consider the presence of a vacancy in the middle of the basal plane, we can see that it is surrounded by total 12 atoms. There are six atoms on the basal plane, numbered as 1–6, respectively. Three atoms are at distance $+\frac{c}{2}$ along the z-axis, numbered as 7–9, respectively, and three atoms are at distance $-\frac{c}{2}$, numbered as 10–12, respectively. We need to consider two jump frequencies: Γ_1 for exchanging position with atoms 1–6 and Γ_2 for exchanging position with atoms 7–12. So the diffusion along the x- and z-axes can be written as

$$D_s = \frac{1}{12}X_V\sum_{i=0}^{12}\Gamma_i\Delta x_i^2 = \frac{1}{12}\left[\Gamma_1\Delta x_1^2+\Gamma_2\Delta x_2^2\cdots+\Gamma_{12}\Delta x_{12}^2\right]$$

$$D_x^s = X_V\frac{1}{12}\begin{bmatrix}\Gamma_1(-a)^2+\Gamma_1(-a/2)^2+\Gamma_1(a/2)^2+\Gamma_1(a)^2+\Gamma_1(a/2)^2+\Gamma_1(-a/2)^2 \\ +\Gamma_2(-a/2)^2+\Gamma_2(0)^2+\Gamma_2(a/2)^2+\Gamma_2(-a/2)^2+\Gamma_2(0)^2+\Gamma_2(a/2)^2\end{bmatrix}$$
$$= \frac{1}{12}X_V a^2(3\Gamma_1+\Gamma_2) \tag{5.83a}$$

$$D_z^s = X_V\frac{1}{12}\begin{bmatrix}\Gamma_1(0)^2+\Gamma_1(0)^2+\Gamma_1(0)^2+\Gamma_1(0)^2+\Gamma_1(0)^2+\Gamma_1(0)^2 \\ +\Gamma_2(c/2)^2+\Gamma_2(c/2)^2+\Gamma_2(c/2)^2+\Gamma_2(-c/2)^2+\Gamma_2(-c/2)^2+\Gamma_2(-c/2)^2\end{bmatrix}$$
$$= \frac{1}{8}\Gamma_2 X_V c^2 \tag{5.83b}$$

One interesting point should be noted here. In the case of an ideal HCP structure, we know that $\frac{c}{a} = \sqrt{\frac{8}{3}}$ and $\Gamma_1 = \Gamma_2$ (note that it has similarities in packing with a FCC structure). So it becomes $D_x = D_Z$. However, this is not true in most of the hexagonal structures, since in general, the ratio of lattice parameters deviates from the ideality. This will result in different jump frequencies also in

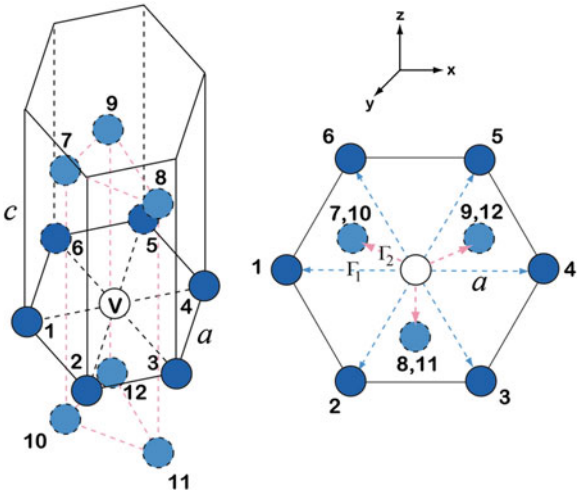

Fig. 5.30 Atomic arrangement and different jump frequencies are shown to explain anisotropy in diffusion in a hexagonal closed packed crystal structure

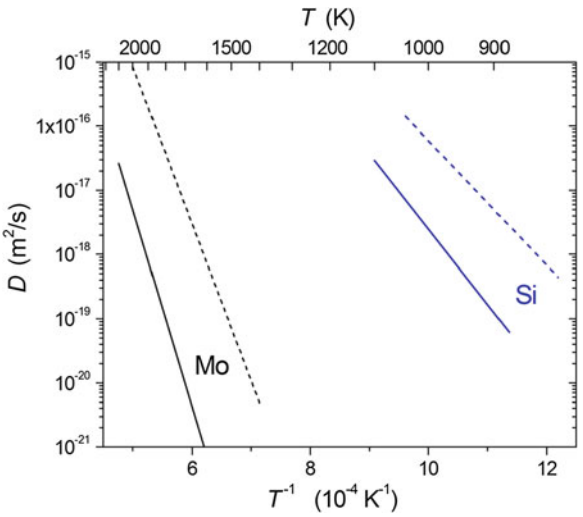

Fig. 5.31 Arrhenius plots of the diffusion coefficients of Mo (*black*) and Si (*blue*) in $MoSi_2$ perpendicular (*dashed lines*) and parallel (*solid lines*) to the tetragonal axis, after [33, 34]

different directions, and certain diffusion anisotropy is measured accordingly (see the experimental examples in Fig. 5.16).

In Sect. 5.2.5, the diffusion anisotropy for interstitial diffusion was documented. As it was stated, the ratio of diffusivities of interstitial atoms in different directions is generally not too large, within a factor of 2–3. On the other hand, the diffusion anisotropy for substitutional atoms can be very pronounced, especially if we consider intermetallic phases. For example, the diffusion anisotropy approaches three to four orders of magnitude for Mo diffusion in $MoSi_2$ and is about an order of magnitude for Si diffusion in $MoSi_2$ (Fig. 5.31). A pronounced anisotropy of Ti

self-diffusion in the $L1_0$-phase TiAl was reported, too. The reason for such huge diffusion anisotropy is the anisotropy of sublattices in the compounds (see general discussion in next sections).

5.3.7 *Effect of Phase Transitions on Substitutional Diffusion*

The effect of crystalline structure on diffusion rates of interstitially and substitutionally diffusing species is most prominent for the case of iron, as shown in Fig. 5.32. The $\alpha \rightarrow \gamma$ phase transition is accompanied by the lattice-type change from more open structure (bcc) to more dense one (fcc), and the diffusion rates drop indeed by orders of magnitude. It is very instructive to compare the diffusivities in δ-Fe and in paramagnetic α-Fe which both reveal the same bcc lattice—the diffusion rates follow almost the same Arrhenius line extrapolated through the γ-phase region, as shown in Fig. 5.32.

Furthermore, magnetic phase transition has a noticeable effect on diffusion of magnetic atoms, such as Fe and Co, as shown in Fig. 5.32. Whereas diffusion of Fe and Co follows linear Arrhenius-type dependencies in the paramagnetic state of α-Fe, it deviates strongly to lower diffusivities in the ferromagnetic state, below T_c in Fig. 5.32, due to additional stiffness of the lattice.

5.4 Diffusion Mechanisms in Intermetallics

So far, we have atomistically considered diffusion in pure metals. Certain complications arise in the case of alloys. We will limit our analysis of *atomistic diffusion mechanisms* by the case of binary AB alloys. Firstly, we will analyze substitutional diffusion in *disordered* binary alloys, and then, the case of *ordered* (intermetallic) AB phases will be considered. These two atomic arrangements are explained in Fig. 5.33a using a BCC lattice as an example.

In completely disordered AB alloy, the probability to find A or B atoms at any site is equal. This situation corresponds to Fig. 5.33a, and the atomic types are represented by gray spheres. The corresponding structure is called A2 one.

Alternatively, if the AB alloy is fully ordered on the BCC lattice, then one type of atoms (say, A) occupies cells corner positions, while other atoms (thus, B) reside at the cell center positions, as shown in Fig. 5.33b. Then, this structure is called as B2 one, and two sublattices—that of A atoms and that of B atoms each of them being a simple cubic lattice—can be introduced. The tendency for an alloy to be in ordered or disordered state is directly related to the corresponding interaction energies between different atomic sorts, i.e., the relationship between $2\varepsilon_{AB}$ and the sum $(\varepsilon_{AA} + \varepsilon_{BB})$ as discussed in Chaps. 1 and 2.

Self-diffusion in such alloys proceeds via migration of vacancies, and it is somehow different in ordered and disordered states.

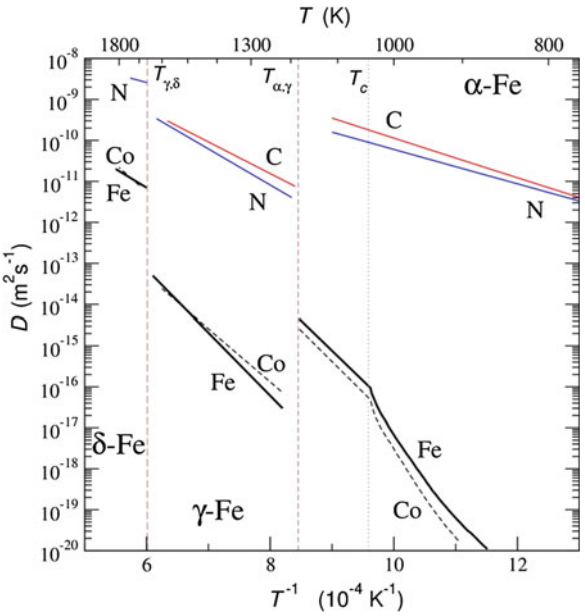

Fig. 5.32 Effect of crystalline structure and magnetic transition on diffusion rates of interstitially diffusing (C and N) and substitutionally diffusing (Fe and Co) species on the example of diffusion in iron

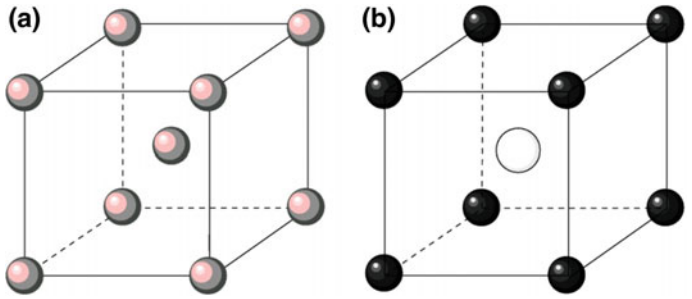

Fig. 5.33 Examples of atomic arrangements in binary AB alloy with disordered A2 (**a**) and ordered B2 (**b**) structures. The A and B atoms are sketched as *black* and *white spheres*. The *gray spheres* in the first figure represent site at which the probabilities to find either A or B atom are equal

5.4.1 Diffusion in Disordered Intermetallic Compounds

In this case, diffusion is mediated by jumps of vacancies, though the particular energy barriers depend on the kind of jumping atom and local environment of it. In a mean field approach, the effect of local environment can be neglected and one has to introduce just two jump frequencies for a vacancy: ω_A and ω_B.

A very useful (and exact as mean field approximation) approach was derived by Manning [35]. His treatment will be sketched here for a binary AB random alloy. The vacancy correlation factor, f_v, is represented as

$$f_v n_v = f_v^A n_A + f_v^B n_B \tag{5.84}$$

where f_v^A and f_v^B are the partial vacancy correlation factors, n_A and n_B are the number of vacancy jumps performed as exchange with the atoms of the sorts A and B, respectively, and n_v is the total number of vacancy jumps for the given time t. The key point of the Manning approach is the introduction of the escape frequency H defined as

$$H = f_v M_0 \omega_v \tag{5.85}$$

Here, ω_v is the average vacancy jump frequency, and M_0 is the function of the geometrical tracer correlation factor f_0 for the given lattice occupied by one sort of atoms,

$$M_0 = 2f_0(1 - f_0) \tag{5.86}$$

The tracer correlation factors of atoms A and B, f_A and f_B, respectively, one can use an expression, which is almost analogous to Eq. 5.54,

$$f_A = \frac{1 + t_A}{1 - t_A} \quad \text{and} \quad f_B = \frac{1 + t_B}{1 - t_B}$$

with $t_A = p_A^+ - p_A^-$ and $t_B = p_B^+ - p_B^-$, where p_A^+ (p_B^+) is the probability for A (B) atom to make the second jump in the same direction as that of the first jump and, correspondingly, p_A^- (p_B^-) is the probability for A (B) atom to make the second jump opposite to the direction of the first jump. Using the escape frequency H and the vacancy–atom exchange frequencies ω_A and ω_B introduced above, the tracer correlation factors can be represented as

$$f_A = \frac{H}{2\omega_A + H} \quad \text{and} \quad f_B = \frac{H}{2\omega_B + H}$$

Within Manning's theory, the tracer correlation factors are related to the partial vacancy correlation factors by the following expressions:

$$f_A = f_0 f_v^A \quad \text{and} \quad f_B = f_0 f_v^B$$

In the mean field approximation, the average vacancy exchange frequency is

$$\omega_v = c_A \omega_A + c_B \omega_B = c_A \omega_A + (1 - c_A)\omega_B \tag{5.87}$$

Here, the vacancy concentration is considered to be negligibly low.

5.4.2 Diffusion Mechanisms in Ordered Intermetallic Compounds

In this case, A and B atoms are not randomly distributed on the same crystalline lattice, as shown in Fig. 5.33b. As it was explained in Chap. 2, generally 4 types of basic substitutional defects can be introduced in ordered AB compound. We will illustrate this point for the B2 binary AB compound, as shown in Fig. 5.33b. We can introduce two sublattices, A and B sublattices, for the perfectly ordered stoichiometric compound, which would exclusively be occupied by A and B atoms, respectively. Since the chemical nature of A and B is considered to be different, it costs different energy to produce vacancy on A or B sublattice and these defects have to be differentiated, as shown in Fig. 5.34a and b.

Two further defects are the *antisite* or *antistructure* atoms when atoms of one sort occupy sites on the wrong sublattice, as shown in Fig. 5.34c, d. As detailed analysis in Chap. 2 has substantiated, the formation energies (as well as formation entropies and formation volumes) of all defects have not necessarily the same, and as a rule, they substantially deviate.

The ordered structure of intermetallic compounds imposes certain limitations on geometrically possible vacancy-mediated diffusion mechanisms. Below, the most important diffusion mechanisms are discussed.

5.4.3 Six-Jump Cycle Mechanism

Originally, this mechanism was proposed for B2 compounds [36], but later it was elaborated for others ordered structures, too. A scheme of this mechanism with a [110] net displacement of the vacancy is shown in Fig. 5.35. One starts with a vacancy on the A sublattice, and after 6 successive jumps, the vacancy exchanges its position with A atom along the face diagonal of the unit cell. During this cyclic movement, disorder in the phase AB increases first—from V_A to $V_B + B_A$ (jump 1), then to $V_A + B_A + A_B$ (jump 2), and finally to $V_B + 2B_A + A_B$ (jump 3)—and then, it is restored to the initial one, i.e., with the only A vacancy—from $V_B + 2B_A + A_B$ to $V_A + B_A + A_B$ (jump 4), then to $V_B + B_A$ (jump 5), and finally to V_A (jump 6).

Thus, as a result of 6 jumps, a vacancy accomplishes one and a half cycle and effectively jumps along the diagonal of the face, as shown in Fig. 5.35. It is clear that first jumps are related to an increase of the energy of the crystal since defects (antisite atoms) are produced. The situation after the 3rd jump represents a most disordered state: one vacancy and three antisite atoms left behind as a result of the first cycle. Following jumps will restore the order in the lattice, and exactly the same ordered state (single vacancy on the initial sublattice) is retained.

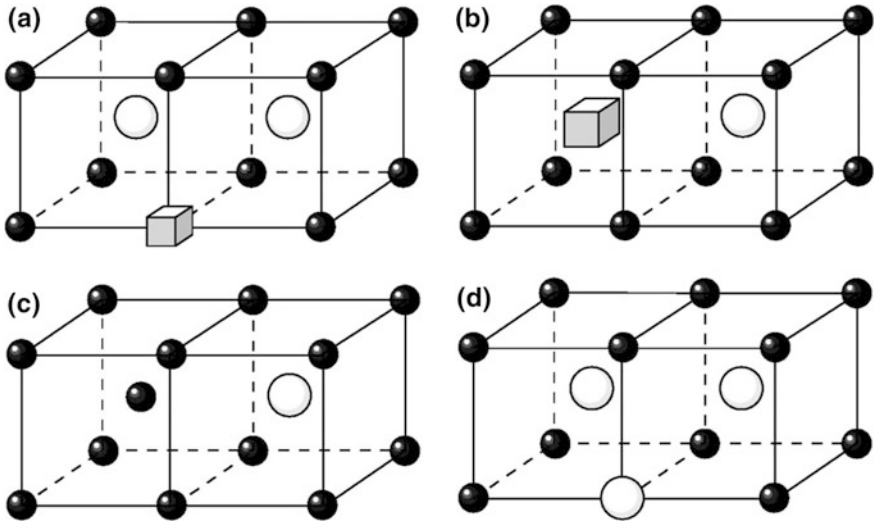

Fig. 5.34 Four types of substitutional defects in ordered AB compound with A and B atoms shown as *black* and *white spheres* and vacancy as a *cube*: vacancy on the **a** A and **b** B sublattices, **c** A atom on the B sublattice, and **d** B atom on the A sublattice

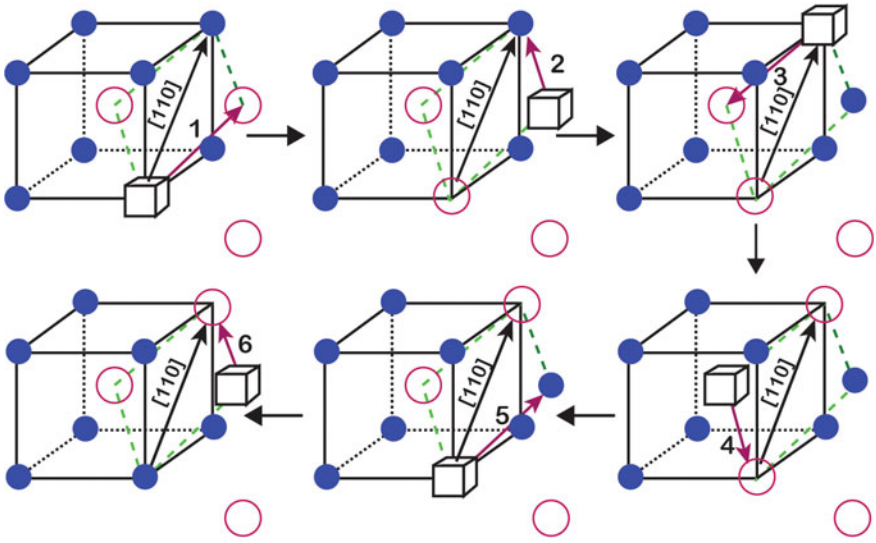

Fig. 5.35 The scheme of the six-jump cycle mechanism with a net [110] displacement of the vacancy V_A

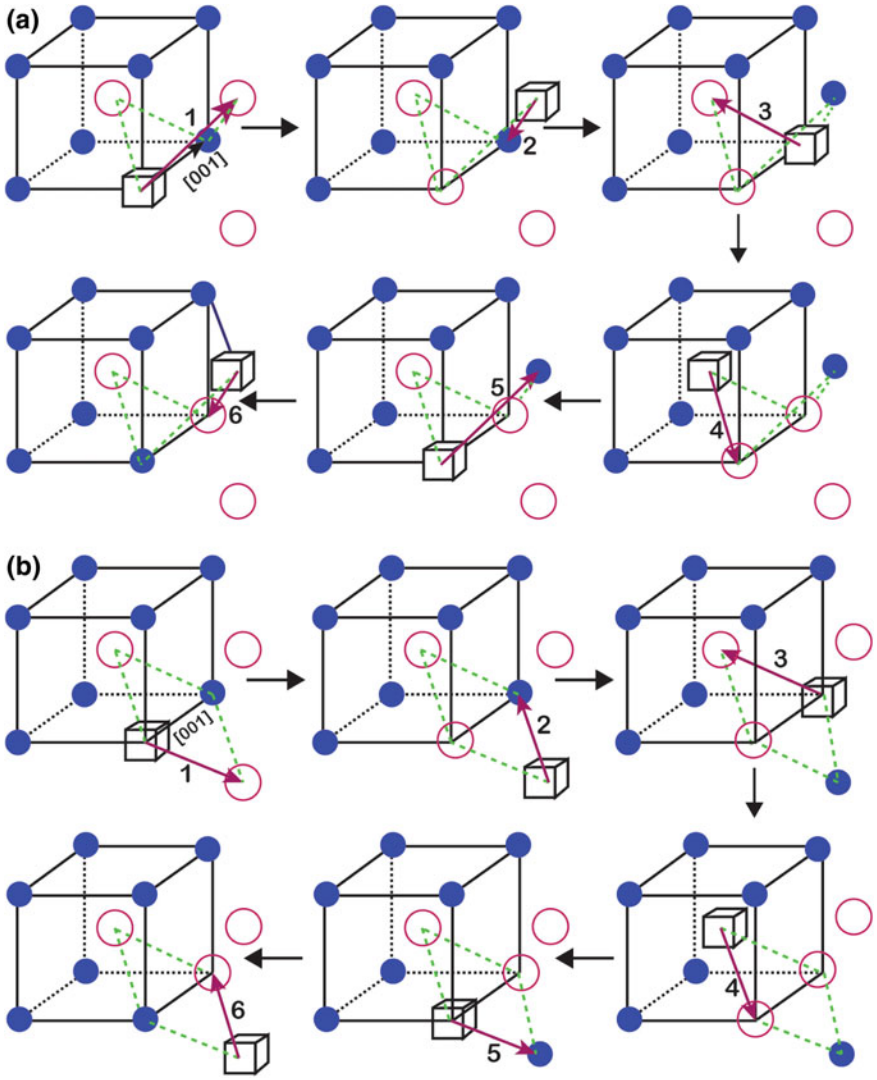

Fig. 5.36 Two variants of the six-jump cycle mechanism with the net [001] displacement of the vacancy—**a** bent and **b** flat cycles. As a result, the vacancy on A sublattice and A atom exchange their positions along the edge of the unit cell

One has to pay attention that two further types of cycles are possible in the B2 lattice, as shown in Fig. 5.36, corresponding to the [001] net displacement of the initial vacancy—the so-called bent (Fig. 5.36a) and flat (Fig. 5.36b) cycles.

It is important that the atoms do not necessarily move along the vectors drawn in Figs. 5.35 and 5.36, and the exact trajectories have to be determined via appropriate atomistic simulations. The vectors, as in each case of such schematic

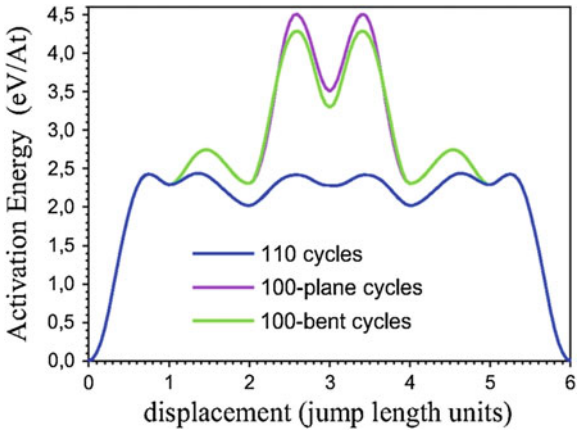

Fig. 5.37 The energy barriers corresponding to different six-jump cycles in the B2 structure of NiAl. The jump sequences were defined in Figs. 5.35 and 5.36, and the abscissa axis represents the distance along jump vectors defined for the whole cycle

representation, just connect the initial and final positions of the vacancy for a particular jump during accomplishing the whole cycle motion.

The energy barriers are not necessarily the same for all types of the cycles. An example of atomistic calculations (allowing relaxation after each jump) is presented in Fig. 5.37 for the case of B2-ordered NiAl (in Figs. 5.35, 5.36, the Ni atoms are A and Al atoms are B). One recognize, e.g., that the 110 cycles are most probable in this structure for NiAl. Further, the atomistic simulation with reliable inter-atomic potentials reveals that the first disordering jump of the vacancy involves typically the highest energy barrier. Subsequent jumps, requiring though a thermal activation, could bring system even to a configuration with a lower total energy with respect to the neighboring configurations, as shown in Fig. 5.37. Of course, the energy of the system is completely restored after the vacancy has accomplished the full sequence of six jumps.

A very important note is due here. Could the temperature dependence of diffusion according to such sophisticated jump sequence be described by a single Arrhenius-type dependence like Eq. 5.74? If yes, how is the activation barrier defined? Is this the highest barrier in the sequence? The numerical simulations give very important hints and predict that diffusion by such highly correlated jump sequence (in particular, for the six-jump cycles) can reasonably be described by an Arrhenius law, Eq. 5.74, and the migration energy can conveniently be represented by a sum of two contributions—the height of the first barrier and the activation energy corresponding to the correlation effects. This can qualitatively be exemplified in Fig. 5.37. According to such viewpoint, the energy barriers for all types of the six-jump cycles are exactly the same and correspond to the height of the first barrier. Still the [001]-type cycles involve very high barriers for the 3rd jumps, as shown in Fig. 5.37, so that the probability of a reverse jump in those sequences is significantly larger and the whole jump sequence will hardly be accomplished, especially at lower temperatures. As the temperature increases, the importance of the difference in the barrier heights decreases, since it is proportional to $\exp(-Q/kT)$, and such sequences

may occur. This strong temperature dependence of the probability of the accomplishment of the cycles corresponds to a large contribution to the effective activation energy. This conclusion is of general importance for diffusion mechanisms which include more than one jump of a defect. The present consideration highlights the importance of careful determination of the correlation effects for the diffusion mechanisms in ordered alloys.

The correlated jumps of the atomic species during accomplishing the cycles impose certain limitations on the quantities which can be measured in a diffusion experiment. Firstly, in a highly ordered state near the stoichiometric composition, the ratio of tracer diffusivities of both components, D_A/D_B, can adopt only the values within the interval

$$\frac{1}{q} \leq \frac{D_A}{D_B} \leq q \tag{5.88}$$

where q was calculated to be 2 [37] and was later corrected to $q \approx 2.034$ by including the correlation effects [38]. The ratio of diffusivities of Ag and Mg in β-AgMg, Zn and Au in β′-AuZn, and Cd and Au in β-AuCd falls into these limits, and this is typically considered as a strong support of the six-jump cycle mechanism in these compounds.

Diffusion by the six-jump cycles is a highly correlated process, as we have already seen. Thus, the correlation factor is supposed to be rather small. However, one should generally distinguish two types of correlations which characterize the six-jump cycles. Considering the individual *cycles* as effective vacancy jump *events* occurring with the given frequency, one can calculate the resulting correlation factors $\tilde{f}_A$ and $\tilde{f}_B$ [38]. For B2 NiAl, Monte Carlo calculations resulted in $\tilde{f}_{Ni} \approx 0.782$ and $\tilde{f}_{Al} \approx 0.860$. In contrast, the tracer correlation factors for Ni and Al atoms in that case were calculated to be $f_{Ni} \approx 0.445$ and $f_{Al} \approx 0.022$, respectively. We note that f_{Ni} is not as small as it was usually anticipated for the six-jump cycle mechanism. This fact should be taken into account when interpreting the results of, e.g., Mössbauer effect experiments, which allowed establishing the geometry of individual atomic jumps and, by comparing the local jump rates with the long-range diffusion data, estimating the corresponding correlation factor.

In [39], the isotope effect was measured for both Au and Zn in the B2-ordered β′-AuZn alloys, with E_{Au} (and correspondingly f_{Au}) being considerably larger than E_{Zn} (f_{Zn}) in Zn-rich alloys (e.g., $E_{Au} = 0.35$ and $E_{Zn} = 0.05$ in the Au-51.85 at.% Zn alloy). This fact resembles the relation between f_{Ni} and f_{Al} in B2-NiAl for the six-jump cycle mechanism [40] and can be explained by the predominant vacancy concentration in the Au sublattice and an increased probability of a reverse jump of a Zn atom which has initiated a six-jump cycle. One may argue that since both atom types in the B2 AB alloy participate in the same cycle, the pertinent correlation factors f_A and f_B have to be similar. However, this is generally not true, as the simulations of correlation effects during diffusion according to the six-jump cycle mechanism in NiAl have shown, and very different correlation factors for the

two components can be obtained. Thus, the large difference between f_A and f_B in an AB compound cannot be considered as an argument against the six-jump cycle mechanism.

The six-jump cycles are to be considered as a subset of a general n-jump cycle mechanism, since, e.g., 3-jump cycles were considered in the $L1_0$ structure of TiAl and 10-jump cycles were introduced to explain diffusion in quasicrystalline compounds. Moreover, higher n cycles can be introduced in the B2 structure, too (with $n = 10$, for example), by a simple inspection of the lattice. In this regard, the six-jump cycles represent simply the n-cycle mechanism with the lowest possible in the given structure number of n successive jumps of a single vacancy in *otherwise perfect* lattice (thus, $n = 3$ for $L1_0$, $n = 6$ for B2, $n = 6$ for $L1_2$, and $n = 10$ for Mackay icosahedrons, respectively, as basic tilling units of icosahedral quasicrystals, etc.).

There is one important point here. The six-jump cycle mechanism was considered for a perfectly ordered lattice containing one vacancy on a given sublattice. In this sense, it was analyzed for the stoichiometric composition of the AB alloy. However, there are basically no objections against the existence of such highly correlated jump sequences in off-stoichiometric AB compounds. As the composition of a given compound deviates from the stoichiometric one, a large amount of (constitutional) defects appear and mutual interaction between different defects has to be considered. If a vacancy performing a six-jump cycle meets an antistructure atom on a particular lattice, the limits in the previous equation are changed [41]. It was shown that q may become significantly larger that unity [41]. Thus, in a less ordered state, experimental values of D_A/D_B being larger than 2 can no longer be considered as an indication that the six-jump cycle mechanism does not operate. One may easily see that such six-jump cycle will be transformed to four-cycle mechanism in the B2 structure if vacancy and antisite atoms reside in different sublattices, as shown in Fig. 5.38. Further subtypes of the general n-jump cycle mechanism could formally be introduced. The sequences differ by activation energies, and the level of correlation of individual jumps and thus with different probabilities could be found by inspection of the results of real simulations using molecular dynamics.

5.4.4 Sublattice Diffusion Mechanism

When one of the components forms a lattice structure which enables the nearest neighbor jumps through the respective sublattice, random jumps of a vacancy on this sublattice will not affect the order in the compound. As an example, this mechanism is schematically presented in Fig. 5.39 for the $L1_2$ structure. It is important that this mechanism can dominate diffusion not only of the majority component, but also of the minority component. In such a case, a minority atom jumps into the "wrong" sublattice and continues its migration through this sublattice. The sublattice diffusion mechanism was extensively analyzed in [42, 43].

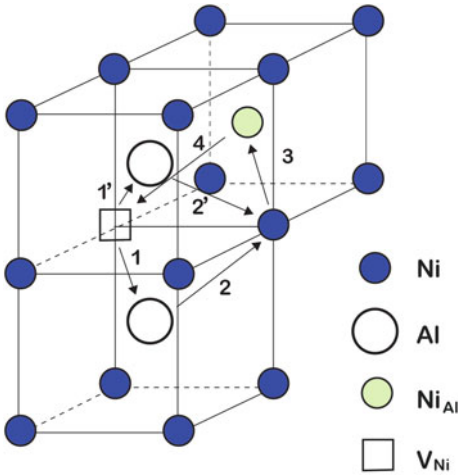

Fig. 5.38 A scheme of 4-jump cycles for the B2 structure. The flat (1–2–3–4) and bent (1′–2′–3–4) cycles are shown. These jump sequences are flowed starting from a vacancy on Ni sublattice (*square*) as a nearest neighbor of a Ni antisite atom, Ni_{Al} (*the shaded circle*). The vacancy first can exchange its position with Al atom occupying the next nearest neighbor position to Ni_{Al} (the jump of type 1′) or Al atom from 4th coordination shell of Ni_{Al} (the jump of type 1). The jumps 2′ or 2 correspond to the most disordered states with two Ni_{Al} and one Al_{Ni} (and a Ni vacancy, of course). The jumps 3 and 4 restore the initial order in the compound

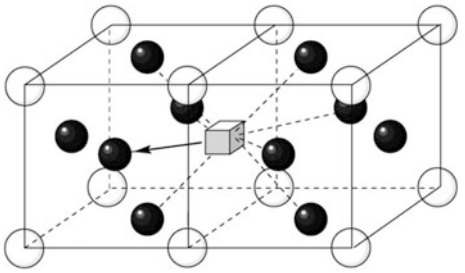

Fig. 5.39 A scheme of sublattice diffusion mechanism for the case of A_3B compound. Here, A and B atoms are represented by *dark* and *bright spheres*, respectively. Eight possible directions of nearest neighbor jumps of a B vacancy are shown by *dashed lines*

It is obvious that the diffusivities of both components are not coupled by a relation similar to Eq. 5.88, if the sublattice diffusion mechanism operates.

The correlation factors for the sublattice diffusion mechanism in the $L1_2$ structure of Ni_3Al are different for diffusion of the majority (i.e., Ni) and minority (i.e., Al) components. The calculations as outlined above provide that $f_{Ni} = 0.689$. The determination of f_{Al} is more intricate, and e.g., a five-frequency model has to be invoked (see Fig. 5.40).

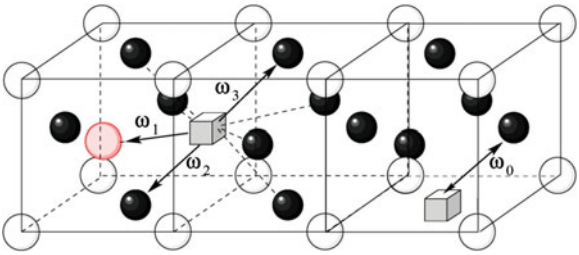

Fig. 5.40 The jump frequencies for a Ni vacancy (*cube*) neighboring an Al antisite atom (*red sphere*). The five frequencies ω_0–ω_4 for a vacancy on the Ni sublattice are indicated: ω_0 is the frequency of Ni vacancy jumps away from the Al antisite atom; ω_1 is the frequency of direct exchange with the Al antisite; ω_2 is the jump frequency between neighboring positions of the Al antisite; ω_3 is the frequency of vacancy jump from first neighbor position of the Al antisite to a more distant neighbor; and ω_4 is the frequency of the reverse jump to ω_3

The somewhat lengthy calculations demonstrate that the Al correlation factor can be expressed in a usual way via the vacancy—Al atom exchange frequency ω_2 and the vacancy escape frequency H:

$$f_{\mathrm{Al}} = \frac{H}{\omega_2 + H} \quad \text{and} \quad H = \frac{10\omega_3 F^z(2\omega_1 + 5\omega_3 F^x)}{2\omega_1 + 5\omega_3(F^z + F^x)}$$

Here, F^x and F^z are functions of ω_4/ω_0, and they are changed in the range of 0.2–1, if ω_4/ω_0 increases from 0 to ∞.

5.4.5 Triple-Defect Diffusion Mechanism

This mechanism was originally proposed by Bakker and Stolwijk for the B2 compound CoGa [44]. It specifies the migration of a triple defect, which represents a bounded entity composed of two transition metal vacancies and one transition metal atom in an antistructural position. The triple-defect mechanism in CoGa was described to correspond to the two nearest neighbor jumps of a Co atom and one next nearest neighbor jump of a Ga atom. In Fig. 5.41, the triple-defect mechanism is shown for the case of the B2-NiAl compound. As a result of the indicated sequence of jumps, the triple defect moves leaving the order in the compound unchanged.

Since a correlated sequence of atomic jumps is involved, the diffusivities of both components in the perfectly ordered state are coupled by Eq. 5.88 with $q = 13.3$.

The correlation factors are supposed to be small for the triple-defect diffusion mechanism. They were calculated for B2-NiAl and $f_{\mathrm{Ni}} \approx 0.05$ at $T = 1{,}300$ K in Ref. [45] using a Monte Carlo method (Fig. 5.42). f_{Ni} depends remarkably on temperature, and the contribution of this temperature dependence to the overall

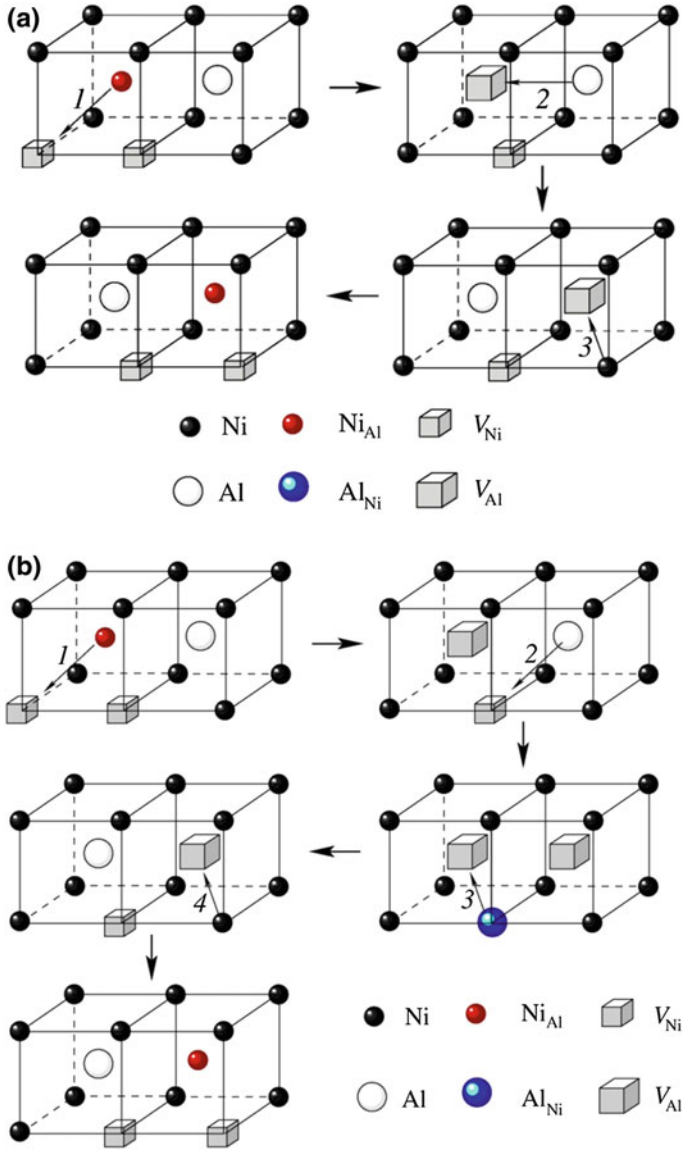

Fig. 5.41 A scheme of the triple-defect mechanism as it can occur in the B2 compound NiAl—either via a sequence of **a** three or **b** four atomic jumps. In the first case, atoms of one kinds, most probably of Al, perform a next nearest neighbor jump within own sublattice to temporary Al vacancy, the jump 2 in (**a**)

activation enthalpy of Ni diffusion by the triple-defect mechanism amounts to 17 kJ/mol. This fact has to be taken into account in interpreting activation enthalpy of diffusion in ordered compounds.

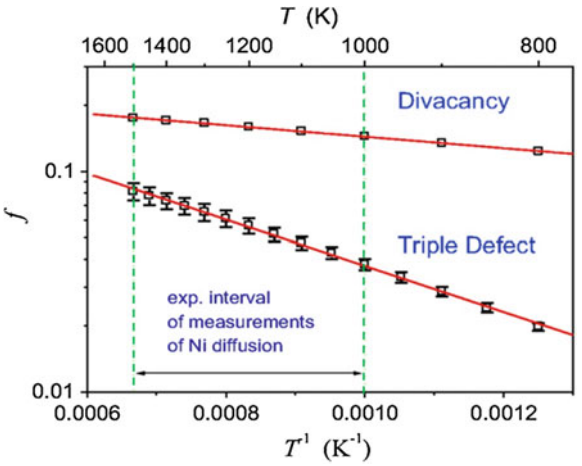

Fig. 5.42 Temperature dependence of correlation factors of Ni diffusion in the B2-phase NiAl determined for triple-defect and divacancy diffusion mechanisms. The divacancy mechanism here is referred to a mechanism of diffusion via a pair of Ni vacancies

5.4.6 Antistructure Bridge Mechanism

This mechanism was originally proposed by Kao and Chang [46] for the B2 structure and was later extended also to $L1_2$ structures [47]. The antistructure bridge (ASB) mechanism is schematically presented in Fig. 5.43a. As a result of the two indicated jumps, the vacancy and the antistructure atom effectively exchange their positions. Since the vacancy can in fact jump up to the 4th or 5th coordination shell from its initial position (depending on the lattice structure), the resulting large geometrical factor of the ASB mechanism increases its contribution to the diffusivity.

It is important to note that the contribution of this mechanism has a percolation nature in the sense that long-range diffusion by the ASB mechanism will occur only if the concentration of the antistructure atoms will be sufficiently high. A relatively high critical concentration for a B2 structure was initially estimated from purely geometrical arguments. The Monte Carlo simulation of this process resulted, however, in a smaller value of the percolation threshold, about 5 %. Such an antistructure atom concentration can indeed exist in intermetallics, and the ASB mechanism becomes important for explaining the observed diffusion behavior in Ni aluminides [45, 48].

In the $L1_0$ structure of the phase TiAl, other types of the ASB mechanism are of prime importance. One of such variant is presented in Fig. 5.43b. After the indicated two jumps (1 + 2), the A vacancy moved perpendicular to the A atom layers using an antistructure A atom as a "bridge." If a further antistructure atom in a suitable nearest neighbor position is available for the vacancy after its second jump, the next ASB sequence may start, as it is indicated in Fig. 5.43b. The Monte Carlo calculation of the percolation threshold for the long-range diffusion by this variant of the ASB mechanism yields about 11 % of the antistructure atoms as the critical concentration.

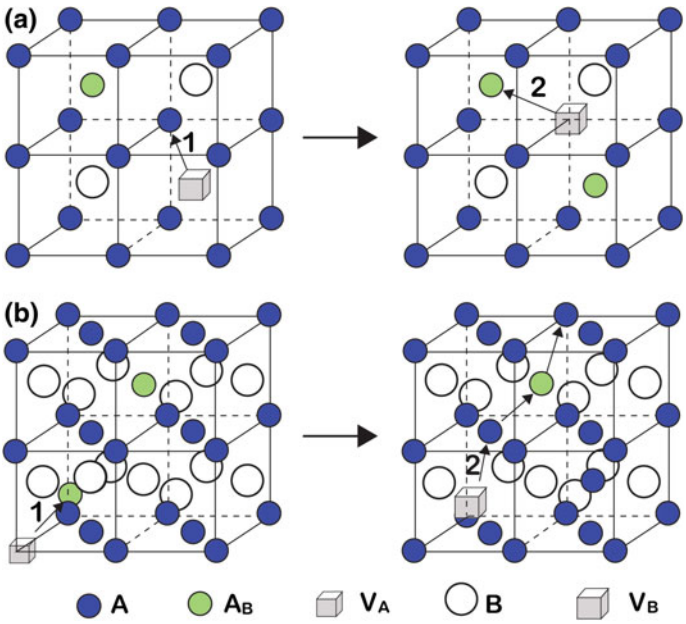

Fig. 5.43 The antistructure bridge mechanism as it can be found in B2 (**a**) and $L1_0$ (**b**) compounds

During the ASB sequence of jumps, only one sort of atoms moves (see Fig. 5.43). Therefore, the diffusivities of the two components are not coupled.

In a strict sense, the genuine ASB mechanism operates only after the percolation threshold is reached. However, in combination with another mechanism (usually the sublattice diffusion mechanism), the ASB mechanism (e.g., jump sequence 1 → 2 in Fig. 5.8b) can substantially contribute already to long-range diffusion without any percolation threshold. One can therefore use the term "ASB mechanism" also in such cases, referring to the specific sequence presented in Fig. 5.43a, b.

5.4.7 Interstitial Diffusion Mechanism

Small metallic atoms could diffuse interstitially in a matrix of a given intermetallic compound. In Fig. 5.44, the solute diffusion of Fe and Ni in pure α-Ti, α_2-Ti_3Al, and in γ-TiAl is presented in comparison with Ti self-diffusion in these materials as a function of the reduced temperature T_m/T. Here, T_m is the melting point of pure Ti or the intermetallic alloys of the stoichiometric composition. Figure 5.44 substantiates that both Fe and Ni are fast diffusers in α-Ti or in α_2-Ti_3Al, [49, 50], while they are "normal" diffusers in γ-TiAl.

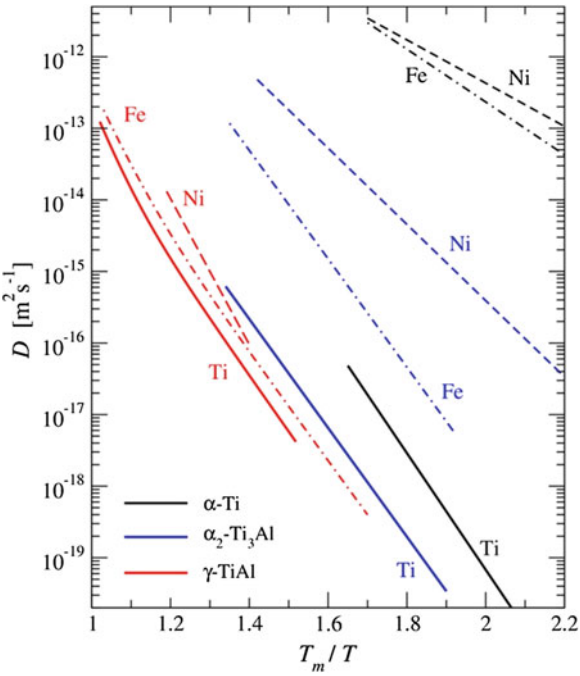

Fig. 5.44 Diffusion rates of Fe and Ni in α-Ti, α_2-Ti_3Al, and γ-TiAl in comparison with the corresponding self-diffusivities of Ti plotted again normalized temperature T_m/T. Here, T_m is the melting point of the corresponding material

This fact correlates with the local arrangements of the atoms which form the octahedral sites for the interstitial diffusion in these compounds, as shown in Fig. 5.45.

The high solubility of nonmetallic interstitial solutes in α_2-Ti_3Al could be attributed to the existence of those octahedral positions in this compound which are exclusively formed by Ti atoms [51]. Unlike pure α-Ti, α_2-Ti_3Al has additional octahedral sites formed by two Al atoms and four Ti atoms, as shown in Fig. 5.45. This fact explains a lower Fe and Ni interstitial solubility and thus a lower diffusivity (in terms of the dissociative mechanism) in α_2-Ti_3Al with respect to α-Ti, since the "mixed" octahedral sites are obviously not energetically favorable for interstitial occupancy. As the inspection of the structure of γ-TiAl shows, only "mixed" octahedral sites exist in this compound. This is most probably the reason why small metallic elements (e.g., Fe and Ni) form only substitutional solutions in TiAl and therefore show "normal" vacancy-mediated diffusion behavior in this compound, as shown in Fig. 5.44.

5.4.8 Other Diffusion Mechanisms

Several other mechanisms, which may be relevant in some specific cases, were proposed for ordered intermetallic compounds. The next nearest neighbor jump

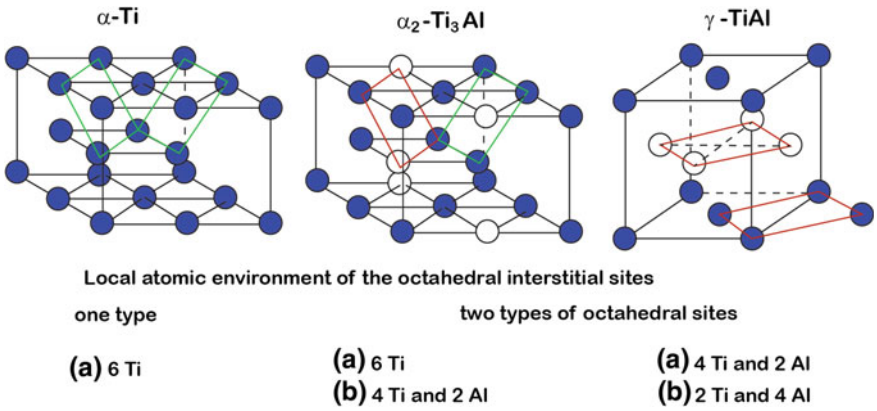

Fig. 5.45 Local atomic environments of octahedral interstitial sites in α-Ti, α_2-Ti_3Al, and γ-TiAl

mechanism may correspond to the lowest activation energy of single Ni vacancy migration in Al-rich NiAl. Also, a divacancy mechanism, with both vacancies belonging to the same sublattice in NiAl, may be suggested. After the given sequence of four atomic jumps, the initial order is completely restored and the divacancy has moved by one step.

5.5 Correlation Factors of Diffusion in Intermetallic Compounds

The calculation of the correlation factors for simple lattices was outlines in Sect. 5.3.3. In ordered intermetallic compounds, the procedure is somehow modified, since the geometry of sublattices and specific diffusion mechanisms have to be taken into account, and it will be presented in this subchapter using $MoSi_2$ as an example. We will limit us for Si diffusion in $MoSi_2$, for which the diffusion mechanism is considered as well established [52]. We will follow the analysis considered in detail in [53].

Generally, diffusion is described by a symmetric diffusivity tensor of rank 2. For a tetragonal crystal like $MoSi_2$, this tensor has two principal components. Diffusion is fully described by the diffusivities along the tetragonal axis, $D_{\|}$, and perpendicular to it, $D_{\perp}$. Denoting the frequencies of type-1 and type-2 jumps as ω_1 and ω_2, respectively (see Fig. 5.46), the tracer diffusivities can be written as

$$D_{\|} = \frac{1}{2}\left(\frac{c}{3}\right)^2 \left(\omega_1 f_{1_{\|}} + \omega_2 f_{2_{\|}}\right) C_V^{eq} = \frac{1}{2}\left(\frac{c}{3}\right)^2 (\omega_1 + \omega_2) f_{\|} C_V^{eq} \tag{5.89}$$

and

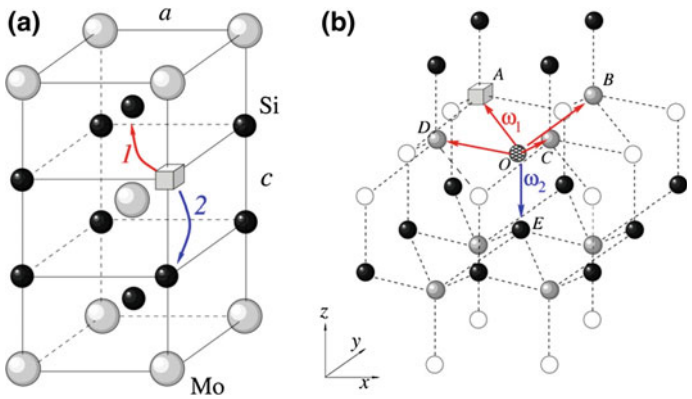

Fig. 5.46 **a** Lattice structure of $MoSi_2$ and **b** the structure of the Si sublattice. The two types of Si vacancy jumps are shown

$$D_{\perp} = \frac{1}{2} a^2 \omega_1 f_{1_{\perp}} C_V^{eq} \tag{5.90}$$

Here, C_V^{eq} is the vacancy concentration on the Si sublattice in thermal equilibrium. $f_{1_{\perp}}$ is the partial correlation factor for diffusion perpendicular to the tetragonal axis. Since type-2 jumps do not contribute to diffusion perpendicular to the tetragonal axis, the partial correlation factor coincides with the total correlation factor in this direction, i.e., $f_{1_{\perp}} = f_{\perp} \cdot f_{1_{||}}$ and $f_{2_{||}}$ are the partial correlation factors for diffusion parallel to the tetragonal axis related to the jump types 1 and 2, respectively. $f_{||}$ is the total correlation factor related to diffusion in this direction. It can be expressed in terms of the partial correlation factors as

$$f_{||} = \frac{\omega_1 f_{1_{||}} + \omega_2 f_{2_{||}}}{\omega_1 + \omega_2} = \frac{f_{1_{||}} + \frac{\omega_2}{\omega_1} f_{2_{||}}}{1 + \frac{\omega_2}{\omega_1}} \tag{5.91}$$

Partial and total correlation factors are functions of the frequency ratio ω_2/ω_1. The anisotropy ratio of diffusion

$$\frac{D_{\perp}}{D_{||}} = \frac{a^2 \omega_1 f_{1_{\perp}}}{\left(\frac{c}{3}\right)^2 \left(\omega_1 f_{1_{||}} + \omega_2 f_{2_{||}}\right)} = \frac{a^2 f_{1_{\perp}}}{\left(\frac{c}{3}\right)^2 \left(f_{1_{||}} + \frac{\omega_2}{\omega_1} f_{2_{||}}\right)} \tag{5.92}$$

is fully described by the correlation factors and is a function of the frequency ratio as well. The strong anisotropy of both Mo and Si diffusion in $MoSi_2$ is documented in Fig. 5.30.

In order to calculate the partial correlation factors f_i, one cannot take advantage of the inversion symmetry, because the Si sublattice sites are not inversion centers, as shown in Fig. 5.46. Moreover, there is no twofold or threefold symmetry around

the direction of the type-1 jumps. We suggest combining Howard's matrix method [10] and a Monte Carlo approach to calculate the correlation factors, as it was described above.

Both types of jumps contribute to diffusion parallel to the tetragonal axis, as shown in Fig. 5.46. Hence, the relevant partial correlation factors can be determined as

$$\mathbf{f}_{||} = \mathbf{I} + 2\mathbf{Z} \cdot \mathbf{T}(\mathbf{E} - \mathbf{T})^{-1} \cdot \mathbf{d} \tag{5.93}$$

where $\mathbf{f}_{||} = (f_{1_{||}}, f_{2_{||}})$ is the column vector of the partial correlation factors, $\mathbf{I}$ the 2-component unit column vector, $\mathbf{E}$ the 2×2 unit matrix, $\mathbf{d} = (|z_1|, |z_2|)$ the column vector of the jump distances $|z_1| = c/6$ and $|z_2| = c/3$ of type-1 and type-2 jumps, $\mathbf{Z} = \begin{Vmatrix} |z_1^{-1}| & 0 \\ 0 & |z_2^{-1}| \end{Vmatrix}$, respectively. $\mathbf{T}$ is a 2×2 matrix with the elements

$$t_{ij} = P_{ij}^{+} - P_{ij}^{-}, \quad i,j = 1,2. \tag{5.94}$$

Here, $P_{ij}^{\pm}$ is the probability that a tracer jump of type i is immediately followed by a tracer jump of type j in the same (+) or opposite (−) direction along the tetragonal axis.

Since only type-1 jumps contribute to diffusion perpendicular to the tetragonal axis (Fig. 5.46), Eq. 5.44 can be simplified, and the relevant correlation factor $f_{\perp}$ can be written as

$$f_{\perp} = \frac{1+t}{1-t} \tag{5.95}$$

with

$$t = P^{+} - P^{-} \tag{5.96}$$

Here, $P^{\pm}$ is the probability that a type-1 jump is immediately followed by a type-1 tracer jump with the same (+) or opposite (−) displacement perpendicular to the tetragonal axis.

5.5.1 Calculation of the Probabilities P

The probabilities $P_{ij}^{\pm}$ and $P^{\pm}$ introduced above have to be determined in order to calculate the correlation factors. Let us start with diffusion along the tetragonal axis. Diffusion perpendicular to the axis is simpler and will be considered afterward.

Figure 5.46b shows the situation immediately after a tracer atom jump of the type 1. The tracer atom is at the site O, whereas the vacancy occupies the neighboring site A after this jump. It is obvious that if the next jump of the tracer is a type-2 jump, the sign of its displacement with respect to the tetragonal axis will be the same as that of the first jump (both jumps displace the tracer atom in the negative direction of the z-axis). Alternatively, if the next jump of the tracer is a type-1 jump (leading to one of the lattice points A, B, C, or D in Fig. 5.46b), the sign of its z component will definitely be opposite to the sign of the z component of the first jump. Therefore, the probabilities are $P_{11}^{+} = 0$, $P_{11}^{-} \neq 0$, $P_{12}^{+} \neq 0$, and $P_{12}^{-} = 0$, and the corresponding matrix elements reduce to $t_{11} = -P_{11}^{-}$ and $t_{12} = P_{12}^{+}$. Considering the situation prevailing just after a tracer jump of type 2, we arrive at the relationships $P_{21}^{+} \neq 0$, $P_{21}^{-} = 0$, $P_{22}^{+} = 0$, and $P_{22}^{-} \neq 0$, and thus $t_{21} = P_{21}^{+}$ and $t_{22} = -P_{22}^{-}$.

Let us suppose that the tracer atom has just performed a jump of type 1. We need to know the probabilities P_{11}^{-} and P_{12}^{+} that the next jump of the tracer atom will be of type 1 or 2, respectively. These two sequential tracer jumps can generally be mediated by the same vacancy or by two different vacancies. As a usual approximation in the encounter model, the vacancy concentration is considered as very small, and thus, a tracer encounter with a next vacancy occurs only after the first encounter has totally been completed (e.g., when the first vacancy has escaped from the tracer atom). Therefore, the individual encounters are well separated in time, and a new vacancy does not disturb the correlations induced by a previous vacancy. In this case, the correlation factors do not depend on the vacancy concentration.

If taking into account that the two successive tracer jumps can generally be induced by the same or by different vacancies, two different contributions to the total probabilities $P_{ij}^{\pm}$ are expected: firstly, a contribution from the encounter with the same vacancy and secondly, a contribution from sequential encounters with the old and the new vacancy. In the latter case, the tracer jump of type i has occurred as a last event of the encounter with the old vacancy (and the vacancy has then escaped from the tracer atom), and the next tracer jump of type j has been induced by a new vacancy through its first exchange with the tracer atom. The second contribution to $P_{ij}^{\pm}$ is important for the $MoSi_2$ structure. This is in contrast to lattice structures with inversion symmetry, where the fresh vacancies equally contribute to both P_{ij}^{+} and P_{ij}^{-}. Hence, they do not affect the resulting correlation factors, which depend only on the differences $t_{ij} = P_{ij}^{+} - P_{ij}^{-}$. However, in the case of a lattice structure, in which the site positions are not inversion centers (this is the case of the Si sublattice of $MoSi_2$), the fresh vacancies may give different contributions to P_{ij}^{+} and P_{ij}^{-}. To illustrate this problem, let us consider the following situation: Suppose a first vacancy has induced a tracer jump of type 1 and has been escaped. After some time, a fresh vacancy will approach the tracer atom from a totally random direction and will induce the next tracer jump. If this next tracer jump is of type 1, it will definitely be in the opposite direction to the first jump of

type 1 with respect to the tetragonal axis. This fact increases the total probability P_{11}^{-}, but, by no means, it changes the value of P_{11}^{+}, which remains zero. Therefore, the total probability P_{11}^{-} must be known to calculate t_{11} and finally to compute the correlation factors.

At first, let us consider the contribution of an encounter of the tracer atom with the same vacancy to $P_{1j}^{\pm}$, $j = 1, 2$. Since the vacancy performs a random walk, it can either induce tracer jumps of type 1 or 2, or escape without inducing any further jump of the tracer atom. Let us denote the probability for the latter event by P_{e_1}, the escape probability after a type-1 jump. Furthermore, we denote the probabilities that the same vacancy induces a type-1 or type-2 jump during its random walk, which follows the initial site exchange with the tracer atom, by $\tilde{P}_{11}^{-}$ and $\tilde{P}_{12}^{+}$, respectively. The sum of all probabilities for the path of a particular vacancy equals unity:

$$\tilde{P}_{11}^{-} + \tilde{P}_{12}^{+} + P_{e_1} = 1 \tag{5.97}$$

A similar relationship holds for the vacancy random walk when the first site exchange resulted in a type-2 jump:

$$\tilde{P}_{21}^{+} + \tilde{P}_{22}^{-} + P_{e_2} = 1 \tag{5.98}$$

The quantities $\tilde{P}_{ij}^{\pm}$ describe the probabilities of sequential jumps of types i and j of a tracer atom caused by *the same vacancy*. In contrast, the $P_{ij}^{\pm}$ denotes the *total* probabilities of sequential jumps of types i and j of the tracer atoms, irrespective of which vacancy has induced these jumps. As explained above, in order to calculate $P_{ij}^{\pm}$, we have to add to $\tilde{P}_{ij}^{\pm}$ the probability that a "fresh" vacancy induces the jump j at its first site exchange with the tracer atom, provided that the "old" vacancy has escaped from the system (remember that this "old" vacancy has previously induced the jump i), i.e.,

$$P_{ij}^{\pm} = \tilde{P}_{ij}^{\pm} + P_{e_i}\tilde{P}_j \tag{5.99}$$

Here, $\tilde{P}_j$ is the probability that a vacancy arriving from an arbitrary lattice position of the Si sublattice at a nearest neighbor position of site O induces the jump j of the tracer atom at its very first site exchange. We have $\tilde{P}_1 + \tilde{P}_2 = 1$, because the "fresh" vacancy can induce either a type-1 or type-2 jump of the tracer atom.

In the absence of driving forces, the flux of fresh vacancies, which induce the jump j at the first site exchange with the tracer atom, is the same as the reverse flux of vacancies escaping after an inverse jump $-j$ without inducing any further jump of the tracer atom, namely $\omega_j P_{e_{-j}} C_V$. On the Si sublattice, a vacancy can induce four jumps of type 1 and one jump of type 2. In view of the lattice symmetry, the escape probabilities for jumps j and $-j$ are equal ($j = 1, 2$). Furthermore, in

thermal equilibrium, the probability to find a vacancy on any site of the Si sublattice is the same. Therefore,

$$\tilde{P}_1 = \frac{4\omega_1 P_{e_1}}{4\omega_1 P_{e_1} + \omega_2 P_{e_2}} \tag{5.100}$$

and

$$\tilde{P}_2 = \frac{\omega_2 P_{e_2}}{4\omega_1 P_{e_1} + \omega_2 P_{e_2}} \tag{5.101}$$

Combining the above equations, the final expression for $P_{ij}^{\pm}$ becomes

$$P_{ij}^{\pm} = \tilde{P}_{ij}^{\pm} + P_{e_j} \frac{n_j \omega_j P_{e_j}}{4\omega_1 P_{e_1} + \omega_2 P_{e_2}}, \quad i,j = 1,2. \tag{5.102}$$

Here, $n_1 = 4$ and $n_2 = 1$ are the numbers of jumps of the corresponding type.

In the case of diffusion perpendicular to the tetragonal axis, only type-1 jumps must be taken into account. Then, one can simply calculate $P^{\pm}$ as

$$P^{\pm} = \tilde{P}^{\pm} \tag{5.103}$$

Here, $\tilde{P}^{\pm}$ is the probability that during a random walk of the given vacancy, the second jump of the tracer atom will occur in the same (+) or opposite (−) direction with respect to the first jump. Due to the symmetry of the structure in the plane perpendicular to the tetragonal axis and in contrast to the previous case of diffusion along the tetragonal axis, the fresh vacancies give equal contributions to both P^{+} and P^{-}. Thus, Eq. 5.95 is not affected by such vacancies, since only the difference $t = P^{+} - P^{-}$ is important in the calculation of the correlation factor $f_{\perp}$.

5.5.2 The Monte Carlo Calculation Scheme

A Monte Carlo approach can be applied to calculate $\tilde{P}_{ij}^{\pm}$ and P_{e_i}, and the structure of Eq. 5.101 suggests the calculation scheme. At first, a tracer atom and a vacancy are placed at the positions O and A on the Si sublattice (Fig. 5.46b). This corresponds to the atomic configuration after a type-1 jump. Then, the random walk of the vacancy is initiated and followed in the computer until the vacancy either escapes (see below) or induces a jump of type j of the tracer atom ($j = 1, 2$). By performing the Monte Carlo runs many times, the probabilities $\tilde{P}_{11}^{-}$, $\tilde{P}_{12}^{+}$, and P_{e_1} are thus determined. Similarly, by simulating the atomic configuration after a type-2 jump and following the random walk of the vacancy, the probabilities $\tilde{P}_{21}^{-}$, $\tilde{P}_{22}^{+}$, and P_{e_2} are determined. From Eq. 5.101, the probabilities $P_{ij}^{\pm}$ are then calculated

using the probabilities $\tilde{P}_{ij}^{\pm}$ and P_{e_i} $(i, j = 1, 2)$ obtained from the Monte Carlo simulation.

The probabilities $\tilde{P}^{\pm}$ are calculated in a similar manner: An atomic configuration after the tracer jump of type 1 is modeled, and the following random walk of the vacancy is considered until it either induces a tracer jump or escapes from the tracer atom. The events resulting in the type-1 jump (with a nonzero displacement perpendicular to the tetragonal axis) are counted, and their probability is determined by appropriate averaging. In view of Eq. 5.102, neither is it necessary to determine the probability that the vacancy escapes nor that it induces a jump of type 2 (with zero displacement perpendicular to the tetragonal axis). The probabilities $\tilde{P}^{\pm}$ can be inserted in Eq. 5.93 instead of the total probabilities $P^{\pm}$, and the relevant correlation factor $f_{\perp}$ can be determined.

In the simulation, the initial vacancy and a tracer atom were introduced into the center of the simulation block. If the vacancy reaches the external boundary of the simulation block in the course of its random walk, we consider it as escaped from the tracer atom. The particular values of $P_{ij}^{\pm}$ and P_{e_i} turned out to depend on the size of the simulation block. However, their combination in Eq. 5.101 approaches a constant value when the size of the simulation block is increased.

The random walk of a vacancy is simulated in a standard manner. On any lattice site, the vacancy can perform either one out of 4 possible jumps of type 1 or one jump of type 2. The corresponding probabilities are $\omega_1/(4\omega_1 + \omega_2)$ and $\omega_2/(4\omega_1 + \omega_2)$, respectively. Since the absolute diffusivities are not addressed here, the frequency ratio ω_2/ω_1 is the only crucial parameter.

All probabilities depend only on this ratio. By using an appropriate random number generator, for each Monte Carlo step, the direction of the vacancy jump is chosen in agreement with the above-mentioned probabilities for the given value of the ratio ω_2/ω_1. The position of the vacancy is then updated, and the next jump direction is selected. Thus, in each Monte Carlo step, the vacancy definitely performs one jump onto a neighbor site, and the probability of the given jump depends on the frequency ratio ω_2/ω_1. The frequency ratio ω_2/ω_1 was changed in the simulations in the wide range from 10^{-5} to 10^{5}.

In the particular calculations, a simulation block of $80 \times 80 \times 80$ unit cells was found to give satisfactory results (the unit cell for the $MoSi_2$ structure is shown in Fig. 5.46a). The random walk of a vacancy was followed until either the vacancy induces a jump of type j of the tracer atom or the vacancy reaches the outer surface of the simulation block. This procedure was repeated for 10^5 to 10^7 times, and the probabilities $\tilde{P}_{ij}^{\pm}$ and P_{e_i} were estimated from suitable averages of the individual Monte Carlo runs. Then, the partial correlation factors were calculated for the chosen ratios of the frequencies ω_2/ω_1.

One comment about the calculation of the probabilities $P^{\pm}$ may be added. Diffusion perpendicular to the tetragonal axis is mediated exclusively by type-1 jumps. Consideration of type-1 jumps solely would correspond to a two-dimensional random walk within a Si bilayer of the $MoSi_2$ structure. *The escape probability in a random walk on a two-dimensional lattice is exactly zero.*

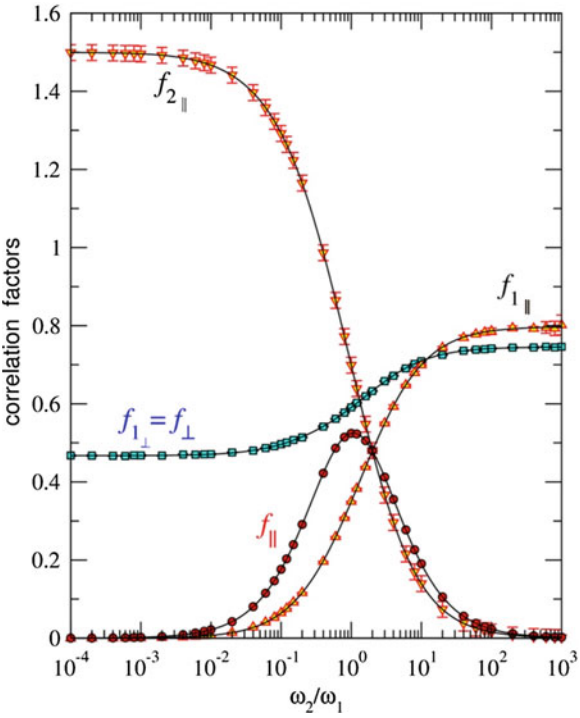

Fig. 5.47 The correlation factors of Si diffusion on the Si sublattice of $MoSi_2$ as a function of the frequency ratio ω_2/ω_1. The *error bars* represent the standard deviations from the mean values. The *solid lines* correspond to Eq. 5.104

However, since in the Si sublattice, type-2 jumps also occur with a probability depending on the ratio ω_2/ω_1, the vacancy can still escape from the tracer atom and randomize. If the ratio ω_2/ω_1 is very small, the vacancy will very rarely jump to another Si bilayer in the MoSi2 structure during the simulation run. However, after a sufficiently large number of jumps, the vacancy will almost have lost its "memory" of the position of the tracer atom and can be considered as "randomized."

The calculated partial and total correlation factors are presented in Fig. 5.47 as functions of the frequency ratio ω_2/ω_1. For practical purposes and for convenient reference, it is useful to express the numerically calculated correlation factors by suitable analytical formula. Appropriate fits can be obtained ratios of polynomial functions:

$$f = \frac{a_0 + a_1\left(\frac{\omega_2}{\omega_1}\right) + a_2\left(\frac{\omega_2}{\omega_1}\right)^2}{b_0 + b_1\left(\frac{\omega_2}{\omega_1}\right) + b_2\left(\frac{\omega_2}{\omega_1}\right)^2 + b_3\left(\frac{\omega_2}{\omega_1}\right)^3} \tag{5.104}$$

with appropriate values of the constants a_i and b_i. The curves in Fig. 5.47 are drawn using such expressions. Note that the rational form of the fitting function has no direct physical background. However, the crystal lattice could be linked to

an electrical network and the correlation factors may be expressed in terms of the resistivity of such a network. It seems reasonable that the resistivity of a network with parallel and series connections is likely expressed by a rational function. Each partial correlation factor is calculated by own set of parameters.

The correlation factor $f_\perp$ for diffusion perpendicular to the tetragonal axis changes monotonically from 0.466 ± 0.002 to 0.748 ± 0.002 when ω_2/ω_1 increases from 10^{-4} to 10^3 (Fig. 5.47, squares), respectively. For $\omega_2/\omega_1 = 0$, diffusion is confined to a Si bilayer and can be considered to be two-dimensional. Then, Si diffusion perpendicular to the tetragonal axis can still occur without type-2 jumps (Fig. 5.46b), and the pertaining correlation factor $f_\perp$ is finite. No long-range diffusion along the tetragonal axis occurs in such a case: A jump with a $+z$ component is immediately followed by a jump with a $-z$ component and vice versa. For $\omega_2/\omega_1 = 0$, the Si sublattice can be considered as a square lattice. The exact correlation factor of vacancy diffusion on a square lattice is known to be 0.4669 which is well reproduced by the Monte Carlo technique.

The partial correlation factor $f_{1_\parallel}$ increases monotonically from almost zero to 0.80 ± 0.02 when ω_2/ω_1 increases in the same range (Fig. 5.47, triangles up). Somehow unexpected is the behavior of $f_{2_\parallel}$, which approaches a value of 1.5 when $\omega_2/\omega_1 \to 0$ (Fig. 5.47, triangles down). As ω_2/ω_1 increases, $f_{2_\parallel}$ drops gradually to zero. The total correlation factor of Si diffusion along the tetragonal axis, $f_\parallel$, remains smaller than unity (Fig. 5.47, circles), although the partial correlation factor $f_{2_\parallel}$ is larger than unity at small values of ω_2/ω_1.

The case of $f_{2_\parallel}$ is very interesting. Forward correlation produced by the specific structure of the Si sublattice in $MoSi_2$ results in $f_{2_\parallel} > 1$ for $\omega_2/\omega_1 \to 0$. Let us analyze this limiting case analytically.

Suppose that a tracer atom has just performed a type-1 jump. Since $\omega_2 \approx 0$, the vacancy performs an almost two-dimensional random walk in the Si bilayer in which the tracer atom is located. Since the escape probability on a two-dimensional lattice is zero, the vacancy will definitely return to the tracer atom and at sometime induces a type-1 jump. The probability for the vacancy to jump into the neighboring Si bilayers and to induce a type-2 jump is practically zero. Thus, for $\omega_2/\omega_1 \to 0$, we have $P_{11}^- \to 1$ and $P_{12}^+ \to 0$. Now consider a random walk of the vacancy just after a type-2 jump of the tracer atom has occurred. The vacancy and the tracer atom are in different Si bilayers, and the probability that the vacancy immediately induces the type-2 backward jump of the tracer atom is almost zero, i.e., $P_{22}^- \approx 0$. However, occasionally, the vacancy will interchange somewhere between the Si bilayers; it can then appear in the same Si bilayer where the tracer atom is located. The probability that the vacancy will jump exactly toward the tracer atom position is negligibly small. Then, after a random walk within the Si bilayer where the tracer atom is located, the vacancy will induce a type-1 jump of the tracer atom. Thus, it is reasonable to suppose that $P_{21}^+ \to 1$ if $\omega_2 \to 0$. Introducing these values of $P_{ij}^\pm$ Eq. 5.102 and taking into account that the escape probabilities are zero, the $\mathbf{T}$ matrix for $\omega_2/\omega_1 \to 0$ becomes

$$\mathbf{T} = \begin{Vmatrix} -1 & 0 \\ 1 & 0 \end{Vmatrix} \tag{5.105}$$

Then, the partial correlation factors turn out to be

$$f_{1_{\|}} = 1 + 2 \cdot \left(-\frac{1}{2}\right) = 0 \tag{5.106}$$

and

$$f_{2_{\|}} = 1 + 2 \cdot \left(\frac{1}{2}\right) \frac{c/6}{c/3} = 1.5 \tag{5.107}$$

These estimates for the limiting case $\omega_2/\omega_1 \to 0$ perfectly agree with the Monte Carlo results of Fig. 5.47.

This example teaches us that though the correlation factors do not exceed unity just by definition, the *partial* correlation factors could be larger than unity, if a *forward correlation* of jumps is involved. Diffusion of Si atoms in $MoSi_2$ represents a textbook example where one of partial correlation factors can be as large as 1.5!

References

1. Y. Adda, J. Philibert and V. Pontikis, Physical Review B 85 (2012) p. 144121-1.
2. K. Kiuchi and R.B. McLlan, Acta Metallurgica 34 (1983) 961.
3. H. Bester and K.W. Lange, Arch Eisenhütttenswes. 43 (1972) 283.
4. J. Takadi, S. Yamamoto and M. Adachi, Z Metallkd 77 (1986) 6.
5. J. Takadi, S. Yamamoto, S. Kikuchi and M. Adachi, Metallurgical Transactions A 17 (1986) 221.
6. J. R. G. da Silva and R. B. McLellan, Materials Science and Engineering 26 (1976) 83.
7. P. Grieveson and E. T. Turkdogan, Trans Metall Soc AIME 230 (1964) 407.
8. J. Agren, Scripta Materialia 20 (1986) 1507.
9. J. C. Slater, Journal of Chemical Physics 41 (1964) 3199.
10. R. E. Howard, Physical Review 144 (1966) 650.
11. Mehrer H. (ed), Diffusion in Solid Metals and Alloys, Landolt-Börnstein, Group II: Crystal and Solid State Physics, Vol 26 (1990) Springer-Verlag, Berlin, pp. 58-62.
12. M. Köppers, Chr. Herzig, M. Friesel, and Y. Mishin, Acta Materialia 45 (1997) 4181.
13. H. Nakajima, M. Koiwa, and S. Ono, Scripta Materialia 17 (1983) 1431.
14. H. Nakajima and M. Koiwa, Titanium Science and Technology Proc. 5th Int. Conf. on Ti, (1985) p. 1759.
15. C. Minkwitz and Chr. Herzig, Defects and Diffusion Forum 143-147 (1997) 61.

16. D. David, G. Beranger, and E.A. Garcia, Journal of the Electrochemical Society 130 (1983) 423.
17. A. Anttila, J. Räisänen, and J. Keinonen, Applied Physics Letters 42 (1983) 498.
18. G.M. Hood, H. Zou, R.J. Schultz, N. Matsuura, J.A. Roy, and J.A. Jackman, Defects and Diffusion Forum 143-147 (1997) 49.
19. H. Nakajima, G.M. Hood, and R.J. Schultz, Philosophical Magazine B 58 (1988) 319.
20. G.M. Hood and R.J. Schultz, Materials Science Forum 15-18 (1987) 475.
21. R.P. Agarwala and A.R. Paul, Journal of Nuclear Materials 58 (1975) 25.
22. I.G. Ritchie and A. Atrens, Journal of Nuclear Materials 67 (1977) 254.
23. A. Anttila, J. Räisänen, and J. Keinonen, Journal of Less Common Metals 96 (1984) 257.
24. I. I. Kovenski, Diffusion in BCC metals, ASM (1965) page 283.
25. D. V. Ignatov, M. S. Model, L. F. Sokirianskii, A. Y. Shinaev, Titanium Sci Techn IV (1973) 2535.
26. R. S. Wasiliewski and G. L. Kehl, Journal of the Institute of Metals 83 (1954) 94.
27. G. B. Gibbs, D.Graham and D. H. Tomlin, Philosophical Magazine 8 (1963) 1269.
28. U. Köhler and Chr. Herzig, Physica Status Solidi B 144 (1987) 243.
29. J. Horvath, F. Dyment, and H. Mehrer, Journal of Nuclear Materials 126 (1984) 206.
30. Chr. Herzig, R. Willecke, and K. Vierrege, Philosophical Magazine A 63 (1991) 949.
31. G.M. Hood, H. Zou, R.J. Schultz, N. Matsuura, J.A. Roy, and J.A. Jackman, Defects and Diffusion Forum 143-147 (1997) 49.
32. A. Chirkov and A. Nazarov, Diffusion Fundamentals 3 (2005) 1.
33. M. Salamon and H. Mehrer, Defect Diffusion Forum, 216-217 (2002) 161.
34. M. Salamon, PhD Thesis, Münster University, Münster, Germany (2003).
35. JR Manning, Diffusion Kinetics for Atoms in Crystals (Princeton, New Jersey: Van Nostrand, 1968).
36. E.W. Elcock and C.W. McCombie, Physical Reiew B 109 (1958) 605.
37. H.A. Domian and H.I. Aaronson, Diffusion in Body-Centered Cubic Metals, editor, American Society for Metals (1965) page 209.
38. M. Arita, M. Koiwa and S. Ishioka, Acta Materialia 37 (1989) 1363.
39. R. Hilgedieck and Chr. Herzig, Z. Metallkd. 74 (1983) 38.
40. S.V. Divinski and Chr. Herzig, Intermetallics 8 (2000) 1357.
41. I.V. Belova and G.E. Murch, Philosophical Magazine A 82 (2002) 269.
42. H. Wever, Defects and Diffusion Forum 83 (1992) 55.
43. H. Numakura, T. Ikeda, M. Koiwa and A. Almazouzi, Philosophical Magazine A 77 (1998) 887.
44. N.A. Stolwijk, M. van Gend and H. Bakker, Philosophical Magazine A 42 (1980) 783.
45. St. Frank, S.V. Divinski, U. Södervall and Chr. Herzig, Acta Materialia 49 (2001) 1399.
46. C.R. Kao and Y.A. Chang, Intermetallics 1 (1993) 237.
47. S.V. Divinski and L.N. Larikov, Journal of Physics: Condensed Matter 9 (1997) 7873.
48. S.V. Divinski, St. Frank, U. Södervall and Chr. Herzig, Acta Materialia 46 (1998) 4369.
49. Chr. Herzig, T. Przeorski and Y. Mishin, Intermetallics 7 (1999) 389.
50. Yu. Mishin and Chr. Herzig, Acta Materialia 48 (2000) 589.
51. Chr. Herzig, T. Przeorski, M. Friesel, F. Hisker and S.V. Divinski, Intermetallics 9 (2001) 461.
52. M. Salamon, A.Strohm, T. Voss, P. Laitinen, I. Riihimaki, S. Divinski, W. Frank, J. Raisanen, H. Mehrer, Philosophical Magazine 84 (2004) 737.
53. S. Divinski, M. Salamon, H. Mehrer, Philosophical Magazine 84 (2004) p. 757.
54. M. O. Zacate, A. Favrot, G. S. Collins, Atom Movement in In_3La Studied via Nuclear Quadrupole Relaxation, Phys. Rev. Lett. 92 (2004) 225901.

Chapter 6
Interdiffusion and the Kirkendall Effect in Binary Systems

This chapter deals with diffusion in the phases with wide homogeneity range. Different approaches, which could be used to estimate the variation of interdiffusion coefficients with composition, are described. Following the Kirkendall effect is introduced along with the estimation of the intrinsic diffusion coefficients. The estimation of the tracer diffusion coefficients from a diffusion couple is also explained.

This chapter considers the continuum approach of diffusion, where the diffusion of components is treated in a continuous medium without going into the details of the atomic mechanism of diffusion. The advantage of this approach is that we can analyze and predict the micro- and/or macroscopic physicochemical changes in applications without going into a complicated atomistic model. In 1896, Sir W. C. Roberts reported for the first time the systematic study of the diffusion of gold in solid lead [1]. From the experiments in the early twentieth century, it was evident that the diffusion coefficient in the solid state is not a constant, but is rather a function of composition and temperature. Earlier in Chap. 3, we introduced the solutions for Fick's second law of diffusion considering the constant diffusion coefficient, which are not usually the case in practical examples. In many systems, diffusion coefficients might vary in the range of a few orders of magnitude. It is not possible to solve the relation considering the variation in the diffusion coefficient with composition, since a particular composition changes location with time in the interdiffusion zone. To clarify, considering the variation of interdiffusion coefficient with composition, Fick's second law can be written as

$$\begin{aligned}\frac{\partial C}{\partial t} &= \frac{\partial}{\partial x}\left(\widetilde{D}\frac{\partial C}{\partial x}\right)\\ &= \frac{\partial \widetilde{D}}{\partial x}\frac{\partial C}{\partial x} + \widetilde{D}\frac{\partial^2 C}{\partial x^2}\end{aligned} \tag{6.1}$$

The term $\partial\widetilde{D}/\partial x$ makes the equation inhomogeneous, and the solution in the closed form is not possible.

A. Paul et al., *Thermodynamics, Diffusion and the Kirkendall Effect in Solids*,
DOI: 10.1007/978-3-319-07461-0_6, © Springer International Publishing Switzerland 2014

However, instead of finding a solution for $C(x, t)$ as done in Chap. 3, it is possible to find the solution for $\widetilde{D} = \widetilde{D}(C)$, that is, the variation in the interdiffusion coefficient with concentration using the Boltzmann parameter.

6.1 Matano–Boltzmann Analysis

Matano [2] with the help of the Boltzmann parameter [3] solved Fick's second law so that we are able to estimate the variation in the interdiffusion coefficients with composition. Frequently, researchers use the Matano–Boltzmann analysis to estimate the interdiffusion coefficients at desired compositions from a measured composition profile. However, the limitation of this method is that it can be used strictly where the partial molar volumes of the components are constant; that is, the total volume does not change with reaction and mixing. This is explained in greater detail later in this chapter in Sect. 6.5. At this point, we are interested to derive the Matano–Boltzmann relation. Consider the case, when two alloys of initial concentrations C_B^- and C_B^+ are coupled and annealed for a reasonably short time t such that after annealing, some parts of the end members still remain unaffected by interdiffusion as shown in Fig. 6.1. The boundary conditions can be written as

$$\begin{aligned} C_B &= C_B^- \quad \text{for } x < 0 \quad \text{at} \quad t = 0 \\ C_B &= C_B^+ \quad \text{for } x > 0 \quad \text{at} \quad t = 0 \end{aligned} \tag{6.2}$$

where "−" and "+" represent the left- and right-hand ends of the diffusion couple. Boltzmann [3] introduced the variable

$$\lambda = \lambda(C_B) = (x - x_o)/t^{1/2} = x/t^{1/2} \tag{6.3}$$

where $x_o = 0$ is the location of the initial contact plane (bonding interface before annealing) and x is the location with respect to this plane. The initial contact plane is also known as the Matano plane in most of the literature on this subject. Equation 6.3 suggests that every concentration, for example, C_B^*, will move from the initial contact plane such that $\lambda^* = \lambda\left(C_B^*\right) = x^*/t^{1/2}$ will have a fixed value. To clarify further, we consider Fig. 6.1. Suppose at the location x_1, the concentration of the plane is C_B^* after an annealing time of t_1. At another annealing time, let us suppose after t_2, the same concentration is to be found at the location of x_2. According to the Boltzmann parameter, the plane corresponding to C_B^* will move such that

$$\lambda^* = \lambda\left(C_B^*\right) = x_1/t_1^{1/2} = x_2/t_2^{1/2} = \text{constant}$$

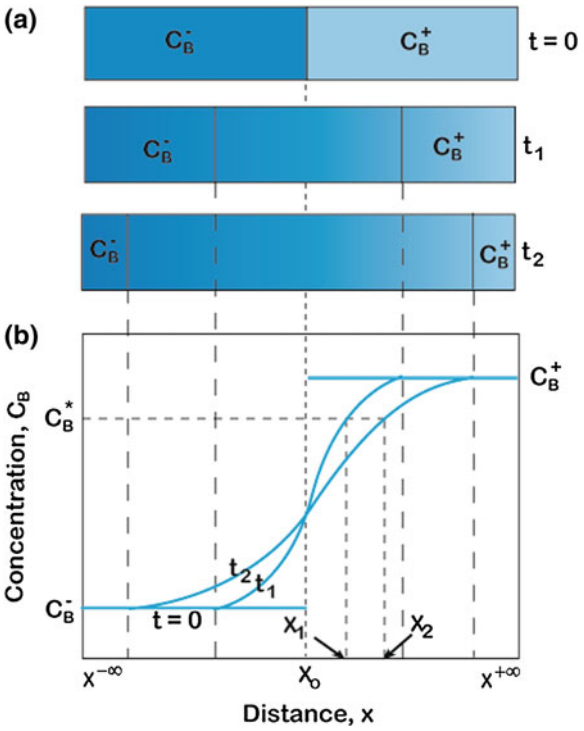

Fig. 6.1 Significance of the Boltzmann parameter is explained with the help of **a** Diffusion couple and **b** its concentration profile

It further indicates that in a diffusion-controlled process (parabolic growth of the phase layer), every concentration in the interdiffusion zone will have a fixed λ value. This means that we can verify the diffusion-controlled process by plotting λ versus $x/t^{1/2}$ after conducting the experiments for different annealing times. The variation of λ estimated at different concentrations with respect to $x/t^{1/2}$ will be the same irrespective of different annealing times. However, note that λ at one particular concentration will depend on the end-member concentrations in the diffusion couple and will have a different value in another diffusion couple with different end members.

Using the Boltzmann parameter given in Eq. 6.3, we obtain

$$\begin{aligned}\frac{\partial C_B}{\partial t} &= \frac{\partial C_B}{\partial \lambda}\frac{\partial \lambda}{\partial t} = -\frac{1}{2}\frac{x}{t^{3/2}}\frac{\partial C_B}{\partial \lambda} \\ \frac{\partial C_B}{\partial x} &= \frac{\partial C_B}{\partial \lambda}\frac{\partial \lambda}{\partial x} = \frac{1}{t^{1/2}}\frac{\partial C_B}{\partial \lambda}\end{aligned} \tag{6.4}$$

And replacing Eq. 6.4 in Fick's second law (Eq. 6.1) results in

$$\begin{aligned}\frac{\partial C_B}{\partial t} &= \frac{\partial}{\partial x}\left(\widetilde{D}\frac{\partial C}{\partial x}\right) - \frac{x}{2t^{\frac{3}{2}}}\frac{\partial C_B}{\partial \lambda} \\ &= \frac{\partial}{\partial x}\left(\frac{\widetilde{D}}{t^{\frac{1}{2}}}\frac{\partial C_B}{\partial \lambda}\right) = \frac{\partial}{t^{\frac{1}{2}}\partial x}\left(\widetilde{D}\frac{\partial C_B}{\partial \lambda}\right)\end{aligned} \tag{6.5}$$

since the concentration profiles under consideration are after a fixed annealing time t. From Eq. 6.3, it is possible to write $\partial\lambda = \partial x/t^{1/2}$. By introducing it in Eq. 6.5, we get

$$-\frac{x}{2t^{3/2}}\frac{\partial C_B}{\partial \lambda} = \frac{1}{t}\frac{\partial}{\partial \lambda}\left(\widetilde{D}\frac{\partial C_B}{\partial \lambda}\right)$$

Again by replacing with the Boltzmann parameter, λ, it can be written with respect to variable λ as

$$-\frac{\lambda}{2}\frac{dC_B}{d\lambda} = \frac{d}{d\lambda}\left(\widetilde{D}\frac{dC_B}{d\lambda}\right) \tag{6.6}$$

Multiplying both the sides by $d\lambda$, we get

$$-\frac{1}{2}\lambda dC_B = d\left(\widetilde{D}\frac{dC_B}{d\lambda}\right) \tag{6.7}$$

The initial conditions of Eq. 6.2 at time $t = 0$ can be rewritten as

$$\begin{aligned} C &= C_B^- \quad \text{at} \quad \lambda = -\infty \\ C &= C_B^+ \quad \text{at} \quad \lambda = +\infty \end{aligned} \tag{6.8}$$

Integrating Eq. 6.7 from the initial concentration C_B^- to the concentration of interest, C_B^* to measure the interdiffusion coefficient, $\widetilde{D}$, results in

$$-\frac{1}{2}\int_{C_B^-}^{C_B^*} \lambda dC_B = \widetilde{D}\frac{dC_B}{d\lambda}\Big|_{C_B^-}^{C_B^*} \tag{6.9}$$

The data are always measured at some fixed time so that t is constant. Replacing the Boltzmann parameter, we arrive at

$$-\frac{1}{2}\int_{C_B^-}^{C_B^*} x dC_B = \widetilde{D}t\frac{dC_B}{dx}\Big|_{C_B^-}^{C_B^*} = \widetilde{D}t\left(\frac{dC_B}{dx}\right)_{C_B^*} - \widetilde{D}t\left(\frac{dC_B}{dx}\right)_{C_B^-} = \widetilde{D}t\left(\frac{dC_B}{dx}\right)_{C_B^*} \tag{6.10}$$

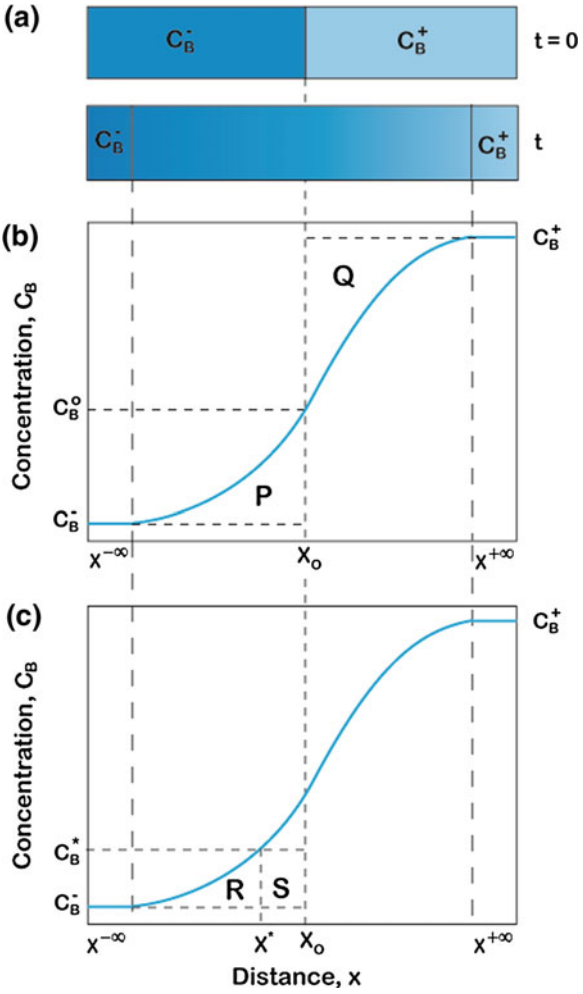

Fig. 6.2 Calculation of the diffusion parameter following Matano–Boltzmann parameter. **a** Diffusion couple, **b** finding the location of the initial contact plane by equalizing the areas P and Q, and **c** estimation of the interdiffusion coefficient is explained

since $\left(\frac{dC_B}{dx}\right)_{C_B^-} = 0$ at the unaffected part of the diffusion couple, where it has a concentration of C_B^- (see Fig. 6.2). Equation 6.10 can thus be rewritten as

$$\widetilde{D}\left(C_B^*\right) = -\frac{1}{2t}\left(\frac{dx}{dC_B}\right)_{C_B^*}\left[\int_{C_B^-}^{C_B^*} x dC_B\right] \tag{6.11}$$

So the interdiffusion coefficient at the concentration of interest C_B^* can be determined using Eq. 6.11. This is explained considering the composition profile developed in a binary A–B system, as presented in Fig. 6.2c. In general, it is easier

to integrate with respect to x in order to estimate the area under the integral. After integrating by parts, the following is obtained

$$\widetilde{D}\left(C_B^*\right) = -\frac{1}{2t}\left(\frac{dx}{dC_B}\right)_{C_B^*}\left[x^*\left(C_B^* - C_B^-\right) - \int_{x^{-\infty}}^{x^*}\left(C_B - C_B^-\right)dx\right] \tag{6.12}$$

since $x^* = x^* - x_o$. The value $x^{-\infty}$ is the location at the unaffected end member of the diffusion couple on the left. Note here that the location parameter is measured with respect to x_o and the concentration is considered from one unaffected part of the diffusion couple (left-hand side in the present case). From Fig. 6.2c, the interdiffusion coefficient can be expressed in terms of the areas as

$$\widetilde{D}\left(C_B^*\right) = \frac{1}{2t}\left(\frac{dx}{dC_B}\right)_{C_B^*}[S+R] \tag{6.13}$$

Note here the missing minus sign, since the values of R and S are actually positive and negative, respectively, in this particular case. To estimate the interdiffusion coefficients using Eq. 6.13, it is necessary to use the absolute values of the areas R and S. However, we should be careful before choosing Eq. 6.13 rather than Eq. 6.12. This is because Eq. 6.13 cannot be used directly if the concentration of interest is on the other side of the initial contact plane. It is nevertheless always safe to refer to Eq. 6.12. This is explained with an example at the end of this section.

It must be clear that we need to determine the location of the initial contact plane (as explained in Fig. 6.2b) for the determination of the interdiffusion coefficients. From the mass balance, we can write

$$\int_{C_B^-}^{C_B^+} x dC_B = 0$$

$$\int_{C_B^-}^{C_B^o} x dC_B + \int_{C_B^o}^{C_B^+} x dC_B = 0 \tag{6.14a}$$

$$\int_{x^{-\infty}}^{x_o}\left(C_B - C_B^-\right)dx = \int_{x_o}^{x^{+\infty}}\left(C_B^+ - C_B\right)dx \tag{6.14b}$$

where C_B^o is the concentration of the component B at x_o after interdiffusion. Note here that the other parts in both the sides after integration by parts are equal to zero since $x_o = 0$. The value $x^{+\infty}$ is the location at the unaffected end member of the

diffusion couple on the right. Equations 6.14a and 6.14b suggests that the location of x_o can be found by equalizing the areas denoted by P and Q, as shown in Fig. 6.2b.

To clarify the estimation methodology, we consider an imaginary diffusion couple in a hypothetical binary system, the one portrayed in Fig. 6.3. For instance, suppose a diffusion couple was made between two alloys of $A_{0.85}B_{0.15}$ and $A_{0.15}B_{0.85}$. Following the explanations given in Chap. 4, only the β phase will grow with a wide homogeneity range of $N_B = 0.4$ to $N_B = 0.6$. For the sake of easy explanation and estimation of $\widetilde{D}$ without the use of any software, we consider that the composition profile inside the product phase in the diffusion couple has a fixed slope. Furthermore, we assume that the molar volume is constant over the whole composition range. Since $C_B = N_B/v_m$, where v_m is the molar volume, Eq. 6.12 can be rewritten as

$$\widetilde{D}\left(N_B^*\right) = -\frac{1}{2t}\left(\frac{dx}{dN_B}\right)_{N_B^*}\left[x^*\left(N_B^* - N_B^-\right) - \int_{x^{-\infty}}^{x^*}\left(N_B - N_B^-\right)dx\right] \tag{6.15}$$

Note here that it is actually possible to consider the molar volume of the different phases for the calculation in real systems. The methodology explained here based on the N_B versus x profile is similar to the calculation from C_B versus x profile using Eq. 6.12. Suppose the diffusion couple was annealed for 100 h and the measured composition profile shows the thickness of the product phase layer as being 200 μm. The composition profile is measured along the dotted line shown on the diffusion couple in Fig. 6.3. The hypothetical composition profile is shown in Fig. 6.4a.

As explained above, the prerequisite of the calculation is finding the location of the initial contact plane. By equalizing the areas P and Q, we find this plane to be located at 150 μm, as can be noted from Fig. 6.4b. Therefore, this location should be set to zero, as shown in Fig. 6.4c. Now suppose, we wish to estimate the interdiffusion coefficient at $N_B = 0.45$, which is located at −50 μm. It will, therefore, be necessary to first estimate the slope. Since it has a fixed slope over the whole product phase, it can be estimated as

$$\frac{dN_B}{dx} = \frac{0.6 - 0.4}{[100 - (-100)] \times 10^{-6}} = \frac{0.2}{200 \times 10^{-6}} = 10^3/\text{m}$$

Further, the areas that are shown in Fig. 6.4c can be written as

$$\begin{aligned} S &= x^*\left(N_B^* - N_B^-\right) = (x^* - x_o)\left(N_B^* - N_B^-\right) \\ &= -50 \times 10^{-6}(0.45 - 0.15) = -15 \times 10^{-6}\,\text{m} \end{aligned}$$

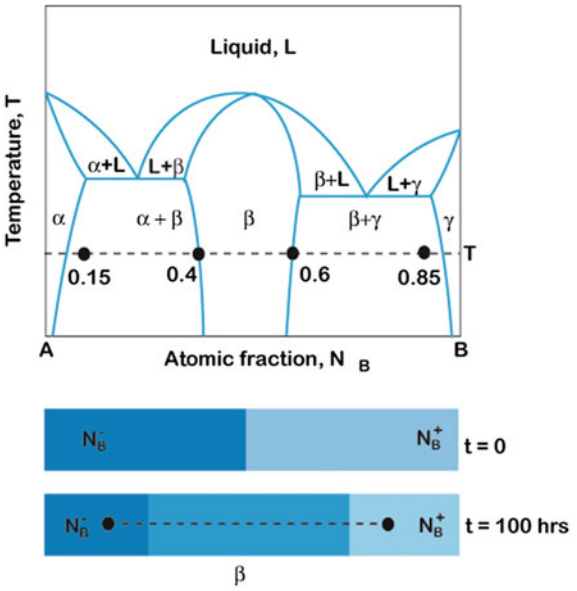

Fig. 6.3 An imaginary diffusion profile is shown based on the alloys in an imaginary binary system

$$R = \int_{x^{-\infty}}^{x^*} (N_B - N_B^-)dx$$

$$= [-50 - (-100)](0.4 - 0.15) + \frac{1}{2}[-50 - (-100)](0.45 - 0.4) = 13.75 \times 10^{-6}\,\text{m}$$

Thus, following Eq. 6.15, for the annealing time of 100 h, the interdiffusion coefficient can be estimated as

$$\widetilde{D}(N_B^* = 0.45) = -\frac{1}{2t}\left(\frac{dx}{dN_B}\right)_{N_B^*}\left[x^*(N_B^* - N_B^-) - \int_{x^{-\infty}}^{x^*}(N_B - N_B^-)dx\right]$$

$$= -\frac{1}{2 \times 100 \times 60 \times 60} \times \frac{1}{10^3}\left[-15 \times 10^{-6} - 13.75 \times 10^{-6}\right]$$

$$= 3.99 \times 10^{-14}\,\text{m}^2/\text{s}$$

Note that this explains the missing minus sign in Eq. 6.13.

Now let us turn to estimate the interdiffusion coefficient at the composition of $N_B = 0.525$. The reader is referred to Fig. 6.4d for the calculation. Note that the composition gradient (dN_B/dx) in this particular case is the same. The areas can be written as

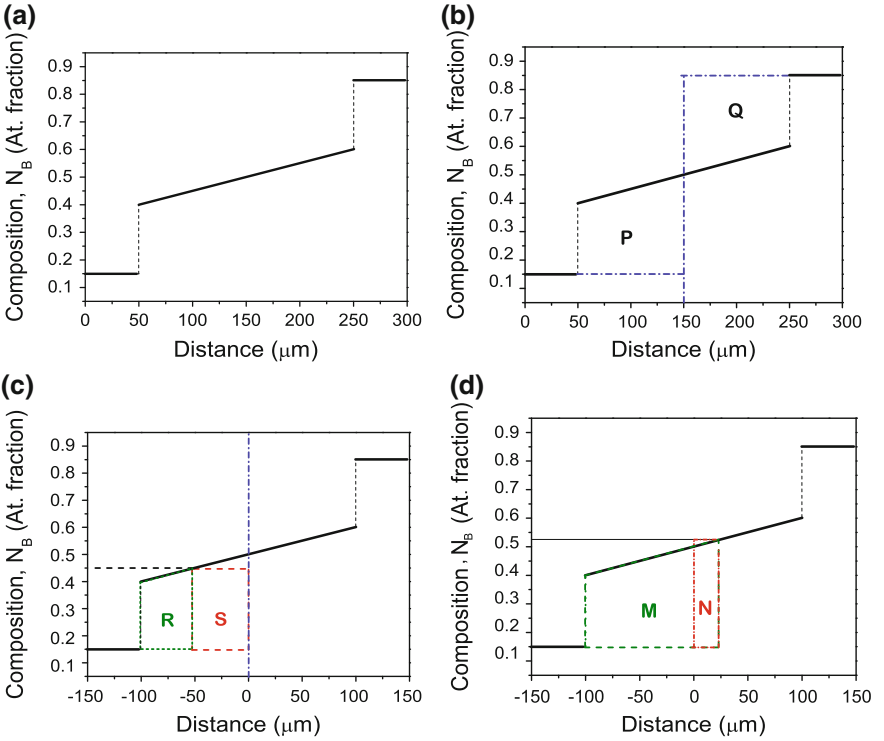

Fig. 6.4 Calculation procedure of the interdiffusion coefficient at the composition of interest. **a** Composition profile, **b** locating the initial contact plane, **c** estimating the interdiffusion coefficient at the composition of interest in the *left-hand side* of the initial contact plane, and **d** estimating the interdiffusion coefficient at the composition of interest in the *right-hand side* of the initial contact plane

$$N = x^*\left(N_B^* - N_B^-\right)$$
$$= (x^* - x_o)\left(N_B^* - N_B^-\right) = 25 \times 10^{-6}(0.525 - 0.15) = 9.375 \times 10^{-6}\,\mathrm{m}$$

$$M = \int_{x^{-\infty}}^{x^*} \left(N_B - N_B^-\right)dx$$
$$= [25 - (-100)](0.4 - 0.15) + \frac{1}{2}[25 - (-100)](0.525 - 0.4) = 39.06 \times 10^{-6}\,\mathrm{m}$$

As a result, the interdiffusion coefficient can be estimated as

$$\widetilde{D}\left(N_B^* = 0.525\right) = -\frac{1}{2t}\left(\frac{dx}{dN_B}\right)_{N_B^*}\left[x^*\left(N_B^* - N_B^-\right) - \int_{x^{-\infty}}^{x^*}\left(N_B - N_B^-\right)dx\right]$$
$$= -\frac{1}{2 \times 100 \times 60 \times 60} \times \frac{1}{10^3}\left[9.375 \times 10^{-6} - 39.06 \times 10^{-6}\right]$$
$$= 4.12 \times 10^{-14}\,\mathrm{m}^2/\mathrm{s}$$

6.2 Limitation of the Matano–Boltzmann Analysis

We have shown previously that the location of the initial contact plane or the Matano plane can be found from the concentration profile, i.e., C_B versus x using the relation $\int_{x^{-\infty}}^{x_o}\left(C_B - C_B^-\right)dx = \int_{x_o}^{x^{+\infty}}\left(C_B^+ - C_B\right)dx$. Ideally, it should also be possible to find this plane from C_A versus x using the relation $\int_{x^{-\infty}}^{x_o}\left(C_A^- - C_A\right)dx = \int_{x_o}^{x^{+\infty}}\left(C_A - C_A^+\right)dx$. Note here that $N_A + N_B = 1$, $N_A^{\pm} + N_B^{\pm} = 1$. Therefore C_B vs. x increases from left to right $(C_B^- < C_B^+)$, C_A vs. x decreases in the same direction $(C_A^- > C_A^+)$. Since there is a unique initial contact plane, we should be able to find the same location by following any of the profiles. However, this is not always the case. As explained in Fig. 6.5, there can be three different situations depending on the variation of the molar volume with composition. It is almost impossible to find a practical system, in which molar volume varies ideally following Vegard's law with the composition as shown in Fig. 6.5a. However, there are a few systems, where the deviation of the molar volume from the straight line connecting the molar volumes of the pure components v_m^A and v_m^B is marginal. Consequently, there will be almost no change in the total volume of the diffusion couple after interdiffusion. In this case, the initial contact planes located from the profiles C_B versus x and C_A versus x will be more or less the same. In fact, if the molar volume varies ideally following Vegard's law $(v_m = N_A v_m^A + N_B v_m^B)$, then the location of this plane found from any of the profiles will be exactly the same. In most of the systems, the molar volume deviates from the ideality. There can be positive deviation, as presented in Fig. 6.5b. Since the compositions that develop in the interdiffusion zone have a higher molar volume than the ideal value, there will be expansion in the diffusion couple, resulting in an increase in the total length of the diffusion couple. Note here that the diffusion profile in the diffusion couple is one dimensional. In this case, two different locations of the initial contact plane are found (as explained later in Sect. 6.5). In fact, both are actually incorrect and we are unable to find the exact location of the initial contact plane. In a system, where the molar volume has a negative deviation from the ideality, the diffusion couple will shrink after interdiffusion, as depicted in Fig. 6.5c. In this case also,

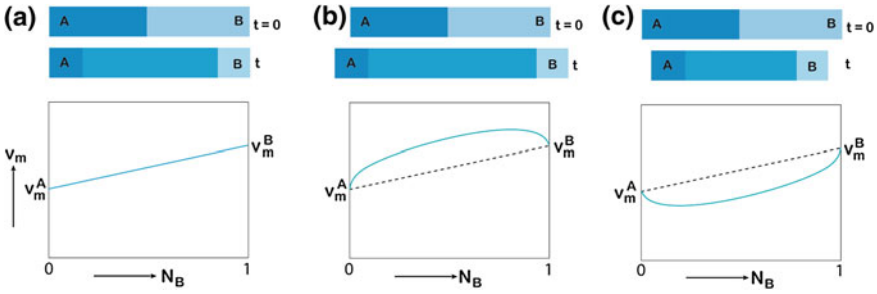

Fig. 6.5 Effect of deviation of molar volume in the diffusion couples is shown for **a** ideal case, **b** positive deviation, and **c** negative deviation

two different values will be found when the initial contact plane is determined from C_A versus x and C_B versus x.

As explained in the previous section, it is necessary to find the location of the initial contact plane for the calculation of the interdiffusion coefficient using the Matano–Boltzmann relation. In most of the systems, the molar volume deviates from ideality. Therefore, we are unable to locate the position of the initial contact plane exactly. This leads to an error in the calculation of the diffusion parameters. To circumvent this problem, relations to estimate $\widetilde{D}$ were developed such that there is no need to find the initial contact plane. Ballufi [4] first derived the solution for the interdiffusion coefficient for systems where the molar volume does not change ideally. Sometime later, Sauer and Freise [5] generalized the Matano–Boltzmann analysis for the same conditions. Wagner [6] then came to a similar relation but by using a simpler and easy-to-understand method. Next came Den Broeder [7] who developed the relation based on a much simpler graphical interpretation. Here, the Den Broeder approach is first explained, as it is fairly easy to follow. After that, we present the Wagner approach, which is very useful to derive the equations to be used for the estimation of few other important diffusion parameters along with the interdiffusion coefficients.

6.3 Den Broeder Approach to Determine the Interdiffusion Coefficient

Den Broeder [7] followed an easy-to-understand graphical approach. The concentration-normalizing variable Y_C is introduced such that

$$Y_C = \frac{C_B - C_B^-}{C_B^+ - C_B^-} \tag{6.16}$$

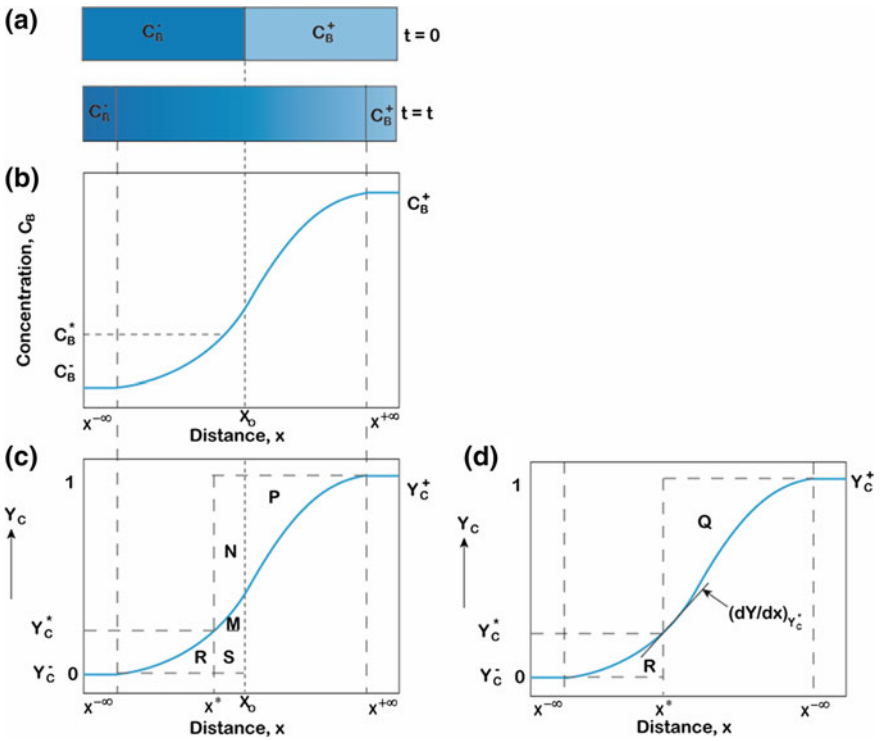

Fig. 6.6 Calculation of the interdiffusion coefficients is shown following Den Broeder's approach. **a** Diffusion couple, **b** concentration profile, **c** derivation of the Den Broeder's approach, and **d** slope at the concentration of interest

This leads to

$$dY_C = \frac{dC_B}{C_B^+ - C_B^-} \tag{6.17}$$

Replacing Eqs. 6.16 and 6.17 in Eq. 6.12 results in

$$\widetilde{D}\left(Y_C^*\right) = -\frac{1}{2t}\left(\frac{dx}{dY_C}\right)_{Y_C^*}\left[x^* Y_c^* - \int_{x^{-\infty}}^{x^*} Y_C dx\right] \tag{6.18}$$

To determine the interdiffusion coefficients using the relation expressed in Eq. 6.18, it is necessary to convert the concentration profile (Fig. 6.6b) to Y_C versus x, as shown in Fig. 6.6c. Note here that $Y_C^- = 0$ and $Y_C^+ = 1$. In terms of the areas shown in Fig. 6.6c, Eq. 6.18 can be expressed as

$$\widetilde{D}\left(Y_C^*\right) = \frac{1}{2t}\left(\frac{dx}{dY_C}\right)_{Y_C^*}[S+R] \tag{6.19}$$

The minus sign is missing in Eq. 6.19 (similar to Eq. 6.13) since the value of S is negative and the value of R is positive. With respect to the position of the initial contact plane x_o we can write

$$R + S + M = P \tag{6.20}$$

By adding N to both sides, we get

$$\begin{aligned} R + S + M + N &= P + N \\ S + M + N &= P + N - R \end{aligned} \tag{6.21}$$

We can further write that

$$S + M + N = (x^* - x_o)Y_C^+ = x^* \tag{6.22a}$$

Since $Y_C^+ = 1$.

$$P + N = \int_{x^*}^{x^{+\infty}} (1 - Y_C)dx \tag{6.22b}$$

$$R = \int_{x^{-\infty}}^{x^*} Y_C dx \tag{6.22c}$$

Replacing 6.22a, 6.22b and 6.22c in 6.21, we get

$$x^* = \int_{x^*}^{x^{+\infty}} (1 - Y_C)dx - \int_{x^{-\infty}}^{x^*} Y_C dx \tag{6.23}$$

Therefore, the following is obtained

$$S = x^* Y_C^* = Y_C^* \int_{x^*}^{x^{+\infty}} (1 - Y_C)dx - Y_C^* \int_{x^{-\infty}}^{x^*} Y_C dx \tag{6.24}$$

$$\begin{aligned} S+R &= Y_C^* \int_{x^*}^{x^{+\infty}} (1-Y_C)dx - Y_C^* \int_{x^{-\infty}}^{x^*} Y_C dx + \int_{x^{-\infty}}^{x^*} Y_C dx \\ &= \left(1-Y_C^*\right) \int_{x^{-\infty}}^{x^*} Y_C dx + Y_C^* \int_{x^*}^{x^{+\infty}} (1-Y_C)dx \end{aligned} \tag{6.25}$$

Replacing Eq. 6.25 in Eq. 6.19 gives

$$\widetilde{D}\left(Y_C^*\right) = \frac{1}{2t}\left(\frac{dx}{dY_C}\right)_{Y_C^*} \left[\left(1-Y_C^*\right) \int_{x^{-\infty}}^{x^*} Y_C dx + Y_C^* \int_{x^*}^{x^{+\infty}} (1-Y_C)dx\right] \tag{6.26}$$

Following Fig. 6.6d, we can express Eq. 6.26 as

$$\widetilde{D}\left(Y_C^*\right) = \frac{1}{2t}\left(\frac{dx}{dY_C}\right)_{Y_C^*} \left[\left(1-Y_C^*\right)R + Y_C^* Q\right] \tag{6.27}$$

This means that it is no longer necessary to locate the initial contact plane. We measure the composition profile, i.e., N_B versus x, by using the composition-measuring techniques. N_B is the atomic fraction of the component B. Dividing the atomic fractions by the respective molar volumes, the concentration profile can then be estimated. The concentration profile is converted into the concentration-normalizing variable Y_C versus x. Next, the interdiffusion coefficients can be estimated by determining the gradient at the point of interest and by estimating the areas R and Q, as shown in Fig. 6.6d, considering the known annealing time t. That means we do not have to consider an ideal variation or a fixed molar volume as required for the calculation using the Matano–Boltzmann analysis. Note here that Sauer-Freise [5] derived the same relation but differently.

6.4 Wagner's Approach to the Calculation of the Interdiffusion Coefficient

From Fick's first law and the relations expressed in Sect. 1.18 (Eq. 1.150), the following is obtained

$$\widetilde{J}_B = -\widetilde{D}\frac{\partial C_B}{\partial x} = -\widetilde{D}\frac{\bar{v}_A}{v_m^2}\frac{\partial N_B}{\partial x} \tag{6.28a}$$

Similarly, the interdiffusion flux with respect to the component A can be expressed as

$$\widetilde{J}_A = -\widetilde{D}\frac{\partial C_A}{\partial x} = -\widetilde{D}\frac{\bar{v}_B}{v_m^2}\frac{\partial N_A}{\partial x} = \widetilde{D}\frac{\bar{v}_B}{v_m^2}\frac{\partial N_B}{\partial x} = \frac{\bar{v}_B}{\bar{v}_A}\widetilde{D}\frac{\bar{v}_A}{v_m^2}\frac{\partial N_B}{\partial x} \tag{6.28b}$$

Since $N_A + N_B = 1$

From Eqs. 6.28a and 6.28b, we can write

$$\bar{v}_A\widetilde{J}_A + \bar{v}_B\widetilde{J}_B = 0 \tag{6.29}$$

So it must be apparent that the interdiffusion fluxes are different when estimated using the concentration profiles of different components. However, the interdiffusion coefficient is a material constant and the value is the same, whether determined with respect to either of the component A or component B.

Using the relations presented in Eq. 1.144 (Sect. 1.18), Eq. 6.28a can be rewritten as

$$\widetilde{J}_B\frac{(N_B\bar{v}_B + N_A\bar{v}_A)}{v_m} = -\widetilde{D}\frac{\bar{v}_A}{v_m^2}\frac{\partial N_B}{\partial x}$$

$$\widetilde{D} = -\frac{v_m\left(N_B\bar{v}_B\widetilde{J}_B + N_A\bar{v}_A\widetilde{J}_B\right)}{\bar{v}_A(\partial N_B/\partial x)}$$

Using Eq. 6.29, we can write

$$\begin{aligned}\widetilde{D} &= -\frac{v_m\left(-N_B\bar{v}_A\widetilde{J}_A + N_A\bar{v}_A\widetilde{J}_B\right)}{\bar{v}_A(\partial N_B/dx)}\\ \widetilde{D} &= \frac{v_m\left(N_B\widetilde{J}_A - N_A\widetilde{J}_B\right)}{\partial N_B/\partial x}\end{aligned} \tag{6.30}$$

From Fick's second law, as expressed in Eq. 3.4, we can write

$$\frac{\partial}{\partial t}\left(\frac{N_B}{v_m}\right) = \frac{\partial C_B}{\partial t} = -\frac{\partial \widetilde{J}_B}{\partial x} \tag{6.31a}$$

$$\frac{\partial}{\partial t}\left(\frac{N_A}{v_m}\right) = \frac{\partial C_A}{\partial t} = -\frac{\partial \widetilde{J}_A}{\partial x} \tag{6.31b}$$

We introduce a composition-normalized variable as

$$Y_B = \frac{N_B - N_B^-}{N_B^+ - N_B^-} \tag{6.32}$$

This can be rewritten as

$$N_B = N_B^+ Y_B + N_B^-(1 - Y_B) \tag{6.33a}$$

Substituting the left-hand side with $N_B = 1 - N_A$

$$\begin{aligned} 1 - N_A &= N_B^+ Y_B + N_B^- (1 - Y_B) \\ 1 - N_A &= N_B^+ Y_B + N_B^- (1 - Y_B) + Y_B - Y_B \\ N_A &= 1 - N_B^+ Y_B - N_B^- (1 - Y_B) - Y_B + Y_B \\ N_A &= \left(Y_B - N_B^+ Y_B\right) + \left[1 - Y_B - N_B^- (1 - Y_B)\right] \\ N_A &= \left(1 - N_B^+\right) Y_B + \left(1 - N_B^-\right)(1 - Y_B) \end{aligned} \tag{6.33b}$$

Substituting Eqs. 6.33a and 6.33b in Eqs. 6.31a and 6.31b, respectively, we arrive at

$$N_B^+ \frac{\partial}{\partial t}\left(\frac{Y_B}{v_m}\right) + N_B^- \frac{\partial}{\partial t}\left(\frac{1 - Y_B}{v_m}\right) = -\frac{\partial \widetilde{J}_B}{\partial x} \tag{6.34a}$$

$$\left(1 - N_B^+\right) \frac{\partial}{\partial t}\left(\frac{Y_B}{v_m}\right) + \left(1 - N_B^-\right) \frac{\partial}{\partial t}\left(\frac{1 - Y_B}{v_m}\right) = -\frac{\partial \widetilde{J}_A}{\partial x} \tag{6.34b}$$

We know the Boltzmann parameter expressed in Eq. 6.3 to be

$$\lambda = \lambda(C_B) = \frac{x}{t^{1/2}} \tag{6.35}$$

By differentiating with respect to t, we get

$$d\lambda = -\frac{1}{2}\frac{x}{t^{3/2}} dt = -\frac{1}{2}\frac{\lambda}{t} dt$$

$$dt = -2t\frac{d\lambda}{\lambda} \tag{6.36}$$

Replacing Eq. 6.36 in Eqs. 6.34a and 6.34b we obtain

$$\frac{\lambda}{2t}\left[N_B^+ \frac{d}{d\lambda}\left(\frac{Y_B}{v_m}\right) + N_B^- \frac{d}{d\lambda}\left(\frac{1 - Y_B}{v_m}\right)\right] = \frac{\partial \widetilde{J}_B}{\partial x} \tag{6.37a}$$

$$\frac{\lambda}{2t}\left[\left(1 - N_B^+\right) \frac{d}{d\lambda}\left(\frac{Y_B}{v_m}\right) + \left(1 - N_B^-\right) \frac{d}{d\lambda}\left(\frac{1 - Y_B}{v_m}\right)\right] = \frac{\partial \widetilde{J}_A}{\partial x} \tag{6.37b}$$

Next, the expressions are rewritten with respect to $\frac{Y_B}{v_m}$ and $\frac{1-Y_B}{v_m}$. Multiplying Eq. 6.37a by $\left(1 - N_B^-\right)$ and Eq. 6.37b by N_B^- and then subtracting the corresponding sides, we get

$$-\frac{\lambda}{2t}\left(N_B^+ - N_B^-\right)\frac{d}{d\lambda}\left(\frac{Y_B}{v_m}\right) = N_B^-\frac{\partial \widetilde{J}_A}{\partial x} - \left(1 - N_B^-\right)\frac{\partial \widetilde{J}_B}{\partial x} \tag{6.38a}$$

In the same way, multiplying Eq. 6.37a by $(1 - N_B^+)$ and Eq. 6.37b by N_B^+ and then subtracting the corresponding sides leads to

$$\frac{\lambda}{2t}\left(N_B^+ - N_B^-\right)\frac{d}{d\lambda}\left(\frac{1 - Y_B}{v_m}\right) = N_B^+\frac{\partial \widetilde{J}_A}{\partial x} - \left(1 - N_B^+\right)\frac{\partial \widetilde{J}_B}{\partial x} \tag{6.38b}$$

By differentiating the Boltzmann parameter with respect to x, we get

$$d\lambda = \frac{dx}{t^{1/2}}$$

Next, we multiply $d\lambda$ to the left-hand side and $dx/t^{1/2}$ to the right-hand side of Eq. 6.38a so that

$$-\frac{\lambda}{2t}\left(N_B^+ - N_B^-\right)d\left(\frac{Y_B}{v_m}\right) = \frac{1}{t^{1/2}}\left[N_B^- d\widetilde{J}_A - \left(1 - N_B^-\right)d\widetilde{J}_B\right]$$

From the Boltzmann parameter, we can write $x = x^{-\infty}, \lambda = \lambda^{-\infty}$ and $x = x^*, \lambda = \lambda^*$.

Integrating for a fixed annealing time t from $\lambda = \lambda^{-\infty}$ to a particular position of interest $\lambda = \lambda^*$ (corresponds to the mole fraction N_B^*), we get

$$-\frac{1}{2t}\left(N_B^+ - N_B^-\right)\int_{\lambda^{-\infty}}^{\lambda^*}\lambda d\left(\frac{Y_B}{v_m}\right) = \frac{1}{t^{1/2}}\left[N_B^-\int_o^{\widetilde{J}_A^*} d\widetilde{J}_A - \left(1 - N_B^-\right)\int_o^{\widetilde{J}_B^*} d\widetilde{J}_B\right]$$

Note that the interdiffusion flux at the unaffected part $x = x^{-\infty}$ or $\lambda = \lambda^{-\infty}$ is zero.

Following integration by parts on the left-hand side, we get

$$\begin{aligned}
-\frac{1}{2t}\left(N_B^+ - N_B^-\right)\left[\frac{\lambda^* Y_B^*}{v_m^*} - \int_{\lambda^{-\infty}}^{\lambda^*}\frac{Y_B}{v_m}d\lambda\right] &= \frac{1}{t^{1/2}}\left[N_B^-\widetilde{J}_A^* - \left(1 - N_B^-\right)\widetilde{J}_B^*\right] \\
\frac{1}{2t}\left(N_B^+ - N_B^-\right)\left[-\frac{\lambda^* Y_B^*}{v_m^*} + \int_{\lambda^{-\infty}}^{\lambda^*}\frac{Y_B}{v_m}d\lambda\right] &= \frac{1}{t^{1/2}}\left[N_B^-\widetilde{J}_A^* - \left(1 - N_B^-\right)\widetilde{J}_B^*\right]
\end{aligned} \tag{6.39a}$$

In the same way, we multiply Eq. 6.38b by $d\lambda$ on the left-hand side and by $dx/t^{1/2}$ on the right-hand side. Following integration from $\lambda = \lambda^*$ to $\lambda = \lambda^{+\infty}$ and then by doing integration by parts on the left-hand side of the equation, we get

$$\frac{1}{2t}\left(N_B^+ - N_B^-\right)\left[\frac{\lambda^*\left(1-Y_B^*\right)}{v_m^*} + \int_{\lambda^*}^{\lambda^{+\infty}} \frac{(1-Y_B)}{v_m} d\lambda\right] = \frac{1}{t^{1/2}}\left[N_B^+ \widetilde{J}_A^* - \left(1-N_B^+\right)\widetilde{J}_B^*\right]$$

Note here the sign because of $(1 - Y_B)$.

$$\frac{1}{2t}\left(N_B^+ - N_B^-\right)\left[-\frac{\lambda^*\left(1-Y_B^*\right)}{v_m^*} - \int_{\lambda^*}^{\lambda^{+\infty}} \frac{(1-Y_B)}{v_m} d\lambda\right] = \frac{1}{t^{1/2}}\left[-N_B^+ \widetilde{J}_A^* + \left(1-N_B^+\right)\widetilde{J}_B^*\right] \tag{6.39b}$$

J_A^* and J_B^* are the fluxes at $\lambda = \lambda^*$. Multiplying Eq. 6.39a by $\left(1 - Y_B^*\right)$ and Eq. 6.39b by Y_B^* and subtracting the corresponding sides, we obtain

$$\begin{aligned}\frac{1}{2t}\left(N_B^+ - N_B^-\right)&\left[\left(1-Y_B^*\right)\int_{\lambda^{-\infty}}^{\lambda^*} \frac{Y_B}{v_m} d\lambda + Y_B^* \int_{\lambda^*}^{\lambda+\infty} \frac{(1-Y_B)}{v_m} d\lambda\right] \\ &= \frac{1}{t^{1/2}}\left[N_B^* \widetilde{J}_A^* - \left(1-N_B^*\right)\widetilde{J}_B^*\right]\end{aligned} \tag{6.40}$$

Note here that the right-hand side of the relation can be found by replacing $Y_B^* = \frac{N_B^* - N_B^-}{N_B^+ - N_B^-}$ and $1 - Y_B^* = \frac{N_B^+ - N_B^*}{N_B^+ - N_B^-}$.

Since $d\lambda = \frac{dx}{t^{1/2}}$, Eq. 6.40 can be written as

$$\begin{aligned}\frac{1}{2t}\left(N_B^+ - N_B^-\right)&\left[\left(1-Y_B^*\right)\int_{\lambda^{-\infty}}^{\lambda^*} \frac{Y_B}{v_m} dx + Y_B^* \int_{\lambda^*}^{\lambda^{+\infty}} \frac{(1-Y_B)}{v_m} dx\right] \\ &= \left[N_B^* \widetilde{J}_A^* - \left(1-N_B^*\right)\widetilde{J}_B^*\right]\end{aligned} \tag{6.41}$$

Previously, we have derived the interdiffusion coefficient with respect to the interdiffusion fluxes $\widetilde{J}_A$ and $\widetilde{J}_B$ in Eq. 6.30. At a particular composition of interest $N_B = N_B^*$, for the fluxes of $\widetilde{J}_A^*$ and $\widetilde{J}_B^*$, it can be written as

$$\widetilde{D}\left(N_B^*\right) = \frac{v_m^*\left(N_B^* \widetilde{J}_A^* - N_A^* \widetilde{J}_B^*\right)}{\left(dN_B/dx\right)_{x^*}} \tag{6.42}$$

Substituting Eq. 6.41 in Eq. 6.42 results in

$$\widetilde{D}\left(N_B^*\right) = \frac{\left(N_B^+ - N_B^-\right)v_m^*}{2t\left(dN_B/dx\right)_{x^*}}\left[\left(1-Y_B^*\right)\int_{x^{-\infty}}^{x^*} \frac{Y_B}{v_m} dx + Y_B^* \int_{x^*}^{x^{-\infty}} \frac{(1-Y_B)}{v_m} dx\right] \tag{6.43}$$

From Eq. 6.32, we can write

$$dY_B = \frac{dN_B}{N_B^+ - N_B^-} \tag{6.44}$$

And replacing Eq. 6.44 in Eq. 6.43, we get

$$\widetilde{D}\left(Y_B^*\right) = \frac{v_m^*}{2t(dY_B/dx)_{x^*}} \left[\left(1 - Y_B^*\right) \int_{x^{-\infty}}^{x^*} \frac{Y_B}{v_m} dx + Y_B^* \int_{x^*}^{x^{+\infty}} \frac{(1 - Y_B)}{v_m} dx \right] \tag{6.45}$$

The calculation procedure is explained in Fig. 6.7. After measuring the composition profile in atomic fraction, presented in Fig. 6.7b, the normalized profile should be plotted, as shown in Fig. 6.7c. Moreover, from the knowledge of the variation of the molar volume with composition, $\frac{Y_B}{v_m}$ and $\frac{1-Y_B}{v_m}$ versus x should be plotted as shown in Fig. 6.7d and e, respectively. If we wish to estimate the interdiffusion coefficient at the composition, N_B^*, which is located at x^* in the diffusion couple, we need to estimate how the gradient $\frac{dY_B}{dx}$ at Y_B^* corresponds to N_B^*. Afterward, the areas $R = \int_{x^{-\infty}}^{x^*} \frac{Y_B}{v_m} dx$ and $S = \int_{x^*}^{x^{+\infty}} \frac{(1-Y_B)}{v_m} dx$ should be determined to estimate the interdiffusion coefficients using the relation expressed in Eq. 6.45.

Further, the difference between the Den Broeder [7] or Sauer-Freise [5] treatment with Wagner's approach [7] should be noted. This should lead to some difference in the diffusion data estimated, especially if the molar volume deviates from the ideality. In fact, for a constant molar volume, these relations are the same.

It should be noted here that when interdiffusion coefficients are estimated over a wide composition range, the impurity diffusion coefficients could be estimated by extending the data to 0 and 100 atomic percent of an element. At 0 at.% B, we have the impurity diffusion coefficient of B in pure A, and at 100 at.% B, we have the impurity diffusion coefficient of A in pure B. This is commonly practiced in many systems.

6.5 Change in Total Volume of the Diffusion Couple

In Sect. 6.2, we have already discussed that there could be a change in the total volume of the diffusion couple depending on the deviation of the molar volume from the ideality. In these couples, we are unable to locate the initial contact plane x_o exactly [8, 9]. In fact, the change in volume is related to the difference (in terms of distance) between the locations found using the profiles C_A versus x and C_B versus x. In this section, we shall show the relation between the changes in total volume with the location of the initial contact planes estimated following a quantitative analysis based on a hypothetical diffusion couple.

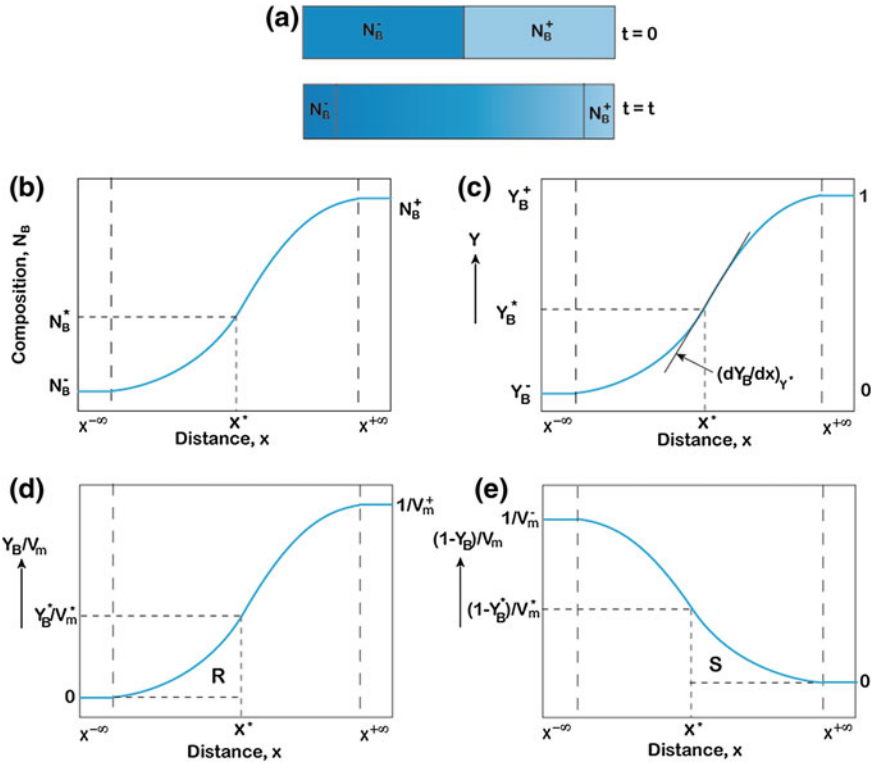

Fig. 6.7 Explanation of the calculation procedure of the interdiffusion coefficient following Wagner's approach. **a** An imaginary diffusion couple, **b** N_B versus x, **c** Y_B versus x profile, **d** Y_B/V_m versus x profile, and **e** $(1 - Y_B)/V_m$ versus x profile

As shown in Fig. 6.8, suppose we couple two alloys N_B^- (or N_A^-, expressed with respect to the element A) and $N_B^+ (N_A^+)$. Note here that N_B^- is a B-lean alloy and N_B^+ is a B-rich alloy, such that $N_B^+ > N_B^-$. Following the same argument, we can write $N_A^+ < N_A^-$. As explained previously, the location of the initial contact plane should be estimated with respect to C_A versus x and C_B versus x. Similarly, it can be determined using the composition-normalized variable, introduced during the derivation of Wagner's relation, from the Y_B/v_m versus x and Y_A/v_m versus x plots, as can be seen from Fig. 6.9. Note that $Y_B = \frac{N_B - N_B^-}{N_B^+ - N_B^-}$ and $Y_A = \frac{N_A - N_A^+}{N_A^- - N_A^+}$. Further, we can write

$$1 - Y_B = 1 - \frac{N_B - N_B^-}{N_B^+ - N_B^-} = \frac{N_B^+ - N_B}{N_B^+ - N_B^-} = \frac{1 - N_A^+ - 1 + N_A}{1 - N_A^+ - 1 + N_A^-} = \frac{N_A - N_A^+}{N_A^- - N_A^+} = Y_A \tag{6.46}$$

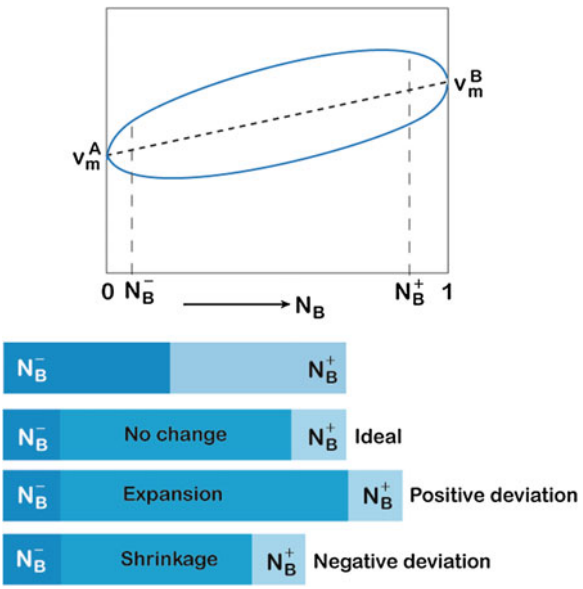

Fig. 6.8 Effect of molar volume change on the dimension of the diffusion couple

This means that it is now possible to identify the initial contact plane with respect to the Y_B/v_m versus x and $(1 - Y_B)/v_m$ versus x plots, as Fig. 6.9 shows, by equalizing the areas P and Q. For the sake of explanation, we consider the initial contact plane found from the Y_B/v_m versus x is x_o^{I} and from the $(1 - Y_B)/v_m$ versus x plot to be x_o^{II}. In terms of mathematical equations, these locations are expressed by equalizing the areas P and Q as

$$\int_{x^{-\infty}}^{x_o^{\mathrm{I}}} \frac{Y_B}{v_m} dx = \int_{x_o^{\mathrm{I}}}^{x^{+\infty}} \left(\frac{1}{v_m^+} - \frac{Y_B}{v_m} \right) dx \tag{6.47a}$$

$$\int_{x^{-\infty}}^{x_o^{\mathrm{II}}} \left(\frac{1}{v_m^-} - \frac{(1 - Y_B)}{v_m} \right) dx = \int_{x_o^{\mathrm{II}}}^{x^{+\infty}} \frac{(1 - Y_B)}{v_m} dx \tag{6.47b}$$

Note that v_m^- is the molar volume of the left-hand side end member with the composition N_B^- and v_m^+ is the molar volume of the right-hand side of the end member with the composition N_B^+.

Furthermore, we can write $P + R = Q + R$. Thus, based on Fig. 6.9a and Eq. 6.47a, the following can be written

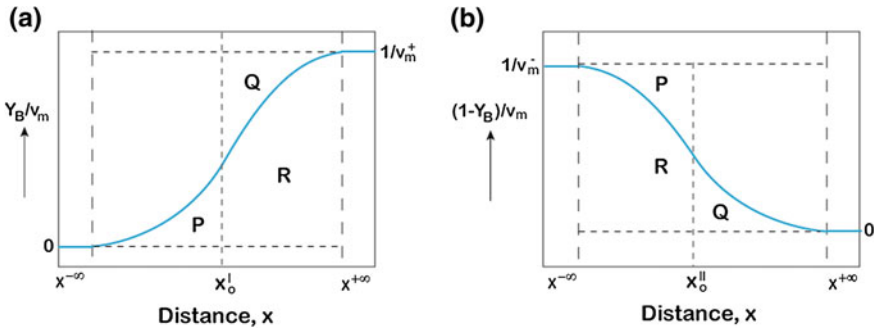

Fig. 6.9 Profiles used for the derivation of the molar volume effect on the total volume of the diffusion couple. **a** Y_B/v_m versus x and **b** $(1 - Y_B)/v_m$ versus x plots

$$\int_{x^{-\infty}}^{x_o^I} \frac{Y_B}{v_m}dx + \int_{x_o^I}^{x^{+\infty}} \frac{Y_B}{v_m}dx = \int_{x_o^I}^{x^{+\infty}} \left(\frac{1}{v_m^+} - \frac{Y_B}{v_m}\right)dx + \int_{x_o^I}^{x^{+\infty}} \frac{Y_B}{v_m}dx$$

$$\int_{x^{-\infty}}^{x^{+\infty}} \frac{Y_B}{v_m}dx = \frac{1}{v_m^+}\int_{x_o^I}^{x^{+\infty}} dx$$

$$\frac{x^{+\infty} - x_o^I}{v_m^+} = \int_{x^{-\infty}}^{x^{+\infty}} \frac{Y_B}{v_m}dx \tag{6.48a}$$

$$x^{+\infty} - x_o^I = v_m^+ \int_{x^{-\infty}}^{x^{+\infty}} \frac{Y_B}{v_m}dx$$

Similarly, with the help of Fig. 6.9b and Eq. 6.47b, we can write

$$\int_{x_o^{-\infty}}^{x_o^{II}} \frac{(1 - Y_B)}{v_m}dx + \int_{x^{-\infty}}^{x_o^{II}} \left(\frac{1}{v_m^-} - \frac{(1 - Y_B)}{v_m}\right)dx = \int_{x_o^{-\infty}}^{x_o^{II}} \frac{(1 - Y_B)}{v_m}dx + \int_{x_o^{II}}^{x^{+\infty}} \frac{(1 - Y_B)}{v_m}dx$$

$$\frac{1}{v_m^-}\int_{x^{-\infty}}^{x_o^{II}} dx = \int_{x^{-\infty}}^{x^{+\infty}} \frac{(1 - Y_B)}{v_m}dx$$

$$\frac{x_o^{II} - x^{-\infty}}{v_m^-} = \int_{x^{-\infty}}^{x^{+\infty}} \frac{(1 - Y_B)}{v_m}dx$$

$$x_o^{II} - x^{-\infty} = v_m^- \int_{x^{-\infty}}^{x^{+\infty}} \frac{(1 - Y_B)}{v_m}dx \tag{6.48b}$$

Adding Eqs. 6.48a and 6.48b, we get

$$\begin{aligned} x_o^{\mathrm{II}} - x^{-\infty} + x^{+\infty} - x_o^{\mathrm{I}} &= v_m^- \int_{x^{-\infty}}^{x^{+\infty}} \frac{(1 - Y_B)}{v_m} dx + v_m^+ \int_{x^{-\infty}}^{x^{+\infty}} \frac{Y_B}{v_m} dx \\ x_o^{\mathrm{II}} - x^{-\infty} + x^{+\infty} - x_o^{\mathrm{I}} &= \int_{x^{-\infty}}^{x^{+\infty}} \frac{v_m^- + \left(v_m^+ - v_m^-\right)}{v_m} Y_B dx \end{aligned} \tag{6.49}$$

When the molar volume varies ideally with the composition, i.e., linear between v_m^- and v_m^+ with respect to N_B (and hence Y_B), we can write

$$v_m = v_m^- + \left(v_m^+ - v_m^-\right) Y_B \tag{6.50}$$

At a particular composition, if the deviation of the molar volume from the connecting line of the molar volumes of the unaffected end members is $+\Delta v_m$ for the positive deviation and $-\Delta v_m$ for the negative deviation, then Eq. 6.50 considering the deviations can be rewritten as

$$\begin{aligned} v_m &= v_m^- + \left(v_m^+ - v_m^-\right) Y_B \pm \Delta v_m \\ v_m \mp \Delta v_m &= v_m^- + \left(v_m^+ - v_m^-\right) Y_B \end{aligned} \tag{6.51}$$

Replacing Eq. 6.51 in Eq. 6.49, we can write

$$\begin{aligned} x_o^{\mathrm{II}} - x^{-\infty} + x^{+\infty} - x_o^{\mathrm{I}} &= \int_{x^{-\infty}}^{x^{+\infty}} \frac{v_m \mp \Delta v_m}{v_m} dx \\ x_o^{\mathrm{II}} - x^{-\infty} + x^{+\infty} - x_o^{\mathrm{I}} &= x^{+\infty} - x^{-\infty} \mp \int_{x^{-\infty}}^{x^{+\infty}} \frac{\Delta v_m}{v_m} dx \\ x_o^{\mathrm{I}} - x_o^{\mathrm{II}} &= \pm \int_{x^{-\infty}}^{x^{+\infty}} \frac{\Delta v_m}{v_m} dx \end{aligned} \tag{6.52}$$

Here, $\int_{x^{-\infty}}^{x^{+\infty}} \frac{\Delta v_m}{v_m} dx$ measures the total volume change of the diffusion couple. Since we have a line profile in the diffusion couple, we can assume that the volume change will be mainly because of the change in the length of the diffusion couple. It must be clear from Eq. 6.52 that in the case of ideal variation of the molar volume ($\Delta v_m = 0$), there will be no difference in the location of the initial contact plane found from the two different profiles. In the case of positive or negative deviation, the difference between the estimated values will be equal to the change in the length of the diffusion couple.

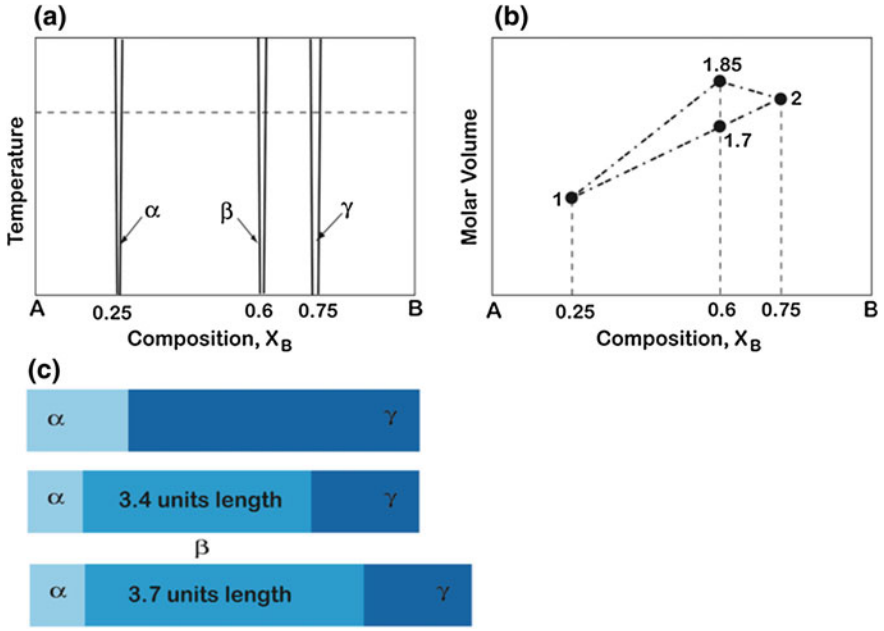

Fig. 6.10 **a** Imaginary phase diagram showing, **b** the positive deviation of the molar volume and **c** its effect on the dimension of the diffusion couple

To explain the effect of the change in the total volume on the estimated values of the initial contact plane, a very simple hypothetical diffusion couple is considered in Fig. 6.10. In the hypothetical phase diagram, as shown in Fig. 6.10a, there are three compounds with narrow homogeneity range α, β, and γ which are present. The average composition of these phases with respect to the element B, N_B are 0.25 ($A_{0.75}B_{0.25}$), 0.6 ($A_{0.4}B_{0.6}$), and 0.75 ($A_{0.25}B_{0.75}$). As discussed in Chap. 4, if we couple α and γ, the β phase will grow in the interdiffusion zone, as Fig. 6.10c shows. If the molar volume varies ideally, as is the case in this system, then if the molar volume of α is 1 unit and γ is 2 units, the molar volume of β will be 1.7 units (see Fig. 6.10b). Additionally, suppose that 0.6 mol of α and 1.4 mol of γ get consumed to produce 2 mol of β. In terms of the reaction equation, we can write

$$0.6A_{0.75}B_{0.25}(\alpha) + 1.4A_{0.25}B_{0.75}(\gamma) \rightarrow 2A_{0.4}B_{0.6}(\beta) \tag{6.53}$$

Since the diffusion couple has a line profile, we can consider the unit cross-sectional area. Consequently, the units consumed or produced can be directly expressed in length units, such that

$$0.6 \times 1(\alpha) + 1.4 \times 2(\gamma) \quad \rightarrow \quad 2 \times 1.7(\beta) = 3.4 \text{ units} \tag{6.54}$$

This further means that 0.6 units of α and 2.8 units of γ get consumed to produce 3.4 units of β. The composition profile developed is shown in Fig. 6.11b.

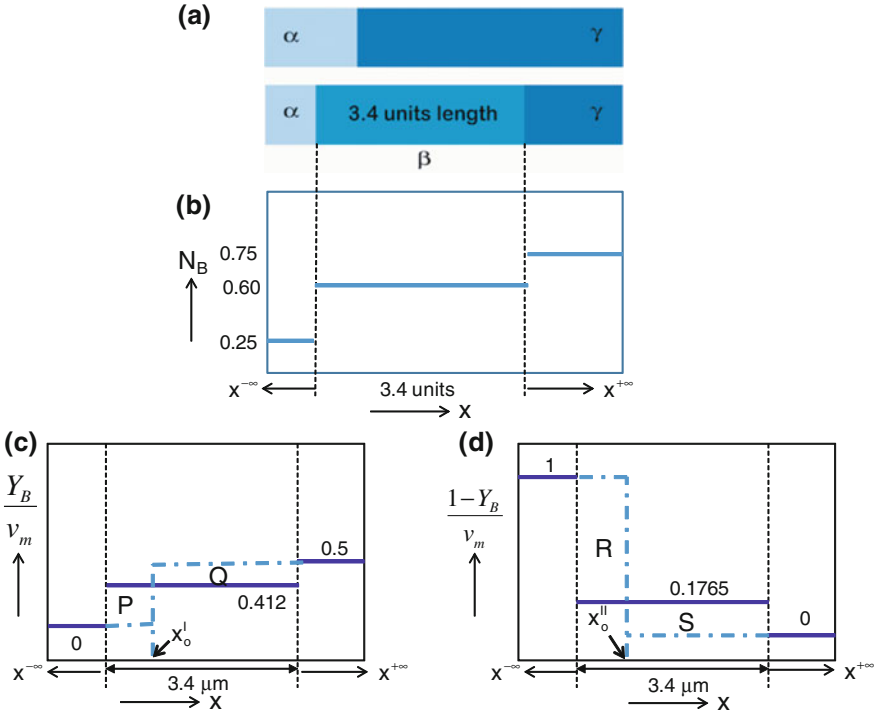

Fig. 6.11 Estimation of the initial contact plane is explained when molar volume varies ideally. **a** Diffusion couple, **b** composition profile, **c** Y_B/v_m versus x plot showing the location of x_o^I, and **d** $(1 - Y_B)/v_m$ versus x plot showing the location of x_o^{II}

Following on from this, the Y_B/v_m versus x and $(1 - Y_B)/v_m$ versus x plots are shown in Fig. 6.11c, d. The values used in Fig. 6.11c, d are estimated as follows

α phase: $N_B^\alpha = N_B^- = 0.25$,

$$Y_B^\alpha = Y_B^- = \frac{N_B - N_B^-}{N_B^+ - N_B^-} = \frac{N_B^\alpha - N_B^\alpha}{N_B^\gamma - N_B^\alpha} = \frac{0.25 - 0.25}{0.75 - 0.25} = 0,$$

$$\frac{Y_B^\alpha}{v_m^\alpha} = \frac{0}{1} = 0; \quad \frac{1 - Y_B^\alpha}{v_m^\alpha} = \frac{1}{1} = 1$$

β phase: $N_B^\beta = N_B = 0.6$,

$$Y_B^\beta = Y_B = \frac{N_B - N_B^-}{N_B^+ - N_B^-} = \frac{N_B^\beta - N_B^\alpha}{N_B^\gamma - N_B^\alpha} = \frac{0.6 - 0.25}{0.75 - 0.25} = 0.7,$$

$$\frac{Y_B^\beta}{v_m^\beta} = \frac{0.7}{1.7} = 0.412; \quad \frac{1 - Y_B^\beta}{v_m^\beta} = \frac{0.3}{1.7} = 0.1765$$

γ phase: $N_B^{\gamma} = N_B^{+} = 0.75$,

$$Y_B^{\gamma} = Y_B^{+} = \frac{N_B - N_B^{-}}{N_B^{+} - N_B^{-}} = \frac{N_B^{\gamma} - N_B^{\alpha}}{N_B^{\gamma} - N_B^{\alpha}} = \frac{0.75 - 0.25}{0.75 - 0.25} = 1,$$

$$\frac{Y_B^{\gamma}}{v_m^{\gamma}} = \frac{1}{2} = 0.5; \quad \frac{1 - Y_B^{\gamma}}{v_m^{\gamma}} = \frac{0}{2} = 0$$

From Eq. 6.54, we know that the actual location of the initial contact plane is 0.6 units from the α/β interface. Now, let us examine whether it is possible to locate this initial contact plane. By equating the areas P and Q in the Y_B/v_m versus x plot—as seen from Fig. 6.11c—we get the location x_o^{I} as

$$(0.412 - 0)x_o^{\mathrm{I}} = (0.5 - 0.412)\left(3.4 - x_o^{\mathrm{I}}\right)$$
$$x_o^{\mathrm{I}} = 0.6$$

Similarly, we find the location of the initial contact plane x_o^{II} from the $(1 - Y_B)/v_m$ versus x plot given in Fig. 6.11d by equating the areas R and S as

$$(1 - 0.1765)x_o^{\mathrm{II}} = 0.1765\left(3.4 - x_o^{\mathrm{II}}\right)$$
$$x_o^{\mathrm{II}} = 0.6$$

This means we are able to locate the exact position of the initial contact plane from any of the profiles when molar volume varies ideally with composition.

Now let us consider the positive deviation of the molar volume for the β phase as 1.85 units, as shown in Fig. 6.10b. Similar to the previous example, we consider the growth of 2 mol of the product phase by consuming 0.6 mol of α and 1.4 mol of γ. The reaction equation is therefore the same, as expressed in Eq. 6.53. However, the units consumed or produced can be directly expressed in length units, such that

$$0.6 \times 1(\alpha) + 1.4 \times 2(\gamma) \rightarrow 2 \times 1.85(\beta) = 3.7 \text{ units} \tag{6.55}$$

This means that 0.6 units of α and 2.8 units of γ get consumed to produce 3.7 units of β, resulting in an expansion of (3.7 − 3.4 =) 0.3 units. There is expansion on both sides of the initial contact plane inside the β phase. Now, let us see what we find from the Y_B/v_m versus x and $(1 - Y_B)/v_m$ versus x plots. The plots are shown in Fig. 6.12.

α phase: $N_B^{\alpha} = N_B^{-} = 0.25$,

$$Y_B^{\alpha} = Y_B^{-} = \frac{N_B - N_B^{-}}{N_B^{+} - N_B^{-}} = \frac{N_B^{\alpha} - N_B^{\alpha}}{N_B^{\gamma} - N_B^{\alpha}} = \frac{0.25 - 0.25}{0.75 - 0.25} = 0;$$

$$\frac{Y_B^{\alpha}}{v_m^{\alpha}} = \frac{0}{1} = 0; \quad \frac{1 - Y_B^{\alpha}}{v_m^{\alpha}} = \frac{1}{1} = 1$$

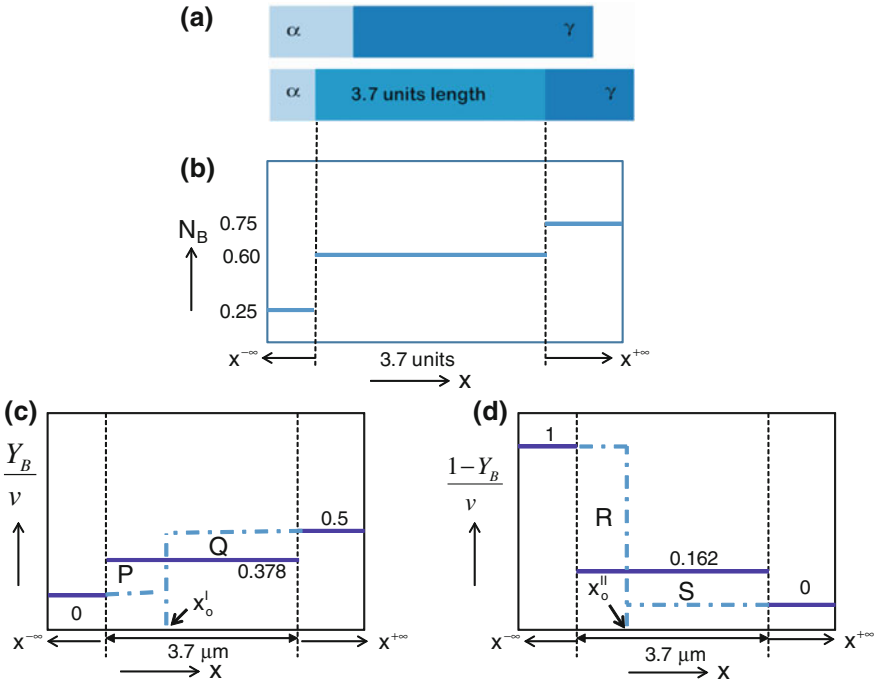

Fig. 6.12 Estimation of the initial contact plane is explained when molar volume deviates positively. **a** Diffusion couple, **b** composition profile, **c** Y_B/v_m versus x plot showing the location of x_o^I, and **d** $(1 - Y_B)/v_m$ versus x plot showing the location of x_o^{II}

β phase: $N_B^\beta = N_B = 0.6$,

$$Y_B^\beta = Y_B = \frac{N_B - N_B^-}{N_B^+ - N_B^-} = \frac{N_B^\beta - N_B^\alpha}{N_B^\gamma - N_B^\alpha} = \frac{0.6 - 0.25}{0.75 - 0.25} = 0.7,$$

$$\frac{Y_B^\beta}{v_m^\beta} = \frac{0.7}{1.85} = 0.378; \quad \frac{1 - Y_B^\beta}{v_m^\beta} = \frac{0.3}{1.85} = 0.162$$

γ phase: $N_B^\gamma = N_B^+ = 0.75$,

$$Y_B^\gamma = Y_B^+ = \frac{N_B - N_B^-}{N_B^+ - N_B^-} = \frac{N_B^\gamma - N_B^\alpha}{N_B^\gamma - N_B^\alpha} = \frac{0.75 - 0.25}{0.75 - 0.25} = 1,$$

$$\frac{Y_B^\gamma}{v_m^\gamma} = \frac{1}{2} = 0.5; \quad \frac{1 - Y_B^\gamma}{v_m^\gamma} = \frac{0}{2} = 0$$

By equating the areas P and Q in the Y_B/v_m versus x plot as shown in Fig. 6.12c, we obtain the location x_o^{I} as

$$(0.378 - 0)x_o^{\mathrm{I}} = (0.5 - 0.378)\left(3.7 - x_o^{\mathrm{I}}\right)$$
$$x_o^{\mathrm{I}} = 0.9$$

Similarly, we find the location of the initial contact plane x_o^{II} from the $(1 - Y_B)/v$ versus x plot, as shown in Fig. 6.12d by equating the areas R and S as

$$(1 - 0.162)x_o^{\mathrm{II}} = 0.162\left(3.7 - x_o^{\mathrm{II}}\right)$$
$$x_o^{\mathrm{II}} = 0.6$$

Thus, we find the two different locations from two different plots. These distances from the α/β interface are 0.6 and 0.9. Actual, initial plane must be located between these two, which we are unable to find. In this case, we have considered just one line compound with a fixed composition. Therefore, when considering homogeneous expansion, we can still locate the exact location of this plane, which should be at $0.6 + 0.6 \times \frac{0.3}{3.4} = 0.653$ units from the α/β interface. This is estimated based on the expansion for the length of 0.6 units consumed from the α phase, that is, the length from the α/β interface in the case of ideal variation of the molar volume. However, in most practical examples, the expansion or the shrinkage of the interdiffusion zone will not be homogeneous and it is almost impossible to locate the exact position of this plane. The Wagner and Den Broeder methods, as discussed in the previous sections, are useful to estimate the interdiffusion coefficients without locating the exact position of the initial contact plane. However, as we shall discuss later in Chap. 8, there is still a need to locate this position for the rationalization of the possibilities of multiple Kirkendall marker planes. We shall discuss how it is possible to still find this location indirectly with a small error (see Sect. 8.4).

6.6 The Kirkendall Effect

Till now, the estimation procedure of the interdiffusion coefficients has been discussed, which is a kind of average of the intrinsic diffusion coefficients of components. In fact, for long, it was a commonly held belief that the diffusivities of the components are the same. Based on this belief, the atomic mechanisms of diffusion were developed. However, on many occasions, scientists researching this field noted a strange behavior. For example, in 1929, Pfeil [10] reported one peculiar phenomenon while studying the oxidation of iron and steel:

> It had frequently been noticed that small particles of foreign matter (such as pieces of muffle) falling on the surface of oxidising iron were gradually buried. The scale grew up round these particles until they finally disappeared beneath the surface, but they could afterwards be found by breaking up the layer of scale.

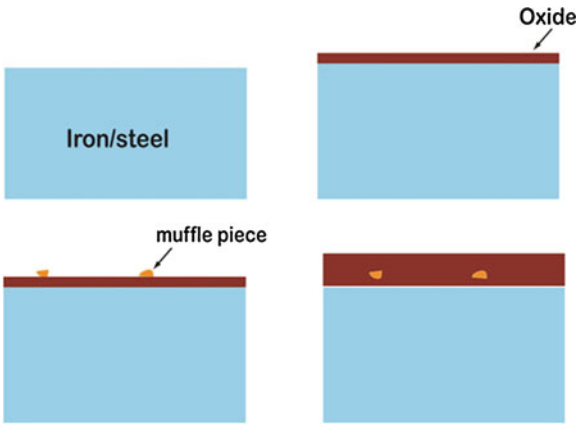

Fig. 6.13 Schematic diagram explaining the movement of debris inside the oxide layer on steel

This is explained with the aid of a schematic diagram in Fig. 6.13. The foreign matter, i.e., the muffle pieces, acted as an inert material and did not take any part in the reaction and the diffusion process. This was an indication that Fe had a higher diffusion rate compared to that of oxygen. After diffusing through the oxide layer, Fe reacted with O_2 to produce the oxide layer. Since the product phase grew at the oxide/air interface, the oxide layer covered the muffle pieces.

As indicated in the book written by Darken and Gurry [11], Hartley [12] was the first to deliberately use foreign inert particles, titanium dioxide, in an organic acetone/cellulose–acetate system, to study the inequality of the diffusing components. Immediately after that, Smigelkas and Kirkendall [13] reported a similar technique to study the inequality of the diffusivities of the components in the Cu–Zn binary system. Instead, they used molybdenum wires as inert markers. Hartley's work went unnoticed in the community working on the metallic systems, and the work published by Kirkendall changed the viewpoints on the atomic mechanism of diffusion. The movement of the inert markers caused by the difference in the diffusion coefficients of the components in an interdiffusion zone is known as the Kirkendall effect.

The experiment followed by Smigelkas and Kirkendall [13] is explained with the help of the schematic diagram represented in Fig. 6.14. A rectangular bar (18×1.9 cm^2) of 70–30 wrought brass (70 wt% Cu–30 wt% Zn) was first prepared. After the standard metallographic preparation of grinding and polishing, 130 μm Mo wires were placed on opposite sides of the surfaces. Next, a 2,500 μm thick electroplated copper layer was deposited. The diffusion couple was then subjected to annealing at 785 °C. At different intervals, a small piece was cross-sectioned and the rest of the block was annealed further. This way, it was possible to examine the movement of the markers at different annealing times. With the increase in annealing time, the thickness of the product phase α brass increased and the distance between the markers decreased. The movement of the markers was estimated after rectifying the volume change in the interdiffusion zone and found to be parabolic with time. It should be noted here that the Mo markers neither took

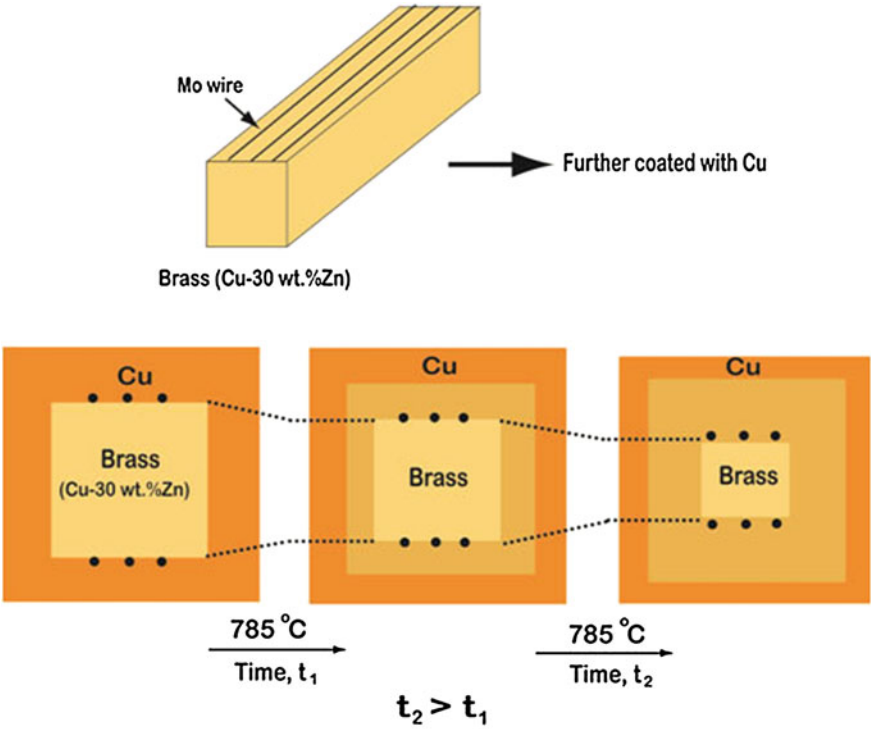

Fig. 6.14 Schematic illustration of the Kirkendall's experiment

part in the diffusion process nor did they react with the diffusing components. The equal diffusivities would have resulted in no movement of the markers because of the transfer of equal amount of material on either side of the Kirkendall plane. The movement of the markers, on the other hand, indicated the unequal diffusion rates of the components in the α brass, Cu(Zn) solid solution. In the manuscript, they reported [13]:

> The movement of the insoluble molybdenum wire was conclusive evidence that the alpha brass was being forced back as a whole (or attracted back) as a result of the diffusing out of the zinc atoms individually.

From this study, two conclusions were drawn which had enormous impact at that time on solid-state diffusion [13]:

1. The rate of diffusion of zinc is much greater than that of copper in alpha brass, and
2. When zinc diffuses more rapidly than copper in alpha brass, the interface shifts to compensate at least partially for the diffusion rate.

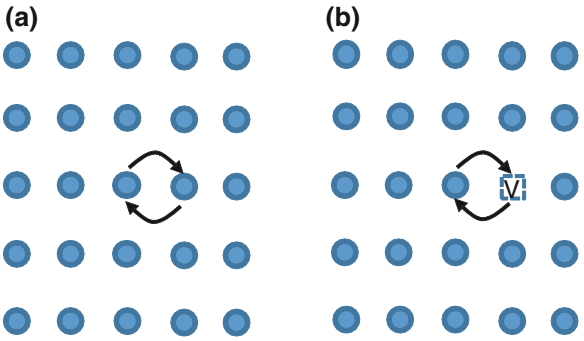

Fig. 6.15 Atomic diffusion mechanisms: **a** direct interchange mechanism and **b** vacancy mechanism

The results reported by Kirkendall not only showed that the diffusion rates of the components in a solid are different, it also helped to establish the vacancy mechanism for substitutional diffusion.

At first, this work was highly criticized mainly by the renowned scientist R. F. Mehl, who was the reviewer of the article and did not accept it immediately for the publication. He felt that this could be an experimental artifact and other factors such as the transport of Zn vapor could have a significant effect. Ultimately, he accepted the article for publication and the manuscript was published along with the comments from many scientists. The impact of the work can be realized from R. F. Mehl's [14] comment:

> If verified, this "Kirkendall effect" would greatly modify not only the treatment of diffusion data but also the theory of mechanism of diffusion. It would, for example, be no longer possible to represent diffusion data in a substitutional solid solution by one coefficient, applying to both metal atoms since the separate coefficients are not equal, but one would have to show two coefficients, one each for each of the two metal atoms.

The historical development of this discussion can be traced by reading the article by Nakajima [15]. Immediately after the publication, R. F. Mehl along with his student da Silva conducted many rigorous studies in many Cu-based solid solutions with different types of markers [16]. Simultaneously, many other groups also worked on this topic. Ultimately, everybody agreed with the results published by Kirkendall, and this phenomenon thereafter was known as the Kirkendall effect.

In the mean time, which might not be known by many, in 1942, Huntington and Seitz also established that substitutional diffusion in metals occurs by a vacancy mechanism [17]. It should be noted here that the second manuscript [18] of Kirkendall's career in which he mentioned for the first time the difference in diffusion coefficients of components was published in the same year (before validating the fact with a detailed experimental work in his third manuscript [13] in 1947). However, because of ongoing Second World War, Huntington and Seitz's paper was overlooked. In fact, before all these developments, Zener [20] proposed a direct interchange mechanism, where, as shown in Fig. 6.15a, two atoms exchange their position directly. If this is true, then there should be no difference in the diffusion rates of components. In their landmark article, Huntington and Seitz [17]

estimated the activation energy for Cu self-diffusion for (i) a direct exchange mechanism, (ii) an interstitial mechanism, and (iii) the vacancy mechanism. They used the experimentally determined activation energy for the tracer diffusion coefficient of Cu for comparison, which varied in the range of 2.1–2.5 eV (202.6–241.2 kJ/mol). Based on their rudimentary calculations, they found the theoretically calculated values to be 17.2 eV (1,659.6 kJ/mol) for the direct interchange mechanism and 10 eV (964.9 kJ/mol) for the interstitial diffusion mechanism. On the other hand, they got a value of about 2.8 eV (270.2 kJ/mol) for the vacancy mechanism in which around 1.8 eV (173.7 kJ/mol) is required for vacancy formation and 1 eV (96.5 kJ/mol) for migration. Therefore, the theoretically estimated activation energy is very close to the value estimated by experiments if the vacancy mechanism of diffusion is considered. They stated that [17]:

> The results of these computations…seem to show beyond a reasonable doubt that the vacancy mechanism of diffusion is greatly preferred over the other two considered here for copper.

In a private communication, Zener criticized this rudimentary calculation. Following this, Huntington and Seitz [19] refined their calculation and found that the true value of the activation energy for the interchange mechanism is close to 10.3 eV (993.8 kJ/mol). They also assumed that the activation energy for interstitial diffusion must be somewhat smaller than the value that they initially estimated. Therefore, they felt that these two mechanisms are dubious for the diffusion of components. Theoretically calculated values are much higher compared to the experimentally estimated values of activation energy.

Zener still believed in a defect-free diffusion mechanism although he did not show any proof against the vacancy mechanism. In 1949, he proposed a new ring mechanism, as explained in Fig. 6.16 [20], where the movement of atoms will produce a ring to exchange positions. He estimated the activation energy required would be 4 eV/atom (386 kJ/mol), which is not as high as the direct interchange mechanism. In the meantime, in 1947, Smigelkas and Kirkendall reported the movement of a fiducial marker in a Cu(Zn) alloy. From the Cu(Zn) alloy, when zinc diffuses away, all the sites are not occupied by the flow of Cu from the opposite direction with the result that vacant sites are left unoccupied. In another sense, there should be a flow of vacancies opposite to the faster diffusing components (here Zn) to compensate for the difference between the Zn and Cu fluxes. Ultimately, this leads to shrinking on the brass side and swelling on the copper side so that the markers move toward the brass side. In many systems, Kirkendall pores form in the interdiffusion zone, which will be discussed in the next section.

After Zener's ring mechanism [20] proposal, Seitz [21] discussed different aspects to defend the vacancy mechanism of diffusion. The main difficulty in accepting the validity of the vacancy mechanism was because of doubts that lingered concerning existence of vacancies. However, he used the Kirkendall marker experiments as a proof of the vacancy mechanism. As already mentioned,

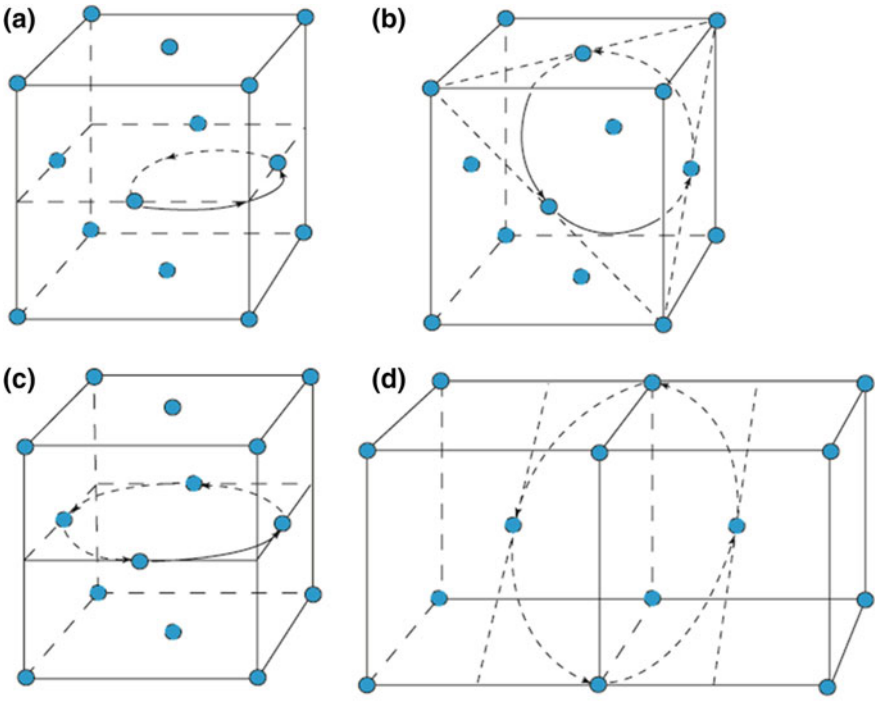

Fig. 6.16 Exchange of atoms by ring mechanism **a** two-, **b** three-, **c** four-ring in FCC lattice, and **d** four-ring in BCC lattice

R. F. Mehl's group experimented on many systems to validate Kirkendall marker experiment. On request, Mehl wrote a letter stating the outcome of the experiments to Seitz as [21]:

> (1) We have repeated this experiment some thirty times, in five metallic systems and at various temperatures. We are able to attain a very satisfactory degree of precision in all measurements, greater than that which Kirkendall attained.
> (2) We were able to demonstrate that the Matano boundary does coincide with the initial boundary in all cases, when correction is made for change of lattice parameter. This, to be sure, is, as you say, merely the law of conservation of mass, with the sole qualification that it demonstrates also that changing percentages of vacancies in the couples are not great enough to affect the experiment, as might be expected.
> (3) The fiducial markers move in all systems studied and at all temperatures by an amount which varies markedly from system to system.
> (4) For a time we entertained the thought that vapor pressure might be the controlling factor, arguing that transport by vapor along the interface between the wire and the alloy might give the movement of the wires observed. We have now investigated all types of markers including various wires, powders and foils. All of them move and by the same amount; even those which are wetted and which actually dissolve partially show the same amount of movement.

Based on these points, Seitz mentioned that [21]:

> It is clear from the start that the Kirkendall experiment cannot be explained naturally in terms of the diffusion mechanism if this is assumed to be exclusively of the interchange type, that is, if one of the possible mechanisms studied by Zener is assumed to predominate completely. For in this case an atom which shifts its position would always do so by moving from one normal position to another and would always be replaced at once by another atom. As a result the lattice array would be maintained completely intact, except for the local expansion or contraction that arises from the variation of the average size of the unit cell with composition, which does not appear to be sufficient to explain the Kirkendall effect.

6.7 Darken Analysis: Relation Between Interdiffusion and Intrinsic Diffusion Coefficients

From Kirkendall's experiment, it was apparent that the diffusion process in solid solutions could not be explained by a single diffusion coefficient. Rather, it is necessary to consider the diffusion rates of all the components. This was first treated mathematically in 1948 by Darken [22]. Almost at the same time, Hartley and Crank [23] studied the same subject and they named the diffusivities of the components as intrinsic diffusion coefficients. Seitz [24] and Bardeen [25] described the diffusion process more extensively. Before discussing the assumptions or the limitations of the Darken analysis, it is pertinent to first explain the concepts introduced by Darken. In Sect. 6.11, we have described different facts and limitations of this analysis.

Let us consider a hypothetical binary diffusion couple of components A and B of the compositions N_B^- (A-rich) and N_B^+ (B-rich), as shown in Fig. 6.17. Before annealing, fiducial (inert) markers are applied at the interface and annealed at an elevated temperature so that interdiffusion takes place. When interdiffusion starts, the markers are trapped at a certain fixed composition and cannot escape at a later stage. Thus, the movement of the markers actually indicates the movement of a particular composition. If the intrinsic diffusivity of D_B is higher than that of D_A at that marker plane (called the Kirkendall plane), then the marker plane will move to the right-hand side from the initial contact interface x_o. The intrinsic flux and the intrinsic diffusion coefficient of the components can be estimated at the Kirkendall marker plane, which are related following Fick's first law as

$$J_A = -D_A\left(\frac{\partial C_A}{\partial x}\right)_K \tag{6.56a}$$

$$J_B = -D_B\left(\frac{\partial C_B}{\partial x}\right)_K \tag{6.56b}$$

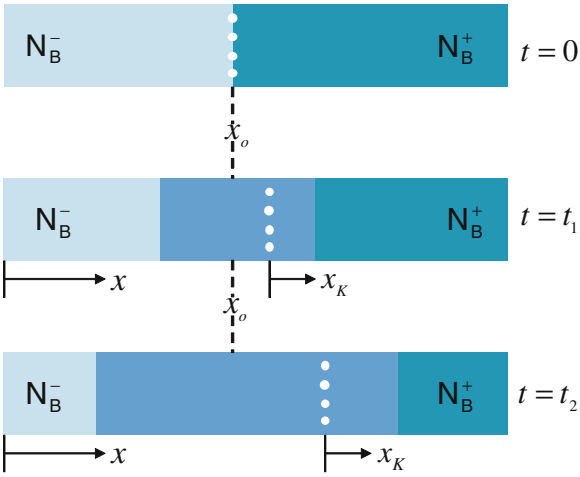

Fig. 6.17 Movement of the inert markers with the increase in annealing time, where $t_2 > t_1 > t = 0$

This Kirkendall reference plane x_K (denoted by K) is not fixed but moves relative to the laboratory frame of reference, that is, the initial contact plane x_o as shown in Fig. 6.17. Suppose the velocity of the Kirkendall marker plane is v_K. Darken [22] explained the relation between the interdiffusion fluxes at the Kirkendall marker planes $\tilde{J}_A$ and $\tilde{J}_B$ measured with respect to x_o and the intrinsic diffusion fluxes J_A and J_B measured with respect to x_K as

$$\tilde{J}_A = J_A + v_K C_A \tag{6.57a}$$

$$\tilde{J}_B = J_B + v_K C_B \tag{6.57b}$$

From Eq. 6.29, in an infinite diffusion couple, the following can be derived

$$\bar{v}_A \tilde{J}_A + \bar{v}_B \tilde{J}_B = \tilde{J}_A^{\text{vol}} + \tilde{J}_B^{\text{vol}} = 0 \tag{6.58}$$

where $\tilde{J}_A^{\text{vol}}$ and $\tilde{J}_B^{\text{vol}}$ are the volume fluxes (volume flux = partial molar volume of component, $\bar{v}_i \times$ molar flux) with respect to elements A and B, respectively. From Eq. 6.58, we arrive at

$$J_A^{\text{vol}} = \bar{v}_A \tilde{J}_A = \bar{v}_A J_A + v_K \bar{v}_A C_A \tag{6.59a}$$

$$J_B^{\text{vol}} = \bar{v}_B \tilde{J}_B = \bar{v}_B J_B + v_K \bar{v}_B C_B \tag{6.59b}$$

Substituting Eqs. 6.59a and 6.59b in Eq. 6.58 and then using the relations expressed in Eqs. 6.56a and 6.56b, we obtain

$$\begin{aligned} -\bar{v}_A D_A \left(\frac{\partial C_A}{\partial x}\right)_K + \bar{v}_A C_A v_K - \bar{v}_B D_B \left(\frac{\partial C_B}{\partial x}\right)_K + \bar{v}_B C_B v_K = 0 \\ \left(\bar{v}_A C_A + \bar{v}_B C_B\right) v_K = \bar{v}_A D_A \left(\frac{\partial C_A}{\partial x}\right)_K + \bar{v}_B D_B \left(\frac{\partial C_B}{\partial x}\right)_K \end{aligned} \tag{6.60}$$

By using the standard thermodynamic relations expressed in Eqs. 1.146 and 1.149, the following can be derived

$$v_K = -(\bar{v}_B J_B + \bar{v}_A J_A) = \bar{v}_B (D_B - D_A) \left(\frac{\partial C_B}{\partial x}\right)_K \tag{6.61a}$$

Similarly, with respect to the concentration profile of the component A, we can derive

$$v_K = \bar{v}_A (D_A - D_B) \left(\frac{\partial C_A}{\partial x}\right)_K \tag{6.61b}$$

Further from Eq. 1.150

$$v_K = \frac{\bar{v}_A \bar{v}_B}{v_m^2} (D_B - D_A) \left(\frac{\partial N_B}{\partial x}\right)_K \tag{6.62}$$

If the molar volume is constant in a phase, then Eq. 6.62 can be written as

$$v_K = (D_B - D_A) \left(\frac{\partial N_B}{\partial x}\right)_K \tag{6.63}$$

The marker velocity can also be estimated directly from the known locations of the initial contact plane x_o and the Kirkendall marker plane x_K. The relation can be derived using the Boltzmann parameter, as expressed above in Eq. 6.3.

$$\begin{aligned} \lambda_K = \lambda(C_K) = \frac{x_K - x_o}{t^{1/2}} = \frac{x_K}{t^{1/2}} \\ v_K = \frac{dx_K}{dt} = \frac{d\left(\lambda_K t^{1/2}\right)}{dt} = \frac{\lambda_K}{2t^{1/2}} = \frac{x_K - x_o}{2t} = \frac{x_K}{2t} \end{aligned} \tag{6.64}$$

Therefore, if it is possible to estimate the location of the initial contact plane correctly, we can therefore estimate the Kirkendall marker velocity using Eq. 6.64.

From Eqs. 6.57b and 6.61a, we can write

$$\begin{aligned} -\widetilde{D} \frac{\partial C_B}{\partial x} = -D_B \frac{\partial C_B}{\partial x} + C_B v_K \\ -\widetilde{D} \left(\frac{\partial C_B}{\partial x}\right)_K = -D_B \left(\frac{\partial C_B}{\partial x}\right)_K + C_B \bar{v}_B (D_B - D_A) \left(\frac{\partial C_B}{\partial x}\right)_K \end{aligned}$$

Utilizing the standard thermodynamic relations that were presented earlier in Sect. 1.18 (Eq. 1.146), this turns into

$$\begin{aligned} -\widetilde{D}\left(\frac{\partial C_B}{\partial x}\right)_K &= -(1 - C_B\bar{v}_B)D_B\left(\frac{\partial C_B}{\partial x}\right)_K - C_B\bar{v}_B D_A\left(\frac{\partial C_B}{\partial x}\right)_K \\ -\widetilde{D}\left(\frac{\partial C_B}{\partial x}\right)_K &= -(C_A\bar{v}_A D_B + C_B\bar{v}_B D_A)\left(\frac{\partial C_B}{\partial x}\right)_K \\ \widetilde{D} &= \bar{v}_A C_A D_B + \bar{v}_B C_B D_A \end{aligned} \tag{6.65}$$

In a rare case, if the molar volume is constant such that $v_m = \bar{v}_A = \bar{v}_B$, Eq. 6.65 reduces to

$$\widetilde{D} = N_A D_B + N_B D_A \tag{6.66}$$

Equation 6.66 is known as the Darken equation.

Note here that the interdiffusion coefficients can be measured at any position in a concentration profile; however, the intrinsic diffusivities can only be measured at compositions indicated by the inert markers. Therefore, Eq. 6.66 can be used only at the marker plane to estimate all the parameters such as interdiffusion and intrinsic diffusion coefficients. At other compositions, only the interdiffusion coefficient can be estimated.

The basic conditions of the previous equations are that the system is under isothermal and isobaric conditions, that no high external force is present (which might cause plastic deformation of the sample or, possibly, pressure-dependent diffusion coefficients), and time-dependent effects are absent such as the recrystallization process. This might cause a gradual transition from the grain boundary diffusion to the much slower bulk (lattice) diffusion.

6.8 Relations for the Estimation of the Intrinsic Diffusion Coefficients

As mentioned previously, the intrinsic diffusivities can be measured only at the Kirkendall plane position, x_K. Heumann [26] and van Loo [27] derived relations following which the intrinsic diffusion coefficients can be estimated from the composition profile. Wagner [6] did not derive these relations; however, on the similar line of treatment, we can derive the same relations. In this section, different ways to estimate the intrinsic diffusion coefficients will be discussed [8]. We shall first explain the Heumann approach. Next, the relations for the calculation of the intrinsic diffusion coefficients will be developed using the approach followed by Wagner for the calculation of the interdiffusion coefficients. These were derived differently by van Loo [27]. In the end, the multifoil technique will be described following which these parameters can be estimated over the whole interdiffusion zone at different compositions in a single diffusion couple instead of at one particular composition by following the previous two methods.

6.8.1 Heumann's Method

As already explained, the markers are trapped in a plane with a particular composition in a diffusion couple and move depending on the relative mobilities of the components. Since the diffusion parameters are fixed for a particular composition at a particular temperature, we can integrate the intrinsic flux of the element B crossing the Kirkendall marker plane over the annealing time t as

$$\Omega_B = -\int_0^t J_B^K dt = D_B \int_0^t \left(\frac{dC_B}{dx}\right)_K dt \tag{6.67}$$

Note here that since the element B diffuses from right to left, the intrinsic flux should be taken as negative.

$$\left(\frac{dC_B}{dx}\right)_K = \left(\frac{dC_B}{d\lambda}\right)_K \frac{d\lambda}{dx} \tag{6.68a}$$

where $\lambda = \lambda(C) = \frac{x}{t^{1/2}}$ is the Boltzmann parameter explained above in Eq. 6.3. Therefore, Eq. 6.68a can be written as

$$\left(\frac{dC_B}{dx}\right)_K = \frac{1}{t^{1/2}} \left(\frac{dC_B}{d\lambda}\right)_K \tag{6.68b}$$

As explained previously that every λ corresponds to one particular concentration in a diffusion couple, we can write Eq. 6.67 as

$$\Omega_B = D_B \left(\frac{dC_B}{d\lambda}\right)_K \int_0^t \frac{dt}{t^{1/2}} = 2D_B t^{1/2} \left(\frac{dC_B}{d\lambda}\right)_K \tag{6.69}$$

Replacing Eq. 6.68b in Eq. 6.69, we get (using the standard thermodynamic relations given in Sect. 1.18)

$$\Omega_B = 2D_B t \left(\frac{dC_B}{dx}\right)_K = 2D_B t \frac{\bar{v}_A}{v_m^2} \left(\frac{dN_B}{dx}\right)_K \tag{6.70a}$$

According to Fig. 6.18, since the direction of the diffusion of the component A is opposite to that of B—that is, from left to right—the sign for the intrinsic flux should be taken positive for component A, and we can write

$$\Omega_A = \int_0^t J_A^K dt = -2D_A t \left(\frac{dC_A}{dx}\right)_K = -2D_A t \frac{\bar{v}_B}{v_m^2} \left(\frac{dN_A}{dx}\right)_K = 2D_A t \frac{\bar{v}_B}{v_m^2} \left(\frac{dN_B}{dx}\right)_K \tag{6.70b}$$

From Eqs. 6.70a and 6.70b, we can write the ratio of the intrinsic diffusion coefficients as

$$\frac{D_B}{D_A} = \frac{\bar{v}_B}{\bar{v}_A}\frac{\Omega_B}{\Omega_A} \tag{6.71}$$

The cumulative intrinsic fluxes Ω that cross the Kirkendall marker plane are shown graphically in Fig. 6.18, which are estimated by taking the differences of the area under the concentration profile at time $t = 0$ and $t = t$, as shown in Fig. 6.18b, c.

In the A-rich side (that is, in the left-hand side), in which the component B has diffused from the right-hand side:

For $t = 0$, the area is X. For $t = t$, the area is $B + P$. Therefore, the difference is $\Omega_B = B + P - X = B + P - (P + Q) = B - Q = B + x_K\left(\frac{1}{v_m^-} - C_A^-\right)$, since x_K is negative in this example.

In the B-rich side, that is, in the right-hand side, in which the component A has diffused from the left-hand side:

For $t = 0$, the area is Y. For $t = t$, the area is $A + R + S$. Consequently, the difference is $\Omega_A = A + R(\text{note } S = Y) = A - x_K C_A^+$. Therefore,

$$\begin{aligned}
\frac{D_B}{D_A} &= \frac{\bar{v}_B}{\bar{v}_A}\frac{B + x_K\left(\frac{1}{v_m^-} - C_A^-\right)}{A - x_K C_A^+} = \frac{\bar{v}_B}{\bar{v}_A}\frac{B + x_K\left(\frac{1}{v_m^-} - \frac{N_A^-}{v_m^-}\right)}{A - x_K\frac{N_A^+}{v_m^+}} \\
\frac{D_B}{D_A} &= \frac{\bar{v}_B}{\bar{v}_A}\frac{\int_{x^{-\infty}}^{x_K}(C_A^- - C_A)dx + x_K\left(\frac{1}{v_m^-} - \frac{N_A^-}{v_m^-}\right)}{\int_{x_K}^{x^{+\infty}}(C_A - C_A^+)dx - x_K\frac{N_A^+}{v_m^+}}
\end{aligned} \tag{6.72a}$$

Note that for a constant molar volume, $(v_m = \bar{v}_A = \bar{v}_B)$, and Eqs. 6.72a and 6.72b, following similar analysis using Fig. 6.17d, e, reduces to

$$\begin{aligned}
\frac{D_B}{D_A} &= \frac{B_1 + x_K\left(1 - N_A^-\right)}{A_1 - x_K N_A^+} \\
\frac{D_B}{D_A} &= \frac{\int_{x^{-\infty}}^{x_K}(N_A^- - N_A)dx + x_K\left(1 - N_A^-\right)}{\int_{x_K}^{x^{+\infty}}(N_A - N_A^+)dx - x_K N_A^+}
\end{aligned} \tag{6.72b}$$

Note here that the need for locating the initial contact plane (i.e., the Matano plane), for the calculation of the intrinsic diffusion coefficients, is similar to its need for the calculation of the interdiffusion coefficient using the Matano–Boltzmann analysis, as explained previously in Sect. 6.1. It is not necessary only in the case of diffusion couples with pure components as the end members, since $N_A^- = 1$

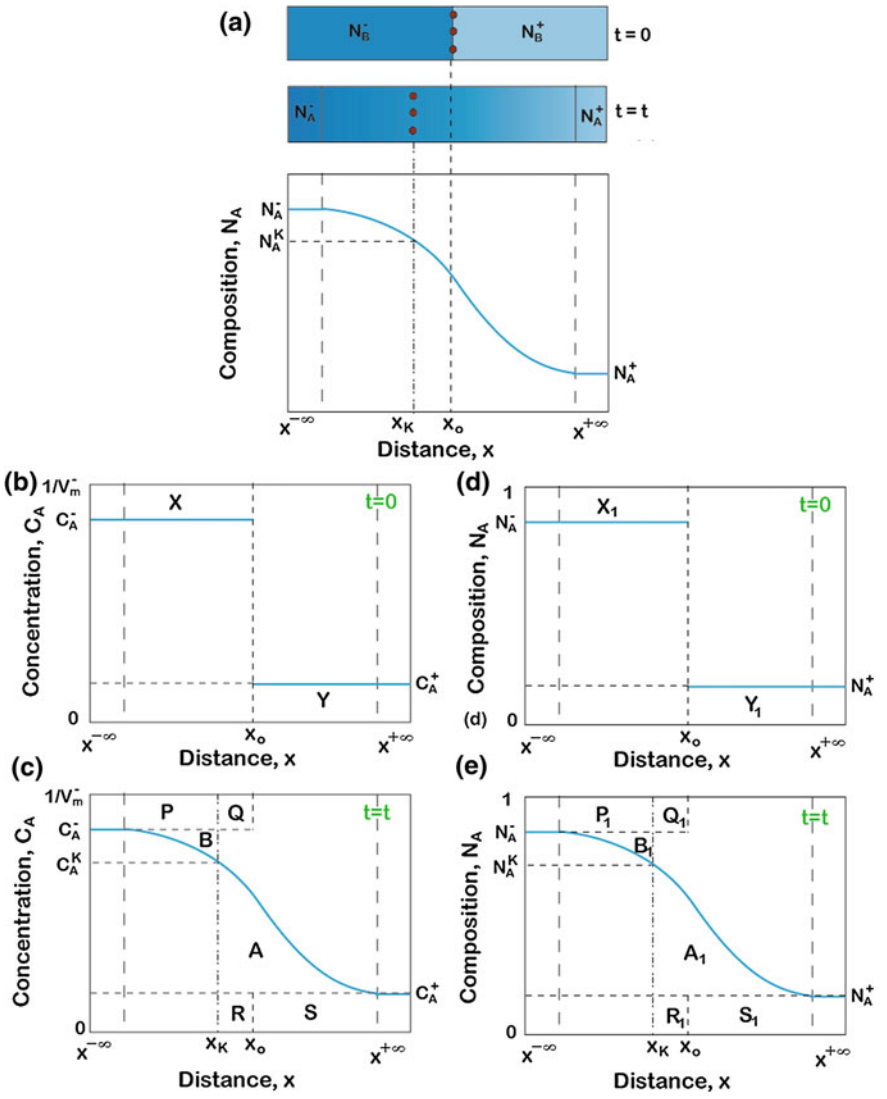

Fig. 6.18 Explanation of the Huemman's approach for estimating the intrinsic diffusion coefficients. **a** An imaginary diffusion couple with corresponding composition profile, **b** Concentration profile before interaction, **c** plot of concentration profile by converting it to $C_A = N_A/V_m$ **d** composition profile, and **e** estimation of the intrinsic diffusion coefficients after considering constant molar volume

(for pure A) and $N_A^+ = 0$ (for pure B). One should be careful about taking proper signs in the above equations, when the marker plane is found in other side of the Matano plane, especially in an incremental couple.

6.8.2 Relations Developed with the Help of Wagner's Treatment

Equation 6.39a and 6.39b at the Kirkendall marker plane can be written as

$$\frac{1}{2t}\left(N_B^+ - N_B^-\right)\left[-\frac{\lambda^K Y_B^K}{v_m^K} + \int_{\lambda^{-\infty}}^{\lambda^K} \frac{Y_B}{v_m} d\lambda\right] = \frac{1}{t^{\frac{1}{2}}}\left[N_B^- \widetilde{J}_A^K - \left(1 - N_B^-\right)\widetilde{J}_B^K\right] \tag{6.73a}$$

$$\frac{1}{2t}\left(N_B^+ - N_B^-\right)\left[-\frac{\lambda^K\left(1 - Y_B^K\right)}{v_m^K} - \int_{\lambda^K}^{\lambda^{+\infty}} \frac{\left(1 - Y_B\right)}{v_m} d\lambda\right] = \frac{1}{t^{\frac{1}{2}}}\left[-N_B^+ \widetilde{J}_A^K + \left(1 - N_B^+\right)\widetilde{J}_B^K\right] \tag{6.73b}$$

To write a relation with respect to $\widetilde{J}_B^K$ only, we multiply Eq. 6.73a by N_B^+ and Eq. 6.73b by N_B^-. Subsequently, we add them and after rearranging, we get [8]

$$\frac{1}{2t}\left(N_B^+ - N_B^-\right)\left[-\lambda^K\left\{\frac{Y_B^K}{v_m^K}N_B^+ + \frac{\left(1 - Y_B^K\right)}{v_m^K}N_B^-\right\} + \left\{N_B^+ \int_{\lambda^{-\infty}}^{\lambda^K} \frac{Y_B}{v_m} d\lambda - N_B^- \int_{\lambda^K}^{\lambda^{+\infty}} \frac{\left(1 - Y_B\right)}{v_m} d\lambda\right\}\right]$$
$$= \frac{1}{t^{\frac{1}{2}}}\left[-N_B^+\left(1 - N_B^-\right)\widetilde{J}_B^K + N_B^-\left(1 - N_B^+\right)\widetilde{J}_B^K\right]$$

Replacing $Y_B^K = \frac{N_B^K - N_B^-}{N_B^+ - N_B^-}$ and $1 - Y_B^K = \frac{N_B^+ - N_B^K}{N_B^+ - N_B^-}$

$$\frac{1}{2t}\left(N_B^+ - N_B^-\right)\left[-\lambda^K \frac{N_B^K}{v_m^K} + \left\{N_B^+ \int_{\lambda^{-\infty}}^{\lambda^K} \frac{Y_B}{v_m} d\lambda - N_B^- \int_{\lambda^K}^{\lambda^{+\infty}} \frac{\left(1 - Y_B\right)}{v_m} d\lambda\right\}\right] = \frac{1}{t^{1/2}}\left[-\left(N_B^+ - N_B^-\right)\widetilde{J}_B^K\right]$$

$$\widetilde{J}_B^K = \frac{t^{1/2}}{2t}\left[\lambda^K \frac{N_B^K}{v_m^K} - N_B^+ \int_{\lambda^{-\infty}}^{\lambda^K} \frac{Y_B}{v_m} d\lambda + N_B^- \int_{\lambda^K}^{\lambda^{+\infty}} \frac{\left(1 - Y_B\right)}{v_m} d\lambda\right]$$

$$\widetilde{J}_B^K = \frac{t^{1/2}}{2t}\lambda^K \frac{N_B^K}{v_m^K} - \frac{t^{1/2}}{2t}\left[N_B^+ \int_{\lambda^{-\infty}}^{\lambda^K} \frac{Y_B}{v_m} d\lambda - N_B^- \int_{\lambda^K}^{\lambda^{+\infty}} \frac{\left(1 - Y_B\right)}{v_m} d\lambda\right]$$

By replacing the Boltzmann parameter $\lambda^K = \frac{x_K}{t^{1/2}}$ and then using the relation of the velocity of the marker plane $v_K = \frac{x_K}{2t}$, as expressed in Eq. 6.64, we arrive at

$$\widetilde{J}_B^K = v_K C_B^K - \frac{t^{1/2}}{2t}\left[N_B^+ \int_{\lambda^{-\infty}}^{\lambda^K} \frac{Y_B}{v_m} d\lambda - N_B^- \int_{\lambda^K}^{\lambda^{+\infty}} \frac{(1-Y_B)}{v_m} d\lambda\right]$$

Note that the concentration of the marker plane is $C_B^K = \frac{N_B^K}{v_m^K}$

From the Boltzmann parameter, we know that $d\lambda = \frac{dx}{t^{1/2}}$ and we can write

$$\widetilde{J}_B^K = v_K C_B^K - \frac{1}{2t}\left[N_B^+ \int_{x^{-\infty}}^{x_K} \frac{Y_B}{v_m} dx - N_B^- \int_{x_K}^{x^{+\infty}} \frac{(1-Y_B)}{v_m} dx\right]$$

Compared to Eq. 6.57b, the intrinsic flux of the element B at the Kirkendall marker plane can be written as

$$J_B^K = -\frac{1}{2t}\left[N_B^+ \int_{x^{-\infty}}^{x_K} \frac{Y_B}{v_m} dx - N_B^- \int_{x_K}^{x^{+\infty}} \frac{(1-Y_B)}{v_m} dx\right]$$

From Fick's first law, it follows that

$$D_B = \frac{1}{2t}\left(\frac{\partial x}{\partial C_B}\right)_K \left[N_B^+ \int_{x^{-\infty}}^{x_K} \frac{Y_B}{v_m} dx - N_B^- \int_{x_K}^{x^{+\infty}} \frac{(1-Y_B)}{v_m} dx\right] \tag{6.74}$$

Further, using the standard thermodynamic relations given in Eq. 1.150

$$D_B = \frac{1}{2t}\frac{v_m^2}{\bar{v}_A}\left(\frac{\partial x}{\partial N_B}\right)_K \left[N_B^+ \int_{x^{-\infty}}^{x_K} \frac{Y_B}{v_m} dx - N_B^- \int_{x_K}^{x^{+\infty}} \frac{(1-Y_B)}{v_m} dx\right] \tag{6.75}$$

Equation 6.75 can be used if we wish to determine the intrinsic diffusion coefficients using the profiles N_B versus x, Y_B/v_m versus x, and $(1-Y_B)/v_m$ versus x.

The equation for the interdiffusion flux $\widetilde{J}_A$ can be written in the same way. Multiplying Eq. 6.73a by $(1-N_B^+)$ and Eq. 6.73b by $\left(1-N_B^-\right)$ and following the similar procedure, the intrinsic diffusivity for the component A can be derived as

$$D_A = \frac{1}{2t}\left(\frac{\partial x}{\partial C_A}\right)_K \left[N_A^+ \int_{x^{-\infty}}^{x_K} \frac{Y_B}{v_m} dx - N_A^- \int_{x_K}^{x^{+\infty}} \frac{(1-Y_B)}{v_m} dx\right] \tag{6.76}$$

By once again utilizing the Eq. 1.150, the following is obtained

$$D_A = \frac{1}{2t}\frac{v_m^2}{\bar{v}_B}\left(\frac{\partial x}{\partial N_A}\right)_K \left[N_A^+ \int_{x^{-\infty}}^{x_K} \frac{Y_B}{v_m} dx - N_A^- \int_{x_K}^{x^{+\infty}} \frac{(1-Y_B)}{v_m} dx\right] \tag{6.77}$$

From Eqs. 6.75 and 6.77, we can write

$$\frac{D_B}{D_A} = \frac{\bar{v}_B}{\bar{v}_A}\left[\frac{N_B^+ \int_{x^{-\infty}}^{x_K} \frac{Y_B}{v_m} dx - N_B^- \int_{x_K}^{x^{+\infty}} \frac{(1-Y_B)}{v_m} dx}{-N_A^+ \int_{x^{-\infty}}^{x_K} \frac{Y_B}{v_m} dx + N_A^- \int_{x_K}^{x^{+\infty}} \frac{(1-Y_B)}{v_m} dx}\right] = \frac{\bar{v}_B}{\bar{v}_A}\left[\frac{N_B^+ R - N_B^- S}{-N_A^+ R - N_A^- S}\right] \tag{6.78}$$

The calculation procedure is shown in Fig. 6.19. R and S are the areas as shown in the figure. Note here that, unlike the Heumann method, there is no need to locate the initial contact position, a task which is not easily accomplished.

In general, instead of estimating the intrinsic diffusion coefficients using Eqs. 6.75 and 6.77 directly, one can estimate the interdiffusion coefficient using Eq. 6.45 and the ratio of diffusivities using Eq. 6.78. Afterward, the intrinsic diffusion coefficients can be estimated using Eqs. 6.65 or 6.66. Note that it is just a matter of choice.

6.8.3 *Multifoil Technique to Estimate the Intrinsic Diffusion Coefficients*

In the example above, we have seen that the intrinsic diffusion coefficients could be estimated only at the Kirkendall marker plane only, since this is the only marked plane that moved from the beginning depending on the relative mobilities of the components. Therefore, many diffusion couples with different end-member compositions need to be prepared (leading to marker planes at different compositions), if we want to determine the intrinsic diffusion coefficients at different compositions. This was done in the β phase of the Ni–Al system [28], which could be a tedious task depending on the system. The multifoil technique is developed in such a way that we are able to estimate these parameters over the whole composition range of interest from only a single experiment. This is explained with the help of experimental results in the Ni–Pt system [29]. In this technique, many foils of two dissimilar materials are stacked together. Therefore, it is relatively easy to follow this technique if the foils could be made. Fortunately, this is relatively straightforward in the case of metals. The number of foils used for these experiments is decided based on the thickness of the interdiffusion zone developed in the bulk diffusion couple experiments. After the interdiffusion process, according to the boundary condition of the equations, some unaffected parts should be left at the ends of the diffusion couple. The back scattered electron image of the

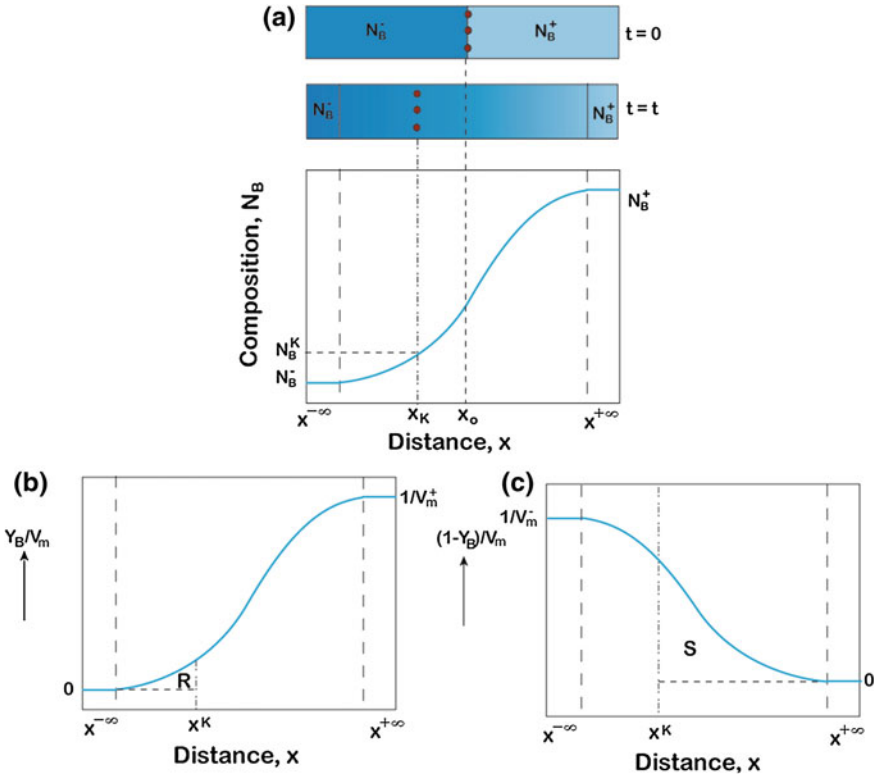

Fig. 6.19 Explanation of van Loo's approach for the estimation of the intrinsic diffusion coefficients. **a** Diffusion couple with corresponding composition profile, **b** Y_B/v_m versus x plot, and **c** $(1 - Y_B)/v_m$ versus x plot

interdiffusion zone developed is shown in Fig. 6.20a. The velocity v of the markers at different planes can be determined by the relation developed by Levasseur and Philibert [30], Cornet [31] and van Loo et al. [32]

$$v = \frac{1}{2t}\left(y - x_o \frac{dy}{dx_o}\right) \tag{6.79}$$

Here, x_o is the initial position of markers before interdiffusion and x is the new position after the interdiffusion, such that $y = (x - x_o)$ is the net displacement. It can be seen that for $x_0 = 0$ (i.e., the Kirkendall plane), according to Eq. 6.79, $v = y/2t$, which is the Kirkendall marker displacement similar to Eq. 6.64.

The composition profile of the Pt/Ni diffusion couple is shown in Fig. 6.20b. The displacement of the markers is measured using the backscattered electron

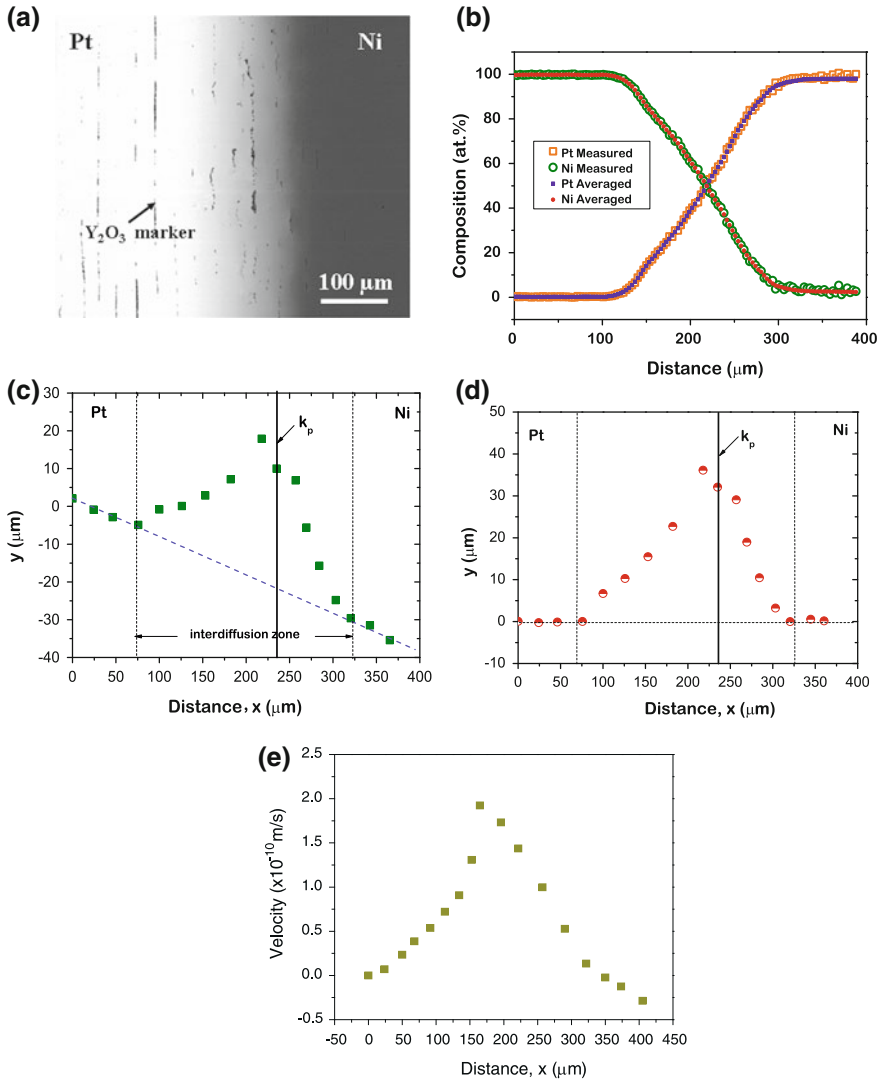

Fig. 6.20 Explanation of procedure for estimating intrinsic diffusion coefficients using multifoil technique. **a** Diffusion couple, **b** composition profile, **c** displacement curve, **d** corrected displacement curve, and **e** the velocity curve of markers [29]

image. All variations of y with x are plotted in Fig. 6.20c. The markers outside the interdiffusion zone also experienced some displacement due to deformations, i.e., creep at annealing temperature. For that, a correction procedure, suggested by Heumann and Grundhoff [33] (followed by van Dal et al. [34]) for plastic deformation, is used in this study. A baseline is drawn which passes through the unreacted parts of the end members, and the difference between the position of

markers and this baseline gives the actual displacement of the markers, which is shown in Fig. 6.20d. Thus, we assume the deformation rate of the end members of the couple to be equal and constant. The difference between the marker displacement measured in the diffusion couple and the value corresponding to the baseline—i.e., the dashed line in Fig. 6.20c giving the actual marker shift (plotted in Fig. 6.20d)—was constructed. It should be noted that the maximum displacement need not to be necessarily at the Kirkendall marker plane only, as is found in this system.

The displacement is then plotted versus x_0 (= $x - y$) to determine dy/dx_o. Following on from this, the velocities of the different marker planes are estimated from Eq. 6.79 as plotted in Fig. 6.20e. Furthermore, we can derive

$$\frac{D_B}{D_A} = \frac{\bar{v}_B D_B}{\bar{v}_B D_A}$$
$$\frac{D_B}{D_A} = \frac{\bar{v}_B(\bar{v}_B C_B + \bar{v}_A C_A) D_B}{\bar{v}_B(\bar{v}_B C_B + \bar{v}_A C_A) D_A}$$

Since, as shown previously in Eq. 1.146, $\bar{v}_B C_B + \bar{v}_A C_A = 1$

$$\frac{D_B}{D_A} = \frac{\bar{v}_B(\bar{v}_A C_A D_B + \bar{v}_B C_B D_B)}{\bar{v}_B \bar{v}_A C_A D_A + \bar{v}_B \bar{v}_B C_B D_A}$$
$$\frac{D_B}{D_A} = \frac{\bar{v}_B[(\bar{v}_A C_A D_B + \bar{v}_B C_B D_A) + \bar{v}_B C_B (D_B - D_A)]}{\bar{v}_B(\bar{v}_A C_A D_B + \bar{v}_B C_B D_A) - \bar{v}_A \bar{v}_B C_A (D_B - D_A)}$$

Since according to Eq. 6.65 $\widetilde{D} = \bar{v}_A C_A D_B + \bar{v}_B C_B D_A$, we can write

$$\frac{D_B}{D_A} = \frac{\bar{v}_B\left[\widetilde{D} + \bar{v}_B C_B (D_B - D_A)\right]}{\bar{v}_B \widetilde{D} - \bar{v}_A \bar{v}_B C_A (D_B - D_A)}$$
$$\frac{D_B}{D_A} = \frac{\widetilde{D} + \bar{v}_B C_B (D_B - D_A)}{\widetilde{D} - \frac{\bar{v}_A \bar{v}_B}{\bar{v}_B} C_A (D_B - D_A)}$$
$$\frac{D_B}{D_A} = \frac{\widetilde{D}\left(\frac{\partial C_B}{\partial x}\right) + \bar{v}_B (D_B - D_A)\left(\frac{\partial C_B}{\partial x}\right) C_B}{\widetilde{D}\left(\frac{\partial C_B}{\partial x}\right) - \bar{v}_B (D_B - D_A)\left(\frac{\partial C_B}{\partial x}\right) \frac{\bar{v}_A}{\bar{v}_B} C_A}$$

Since according to Eqs. 6.61a and 6.61b $v = \bar{v}_B (D_B - D_A)\left(\frac{\partial C_B}{\partial x}\right)$, we can write

$$\frac{D_B}{D_A} = \frac{\widetilde{D}(\partial C_B/\partial x) + v C_B}{\widetilde{D}(\partial C_B/\partial x) - v \frac{\bar{v}_A}{\bar{v}_B} C_A}$$
$$\frac{D_B}{D_A} = \frac{1 + \frac{v}{\widetilde{D}(\partial C_B/\partial x)} C_B}{1 - \frac{v}{\widetilde{D}(\partial C_B/\partial x)} C_A \frac{\bar{v}_A}{\bar{v}_B}}$$

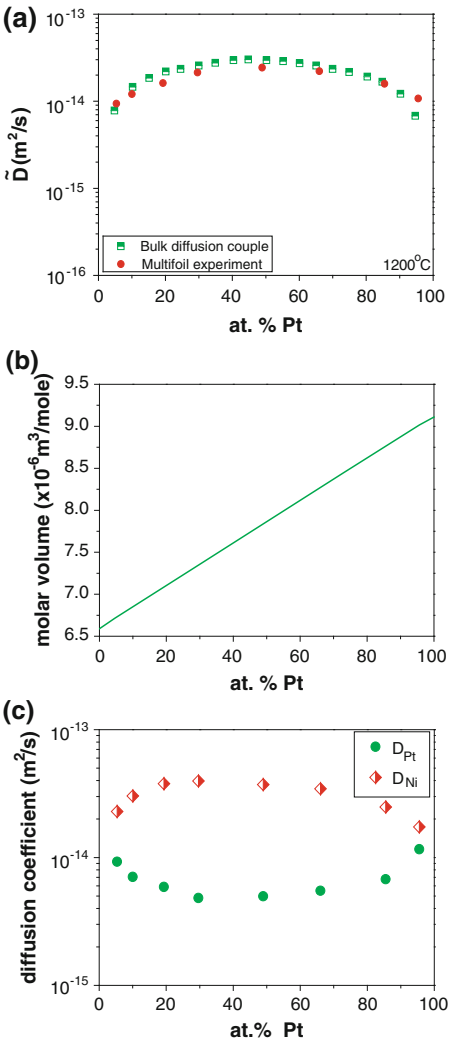

Fig. 6.21 Estimation of diffusion parameters following multifoil technique as discussed in previous figure: **a** interdiffusion coefficients, **b** molar volume, and **c** the intrinsic diffusion coefficients in the Ni–Pt system [29]

$$\frac{D_B}{D_A} = \frac{1 + f\,C_B}{1 - f\,C_A(\bar{v}_A/\bar{v}_B)} \quad \text{where } f = \frac{v}{\widetilde{D}(\partial C_B/\partial x)} \tag{6.80}$$

Therefore, from the values of v, as shown in Fig. 6.20e, it is possible to estimate D_B/D_A. After estimating $\widetilde{D}$ following previously explained approaches, we can the estimate intrinsic diffusion coefficients using Eq. 6.65. The interdiffusion coefficients estimated in a bulk diffusion couple must be compared with the estimated values from a multifoil experiment in order to validate the results. It can be seen in Fig. 6.21a that the interdiffusion coefficients are more or less the same. This helps to understand if stacking of foils created any problem in the diffusion couple. The

variation of the molar volume is shown in Fig. 6.21b. The intrinsic diffusion coefficients that were subsequently estimated by multifoil technique are given in Fig. 6.21c.

6.9 Different Ways to Detect the Kirkendall Marker Plane

As already explained, it is important to use inert markers at the mating interface of a diffusion couple and anneal it to detect the Kirkendall marker plane after interdiffusion. Following, these inert particles are found under a scanning electron microscope (SEM) by image analysis or by detecting the X-ray peak originated from the material used as marker in an energy dispersive spectrometer (EDS) or wavelength dispersive spectrometer (WDS) detectors. Depending on the system in which they are used, different materials are used as markers, and these materials can be used in wire or powder form. Powders are used more often because of ease of use. It is important to note that the markers selected do not react with the diffusing components, which will otherwise not move ideally depending on their relative mobilities. Markers are made from should be impervious to the diffusing components, and there should be enough space between them to not hinder the movement of the diffusing components. Marker size should be much smaller than the total interdiffusion zone thickness. On the other hand, the markers should not be so small that they are dragged along by the grain boundaries, a phenomenon we have often witnessed, especially when we have used the particles in powder form and the particle size was less than 0.1 μm. As already mentioned, Kirkendall and many others preferred to use Mo or W wires as inert markers. Due to the difficulties in placing the wires, powders are used more commonly these days. These are dispersed in acetone, and a small drop is placed on a metallographically prepared smooth surface of one of the couple halves. The acetone evaporates leaving the particles distributed evenly on the surface. Distribution could be checked in an optical microscope. In general, we prefer, on average around 20–30 μm spacing between the particles for average particle size of 1–2 μm. However, strictly speaking, it is difficult to achieve very good control over the distribution of the particles and the desired distribution pattern might not be achieved in first attempt. This process is repeated after cleaning the surface with acetone until we have an acceptable distribution pattern. It is not possible to achieve a perfectly even distribution; however, having too many particles clumped together in many locations should be avoided. Once satisfied, another couple half is placed above and clamped in a fixture to place it in the calibrated furnace for annealing. According to our experience, a marker size of 1–5 μm works well depending on the system and the thickness of the interdiffusion zone. Different refractory metal and oxide powders such as W, Mo, ThO_2, TiO_2, and Y_2O_3 are used in metallic systems. Similarly, Au and Pt particles are used in oxides. ThO_2 acts as the best marker in most of the metallic systems, since this is one of the

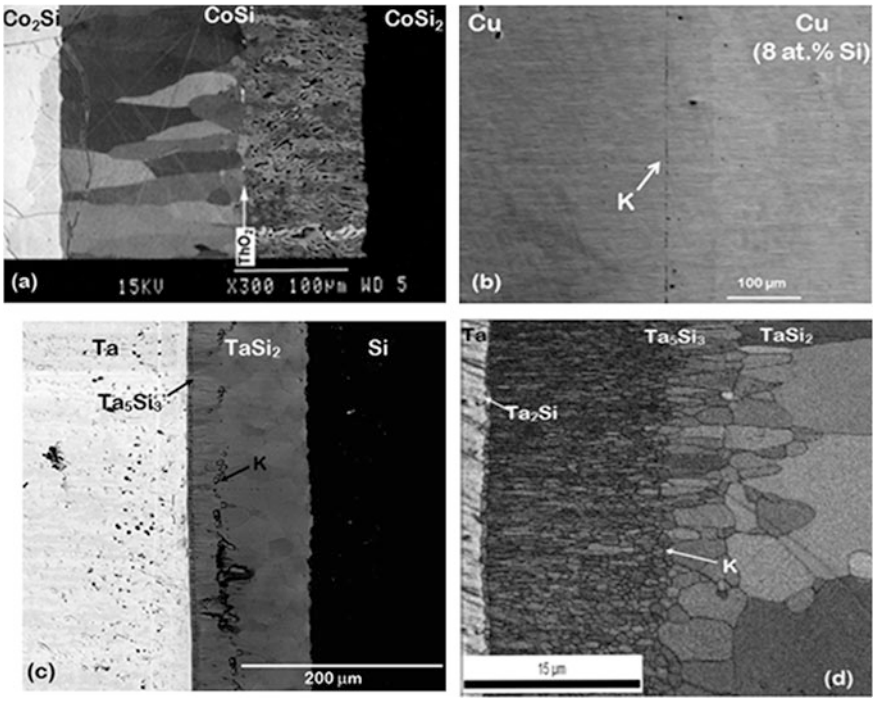

Fig. 6.22 Kirkendall marker plane positions (*K*) are shown in **a** $Co_2Si/CoSi_2$ [36, 37], **b** Cu/Cu(8 at.% Si), **c** Ta/Si, and **d** $Ta/TaSi_2$ diffusion couples [38]

highly inert oxides. Furthermore, very high atomic number of Th makes it easily detectable with a white contrast in a scanning electron image, as shown in Fig. 6.22a [35–37]. Sometimes, debris accumulated during grinding and polishing on the surface also acts as inert markers and is found at the Kirkendall marker plane along with the inert particles that have been deliberately used. Even the scratches act as a negative surface and are found at this plane in the form of a line of pores, since the components cannot diffuse through it. For example, as Fig. 6.22b [9] demonstrates, in the Cu/(Cu-8 at.% Si), the location of the marker plane could be detected easily by the presence of pores and TiO_2 particles on the same line. In fact, the presence of such a straight line of pores could be considered confidently as the Kirkendall plane even when markers are not used. The location of the marker plane could also be located with the help of duplex morphology that develops in the interdiffusion zone. As explained in greater detail later in Chap. 8, this indicates the location of the marker plane, as it is found in Fig. 6.22c [38]. This is frequently of great help, especially in situations when we cannot use markers. For example, in many refractory metal–silicon systems, we could not grow the interdiffusion zone when inert particles were used since both the materials are very hard and do not make a successful contact if markers are used. In that case, by detecting the presence of duplex morphology, it is possible to identify the

location of the Kirkendall marker planes, as shown in the Ta/Si and $TaSi_2$/Ta diffusion couples, given in Fig. 6.22c, d [38]. In the Ta/Si couple, the location of the Kirkendall marker plane could easily be detected by the presence of both duplex morphology and the line of pores. Duplex morphology is found since the phase layer grows differently from the two interfaces. Larger grains are found on the Si side since the phase layer grows on this single crystal. On the other hand, another sublayer grows on the Ta_5Si_3 phase with much finer grains since Ta_5Si_3 possesses very small grains. A similar duplex morphology is found in the Ta_5Si_3 phase that is grown between Ta and $TaSi_2$. Grain morphology could be detected by different techniques, for example, by etching with an etchant under a polarized microscope [35–37], or an electron backscattered diffraction (EBSD) detector [38]. Figure 6.22c is an SEM image taken after etching with an acid mixture of HNO_3 and HF, and Fig. 6.22d is a non-indexed EBSD image.

6.10 Phenomenological Equations: Darken's Analysis for the Relations Between the Interdiffusion, Intrinsic, and Tracer Diffusion Coefficients

To gain deeper insights into the phenomenological process, it is crucial to understand this process from a thermodynamical point of view. As discussed earlier in Chap. 4, we have seen how the chemical potential gradient better explains the diffusion process compared to the concentration gradient. In fact, in n component system, an equilibrium condition could be defined with respect to T, P, and the chemical potential of the components μ_1, $\mu_2 \ldots \mu_n$. Therefore, as previously covered in Chaps. 1 and 4, the flux of the element i can be expressed with respect to its gradient as

$$J_i = -L_{i1}\frac{d\mu_1}{dx} - L_{i2}\frac{d\mu_2}{dx} \ldots - L_{in}\frac{d\mu_n}{dx} - L_{iT}\frac{dT}{dx} - L_{iP}\frac{dP}{dx} \tag{6.81a}$$

Similarly, if any other driving forces such as electric potential, hydrostatic stress, etc., are present, then the additional terms should be added. If we consider the experimental condition under constant temperature and pressure—with no other external driving forces present—then, in a one-dimensional AB binary diffusion profile, we can write

$$\begin{aligned} J_A &= -L_{AA}\frac{d\mu_A}{dx} - L_{AB}\frac{d\mu_B}{dx} - L_{AV}\frac{d\mu_v}{dx} \\ J_B &= -L_{BA}\frac{d\mu_A}{dx} - L_{BB}\frac{d\mu_B}{dx} - L_{BV}\frac{d\mu_v}{dx} \\ J_v &= -L_{VA}\frac{d\mu_A}{dx} - L_{VB}\frac{d\mu_B}{dx} - L_{VV}\frac{d\mu_v}{dx} \end{aligned}$$

Note here that this last equation is relevant when a vacancy diffusion mechanism is operative. However when the vacancies are in equilibrium, the chemical

potential of the vacancy should, therefore, be considered to be zero. As mentioned earlier, we have not discussed the assumptions of Darken analysis. Nonetheless, it takes mainly two assumptions: (i) vacancies remain in equilibrium at every concentration of the interdiffusion zone and (ii) the off-diagonal phenomenological constants are zero. Therefore, we have $\mu_v \approx 0, \frac{d\mu_v}{dx} \approx 0, L_{AB} = 0$ and $L_{BA} = 0$, meaning that the flux of the components can be written as

$$J_A = -L_{AA} \frac{d\mu_A}{dx} \tag{6.81b}$$

$$J_B = -L_{BB} \frac{d\mu_B}{dx} \tag{6.81c}$$

If F is the force due to the chemical potential an dv_B is the velocity of the component B, then the mobility of B can be written as $M_B = v_B\ F$. Therefore, the flux of element B can be written as

$$J_B = C_B v_B = M_B F C_B \tag{6.82}$$

Since the force is equal to the chemical potential gradient where the atoms diffuse down the gradient, we can write $F = -\frac{d\mu_B}{dx}$. Consequently, Eq. 6.82 can be written as

$$J_B = -M_B C_B \frac{d\mu_B}{dx} \tag{6.83}$$

In comparison with Eq. 6.81c, the phenomenological constant can be written as $L_B = M_B C_B$. When comparing it with Fick's first law, we can write

$$D_B = M_B C_B \frac{d\mu_B}{dC_B} = M_B \frac{N_B}{v_m} \frac{d\mu_B}{dC_B} \tag{6.84}$$

Further using the standard thermodynamic relation in Eq. 1.150

$$D_B = \frac{v_m}{\bar{v}_A} M_B N_B \frac{d\mu_B}{dN_B} = \frac{v_m}{\bar{v}_A} M_B \frac{d\mu_B}{d \ln N_B} \tag{6.85}$$

Furthermore,

$$\mu_B = \mu_B^o + RT\ \ln a_B = \mu_B^o + RT(\ln N_B + \ln \gamma_B) \tag{6.86}$$

Substituting Eq. 6.86 in Eq. 6.85

$$D_B = \frac{v_m}{\bar{v}_A} M_B RT \frac{d\ \ln a_B}{d\ \ln N_B} = \frac{v_m}{\bar{v}_A} M_B RT \left(1 + \frac{d\ \ln \gamma_B}{d\ \ln N_B}\right) \tag{6.87}$$

In the measurement of the tracer diffusion coefficient, as explained previously in Chap. 5, there is no driving force for diffusion. Moreover, since this is a measurement in a single-composition alloy, the volume terms are unnecessary. Thus, it is possible to write the tracer diffusion coefficient with respect to the mobility term from Eq. 6.87 as

$$D_B^* = M_B^* RT \tag{6.88}$$

The above relation is known as the Nernst–Einstein relation.

Substituting Eq. 6.88 in Eq. 6.87, we get

$$D_B = D_B^* \frac{v_m}{\bar{v}_A} \frac{d\ln a_B}{d\ln N_B} = D_B^* \frac{v_m}{\bar{v}_A} \left(1 + \frac{d\ln \gamma_B}{d\ln N_B}\right) \tag{6.89a}$$

In the same way, for the component A

$$D_A = D_A^* \frac{v_m}{\bar{v}_B} \frac{d\ln a_A}{d\ln N_A} = D_A^* \frac{v_m}{\bar{v}_B} \left(1 + \frac{d\ln \gamma_A}{d\ln N_A}\right) \tag{6.89b}$$

According to the Gibbs–Duhem relation derived much earlier in Chap. 1 (Eqs. 1.134 and 1.139), we know that $\frac{d\ln a_A}{d\ln N_A} = \frac{d\ln a_B}{d\ln N_B}$. Substituting Eqs. 6.89a and 6.89b in Eq. 6.65, we arrive at

$$\widetilde{D} = \left(N_A D_B^* + N_B D_A^*\right)\left(\frac{d\ln a_B}{d\ln N_B}\right) \tag{6.90}$$

This relation was first proposed by Darken [22].

The ratio of intrinsic diffusivities in terms of tracer diffusivities can be expressed by

$$\frac{D_B}{D_A} = \frac{\bar{v}_B}{\bar{v}_A} \frac{D_B^*}{D_A^*} \tag{6.91}$$

Comparing Eqs. 6.78 and 6.91

$$\frac{D_B^*}{D_A^*} = \left[\frac{N_B^+ \int_{x^{-\infty}}^{x_K} \frac{Y_B}{v_m} dx - N_B^- \int_{x_K}^{x^{+\infty}} \frac{(1-Y_B)}{v_m} dx}{-N_A^+ \int_{x^{-\infty}}^{x_K} \frac{Y_B}{v_m} dx + N_A^- \int_{x_K}^{x^{+\infty}} \frac{(1-Y_B)}{v_m} dx}\right] \tag{6.92}$$

Using this relation, it is possible to estimate the ratio of tracer diffusion coefficients at the Kirkendall marker plane using the composition profile. The velocity of the Kirkendall marker plane from Eqs. 6.61a, 6.89a and 6.89b can be written as

$$v_K = \bar{v}_B \left(D_B^* \frac{v_m}{\bar{v}_A} - D_A^* \frac{v_m}{\bar{v}_B} \right) \Theta \left(\frac{\partial C_B}{\partial x} \right)_K \tag{6.93}$$

where $\Theta = \frac{d \ln a_A}{d \ln N_A} = \frac{d \ln a_B}{d \ln N_B}$ is known as the thermodynamic factor.

6.11 Limitations of the Relations Developed by Darken and Manning's Correction for the Vacancy Wind Effect

After the above analysis by Darken, Bardeen [25] made a thorough analysis and explained that the relations developed by Darken can be derived by considering enough sources and sinks for vacancies to maintain this equilibrium ($d\mu_v/dx \approx 0$) over the interdiffusion zone. Subsequently, Seitz [39] showed further that everywhere inside the interdiffusion zone vacancies should be at equilibrium ($\mu_v \approx 0$). He further explained that Darken's relations (Eq. 6.66) could be used in both substitutional and interstitial diffusion. Bardeen and Herring [40] argued (based on the experimental results available in the 1950s) that Darken's relations are fulfilled in most of the diffusion couples. Therefore, a volume of vacancies should be created on one side of the couple and absorbed on the other side. This volume is equivalent to the volume shift by the Kirkendall marker plane, that is, the shift distance $x_K = x_K - x_o$ multiplied by the cross-sectional area of the couple. This point is clarified in Fig. 6.23. In this example, the component A has a higher diffusion rate compared to B. Therefore, the vacancies flow in the same direction of the component B, which has the lower diffusion rate of the two. Following Eqs. 1.149 and 6.61a, we can write [41]

$$v_K = v_m J_V = -(\bar{v}_B J_B + \bar{v}_A J_A) \tag{6.94}$$

The dJ_V/dx versus x plot gives the idea in which part vacancies are created (positive) and absorbed (negative). Analysis indicates that grain boundaries, pores, cracks [39], and interfaces [41] act as a source and sink for vacancies. Doo and Balluffi [42] presented the proof on the role of edge dislocations related to the Kirkendall marker shift. Its role as sink and source is explained more clearly in Fig. 6.24 with the aid of a schematic illustration of the lattice planes and dislocations. The vacancies are flowing from right to left since there is a net flux of atoms from left to right. On the left, the dislocations act as sinks, where the atoms are replaced by vacancies from the extra plane. On the right, they act as sources, where the atoms are added to the extra planes [43]; that is, the vacancies are created and move to neighboring positions.

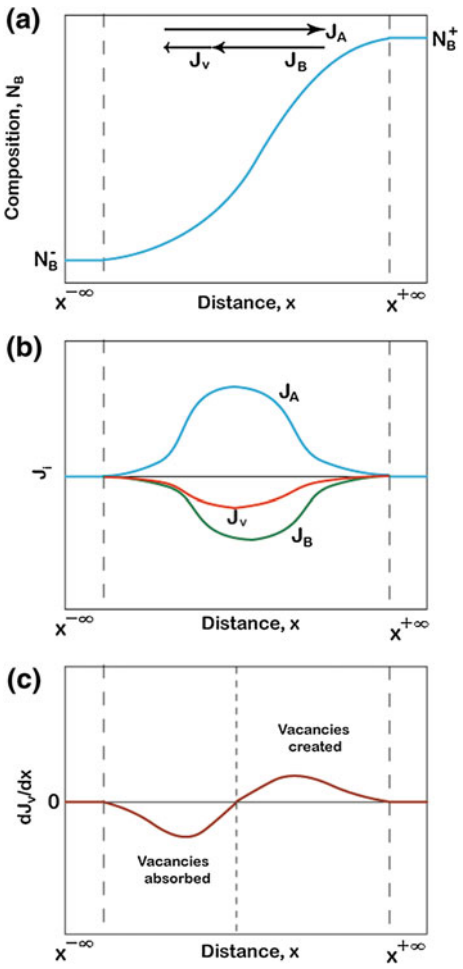

Fig. 6.23 Flow of vacancies depending on the intrinsic fluxes is explained **a** composition profile, **b** flux of components, and **c** creation and annihilation of vacancies

One interesting feature noticed in many diffusion couples is that pores are found on the side of the diffusion couple toward which the marker plane moves. In the beginning, the reason for the formation of voids was not clear and was believed that this might be incidental in a few diffusion couples [44]. However, over time, it became clear that this must be related to the Kirkendall effect. Branes [45] found that the volume of these pores is considerable and influences the Kirkendall plane shift. In the absence of any voids, the marker plane movement would be more [35]. Therefore, these two can be considered as competitive phenomena. In some couples, as can be seen in Fig. 6.22a, the content of pores is very high. In general, the lack of sinks is considered to be a valid explanation for finding these pores, especially if one component has a much higher diffusion rate compared to the other, as is the case in the CoSi phase. The diffusion rate of Si is around 30 times

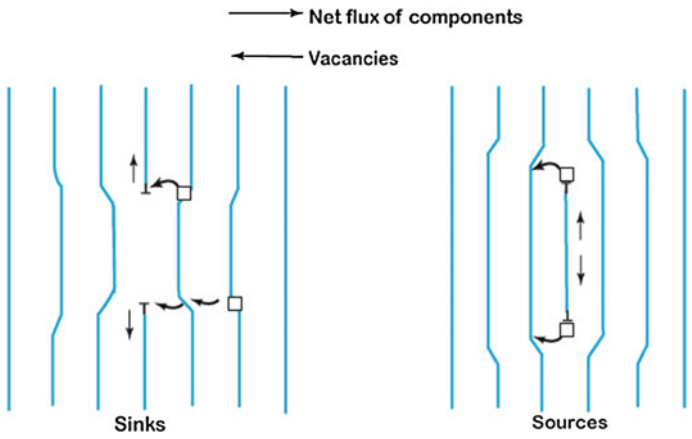

Fig. 6.24 Edge dislocations as sink and source of vacancies are explained

higher than that of Co in this phase [36]. Similar behavior was found in the Nb_5Si_3 phase, as shown in Fig. 6.25a, in which one side of the Kirkendall marker plane is covered by pores [46]. The diffusion rate of Si is approximately 100 times higher than that of Nb in this phase. The area fraction of the pores in the Cu_3Sn phase is found to be noticeably less, as seen from the Cu/Sn system shown in Fig. 6.25b [8]. It is believed that the distribution of the pores is affected by the impurities present in the end members. Note here that the diffusion rate of Cu is almost 30 times higher than that of Sn in this phase [47]. The differences in pore volume vary from system to system, and these differences may be due to the difference in the availability of sinks, the relative mobilities of the components, or the presence of impurities or inclusions, for instance. When the pore volume is substantial, this factor should be considered in the calculation of the diffusion parameters, as was done in the Co–Si system [36].

Along with the formation of pores, the development of stress in the diffusion couple and the deformation of the diffusion couple are also associated with the Kirkendall effect. Previously, the Kirkendall effect has been discussed based on the movement of the markers and the shrinkage on one side with the corresponding swelling on the other side of the couple based on a one-dimensional diffusion (i.e., composition) profile. With the accumulation of vacancies and/or pore formation, tensile stress develops on one side of the couple and compressive stress develops on the other side where an extra amount of atoms are accommodated. This may result in a three-dimensional change in the diffusion couple, as shown in Fig. 6.26 [48]. After annealing for time t, Fig. 6.26b shows one-dimensional deformation, whereas Fig. 6.26c presents the volume deformation. In this case, there will be equal deformation in all directions, which is one-third of the total deformation in one-dimensional deformation case. The dots on the figure represent the markers showing the deformation areas. For further reading on deformation and bending, the reader is referred to the manuscripts by Boettinger et al. [49] and Daruka et al.

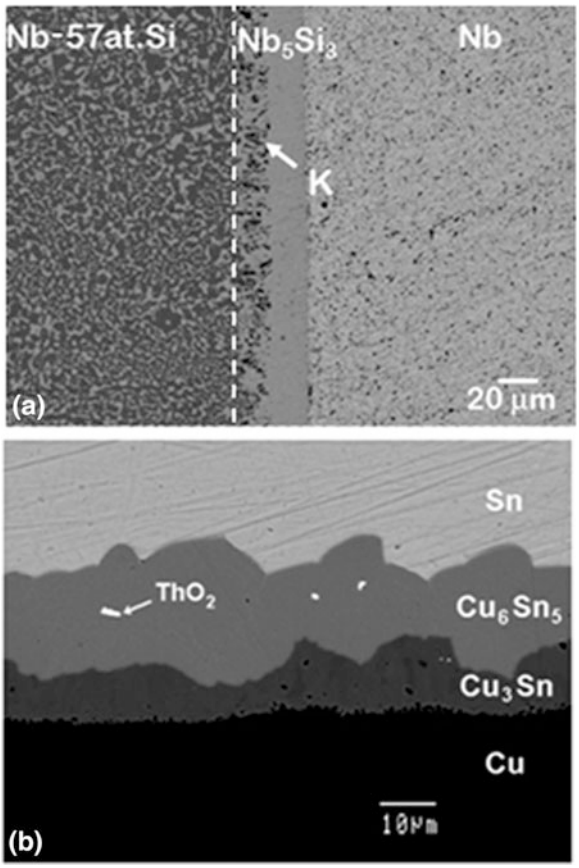

Fig. 6.25 Evolution of the Kirkendall voids in different systems is explained in the **a** Nb_5Si_3 [46] and **b** Cu_3Sn phases [8]

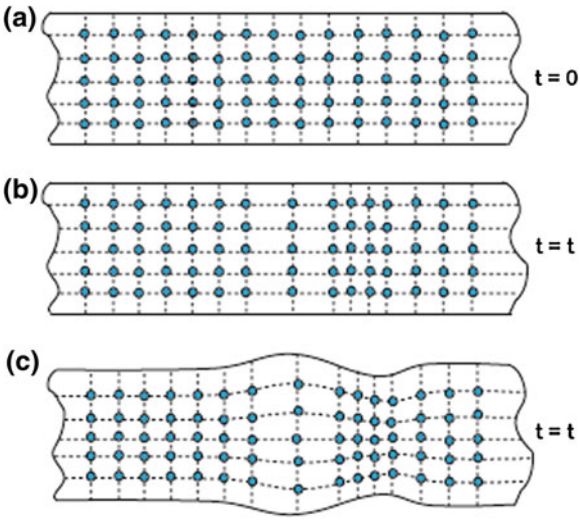

Fig. 6.26 **a** Deformation of diffusion couple and distribution of inert particles are shown before the experiments and when deformation is **b** one dimensional and **c** three dimensional. *Dots* indicate the markers at different planes

[50]. It should be noted here that the deformation or bending of the sample could be significant in a thin-film diffusion couple.

Darken's treatment correlates the interdiffusion, intrinsic, and tracer diffusion coefficients of the components with the aid of the thermodynamic factor. As explained, in a binary system, the intrinsic diffusivities of the components are different. When diffusion is controlled by a vacancy mechanism, the net flow of matter in one direction will be balanced by a flow of vacancies in the opposite direction. Manning explained that the net flux of vacancies creates a vacancy wind effect during interdiffusion [51, 52]. According to this theory, the flow of vacancies will make a jump of some extra vacancies. The jump of extra vacancies means an increase in the diffusion rate of the faster diffusing components and a decrease in the diffusion rate of the slower diffusing component than what is expected when adopting the relations developed by Darken. To accommodate this effect, he incorporated a *correction factor* into the equations developed by Darken. Naturally, these modified equations are known as the Darken–Manning equations.

Assuming there is no supersaturation, binding of vacancies, and no clustering in the alloy, Manning modified Eqs. 6.89a and 6.89b using a random alloy model as

$$D_A = \frac{v_m}{\bar{v}_B} D_A^* \Theta (1 + W_A) \tag{6.95a}$$

$$D_B = \frac{v_m}{\bar{v}_A} D_B^* \Theta (1 - W_B) \tag{6.95b}$$

where the vacancy wind factor $W_i = \frac{2N_i\left(D_A^* - D_B^*\right)}{\mathrm{M_o}\left(N_A D_A^* + N_B D_B^*\right)}$, M_o is a constant, which depends on the crystal structure of the system, N_i is the mole fraction of component i, and Θ is the thermodynamic factor $d\ln a_A / d\ln N_A = d\ln a_B / d\ln N_B$. Replacing Eqs. 6.95a and 6.95b in Eq. 6.65 and after some simple arithmetic, we arrive at

$$\widetilde{D} = \left(N_A D_B^* + N_B D_A^*\right)\ \Theta\ W_{AB} \tag{6.96}$$

where $W_{AB} = 1 + \frac{2N_A N_B\left(D_A^* - D_B^*\right)^2}{M_o\left(N_A D_B^* + N_B D_A^*\right)\left(N_A D_A^* + N_B D_B^*\right)}$

In the same way, the Kirkendall marker velocity was modified to

$$v_K = \bar{v}_B \left(\frac{v_m}{\bar{v}_A} D_B^* - \frac{v_m}{\bar{v}_B} D_A^* \right) \alpha\, \Theta \frac{\partial C_B}{\partial x} = \frac{1}{v_m} \left(\bar{v}_B D_B^* - \bar{v}_A D_A^* \right) \alpha\ \Theta \frac{\partial N_B}{\partial x} \tag{6.97}$$

where $\alpha = 1/f$ and f is the correlation factor for self-diffusion. Last equation can be written after modifying the relation using equations in Sect. 1.18.

The values of M_o and α for face centered cubic, body-centered cubic, simple cubic, and diamond structure are 7.15, 5.33, 3.77, 2 and 1.280, 1.375, 1.531, 2, respectively.

Many experiments have been conducted to compare the experimental results on intrinsic diffusion coefficients and those estimated by the Manning method from the tracer diffusion coefficients. The outcome is ambiguous. Schmatz et al. [53] and Iorio et al. [54] found that Manning's correction led to a better match between the ratio of self-diffusivities estimated from the Kirkendall effect and the ratio determined by radioactive tracer measurements. However, there was significant disagreement in the absolute values of the self-diffusivities between those experimentally determined and those estimated using the Manning approach. Kohn et al. [55] also found discrepancies between experimental and estimated values. Meyer [56] and Dallwitz [57] estimated the Kirkendall marker shift and found good agreement between experimentally determined results and the values predicted by Manning's model. Carlson [58] found that the vacancy wind effect is an important parameter for intrinsic diffusion fluxes and determined these values at different compositions for the V–Ti system. Later, Manning [59], Dayananda [60], and Belova and Murch [61] have extended this approach to consider the vacancy wind effect in multicomponent systems. The presence of the vacancy wind effect rather indicates that the off-diagonal phenomenological constants, which are assumed to be zero for the derivation of Darken's relations (Eq. 6.90), are not actually zero.

As already mentioned, Darken's relations can be used when vacancies are in thermal equilibrium, meaning that enough sources and sinks for the vacancies must be present in the interdiffusion zone to keep the vacancies in thermal equilibrium. As mentioned by Gusak et al. [62], Nazarov and Gurov [63, 64] analyzed the condition considering a non-equilibrium vacancy concentration in a binary diffusion couple by neglecting the sources and sinks to derive the relation

$$\widetilde{D} = \frac{D_A^* D_B^*}{N_A D_A^* + N_B^* D_B^*} \Theta \tag{6.98}$$

As commented by Gusak et al. [62] Darken's relation expressed in Eq. 6.90 is controlled by the faster diffusing component, whereas the relation developed by Nazarov–Gurov is controlled by the slower diffusing component. The significance of all this is that the Nazarov–Gurov relation could be important in the nanoscale interdiffusion process, where a non-ideal concentration of vacancies could be found. Darken's relation, on the other hand, is highly relevant in the macro and bulk samples. In fact, the Nazarov–Gurov relation could be important at the very initial stage of the diffusion couple; however, Darken's relation will prevail when annealing time is higher [65].

References

1. W.C. Roberts-Austen, Phil. Trans. Roy. Soc. A187 (1896) 383
2. C. Matano, Jap. J. Phys. 8 (1933) 109
3. L. Boltzmann, Ann. Physik. 53 (1894) 959
4. R.W. Ballufi, Acta Met. 8 (1960) 871
5. F. Sauer and V. Freise, Z. Electrochem. 66 (1962) 353
6. C. Wagner, Acta Met. 17 (1969) 99
7. F.J.A. den Broeder, Scripta Met. 3 (1969) 321
8. A. Paul, The Kirkendall effect in solid state diffusion. PhD Thesis, Technische Universiteit Eindhoven, The Netherlands, 2004
9. S. Santra, H. Dong, T. Laurila, A. Paul, Proceedings of the Royal Society A 470 (2013) 20130464.
10. L.B. Pfeil, J. Iron Steel 119 (1929) 501
11. L.S. Darken and R.W. Gurry, Physical chemistry of metals, McGraw Hill Book Company, Columbus, OH 43218, USA, 1953.
12. G.S. Hartley, Trans. Faraday Soc. 46 (1946) 6
13. A.D. Smigelkas and E.O. Kirkendall, Trans. AIME 171 (1947) 130
14. R.F. Mehl, Trans. AIME 171 (1947) 135
15. H. Nakajima, JOM 49 (1997) 15
16. L.C.C. da Silva and R.F. Mehl, Trans. AIME 191 (1951) 155
17. H.B. Huntington and F. Seitz, Phys. Rev. 61 (1942) 315
18. E.O. Kirkendall, *Trans. AIME,* 147 (1942) 104
19. H.B. Huntington and F. Seitz, Phys. Rev. 76 (1949) 1728
20. C. Zener, Acta Cryst. 3 (1950) 346
21. F. Sietz, Acta Cryst. 3 (1950) 355
22. L.S. Darken, Trans. Met. Soc. AIME 175 (1948) 184
23. G.S. Hartley and J. Crank, Trans. Faraday Soc. 45 (1949) 801
24. F. Seitz, Phys. Rev. 74 (1948) 1513
25. J. Bardeen, Phys. Rev. 1 (1949) 1403
26. T. Heumann, Z. Phys. Chem. 201 (1952)168
27. F.J.J. van Loo, Acta Met. 18 (1970) 1107
28. A Paul, AA Kodentsov, FJJ Van Loo, Journal of alloys and compounds 403 (2005) 147
29. VD Divya, U Ramamurty, A Paul, Journal of Materials Research 26 (2011) 2384
30. J. Levasseur and J. Philibert: J. Phys. Stat. Sol. B, 21 (1967) K1
31. J.F. Cornet: J. Phys. Chem. Solids 35, (1974) 1247
32. F.J.J. van Loo, G.F. Bastin and G.D. Rieck, Science of Sintering, 11 (1979) 9
33. T. Heumann, and K. J. Grundhoff. Z. Metallkd. 63 (1972) 173
34. M.J.H. van Dal, M.C.L.P. Pleumeeres, A.A. Kodenstov and F.J.J. van Loo, Acta Met. 48, (2000) 385
35. MJH Van Dal, D Huibers, AA Kodentsov, FJJ Van Loo, Intermetallics 9 (2001) 409
36. MJH Van Dal, AA Kodentsov, FJJ Van Loo, Intermetallics 9 (2001) 451
37. A Paul, MJH Van Dal, AA Kodentsov, FJJ Van Loo, Acta Materialia 52 (2004) 623
38. S.Roy and A. Paul, Philosophical Magazine 92 (2012) 4215
39. F. Seitz, Acta Metall. 1 (1953) 355
40. J. Bardeen and C. Herring, Imperfections in nearly Perfect crystals, Wiley, New York, 1952.
41. F.J.J. van Loo, Prog. Solid State Chem. 20 (1990) 47
42. V.Y. Doo and R.W. Balluffi, Acta Met. 6(1958) 428
43. Y. Adda and J. Philibert, Atom movements and mass transport in solids, Les Éditions de Physique, Les Ulis, 1991.
44. L.C. Correa Da Silva and R.F. Mehl, Trans. Amer. Inst. Min. Met. Eng. 191 (1951) 155
45. R.S. Branes, Effects associated with the Flow of Vacancies in Intermetallic Diffusion, Proc. Phys. Soc. 65B (1952) 512

46. S Prasad, A Paul, Acta Materialia 59 (2011) 1577
47. A Paul, C Ghosh, WJ Boettinger, Metallurgical and Materials Transactions A 42 (2011) 952
48. J. Schlipf, Acta Metall. 21 (1973) 435
49. W.J. Boettinger, G.B. McFadden, S.R. Coriell, R.F. Sekerka, J.A. Warren, Acta Mat. 53 (2005) 1995
50. I. Daruka, I.A. Szabó, D.L. Beke, C. Cserháti, A. Kodentsov, F.J.J. Van Loo, 44 (1996) 4981
51. J.R. Manning, Phys. Rev. 124 (1961) 470
52. J.R. Manning, Acta Met. 15 (1967) 817
53. D.J. Schmatz, H.A. Domain and H.I. Aaronson, J. Appl. Phys. 37 (1966) 1741
54. N.R. Iorio, M.A. Dayananda and R.E. Grace, Met. Trans. 4 (1973) 1339
55. A. Kohn, J. Levasseur, J. Philibert and M. Wanin, Acta Met. 18 (1970) 163
56. R.O. Meyer, Phys. Rev. 181 (1969) 1086
57. M.J. Dallwitz, Acta Met. 20 (1972) 1229
58. P.T. Carlson, Met. Trans. A 7A (1975) 199-208
59. J.R. Manning, Metallurgical and Materials Transactions B, 1 (1970) 499
60. M.A. Dayananda, Met. Trans. 2 (1971) 334
61. I.V. Belova, G.E. Murch, Act Mat. Volume 55 (2007) Pages 627
62. A.M.Gusak , S.V. Kornienko, G.V.Lutsenko, Defect and Diffusion Forum, 264 (2007) 109
63. A.V.Nazarov and K.P.Gurov: Phys. Metal. Metallogr. Vol. 37 (1974), 496
64. A.V.Nazarov and K.P.Gurov: Phys. Metal. Metallogr. Vol. 38 (1974) 486
65. H. Mehrer, Diffusion in solids: fundamentals, methods, materials, diffusion-controlled processes, Springer-Verlag GmbH, Berlin Germany, 2007

Chapter 7
Growth of Phases with Narrow Homogeneity Range and Line Compounds by Interdiffusion

In this chapter, the growth of the line compounds and the phases with narrow homogeneity range by reactive diffusion is discussed. The concept of the integrated diffusion coefficient is introduced. In the end, few case studies are given to explain the estimation procedure of the diffusion coefficients.

7.1 Time-Dependent Growth of the Phase Layer

In the previous chapter, we covered how interdiffusion works in a solid solution or—to put it another way—how the interdiffusion process affects the growth of phases with a wide composition range. In this present chapter, the growth of the phases with a narrow homogeneity range and the line compounds will be presented. Earlier, we showed that it is possible to validate the assumption that diffusion controls the process under investigation by using the Boltzmann parameter. However, in the case of line compounds, this must be verified by examining the parabolic nature of the growth. To simplify the discussion, let us consider an interdiffusion zone, where only a single-phase layer grows. In a diffusion-controlled process, the rate of increase in layer thickness is inversely proportional to the layer thickness itself. This arises from the fact that the amount of diffusing flux decreases with the increase in layer thickness, because the atoms have to diffuse a longer distance. Therefore, the following can be written

$$\frac{dx}{dt} \propto \frac{1}{x} \tag{7.1a}$$

$$\frac{dx}{dt} = k\frac{1}{x} \tag{7.1b}$$

where x is the layer thickness, t is the time, and k is a constant. Integrating Eq. 7.1b from zero layer thickness at time zero to the layer thickness of Δx after the annealing time of t, we get

A. Paul et al., *Thermodynamics, Diffusion and the Kirkendall Effect in Solids*,
DOI: 10.1007/978-3-319-07461-0_7,

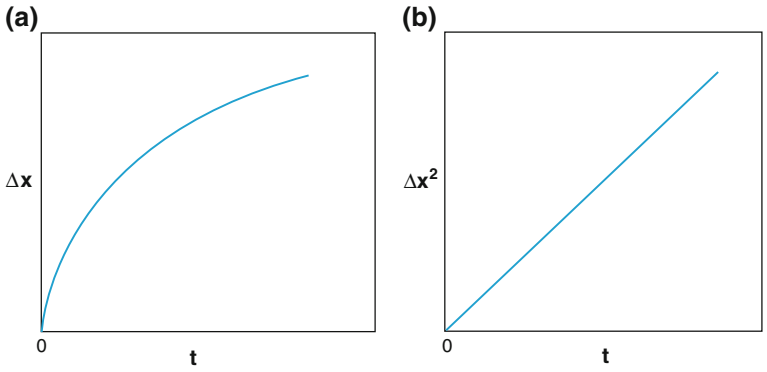

Fig. 7.1 Plots of the growth of a phase layer during diffusion-controlled process **a** Δx versus t and **b** Δx^2 versus t

$$\Delta x^2 = 2k_p t \tag{7.2}$$

where k_p is the parabolic growth constant. Thus, the parabolic nature of the growth is checked by plotting Δx versus t or Δx^2 versus t, as discussed in Figs. 7.1, 7.3, 7.4, 7.5 and 7.6. Sometimes, instead plotting, Δx versus $t^{1/2}$ plot Δx^2 versus t is found from which the parabolic growth constant can be estimated from the slope $\left(= 2k_p\right)$, as presented in Fig. 7.1b. In fact, it is also a common practice to plot Δx versus t to verify the parabolic nature of the growth, as shown in Fig. 7.1a.

The activation energy for the growth of a phase can be determined by conducting diffusion experiments at different temperatures. According to the Arrhenius equation,

$$k_p = k_p^o \exp\left(-\frac{Q_g}{RT}\right) \tag{7.3}$$

where ${k_p}^o$ is the pre-exponential factor, R is the gas constant, and Q_g is the activation energy for growth. The activation energy can be estimated from the slope $\left(-Q_g/R\right)$ of the $\ln k_p$ versus $1/T$ plot, as can be seen from Fig. 7.2. Rather the zero thickness at zero annealing time should not be added to the experimentally measured data points.

Under ideal conditions, the layer thickness at the beginning of the experiment is zero. However, for a number of reasons, different kinds of situation can be encountered. The thickness of the phase layer is always measured after a certain annealing time. When the line is extrapolated to $t = 0$, sometimes, it may intersect the y-axis (axis for thickness) at some positive value of Δx_i. This can be realized from Fig. 7.3. One of the reasons to find this kind of behavior is because of the growth during the heating and cooling cycles at the time of the heat treatment. Most of the experiments are conducted in vacuum or under flowing inter-gases. In

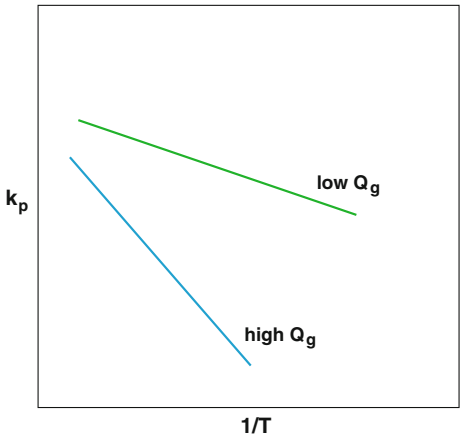

Fig. 7.2 Arrhenius plot explaining the activation energies

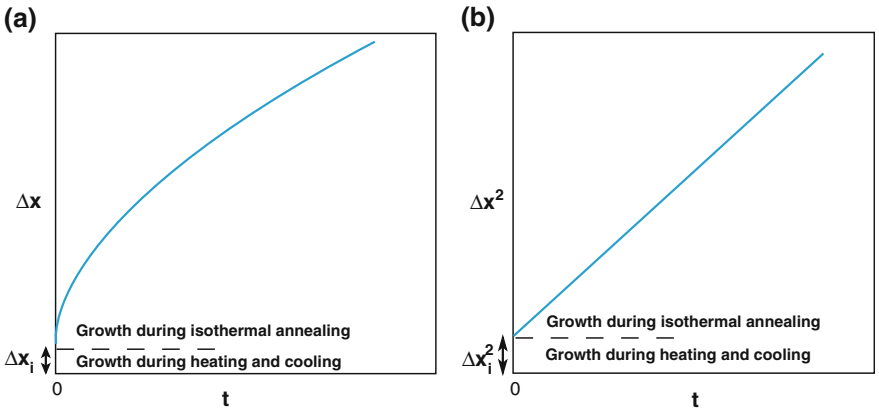

Fig. 7.3 Parabolic growth plots showing the effect of growth during heating and cooling cycles in the furnace

these cases, the sample has to be placed in the furnace first and only then heated to the desired temperature. After the completion of annealing at a specific temperature, the growth of the phase layer during the cooling down period could be avoided by quenching the sample immediately. However, if the interface is weak—for example, in a metal/silicon diffusion couples—or if we like to avoid oxidation, furnace cooling is preferred. In the calculations, only the isothermal annealing time at the desired temperature is taken into account. Therefore, Δx_i indicates the growth of layer thickness during the heating and cooling cycles. If the activation energy for growth is low, this contribution can be significant. The contribution will be smaller, however, when the activation energy is high. This can be understood from the fact that the activation energy indicates the difference in

growth rate at different temperatures, as shown in Fig. 7.2. Keeping the sample at the desired annealing temperature for a relatively long time, we can minimize this contribution to the overall growth.

It is not very straightforward to understand whether the positive value of Δx_i indicates only the growth of the phase layer during the heating and cooling cycles. In interdiffusion, both lattice and grain boundary diffusion might play a significant role. In the beginning, when the size of the grains is very small (representing a high grain boundary area), the growth of the phase might happen mainly due to the flux diffused via the grain boundaries. However, with an increase in annealing time, grains also grow along with the layer thickness. Therefore, after a certain annealing time, the diffusion process could be controlled by the lattice diffusion. In this case, if Δx^2 is plotted with respect to t for short annealing times, the transition will be clear from the curve, as shown in Fig. 7.4b. In most of the cases, however, this will be difficult to find because of very small transition time. Therefore, if the experiments are conducted by choosing the annealing times in the later stage where the lattice diffusion-controlled growth process has already started after the initial grain boundary diffusion-controlled process, Δx_i will be positive. Then, it will be difficult to understand whether this is because of the heating and cooling cycles or because of the initial grain boundary diffusion. It should be noted here that this is not a problem to determine the parabolic growth constant, since it can be estimated from the slope directly. In terms of an equation, it can be written as

$$\Delta x^2 - \Delta x_i^2 = 2k_p t \tag{7.4}$$

However, if we wish to examine the reason for finding the positive Δx_i value, one experiment should be conducted by heating to the desired temperature and then cooling without holding it for isothermal annealing.

Many times immediately after the start of annealing, the layer cannot start growing. This can be realized from Fig. 7.5. This phenomenon is generally found when the surface layer is covered by a thin oxide layer—something which is very commonly found in couples with Al, as was found in the Ti/Al diffusion couple [1, 2]. It might have an incubation period of many hours during which the growth of the phase was reaction controlled. Once the oxide layer is completely broken, the diffusion-controlled parabolic growth of the phase is found. Sometimes, the small broken pieces of oxide are found in the product phase itself [1]. The parabolic growth constant in this case is estimated from

$$\Delta x^2 = 2k_p(t - t_o) \tag{7.5}$$

Many times, [2–4], a carbon or phosphorous segregated layer could be present at one of the material surfaces. A very small concentration, even in the range of a few parts per million, is enough to create problem at the initial stage of the growth process. This might even lead to a different diffusion process in the beginning and even might become a reaction-controlled process because of the limited amount of impurities.

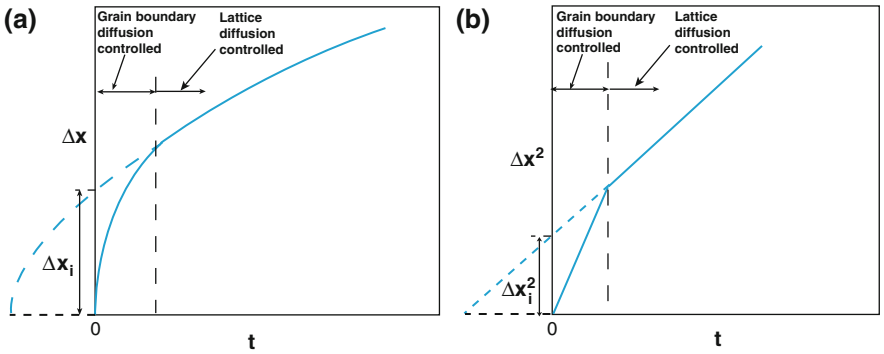

Fig. 7.4 Parabolic growth plots showing the effect of transition from grain boundary diffusion to lattice diffusion

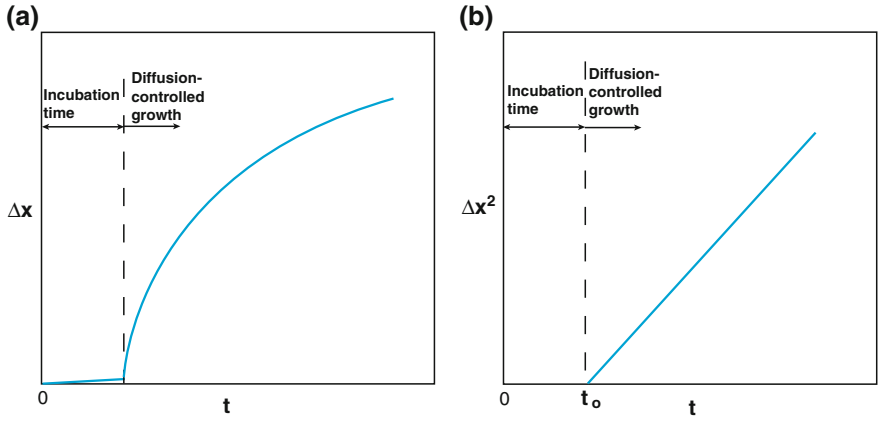

Fig. 7.5 Parabolic growth constant plots showing incubation time

The growth of the phase layer at the initial stage could be reaction controlled, where the layer grows linearly with time. After a certain annealing time, the growth process might become diffusion controlled, as shown in Fig. 7.6. Dybkov has discussed this topic extensively in his book [5]. In a thin-film couple, because of the stress developed during deposition, the growth of the phase could, in fact, be reaction controlled. Sometimes, especially in this condition, nucleation of the product phase could be difficult because of the low driving force for the formation and the high interfacial energy. In such cases, a non-equilibrium phase(s) could be formed. However, in the bulk diffusion couple of solid materials (that is not porous), this is not so common. Even if it is there, in the very beginning, the parabolic growth constant estimated using the Eq. 7.5 does not draw any significant error. Pieraggi [6] has discussed extensively on the right choice of plotting between Δx versus t or Δx^2 versus t for oxide layer growth cases, where the initial

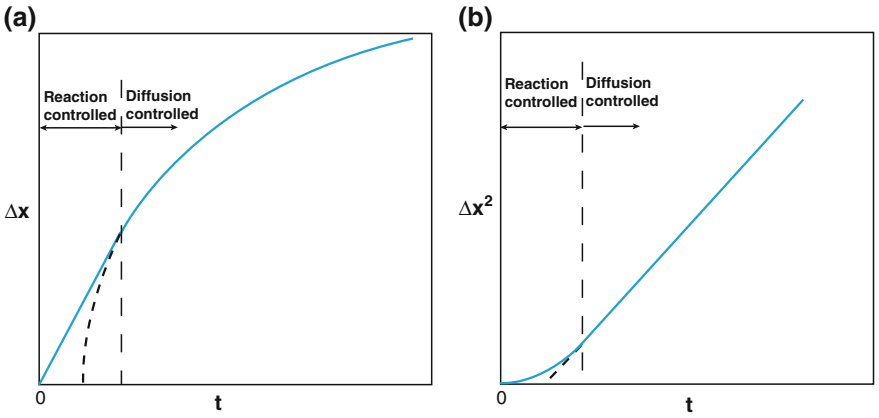

Fig. 7.6 Parabolic growth plots showing transition from reaction-controlled to diffusion-controlled growth

fast growth rate does not contribute to the steady-state growth at the later stage. However, oxide systems are beyond the scope of discussion in this book. Interested readers are referred to the manuscript by Pieraggi [6] or to the summary of the outcome by van Loo [2].

If the aim is to ultimately conduct the experiments to determine the activation energy for growth, then time-dependent experiments ideally should be conducted at every temperature, in the case that Δx_i is positive or there is an incubation time. On the other hand, it can be neglected, if these are small. It is also possible to consider similar deviation, if the temperature range of a particular study is not very high. This value might not be very different at differing temperatures within a short temperature range. It is easy to appreciate the need to conduct time-dependent experiments at every temperature based on the results plotted with respect to the Arrhenius equation for the calculation of the activation energy, as shown in Fig. 7.2. If the data points fall more or less on the line, this indicates that the deviation in the temperature range of interest will be similar. It should be noted here that sometimes data are fit by considering zero thickness at zero annealing time, as shown in Fig. 7.7b in the Mg/Ni diffusion couple [7]. When experimental data points are extrapolated to zero time, these will never lead to zero thickness exactly because of error associated with the experiments even if there are no issues at the initial stages as discussed above. However, there is nothing wrong to show the graph, as presented in Fig. 7.7c, which is drawn after extracting the data points from Fig. 7.7b. With such a small error, one can conveniently consider that the system is not affected by the factors discussed above at the initial stage.

If local equilibrium is achieved in an interdiffusion zone, as shown by Wagner [8], Gurov et al. [9], and Kidson [10], all the phase layers contained in the phase diagram should be present in the interdiffusion zone. Local equilibrium is, in general, found in the bulk diffusion couple, and it is expected that all phase layers

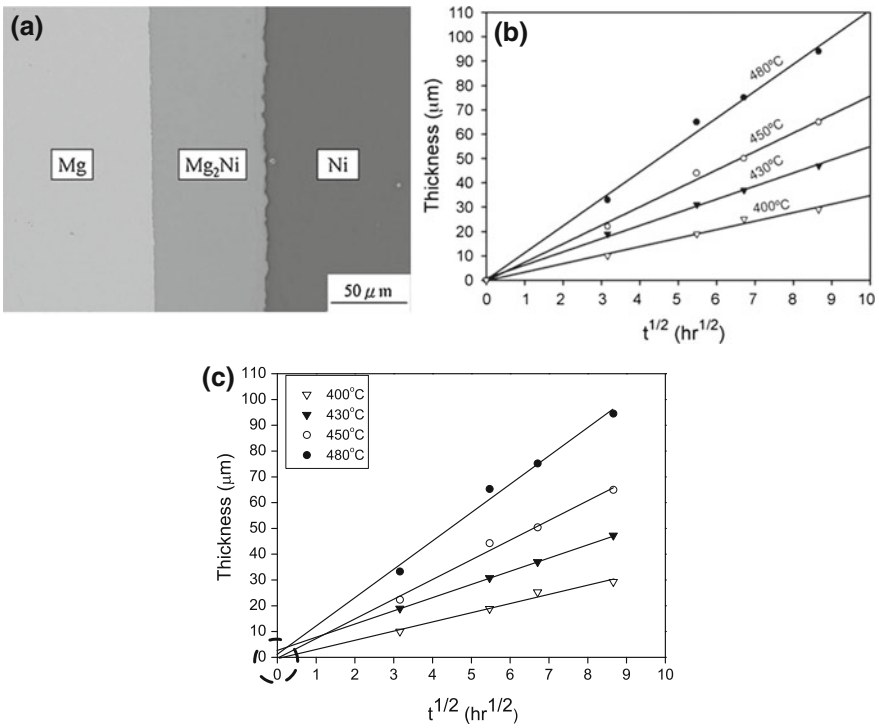

Fig. 7.7 **a** Mg/Ni diffusion couple annealed at 480 °C for 45 h. Growth of the product phases with respect to square root time are shown for **b** considering zero thickness at zero time and **c** without considering it in the data fit [7]

start growing together. However, it is also true that the growth rates of one or more phases are much lower compared to the growth rate of other phases. In such cases, the phases with slower growth rates might actually be present in the interdiffusion zone, but proper analysis, for example, under a transmission electron microscope (TEM) is required to detect the phase. In the Mo–Si system [11], three phases, $MoSi_2$, Mo_5Si_3, and Mo_3Si, should be present in the interdiffusion zone of the Mo/Si diffusion couple. However, the interdiffusion zone was mainly covered by the $MoSi_2$ phase with a very thin layer of the Mo_5Si_3 phase [12]. Mo_3Si phase was not detected at all. Our calculation showed that the thickness of Mo_3Si in this couple is in the nanometer range, which is not possible to detect under a scanning electron microscope. TEM analysis by Yoon et al. [13] showed the presence of this phase. The same phase was grown with reasonable thickness in Mo/Mo_5Si_3 incremental couple [14]. In the Au/Sn diffusion couple, the Au_5Sn phase was not found; however, it was revealed after etching the sample [15]. Even in the bulk diffusion couples, sometimes, a sequential rather than a simultaneous phase growth is sometimes suspected [16]. However, the initial time for the sequential growth could be so small that validating this fact experimentally is difficult. In the

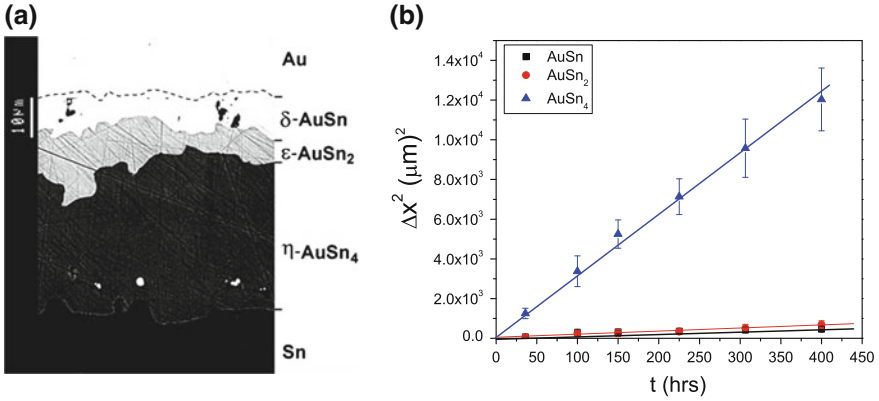

Fig. 7.8 **a** Au/Sn diffusion couple at 180 °C for 36 h [15]. **b** Growth of the phase layers with respect to time at 180 °C [23]

thin-film couple, instead of simultaneous growth, sequential growth is very common and the phases may not grow parabolically with time [17]. Nucleation problem is also encountered frequently especially in the thin-film couples [18–21].

In multiphase growth, if all the phases grow parabolically with time, the growth of the total interdiffusion zone will also be parabolic with time. Quite often, the phase(s) grow with more or less straight interface, and it is relatively easy to check the parabolic nature of the growth, as can be seen in the Mg–Ni system which is reproduced in Fig. 7.7 [7]. However, many times [22], as found in the Au/Sn diffusion couple, one or more phase layers could be very wavy, and this leads to a high standard deviation in the calculation of the parabolic growth constant, as shown in Fig. 7.8 [23].

In the end, it should be noted that the parabolic growth constant is not a material constant since the thickness of a particular phase layer changes with the change in composition of the end members. It is therefore not straightforward to discuss the diffusion behavior based on the parabolic growth constant calculations. In a particular condition, the activation energy for growth could be the same as the activation energy for the diffusion coefficient (single-phase growth of a line compound in the interdiffusion zone). In most conditions (multiphase growth), however, these are actually different. Therefore, incorrect conclusions may be drawn if the diffusion behavior is discussed solely based on the calculation of the parabolic growth constant. It is always safe to consider the diffusion coefficients, since the diffusion coefficient is a material constant. In fact, as will be discussed, the thickness of a particular phase layer is grown differently in different couples with different end members such that the diffusion coefficients of the phases remain constant.

7.2 Calculation of the Diffusion Parameters in Line Compounds or the Phases with Narrow Homogeneity Range: Concept of the Integrated Diffusion Coefficient

The relations derived in Chap. 6 cannot be used to estimate the diffusion coefficients for compounds with a narrow homogeneity range. To explain this, we consider an imaginary phase diagram as shown in Fig. 7.9a. An alloy in the α phase ($N_B{}^-$) is coupled with an alloy in the γ phase ($N_B{}^+$). Following the arguments discussed in Chap. 4, the α, β, and γ phases with a composition profile shown in Fig. 7.9b could grow in the interdiffusion zone. In the β phase, the composition profile will have a negligible gradient since this phase has a very narrow composition range. Previously in Chap. 6, the relation for the interdiffusion coefficient (Eq. 6.45) was derived as

$$\tilde{D}(Y_B{}^*) = \frac{v_m{}^*}{2t(dY_B/dx)_{Y_B{}^*}} \left[(1 - Y_B{}^*) \int_{x^{-\infty}}^{x^*} \frac{Y_B}{v_m} dx + Y_B{}^* \int_{x^*}^{x^{+\infty}} \frac{(1 - Y_B)}{v_m} dx \right] \tag{7.6}$$

To determine the interdiffusion coefficient, it is necessary to calculate the gradient $\frac{dY_B}{dx} = \frac{1}{N_B^+ - N_B^-} \frac{dN_B}{dx}$, which is almost impossible to determine in the β phase. To overcome this problem, Wagner [8] introduced the concept of the integrated diffusion coefficient $\tilde{D}_{\text{int}}$—which is the interdiffusion coefficient $\tilde{D}$ integrated over the unknown composition range, let us say $\Delta N_B^\beta = N_B^{\beta 2} - N_B^{\beta 1}$. In mathematical terms, it is expressed as

$$\tilde{D}_{\text{int}}^\beta = \int_{N_B^{\beta 1}}^{N_B^{\beta 2}} \tilde{D} dN_B \tag{7.7}$$

The interdiffusion coefficient may not vary significantly in the narrow composition range, and hence, Eq. 7.7 can be written as

$$\tilde{D}_{\text{int}}^\beta = \tilde{D}\left(N_B^{\beta_2} - N_B^{\beta_1}\right) = \tilde{D}\Delta N_B^\beta \tag{7.8}$$

Frequently, the phase might grow with only a small composition range (not very narrow). It remains, however, difficult to calculate the composition gradient with minimum error. Often, a phase might have a reasonably wide composition range, yet the gradient changes very sharply near the interface, or it does not grow with the complete measureable composition range. If the actual composition range is known, the average interdiffusion diffusion coefficient is estimated from the integrated diffusion coefficient using the relation

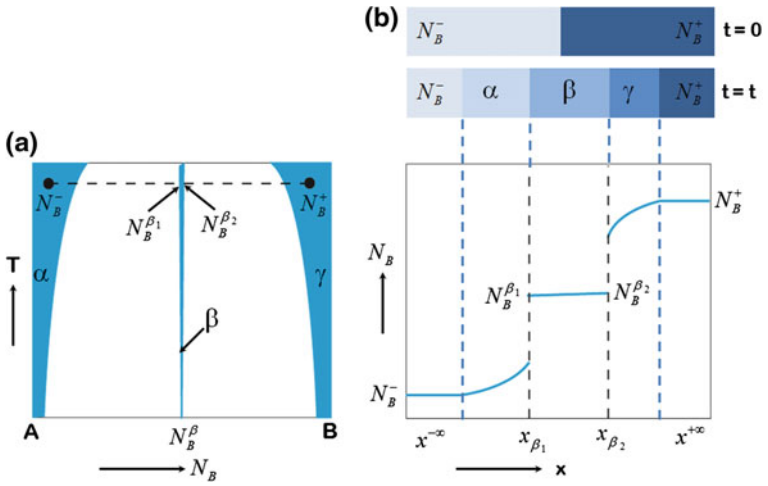

Fig. 7.9 **a** Lower part of an imaginary phase diagram and **b** a possible composition profile of the diffusion couple

$$\tilde{D}_{av} = \frac{\tilde{D}^{\beta}_{\text{int}}}{\Delta N_B{}^{\beta}} \tag{7.9}$$

We can derive the relation for the estimation of the integrated diffusion coefficient from a composition profile with the help of relations expressed in Eqs. 7.6 and 7.8. The term inside the brackets in Eq. 7.6 can be separated into three parts in the interdiffusion zone (see Fig. 7.9) as

$$\tilde{D}\left(Y_B^{\beta}\right) = \frac{v_m^{\beta}}{2t}\left(\frac{dx}{dY_B}\right)_{\beta}\left[(1-Y_B^{\beta})\int_{x^{-\infty}}^{x_{\beta_1}}\frac{Y_B}{v_m}dx + (1-Y_B^{\beta})\int_{x_{\beta_1}}^{x_{\beta_2}}\frac{Y_B}{v_m}dx + Y_B^{\beta}\int_{x_{\beta_2}}^{x^{+\infty}}\frac{1-Y_B}{v_m}dx\right] \tag{7.10}$$

Since we are seeking to calculate the diffusion parameter in the β phase, which has an average (or stoichiometric) composition of N_B^{β}, both $Y_B{}^{\beta}$ and v_m^{β} can be considered as constant. Therefore, Eq. 7.10 can be written as

$$\tilde{D}\left(Y_B^{\beta}\right) = \frac{v_m^{\beta}}{2t}\left(\frac{dx}{dY_B}\right)_{\beta}\left[\left(1-Y_B^{\beta}\right)\int_{x^{-\infty}}^{x_{\beta_1}}\frac{Y_B}{v_m}dx + \frac{\left(1-Y_B^{\beta}\right)Y_B^{\beta}}{v_m^{\beta}}\int_{x_{\beta_1}}^{x_{\beta_2}}dx + Y_B^{\beta}\int_{x_{\beta_2}}^{x^{+\infty}}\frac{1-Y_B}{v_m}dx\right]$$

$$\tilde{D}\left(Y_B^{\beta}\right) = \frac{v_m^{\beta}}{2t}\left(\frac{dx}{dY_B}\right)_{\beta}\left[\left(1-Y_B^{\beta}\right)\int_{x^{-\infty}}^{x_{\beta_1}}\frac{Y_B}{v_m}dx + \frac{\left(1-Y_B^{\beta}\right)Y_B^{\beta}}{v_m^{\beta}}\Delta x_{\beta} + Y_B^{\beta}\int_{x_{\beta 2}}^{x^{+\infty}}\frac{1-Y_B}{v_m}dx\right] \tag{7.11}$$

The thickness of the β phase is $\Delta x_\beta = x_{\beta_2} - x_{\beta_1}$. Further, we can write

$$\left(\frac{dx}{dY_B}\right)_\beta = \left(N_B^+ - N_B^-\right)\left(\frac{dx}{dN_B}\right)_\beta = \left(N_B^+ - N_B^-\right)\frac{\Delta x_\beta}{\Delta N_\beta} \tag{7.12}$$

Replacing Eq. 7.12 in Eq. 7.11, we arrive at

$$\tilde{D}_{\text{int}}^{\beta} = \tilde{D}\Delta N_\beta = \frac{v_m^\beta}{2t}\Delta x_\beta\left(N_B^+ - N_B^-\right) \times \left[\left(1 - Y_B^\beta\right)\int_{x^{-\infty}}^{x_{\beta_1}} \frac{Y_B}{v_m}dx + \frac{\left(1 - Y_B^\beta\right)Y_B^\beta}{v_m^\beta}\Delta x_\beta + Y_B^\beta\int_{x_{\beta 2}}^{x^{+\infty}} \frac{1 - Y_B}{v_m}dx\right]$$

Since $Y_B = \frac{N_B - N_B^-}{N_B^+ - N_B^-}$; $\quad Y_B^\beta = \frac{N_B^\beta - N_B^-}{N_B^+ - N_B^-}$, the above relation can be written as

$$\tilde{D}_{\text{int}}^{\beta} = \frac{\left(N_B{}^\beta - N_B{}^-\right)\left(N_B{}^+ - N_B{}^\beta\right)}{N_B{}^+ - N_B{}^-}\frac{\left(\Delta x_\beta\right)^2}{2t} + \frac{v_m{}^\beta}{2t}\left(N_B{}^+ - N_B{}^-\right)\Delta x_\beta\left[\left(1 - Y_B{}^\beta\right)\int_{x^{-\infty}}^{x_{\beta_1}} \frac{Y_B}{v_m}dx + Y_B{}^\beta\int_{x_{\beta_2}}^{x^{+\infty}} \frac{1 - Y_B}{v_m}dx\right]$$

$$\tilde{D}_{\text{int}}^{\beta} = \frac{\left(N_B^\beta - N_B^-\right)\left(N_B^+ - N_B^\beta\right)}{N_B^+ - N_B^-}\frac{\left(\Delta x_\beta\right)^2}{2t} + \frac{\Delta x_\beta}{2t}\left[\frac{N_B^+ - N_B^\beta}{N_B^+ - N_B^-} \times \int_{x^{-\infty}}^{x^{\beta_1}} \frac{v_m^\beta}{v_m}\left(N_B - N_B^-\right)dx + \frac{N_B^\beta - N_B^-}{N_B^+ - N_B^-} \times \int_{x^{\beta_2}}^{x^{+\infty}} \frac{v_m^\beta}{v_m}\left(N_B^+ - N_B\right)dx\right] \tag{7.13a}$$

Note here that the first term that is the term outside the bracket accounts for the profile of the phase of interest (β) to calculate the integrated diffusion coefficient. The first term inside the bracket accounts for the composition profile of the phases on the left-hand side, whereas the second term accounts for the phases present on the right-hand side of the phase of interest β. Numerous cases contain many line compounds or the phases with a narrow homogeneity in the interdiffusion zone. The composition profile in the solid solution in the ends of the couple might be negligible compared to the thickness of the phases with a narrow homogeneity range. In that case, Eq. 7.13a can therefore be written as

$$\tilde{D}_{\text{int}}^{\beta} = \frac{\left(N_B^{\beta} - N_B^{-}\right)\left(N_B^{+} - N_B^{\beta}\right)}{N_B^{+} - N_B^{-}} \frac{\left(\Delta x_{\beta}\right)^2}{2t} + \frac{\Delta x_{\beta}}{2t} \frac{1}{N_B^{+} - N_B^{-}} \left[\left(N_B^{+} - N_B^{\beta}\right) \sum_{i=2}^{\beta-1} \frac{v_m^{\beta}}{v_m^{i}} \left(N_B^{i} - N_B^{-}\right) \Delta x_i + \left(N_B^{\beta} - N_B^{-}\right) \sum_{i=\beta+1}^{n-1} \frac{v_m^{\beta}}{v_m^{i}} \left(N_B^{+} - N_B^{i}\right) \Delta x_i \right] \tag{7.13b}$$

$$\tilde{D}_{\text{int}}^{\beta} = \frac{\left(N_B^{\beta} - N_B^{-}\right)\left(N_B^{+} - N_B^{\beta}\right)}{N_B^{+} - N_B^{-}} k_p^{\beta} + \frac{\Delta x_{\beta}}{2t} \frac{1}{N_B^{+} - N_B^{-}} \left[\left(N_B^{+} - N_B^{\beta}\right) \sum_{i=2}^{\beta-1} \frac{v_m^{\beta}}{v_m^{i}} \left(N_B^{i} - N_B^{-}\right) \Delta x_i + \left(N_B^{\beta} - N_B^{-}\right) \sum_{i=\beta+1}^{n-1} \frac{v_m^{\beta}}{v_m^{i}} \left(N_B^{+} - N_B^{i}\right) \Delta x_i \right] \tag{7.13c}$$

since $k_p^{\beta} = \frac{\left(\Delta x_{\beta}\right)^2}{2t}$. Note here that the end members are numbered as 1 and n. $(n-2)$ phases—i.e., from 2 to $(n-1)$—grow in the interdiffusion zone. As shown in Fig. 7.10, suppose three phases, α, β, and γ grow and we wish to calculate the integrated diffusion coefficient of the β phase. Equation 7.13b can then be expressed as

$$\tilde{D}_{\text{int}}^{\beta} = \frac{a \times b}{a+b} \frac{\left(\Delta x_{\beta}\right)^2}{2t} + \frac{\Delta x_{\beta}}{2t} \frac{1}{a+b} \left[b \left(\frac{v_m^{\beta}}{v_m^{\alpha}} P \right) + a \left(\frac{v_m^{\beta}}{v_m^{\gamma}} Q \right) \right] \tag{7.14a}$$

where $a = N_B{}^{\beta} - N_B{}^{-}$, $b = N_B^{+} - N_B^{\beta}$, $P = \Delta x_{\alpha}(N_B{}^{\alpha} - N_B{}^{-})$, and $Q = \Delta x_{\gamma}(N_B^{+} - N_B^{\gamma})$.

The integrated diffusion coefficients for the α and the γ phases can be estimated, following Fig. 7.11 from

$$\tilde{D}_{\text{int}}{}^{\alpha} = \frac{c \times d}{c+d} \frac{\left(\Delta x_{\alpha}\right)^2}{2t} + \frac{\Delta x_{\alpha}}{2t} \frac{1}{c+d} \left[d(0) + c \left(\frac{v_m^{\alpha}}{v_m{}^{\beta}} M + \frac{v_m{}^{\alpha}}{v_m{}^{\gamma}} N \right) \right] \tag{7.14b}$$

where $c = N_B^{\alpha} - N_B^{-}$, $d = N_B{}^{+} - N_B{}^{\alpha}$,$M = \Delta x_{\beta}(N_B^{+} - N_B^{\beta})$, and $N = \Delta x_{\gamma}(N_B^{+} - N_B^{\gamma})$. It should be noted here that the first term inside the bracket becomes zero as no phase(s) are present on the left-hand side of the phase of interest.

$$\tilde{D}_{\text{int}}^{\gamma} = \frac{e \times f}{e+f} \frac{\left(\Delta x_{\gamma}\right)^2}{2t} + \frac{\Delta x_{\gamma}}{2t} \frac{1}{e+f} \left[f \left(\frac{v_m^{\gamma}}{v_m^{\alpha}} R + \frac{v_m^{\gamma}}{v_m^{\beta}} S \right) + e(0) \right] \tag{7.14c}$$

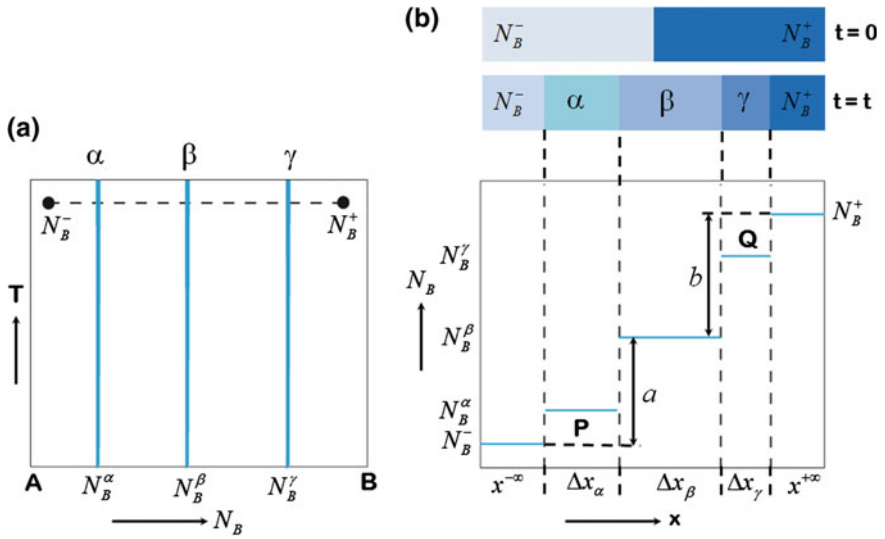

Fig. 7.10 **a** Lower part of an imaginary phase diagram with three line compounds and **b** a possible composition profile of the diffusion couple showing the estimation of the integrated diffusion coefficient for the β phase

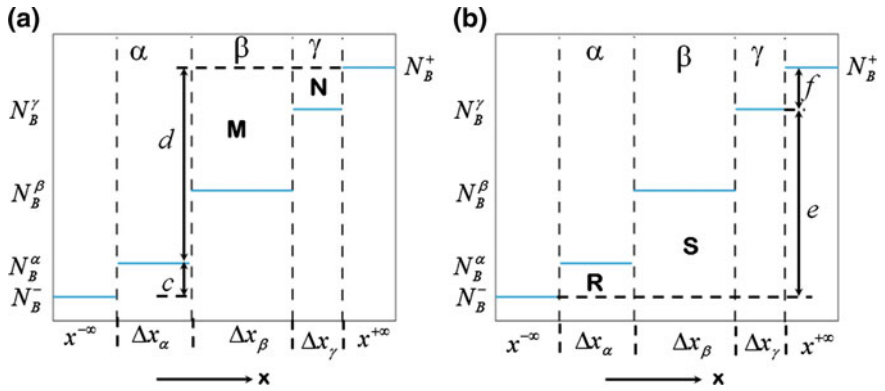

Fig. 7.11 Composition profiles showing the estimation of the integrated diffusion coefficients for the **a** α-phase and **b** β-phase

where $e = N_B{}^{\gamma} - N_B{}^{-}, f = N_B^{+} - N_B^{\gamma}, R = \Delta x_{\alpha}(N_B{}^{\alpha} - N_B{}^{-})$, and $S = \Delta x_{\beta}(N_B^{\beta} - N_B^{-})$. It should be noted here that the second term inside bracket becomes zero as no phase(s) are present on the right-hand side of the phase of interest.

In cases where only the β phase grows in the interdiffusion zone, (see Fig. 7.12), such that no other phases are present on the left- and right-hand sides of the product phase, Eq. 7.14a is then simplified to

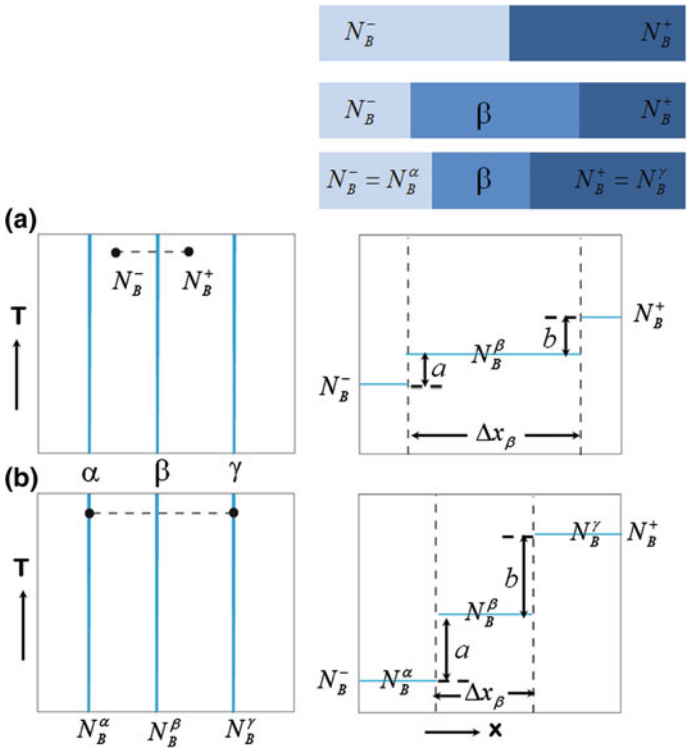

Fig. 7.12 Estimation of the integrated diffusion coefficient in an incremental diffusion couple is explained for **a** a diffusion couple with two phase mixtures as the end members and **b** single phases as the end members

$$\tilde{D}_{\text{int}}^{\beta} = \frac{a \times b}{a+b} \frac{\left(\Delta x_\beta\right)^2}{2t} = \frac{a \times b}{a+b} k_p^\beta \tag{7.15}$$

where $k_p{}^\beta$ is the parabolic growth constant of the β phase.

7.3 Calculation of the Average Interdiffusion Coefficient

Often, a phase grows in the interdiffusion zone, which has a composition range of only a few percent. Nevertheless, it still may not be possible to estimate the composition gradient with the minimum of error. For example, when Ni and Mo were coupled at 1,150 °C for 9 h, the interdiffusion zone developed with the Ni(Mo) solid solution and the σ phase following the phase diagram, as shown in Fig. 7.13 [24]. After plotting the average smoothened composition profile on the

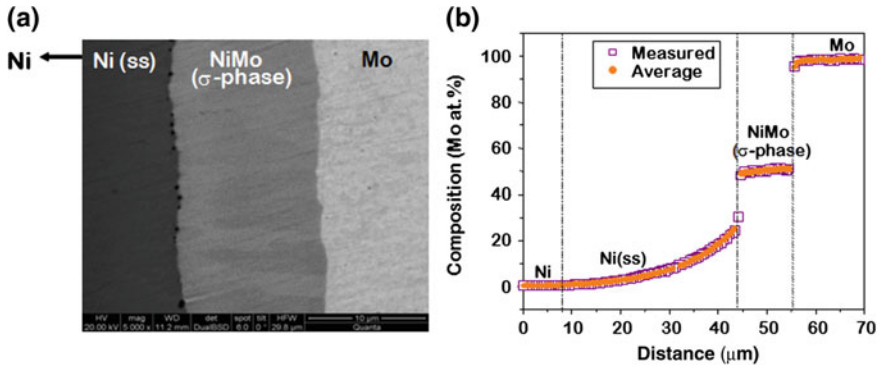

Fig. 7.13 **a** SEM image of a Ni/Mo diffusion couple (Ni end member is further away from the image shown) and **b** composition profile at 1,150 °C for 9 h

measured profile, it was not possible to calculate the interdiffusion coefficients in the σ phase with a small margin of error because of the small composition gradient. On the other hand, this phase is not a line compound or does not grow with a very small composition range. Thus, the calculation of the integrated diffusion coefficient is not very suitable. In this kind of system, it is very common practice to calculate an average interdiffusion coefficient. Two different approaches could be followed to estimate this. It can be estimated by dividing $\tilde{D}_{\text{int}}$ with the known composition range of the phase $\Delta N_B{}^{\beta}$ as expressed in Eq. 7.9. For that, first, it is necessary to determine the integrated diffusion coefficient for the phase. Therefore, to apply the relations derived in the previous section, an average composition profile with a zero gradient is first determined from the measured composition profile in the phase of interest following

$$N^{\beta}_{B(av)} = \frac{\int_{N_B^{\beta}{}_1}^{N_B^{\beta}{}_2} N_B dx}{\Delta x_{\beta}} \tag{7.16}$$

Next, the average composition profile is plotted with the help of the known thickness of the phase. For instance, in the case of the Ni–Mo system, only the average composition profile for the σ-NiMo phase should be plotted without changing anything in the Ni(Mo) solid solution. Subsequently, the appropriate equation—as discussed in the previous section—is used to calculate the integrated diffusion coefficient. In this particular system, Eq. 7.13a should be used. The average interdiffusion coefficient is then estimated using the relation expressed in Eq. 7.9.

Another approach can also be followed to determine this parameter by estimating the interdiffusion flux $\tilde{J}$. Following Fick's first law, considering constant molar volume for the phase of interest, we can write

$$\tilde{J} = -\tilde{D}\frac{dC}{dx} = -\tilde{D}\frac{1}{v_m^{\beta}}\frac{dN_B}{dx} \tag{7.17}$$

Generally, in a phase with a small composition range, the variation of the lattice parameters with composition is not known. Therefore, an average constant molar volume is considered, which is estimated based on the lattice parameter data of stoichiometric composition. Replacing Eqs. 7.17 and 7.7, we get

$$\tilde{D}_{\text{int}}^{\beta} = \int_{N_B^{\beta 1}}^{N_B^{\beta 2}} \tilde{D}dN_B = -v_m^{\beta}\int_{x_{\beta 1}}^{x_{\beta 2}} \tilde{J}dx \tag{7.18}$$

Therefore, $\tilde{D}_{\text{int}}^{\beta}$ can be estimated after calculating the variation of $\tilde{J}$ with composition and then integrating it over the length of the phase of interest. The value $\tilde{J}$ can be estimated using the relation developed by Den Broeder for the interdiffusion coefficient (Eq. 6.26) expressed as

$$\tilde{D}\left(Y_C^*\right) = \frac{1}{2t}\left(\frac{dx}{dY_C}\right)_{Y_C^*}\left[\left(1-Y_C^*\right)\int_{x^{-\infty}}^{x^*} Y_C dx + Y_C^*\int_{x^*}^{x^{+\infty}} (1-Y_C)dx\right]$$

Since according to Eq. 6.16, the concentration-normalized variable is expressed as $Y_C = \frac{C_B - C_B^-}{C_B^+ - C_B^-}$

$$\tilde{D}\left(Y_C^*\right)\frac{dC_B}{dx} = \frac{\left(C_B^+ - C_B^-\right)}{2t}\left[\left(1-Y_C^*\right)\int_{x^{-\infty}}^{x^*} Y_C dx + Y_C^*\int_{x^*}^{x^{+\infty}} (1-Y_C)dx\right]$$

Therefore, using Fick's first law, we can write

$$\tilde{J}\left(Y_C^*\right) = -\frac{\left(C_B^+ - C_B^-\right)}{2t}\left[\left(1-Y_C^*\right)\int_{x^{-\infty}}^{x^*} Y_C dx + Y_C^*\int_{x^*}^{x^{+\infty}} (1-Y_C)dx\right] \tag{7.19a}$$

After calculating the flux in the composition range of the phase of interest, the integrated diffusion coefficient can be estimated by integrating the flux over the phase layer thickness in accordance with Eq. 7.18. This can also be estimated using the expression of the composition-normalized variable used by Wagner [8] to develop the relation for the interdiffusion coefficient, expressed by (Eq. 6.45)

$$\tilde{D}\left(Y_B^*\right) = \frac{v_m^*}{2t(dY_B/dx)_{Y_B^*}}\left[\left(1-Y_B^*\right)\int_{x^{-\infty}}^{x^*}\frac{Y_B}{v_m}dx + Y_B^*\int_{x^*}^{x^{+\infty}}\frac{(1-Y_B)}{v_m}dx\right]$$

$$\tilde{D}\frac{dN_B}{dx} = \frac{v_m^*\left(N_B^+ - N_B^-\right)}{2t}\left[\left(1-Y_B^*\right)\int_{x^{-\infty}}^{x^*}\frac{Y_B}{v_m}dx + Y_B^*\int_{x^*}^{x^{+\infty}}\frac{(1-Y_B)}{v_m}dx\right]$$

where $Y_B = \frac{N_B - N_B^-}{N_B^+ - N_B}$. Fick's first law, with the help of Eq. 1.150, can be written as

$$\tilde{J} = -\tilde{D}\frac{dC_B}{dx} = -\tilde{D}\left(\frac{\bar{v}_A}{v_m^2}\right)\frac{dN_B}{dx}$$

Replacing this in the previous equation, we get

$$\tilde{J} = -\frac{\bar{v}_A^*}{v_m^*}\frac{\left(N_B^+ - N_B^-\right)}{2t}\left[\left(1-Y_B^*\right)\int_{x^{-\infty}}^{x^*}\frac{Y_B}{v_m}dx + Y_B^*\int_{x^*}^{x^{+\infty}}\frac{(1-Y_B)}{v_m}dx\right] \tag{7.19b}$$

If we consider a constant molar volume in the phase of interest, we can write $v_m^* = v_A^*$. Therefore, the relation for the interdiffusion flux can be written as

$$\tilde{J} = -\frac{\left(N_B^+ - N_B^-\right)}{2tv_m}\left[\left(1-Y_B^*\right)\int_{x^{-\infty}}^{x^*}Y_B dx + Y_B^*\int_{x^*}^{x^{+\infty}}(1-Y_B)dx\right] \tag{7.19c}$$

Note that for constant molar volume, Eq. 7.19a will be the same as Eq. 7.19c. We have noticed in many cases that the last approach that is the determination of the average interdiffusion coefficient by integrating the interdiffusion flux gives smaller error than averaging the composition profile following Eq. 7.16

7.4 Comments on the Relations Between the Parabolic Growth Constants, Integrated and Average Interdiffusion Coefficients

One important fact can be explained with the help of Eq. 7.15 and Fig. 7.12. Previously, we stated that the parabolic growth constant is not a material constant. In fact, the integrated diffusion coefficient is a material constant and it has a fixed value at a particular stoichiometric composition of the compound and the temperature. Moreover, this means that at a particular temperature, the integrated diffusion coefficient is constant irrespective of the end-member composition. However, the parabolic growth constant or the thickness of the phase layer actually

depends on the composition of the end members. It is explained in Fig. 7.12. When the compositions of the end members are closer to the product phase, it will grow with a higher thickness compared to the one having a larger difference in the end-member composition. For example, we consider that the composition of the product phase β is $N_B{}^{\beta} = 0.5$. Suppose, in Fig. 7.12a, the end-member compositions are $N_B^- = 0.45$ and $N_B{}^+ = 0.55$. Therefore, from Eq. 7.15, the parabolic growth constant in this case would be

$$k_p^{\beta}(a) = \frac{0.10}{0.05 \times 0.05} \times \tilde{D}_{\text{int}}^{\beta} \tag{7.20a}$$

In the second case, as shown in Fig. 7.12b, suppose the end-member compositions are $N_B^- = N_B^{\alpha} = 0.35$ and $N_B^+ = N_B^{\gamma} = 0.65$. We can write

$$k_p^{\beta}(b) = \frac{0.30}{0.15 \times 0.15} \times \tilde{D}_{\text{int}}^{\beta} \tag{7.20b}$$

Therefore, for the same annealing time, we can write

$$\frac{k_p^{\beta}(a)}{k_p^{\beta}(b)} = \frac{0.10}{0.30} \times \frac{0.15 \times 0.15}{0.05 \times 0.05} = 3 \tag{7.20c}$$

This now means that the parabolic growth constant in the first case will be 3 times higher. If the annealing time is the same, the ratio of the layer thickness will be (since $\Delta x^2 = 2k_p t$)

$$\frac{\Delta x_{\beta}(a)}{\Delta x_{\beta}(b)} = \sqrt{3} = 1.73 \tag{7.20d}$$

This indicates that in the first diffusion couple, the layer thickness will be 1.73 times higher than the second diffusion couple. A physical explanation for this can be easily understood. In the first case (Fig. 7.12a), the end members have a phase mixture of ($\alpha + \beta$) and ($\beta + \gamma$) between which the β phase grows. The component A dissociates from the α phase at one interface and then diffuses through the β phase to reach to the other interface and reacts with the γ phase to produce the β phase. Similarly, B dissociates from the γ phase and then diffuses to other phase and reacts with the α phase to produce the β phase. In this way, dissociation and reaction of the α and γ phases produces the β phase. Moreover, the β phase that already exists in the end members directly adds to the β product phase in the interdiffusion zone. On the other hand, in the second case (Fig. 7.12b), the β phase is not present in the end members. The product β phase grows by dissociation and reaction only. Therefore, the growth rate in the first case is higher, which is shown by the derivations above. Read Chap. 8 for a better understanding of such mechanisms.

Furthermore, it also should be noted that, in an incremental diffusion couple (if only one phase grows), the thickness of the phase layer is always higher than the

thickness of the same phase grown in a multiphase interdiffusion zone. In fact, many times, we are not able to calculate the diffusion parameter of a phase in a multiphase interdiffusion since it does not grow with reasonable thickness. To determine the diffusion parameter with a smaller error in that phase, an incremental diffusion couple is conducted such that the phase of interest grows with a higher thickness [25–27]. This can be understood from Eq. 7.13c. In an incremental couple, only the first part of the equation is relevant, whereas in multiphase growth, the first part is related to the phase of interest and the second part is relevant for the other phases. In an incremental couple, the components can dissociate at the interfaces and diffuse through the phase of interest only for the growth of this phase. On the other hand, in a couple with multiphase growth, the components have to diffuse through all the phases, which grow together but at different rates. Moreover, simultaneous growth and consumption process at the interfaces make the diffusion process very complicated, which will be discussed in detail in Chap. 8. In fact, Wagner [8] named the parabolic growth constant estimated in a diffusion couple of end members with pure components as the parabolic growth constant of the first kind, k_p^{I}. When the parabolic growth constant is estimated in an incremental diffusion couple with a single phase in the interdiffusion zone, it is referred to as the parabolic growth constant of the second kind, k_P^{II}.

Here, two important facts should be noted. In two different incremental diffusion couples with different end-member compositions, when the same phase grows in an interdiffusion zone, the parabolic growth constant values will be different. After measuring the growth rate at different temperatures, when the parabolic growth constants are plotted following the Arrhenius equation, as expressed in Eq. 7.3, the difference will be in the pre-exponential factor only. The activation energy for the parabolic growth will be same in both the cases. However, when the growth of a particular phase is compared between an incremental couple and the couple with the end members where other phase(s) also grow (multiphase growth), the key values—i.e., the parabolic growth constants, the pre-exponential factors, and the activation energies—will all be different. This is the reason why the parabolic growth constant is not a material constant but rather depends on the composition of the end members. On the other hand, the integrated diffusion coefficient is a material constant and it is the same for a particular phase, irrespective of the end-member composition. In fact, a phase under different conditions grows such that the integrated diffusion coefficient is the same.

To continue with the discussion on the activation energy for the parabolic growth constant and the integrated diffusion coefficient, another important fact should be noted. Replacing Eq. 7.3 in Eq. 7.15, we obtain

$$\tilde{D}_{\mathrm{int}} = \frac{a \times b}{a + b} \times k_p^o \exp\left(-\frac{Q_g}{RT}\right) \tag{7.21a}$$

Similarly, the Arrhenius equation for the integrated interdiffusion coefficient could be written as

$$\tilde{D}_{\text{int}} = \tilde{D}^{o}_{\text{int}} \exp\left(-\frac{Q_D}{RT}\right) \tag{7.21b}$$

By comparing the relations above, it can be easily understood that when in an incremental diffusion couple a single phase grows in the interdiffusion zone, the activation energy for both—the parabolic growth constant and the integrated diffusion coefficient—is the same. The difference is in the pre-exponential terms only. However, it is not true for the phase when it grows with other phases in the interdiffusion zone. In multiphase growth, the parabolic growth constant of a phase is nonetheless estimated directly from the measured thickness of that phase only. However, for the calculation of the integrated diffusion coefficient, the thickness and the composition of the other phases are also used, as explained in Eq. 7.13a. In multiphase growth, when one particular phase grows with a much higher thickness than that of the other thin phases, we have seen that the difference between the activation energies of the parabolic growth constants and the integrated diffusion coefficients is much less for the thick phase. However, it could be significantly different in the case of a phase with much lower thickness. The comments above are also true when the activation energy for the parabolic growth constants and the average interdiffusion coefficients are compared. These are shown in the Fe–Nb system, as presented in Fig. 7.14 for the $NbFe_2$ and NbFe phases. The $NbFe_2$ phase grows with a much higher thickness, and there is not much difference in the activation energy for the parabolic growth constant and the average interdiffusion coefficient. On the other hand, the NbFe phase grows with a small thickness and there is a high difference in the activation energies [28].

In many cases, for example, during the interaction of Cu with Sn-based solder, as shown in Fig. 7.15 [29], where two phases Cu_3Sn and Cu_6Sn_5 grow in the interdiffusion zone, we cannot estimate the diffusion parameters. Although the solder is a multicomponent alloy, only Sn from the solder along with the Cu from the Cu printed wiring board takes part in the interdiffusion process. We may feel optimistic that it is possible to estimate the diffusion parameters by considering it as a binary Cu/Sn system. However, we cannot do so. It should be noted here that the condition for the use of the relations derived for the calculation of the diffusion parameters is valid only when we are able to measure the concentration profile up to the unaffected zone in the couple. It is not possible to estimate exactly how much length is affected in the solder alloy, and it is even almost impossible to find the average composition profile because of presence of a phase mixture.

When only one phase layer grows in the interdiffusion zone, in such couples, it is common practice to calculate the interdiffusion coefficient using the relation $\Delta x = 2\sqrt{\tilde{D}t}$. This relation is written based on the error function analysis explained previously in Chap. 3, with the consideration that the interdiffusion coefficient is constant. However, sometimes, this relation is used even when more than one phase layer grows at the interface. This is incorrect, since in this calculation, the diffusion parameter for the phase of interest is incorrectly estimated without considering the growth of the other phases. Sometimes, one interdiffusion

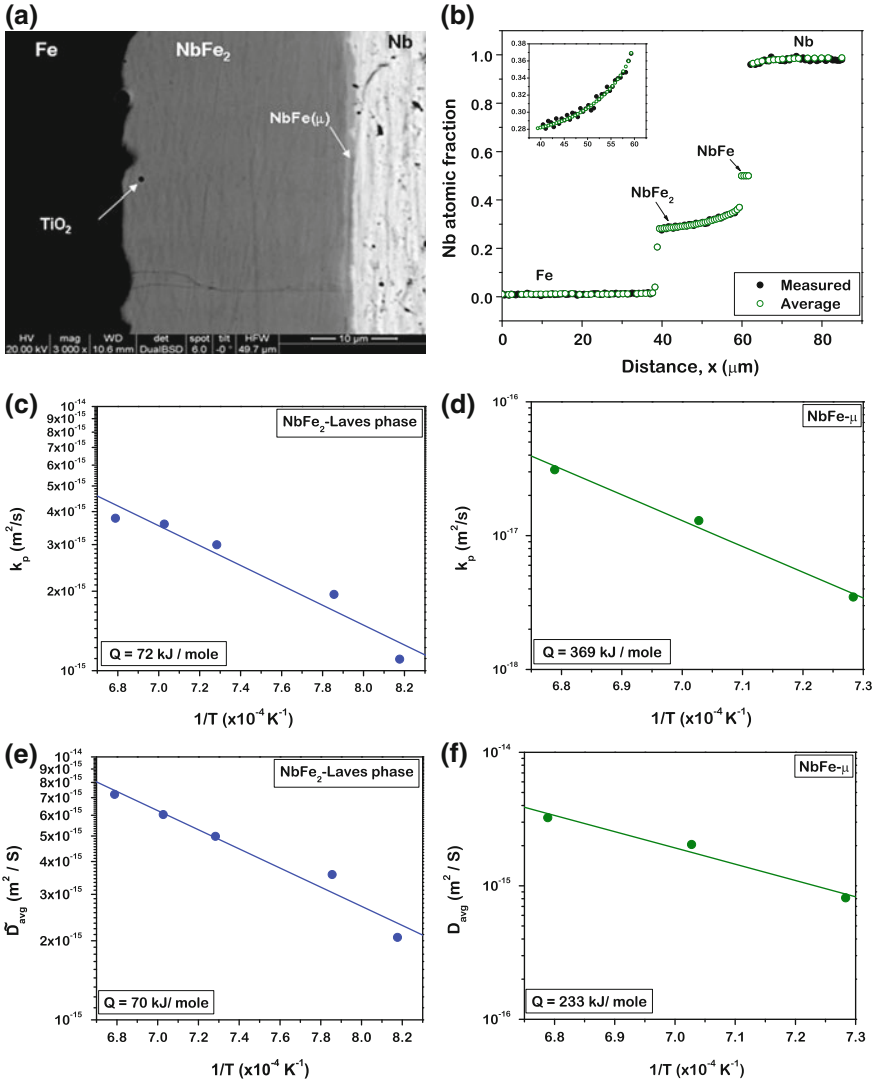

Fig. 7.14 **a** Fe/Nb diffusion couple annealed at 1,150 °C for 25 h, **b** measured composition profile, Arrhenius plots of the parabolic growth constants for **c** $NbFe_2$ and **d** NbFe phases, Arrhenius plots of the average interdiffusion coefficients for **e** $NbFe_2$ and **f** NbFe phases

coefficient is estimated taking the thickness of all the phases together. Note that this is also not correct, since different phases have different compositions and they will have different diffusion coefficients and perhaps different diffusion mechanisms. We commented previously, that when all the phases grow parabolically with time, the total thickness of the interdiffusion zone would also be parabolic with time. By considering this fact, sometimes, the activation energy for growth is

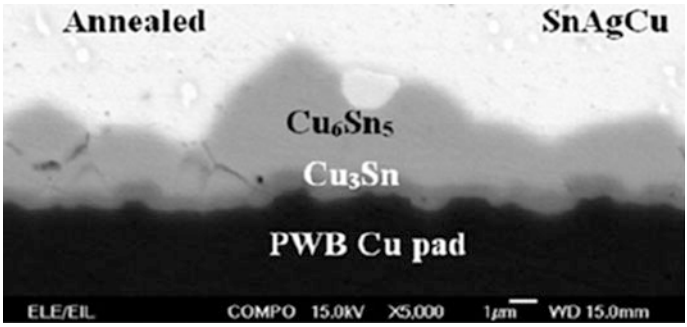

Fig. 7.15 Reaction layers formed in the reaction of Sn-based SnAgCu (*SAC*) solder and Cu after annealing at 110 °C for 750 h

estimated after calculating the parabolic growth constant from the total layer thickness. This is again incorrect, since the activation energy indicates the diffusion and the growth mechanisms that are different for different phases. One single value for all the phases together does not have any physical significance.

7.5 Calculation of the Ratio of the Intrinsic Diffusion Coefficients

In the previous chapter, we have derived the relations for the intrinsic diffusion coefficient for the components, as expressed in Eqs. 6.74 and 6.76. However, again because of the same problem, as discussed before, we cannot calculate a very small composition gradient in the line compounds (or the phases with a narrow homogeneity range) and it is not possible to calculate the absolute values of the intrinsic diffusion coefficients. It is, however, possible to calculate the ratio of diffusivities (Eq. 6.78), using the relation

$$\frac{\bar{v}_A D_B}{\bar{v}_B D_A} = \left[\frac{N_B^+ \int_{x^{-\infty}}^{x_K} \frac{Y_B}{v_m} dx - N_B^- \int_{x_K}^{x^{+\infty}} \frac{(1-Y_B)}{v_m} dx}{-N_A^+ \int_{x^{-\infty}}^{x_K} \frac{Y_B}{v_m} dx + N_A^- \int_{x_K}^{x^{+\infty}} \frac{(1-Y_B)}{v_m} dx} \right] \tag{7.22}$$

In the above relation, it can be seen that we still need to determine the partial molar volumes of the components. In general, since the phases under consideration have a very narrow homogeneity range, the details concerning the variation of the molar volume in that small composition range are not known. Therefore, it is also impossible to calculate the ratio of the intrinsic diffusion coefficients correctly. However, from the relation expressed in Eq. 6.92, we can write

$$\frac{D_B^*}{D_A^*} = \left[\frac{N_B^+ \int_{x^{-\infty}}^{x_K} \frac{Y_B}{v_m} dx - N_B^- \int_{x_K}^{x^{+\infty}} \frac{(1-Y_B)}{v_m} dx}{-N_A^+ \int_{x^{-\infty}}^{x_K} \frac{Y_B}{v_m} dx + N_A^- \int_{x_K}^{x^{+\infty}} \frac{(1-Y_B)}{v_m} dx} \right] \tag{7.23}$$

Thus, at the location of the Kirkendall marker plane, we can calculate directly the ratio of the tracer diffusion coefficients. However, again, in Eq. 7.23, we have disregarded the contribution from the vacancy wind effect. Considering the vacancy wind effect, Eq. 7.23 can be written correctly as

$$\frac{D_B^*(1-W_B)}{D_A^*(1+W_A)} = \left[\frac{N_B^+\int_{x^{-\infty}}^{x_K}\frac{Y_B}{v_m}dx - N_B^-\int_{x_K}^{x^{+\infty}}\frac{(1-Y_B)}{v_m}dx}{-N_A^+\int_{x^{-\infty}}^{x_K}\frac{Y_B}{v_m}dx + N_A^-\int_{x_K}^{x^{+\infty}}\frac{(1-Y_B)}{v_m}dx}\right] \tag{7.24}$$

where $W_i = \frac{2N_i(D_A^*-D_B^*)}{M_o(N_AD_A^*+N_BD_B^*)}$.

For most intermetallic compounds that have a complicated crystal structure, the value of the structure factor M_o is not readily available. For this reason, we calculate the ratio of the tracer diffusion coefficients using the relation expressed in Eq. 7.23, i.e., by neglecting the role of the vacancy wind effect. Because of this assumption, we cannot estimate the ratio of the tracer diffusion coefficients correctly; however, it is still very useful, to understand the atomic mechanism of diffusion. In many cases, this does not greatly affect the estimated values and error falls within the limit of experimental error that one typically expects from the experimental procedure.

The calculation procedures to determine the ratio of the tracer diffusion coefficients are explained in Fig. 7.16. Note here that we need to calculate the integrals $\Phi = \int_{x^{-\infty}}^{x_K}\frac{Y_B}{v_m}dx$ and $\Psi = \int_{x_K}^{x^{+\infty}}\frac{(1-Y_B)}{v_m}dx$ on the either side of the Kirkendall marker plane, located at x_K, and indicated by the white dotted markers on the schematic diffusion couple. When we calculate the ratio of the tracer diffusion coefficients in a line compound by neglecting the contribution of the vacancy wind effect, Eq. 7.23 can be rewritten as

$$\frac{D_B^*}{D_A^*} = \left[\frac{N_B^+\Phi - N_B^-\Psi}{-N_A^+\Phi + N_A^-\Psi}\right] \tag{7.25}$$

In few cases, such as that presented in Fig. 7.16a, there could be a phase of interest with narrow composition range in which the marker plane is located. On both sides of this phase, composition varies continuously. In this case, the values of Φ and Ψ are

$$\Phi = \left(\int_{x^{-\infty}}^{x_{\beta_1}}\frac{(N_B - N_B^-)}{v_m}dx + \frac{\left(N_B^\beta - N_B^-\right)}{v_m^\beta}\Delta x_{\beta_1}\right) = \left(\int_{x^{-\infty}}^{x_{\beta_1}}\frac{(N_B - N_B^-)}{v_m}dx + \frac{R1}{v_m^\beta}\right) \tag{7.26a}$$

$$\Psi = \left(\int_{x_{\beta_2}}^{x^{+\infty}}\frac{(N_B^+ - N_B)}{v_m}dx + \frac{\left(N_B^+ - N_B^\beta\right)}{v_m^\beta}\Delta x_{\beta_2}\right) = \left(\int_{x_{\beta_2}}^{x^{+\infty}}\frac{(N_B^+ - N_B)}{v_m}dx + \frac{S1}{v_m^\beta}\right) \tag{7.26b}$$

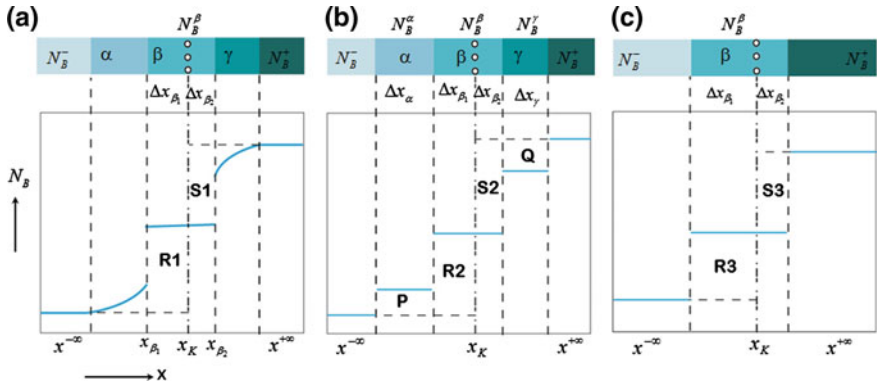

Fig. 7.16 Imaginary composition profiles explaining the estimation of the ratio of diffusivities of the components for different conditions

Note here that after converting Y_B to N_B, we have not included the factor $(N_B^+ - N_B^-)$. This is because the same term is present in both numerator and denominator in Eq. 7.25 to cancel out each other. Sometimes, in multiphase growth, all the phases grow either as line compounds or with a narrow composition range, as expressed in Fig. 7.16b. In this case, the values of Φ and Ψ can be written as

$$\Phi = \frac{\left(N_B^{\alpha} - N_B^{-}\right)}{v_m^{\alpha}}\Delta x_{\alpha} + \frac{\left(N_B^{\beta} - N_B^{-}\right)}{v_m^{\beta}}\Delta x_{\beta_1} = \frac{P}{v_m^{\alpha}} + \frac{R2}{v_m^{\beta}} \tag{7.27a}$$

$$\Psi = \frac{\left(N_B^{+} - N_B^{\gamma}\right)}{v_m^{\gamma}}\Delta x_{\gamma} + \frac{\left(N_B^{+} - N_B^{\beta}\right)}{v_m^{\beta}}\Delta x_{\beta_2} = \frac{Q}{v_m^{\gamma}} + \frac{S2}{v_m^{\beta}} \tag{7.27b}$$

If an incremental diffusion couple experiment is conducted such that only one phase grows in the interdiffusion zone, as shown in Fig. 7.16c, then these values can be written as

$$\Phi = \frac{\left(N_B^{\beta} - N_B^{-}\right)}{v_m^{\beta}}\Delta x_{\beta_1} = \frac{R3}{v_m^{\beta}} \tag{7.28a}$$

$$\Psi = \frac{\left(N_B^{+} - N_B^{\beta}\right)}{v_m^{\beta}}\Delta x_{\beta_2} = \frac{S3}{v_m^{\beta}} \tag{7.28b}$$

7.6 Calculation of the Tracer Diffusion Coefficients

The previous chapter contained an explanation of the procedure for estimating the tracer diffusion coefficients in a diffusion couple indirectly by using the interdiffusion coefficients, the ratio of the intrinsic diffusion coefficients, and the thermodynamic factor. It can also be estimated directly (without calculating the interdiffusion coefficient) by using the absolute values of the intrinsic diffusion coefficients and the thermodynamic factor. As explained in the previous section, we can estimate only the ratio of the tracer diffusion coefficients in the phases with a narrow homogeneity range. Consequently, we need to relate the integrated diffusion coefficients with the ratio of the tracer diffusion coefficients and thermodynamic parameters (driving forces) to estimate the absolute values of the tracer diffusion coefficients. We consider a hypothetical incremental diffusion couple of α and γ, as shown in Fig. 7.17, where only a single β phase grows at the interface. Further, α is A-rich phase and γ is B-rich phase. This means that A dissociates from α at the interface I and then diffuses to the interface II. At this interface, A reacts with γ to produce the β phase. Concurrently, B dissociates from γ and then diffuses to the interface I. At this interface, it reacts with α to produce the β phase. From the chemical potential point of view (see Chaps. 1 and 4), A diffuses from the interfaces I to II because $\mu_A^{\mathrm{I}} > \mu_A^{\mathrm{II}}$. Simultaneously, B diffuses from the interface II to I because $\mu_B^{\mathrm{II}} > \mu_B^{\mathrm{I}}$, as explained in Fig. 7.17. Replacing the relation between the interdiffusion coefficient and the tracer diffusion coefficient as expressed in Eq. 6.90 (see Chap. 6) in Eq. 7.7, we get

$$\begin{aligned}\tilde{D}_{\mathrm{int}} &= \int_{N_B^{\beta 1}}^{N_B^{\beta 2}} \left(N_A^{\beta} D_B^{*} + N_B^{\beta} D_A^{*}\right)\left(\frac{d\ln a_B}{d\ln N_B}\right) dN_B \\ \tilde{D}_{\mathrm{int}} &= \int_{a_B^{\mathrm{I}}}^{a_B^{\mathrm{II}}} \left(N_A^{\beta} D_B^{*} + N_B^{\beta} D_A^{*}\right) N_B^{\beta} d\ln a_B\end{aligned} \tag{7.29}$$

where $a_B{}^{\mathrm{I}}$ and a_B^{II} are the activities of the component B at the interfaces I and II, respectively. Since we are considering an average composition of the phase with a very narrow homogeneity range and at that composition, it will have the fixed tracer diffusion coefficient of the components. This can therefore be written as

$$\tilde{D}_{\mathrm{int}} = \int_{a_B^{\mathrm{I}}}^{a_B^{\mathrm{II}}} \left(N_A^{\beta} D_B^{*} + N_B^{\beta} D_A^{*}\right) N_B^{\beta} d\ln a_B = \left(N_A^{\beta} D_B^{*} + N_B^{\beta} D_A^{*}\right) N_B^{\beta} \left[\ln a_B^{\mathrm{II}} - \ln a_B^{\mathrm{I}}\right] \tag{7.30}$$

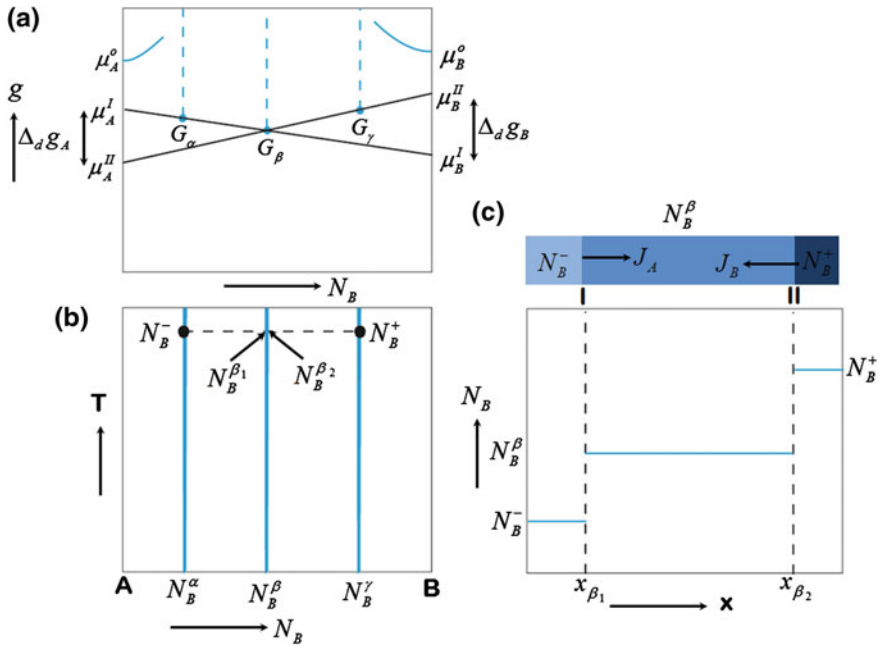

Fig. 7.17 Imaginary **a** free energy diagram, **b** phase diagram, and **c** composition profile explaining the estimation of the tracer diffusion coefficients from an incremental diffusion couple

From the relations between the activities and the chemical potential of the components as derived in Chap. 1, we can write

$$\mu_B^{\mathrm{I}} = \mu_B^o + RT \ln a_B^{\mathrm{I}} \tag{7.31a}$$

$$\mu_B^{\mathrm{II}} = \mu_B^o + RT \ln a_B^{\mathrm{II}} \tag{7.31b}$$

From Eqs. 7.31a and 7.31b, we can express the relation for the driving force for diffusion of the component B as

$$\Delta_d g_B = \mu_B^{\mathrm{I}} - \mu_B^{\mathrm{II}} = -RT\left(\ln a_B^{\mathrm{II}} - \ln a_B^{\mathrm{I}}\right) \tag{7.32}$$

Replacing Eq. 7.32 in Eq. 7.30, we get

$$\tilde{D}_{\mathrm{int}}^{\beta} = -\left(N_A^{\beta} D_B^* + N_B^{\beta} D_A^*\right) \frac{N_B^{\beta} \Delta_d g_B}{RT} \tag{7.33a}$$

It should be noted here that $N_B^{\beta} \Delta_d g_B = N_A^{\beta} \Delta_d g_A$ (see Sect. 7.7.2). Thus, the same relation, with respect to the driving force for diffusion of the component A, can be written as

$$\tilde{D}_{\text{int}}^{\beta} = -\left(N_A^{\beta} D_B^* + N_B^{\beta} D_A^*\right) \frac{N_A^{\beta} \Delta_d g_A}{RT} \tag{7.33b}$$

If the product phase β grows between the pure end members A and B such that no other phases are present in the phase diagram, it is possible to write Eq. 7.33a as

$$\tilde{D}_{\text{int}}^{\beta} = -\left(N_A^{\beta} D_B^* + N_B^{\beta} D_A^*\right) \frac{\Delta_f g_{\beta}}{RT} \tag{7.34}$$

where$\Delta_f g_{\beta}$ is the free energy for the formation of the β phase. Therefore, by estimating the ratio of the tracer diffusion coefficients, the integrated diffusion coefficients, and the driving force for diffusion of the components, the absolute values of the tracer diffusion coefficients can be estimated.

One important fact should be noted here that the integrated diffusion coefficients and the ratio of the tracer diffusion coefficients could be estimated from any type of diffusion couple—whether an incremental diffusion couple or a couple with pure end members. However, the driving force for diffusion should be estimated considering the growth of the product phase in an incremental couple from the adjacent phases in the phase diagram. Similarly, even if the diffusion parameters in the product β phase are estimated in an incremental couple with phase mixtures of $\alpha + \beta$ and $\beta + \gamma$ as the end members (for, e.g., see Fig. 7.12a), the driving force for diffusion should be estimated as if the layer is grown between the pure α and γ phases as the end members. Note here that the diffusion coefficients are the material constants and would have the same values irrespective of the different end members.

7.7 The Kirkendall Marker Velocity in a Line Compound

In the previous chapter, we have derived the relation for the velocity of the marker plane (Eq. 6.61) as

$$v_K = \bar{v}_B (D_B - D_A) \left(\frac{\partial C_B}{\partial x}\right)_K \tag{7.35}$$

Since we cannot determine the absolute values of the intrinsic diffusion coefficients in the line compound, the relation must be derived differently. Using standard thermodynamic relations (Eq. 1.150) together with Eq. 7.35, the following can be written

$$v_K = \frac{\bar{v}_A \bar{v}_B}{v_m^2}(D_B - D_A)\left(\frac{\partial N_B}{\partial x}\right)_K \tag{7.36}$$

Integrating Eq. 7.36 over the composition range from $N_B{}^{\beta_1}$ to $N_B^{\beta_2}$ and the position range (that is the thickness) from x_{β_1} to x_{β_2},

$$\int_{x_{\beta_1}}^{x_{\beta_2}} v_K dx = \int_{N_B^{\beta_1}}^{N_B^{\beta_2}} \frac{\bar{v}_A \bar{v}_B}{v_m^2}(D_B - D_A) dN_B \tag{7.37}$$

Further, we know from Eq. 6.65 that

$$\tilde{D} v_m = N_A \bar{v}_A D_B + N_B \bar{v}_B D_A \tag{7.38}$$

Using Eq. 7.38 in Eq. 7.37, we arrive at

$$v_K \Delta x_\beta = \frac{\bar{v}_A \bar{v}_B}{v_m^2}(D_B - D_A) \int_{N_B^{\beta 1}}^{N_B^{\beta 2}} \frac{\tilde{D} v_m}{N_A \bar{v}_A D_B + N_B \bar{v}_B D_A} dN_B$$

Here, we are considering the phase with a narrow homogeneity range or a line compound with an almost fixed or an average composition. Consequently, it is possible to consider the intrinsic diffusion coefficients and molar volume of the β phase as more or less constant. It will, therefore, almost have a fixed velocity. Thus, we can write

$$v_K \Delta x_\beta = \frac{\bar{v}_A \bar{v}_B}{v_m} \frac{D_B - D_A}{N_A \bar{v}_A D_B + N_B \bar{v}_B D_A} \int_{N_B^{\beta 1}}^{N_B^{\beta 2}} \tilde{D} dN_B \tag{7.39}$$

From the definition of the integrated diffusion coefficient (Eq. 7.7) and dividing both numerator and denominator by $\bar{v}_B D_A$ in Eq. 7.39, the velocity can be written as [30]

$$v_K = \frac{\bar{v}_A}{v_m} \frac{\frac{D_B}{D_A} - 1}{\left(\frac{\bar{v}_A D_B}{\bar{v}_B D_A}\right) N_A + N_B} \frac{\tilde{D}_{\text{int}}}{\Delta x_\beta} \tag{7.40}$$

Again, it is almost impossible to calculate the partial molar volumes of the phase and the exact velocity is thus impossible to calculate. Mostly, we consider $v_m = \bar{v}_A = \bar{v}_B$ and calculate the velocity of the marker plane in a line compound. It can be seen that to calculate the velocity of the marker plane, it is first necessary to

calculate the intrinsic (or the ratio of the intrinsic) diffusion coefficient from the composition profile. We can derive a simpler relation to estimate this value directly from the composition profile. We denote $\phi = \int_{x^{-\infty}}^{x_K} \frac{Y}{v_m} dx$ and $\psi = \int_{x_K}^{x^{+\infty}} \frac{1-Y}{v_m} dx$. Therefore, the relation for the intrinsic diffusion coefficients, as expressed in Eqs. 6.75 and 6.77, can be written as

$$D_B = \frac{1}{2t} \frac{v_m^2}{\bar{v}_A} \left(\frac{\partial x}{\partial N_B} \right)_K \left(N_B^+ \phi - N_B^- \psi \right) \tag{7.41a}$$

$$D_A = \frac{1}{2t} \frac{v_m^2}{\bar{v}_B} \left(\frac{\partial x}{\partial N_A} \right)_K \left(N_A^+ \phi - N_A^- \psi \right) \tag{7.41b}$$

Replacing Eq. 7.41a, b in Eq. 7.36, we get

$$v_K = \frac{\bar{v}_A \bar{v}_B}{v_m^2} \left[\frac{1}{2t} \frac{v_m^2}{\bar{v}_A} \left(\frac{\partial x}{\partial N_B} \right)_K \left(N_B^+ \phi - N_B^- \psi \right) - \frac{1}{2t} \frac{v_m^2}{\bar{v}_B} \left(\frac{\partial x}{\partial N_A} \right)_K \left(N_A^+ \phi - N_A^- \psi \right) \right] \left(\frac{\partial N_B}{\partial x} \right)_K$$

Since $N_A + N_B = 1$ that is $dN_A + dN_B = 0$, we can write

$$\begin{aligned} v_K &= \frac{1}{2t} \left[\bar{v}_B \left(N_B^+ \phi - N_B^- \psi \right) + \bar{v}_A \left(N_A^+ \phi - N_A^- \psi \right) \right] \\ v_K &= \frac{1}{2t} \left[\left(\bar{v}_B N_B^+ + \bar{v}_A N_A^+ \right) \phi - \left(\bar{v}_B N_B^- + \bar{v}_A N_A^- \right) \psi \right] \end{aligned} \tag{7.42a}$$

In a diffusion couple with pure components as end members, $N_B^- = 0$, $N_A{}^- = 1$, $N_B^+ = 1$, and $N_A^+ = 0$. Therefore, Eq. 7.42a reduces to [26]

$$v_K = \frac{1}{2t} \left[\bar{v}_B \phi - \bar{v}_A \psi \right] \tag{7.42b}$$

The advantage of using Eq. 7.42a is that this makes it possible to determine the velocity of the marker plane directly from the Y/v_m versus x plot. Furthermore, this relation can be used in any phase with wide homogeneity range or a line compound. In order to calculate the partial molar volumes in a line compound or in a phase where the variation of the molar volume with composition is not known, the approximate velocity of the marker plane can be estimated by considering $\bar{v}_B = \bar{v}_A = v_m$.

It should be noted here that we have composition jumps between the end members and the product phases in multiphase growth. Mathematically, we cannot differentiate the composition profile anywhere if it is not continuous at some points. Therefore, we actually assume a sharp, but continuous change in composition at those points. On the other hand, we highlight that

all important relations, i.e., those for the estimation of the integrated diffusion coefficient using Eq. 7.13a, the interdiffusion flux using Eq. 7.19a, and the ratio of diffusivities by Eqs. 7.22 and 7.23, were derived without any differentiation of the composition profile, and thus, the obtained formulas are mathematically correct.

7.8 Case Studies

7.8.1 Calculation of the Integrated and the Ratio of the Tracer Diffusion Coefficients

We consider a diffusion couple of Nb/Si annealed at 1,250 °C for 24 h [27]. According to the phase diagram shown in Fig. 7.18a, two phase layers Nb_5Si_3 and $NbSi_2$ are expected to grow at the interface, as can be seen in Fig. 7.18b. According to the composition analysis, the composition profile in the Nb(Si) and Si(Nb) was negligible and can be neglected. Since the phases are actually line compounds, the composition profile can be drawn after measuring the thickness of the phase layers, as shown in Fig. 7.19a. "K" denotes the location of the Kirkendall marker plane. Therefore, we can calculate the integrated diffusion coefficients for both the phases and the ratio of the tracer diffusion coefficients in the $NbSi_2$ phase. The thicknesses of the phase layers are mentioned in the profile. The calculated molar volumes of the phases are $v_m^{Nb_5Si_3} = 9.6 \times 10^{-6}$ and $v_m{}^{NbSi_2} = 8.7 \times 10^{-6}\ m^3/mol$.

The integrated diffusion coefficients can be estimated as (see Fig. 7.19b, c)

$$\tilde{D}_{int}^{Nb_5Si_3} = \frac{a \times b}{a+b}\frac{\Delta x_{Nb_5Si_3}^2}{2t} + \frac{\Delta x_{Nb_5Si_3}}{2t}\left[\frac{b(0) + a\left(\frac{v_m^{Nb_5Si_3}}{v_m^{NbSi_2}}P\right)}{a+b}\right] = 4.4 \times 10^{-16}\ m^2/s$$

where $a = \frac{3}{8} - 0 = \frac{3}{8}$, $b = 1 - \frac{3}{8} = \frac{5}{8}$, $\Delta x_{Nb_5Si_3} = 4.7 \times 10^{-6}$ m, $2t = 2 \times 24 \times 60 \times 60 = 172,800$ s, and $P = \left(1 - \frac{2}{3}\right) \times 110.2 \times 10^{-6}$ m.

$$\tilde{D}_{int}^{NbSi_2} = \frac{c \times d}{c+d}\frac{\Delta x_{NbSi_2}^2}{2t} + \frac{\Delta x_{NbSi_2}}{2t}\left[\frac{d\left(\frac{v_m^{NbSi_2}}{v_m^{Nb_5Si_3}}Q\right) + c(0)}{c+d}\right] = 1.6 \times 10^{-14}\ m^2/s$$

where $c = \frac{2}{3} - 0 = \frac{2}{3}$, $d = 1 - \frac{2}{3} = \frac{1}{3}$, $\Delta x_{Nb_5Si_3} = 110.2 \times 10^{-6}$ m, $2t = 2 \times 24 \times 60 \times 60 = 172,800$ s, and $Q = \left(1 - \frac{3}{8}\right) \times 4.7 \times 10^{-6}$ m.

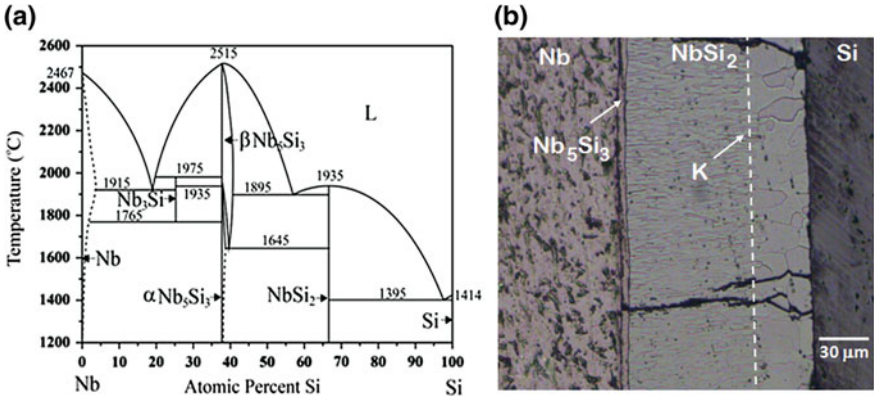

Fig. 7.18 **a** Nb–Si phase diagram [31] and **b** Nb/Si diffusion couple annealed at 1,250 °C for 24 h [27]

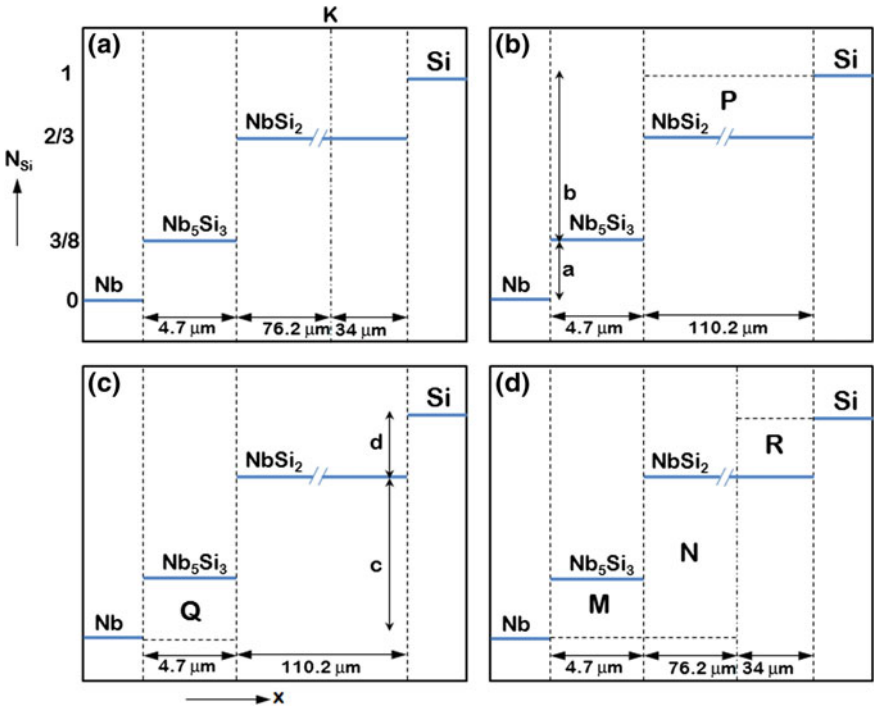

Fig. 7.19 Estimation of the diffusion parameters from the composition profile in the Nb–Si system is explained. **a** Composition profile, estimation of the integrated diffusion coefficient for **b** Nb_5Si_3, **c** $NbSi_2$, and **d** estimation of the ratio of diffusivities in the $NbSi_2$ phase

The ratio of the diffusivities can be estimated as (see Fig. 7.19d)

$$\frac{D^*_{\mathrm{Si}}}{D^*_{\mathrm{Nb}}} = \left[\frac{N^+_{\mathrm{Si}}\Phi - N^-_{\mathrm{Si}}\Psi}{-N^+_{\mathrm{Nb}}\Phi + N^-_{\mathrm{Nb}}\Psi}\right] = 4.62$$

where $\Phi = \frac{M}{v_m^{\mathrm{Nb_5Si_3}}} + \frac{N}{v_m^{\mathrm{NbSi_2}}}$, $\Psi = \frac{R}{v_m^{\mathrm{NbSi_2}}}$, $M = \left(\frac{3}{8} - 0\right) \times 4.7 \times 10^{-6}$ m, $N = \left(\frac{2}{3} - 0\right) \times 76.2 \times 10^{-6}$ m, $R = \left(1 - \frac{2}{3}\right) \times 34 \times 10^{-6}$ m, $N^-_{\mathrm{Si}} = 0$, $N_{\mathrm{Si}}{}^+ = 1$, $N^-_{\mathrm{Nb}} = 1$, and $N_{\mathrm{Nb}}{}^+ = 0$.

7.8.2 Calculation of the Absolute Values of the Tracer Diffusion Coefficients

Let us consider the incremental diffusion couple between $Co_{0.48}Si_{0.52}$ and Si [25, 30]. From the Co–Si phase diagram shown in Fig. 7.20a [31], it can be seen that the $Co_{0.48}Si_{0.52}$ alloy consists of two phases, CoSi and $CoSi_2$. Therefore, in the diffusion couple, as expected, only the $CoSi_2$ phase is grown, as shown in Fig. 7.20b. The couple was annealed at 1,186 °C for 100 h. ThO_2 particles were used to detect the location of the Kirkendall marker plane. The length of the phase layer on either side of the marker plane is shown. With the aim of calculating the absolute values at the Kirkendall marker plane, we should first determine the integrated diffusion coefficients and the ratio of the tracer diffusion coefficients. These are

$$\begin{aligned}
\tilde{D}^{\mathrm{CoSi_2}}_{\mathrm{int}} &= \frac{ab}{a+b}\frac{\Delta x^2_{\mathrm{CoSi_2}}}{2t} \\
&= \frac{(2/3 - 0.52)(1 - 2/3)}{1 - 0.52}\frac{\left(154.4 \times 10^{-6}\right)^2}{2 \times 100 \times 60 \times 60} = 3.3 \times 10^{-15}\ \mathrm{m^2/s} \\
\frac{v_{\mathrm{Co}}}{v_{\mathrm{Si}}}\frac{D_{\mathrm{Si}}}{D_{\mathrm{Co}}} = \frac{D^*_{\mathrm{Si}}}{D^*_{\mathrm{Co}}} &= \left[\frac{N^+_{\mathrm{Si}}R - N^-_{\mathrm{Si}}S}{-N^+_{\mathrm{Co}}R + N^-_{\mathrm{Co}}S}\right] \\
&= \left[\frac{1 \times (2/3 - 0.52) \times 102.2 - 0.52 \times (1 - 2/3) \times 52.2}{-0 \times (2/3 - 0.52) \times 102.2 + 0.48 \times (1 - 2/3) \times 52.2}\right] = 0.7
\end{aligned}$$

Now, we need to calculate the driving force for diffusion of the components through the $CoSi_2$ phase. As mentioned earlier, we need to consider as if the product phase is grown between the pure CoSi and Si end members. Since the diffusion parameters are the material constants, the values estimated above would be the same. The free energy of the phases at 1,186 °C is estimated using the thermodynamic parameters, as listed in Table 7.1. First, the enthalpy and the entropy at the temperature of interest are estimated using the relations

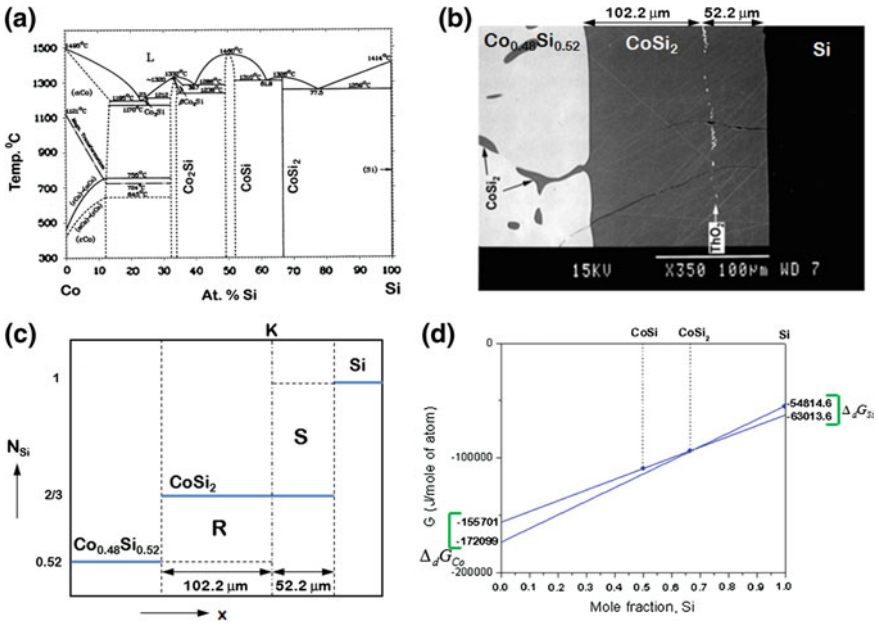

Fig. 7.20 **a** Co–Si phase diagram, **b** $Co_{0.48}Si_{0.52}$/Si diffusion couple annealed at 1,186 °C for 100 h, **c** composition profile, and **d** the estimation of the driving forces [25, 30]

Table 7.1 Thermodynamic parameters in Co–Si system are tabulated

	Details of C_p values		
	CoSi	$CoSi_2$	Si
A	49.16	70.86	23.698
B × 10^{-3}	12.1	I8.66	3.305
C × 10^5	7.54	9.93	4.351
S_{298}	43.2 J/mol.K	64.2 J/mol.K	18.81 J/mol.K
h_{298}	−94,600 J (mole of CoSi)	−98,700 J (mole of $CoSi_2$)	0

$$h_T = h_{298} + \int_{298}^{T} C_P dT \tag{7.43a}$$

$$s_T = s_{298} + \int_{298}^{T} \frac{C_P}{T} dT \tag{7.43b}$$

where $C_p = A + BT - \frac{C}{T^2}$

After this, the free energies of the phases are estimated using the relation $g = h - Ts$. The values are estimated as $g(\mathrm{CoSi}) = -218{,}714.9$ J/mole of CoSi, $g(\mathrm{CoSi_2}) = -281{,}727.8$ J/mol of $\mathrm{CoSi_2}$, and $g(\mathrm{Si}) = -54{,}814.57$ J/mole of atom. To estimate the driving forces from a free energy diagram—which is drawn with respect to per mol of atom—it is necessary to divide the values of g estimated for CoSi and $\mathrm{CoSi_2}$ by the number of atoms in the compound that is 2 and 3, respectively. This leads to $g(\mathrm{CoSi}) = -109{,}357.45$ J/mole of atom and $g(\mathrm{CoSi_2}) = -93{,}909.27$ J/mole of atom. We can use the estimated value of the Si free energy as it is. After plotting the values, as shown in Fig. 7.20d, we get $\Delta_d g_{\mathrm{Si}} = -8{,}199$ J/mol of Si atom and $\Delta_d g_{\mathrm{Co}} = -16{,}398$ J/mol of Co atom. Previously, we stated that $N_{\mathrm{Si}}\Delta_d g_{\mathrm{Si}} = N_{\mathrm{Co}}\Delta_d g_{\mathrm{Co}}$. It can be seen that this is true since $N_{\mathrm{Si}} = 2/3$ and $N_{\mathrm{Co}} = 1/3$. Next, the absolute values of the tracer diffusion coefficients are determined using the relations

$$\tilde{D}_{\mathrm{int}} = 3.3 \times 10^{-15}\ \mathrm{m^2/s} = -\left(N_{\mathrm{Co}}D^*_{\mathrm{Si}} + N_{\mathrm{Si}}D^*_{\mathrm{Co}}\right)\frac{N_{\mathrm{Si}}\Delta_d g_{\mathrm{Si}}}{RT}$$

$$\frac{D^*_{\mathrm{Si}}}{D^*_{\mathrm{Co}}} = 0.7$$

The values are estimated as $D^*_{\mathrm{Co}} = 8.25 \times 10^{-15}\ \mathrm{m^2/s}$, $D^*_{\mathrm{Si}} = 5.77 \times 10^{-15}\ \mathrm{m^2/s}$.

The estimated values of the driving forces demonstrate that $N_{\mathrm{Si}}\Delta_d g_{\mathrm{Si}} = N_{\mathrm{Co}}\Delta_d g_{\mathrm{Co}}$. We can demonstrate that this is true in a different way with respect to the reaction/diffusion at the interfaces. This is explained with the help of Fig. 7.21. It can be seen that Si diffuses to the interface I and reacts with CoSi to produce the $\mathrm{CoSi_2}$ phase. Co dissociates at the same interface from CoSi to produce the product phase at the same interface. The dissociated Co diffuses through the $\mathrm{CoSi_2}$ product phase and reacts with Si at the interface II to produce the $\mathrm{CoSi_2}$ product phase. In terms of a reaction at the interfaces, we can write

Interface I

$$2\mathrm{CoSi} = [\mathrm{Co}]_d + \mathrm{CoSi_2} \tag{7.44a}$$

$$\mathrm{CoSi} + [\mathrm{Si}]_d = \mathrm{CoSi_2} \tag{7.44b}$$

Interface II

$$2\mathrm{Si} + [\mathrm{Co}]_d = \mathrm{CoSi_2} \tag{7.44c}$$

Note here that the above interface reactions do not control the growth of the phase. Rather, the diffusion of the components through the product phase controls the growth process. From Eq. 7.44b, we can write the energy change per mol of moving Si atom as

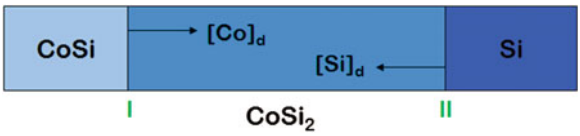

Fig. 7.21 A schematic representation of the CoSi/Si diffusion couple

$$\Delta_d g_{\mathrm{Si}} = g(\mathrm{CoSi_2}) - g(\mathrm{CoSi}) - g(\mathrm{Si}) \tag{7.45a}$$

Since the same Co atoms are involved in producing the product phase at both interfaces, by adding Eqs. 7.44a and 7.44c, we can write

$$2\mathrm{CoSi} + 2\mathrm{Si} = 2\mathrm{CoSi_2}$$

Therefore, the energy change per mol of a moving Co atom can be written as

$$\Delta_d g_{\mathrm{Co}} = 2g(\mathrm{CoSi_2}) - 2g(\mathrm{CoSi}) - 2g(\mathrm{Si}) \tag{7.45b}$$

Comparing Eqs. 7.45a and 7.45b, we can write

$$\begin{aligned} \Delta_d g_{\mathrm{Co}}^{\mathrm{CoSi_2}} &= 2\Delta_d g_{\mathrm{Si}}^{\mathrm{CoSi_2}} \\ \frac{1}{3}\Delta_d g_{\mathrm{Co}}^{\mathrm{CoSi_2}} &= \frac{2}{3}\Delta_d g_{\mathrm{Si}}^{\mathrm{CoSi_2}} \\ N_{\mathrm{Co}}^{\mathrm{CoSi_2}}\Delta_d g_{\mathrm{Co}}^{\mathrm{CoSi_2}} &= N_{\mathrm{Si}}^{\mathrm{CoSi_2}}\Delta_d g_{\mathrm{Si}}^{\mathrm{CoSi_2}} \end{aligned}$$

7.8.3 *Diffusion Studies in the Ti-Si System and the Significance of the Parabolic Growth Constant*

Ti–Si is one of the important refractory metal–silicon systems used extensively in the very large-scale integrated (VLSI) industry. The C54 phase $TiSi_2$ is used as a contact because of its low resistivity and excellent thermal stability. This material is grown by depositing a thin film of Ti on Si. Later, self-aligned silicide (salicide) is grown at the interface by a diffusion-controlled process. Therefore, extensive studies have been conducted in this system in order to understand the growth of the phases mainly in the thin-film condition because of the relevance of such studies. Time-dependent experiments were conducted, and the growth of the phase was found to follow the parabolic growth law (that is, diffusion-controlled growth) [32]. However, studies in the thin-film condition might not be suitable to develop a basic understanding of both the phase growth mechanism and the atomic mechanism of diffusion, which is explained in more detail later in Chap. 11.

Interdiffusion in the bulk solid-state condition is ideal for fundamental studies. As shown in Fig. 7.22a, the $TiSi_2$, TiSi, and Ti_5Si_4 phases are grown with a higher

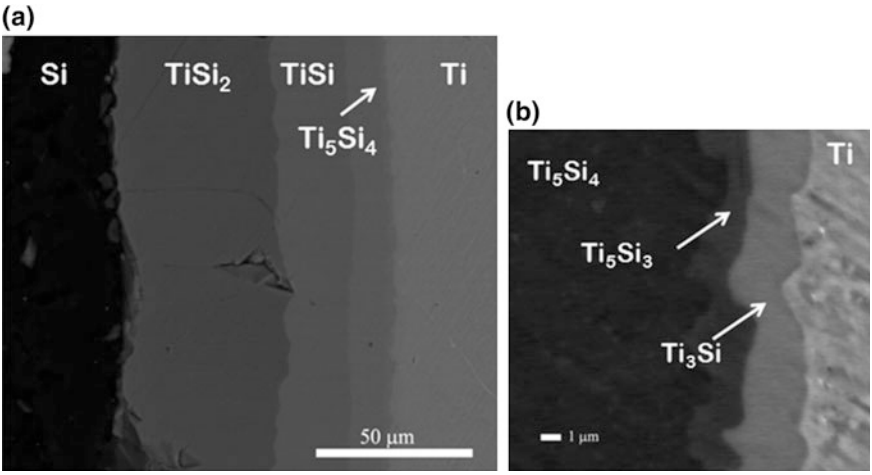

Fig. 7.22 **a** Ti/Si couple annealed at 1,200 °C for 16 h showing the thicker phases and **b** image of the same couple near the Ti end member showing the presence of other phases [32]

Table 7.2 Thicknesses of phases grown at different temperatures after 16 h of annealing

Temperature (°C)	(Δx $TiSi_2$ in μm)	Δx (TiSi in μm)	Δx (Ti_5Si_4 in μm)
1,150	39 ± 1.1	23 ± 0.5	9 ± 0.3
1,175	43 ± 0.6	24 ± 0.4	12 ± 0.3
1,200	52 ± 0.8	24 ± 0.6	14 ± 0.4
1,225	60 ± 0.5	25 ± 0.6	15 ± 0.7
1,250	67 ± 0.9	25 ± 0.7	18 ± 0.4

thickness at 1,200 °C after an annealing period of 16 h. A closer examination reveals the presence of two other phases, Ti_5Si_3 and Ti_3Si, as shown in Fig. 7.22b. Since these are present as very thin layers, we consider only the first three phases for analysis. Since the parabolic growth of the interdiffusion zone has been already confirmed by many researchers in this system, at first, the temperature-dependent experiments were conducted to estimate the activation energies. The thicknesses of the phase layers (Δx) are tabulated in Table 7.2. Some interesting behavior concerning the growth of TiSi phase can be noticed. The increase in layer thickness with increasing annealing temperature is negligible.

There could be two reasons for this behavior. As already discussed, in an incremental couple, when only one phase layer grows in the interdiffusion zone, it is not affected by any other phases. On the other hand, the growth kinetics of a phase in multiphase interdiffusion depends on the growth of neighboring phases, which is discussed in detail subsequently in Chap. 8. Ideally, all the phases should grow according to their own diffusion parameters since these are the material constants. This means that the thicknesses of the phase layers are adjusted depending on the end-member compositions such that the diffusion parameters

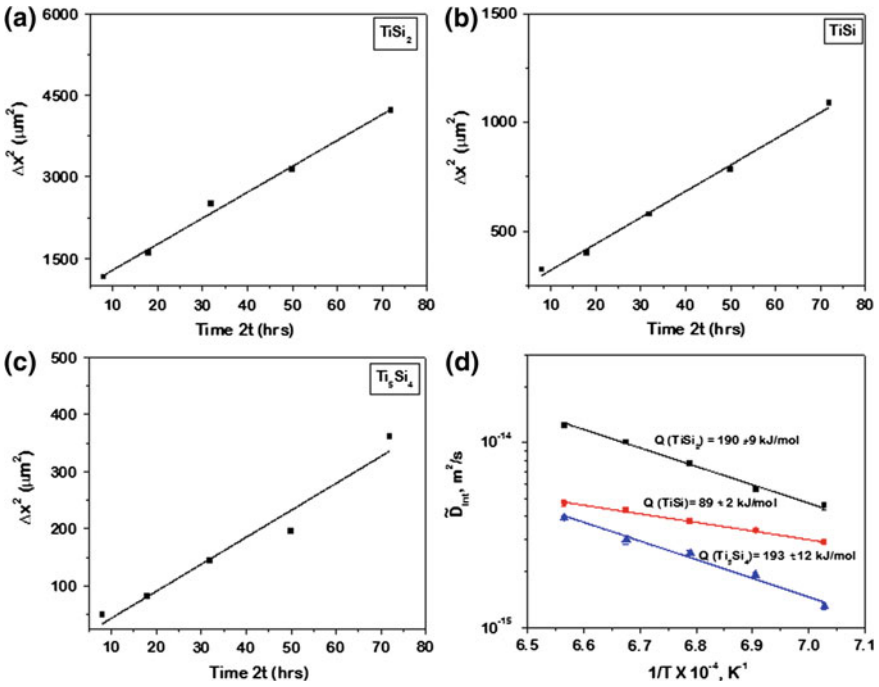

Fig. 7.23 Time-dependent experiments at 1,200 °C for 4, 9, 16, 25, and 36 h are shown by Δx^2 versus $2t$ plots for **a** $TiSi_2$, **b** TiSi, **c** Ti_5Si_4, and **d** the integrated diffusion coefficients for $TiSi_2$, TiSi, and Ti_5Si_4 plotted following the Arrhenius equation [32]

remain the same. There is, therefore, a possibility that the growth rate of the other phase changed with temperature in such a way that the growth rate of TiSi phase did not vary significantly with temperature. This also means that the activation energy for the growth of this phase is relatively low compared to the other phases. Secondly, it is possible that this phase could not grow ideally—that is, parabolically with time—in a multiphase interdiffusion zone, as was found, for instance, in the Ti–Al system [1]. To investigate this, time-dependent experiments were conducted at 1,200 °C. As can be seen clearly from Fig. 7.23a–c, all three phases grow by a diffusion-controlled process since a linear dependence of the phase thickness squares Δx^2 versus time $2t$ is found. This fact indicates that the activation energy for the interdiffusion of TiSi phase must be low compared to the other phases, as discussed above, which is clear from Fig. 7.23d. Another important point should be noted here: We might ask whether time-dependent experiments should be conducted at every temperature, especially when $\Delta x \neq 0$ at $t = 0$, as it is found in this particular system. This can be decided based on the temperature-dependent experiments. If the growth of the phase layer is affected differently at different temperatures, data points will not fall on a line in the Arrhenius plot. Figure 7.23d shows that these points do actually fall on a line for all the phases in

this system, this indicates that the phases are affected similarly at the initial stage in the temperature range of our interest. This is true for most of the systems, if experiments are conducted relatively within a small temperature range.

References

1. F. J. J. van Loo and G.D. Rieck, Acta Metallurg. 21 (1973) 61–71
2. F. J. J. van Loo, Prog. Solid State Chem. 20 (1990) 47–99
3. C.P. Heijwegen and G.D. Rieck, Metall. Trans. 4 (1973) 2159–2167
4. G.M. Becht, F.J.J. van Loo and R. Metselaar, Reactivity of Solids 6 (1988) 45–59.
5. V.I. Dybkov, Solid state reaction kinetics, IPMS Publications, Kyiv, 2013.
6. B. Pieraggi, Oxidation of Metals 27 (1987) 177–185
7. M.Y. Tsai, M.H. Chou, C.R. Kao, J. Alloys Comp. 471 (2009) 90–92
8. C. Wagner, Acta Metall. 17 (1969) 99–107
9. K.P. Gurov, V.N. Pimenov and Y.E. Ugaste, Fiz. metal, metalloved. 32 (1971) 103
10. G.V. Kidson, J. Nucl. Mater. 3 (1961) 21–29
11. A. B Gokhale, G. J Abbaschian, J. Phase Equilibria 12 (1991) 493–498
12. S. Prasad and A. Paul, Intermetallics 19 (2011) 1191–1200
13. J.K. Yoon, J.Y. Byun, G.H. Kim, J.S. Kim, C.S Choi. Thin Solid Films 405 (2002) 170–178
14. J.K. Yoon, J.K. Lee, K.H. Lee, J.Y. Byun, G.H. Kim, K.T. Hong, Intermetallics 11 (2003) 687–696
15. A. Paul, A.A. Kodentsov, F.J.J. van Loo, Z. Metallkunde 95 (2004) 913–920
16. A. Paul, C. Ghosh and W.J. Boettinger, Metall. Mater. Trans. A 42A (2011) 952–963
17. K. N. Tu, G. Ottaviani, U. Gösele and H. Föll, J. Appl. Phys. 54 (1983) 758–763
18. V.I. Dybkov, J. Mater. Sic. 21 (1986) 3078–3084
19. F.M. d'Heurle, J. Mater.Res. 3 (1988) 167–195
20. D.S. Williams, R.A. Rapp and J.P. Hirth, Thin Solid Films 142 (1986) 47–64
21. U. Gösele and K.N. Tu, J. Appl. Phys. 66 (1989) 2619–2626
22. A. Paul, M.J.H. van Dal, A.A. Kodentsov and F.J.J. van Loo, Acta Mater. 52 (2004) 623–630
23. A. Paul, A.A. Kodentsov, F.J.J. van Loo, unpublished research
24. V.D. Divya, S.S.K. Balam, U. Ramamurty and A. Paul, Scripta Materialia 62 (2010) 621–624
25. M.J.H van Dal, A.A Kodentsov, F.J.J van Loo, Intermetallics, 9 (2001) 451–456
26. A. Paul, The Kirkendall effect in solid state diffusion, PhD Thesis, Technische Universiteit Eindhoven, Eindhoven, The Netherlands, 2004
27. S. Prasad and A. Paul, Acta Materialia 59 (2011) 1577–1585
28. S.S.K. Balam, and A. Paul, Metall. Mater. Trans. 41A (2010) 2175–2179.
29. T. Laurila, J. Karppinen, V.Vuorinen, A. Paul and M. Paulasto-Kröckel, Journal of Electronic Materials 40 (2011) 1517
30. M.J.H. van Dal, Microstructural stability of the Kirkendall plane, PhD thesis, Technische Universiteit Eindhoven, The Netherlands, 2001
31. M.E. Schlesinger, H. Okamoto, A.B. Gokhale and R. Abbaschian, Journal of Phase Equilibria 14(1993) 502
32. S. Roy, S. Divinski and A. Paul, Philosophical Magazine 94 (2014) 683.

Chapter 8
Microstructural Evolution of the Interdiffusion Zone

In this chapter, previously unknown behavior of marker plane is shown. In most of the cases, we find the markers along one particular plane; however, in certain condition, these might spread. Sometimes, markers split into more than one planes. A characteristic microstructural feature is found to develop depending on the number and location of the marker planes. This led to development of a physico-chemical approach explaining the microstructural evolution in the interdiffusion zone.

As already discussed in Chap. 6, the discovery of the Kirkendall effect [1, 2] is one of the most important developments in the area of solid-state diffusion. This helped to validate the vacancy-mediated substitutional diffusion. For long, it was known that the markers accumulate at a single plane with a fixed composition. However, sometimes, an unusual behavior of the marker plane has been reported in the literature on this subject. Bastin and Rieck [3] placed W wire at the interface of a Ni/Ti diffusion couple before annealing it at 800 °C for 72 h. Three phases, Ti_2Ni, TiNi, and $TiNi_3$, were grown in the interdiffusion zone. Surprisingly, the authors found pieces of broken W wire in different phases, as if these markers tried to move to different planes simultaneously. Much later, in 1993, Shimozaki et al. [4] reported another unusual behavior in the β′-AuZn phase grown by interdiffusion in the $Au/Au_{0.36}Zn_{0.64}$ diffusion couple. As discussed in Chap. 6, the position of the marker plane could be detected by the presence of a line of pores that developed because of the negative surface (such as scratches or by the presence of debris left on the metallographically prepared bonding surfaces). In general, the markers used to detect the Kirkendall plane are also found along with these on the same plane. Shimozaki et al. used 5-μm-diameter W wire as an inert marker. To their surprise, they found the wires at one plane and the traces (pores caused by scratches or debris) of the original interface at another plane. In both cases, the actual reason for such behavior was not known. In the meantime, following theoretical analysis, Cornet and Calais [5] and van Loo et al. [6] described the possibility of finding more than one Kirkendall marker plane in an interdiffusion zone. In their analysis, they considered a diffusion couple of α and β with a single interface between them. First, they showed that depending on the initial composition of the end members, the same interface can act as both a source and a sink for vacancies when one particular

A. Paul et al., *Thermodynamics, Diffusion and the Kirkendall Effect in Solids*,
DOI: 10.1007/978-3-319-07461-0_8,

component diffuses at a faster rate in both the phases. If $D_A/D_B > 1$ in one phase and $D_A/D_B < 1$ in the other phase, depending on the initial end-member compositions, there could be two Kirkendall planes present in the interdiffusion zone. In that case, the inert markers placed at the initial contact plane have to split and will accumulate at two different planes: one in the α phase and the other in the β phase. In fact, we should consider a marker plane in each phase. Depending on the end-member compositions, the intrinsic diffusion coefficients and the interdiffusion coefficients, it is possible to actually find one or more than one marker planes. After the manuscript published by Shimozaki et al. extensive studies were conducted in several systems including the Ni–Ti and the Au–Zn systems in order to demonstrate the previously unknown behavior of the marker planes [7–13]. Now, we know that the inert markers could be stable to be found in one plane. Under certain circumstances, we might notice some unstable behavior, in which, instead of accumulation in one plane, the markers might spread over a wider area. Depending on the end-member compositions and diffusivities, more than one plane also could be found in a single phase or in different phases. Based on which, a physico-chemical approach is developed to explain the morphologies in a multiphase interdiffusion zone depending on the presence of a single or multiple Kirkendall planes.

8.1 Stable, Unstable, and Multiple Kirkendall Marker Planes

In Chap. 6, we have seen that the intrinsic diffusion coefficients can be estimated over the composition range using an incremental diffusion couple by making several diffusion couples with different end members or from a single diffusion couple by making a multifoil diffusion couple. Once the intrinsic diffusion coefficients (D_A and D_B) are calculated, the velocity at a different composition in a particular diffusion couple can be determined from the knowledge of these diffusion parameters at different compositions and the concentration gradient measured at those compositions following the relation as expressed in Eq. 6.61

$$v_K = \bar{v}_B (D_B - D_A) \left(\frac{\partial C_B}{\partial x} \right)_K \tag{8.1}$$

The velocity of the Kirkendall plane (or the composition of the Kirkendall marker plane) can also be determined directly by locating the initial contact plane x_o and the Kirkendall marker plane x_K from the relation as expressed in Eq. 6.64

$$v_K = \frac{x_K - x_o}{2t} = \frac{x_K}{2t} \tag{8.2}$$

Therefore, at the intersection point of these two lies the location of the Kirkendall marker plane, since both have the same velocity at this plane [7, 8]. To explain

further in a simplified system, let us consider, the constant molar volume of a system, such that $v_A = v_B = v_m$ and a constant interdiffusion coefficient $\tilde{D}$ over the whole concentration range. Therefore, Fick's second law reduces to

$$\frac{\partial N_B}{\partial t} = \tilde{D}\frac{\partial^2 N_B}{\partial x^2} \tag{8.3}$$

The solution of Eq. 8.3 with respect to error function can be written as [7, 8, 10]

$$N_B = \frac{1}{2}\mathrm{erfc}\left(\frac{x}{2\sqrt{\tilde{D}t}}\right) \tag{8.4}$$

For a constant molar volume, Eq. 8.1 can be written as

$$v = (D_B - D_A)\frac{\partial N_B}{\partial x} \tag{8.5}$$

Further, the Darken relation (Eq. 6.65) can be expressed as

$$\tilde{D} = N_A D_B + N_B D_A \tag{8.6}$$

If we would like to consider a constant ratio of diffusivities, Eq. 8.5, with the help of Eq. 8.6 can be written as

$$v = \tilde{D}\left(\frac{\frac{D_B}{D_A} - 1}{N_A\frac{D_B}{D_A} + N_B}\right)\frac{\partial N_B}{\partial x} \tag{8.7}$$

With the help of Eq. 8.4, Eq. 8.7 can be written as

$$v = \tilde{D}\left(\frac{\frac{D_B}{D_A} - 1}{N_A\frac{D_B}{D_A} + N_B}\right)\left(\frac{-1}{\sqrt{\pi}}\frac{1}{2\sqrt{\tilde{D}t}}\right)\exp\left[-\left(\frac{x}{2\sqrt{\tilde{D}t}}\right)^2\right] \tag{8.8}$$

After plotting v versus x using Eq. 8.8, the location of the Kirkendall plane can be rationalized by the intersection of the straight line—expressed by Eq. 8.2—that goes through $x = 0$. The velocity diagram, as shown in Fig. 8.1, is estimated for $\tilde{D} = 10^{-14}\,\mathrm{m^2/s}$, $D_A/D_B = 3$, $t = 10^6$ s and for the constant molar volume [7, 10].

Note that in an actual case, the ratios of the diffusivities are not constant over the whole composition range and even the molar volume might change drastically. In that case, Eqs. 8.1 and 8.2 should be used to construct the velocity curve. Cornet and Calais [5] explained the possibility of finding multiple Kirkendall marker planes in a theoretical analysis. Much later, the group of van Loo [7–13] conducted extensive experimental studies to show the different possibilities of the marker planes and explained these behaviors with the help of theoretical analysis that has been developed based on the work by Cornet and Calais [5]. Now, we know that a

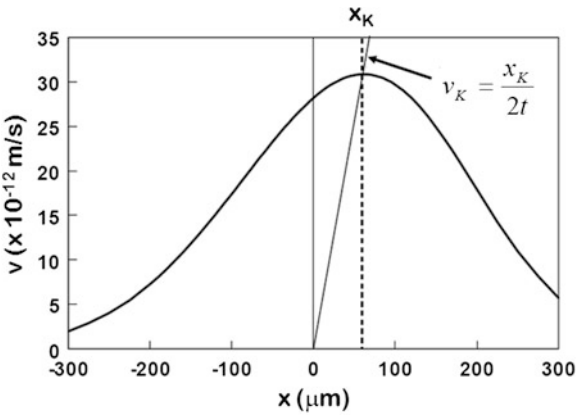

Fig. 8.1 Velocity diagram showing the location of the Kirkendall marker plane [7]

stable marker plane can be present in a system such that all the inert markers accumulate along a single composition indicating the position of the Kirkendall marker plane. On the other hand, markers can be unstable such that they spread over a composition or region in the interdiffusion zone. In a few special cases, markers have been known to bifurcate or trifurcate. There is a possibility of bifurcation in a single phase or in two different phases.

Before showing the experimental results, it is necessary to understand the condition in which different kinds of behavior could be found [7, 8]. We consider a system where in the A-rich side A has a higher diffusion rate compared to B and in the B-rich side B has a higher diffusion rate compared to A. In such a case, according to Eq. 8.1, as shown in Fig. 8.2, the velocity will have a negative value in the A-rich side and positive values in the B-rich side. We have considered the left-hand side of the diffusion couple as being A-rich and the right-hand side of the couple as being B-rich. Following, the number and nature of the marker plane will depend on the location of the intersection on the velocity curve by the straight line determined by Eq. 8.2. Depending on the end-member compositions, the interdiffusion coefficients and the intrinsic diffusion coefficients, the straight line estimated from the position of the marker plane might intersect the velocity curve at a point, where it has a negative gradient $dv/dx < 0$. This point is shown in Fig. 8.2a. In this case, it will have a stable marker plane such that all the markers will accumulate at this Kirkendall marker plane located at x_K. At the very initial stage, if for any reason, the markers move ahead of this plane, they will slow down due to lower velocity and come back to the stable plane. On the other hand, if the markers are left behind this plane, they will move faster because of the higher velocity and drift to the marker plane. Therefore, the marker plane acts as the attractor for the markers to accumulate the inert particles from the nearby positions.

As shown in Fig. 8.2b, by changing the end-member compositions in the same system, the position of the initial contact plane $x_o = 0$ might move such that the straight line intersects the velocity curve at a point where it has a positive gradient

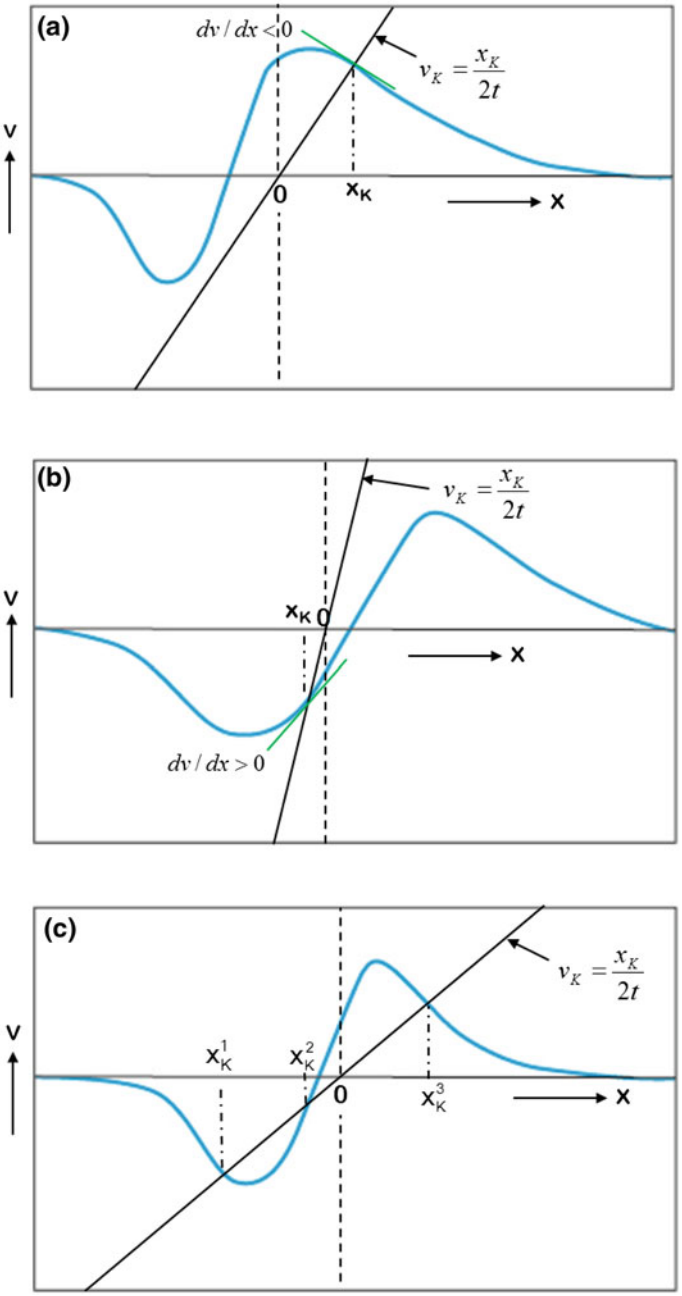

Fig. 8.2 Imaginary velocity diagrams showing the possibility of finding **a** a stable marker plane, **b** an unstable marker plane, and **c** bifurcation of the marker plane in the same system [7]

$dv/dx > 0$. It should be noted here that the slope of the line, $v_K = \frac{x_K}{2t}$ also changes with the change in end-member compositions. Following a similar line of discussion, the stability of the movement of the inert markers can be explained. At the very initial stage, for any perturbation, if the markers are left behind, they will slow down because of lower velocity. On the other hand, if the markers move ahead, they will move faster to go even further away. Therefore, it will show unstable marker behavior, where the markers will be spread over a larger area.

In another diffusion couple with different end members, a situation might arise where the straight line intersects the velocity curve at three points, as shown in Fig. 8.2c. An unstable marker plane is present at x_K^2 between two stable planes at x_K^1 and x_K^3. At the very initial stage, since the markers move away from the unstable marker plane, the markers will be attracted by the stable planes. Therefore, in this diffusion couple, two stable marker planes—that is the bifurcation of the marker plane—will be found.

The conditions of finding stable and unstable Kirkendall marker planes were examined experimentally in the Ni–Pd and Fe–Pd systems, as shown in Fig. 8.3 [9]. ThO_2 particles were used as inert markers. As discussed in the previous chapter, the velocity curves were determined following a multifoil technique. The intersection points—indicating the location of the Kirkendall marker planes—are found by plotting the straight line from the estimated location of the initial contact plane and the known location of the Kirkendall marker plane. It can be seen that $dv/dx < 0$ at the point of intersection in the Ni–Pd system, where a stable marker plane is found. On the other hand, in the Fe–Pd system $dv/dx > 0$ at the point of intersection and it has an unstable Kirkendall plane. In the Fe–Pd system, since there is no particular marker plane present, a plane approximately in the middle of the marker region was considered for the construction of the velocity diagram.

Experimental evidence indicating the presence of stable, unstable, and the bifurcation of the marker plane was found in the β′-AuZn phase in the diffusion couples with different end-member compositions [8]. From the tracer diffusion data available in the literature published on the subject, it was known that Au is the faster diffusing component in the Au-rich and Zn is the faster diffusing component in the Zn-rich side of this phase. Therefore, it was expected to find the situations, as explained in Fig. 8.2. As shown in Fig. 8.4, in a diffusion couple of $Au_{0.66}Zn_{0.34}/Au_{0.34}Zn_{0.66}$, a stable Kirkendall marker plane was found. As presented in Fig. 8.5, by changing the end-member compositions, an unstable Kirkendall marker plane was found in the same phase in a $Au_{0.70}Zn_{0.30}/Au_{0.40}Zn_{0.60}$ diffusion couple. The Kirkendall marker location—as shown in a rectangle denoted by B in Fig. 8.5b—is shown in Fig. 8.5c where an array of markers are to be seen spreading over a region. By changing the end-member compositions of the diffusion couple, as shown in Fig. 8.6, the bifurcation of the Kirkendall marker plane was found. One Kirkendall plane was found in the Au-rich and another in the Zn-rich side of the β′-AuZn phase.

However, rationalization with the help of a velocity diagram was not possible because of difficulties in determining the intrinsic diffusion coefficients over the

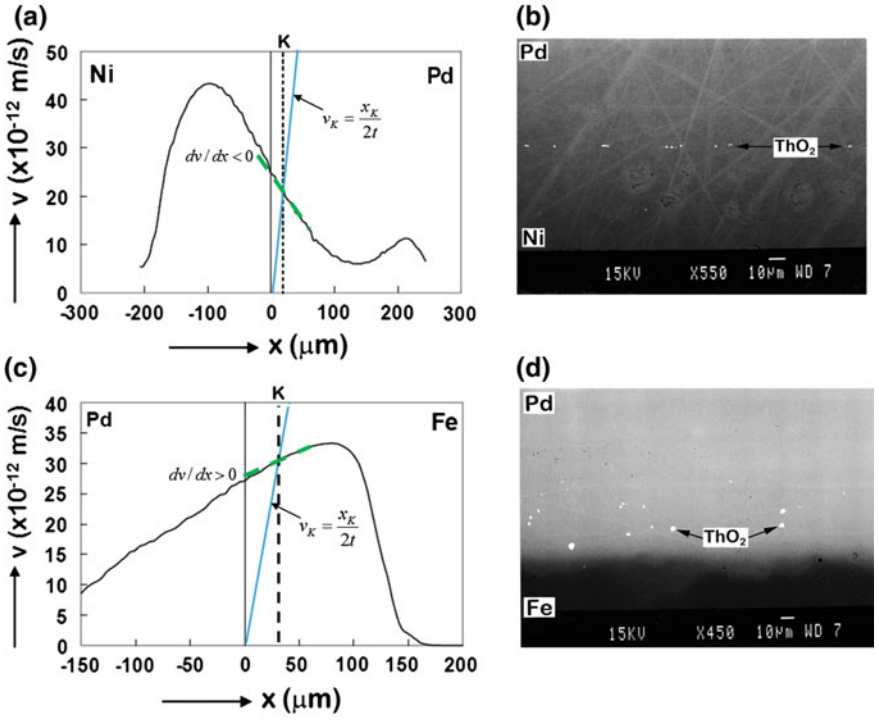

Fig. 8.3 **a** Velocity diagram constructed experimentally in the Ni–Pd system and **b** experimentally found a stable marker plane. **c** Velocity diagram constructed experimentally in the Fe–Pd system and **d** experimentally found unstable marker plane [9]

whole composition range in the β′-AuZn phase. Absence of the data on lattice parameter variation and Zn evaporation during melting complicated the analysis. Similar bifurcation of the Kirkendall marker plane was found in the β-NiAl phase, as shown in Fig. 8.7 in a diffusion couple of $Ni_{41.7}Al_{58.3}/Ni_{72.24}Al_{27.76}$ at 1,000 °C. The optical micrograph in Fig. 8.7b presents the whole interdiffusion zone, and the back scattered electron image in Fig. 8.7c exhibits the position of the two marker planes shown by the presence of ThO_2 particles. One marker plane was found in the Ni-rich and another in the Al-rich side of the β-NiAl phase [11]. To estimate the intrinsic diffusion coefficients over the homogeneity range in this phase, many incremental diffusion couple experiments were conducted such that marker positions are found at different compositions. The composition of the diffusion couples and the annealing times are listed in Table 8.1 along with the couple in which bifurcation of the marker plane was found.

The estimated interdiffusion coefficients and the ratio of the intrinsic diffusion coefficients are shown in Fig. 8.8a and b. From the average of these values, the intrinsic diffusion coefficients are estimated using Eq. 6.66, as shown in Fig. 8.8c. The velocity curve was determined with the help of the concentration gradient

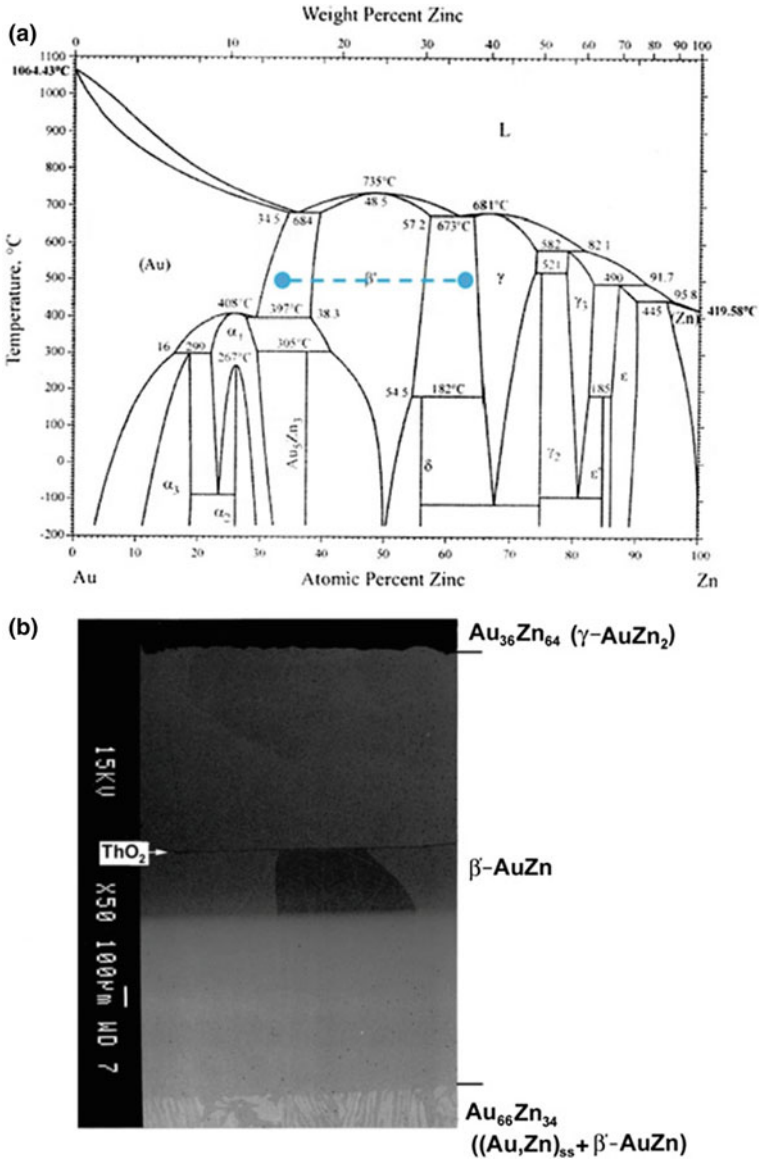

Fig. 8.4 **a** Compositions for a diffusion couple indicating on the Au–Zn phase diagram in which **b** a single marker plane is found [8]

obtained from the measured composition profile in the diffusion couple showing bifurcation of the marker plane, as shown in Fig. 8.9a. Afterward, the straight line determined from $v_K = (x_K - x_o)/2t = x_K/2t$ is drawn by calculating the initial contact plane and from knowledge of the known location of the marker plane. In

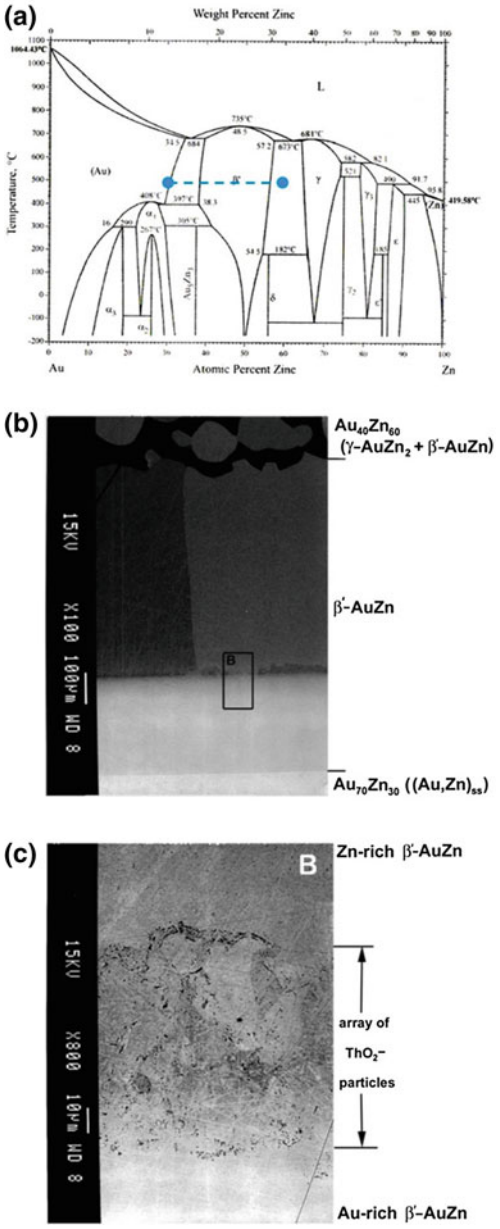

Fig. 8.5 **a** Compositions for a diffusion couple indicating on the Au–Zn phase diagram in which **b** unstable marker plane is found, **c** shows the marker region [8]

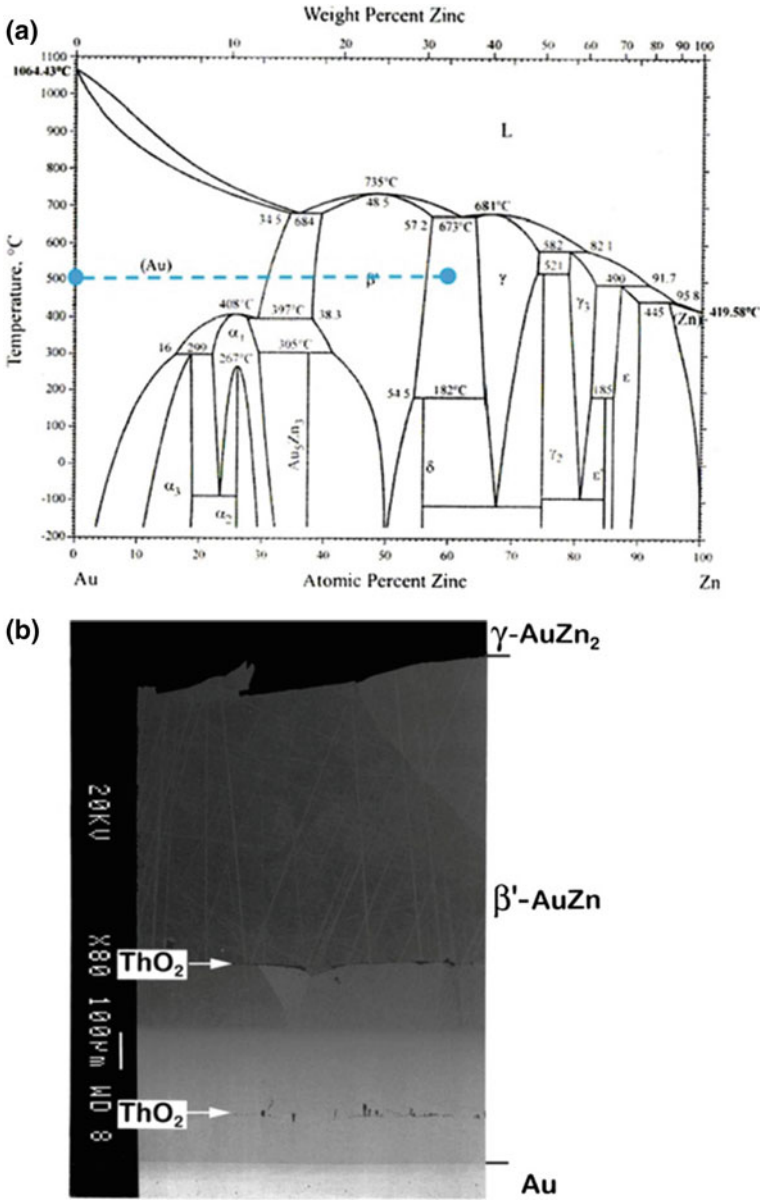

Fig. 8.6 **a** Compositions for a diffusion couple indicating on the Au–Zn phase diagram in which **b** a bifurcation of the marker plane is found [8]

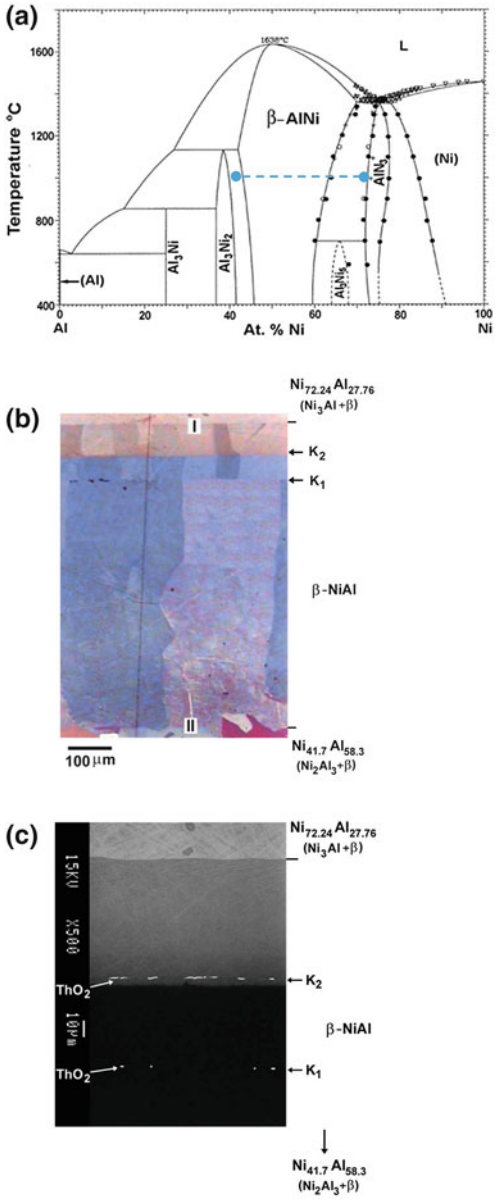

Fig. 8.7 **a** Compositions for a diffusion couple indicating on the Ni–Al phase diagram in which **b** a bifurcation of the marker plane is found in the β-NiAl phase (polarized light microscope image), **c** back scattered electron image clearly shows the location of the marker planes [11]

Table 8.1 Details of the incremental diffusion couple experiments conducted at 1,000 °C are listed

Couple no.	Diffusion couple	Time (h)
1	$Ni_{49.8}Al_{50.2}/Ni_{72.24}Al_{27.76}$	100
2	$Ni_{49.8}Al_{50.2}/Ni_{66.24}Al_{33.76}$	24
3	$Ni_{46}Al_{54}/Ni_{72.24}Al_{27.76}$	24
4	$Ni_{46}Al_{54}/Ni_{66.24}Al_{33.76}$	24
5	$Ni_{46}Al_{54}/Ni_{57.5}Al_{42.5}$	100
6	$Ni_{46}Al_{54}/Ni_{57.5}Al_{42.5}$	24
7	$Ni_{46}Al_{54}/Ni_{49.8}Al_{50.2}$	100
8	$Ni_{49.8}Al_{50.2}/Ni_{57.5}Al_{42.5}$	100
9	$Ni_{46}Al_{54}/Ni_{52.2}Al_{47.8}$	100
10	$Ni_{46}Al_{54}/Ni_{52.2}Al_{47.8}$	24
11	$Ni_{41.7}Al_{58.3}/Ni_{72.24}Al_{27.76}$	24
12	$Ni_{46}Al_{54}/Ni_{54}Al_{46}$	24

the velocity diagram given in Fig. 8.9b, we see that this straight line intersects the velocity curve at two points where it has a negative gradient. There is a jump in the middle of the velocity curve since the composition profile does not grow with any measurable thickness near the stoichiometric composition because of the low interdiffusion coefficients.

The bifurcation of the Kirkendall marker plane shown in the previous examples is found in a single phase. Bifurcation in different phases is found more often than that in a single phase such as in Ag–Zn, Co–Si, Ni–Ti, and Au–Sn systems. The examples for Ag–Zn [12], Co–Si [14, 15], and Ni–Ti [10] systems are shown in Fig. 8.10. In fact, the study on the Ni–Ti system was conducted since this is one of the first systems indicating the likelihood of more than one Kirkendall marker plane. Trifurcation of the Kirkendall marker plane is very rare and it was found in the Ti–Al system [16], which was in fact predicted from the data reported on diffusion parameters before the experimental proof. Theoretically, these behaviors of the marker planes were studied by Höglund and Ågren [17] and Boettinger et al. [18].

8.2 A Physicochemical Approach to Explain the Morphological Evolution in an Interdiffusion Zone

It has been seen in many examples that a characteristic morphology develops in the product phase when grown by reactive diffusion. For example, three incremental diffusion couples in different systems are shown in Fig. 8.11 [14, 15, 19, 20]. It can be seen that a duplex morphology is present whenever there is a Kirkendall marker plane present. In Fig. 8.10a, the bifurcation of the marker plane is shown in the Ag–Zn system [12]. The grain morphologies in different phases are shown in Fig. 8.12. In the ε-$AgZn_3$ and γ-Ag_5Zn_8 phases, the marker planes are

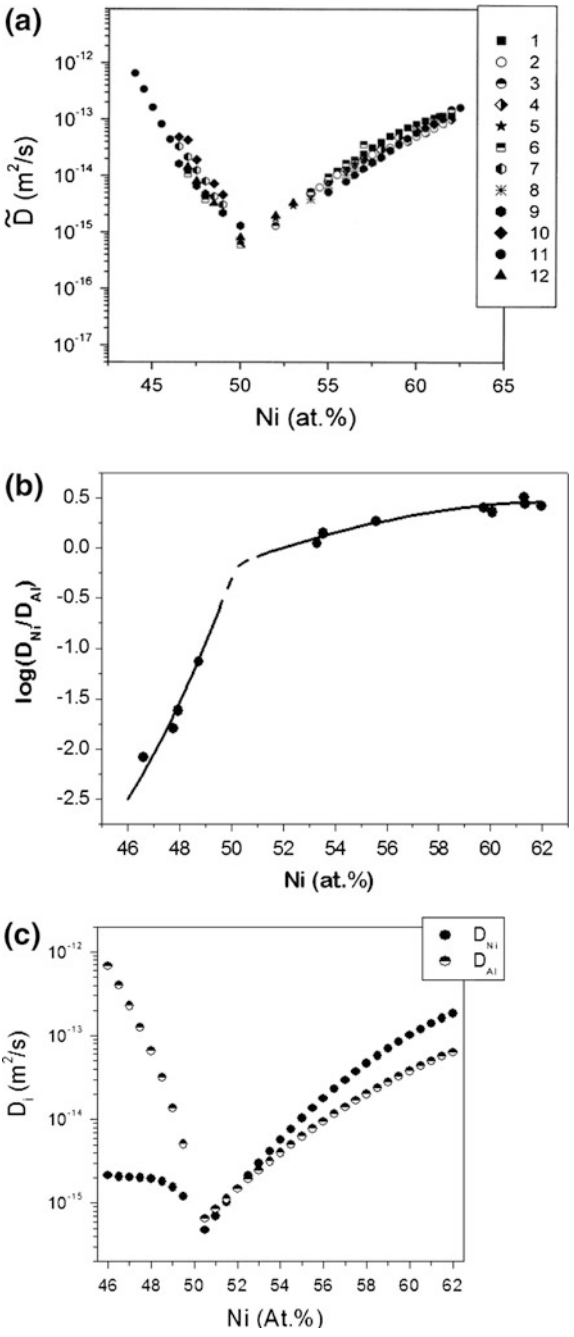

Fig. 8.8 **a** The interdiffusion coefficients, **b** the ratio of the intrinsic diffusion coefficients and **c** the estimated intrinsic diffusion coefficients at different compositions in the β-NiAl phase at 1,000 °C [11]

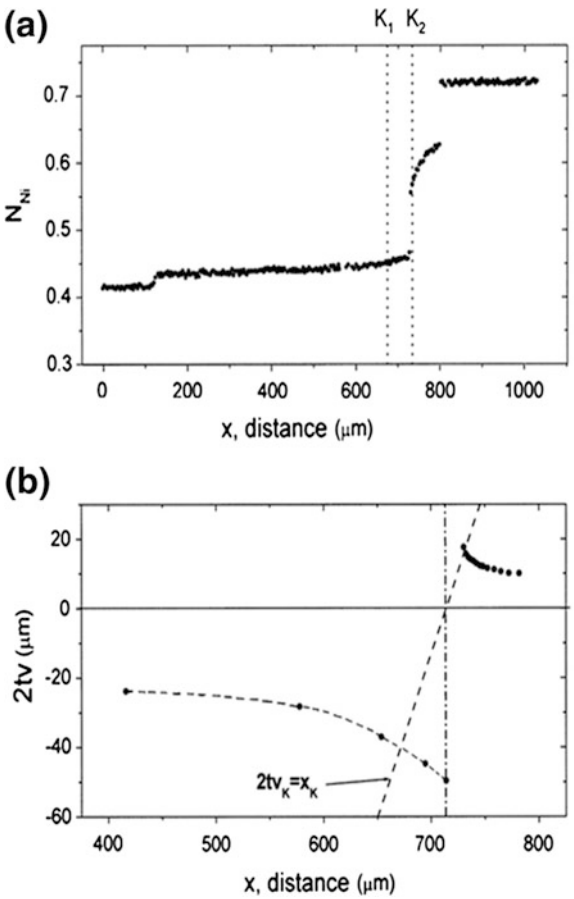

Fig. 8.9 **a** Composition profile and **b** the velocity diagram rationalization of the bifurcation of the marker plane [11]

present and the duplex morphology is also evident. On the other hand, there is no marker plane present in the β-AgZn phase, where uniform and continuous grain morphology is present.

The experimental results shown above indicate that the phase layer grows differently at different interface interphases. In reactive diffusion, the product phase layers are grown because of the reaction/dissociation of the diffusing component from the interfaces. Although the phases are grown by the reactions and/or dissociation at the interface interphases, growth of the phases are not controlled by these processes. We are considering the systems, in which diffusion of components through the phase layers takes longer time to control the growth process. There are many examples, especially in thin-film conditions, where the growth of the phase is reaction controlled, which are not considered here. Before estimating the diffusion parameters with the help of a physicochemical approach,

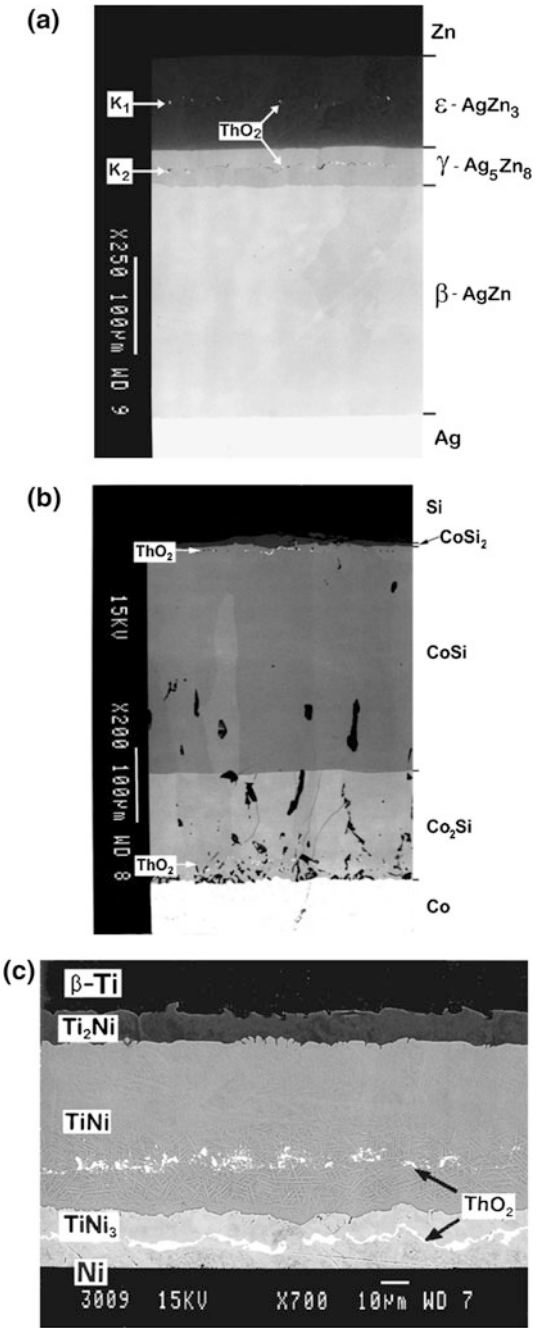

Fig. 8.10 Experimental evidences of bifurcations in **a** Ag–Zn [12], **b** Co–Si [14, 15], and **c** Ni–Ti [10] systems

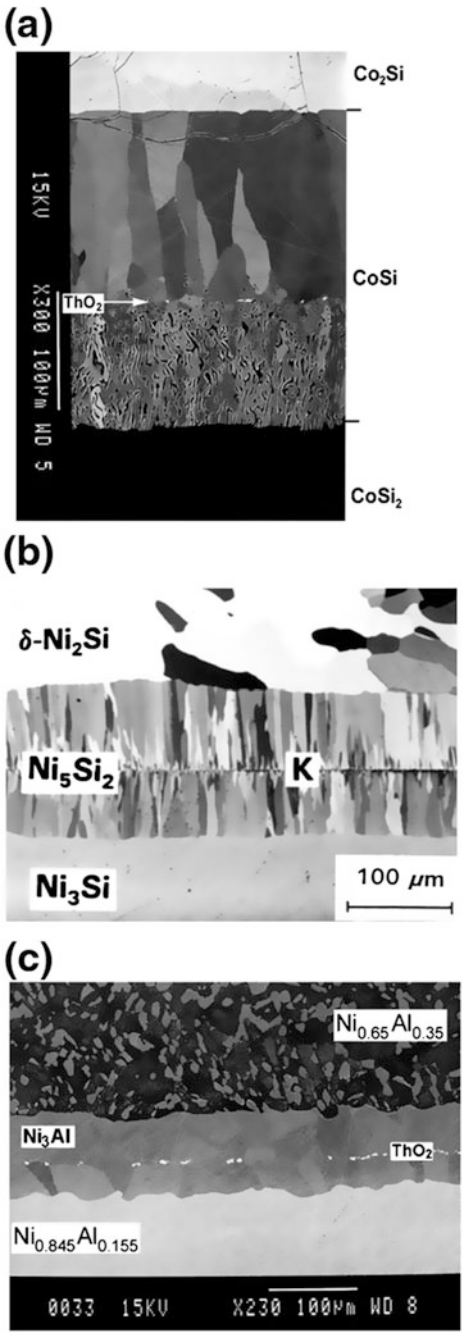

Fig. 8.11 Duplex morphology in the presence of the Kirkendall marker plane in different phases **a** CoSi [14, 15], **b** Ni_5Si_2 [19], and **c** Ni_3Al [20]

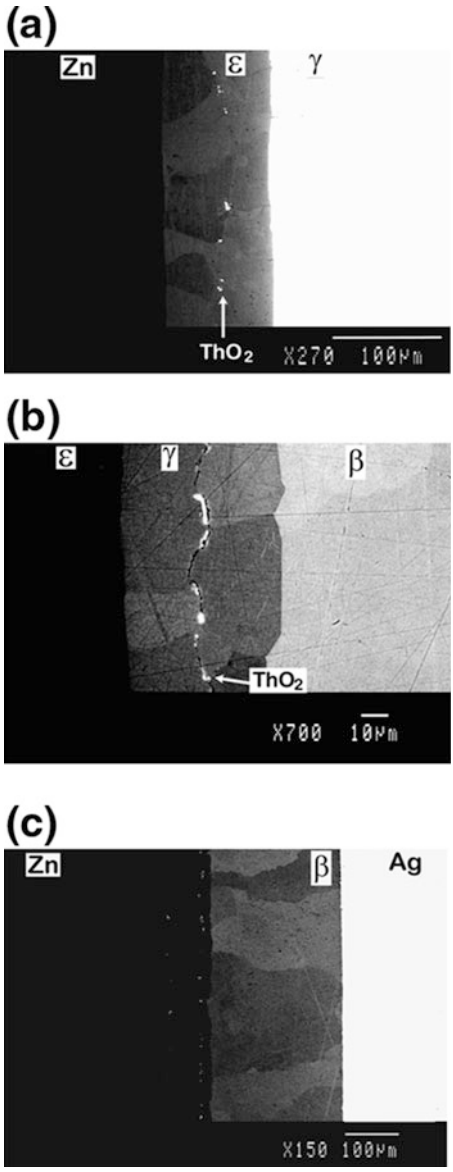

Fig. 8.12 Duplex morphology in the presence of the Kirkendall marker plane in **a** ε-phase, **b** γ-phase and **c** a uniform grain morphology in the β-phase because of the absence of any marker plane [12]

which is developed considering the reactions and dissociations at the interfaces in real systems along with the diffusion of the component through the phase layer, we shall first show that this approach is equivalent to the relations developed in the previous chapters.

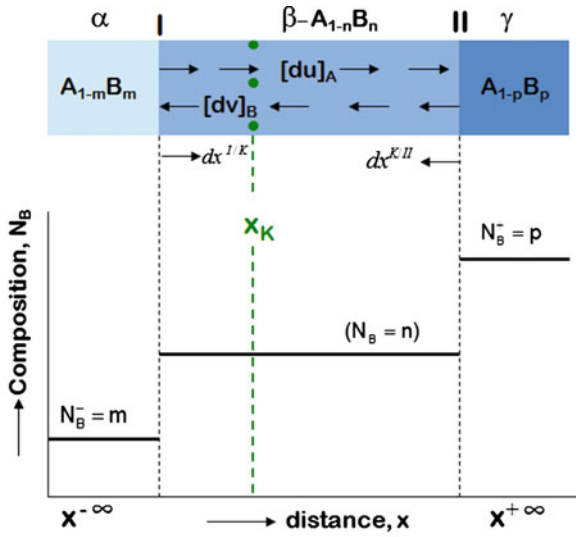

Fig. 8.13 A schematic diagram explaining the physicochemical approach

For the sake of simplicity, let us consider a diffusion couple of α and γ phases in which a line compound β grows in an interdiffusion zone, as shown in Fig. 8.13 [21]. The stoichiometric compositions of the α, β, and γ phases are $A_{1-m}B_m$, $A_{1-n}B_n$, and $A_{1-p}B_p$, respectively. Suppose α is an A-rich and β is a B-rich phase. Therefore, as shown in the figure, A dissociates from the α phase at the interface I to produce the product β phase. The dissociated A then diffuses to the interface II and reacts with the γ phase to produce the β phase. At the same time, B dissociates from the γ phase at the interface II to produce the β phase. The dissociated B diffuses to the interface I to produce the β phase. Therefore, at both interfaces, the product phase β is grown by the dissociation and reaction of the components. Suppose, $[du]_A$ mol/m^2 is the flux of the component A crossing the Kirkendall marker plane in the short period of time dt. Similarly, the flux of the component B that crosses the marker plane in that short period of time is $[dv]_B$ mol/m^2. The location of the marker plane in the interdiffusion zone is shown by filled circles, and the location is denoted as x_K. It is evident that the thickness of the product phase that is grown in the left-hand side of the marker plane is due to the reaction and dissociation at the interface I. On the other hand, the right-hand side of the product phase from the Kirkendall marker plane is grown because of the reaction and dissociation at the interface II. Therefore, we should write the reaction and dissociation equations at the two different interfaces.

Reaction dissociation equations at the interface I:

$$\frac{n}{n-m}du\mathrm{A}_{1-m}\mathrm{B}_m(\alpha\,\text{phase}) \rightarrow du\,[\mathrm{A}]_d + \frac{m}{n-m}du\mathrm{A}_{1-n}\mathrm{B}_n(\beta\,\text{phase})$$

dissociation of A

$$\frac{1-n}{n-m}dv\mathrm{A}_{1-m}\mathrm{B}_m(\alpha\,\text{phase}) + dv\,[\mathrm{B}]_d \rightarrow \frac{1-m}{n-m}dv\mathrm{A}_{1-n}\mathrm{B}_n(\beta\,\text{phase})$$

reaction of B.

Reaction dissociation equations at the interface II:

$$\frac{n}{p-n}du\mathrm{A}_{1-p}\mathrm{B}_p(\gamma\,\text{phase}) + du\,[\mathrm{A}]_d \rightarrow \frac{p}{p-n}du\mathrm{A}_{1-n}\mathrm{B}_n(\beta\,\text{phase})$$

reaction of A

$$\frac{1-n}{p-n}dv\mathrm{A}_{1-p}\mathrm{B}_P(\gamma\,\text{phase}) \rightarrow dv\,[\mathrm{B}]_d + \frac{1-p}{p-n}dv\mathrm{A}_{1-n}\mathrm{B}_n(\beta\,\text{phase})$$

dissociation of A.

The amount of the β phase produced at the interface I is $\frac{1}{n-m}[mdu + (1-m)dv]$ mol/m^2 and at the interface II is $\frac{1}{p-n}[pdu + (1-p)dv]$ mol/m^2. Suppose, the molar volume of the product β phase is v_m, which will be written as v_m^β at latter stage. Suppose, the thicknesses of the phase layer grown from the interfaces I and II in this short period of time dt is $dx^{\mathrm{I/K}}$ and $dx^{\mathrm{K/II}}$, respectively. Therefore, we can write

$$\frac{1}{n-m}[mdu + (1-m)dv]\,v_m = dx^{\mathrm{I/K}} \tag{8.9a}$$

$$\frac{1}{p-n}[pdu + (1-p)dv]\,v_m = dx^{\mathrm{K/II}} \tag{8.9b}$$

Furthermore, we can write both the left- and right-hand sides of the end members, as well as the composition of the product phases as $m = N_\mathrm{B}^-$, $p = N_\mathrm{B}^+$ and $n = N_\mathrm{B}$. Therefore, Eqs. 8.9a and 8.9b can be rewritten as

$$N_\mathrm{B}^- du + (1-N_\mathrm{B}^-)dv = \frac{N_\mathrm{B}-N_\mathrm{B}^-}{v_m}dx^{\mathrm{I/K}} \tag{8.10a}$$

$$N_\mathrm{B}^+ du + (1-N_\mathrm{B}^+)\,dv = \frac{N_\mathrm{B}^+-N_\mathrm{B}}{v_m}dx^{\mathrm{K/II}} \tag{8.10b}$$

If the fluxes of the diffusing components A and B are 0 at time $t = 0$ and become u and v after the annealing time t, we can write Eqs. 8.10a and 8.10b by integrating as

$$N_{\mathrm{B}}^{-}\int_{o}^{u} du + (1-N_{\mathrm{B}}^{-})\int_{o}^{v} dv = \int_{x^{-\infty}}^{x_{\mathrm{K}}} \frac{N_{\mathrm{B}}-N_{\mathrm{B}}^{-}}{v_m}dx$$

$$N_{\mathrm{B}}^{-}u + (1-N_{\mathrm{B}}^{-})v = \int_{x^{-\infty}}^{x_{\mathrm{K}}} \frac{N_{\mathrm{B}}-N_{\mathrm{B}}^{-}}{v_m}dx \tag{8.11a}$$

$$N_{\mathrm{B}}^{+}\int_{o}^{u} du + (1-N_{\mathrm{B}}^{+})\int_{o}^{v} dv = \int_{x_{\mathrm{K}}}^{x^{+\infty}} \frac{N_{\mathrm{B}}-N_{\mathrm{B}}^{-}}{v_m}dx$$

$$N_{\mathrm{B}}^{+}u + (1-N_{\mathrm{B}}^{+})v = \int_{x_{\mathrm{K}}}^{x^{+\infty}} \frac{N_{\mathrm{B}}^{+}-N_{\mathrm{B}}}{v_m}dx \tag{8.11b}$$

Now, we would like to write the expressions separately for u and v. Multiplying Eq. 8.11a by $(1-N_{\mathrm{B}}^{+})$ and Eq. 8.11b by $\left(1-N_{\mathrm{B}}^{-}\right)$ and then by subtracting, we get

$$N_{\mathrm{B}}^{-}(1-N_{\mathrm{B}}^{+})u - N_{\mathrm{B}}^{+}(1-N_{\mathrm{B}}^{-})u = (1-N_{\mathrm{B}}^{+})\int_{x^{-\infty}}^{x_{\mathrm{K}}} \frac{N_{\mathrm{B}}-N_{\mathrm{B}}^{-}}{v_m}dx - (1-N_{\mathrm{B}}^{-})\int_{x_{\mathrm{K}}}^{x^{+\infty}} \frac{N_{\mathrm{B}}^{+}-N_{\mathrm{B}}}{v_m}dx$$

$$u = -\left[(1-N_{\mathrm{B}}^{+})\int_{x^{-\infty}}^{x_{\mathrm{K}}} \frac{N_{\mathrm{B}}-N_{\mathrm{B}}^{-}}{N_{\mathrm{B}}^{+}-N_{\mathrm{B}}^{-}}\frac{1}{v_m}dx - (1-N_{\mathrm{B}}^{-})\int_{x_{\mathrm{K}}}^{x^{+\infty}} \frac{N_{\mathrm{B}}^{+}-N_{\mathrm{B}}}{N_{\mathrm{B}}^{+}-N_{\mathrm{B}}^{-}}\frac{1}{v_m}dx\right]$$

Introducing the composition normalizing variable $Y_{\mathrm{B}} = \frac{N_{\mathrm{B}}-N_{\mathrm{B}}^{-}}{N_{\mathrm{B}}^{+}-N_{\mathrm{B}}^{-}}$ such that $1-Y_{\mathrm{B}} = \frac{N_{\mathrm{B}}^{+}-N_{\mathrm{B}}}{N_{\mathrm{B}}^{+}-N_{\mathrm{B}}^{-}}$, we can write

$$u = -\left[(1-N_{\mathrm{B}}^{+})\int_{x^{-\infty}}^{x_{\mathrm{K}}} \frac{Y_{\mathrm{B}}}{v_m}dx - (1-N_{\mathrm{B}}^{-})\int_{x_{\mathrm{K}}}^{x^{+\infty}} \frac{1-Y_{\mathrm{B}}}{v_m}dx\right]$$

$$u = -\left[N_{\mathrm{A}}^{+}\int_{x^{-\infty}}^{x_{\mathrm{K}}} \frac{Y_{\mathrm{B}}}{v_m}dx - N_{\mathrm{A}}^{-}\int_{x_{\mathrm{K}}}^{x^{+\infty}} \frac{1-Y_{\mathrm{B}}}{v_m}dx\right] \tag{8.12a}$$

Multiplying Eq. 8.11a by N_{B}^{-} and Eq. 8.11b by N_{B}^{+} and then by subtracting, we get

$$N_{\mathrm{B}}^{+}(1-N_{\mathrm{B}}^{-})v\ -N_{\mathrm{B}}^{-}(1-N_{\mathrm{B}}^{+})v=N_{\mathrm{B}}^{+}\int_{x^{-\infty}}^{x_{\mathrm{K}}}\frac{N_{\mathrm{B}}-N_{\mathrm{B}}^{-}}{v_m}dx-N_{\mathrm{B}}^{-}\int_{x_{\mathrm{K}}}^{x^{+\infty}}\frac{N_{\mathrm{B}}^{+}-N_{\mathrm{B}}}{v_m}dx$$

$$v=N_{\mathrm{B}}^{+}\int_{x^{-\infty}}^{x_{\mathrm{K}}}\frac{N_{\mathrm{B}}-N_{\mathrm{B}}^{-}}{N_{\mathrm{B}}^{+}-N_{\mathrm{B}}^{-}}\frac{1}{v_m}dx-N_{\mathrm{B}}^{-}\int_{x_{\mathrm{K}}}^{x^{+\infty}}\frac{N_{\mathrm{B}}^{+}-N_{\mathrm{B}}}{N_{\mathrm{B}}^{+}-N_{\mathrm{B}}^{-}}\frac{1}{v_m}dx$$

$$v=N_{\mathrm{B}}^{+}\int_{x^{-\infty}}^{x_{\mathrm{K}}}\frac{Y_{\mathrm{B}}}{v_m}dx-N_{\mathrm{B}}^{-}\int_{x_{\mathrm{K}}}^{x^{+\infty}}\frac{1-Y_{\mathrm{B}}}{v_m}dx \tag{8.12b}$$

The intrinsic flux of A that is J_{A} and the intrinsic flux of B that is J_{B} can be related to u and v. It is a fact that the intrinsic fluxes are inversely proportional to $t^{1/2}$. Moreover, the sign of the flux of A should be taken as positive since it diffuses from left to right and the flux of B should be taken as negative since it diffuses from right to left. Therefore, we can write

$$u=\int_0^u du=\int_0^t J_{\mathrm{A}}\,dt=\int_0^t\frac{k}{t^{1/2}}dt=\frac{kt^{1/2}}{1/2}=2tJ_{\mathrm{A}}=-2tD_{\mathrm{A}}\frac{\partial C_{\mathrm{A}}}{\partial x} \tag{8.13a}$$

$$v=\int_0^v dv=-\int_0^t J_{\mathrm{B}}\,dt=-\int_0^t\frac{k}{t^{1/2}}dt=-2tJ_{\mathrm{B}}=2tD_{\mathrm{B}}\frac{\partial C_{\mathrm{B}}}{\partial x} \tag{8.13b}$$

where k is the proportionality constant. Note here that $J_i=-D_i\frac{\partial C_i}{\partial x}$. From Eqs. 8.12 and 8.13a, we can write

$$D_{\mathrm{A}}=\frac{1}{2t}\left(\frac{\partial x}{\partial C_{\mathrm{A}}}\right)\left[N_{\mathrm{A}}^{+}\int_{x^{-\infty}}^{x_{\mathrm{K}}}\frac{Y}{v_m}dx-N_{\mathrm{A}}^{-}\int_{x_{\mathrm{K}}}^{x^{+\infty}}\frac{1-Y}{v_m}dx\right] \tag{8.14a}$$

$$D_{\mathrm{B}}=\frac{1}{2t}\left(\frac{\partial x}{\partial C_{\mathrm{B}}}\right)\left[N_{\mathrm{B}}^{+}\int_{x^{-\infty}}^{x_{\mathrm{K}}}\frac{Y}{v_m}dx-N_{\mathrm{B}}^{-}\int_{x_{\mathrm{K}}}^{x^{+\infty}}\frac{1-Y}{v_m}dx\right] \tag{8.14b}$$

Note that these are the relations developed by van Loo [22] and are those that we derived earlier in Chap. 6 following the approach by Wagner [13]. From the standard thermodynamic relations $\partial C_A=\left(\bar{v}_B/v_m^2\right)\partial N_A$, $\partial C_B=\left(\bar{v}_A/v_m^2\right)\partial N_B$ (Eq. 1.150), we can write the ratio of the intrinsic diffusion coefficients as

$$\frac{\bar{v}_A D_B}{\bar{v}_B D_A} = \frac{J_B}{J_A} = \frac{v}{u} \tag{8.15a}$$

Following Eq. 6.91, we can write this with respect to the ratio of the tracer diffusion coefficients as

$$\frac{D_B^*}{D_A^*} = \frac{\bar{v}_A D_B}{\bar{v}_B D_A} = \frac{J_B}{J_A} = \frac{v}{u} \tag{8.15b}$$

Therefore, since the partial molar volumes are not known in a phase with a narrow homogeneity range, we actually measure the ratio of the tracer diffusion coefficients after neglecting the role of the vacancy wind effect, as explained in Chap. 6.

Previously in Chap. 6, we derived the relation between the interdiffusion coefficients and the intrinsic diffusion coefficients as

$$\tilde{D} = C_A \bar{v}_A D_B + C_B \bar{v}_B D_A \tag{8.16}$$

since $N_B + N_A = 1$, $C_i = \frac{N_i}{v_m}$, we can write the interdiffusion coefficients with respect to u and v with the help of Eqs. 8.13a and 8.13b as [21]

$$\tilde{D} = \frac{v_m}{2t} \frac{\partial x}{\partial N_B} [N_B u + N_A v] \tag{8.17}$$

In the case of a compound with a very narrow homogeneity range, since we cannot measure the composition profile, the integrated diffusion coefficient is measured. With respect to u and v, we can express this as [23]

$$\tilde{D}_{int}^{\beta} = \int_{N_B^I}^{N_B^{II}} \tilde{D}\, dN_B = \int_{x_\beta^I}^{x_\beta^{II}} \frac{v_m}{2t} [N_B u + N_A v]\, dx = \frac{v_m^\beta}{2t} \left[N_B^\beta u + N_A^\beta v \right] \Delta x_\beta \tag{8.18}$$

As explained in Chap. 6, here the unknown composition range of the β phase is $N_B^{II} - N_B^I$, the thickness of the phase layer is $\Delta x_\beta = x_\beta^{II} - x_\beta^I$. The average molar volume of the phase v_m^β and the composition N_B^β can be considered as constant and during a fixed annealing time of t fixed amount of fluxes, u and v transfer through the Kirkendall marker plane. The values of u and v can be estimated from the composition profile using the relations expressed in Eqs. 8.12a and 8.12b. It should be noted here that by replacing these relations in Eqs. 8.17 and 8.18, we can derive the same relations for the interdiffusion coefficient and the integrated diffusion coefficient as derived by Wagner, which are described in Chaps. 6 and 7.

The velocity of the marker plane following Eq. 6.62 can be estimated by

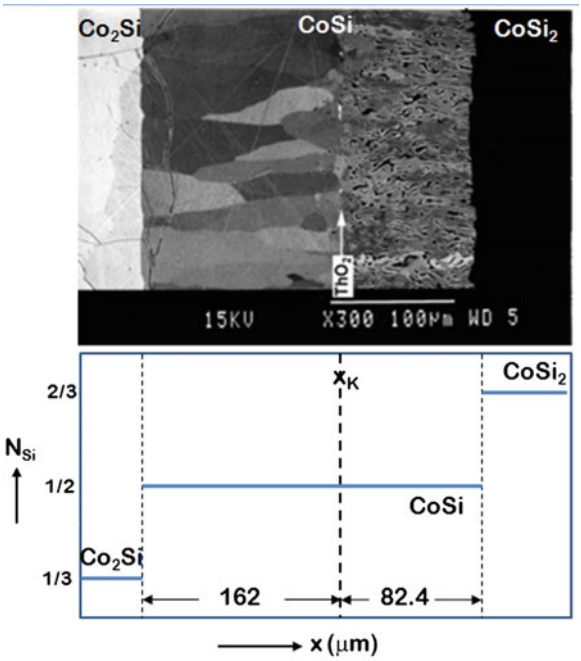

Fig. 8.14 Interdiffusion zone of the CoSi phase in a diffusion couple of Co_2Si/$CoSi_2$ annealed at 1,000 °C for 49 h and use of the physicochemical approach for the estimation of the diffusion parameter [14]

$$v_K = -(\bar{v}_A J_A + \bar{v}_B J_B)$$

Replacing Eq. 8.13a in the above equation, we get

$$v_K = -\left(\bar{v}_A \frac{u}{2t} - \bar{v}_B \frac{v}{2t}\right) = \frac{1}{2t}(\bar{v}_B v - \bar{v}_A u) \tag{8.19a}$$

If the values of the partial molar volumes are not known—for instance, in a phase with a narrow homogeneity range—we consider $v_m = \bar{v}_A = \bar{v}_B$, where v_m is the molar volume of the product phase. Therefore, we can write

$$x_K = 2tv_K = v_m(v - u) \tag{8.19b}$$

It can be understood from the above discussion that the phase layer grows differently from the two different interfaces and we should expect a duplex morphology separated by a Kirkendall marker plane as shown in Fig. 8.11. Therefore, one expects the same values of diffusion coefficients when derived following different approaches explained in Chaps. 6 and 7 or this chapter. The physicochemical approach has an additional benefit that it sheds light on the morphological evolutions in the interdiffusion zone.

8.3 The Application of the Physicochemical Approach in an Incremental Diffusion Couple with a Single Product Phase

Let us now apply this physicochemical approach to estimate the integrated diffusion coefficient and the ratio of the tracer diffusion coefficients in real systems. We consider the growth of CoSi in a diffusion couple of Co_2Si and $CoSi_2$ annealed at 1,100 °C for 49 h, as shown in Fig. 8.11a. The description of the analysis is presented in Fig. 8.14 [16, 21]. It is to be anticipated that Co will dissociate from the Co-rich phase Co_2Si at the interface I to produce the CoSi product phase. Co will then diffuse to the interface II to react with the $CoSi_2$ phase and produce the CoSi phase. Similarly, Si dissociates from the Si-rich phase (the $CoSi_2$ phase at the interface II) to produce the CoSi phase. The dissociated Si diffuses to the interface I to react with the Co_2Si phase and produce the CoSi phase.

In terms of chemical reaction equations:

At the interface I (Co_2Si/CoSi)

$$3u\mathrm{Co}_{2/3}\mathrm{Si}_{1/3} \rightarrow [u]_{\mathrm{Co}} + 2u\mathrm{Co}_{1/2}\mathrm{Si}_{1/2}$$
$$3v\mathrm{Co}_{2/3}\mathrm{Si}_{1/3} + [v]_{\mathrm{Si}} \rightarrow 4v\mathrm{Co}_{1/2}\mathrm{Si}_{1/2}$$

At the interface II (CoSi/$CoSi_2$)

$$3u\mathrm{Co}_{1/3}\mathrm{Si}_{2/3} + [u]_{\mathrm{Co}} \rightarrow 4u\mathrm{Co}_{1/2}\mathrm{Si}_{1/2}$$
$$3v\mathrm{Co}_{1/3}\mathrm{Si}_{2/3} \rightarrow [v]_{\mathrm{Si}} + 2v\mathrm{Co}_{1/2}\mathrm{Si}_{1/2}$$

The parameters $[u]_{\mathrm{Co}}$ and $[v]_{\mathrm{Si}}$ are the number of moles of Co and Si atoms, respectively, transferred per unit area of the reaction layer during the total diffusion time. Following on from this, we can write

$$(2u + 4v)\, v_m^{\mathrm{CoSi}} = \Delta x_{\mathrm{CoSi}}^{\mathrm{I}} \tag{8.20a}$$

$$(4u + 2v)\, v_m^{\mathrm{CoSi}} = \Delta x_{\mathrm{CoSi}}^{\mathrm{II}} \tag{8.20b}$$

Note that the same relations can be obtained directly from Eq. 8.11.

$$N_{\mathrm{Si}}^{-}u + \left(1 - N_{\mathrm{Si}}^{-}\right)v = \int_{x^{-\infty}}^{x_{\mathrm{K}}} \frac{N_{\mathrm{Si}} - N_{\mathrm{Si}}^{-}}{v_m^{\mathrm{CoSi}}}\, dx = \frac{N_{\mathrm{Si}} - N_{\mathrm{Si}}^{-}}{v_m^{\mathrm{CoSi}}} \int_{x^{-\infty}}^{x_{\mathrm{K}}} dx = \frac{N_{\mathrm{Si}} - N_{\mathrm{Si}}^{-}}{v_m^{\mathrm{CoSi}}} \Delta x_{\mathrm{CoSi}}^{\mathrm{I}}$$

$$N_{\mathrm{Si}}^{+}u + \left(1 - N_{\mathrm{Si}}^{+}\right)v = \int_{x_{\mathrm{K}}}^{x^{+\infty}} \frac{N_{\mathrm{Si}}^{+} - N_{\mathrm{Si}}}{v_m^{\mathrm{CoSi}}}\, dx = \frac{N_{\mathrm{Si}}^{+} - N_{\mathrm{Si}}}{v_m^{\mathrm{CoSi}}} \int_{x_{\mathrm{K}}}^{x^{+\infty}} dx = \frac{N_{\mathrm{Si}}^{+} - N_{\mathrm{Si}}}{v_m^{\mathrm{CoSi}}} \Delta x_{\mathrm{CoSi}}^{\mathrm{II}}$$

In this example, $N_{\mathrm{Si}}^{-} = 1/3$, $1 - N_{\mathrm{Si}}^{-} = 2/3$, $N_{\mathrm{Si}}^{+} = 2/3$, $1 - N_{\mathrm{Si}}^{+} = 1/3$, $N_{\mathrm{Si}} = 1/2$ and $1 - N_{Si} = 1/2$. We are considering a phase with a narrow composition range that is an average composition and the constant molar volume of the phase. It can be seen that from the composition values written above, we get the same relations in Eq. 8.20.

The thicknesses of the sublayers measured from the microstructure shown in Fig. 8.14 are $\Delta x_{\mathrm{CoSi}}^{\mathrm{I}} = 162\ \mu\mathrm{m}$. Note here that the actual length of $\Delta x_{\mathrm{CoSi}}^{\mathrm{II}}$ is measured as 107 μm (approximately 23 %); however, the length of $\Delta x_{\mathrm{CoSi}}^{\mathrm{II}} = 82.4\ \mu\mathrm{m}$ is considered for the calculation because of the presence of pores in this sublayer [14, 15]. The molar volume of the CoSi phase is $v_m^{\mathrm{CoSi}} = 6.6 \times 10^{-6}\ \mathrm{m^3/mol}$. Using these values, we find $u = 0.07$ and $v = 6.1\ \mathrm{mol/m^2}$. Therefore, the integrated diffusion coefficient and the ratio of the tracer diffusion coefficients can be estimated using the relations expressed in Eqs. 7.15b and 7.18 as (for an annealing time of 49 h)

$$\frac{D_{\mathrm{Si}}^{*}}{D_{\mathrm{Co}}^{*}} = \frac{v}{u} = 87$$

$$\begin{aligned}\tilde{D}_{\mathrm{int}}^{\mathrm{CoSi}} &= \frac{v_m^{\mathrm{CoSi}}}{2t}\left[N_{\mathrm{Si}}^{\mathrm{CoSi}}u + N_{\mathrm{Co}}^{\mathrm{CoSi}}v\right]\Delta x_{\beta} \\ &= \frac{6.60 \times 10^{-6}}{2 \times 49 \times 60 \times 60}\left[\frac{1}{2} \times 0.07 + \frac{1}{2} \times 6.1\right](162 + 82.4) \times 10^{-6} \\ &= 1.41 \times 10^{-14}\ \mathrm{m^2/s}\end{aligned}$$

Once again, it was possible to calculate the same values using the relations shown in Chap. 7 (Eq. 7.15).

$$\begin{aligned}\tilde{D}_{\mathrm{int}}^{\mathrm{CoSi}} &= \frac{\left(N_{\mathrm{Si}}^{\mathrm{CoSi}} - N_{\mathrm{Si}}^{\mathrm{Co_2Si}}\right)\left(N_{\mathrm{Si}}^{\mathrm{CoSi_2}} - N_{\mathrm{Si}}^{\mathrm{CoSi}}\right)}{\left(N_{\mathrm{Si}}^{\mathrm{CoSi_2}} - N_{\mathrm{Si}}^{\mathrm{Co_2Si}}\right)}\frac{\Delta x_{\mathrm{CoSi}}^{2}}{2t} \\ &= \frac{1/6 \times 1/6}{1/3} \times \frac{(162 + 82.4) \times 10^{-6}}{2 \times 49 \times 60 \times 60} \\ &= 1.41 \times 10^{-14}\ \mathrm{m^2/s}\end{aligned}$$

Now, let us consider an incremental couple in which a single product phase grows from the end members with two phase alloys, as shown in Fig. 8.15 [23]. One of the end members has a composition of $Co_{0.81}Si_{0.19}$. It can be observed from the phase diagram and the alloy in the end member that it is a phase mixture of ε-Co—that is, ε-Co(Si) solid solution with a composition of $Co_{0.83}Si_{0.17}$ at 1,100 °C. Another alloy used as an end member has an average composition of $Co_{0.52}Si_{0.48}$, meaning that it is a phase mixture of Co_2Si and CoSi phases. The volume fraction of the phases can be estimated by the lever rule, as explained in Chap. 1.

Before proceeding to the reaction equations, it is necessary to understand the mechanism by which the product phase grows at the interdiffusion zone. Note that

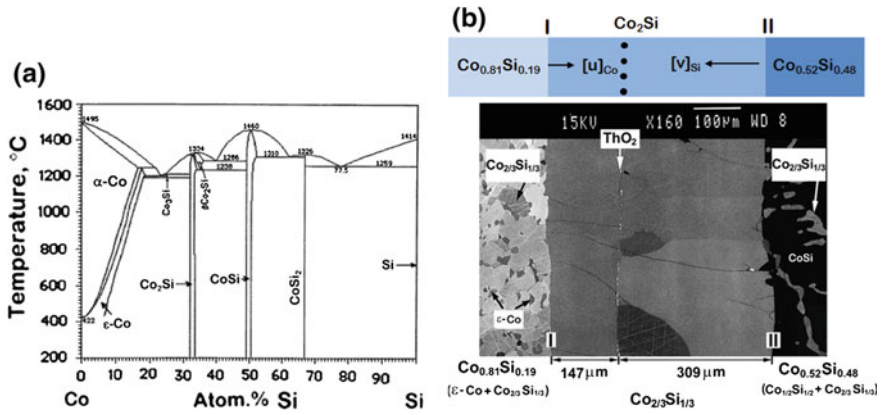

Fig. 8.15 **a** Co–Si phase diagram and **b** use of the physicochemical approach in the Co_2Si phase grown at 1,100 °C after annealing for 100 h [23]

only the ε-Co(Si) phase from the left-hand side end member and the CoSi phase from the right-hand side end member will take part in the reaction or the dissociation process. The Co_2Si phase that is already present in the alloy will directly add to the product phase. This is the reason, as explained in Chap. 7 (Sect. 7.4), the growth rate of a product phase is different depending on the end-member compositions. If we select alloys having a composition closer to the product phase, the growth kinetics of the phase will be higher since the amount of this phase—which can be directly added to the product phase—is higher. The reaction dissociation equations at the interfaces can be written as [23].

At the interface I ($Co_{0.81}Si_{0.19}$/Co_2Si)

$$2.04u\mathrm{Co}_{0.83}\mathrm{Si}_{0.17}(\varepsilon) \rightarrow [u]_{\mathrm{Co}} + 1.04u\mathrm{Co}_{2/3}\mathrm{Si}_{1/3}$$
$$4.06v\mathrm{Co}_{0.83}\mathrm{Si}_{0.17}(\varepsilon) + [v]_{\mathrm{Si}} \rightarrow 5.06v\mathrm{Co}_{2/3}\mathrm{Si}_{1/3}$$

At the interface II (CoSi/$CoSi_2$)

$$2u\mathrm{Co}_{1/2}\mathrm{Si}_{1/2} + [u]_{\mathrm{Co}} \rightarrow 3u\mathrm{Co}_{2/3}\mathrm{Si}_{1/3}$$
$$4v\mathrm{Co}_{1/2}\mathrm{Si}_{1/2} \rightarrow [v]_{\mathrm{Si}} + 3v\mathrm{Co}_{2/3}\mathrm{Si}_{1/3}$$

The parameters $[u]_{Co}$ and $[v]_{Si}$ are the number of moles of Co and Si atoms, respectively, transferred per unit area of the reaction layer during the total diffusion time. Therefore, $(1.04u + 5.06v)$ moles of the Co_2Si phase are produced at the interface I caused by the dissociation and reaction processes. Moreover, as already discussed for the $(2.04u + 4.06v)$ moles of the ε-Co(Si) phase that is consumed at the interface I, a portion of the Co_2Si phase will be directly added to the product phase. Following the lever rule, we know that in an alloy with an average composition of $Co_{0.81}Si_{0.19}$, the ratio of the mole fractions of the Co_2Si

phase to the ε-Co(Si) phase with a composition of $Co_{0.83}Si_{0.17}$ is $\frac{0.19-0.17}{1/3-0.19} = 0.14$. For the consumption of $(2.04u + 4.06v)$ moles of the ε-Co(Si) phase at this interface, $0.14(2.04u + 4.06v)$ moles of the Co_2Si phase will be directly added to the product phase. Therefore, the growth of the Co_2Si phase from the interface I can be written as

$$\begin{aligned}&[(1.04u + 5.06v) + 0.14(2.04u + 4.06v)]v_{\mathrm{m}}^{\mathrm{Co_2Si}} = \Delta x^{I}_{Co_2Si}\\&(1.3u + 5.6v)v_{\mathrm{m}}^{\mathrm{Co_2Si}} = \Delta x^{I}_{Co_2Si}\end{aligned} \tag{8.21a}$$

Similarly, at the interface II, $(3u + 3v)$ moles of the Co_2Si phase are produced by the reaction and dissociation processes. Since $(2u + 4v)$ moles of CoSi are consumed at this interface, a portion of the Co_2Si phase will be directly added to the product phase. Following the lever rule, the ratio of moles of the Co_2Si phase to the CoSi phase in an alloy with an average composition of a $Co_{0.52}Si_{0.48}$ alloy is $\frac{0.5-0.48}{0.48-1/3} = 0.136$. For the consumption of $(2u + 4v)$ moles of CoSi, $0.136(2u + 4v)$ moles of the Co_2Si phase will be directly added to the product phase. Therefore, the growth of the Co_2Si phase from the interface II can be written as

$$\begin{aligned}&[(3u + 3v) + 0.136(2u + 4v)]v_{\mathrm{m}}^{\mathrm{Co_2Si}} = \Delta x^{II}_{Co_2Si}\\&(3.3u + 3.5v)v_{\mathrm{m}}^{\mathrm{Co_2Si}} = \Delta x^{II}_{Co_2Si}\end{aligned} \tag{8.21b}$$

The same relations can be obtained directly from Eq. 8.11.

$$N_{\mathrm{Si}}^{-}u + (1 - N_{\mathrm{Si}}^{-})v = \int_{x^{-\infty}}^{x_{\mathrm{K}}} \frac{N_{\mathrm{Si}} - N_{\mathrm{Si}}^{-}}{v_m^{\mathrm{Co_2Si}}}dx = \frac{N_{\mathrm{Si}} - N_{\mathrm{Si}}^{-}}{v_m^{\mathrm{Co_2Si}}}\int_{x^{-\infty}}^{x_{\mathrm{K}}} dx = \frac{N_{\mathrm{Si}} - N_{\mathrm{Si}}^{-}}{v_m^{\mathrm{Co_2Si}}}\Delta x^{\mathrm{I}}_{\mathrm{Co_2Si}}$$

$$N_{\mathrm{Si}}^{+}u + (1 - N_{\mathrm{Si}}^{+})v = \int_{x_{\mathrm{K}}}^{x^{+\infty}} \frac{N_{\mathrm{Si}}^{+} - N_{\mathrm{Si}}}{v_m^{\mathrm{Co_2Si}}}dx = \frac{N_{\mathrm{Si}}^{+} - N_{\mathrm{Si}}}{v_m^{\mathrm{Co_2Si}}}\int_{x_{\mathrm{K}}}^{x^{+\infty}} dx = \frac{N_{\mathrm{Si}}^{+} - N_{\mathrm{Si}}}{v_m^{\mathrm{Co_2Si}}}\Delta x^{\mathrm{II}}_{\mathrm{Co_2Si}}$$

In this example, $N_{\mathrm{Si}}^{-} = 0.19$, $1 - N_{\mathrm{Si}}^{-} = 0.81$, $N_{\mathrm{Si}}^{+} = 0.48$, $1 - N_{\mathrm{Si}}^{+} = 0.52$, $N_{\mathrm{Si}} = 1/3$ and $1 - N_{\mathrm{Si}} = 2/3$. It can be seen that from the composition values written above, we arrive at the same relations as those in Eq. 8.21.

The thicknesses of the sublayers measured from the microstructure shown in Fig. 8.15 are $\Delta x^{\mathrm{I}}_{\mathrm{Co_2Si}} = 147\,\mu\mathrm{m}$ and $\Delta x^{\mathrm{II}}_{\mathrm{Co_2Si}} = 309\,\mu\mathrm{m}$. The molar volume of the Co_2Si phase is $v_m^{\mathrm{Co_2Si}} = 6.56 \times 10^{-6}\ \mathrm{m^3/mol}$. Using these values, we find $u = 13.55$ and $v = 0.78$. Therefore, the integrated diffusion coefficient and the ratio of the tracer diffusion coefficients can be estimated using the relations expressed in Eqs. 8.15b and 8.18 as (for an annealing time of 100 h)

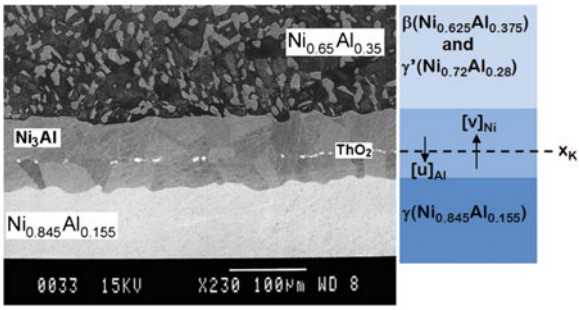

Fig. 8.16 Use of the physicochemical approach in Ni_3Al phase grown in a diffusion couple at 1,000 °C annealed for 196 h [20]

$$\frac{D^*_{Si}}{D^*_{Co}} = \frac{v}{u} = 0.06$$

$$\tilde{D}^{Co_2Si}_{int} = \frac{v_m^{Co_2Si}}{2t}\left[N_{Si}^{Co_2Si}u + N_{Co}^{Co_2Si}v\right]\Delta x_{Co_2Si}$$

$$= \frac{6.56\times10^{-6}}{2\times100\times60\times60}\left[\frac{1}{3}\times13.55+\frac{2}{3}\times0.78\right](147+309)\times10^{-6}$$

$$= 2.1\times10^{-14}\,m^2/s$$

It should be pointed out here that the relations developed in this chapter could also be used to calculate the diffusion parameters at the Kirkendall marker plane where the composition varies in the interdiffusion zone. For example, as shown in Fig. 8.16 in a $Ni_{0.65}Al_{0.35}/Ni_{0.845}Al_{0.155}$ diffusion couple, the γ' phase grows in the interdiffusion zone [21]. It can be understood from the Ni–Al phase diagram in Fig. 4.11a [24] that $Ni_{0.65}Al_{0.35}$ is a phase mixture of the β-NiAl phase with the composition of the $Ni_{0.625}Al_{0.375}$ (dark matrix) and the γ'-Ni_3Al phase (gray precipitates) having the composition of $Ni_{0.72}Al_{0.28}$. The other end member with a composition of $Ni_{0.845}Al_{0.155}$ is a γ-Ni(Al) solid-solution phase [20]. Unlike the previous examples, in this case, there will be composition redistribution after the γ' phase gets added to the product phase from the end member.

The composition profile of the interdiffusion zone is shown in Fig. 8.17a. We consider that u and v in mol/m^2 are the fluxes of Al and Ni crossing the Kirkendall marker plane for the total annealing time of 196 h. The relations expressed in Eq. 8.11 for this diffusion couple can be written as

$$0.65u + 0.35v = \int_{x^{-\infty}}^{x_K} \frac{N_{Ni} - 0.65}{v_m}\,dx \tag{8.22a}$$

$$0.845u + 0.155v = \int_{x_K}^{x^{+\infty}} \frac{0.845 - N_{Ni}}{v_m}\,dx \tag{8.22b}$$

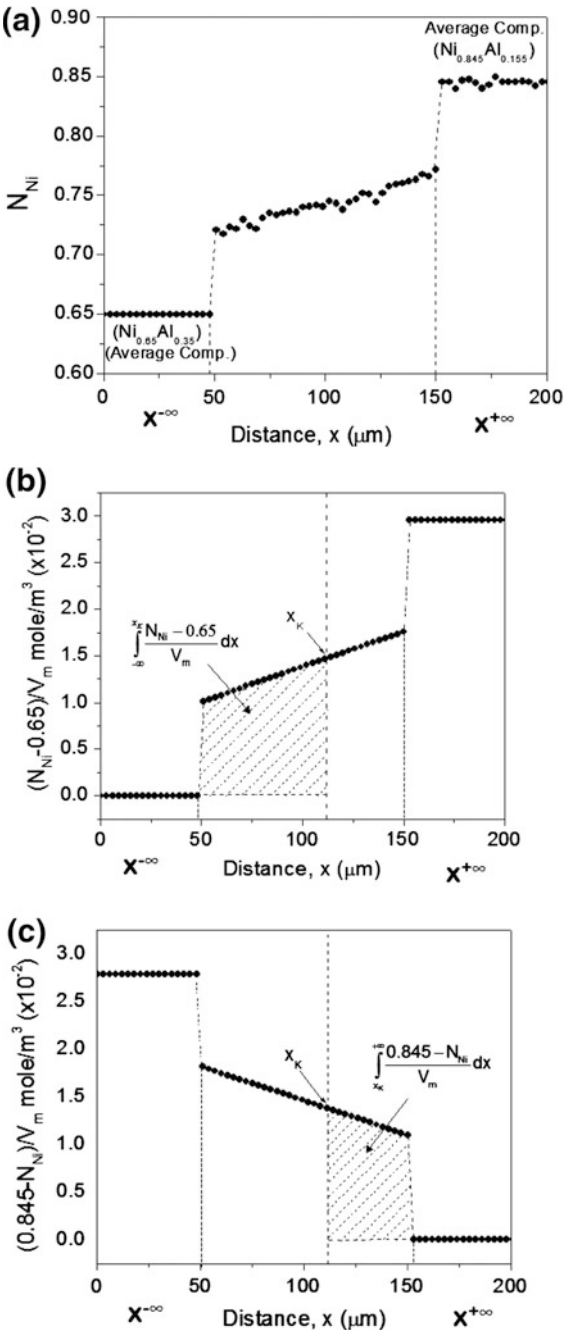

Fig. 8.17 Explanation of estimation of the diffusion parameters by physicochemical approach in Ni_3Al [21]

Note here that $N_B^- = 0.65$, $1 - N_B^- = 0.35$, $N_B^+ = 0.845$ and $1 - N_B^+ = 0.155$. The $(N_{Ni} - 0.65)/v_m$ versus x and $(0.845 - N_{Ni})/v_m$ versus x plots are given in Fig. 8.17b and c, respectively, to determine the values of u and v. The variation in the molar volume of the Ni_3Al phase with composition is available in published work as [20]

$$v_m = 6.60 + 0.823(1 - N_{Ni}) + 0.965\left(1 - N_{Ni}\right)^2 \tag{8.22c}$$

The partial molar volumes of Ni and Al from Eq. 8.22c are estimated as 6.54×10^{-6} and 7.85×10^{-6} m^3/mol.

The values under integral are determined graphically from Fig. 8.17b and c and the values of u and v using Eq. 8.22 are found to be 0.28 and 1.67 mol/m^2, respectively. The slope $d(N_{Ni}/v_m)/dx$ is found to be 7.49×10^7 mol/m^4. Following, the values of the intrinsic diffusion coefficients of the component are estimated as $D_{Ni} = 1.58 \times 10^{-14}$ and $D_{Al} = 3.2 \times 10^{-15}$ m^2/s.

8.4 The Application of the Physicochemical Approach to Explain the Multiphase Growth

The diffusion process for multiphase growth is highly complicated in comparison with the growth of a single phase in an interdiffusion zone. Instead of considering the calculated diffusion parameters from a single composition profile, we shall use the diffusion parameters estimated from the incremental diffusion couples to explain the morphological evolution during multiphase growth. Since there is an extensive data available for the Co–Si system, we shall consider this. A similar method can be used in the other systems once the diffusion process is understood in this system. The useful data at 1,100 °C are listed in Table 8.2 [16]. We consider a diffusion couple of Co/$CoSi_2$, in which, according to the phase diagram shown in Fig. 8.15a, two phases (Co_2Si and CoSi) should grow in the interdiffusion zone. Such a schematic diffusion couple is shown in Fig. 8.18. As shown in this figure, it is necessary to consider a Kirkendall marker plane in both the phases. Following, we consider that the total flux of Co and Si that crosses the Kirkendall marker plane in the Co_2Si phase is $[m]_{Co}$ and $[n]_{Si}$, respectively. Similarly, the total flux of Co and Si that crosses the Kirkendall marker plane in the CoSi phase is $[p]_{Co}$ and $[q]_{Si}$, respectively. The growth of the Co_2Si phase at the interface I occurs by the reaction of Co with the Si-diffused component through this phase after the dissociation at the interface II. At the interface II, the same phase grows because of the dissociation of Si from the CoSi phase. At the same time, the phase also grows because of the reaction between CoSi and Co that diffuses from the interface I. At the same time, the CoSi phase grows at the interface II because of the dissociation of Co from the Co_2Si phase and the reaction of Si with the same phase. The dissociated Co diffuses through the CoSi product phase and reacts with

Table 8.2 The integrated diffusion coefficients $\left(\tilde{D}_{\text{int}}\right)$, molar volumes of the Co-silicides (v_m), and the ratio of tracer diffusivities of Si and Co $\left(\frac{\bar{v}_{\text{Co}} D_{\text{Si}}}{\bar{v}_{\text{Si}} D_{\text{Co}}}\right)$ at 1,100 °C in different phases are listed

	Phases	
	Co_2Si	CoSi
$\tilde{D}_{\text{int}}(\text{m}^2/\text{s})$	$(1.5 \pm 0.5) \times 10^{-14}$	$(4.6 \pm 0.3) \times 10^{-14}$
$\frac{D^*_{\text{Si}}}{D^*_{\text{Co}}} = \left(\frac{\bar{v}_{\text{Co}} D_{\text{Si}}}{\bar{v}_{\text{Si}} D_{\text{Co}}}\right)$	0.06 ± 0.025	35 ± 15
v_m (m^3 mol^{-1})	6.56×10^{-6}	6.60×10^{-6}

These are the average values obtained from many different diffusion couples. Therefore, the data considered for Co_2Si in this table are different from the data obtained in a particular diffusion couple, as discussed in the previous example

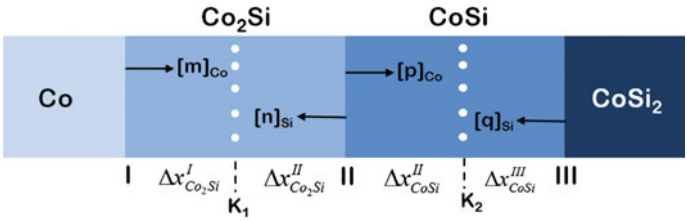

Fig. 8.18 A schematic diagram explaining the physicochemical approach in a Co/$CoSi_2$ diffusion couple

the $CoSi_2$ phase to produce CoSi. Si that reacts with the Co_2Si phase at the interface II is actually produced by the dissociation from the $CoSi_2$ phase at the interface III to produce the CoSi product phase. Therefore, it must be clear that the Co_2Si and CoSi phases at the interfaces grow by consuming the neighboring phase(s) and at the same time become consumed because of the growth of the neighboring phase(s).

In terms of reaction equations, these can be written as:

At the interface I (Co/Co_2Si on the Co_2Si side)

$$2n\text{Co} + n\,[\text{Si}]_d \rightarrow 3n\text{Co}_{2/3}\text{Si}_{1/3}$$

At the interface II (Co_2Si/CoSi on the Co_2Si side)

$$4n\text{Co}_{1/2}\text{Si}_{1/2} \rightarrow n[\text{Si}]_d + 3n\text{Co}_{2/3}\text{Si}_{1/3}$$

$$2m\text{Co}_{1/2}\text{Si}_{1/2} + m\,[\text{Co}]_d \rightarrow 3m\text{Co}_{2/3}\text{Si}_{1/3}$$

At the interface II (Co_2Si/CoSi on the CoSi side)

$$3p\mathrm{Co}_{2/3}\mathrm{Si}_{1/3} \rightarrow p[\mathrm{Co}]_d + 2p\mathrm{Co}_{1/2}\mathrm{Si}_{1/2}$$
$$3q\mathrm{Co}_{2/3}\mathrm{Si}_{1/3} + q[\mathrm{Si}]_d \rightarrow 4q\mathrm{Co}_{1/2}\mathrm{Si}_{1/2}$$

At the interface III (CoSi/$CoSi_2$ on the CoSi side)

$$3p\mathrm{Co}_{1/3}\mathrm{Si}_{2/3} + p[\mathrm{Co}]_d \rightarrow 4p\mathrm{Co}_{1/2}\mathrm{Si}_{1/2}$$
$$3q\mathrm{Co}_{1/3}\mathrm{Si}_{2/3} \rightarrow q[\mathrm{Si}]_d + 2q\mathrm{Co}_{1/2}\mathrm{Si}_{1/2}$$

Therefore, $3n$ moles of the Co_2Si phase are produced at the interface I. At the interface II, $(3m + 3n)$ moles of Co_2Si are produced and at the same time $(3p + 3q)$ moles get consumed. At the same interface, on the other side, $(2p + 4q)$ moles of CoSi are produced; however, $(4n + 2\ m)$ moles get consumed. At the interface III, $(4p + 2q)$ moles of CoSi are produced.

$$\begin{aligned}
&v_m^{\mathrm{Co}_{2/3}\mathrm{Si}_{1/3}} \times 3n = \Delta x^{\mathrm{I}}_{\mathrm{Co_2Si}} \\
&v_m^{\mathrm{Co}_{2/3}\mathrm{Si}_{1/3}} \times (3m + 3n - 3p - 3q) = \Delta x^{\mathrm{II}}_{\mathrm{Co_2Si}} \\
&v_m^{\mathrm{Co}_{\frac{1}{2}}\mathrm{Si}_{\frac{1}{2}}} \times (2p + 4q - 4n - 2m) \\
&v_m^{\mathrm{Co}_{\frac{1}{2}}\mathrm{Si}_{\frac{1}{2}}} \times (4p + 2q)
\end{aligned} \tag{8.23a}$$

The integrated diffusion coefficients can be written as

$$\begin{aligned}
\tilde{D}^{Co_2Si}_{\mathrm{int}} &= \frac{v_m^{Co_2Si}}{2t}\left[N_{Si}^{Co_2Si}m + N_{Co}^{Co_2Si}n\right]\left(\Delta x^{I}_{Co_2Si} + \Delta x^{II}_{Co_2Si}\right) \\
\tilde{D}^{CoSi}_{\mathrm{int}} &= \frac{v_m^{CoSi}}{2t}\left[N_{Si}^{CoSi}p + N_{Co}^{Co_2Si}q\right]\left(\Delta x^{II}_{CoSi} + \Delta x^{III}_{CoSi}\right)
\end{aligned} \tag{8.23b}$$

The ratio of the diffusivities can be written as

$$\begin{aligned}
\left.\frac{D^*_{Si}}{D^*_{Co}}\right|_{Co_2Si} &= \left.\frac{\bar{v}_{Co}D_{Si}}{\bar{v}_{Si}D_{Co}}\right|_{Co_2Si} = \frac{n}{m} \\
\left.\frac{D^*_{Si}}{D^*_{Co}}\right|_{CoSi} &= \left.\frac{\bar{v}_{Co}D_{Si}}{\bar{v}_{Si}D_{Co}}\right|_{CoSi} = \frac{q}{p}
\end{aligned} \tag{8.23c}$$

Using the molar volume values, the integrated diffusion coefficients and the ratio of the intrinsic (or tracer diffusion coefficients), as listed in Table 8.2, we find the values for 100 hrs as

$\Delta x^{\mathrm{I}}_{\mathrm{Co_2Si}} = 32\,\mu\mathrm{m}$, $\Delta x^{\mathrm{II}}_{\mathrm{Co_2Si}} = 133\,\mu\mathrm{m}$, $\Delta x^{\mathrm{II}}_{\mathrm{CoSi}} = 168.5\,\mu\mathrm{m}$, $\Delta x^{\mathrm{II}}_{CoSi} = 294.5\,\mu\mathrm{m}$, $m = 26.8, n = 1.6, p = 0.6$ and $q = 21.0\ \mathrm{mol/m^2}$.

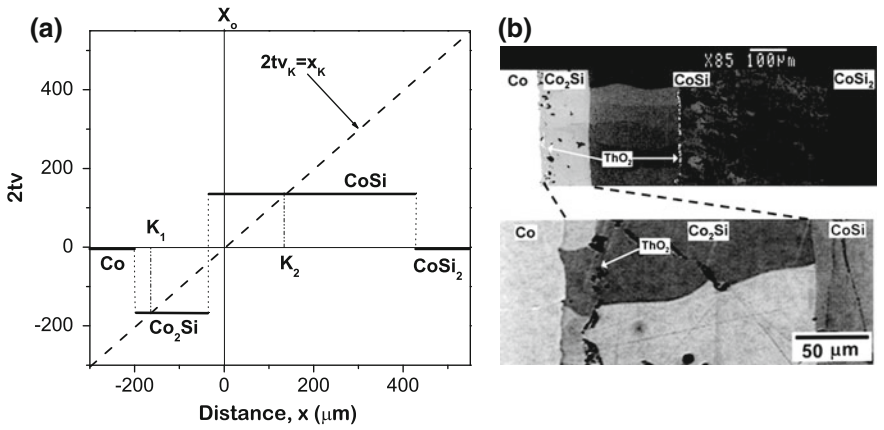

Fig. 8.19 **a** A velocity diagram and **b** the interdiffusion zone showing the location of the marker planes in a Co/$CoSi_2$ diffusion couple [14] annealed at 1100 °C for 100 h

One interesting fact should be noted here that the thicknesses of all the sublayers $\Delta x^{\mathrm{II}}_{\mathrm{Co_2Si}}$ and $\Delta x^{\mathrm{II}}_{\mathrm{CoSi}}$ are positive, despite getting consumed by the neighboring phases at the interface II. This means that both phases will have the Kirkendall marker plane. In other sense, bifurcation of the Kirkendall marker plane is expected. This can be shown with respect to the velocity diagram construction. The velocity of the phases can be estimated as

$$v_m^{\mathrm{Co_2Si}}(n-m) = 2tv_{\mathrm{K}}^{\mathrm{Co_2Si}} = x_{\mathrm{K}}^{\mathrm{Co_2Si}} = -165.3\,\mu\mathrm{m}$$
$$v_m^{\mathrm{CoSi}}(q-p) = 2tv_{\mathrm{K}}^{\mathrm{CoSi}} = x_{\mathrm{K}}^{\mathrm{CoSi}} = 134.6\,\mu\mathrm{m}$$

Note that we have assumed the partial molar volume of the component to be equal to the molar volume of the phase.

It should be noted here that for the velocity diagram plot, we have not determined the initial contact plane—which is not possible to determine correctly—as already explained in Chap. 6. It can be seen that the range of the y and x axes is kept the same such that the straight line $2tv_{\mathrm{K}} = x_{\mathrm{K}}$ will have an angle of 45°. Accordingly, the straight line can just be drawn from one corner to the other as is done in Fig. 8.19a. The location of the initial contact plane is the position at which it intersects $2tv = 0$. The positions of the intersection points by the straight line $2tv_{\mathrm{K}} = x_{\mathrm{K}}$ on the line representing the velocity of the phases indicate the location of the Kirkendall marker plane. Since we have considered the phases with an average composition, the velocity of the phase is drawn by the straight lines. The interdiffusion zone in the Co/$CoSi_2$ phase is shown in Fig. 8.19b. It can be seen that the thicknesses of the phase layers are similar within the range of experimental error. As estimated, both phases contain the Kirkendall marker plane. The presence of duplex morphology is also evident in both phases suggesting the location of the marker planes. Note here that there was a very small dissolution of Si in the

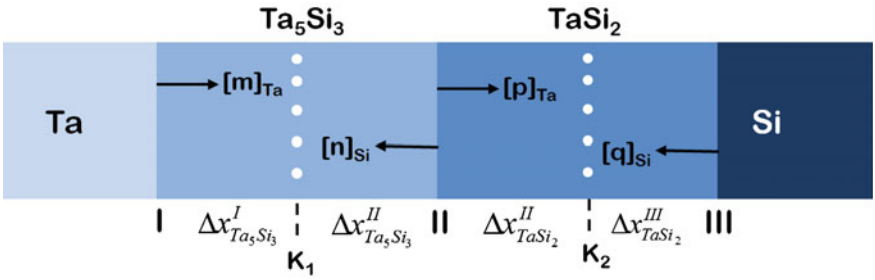

Fig. 8.20 A schematic diagram explaining the physicochemical approach in a Ta/Si diffusion couple

Table 8.3 The integrated diffusion coefficients, $\left(\tilde{D}_{\text{int}}\right)$ molar volumes of the Ta-silicides (v_m) and the intrinsic flux ratios of Si and Ta $\left(\frac{\tilde{v}_{\text{Ta}} D_{\text{Si}}}{\tilde{v}_{\text{Si}} D_{\text{Ta}}}\right)$ at 1,250 °C in different phases are listed [24]

	Phase	
	Ta_5Si_3	$TaSi_2$
$\tilde{D}_{\text{int}}(\text{m}^2/\text{s})$	1.41×10^{-16}	5.02×10^{-14}
$\frac{D_{\text{Si}}^*}{D_{\text{Ta}}^*} = \frac{\tilde{v}_{\text{Ta}} D_{\text{Si}}}{\tilde{v}_{\text{Si}} D_{\text{Ta}}}$	5.8	1.1
v_m (m^3 mol^{-1})	9.48×10^{-6}	8.71×10^{-6}

Co end member, which is neglected in this analysis [16]. This results a minor error in the estimated values.

Now, let us turn to consider a Ta–Si system where there are four intermediate phases [25]; however, only two phases ($TaSi_2$ and Ta_5Si_3) could be detected in the interdiffusion zone. There was an indication that the other phases have a much lower growth rate such that they may be present as very thin layers—but are almost impossible to detect under a scanning electron microscope. Therefore, for our analysis, we can consider the presence of two phases only in the interdiffusion zone, as shown in Fig. 8.20. We shall consider a diffusion couple annealed at 1,250 °C for 9 h. This couple is presented schematically in Fig. 8.20 to explain the dissociation and reaction processes occurring at different interfaces. All details of the integrated diffusion coefficients, the ratio of the diffusivities, and the molar volumes are listed below in Table 8.3.

In the same line of discussion, as described in the previous example, we can write the reaction dissociation equations at the interfaces as

At the interface I

$$\frac{5}{3}\, n\,\text{Ta} + [n]_{\text{Si}} \rightarrow \frac{8}{3}\, n\,\text{Ta}_{5/8}\text{Si}_{3/8}$$

At the interface II (Ta_5Si_3 side)

$$\frac{9}{7}\,m\,\mathrm{Ta}_{1/3}\mathrm{Si}_{2/3} + [m]_{\mathrm{Ta}} \rightarrow \frac{16}{7}\,m\,\mathrm{Ta}_{5/8}\mathrm{Si}_{3/8}$$
$$\frac{15}{7}\,n\,\mathrm{Ta}_{1/3}\mathrm{Si}_{2/3} \rightarrow [n]_{\mathrm{Si}} + \frac{8}{7}\,n\,\mathrm{Ta}_{5/8}\mathrm{Si}_{3/8}$$

Interface II ($TaSi_2$ side)

$$\frac{8}{7}\,q\,\mathrm{Ta}_{5/8}\mathrm{Si}_{3/8} + [q]_{\mathrm{Si}} \rightarrow \frac{15}{7}\,q\,\mathrm{Ta}_{1/3}\mathrm{Si}_{2/3}$$
$$\frac{16}{7}\,p\,\mathrm{Ta}_{5/8}\mathrm{Si}_{3/8} \rightarrow [p]_{\mathrm{Ta}} + \frac{9}{7}\,p\,\mathrm{Ta}_{1/3}\mathrm{Si}_{2/3}$$

Interface III

$$2\,p\,Si + [\,p\,]_{Ta} \rightarrow 3\,p\,Ta_{1/3}Si_{2/3}$$

Accordingly, the thicknesses of the sublayers can be related to the mole of the product phases formed at the different interfaces can be written as

$$\begin{aligned}
&\frac{8}{3}n \times v_m^{\mathrm{Ta_5Si_3}} = \Delta x^{\mathrm{I}}_{\mathrm{Ta_5Si_3}} \\
&\left[\left(\frac{16}{7}m + \frac{8}{7}n\right) - \left(\frac{16}{7}p + \frac{8}{7}q\right)\right] \times v_m^{\mathrm{Ta_5Si_3}} = \Delta x^{\mathrm{II}}_{\mathrm{Ta_5Si_3}} \\
&\left[\left(\frac{15}{7}q + \frac{9}{7}p\right) - \left(\frac{15}{7}n + \frac{9}{7}m\right)\right] \times v_m^{\mathrm{TaSi_2}} = \Delta x^{\mathrm{II}}_{\mathrm{TaSi_2}} \\
&3p \times v_m^{\mathrm{TaSi_2}} = \Delta x^{\mathrm{III}}_{\mathrm{TaSi_2}}
\end{aligned} \tag{8.24a}$$

Following, the integrated diffusion coefficients and the ratio of the diffusivities of the components can be written as

$$\begin{aligned}
\tilde{D}^{Ta_5Si_3}_{\mathrm{int}} &= \frac{v_m^{Ta_5Si_3}}{2t}\left[N_{Ta}^{Ta_5Si_3}\,n + N_{Si}^{Ta_5Si_3}\,m\right]\left(\Delta x^{I}_{Ta_5Si_3} + \Delta x^{II}_{Ta_5Si_3}\right) \\
\tilde{D}^{TaSi_2}_{int} &= \frac{v_m^{TaSi_2}}{2t}\left[N_{Ta}^{TaSi_2}\,q + N_{Si}^{TaSi_2}\,p\right]\left(\Delta x^{II}_{TaSi_2} + \Delta x^{III}_{TaSi_2}\right)
\end{aligned} \tag{8.24b}$$

$$\begin{aligned}
\left.\frac{D^*_{Si}}{D^*_{Ta}}\right|_{Ta_5Si_3} &= \frac{n}{m} \\
\left.\frac{D^*_{Si}}{D^*_{Ta}}\right|_{TaSi_2} &= \frac{q}{p}
\end{aligned} \tag{8.24c}$$

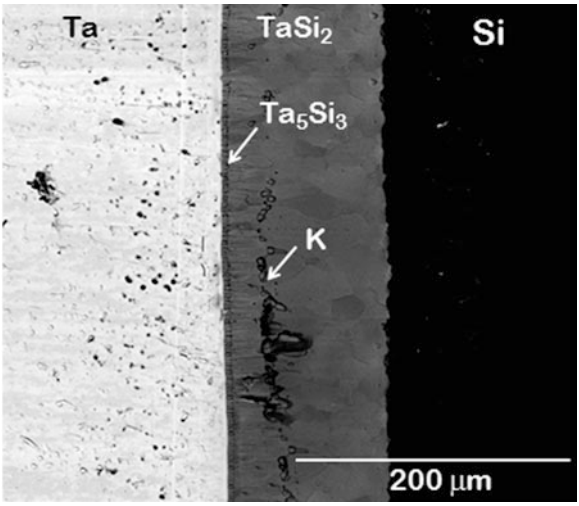

Fig. 8.21 Interdiffusion zone of the Ta/Si diffusion couple annealed at 1,250 °C for 9 h

Using the values in the Table 8.3 for 9 h, we get

$$\Delta x^{\mathrm{I}}_{\mathrm{Ta_5Si_3}} = 64.07,\ \Delta x^{\mathrm{II}}_{\mathrm{Ta_5Si_3}} = -63.52,\ \Delta x^{\mathrm{II}}_{\mathrm{TaSi_2}} = 42.7 \text{ and } \Delta x^{\mathrm{III}}_{\mathrm{TaSi_2}} = 78.15\ \mu\mathrm{m}$$
$$m = 0.437, n = 2.535, p = 2.99 \text{ and } q = 3.29\ \mathrm{mol/m^2}.$$

Unlike the example, as discussed before, all sublayer thicknesses do not have positive values. This would indicate that $\Delta x^{\mathrm{II}}_{\mathrm{Ta_5Si_3}}$ gets consumed at the interface II because of the growth of $\Delta x^{\mathrm{II}}_{\mathrm{TaSi_2}}$. Therefore, the total thickness of the Ta_5Si_3 phase is $\Delta x^{\mathrm{I}}_{\mathrm{Ta_5Si_3}} + \Delta x^{\mathrm{II}}_{\mathrm{Ta_5Si_3}} = 0.55$ μm. This further means that there will be a Kirkendall marker plane in the $TaSi_2$ phase and no marker plane in the Ta_5Si_3 phase. This is indeed to be found also in the Ta/Si couple as shown in Fig. 8.21. The location of the marker plane is evident from the presence of pores and the duplex morphology, as discussed in greater depth in Chap. 6.

Now, let us consider the Ag–Zn system, as shown in Figs. 8.10a and 8.12. The Zn/Ag couple was annealed at 370 °C for 5 h, and analysis can be done to understand the reason for not finding any Kirkendall marker plane in the β-AgZn phase [13, 26]. The composition profile is given in Fig. 8.22. It can be seen that the phases have a wide homogeneity range. To simplify the analysis, we consider an average composition of the phases, which is estimated from

$$N^{\theta}_{\mathrm{Ag}}\Big|_{\mathrm{ave}} = \frac{\int_{N^{-\theta}_{\mathrm{Ag}}}^{N^{+\theta}_{\mathrm{Ag}}} N_{\mathrm{Ag}}\,dx}{\Delta x_{\theta}} \tag{8.25}$$

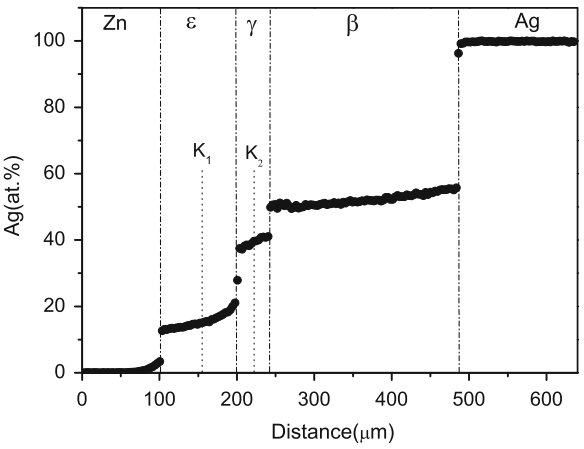

Fig. 8.22 Composition profile of the Ag/Zn diffusion couple annealed at 370 °C for 5 h

where θ is the phase of interest, $N_{Ag}^{-\theta}$ and $N_{Ag}^{+\theta}$ are the phase boundary compositions, and Δx_θ is the thickness of the interested phase. The estimated average compositions of the ε, γ and β phases are $Ag_{0.154}Zn_{0.846}$, $Ag_{0.394}Zn_{0.606}$, and $Ag_{0.521}Zn_{0.479}$, respectively. For our analysis without complication, we ignore the dissolution of Ag in Zn and Zn in Ag, since the composition profiles developed in these solid solutions are small.

The schematic diffusion couple is presented above in Fig. 8.23. Based on the average compositions of the phases, the reaction/dissociation equations at different interfaces can be written as

Interface I—$Zn/AgZn_3$ ($AgZn_3$ side)

$$5.49nZn + [n]_{Ag} \rightarrow 6.49nAg_{0.154}Zn_{0.846}(\varepsilon)$$

Reaction of Ag with Zn

Interface II—$AgZn_3/Ag_5Zn_8$ ($AgZn_3$ side)

$$0.64mAg_{0.394}Zn_{0.606}\ (\gamma) + [m]_{Zn} \rightarrow 1.64mAg_{0.154}Zn_{0.846}(\varepsilon)$$

Reaction of Zn with Ag_5Zn_8

$$3.53nAg_{0.394}Zn_{0.606}(\gamma) \rightarrow [n]_{Ag} + 2.53nAg_{0.154}Zn_{0.846}(\varepsilon)$$

Dissociation of Ag from Ag_5Zn_8

Interface II—$AgZn_3/Ag_5Zn_8$ (Ag_5Zn_8 side)

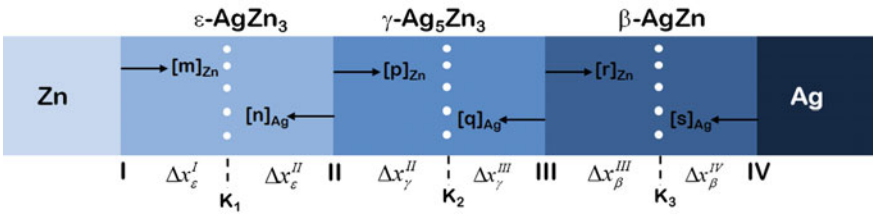

Fig. 8.23 A schematic diagram explaining the physicochemical approach in the Ag/Zn diffusion couple

$$1.64p\mathrm{Ag}_{0.154}\mathrm{Zn}_{0.846}(\varepsilon) \rightarrow [p]_{\mathrm{Zn}} + 0.64p\mathrm{Ag}_{0.394}\mathrm{Zn}_{0.606}(\gamma)$$

Dissociation of Zn from $AgZn_3$

$$2.53q\mathrm{Ag}_{0.154}\mathrm{Zn}_{0.846}(\varepsilon) + [q]_{\mathrm{Ag}} \rightarrow 3.53q\mathrm{Ag}_{0.394}\mathrm{Zn}_{0.606}(\gamma)$$

Reaction of Ag with $AgZn_3$

Interface III—Ag_5Zn_8/AgZn (Ag_5Zn_8 side)

$$3.10p\mathrm{Ag}_{0.521}\mathrm{Zn}_{0.479}(\beta) + [p]_{\mathrm{Zn}} \rightarrow 4.10p\mathrm{Ag}_{0.394}\mathrm{Zn}_{0.606}(\gamma)$$

Reaction of Zn with AgZn

$$4.77q\mathrm{Ag}_{0.521}\mathrm{Zn}_{0.479}(\beta) \rightarrow [q]_{\mathrm{Ag}} + 3.77q\mathrm{Ag}_{0.394}\mathrm{Zn}_{0.606}(\gamma)$$

Dissociation of Ag from AgZn

Interface III—Ag_5Zn_8/AgZn (AgZn side)

$$4.10r\mathrm{Ag}_{0.394}\mathrm{Zn}_{0.606}(\gamma) \rightarrow [r]_{\mathrm{Zn}} + 3.10r\mathrm{Ag}_{0.521}\mathrm{Zn}_{0.479}(\beta)$$

Dissociation of Zn from Ag_5Zn_8

$$3.77s\mathrm{Ag}_{0.394}\mathrm{Zn}_{0.606}\ (\gamma) + [s]_{\mathrm{Ag}} \rightarrow 4.77s\mathrm{Ag}_{0.521}\mathrm{Zn}_{0.479}(\beta)$$

Reaction of Ag with Ag_5Zn_8

Interface IV—AgZn/Ag (AgZn side)

$$1.09r\mathrm{Ag} + [r]_{\mathrm{Zn}} \rightarrow 2.09r\mathrm{Ag}_{0.521}\mathrm{Zn}_{0.479}(\beta)$$

Reaction of Zn with Ag.

Here, m, n, p, q, r, and s are the fluxes (moles/m^2) of the components as shown in Fig. 8.23. The product phases produced at different interfaces can be related to the thicknesses of the sublayers as

$$\begin{aligned}
v_m^{\varepsilon}(6.49n) &= \Delta x_{\varepsilon}^{\mathrm{I}} \\
v_m^{\varepsilon}(1.64m + 2.53n - 1.64p - 2.53q) &= \Delta x_{\varepsilon}^{\mathrm{II}} \\
v_m^{\gamma}(0.64p + 3.53q - 0.64m - 3.53n) &= \Delta x_{\gamma}^{\mathrm{II}} \\
v_m^{\gamma}(4.10p + 3.77q - 4.10r - 3.77s) &= \Delta x_{\gamma}^{\mathrm{III}} \\
v_m^{\beta}(3.10r + 4.77s - 3.10p - 4.77q) &= \Delta x_{\beta}^{\mathrm{III}} \\
v_m^{\beta}(2.09r) &= \Delta x_{\beta}^{\mathrm{IV}}
\end{aligned}$$

The molar volumes of the ε, γ and β phases are 9.20×10^{-6}, 9.44×10^{-6} and 9.46×10^{-6} m^3/mol. The sublayer thicknesses in the ε and γ phases measured directly from the Ag–Zn diffusion couple as shown in Fig. 8.24 are $\Delta x_{\varepsilon}^{\mathrm{I}} = 48.6$, $\Delta x_{\varepsilon}^{\mathrm{II}} = 50.2$, $\Delta x_{\gamma}^{\mathrm{II}} = 16.65$, $\Delta x_{\gamma}^{\mathrm{III}} = 24.45$ and $\left(\Delta x_{\beta}^{\mathrm{III}} + \Delta x_{\beta}^{\mathrm{IV}}\right) = 244\,\mu\mathrm{m}$. The ratio of the diffusivities in the β-AgZn phase was estimated using an incremental couple as $\frac{r}{s} = \frac{V_{\mathrm{Ag}} D_{\mathrm{Zn}}}{V_{\mathrm{Zn}} D_{\mathrm{Ag}}} = 6.5$. From these, the rest of the parameters are estimated as $m = 19.62$, $n = 0.81$, $p = 13.88$, $q = 2.37$, $r = 13.52$, $s = 2.08$ mol/m^2, and $\Delta x_{\beta}^{\mathrm{III}} = -23.72$ and $\Delta x_{\beta}^{\mathrm{IV}} = 267.72$ mm. Therefore, the negative value of $\Delta x_{\beta}^{\mathrm{III}}$ is suggestive of the consumption of the sublayer by the neighboring phase and the absence of the Kirkendall marker plane in the β phase.

Now, let us consider different locations of the marker planes and the kind of morphology to be expected in the interdiffusion zone. Our discussion shall be based upon only two product phases in the interdiffusion zone; the description is, however, the same when a different number of phases are formed. Typically, we expect to find one of the three examples given in Fig. 8.24.

Suppose, two phases (A_2B and AB_2) are grown in the interdiffusion zone of a hypothetical A/B diffusion couple. There is a possibility that the marker planes are present in both the phases, as shown in Fig. 8.24a, meaning that the thicknesses of all the sublayers are positive and duplex morphology should be expected in both the phases. It should be noted here that finding more than one Kirkendall plane in an interdiffusion zone is not very common—with very few rare examples being found till date [27]. In most cases, a single marker plane is present in one of the phases—as shown in Fig. 8.24b—which signifies that the thicknesses of the sublayers $\Delta x_{\mathrm{A_2B}}^{\mathrm{I}}$ and $\Delta x_{\mathrm{A_2B}}^{\mathrm{II}}$ are positive in the A_2B phase. $\Delta x_{\mathrm{AB_2}}^{\mathrm{II}}$ is negative, which

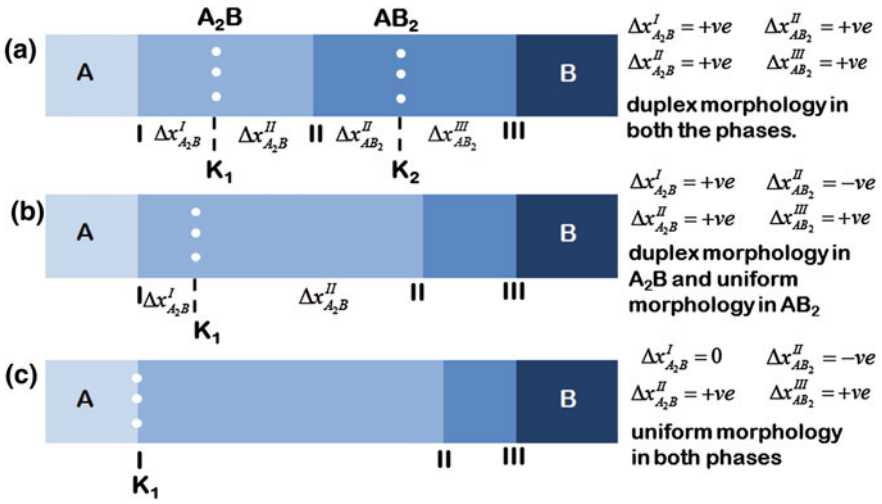

Fig. 8.24 Schematic representation of the diffusion couple explaining the situation for finding **a** bifurcation of the marker plane **b** a single Kirkendall marker plane in the A_2B phase and **c** a single marker plane at A/A_2B phase

means that this part is consumed because of the growth of the $\Delta x^{\mathrm{II}}_{\mathrm{A_2B}}$. However, $\Delta x^{\mathrm{III}}_{\mathrm{AB_2}}$ is positive. This suggests that duplex morphology is to be expected in the A_2B phase and a uniform morphology is expected in the AB_2 phase. There could be many examples where the marker plane is present at one of the interfaces of the end-member/product phase, as shown in Fig. 8.24c. Very frequently, it is concluded (based on the similar location of the marker plane) that one of the components has a much higher diffusion rate compared to the other in both phases. This is not correct. For example, if the marker plane is present at the A/A_2B interface, it is true that A has a much higher diffusion rate compared to B in the A_2B phase. However, it is not indicative of the relative mobilities of the components in the AB_2 phase. There could be a comparable diffusion rate of both the components in this phase. Due to the significantly higher diffusion rate of A and negligible diffusion rate of B in the A_2B phase, $\Delta x^{\mathrm{I}}_{\mathrm{AB_2}}$ will be negligible and $\Delta x^{\mathrm{II}}_{\mathrm{AB_2}}$ will be almost equal to the total thickness of the A_2B phase. Moreover, due to the very high flux of A through this phase, the growth rate of this product phase is very high at the interface II and might consume the whole of $\Delta x^{\mathrm{II}}_{\mathrm{AB_2}}$ and a part of $\Delta x^{\mathrm{III}}_{\mathrm{AB_2}}$ such that $\Delta x^{\mathrm{II}}_{\mathrm{AB_2}}$ will have a negative value. Therefore, both the phases will have a uniform morphology. It should be noted here that, sometimes, even if the possibility of bifurcation of the marker plane is expected in an interdiffusion zone, the markers in both the phases might not be found. This was seen in the Cu–Sn system, where the Cu_3Sn and Cu_6Sn_5 phases are seen to be growing at the interdiffusion zone [28]. The marker plane was found only in the Cu_6Sn_5 phase; however, according to the analysis based on the diffusion parameters in the phases, the

marker plane should be present in both the phases. To find the marker planes in both the phases, it is important that both phases should start growing together from the beginning to trap the markers. This is, in general, found in bulk diffusion couples, as discussed till now. In thin films, on the other hand, sequential phase growth is very frequently reported. The presence of the marker plane only in the Cu_6Sn_5 phase, however, indicates the sequential growth of the phases, where the Cu_3Sn phase, most probably, started growing after some incubation period. If this is true, once all the markers get trapped in the Kirkendall marker plane in the Cu_6Sn_5 phase, no markers will be left in the Cu_3Sn phase after it starts growing.

8.5 Effect of Electrical Current on the Microstructural Evolution of the Diffusion Zone

The physicochemical approach can also be utilized to rationalize the effect of additional driving forces, such as electric field, on the growth of interfacial phases. Figure 8.25 shows a cross section of the component with the directions of the current and electron flux. The electron flux enters the component from the source contact and leaves from the drain contact. In the forthcoming analysis of the effect of the electron flow on the IMC, growth only the on the printed wiring board (PWB) side is considered. This is because, at the component side, the presence of Ag finish will make the analysis less quantitative.

Figure 8.26 shows the interfacial microstructures from solder—PWB interfaces from the samples that have been annealed at 110 °C for 750 h and both the drain as well as source contacts after 750 h of constant current stressing.

Due to the relatively complex geometry of the interconnections and the differences in cross-sectional areas, the current crowding effects and thus the differences in current densities cannot be easily addressed. However, even if only the direction of the electron flux is taken into consideration, the marked differences in the total IMC growth kinetics as well as the relative thicknesses of the Cu_6Sn_5 and Cu_3Sn intermetallic compounds can be observed when these differences are compared with the results obtained using the diffusion couple experiments [29, 30]. Closer examination of Table 8.4 and Fig. 8.26 reveals that when the flow of electrons is toward the PWB, the η and ε phase layers are almost of the same thickness, whereas in the opposite situation, the thickness of Cu_3Sn is drastically reduced.

The thickness ratio of Cu_6Sn_5 to Cu_3Sn is unusually high in the case of the annealed samples (Table 8.4) when compared to the earlier results from the Cu/Sn(X) diffusion couples [31–35]. It is known that impurity and alloying components can drastically change the growth kinetics of the IMC compounds [32]. Hence, it is not surprising that the IMC ratio differs from that observed with high purity materials. Based on our previous experiments, it is known that alloying components (like Ni) in copper increase the Sn flux through Cu_6Sn_5 but have no measurable effect on the intrinsic fluxes inside Cu_3Sn. This, in turn, results in a

Fig. 8.25 SEM micrograph of the structure of the component used in the electromigration study

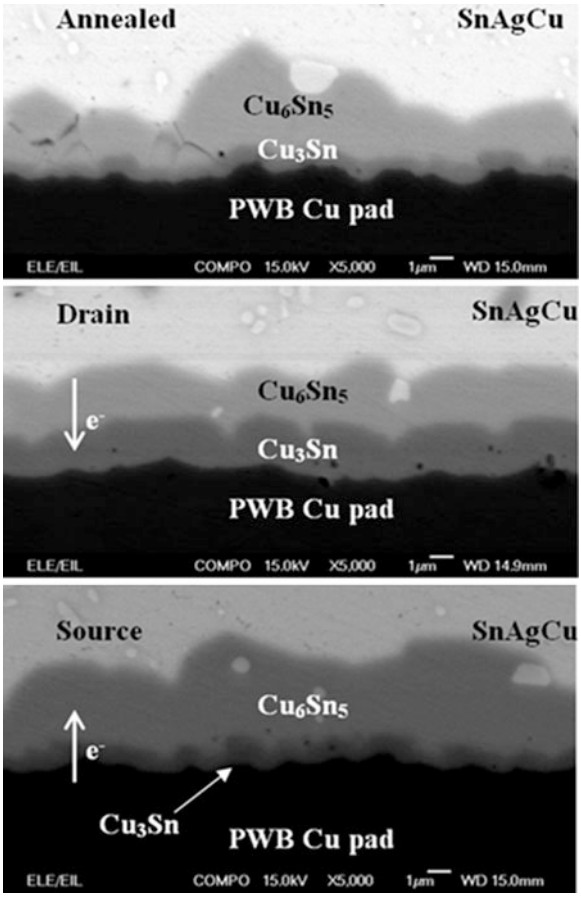

Fig. 8.26 SEM micrograph showing the interfacial reaction layer structure depending on the direction of the electron flux [29]

lower growth rate of Cu_3Sn than in the case of a pure Cu/Sn diffusion couple. The decrease in the growth rate of Cu_3Sn can be understood when it is noticed that the growth of the reaction layers in multiphase diffusion couples is dependent on each other. Thus, when the formation rate of Cu_6Sn_5 at the Cu_3Sn/Cu_6Sn_5 interface increases, more and more Cu_3Sn is consumed by the growing η layer. As the fluxes of either Sn or Cu inside Cu_3Sn are not significantly altered, this results in the observed growth behavior. A similar (but slightly different) effect using the electron flux can be observed here as discussed below. Regarding the annealed

Table 8.4 Thickness data of the intermetallic compounds grown at the interface

	Cu_3Sn	Cu_6Sn_5	Cu_6Sn_5 to Cu_3Sn ratio
No current	0.8 μm 0.093 mol/m^2	3 μm 0.283 mol/m^2	3.8
Constant current from PWB	2.1 μm 0.244 mol/m^2	2.3 μm 0.217 mol/m^2	1.1
Constant current from solder	0.9 μm (∼no change) 0.1 mol	3.8 μm 0.36 mol/m^2	4.2

samples, it is to be noted that in this case, the Cu–Sn IMCs are growing between the Cu and SnAgCu solder instead of between Cu and pure Sn. Based on the experimental results [34], it is known that the thickness of Cu_3Sn is smaller when growth takes place in the Cu/SnAgCu diffusion couple than in the Sn/Cu diffusion couple at the same temperature. This can be understood when considering how the presence of Ag and Cu in solder affects the activities of the diffusing components. The presence of Cu in the solder decreases the driving force for diffusion of Cu from the Cu-substrate to the solder as the activity difference decreases. Likewise, the lowering of the activity of Sn in the solder (because of the presence of Ag) reduces the driving force for diffusion of Sn toward the Cu-substrate, thus reducing the Sn flux. These two effects combine to produce the observed difference between the Cu/Sn and Cu/SnAgCu reaction couples. Finally, it is emphasized that also the slightly lower temperature used here (110 °C instead of 125 °C which is used in the reference cases [34, 35]) will itself contribute to the observed smaller thickness ratio of Cu_3Sn to Cu_6Sn_5.

From the results of the steady current experiments, it can be seen that in the drain contact, the electron flux comes from the solder side to the interface. Thus, the PWB pad is acting as the anode, meaning that the Sn flux toward the PWB is increased in both IMC layers whereas the flux of Cu from the PWB is decreased, which, based on the experimental results, seems to favor the growth of Cu_3Sn. This can be analyzed in more detail with the help of Fig. 8.27 and the following reaction equations.'

The reaction scheme

The reactions occurring at different interfaces of the reaction couple, as shown in Fig. 8.27, can be expressed as follows

Interface I:

$$3q\mathrm{Cu} + q[\mathrm{Sn}]_d \rightarrow 4q\mathrm{Cu}_{3/4}\mathrm{Sn}_{1/4}$$

Interface II Cu_3Sn side:

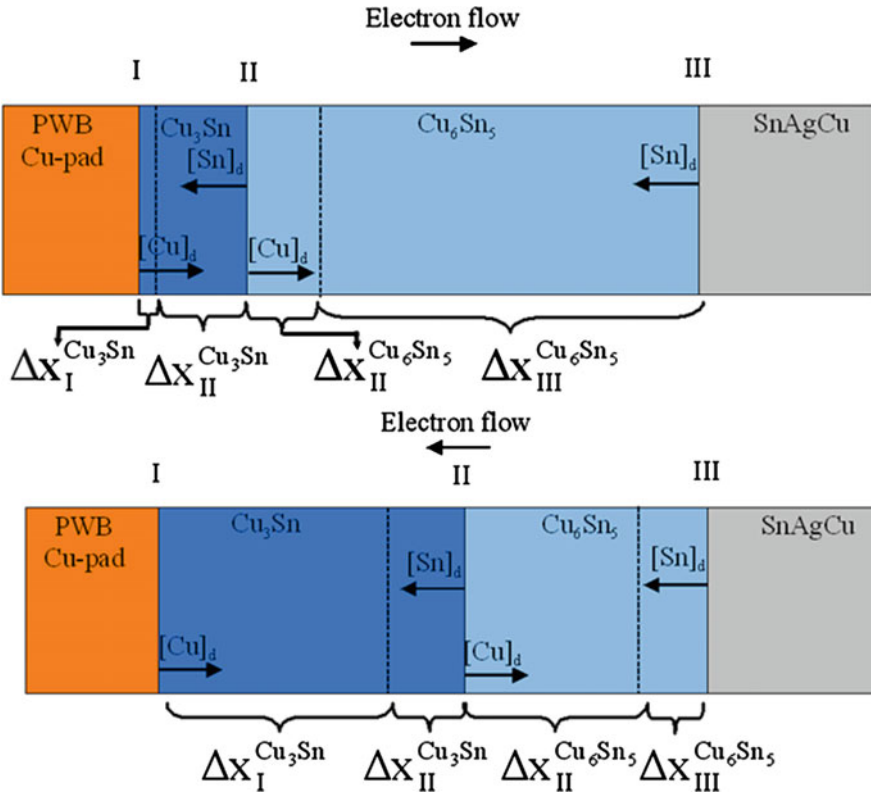

Fig. 8.27 Schematic presentation of the interfacial reactions occurring in the reaction couple

$$\frac{11}{9}p\mathrm{Cu}_{6/11}\mathrm{Sn}_{5/11} + p[\mathrm{Cu}]_d \rightarrow \frac{20}{9}p\mathrm{Cu}_{3/4}\mathrm{Sn}_{1/4}$$
$$\frac{11}{3}q\mathrm{Cu}_{6/11}\mathrm{Sn}_{5/11} \rightarrow q[\mathrm{Sn}]_d + \frac{8}{3}q\mathrm{Cu}_{3/4}\mathrm{Sn}_{1/4}$$

Interface II Cu_6Sn_5 side:

$$\frac{20}{9}r\mathrm{Cu}_{3/4}\mathrm{Sn}_{1/4} \rightarrow r[\mathrm{Cu}]_d + \frac{11}{9}r\mathrm{Cu}_{6/11}\mathrm{Sn}_{5/11}$$
$$\frac{8}{3}s\mathrm{Cu}_{3/4}\mathrm{Sn}_{1/4} + s[\mathrm{Sn}]_d \rightarrow \frac{11}{3}s\mathrm{Cu}_{6/11}\mathrm{Sn}_{5/11}$$

Interface III:

$$\frac{5}{6}r\mathrm{Sn} + r[\mathrm{Cu}]_d \rightarrow \frac{11}{6}r\mathrm{Cu}_{6/11}\mathrm{Sn}_{5/11}$$

Table 8.5 Summary of the experimental results

	Cu_6Sn_5 (μm)	Cu_3Sn (μm)	IMC tot (μm)
After soldering			
No current	1	0.1	1.1
Drain	1	0.1	1.1
Source	1	0.1	1.1
1,500 Cycles			
No current	1.8	1.4	3.2
Drain	2.4	1.2	3.6
Source	3.6	0.3	3.9
3,000 Cycles			
No current	1.9	1.9	3.8
Drain	2.7	1.5	4.2
Source	4.4	0.5	4.9

Here, p and q are the moles of Cu and Sn, respectively, transferred per unit area through the Cu_3Sn phase during the total diffusion time t. Similarly, r and s are the number of moles of Cu and Sn transported during interaction per unit area through the Cu_6Sn_5-phase layer. From the equations written above, it is clear that at the interface II, not only $\left(\frac{20}{9}p + \frac{8}{3}q\right)$ moles of Cu_3Sn grow, but also $\left(\frac{20}{9}r + \frac{8}{3}s\right)$ moles get consumed because of the growth of the Cu_6Sn_5 phase. Similarly, $\left(\frac{11}{9}r + \frac{11}{3}s\right)$ moles of Cu_6Sn_5 grow at the same interface, but $\left(\frac{11}{9}p + \frac{11}{3}q\right)$ moles get consumed by the Cu_3Sn phase.

The thickness of the parts of the product phase layers resulting from the interfacial reactions given above can be expressed as

$$
\begin{aligned}
&4q \times v_m^{Cu_3Sn} = \Delta x_{\mathrm{I}}^{Cu_3Sn} \\
&\left(\frac{20}{9}p + \frac{8}{3}q - \frac{20}{9}r - \frac{8}{3}s\right) \times v_m^{Cu_3Sn} = \Delta x_{\mathrm{II}}^{Cu_3Sn} \\
&\left(\frac{11}{9}r + \frac{11}{3}s - \frac{11}{9}p - \frac{11}{3}q\right) \times v_m^{Cu_6Sn_5} = \Delta x_{\mathrm{II}}^{Cu_6Sn_5} \\
&\frac{11}{6}r \times v_m^{Cu_6Sn_5} = \Delta x_{\mathrm{III}}^{Cu_6Sn_5}
\end{aligned}
$$

where $\Delta x_{\mathrm{I}}^{Cu_3Sn}$ and $\Delta x_{\mathrm{II}}^{Cu_3Sn}$ are the thicknesses of the sublayers in the Cu_3Sn phase. $\Delta x_{\mathrm{II}}^{Cu_6Sn_5}$ and $\Delta x_{\mathrm{III}}^{Cu_6Sn_5}$ are the thicknesses of sublayers in the Cu_6Sn_5 phase. These sublayers are separated by the Kirkendall marker planes in these phases. In Table 8.5, the experimental results about the effect of the electron flow on the growth of the IMCs are presented in a different way. In addition to thickness, the amount of each phase has been tabulated in terms of mole/m^2 for the sake of discussion.

PWB as the anode

Let us first consider that there is an equal increase in the flux of Sn and an equal decrease in the flux of Cu in both the phases. First, the two cases will be addressed separately and then the combined effect of the changes in the Cu and Sn fluxes is addressed.

(i) Increase in the Sn flux through the phases:

Owing to the diffusion of Sn, 4 parts (in terms of moles) of the Cu_3Sn product phase will grow at the interface I plus a further 8/3 parts at the interface II by consuming the Cu_6Sn_5 phase. On the other hand, 8/3 parts will get consumed because of the growth of the Cu_6Sn_5 phase at the interface II. So, in total, there will be a net gain of 4 parts of the Cu_3Sn phase in this case.

Similarly, 11/3 parts of the Cu_6Sn_5 phase will grow at the interface II and the same amount will get consumed because of the growth of the Cu_3Sn phase at that interface. So, there should be no net change in the layer thickness of the Cu_6Sn_5 phase.

(ii) Decrease in the Cu flux through the phases:

If the flow of Cu decreases at the same rate through both the phases, there will be 20/9 parts (in terms of moles) less production of Cu_3Sn at the interface II. Further, because of the decreased diffusion rate of Cu through the Cu_6Sn_5 phase, there will be 20/9 less consumption of the Cu_3Sn phase at the interface II. So, there should be no net change in the layer thickness of the Cu_3Sn phase because of the flow of electrons from solder to the PWB.

On the other hand, as a result of the lower production of the Cu_3Sn phase at the interface II, there will be 11/9 parts less consumption of the Cu_6Sn_5 phase at that interface. At the same time (because of the decreased flow rate of Cu through the Cu_6Sn_5 phase), there will 11/9 parts less production of the Cu_6Sn_5 phase due to the dissociation of the Cu_3Sn phase at the interface II. Finally, there will be lower production of 11/6 parts of the Cu_6Sn_5 phase at the interface III. So, there should be a net loss in the thickness of the Cu_6Sn_5 phase compared to the situation when there is no flow of electrons.

(iii) Combined effect of Sn and Cu fluxes

Thus, if the Cu and Sn fluxes are affected similarly in both the phases, then for every 4 parts of Cu_3Sn phase increase there will be a corresponding 11/6 parts decrease in the layer thickness of the Cu_6Sn_5 phase. This means that for a one-part increase in the thickness of the Cu_3Sn phase, there will be a corresponding 0.46 parts decrease in the thickness of the Cu_6Sn_5 phase. In our experimental results, we actually get for a 0.151 parts (mol/m^2) increase in the thickness of the Cu_3Sn phase a corresponding decrease of 0.066 parts in the Cu_6Sn_5 phase. This can be put in another way: for a 1-part Cu_3Sn phase increase, we get 0.44 parts of decrease in the Cu_6Sn_5 phase. This is very close to the analysis presented above and can thus

be taken to indicate that the components (Sn and Cu) are indeed affected in a similar fashion by the electron flow. To conclude, it is now self-evident that it is time to reexamine the assumption that Sn should be strongly affected by the electron flux owing to its higher effective valence (Z*).

PWB as the cathode

Again, we consider there to be an equal decrease of Sn flux and an increase of Cu in both the phases. The good match between the analysis results based on this assumption with the experimental results, shown above, gives us further confidence that this approach is justified.

(i) Increase in Cu flux through the phases:

When the amount of Cu_3Sn increases by 20/9 parts (in moles) by consuming the Cu_6Sn_5 phase at the interface II because of the increase of Cu flux, 20/9 parts of the same phase will get consumed because of the growth of the Cu_6Sn_5 phase at the same interface. So, there will be no net gain or loss in the thickness of the Cu_3Sn phase because of the increase in the diffusion rate of Cu. Owing to the increase in the flow of Cu through the Cu_3Sn phase, the increased consumption of 11/9 of the Cu_6Sn_5 phase will occur at the interface II. However, at the same time, 11/9 parts of the same phase will grow by dissociation of the Cu_3Sn phase, because of the increase in flow of Cu through this phase. A further increase of 11/6 parts of the Cu_6Sn_5 phase will occur due to the increase in the flow of Cu through the η phase. So, there should be no net gain in the thickness of the Cu_3Sn phase, but a net gain of 11/6 parts in the thickness of the Cu_6Sn_5 phase.

(ii) Decrease in Sn flux through the phases:

Owing to the decreased diffusion rate of Sn through the Cu_3Sn phase, there will be a corresponding 4 parts decrease in the layer thickness. Similarly, there will be 8/3 parts less produced at the interface II caused by the dissociation of the Cu_6Sn_5 phase. Furthermore, because of the decreased diffusion rate of Sn through the Cu_6Sn_5 phase, the consumption of the same phase will be 8/3 parts less at the same interface. So, the net loss for the Cu_3Sn should be 4 parts.

Because of the decrease of Sn flux through the Cu_6Sn_5 phase, there will be 11/3 parts less production of the phase at the interface II by consuming the Cu_3Sn phase. At the same time, there will be 11/3 parts less consumption of the same phase because of the low diffusion rate of Sn through the Cu_3Sn phase. So, there should be no net gain in the Cu_6Sn_5 phase layer thickness because of low flux of Sn through both the phases.

(iii) Combined effect of Sn and Cu fluxes

When we consider the increase in the flow of Cu and the corresponding decrease in the flow of Sn to occur equally through both the phases, there will be a net gain of 11/6 parts in the thickness of Cu_6Sn_5 and a net decrease of 4 parts in the thickness of the Cu_3Sn phase. However, the diffusion rate of Sn is known to be

Table 8.6 Summary of the experimental and theoretical results

PWB side acting as	Effect of electron flux				Theoretical result		Experimental result	
	Flux of Sn in ε	Flux of Cu in ε	Flux of Sn in η	Flux of Cu in η	Thickness of ε	Thickness of η	Thickness of ε	Thickness of η
Anode	⇑	⇓	⇑	⇓	⇑	⇓	⇑	⇓
Cathode	⇓	⇑	⇓	⇑	± 0	⇑	±0	⇑

small compared to that of Cu in the Cu_3Sn phase, as shown in the ratios of the tracer diffusion coefficients [28]

$$\left.\frac{D^*_{Cu}}{D^*_{Sn}}\right|_{Cu_3Sn} = \frac{p}{q} \approx 30$$

$$\left.\frac{D^*_{Cu}}{D^*_{Sn}}\right|_{Cu_6Sn_5} = \frac{r}{s} \approx 0.35$$

Consequently, the role of Sn in this phase can be neglected—especially in this particular case as the diffusion of Sn is further hindered by the electron flux.

Overall, therefore, there should be an increase in the layer thickness of the Cu_6Sn_5 phase, which is what we see in the experiment. The results from the above analysis and from the experiments are summarized in Table 8.6.

References

1. E.O. Kirkendall, Diffusion of Zinc in Alpha Brass, Transaction of AIME 147 (1942) pp. 104
2. A.D. Smigelkas and E.O. Kirkendall, Zinc diffusion in alpha brass, Transaction of AIME 171 (1947) 130
3. G.F. Bastin and G.D. Rieck, Metallurgical Transactions 5 (1974) 1817
4. T. Shimozaki, Y. Goda, Y. Wakamatsu and M. Onishi, Defects and Diffusion Forum 95-98 (1993) 629
5. J.-F. Cornet and D. Calais, Journal of Physics and Chemistry of Solids 33 (1972) 1675-84
6. F.J.J. van Loo, B. Pieraggi and R.A. Rapp, Acta Metallurgica et Materialia 38 (1990) 1769
7. M.J.H van Dal, A.M. Gusak, C. Cserháti, A.A. Kodentsov and F.J.J van Loo, Physical Review Letters 86 (2001) 3352
8. M.J.H. van Dal, A.M. Gusak, C. Cserháti, A.A. Kodentsov and F.J.J. van Loo, Philosophical Magazine A, 82 (2002) 943
9. M.J.H. van Dal, M.C.L.P Pleumeekers, A.A. Kodentsov and F.J.J. van Loo, Acta Materialia 48 (2000) 385
10. M.J.H. van Dal, Microstructural stability of the Kirkendall plane, PhD thesis, Technische Universetiet Eindhoven, The Netherlands, 2001.
11. A. Paul, A.A. Kodentsov and F.J.J. van Loo, Acta Materialia 52 (2004) 4041
12. A. A. Kodentsov, A. Paul, Frans J.J. van Loo, Zeitschrift für Metallkunde 95 (2004) 258
13. A. Paul, The Kirkendall effect in solid state diffusion, PhD thesis, Technische Universetiet Eindhoven, The Netherlands, 2004.
14. M.J.H. van Dal, D.G.G.M. Huibers, A.A. Kodentsov, F.J.J. van Loo, Intermetallics 9 (2001) 409

15. M.J.H. van Dal, A.A. Kodentsov and F.J.J. van Loo, Intermetallics 9 (2001) 451
16. A. Paul, M.J.H. van Dal, A.A. Kodentsov and F.J.J. van Loo, Acta Materialia 52 (2004) 623-
17. L. Höglund, & J. Ågren, Acta Materialia 49 (2001) 1311
18. W.J. Boettinger, J.E. Guyer, C.E. Campbell and G.B. McFadden, Proceeding of the Royal Society London A 463 (2007) 3347
19. J.H. Gülpen, A.A. Kodentsov, F.J.J. van Loo, Zeitschrift für Metallkunde 86 (1995) 530.
20. C. Cserháti, A. Paul, A.A. Kodentsov, M.J.H. van Dal, F.J.J. van Loo, Intermetallics 11 (2003) 291-297.
21. C. Ghosh and A. Paul, Acta Materialia 55 (2007) 1927
22. F.J.J. van Loo, Acta Metallurgica 18 (1970) 1107
23. A. Paul, A.A. Kodentsov and F.J.J. van Loo, Intermetallics, 14 (2006) 1428
24. H. Okamoto, Journal of Phase Equilibria and diffusion 25 (2004) 394
25. S. Roy and A. Paul, Philosophical Magazine, 92 (2012) 4215
26. A.A. Kodentsov, A. Paul, and F.J.J. van Loo, Defects and Diffusion Forum 258-260 (2006) 182
27. A. Paul, Journal of Materials Science: Materials in Electronics 22 (2011) 833
28. A. Paul, C. Ghosh and W.J. Boettinger, Metallurgical and Materials Transactions A 42A (2011) 952
29. T. Laurila, J. Karppinen, V.Vuorinen, A. Paul and M. Paulasto-Kröckel, Journal of Electronic Materials 40 (2011) 1517
30. T. Laurila, J. Karppinen, V. Vuorinen, J. Li, A.Paul and M. Paulasto-Kröckel, Journal of Electronic Materials 41 (2012)
31. J. Dekker, A. Lodder and J. van Ek, Physical Review B 56 (1997) 12167-12177
32. T. Laurila, V. Vuorinen, and M. Paulasto-Kröckel, Materials Science and Engineering Reprts, R68, (2010) 1
33. V. Vuorinen, T. Laurila, T. Mattila, E. Heikinheimo, J. Kivilahti, Journal of Electronic Materials 36 (2007) 1355
34. J. Hurtig, Master's Thesis, Helsinki University of Technology, (2006).
35. T. Laurila, J. Hurtig, V. Vuorinen, and J.K. Kivilahti, Microelectronics Reliability 49 (2009) 242

Chapter 9
Interdiffusion in Multicomponent Systems

In this Chapter, estimation of the diffusion parameters in the multicomponent system is explained. A pseudobinary approach simplifying the mathematical conditions is also described. Finally the use of diffusion couple establishing the phase diagram is presented.

In the previous chapters, we have explained the diffusion analysis in binary systems. In fact, it is relatively easy to study interdiffusion when only two components take part in the diffusion process. This is the reason that the majority of systems studied are binary systems. With an increase in the number of components, the study of interdiffusion either becomes (at best) rather difficult or (at worst) close to impossible. Even, the physical meaning of some of the parameters involved are not very easy to understand [1]. Research is going on to develop an easier approach for the study of multicomponent systems. In this chapter, we shall introduce the concept very briefly without going into too much complexity—something that could be difficult for new students of the diffusion process to understand. A book written by Kirkaldy and Young [2] will shed further light on this topic. A comprehensive review written by Dayananda in Ref. [3] could be very useful to understand the details on the evolution of the composition in ternary and quaternary systems. The main difference between binary and multicomponent systems is that in binary systems, we neglect the cross-terms. On the other hand, these are important to consider in multicomponent systems, which might have strong influence. This fact as well as the influence of vacancies on diffusion in binary alloys in general will be clear after the discussion below and from the note in the end of the Sect. 9.4.

9.1 Interdiffusion and Intrinsic Diffusion Coefficients in Multicomponent Systems

The interdiffusion flux of an i-th component in a multicomponent system based on Onsager's formulism [4, 5] can be written as

A. Paul et al., *Thermodynamics, Diffusion and the Kirkendall Effect in Solids*,
DOI: 10.1007/978-3-319-07461-0_9,

$$\tilde{J}_u = -\sum_{v=1}^{n-1} \tilde{D}_{uv}^{n} \frac{\partial C_v}{\partial x} \tag{9.1a}$$

The interdiffusion fluxes estimated from the composition profiles of different components are related by (following the same line of discussion in Chap. 6 for binary systems)

$$\sum_{u=1}^{n} \bar{v}_u \tilde{J}_u = \bar{v}_1 \tilde{J}_1 + \bar{v}_2 \tilde{J}_2 + \cdots\cdots + \bar{v}_n \tilde{J}_n = 0 \tag{9.1b}$$

where $\tilde{J}_u$ is the interdiffusion flux of the component u, $\tilde{D}$ is the interdiffusion coefficient, C is the concentration, x is the position parameter, $\bar{v}_u$ is the partial molar volume, and n is the dependent variable. From Eq. 9.1b, it can be understood that we need to estimate the interdiffusion fluxes for $(n-1)$ components. The flux for the n-th component can be determined from these values. Compositions of different components are related by $N_1 + N_2 + \cdots\cdots + N_n = 1$. Therefore, if we consider the n-th component as the dependent variable, the interdiffusion fluxes can be expressed with $(n-1)$ components. This means that the total $(n-1)^2$ interdiffusion coefficients are required to express the interdiffusion fluxes of all the $(n-1)$ independent components.

Following Eq. 9.1a, in a ternary system ($n = 3$), $\tilde{J}_1$ and $\tilde{J}_2$ can be expressed as

$$\tilde{J}_1 = -\tilde{D}_{11}^{3} \frac{\partial C_1}{\partial x} - \tilde{D}_{12}^{3} \frac{\partial C_2}{\partial x} = -\tilde{D}_{11}^{3} \frac{1}{v_m} \frac{\partial N_1}{\partial x} - \tilde{D}_{12}^{3} \frac{1}{v_m} \frac{\partial N_2}{\partial x} \tag{9.2a}$$

$$\tilde{J}_2 = -\tilde{D}_{21}^{3} \frac{\partial C_1}{\partial x} - \tilde{D}_{22}^{3} \frac{\partial C_2}{\partial x} = -\tilde{D}_{21}^{3} \frac{1}{v_m} \frac{\partial N_1}{\partial x} - \tilde{D}_{22}^{3} \frac{1}{v_m} \frac{\partial N_2}{\partial x} \tag{9.2b}$$

The second part of the relations above is true for a constant molar volume, v_m. In most ternary systems, the change in lattice parameters with composition is not known and an average molar volume is considered for the estimations. Following Eq. 9.1b, $\tilde{J}_3$ can be related by (for the constant molar volume and constant partial molar volumes of the components)

$$\tilde{J}_1 + \tilde{J}_2 + \tilde{J}_3 = 0 \tag{9.3}$$

The average molar volume can be estimated by taking the weighted fraction of the molar volumes of the pure components that is $v_m(av) = \frac{1}{n}\sum_{i=1}^{n} v_m^i$, where v_m^i is the molar volume of the pure component i. In Eqs. 9.2a and 9.2b, $\tilde{D}_{11}^{3}$ and $\tilde{D}_{22}^{3}$ are the main (or direct) interdiffusion coefficients, which represent the influence of the concentration gradient of one component on the diffusion rate of the same component. $\tilde{D}_{12}^{3}$ and $\tilde{D}_{21}^{3}$ are the cross- or indirect interdiffusion coefficients, which represent the influence of the concentration gradient of one component on the

diffusion rate of the other component. The third component is considered as the dependent variable. Therefore, the values of $\tilde{D}^3_{11}$, $\tilde{D}^3_{12}$, $\tilde{D}^3_{21}$, and $\tilde{D}^3_{22}$ are required to relate or to calculate the interdiffusion fluxes in a ternary system.

The estimation of these parameters, however, is not as straightforward as in a binary system. These parameters can only be determined at the point of intersection of the composition profiles from two different diffusion couples. For example, in a Ni–Co–Pt system, the diffusion couples were made with different compositions and annealed at 1,200 °C for 25 h. [6]. It can be seen in Fig. 9.1a that the two composition profiles are found to intersect at a composition shown by a red circle. In each diffusion couple, the interdiffusion flux of the two components can be determined from the measured composition profile. The composition profile of Co(25Pt)/Ni is shown in Fig. 9.1b. Kirkaldy [7] explained that it is possible to use the Matano–Boltzmann analysis to determine the interdiffusion flux. A few years later, the same was discussed by Philibert and Guy [8]. Therefore, the interdiffusion flux of each component i can be determined using the relation [from Eq. 7.19a]

$$\tilde{J}_i\left(Y_{C_i}\right) = -\frac{\left(C_i^+ - C_i^-\right)}{2t}\left[\left(1 - Y_{C_i}\right)\int_{x^{-\infty}}^{x^*} Y_{C_i}dx + Y_{C_i}\int_{x^*}^{x^{+\infty}} \left(1 - Y_{C_i}\right)dx\right] \quad (9.4a)$$

where $Y_{C_i} = \frac{C_i - C_i^-}{C_i^+ - C_i^-}$. Since, we generally consider a constant molar volume caused by an unknown variation of the molar volume in a ternary system, we can write

$$\tilde{J}_i(Y_i) = -\frac{\left(N_i^+ - N_i^-\right)}{2tv_m}\left[\left(1 - Y_i\right)\int_{x^{-\infty}}^{x^*} Y_i dx + Y_i\int_{x^*}^{x^{+\infty}} \left(1 - Y_i\right)dx\right] \quad (9.4b)$$

where $Y_i = \frac{N_i - N_i^-}{N_i^+ - N_i^-}$. Note that the same relation can be written, when the flux is estimated using Wagner's relation considering the constant molar volume, as can be seen in Eq. 7.19c. The variation of the interdiffusion flux estimated from the composition profile in Fig. 9.1b is shown in Fig. 9.1c. The correctness of the estimation can be checked by examining whether the summation of the interdiffusion fluxes that is $\tilde{J}_{Ni} + \tilde{J}_{Co} + \tilde{J}_{Pt} = 0$ because of the consideration of the constant molar volume. Note that depending on the direction of the diffusing component, if the interdiffusion fluxes for Co and Pt are positive, the interdiffusion flux of Ni should be negative. By considering Ni as a dependent variable, we calculate the interdiffusion fluxes of the independent variables Co and Pt at the composition of the intersection point. Accordingly, we can write

$$\tilde{J}_{Co}(\text{couple 1}) = -\tilde{D}^{Ni}_{CoCo}\frac{1}{v_m}\left(\frac{\partial N_{Co}}{\partial x}\right)_{\text{Couple 1}} - \tilde{D}^{Ni}_{CoPt}\frac{1}{v_m}\left(\frac{\partial N_{Pt}}{\partial x}\right)_{\text{Couple 1}} \quad (9.5a)$$

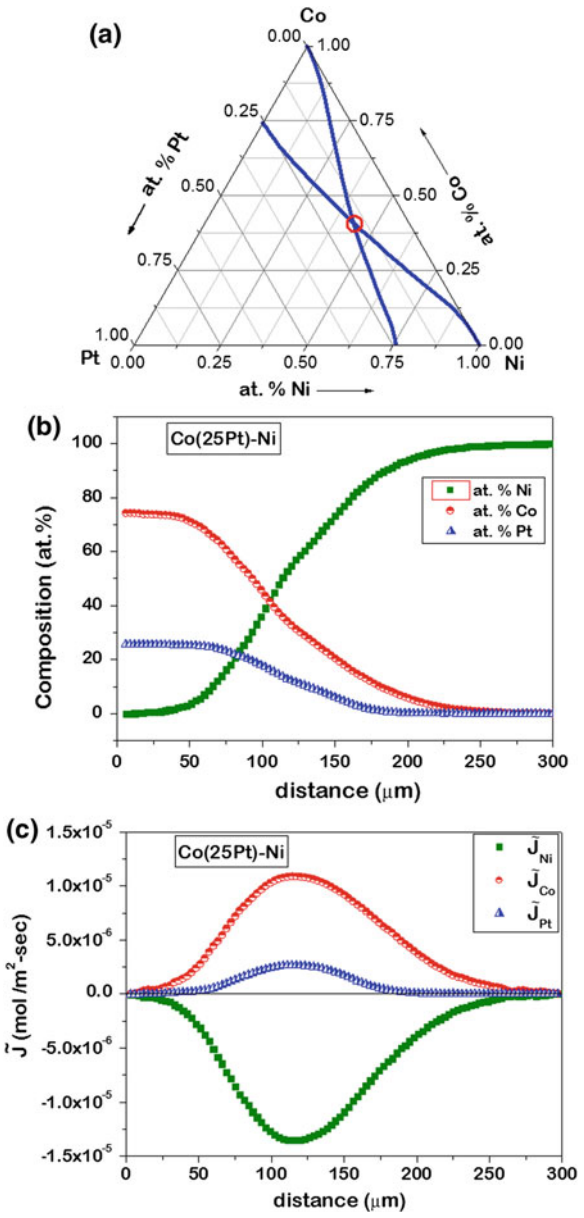

Fig. 9.1 Composition profiles of diffusion couples in Ni–Co–Pt system annealed at 1,200 °C for 25 h are shown on **a** Ni–Co–Pt Gibb's triangle. **b** Composition-distance profile of the Co(25Pt)/Ni diffusion couple and **c** estimated variation of interdiffusion fluxes of components [6]

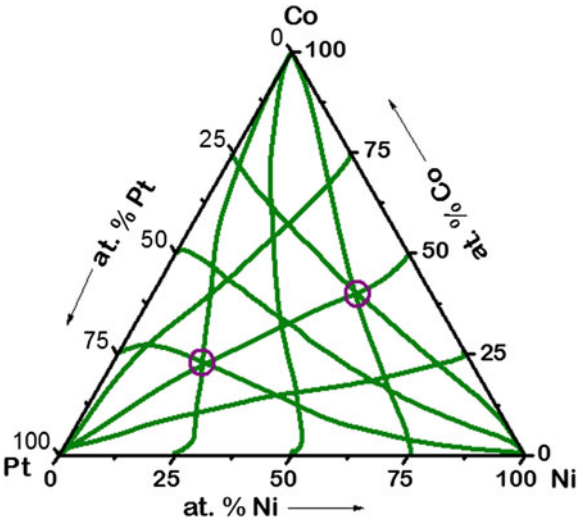

Fig. 9.2 Composition profiles developed in different diffusion couples of Co–Ni–Pt system annealed at 1,200 °C for 25 h are shown in the Gibbs triangle. Profiles with *dotted lines* indicate the presence of uphill diffusion. Compositions at which three profiles intersect are shown by *circles* [6]

$$\tilde{J}_{\mathrm{Pt}}(\text{couple 1}) = -\tilde{D}^{\mathrm{Ni}}_{\mathrm{PtCo}} \frac{1}{v_m} \left(\frac{\partial N_{\mathrm{Co}}}{\partial x}\right)_{\text{Couple 1}} - \tilde{D}^{\mathrm{Ni}}_{\mathrm{PtPt}} \frac{1}{v_m} \left(\frac{\partial N_{\mathrm{Pt}}}{\partial x}\right)_{\text{Couple 1}} \tag{9.5b}$$

Similarly, at the same intersection point, we can calculate the interdiffusion fluxes of these two components from the composition profile that is developed in the second diffusion couple (Ni25Pt)/Co. These fluxes are related to the interdiffusion coefficients as

$$\tilde{J}_{\mathrm{Co}}(\text{couple 2}) = -\tilde{D}^{\mathrm{Ni}}_{\mathrm{CoCo}} \frac{1}{v_m} \left(\frac{\partial N_{\mathrm{Co}}}{\partial x}\right)_{\text{Couple 2}} - \tilde{D}^{\mathrm{Ni}}_{\mathrm{CoPt}} \frac{1}{v_m} \left(\frac{\partial N_{\mathrm{Pt}}}{\partial x}\right)_{\text{Couple 2}} \tag{9.5c}$$

$$\tilde{J}_{Pt}(\text{couple 2}) = -\tilde{D}^{\mathrm{Ni}}_{\mathrm{PtCo}} \frac{1}{v_m} \left(\frac{\partial N_{\mathrm{Co}}}{\partial x}\right)_{\text{Couple 2}} - \tilde{D}^{\mathrm{Ni}}_{\mathrm{PtPt}} \frac{1}{v_m} \left(\frac{\partial N_{\mathrm{Pt}}}{\partial x}\right)_{\text{Couple 2}} \tag{9.5d}$$

The interdiffusion coefficients are the material constants, and these should be the same at that particular composition. Therefore, solving the above equations, four interdiffusion coefficients can be estimated at the point of intersection from two separate diffusion profiles.

The interdiffusion coefficients in a ternary system were first time estimated by Zeibold and Ogilvie [9] in the Cu–Au–Ag system. It must be apparent that many diffusion couples should be prepared to calculate the variation of the interdiffusion coefficients with composition over the whole composition range in a ternary system. The diffusion couples prepared in the Ni–Co–Pt system, which were annealed at 1,200 °C for 25 h, are shown in Fig. 9.2 [6]. The interdiffusion coefficients can be estimated at all the compositions where the diffusion profiles have intersected. Variation of the data are shown in Fig. 9.3.

Table 9.1 The main and cross-interdiffusion coefficients estimated at the composition where three intersecting diffusion profiles in the Co–Ni–Pt are listed [6]

Composition at. %	$\tilde{D}^{Ni}_{CoCo}$ (10^{-14} m^2/s)	$\tilde{D}^{Ni}_{CoPt}$ (10^{-15} m^2/s)	$\tilde{D}^{Ni}_{PtCo}$ (10^{-15} m^2/s)	$\tilde{D}^{Ni}_{PtPt}$ (10^{-14} m^2/s)
Ni = 19.8, Co = 22.7 and Pt = 57.5	0.8	−5	−6.2	1.1
	0.3	−1.7	−6.9	1.2
	1.2	−1.9	−7.1	1.2
Ni = 43, Co = 40 and Pt = 17	1.7	−7.1	−0.9	0.4
	1.5	−2.5	−1.2	1.3
	0.9	−3	−0.2	0.8

A relatively high rate of error is expected in the estimation of these ternary-system parameters (compared to any binary system) because of the requirements of two diffusion profiles. This can be explained with the estimated data in the Ni–Co–Pt system. As circled in Fig. 9.2, there are two compositions, at which three different composition profiles have intersected. We should, therefore, be able to estimate the interdiffusion coefficients by considering any of the two diffusion couples at the same intersection points. The estimated values are listed in Table 9.1. The data of three rows at both compositions are estimated, considering three different combinations. It can be seen that there is no change in the sign of the diffusion coefficients; however, there was a relatively high difference between the diffusion parameters estimated.

Another important question is which component should be considered as a dependent component. As explained by Kirkaldy and Young [2], the dependent variable should be chosen such that the conditions written below are fulfilled—conditions that are derived based on the thermodynamic requirements and stability of the solutions

$$\tilde{D}^3_{11} + \tilde{D}^3_{22} > 0 \tag{9.6a}$$

$$(\tilde{D}^3_{11} + \tilde{D}^3_{22})^2 \geq 4(\tilde{D}^3_{11}\tilde{D}^3_{22} - \tilde{D}^3_{12}\tilde{D}^3_{21}) \tag{9.6b}$$

$$(\tilde{D}^3_{11}\tilde{D}^3_{22} - \tilde{D}^3_{12}\tilde{D}^3_{21}) \geq 0 \tag{9.6c}$$

In general, when the diffusion experiments are conducted in a small section, it is a common practice to consider the solvent component (that is, the major component) as the dependent variable. Of course, it is still wise to check whether the above conditions written in Eqs. 9.6a, 9.6b and 9.6c are met. When the experiments are covered in the whole composition range, after estimation of the data, it is necessary to check for which component the conditions for the dependent variable is fulfilled at all compositions. Repeatedly—as it was in the case of the Ni–Co–Pt system—the conditions are met when we consider any of the components as the dependent variable. It should be noted at this point that presenting data with

respect to one dependent variable is sufficient, since the interdiffusion coefficients considering different components as dependent variables are related by [10]

$$\tilde{D}^2_{11} = \tilde{D}^3_{11} - \tilde{D}^3_{12} \tag{9.7a}$$

$$\tilde{D}^2_{13} = -\tilde{D}^3_{12} \tag{9.7b}$$

$$\tilde{D}^2_{31} = \tilde{D}^3_{22} + \tilde{D}^3_{12} - \tilde{D}^3_{11} - \tilde{D}^3_{21} \tag{9.7c}$$

$$\tilde{D}^2_{33} = \tilde{D}^3_{22} + \tilde{D}^3_{12} \tag{9.7d}$$

$$\tilde{D}^1_{22} = \tilde{D}^3_{22} - \tilde{D}^3_{21} \tag{9.7e}$$

$$\tilde{D}^1_{23} = -\tilde{D}^3_{21} \tag{9.7f}$$

$$\tilde{D}^1_{32} = \tilde{D}^3_{11} + \tilde{D}^3_{21} - \tilde{D}^3_{22} - \tilde{D}^3_{12} \tag{9.7g}$$

$$\tilde{D}^1_{33} = \tilde{D}^3_{11} + \tilde{D}^3_{21} \tag{9.7h}$$

The variation of the interdiffusion coefficients estimated in the Ni–Co–Pt system is shown in Fig. 9.3.

The interdiffusion fluxes that are estimated based on the composition profile of a particular component are related to the intrinsic fluxes of the components by [3]

$$\tilde{J}_u = J_u - N_u \sum_{k=1}^{n} J_k \tag{9.8a}$$

In a ternary system, these can be written as

$$\tilde{J}_1 = (1 - N_1)J_1 - N_1(J_2 + J_3) = (N_2 + N_3)J_1 - N_1(J_2 + J_3) \tag{9.8b}$$

$$\tilde{J}_2 = (1 - N_2)J_2 - N_2(J_1 + J_3) = (N_1 + N_3)J_2 - N_2(J_1 + J_3) \tag{9.8c}$$

$$\tilde{J}_3 = (1 - N_3)J_3 - N_3(J_1 + J_2) = (N_1 + N_2)J_3 - N_3(J_1 + J_2) \tag{9.8d}$$

where J_u is the intrinsic flux of the component u. Furthermore, the intrinsic flux is related to the intrinsic diffusion coefficients by [3]

$$J_u = -\sum_{v=1}^{n-1} D^n_{uv} \frac{\partial C_v}{\partial x} \tag{9.9a}$$

In a ternary system, we can write

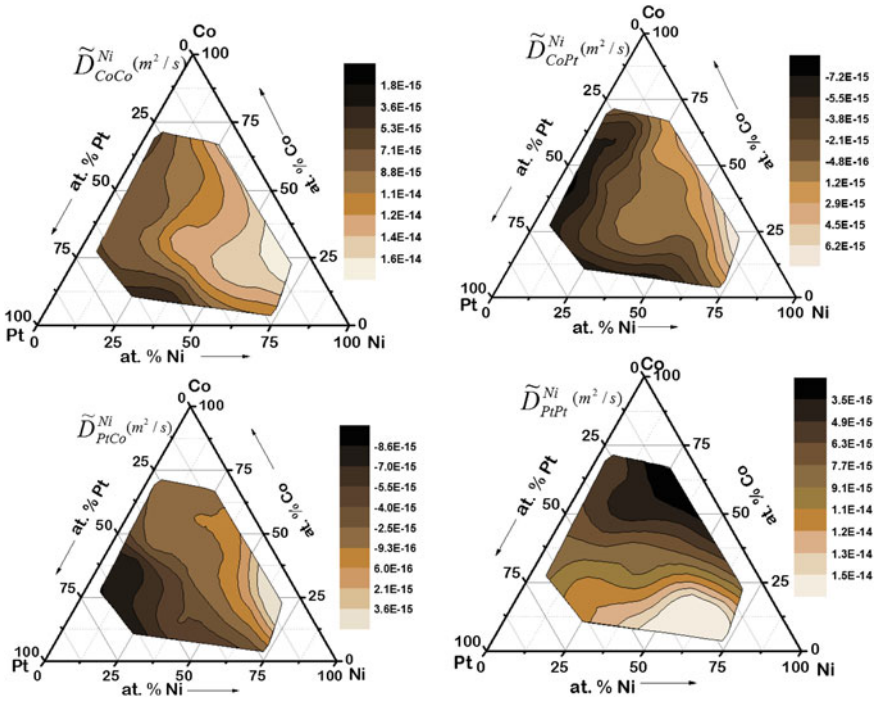

Fig. 9.3 Main interdiffusion coefficients $\tilde{D}^{\mathrm{Ni}}_{\mathrm{CoCo}}$ and $\tilde{D}^{\mathrm{Ni}}_{\mathrm{PtPt}}$ and the cross-interdiffusion coefficients $\tilde{D}^{\mathrm{Ni}}_{\mathrm{CoPt}}$ and $\tilde{D}^{\mathrm{Ni}}_{\mathrm{PtCo}}$ calculated at common intersecting compositions in the Co–Ni–Pt system [6]

$$J_1 = -D^3_{11}\frac{\partial C_1}{\partial x} - D^3_{12}\frac{\partial C_2}{\partial x} \tag{9.9b}$$

$$J_2 = -D^3_{21}\frac{\partial C_1}{\partial x} - D^3_{22}\frac{\partial C_2}{\partial x} \tag{9.9c}$$

$$J_3 = -D^3_{31}\frac{\partial C_1}{\partial x} - D^3_{32}\frac{\partial C_2}{\partial x} \tag{9.9d}$$

The interdiffusion coefficients are related to the intrinsic diffusion coefficients by [3]

$$\tilde{D}^n_{uv} = D^n_{uv} - N_u \sum_{k=1}^{n} D^n_{kv} \tag{9.10a}$$

In a ternary system, the four main and cross-interdiffusion coefficients are related by

$$\tilde{D}_{11}^{n} = D_{11}^{n} - N_1\left(D_{11}^{n} + D_{21}^{n} + D_{31}^{n}\right) \tag{9.10b}$$

$$\tilde{D}_{12}^{n} = D_{12}^{n} - N_1\left(D_{12}^{n} + D_{22}^{n} + D_{32}^{n}\right) \tag{9.10c}$$

$$\tilde{D}_{21}^{n} = D_{21}^{n} - N_2\left(D_{11}^{n} + D_{21}^{n} + D_{31}^{n}\right) \tag{9.10d}$$

$$\tilde{D}_{22}^{n} = D_{22}^{n} - N_2\left(D_{12}^{n} + D_{22}^{n} + D_{32}^{n}\right) \tag{9.10e}$$

Lane and Kirkaldy [11] described the requirements of these six intrinsic diffusion coefficients to describe the intrinsic or interdiffusion fluxes and the interdiffusion coefficients. From the relations above, it must be clear that these can be estimated at the composition of the intersection from the two diffusion couples with an additional condition that the inert particles used as markers (indicating the position of the Kirkendall plane) are also located at that composition. Six intrinsic fluxes can be estimated at this composition using the method developed by Heumann as explained previously in Sect. 6.11a, [12, 13] or the relation developed in Sect. 6.8b, which is expressed as

$$J_i^K = -\frac{1}{2t}\left[N_i^{+}\int_{x^{-\infty}}^{x_K}\frac{Y_i}{v_m}dx - N_i^{-}\int_{x_K}^{x^{+\infty}}\frac{(1-Y_i)}{v_m}dx\right] \tag{9.11a}$$

For constant molar volume, it can be written as

$$J_i^K = -\frac{1}{2tv_m}\left[N_i^{+}\int_{x^{-\infty}}^{x_K} Y_i dx - N_i^{-}\int_{x_K}^{x^{+\infty}}(1-Y_i)dx\right] \tag{9.11b}$$

Since there is very little chance of getting the markers at the point of intersection, which is very difficult to predict, it is very rare for anyone to estimate the intrinsic diffusion coefficients following this method. For example, Sohn and Dayananda [14] estimated these six intrinsic diffusion coefficients at one composition in the Fe–Ni–Al system. Dayananda [15] developed an approach in which the intrinsic diffusion coefficients can be estimated from a single vapor/solid diffusion couple. Therefore, this method is restricted to systems, where the components are able to react in the vapor phase (such as Zn and Mg) with solid alloys. This approach was applied in the Cu–Zn–Mn [16] and Ag–Zn–Cd [17] systems.

The existence of the zero flux plane (ZFP) in the interdiffusion zone of different multicomponent systems is shown by Dayananda et al. in many systems [14, 18, 19]. This is associated with the uphill diffusion of a component in a particular part of the interdiffusion zone and the downhill diffusion in the other part. This can be explained with the help of the CoPt/Ni diffusion couples in the Ni–Co–Pt system, with varying compositions of CoPt alloys, as shown in Fig. 9.2. The composition profiles and the estimated interdiffusion fluxes are presented in Fig. 9.4, where it

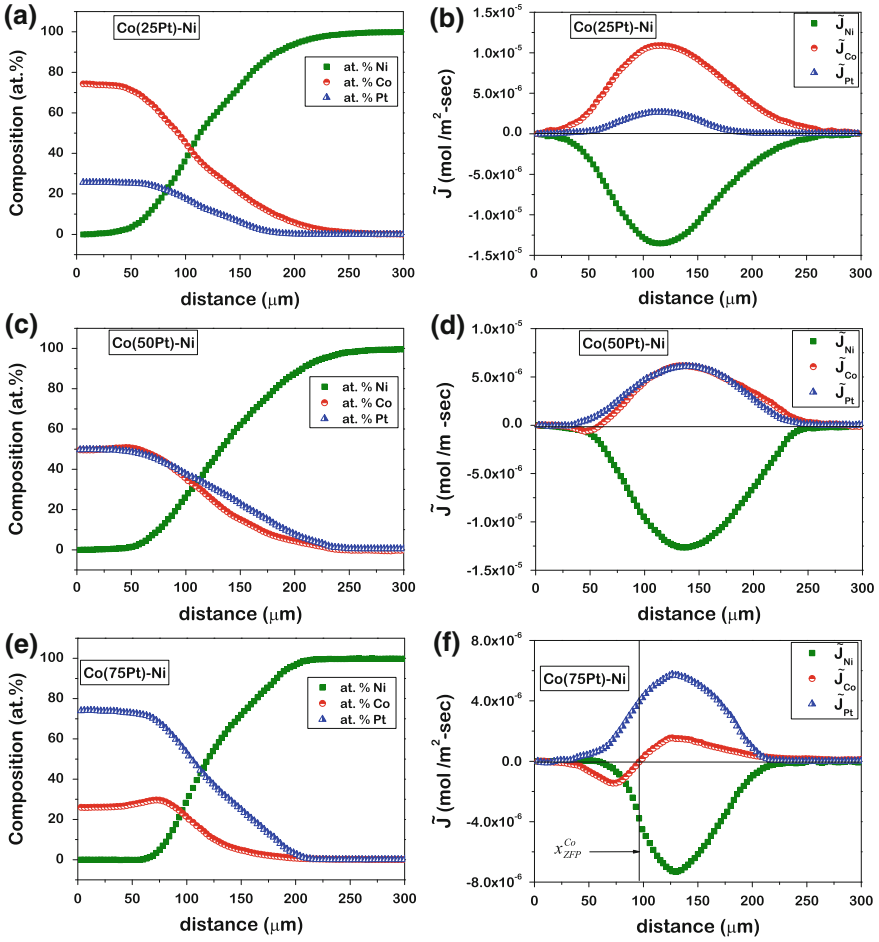

Fig. 9.4 Composition profiles developed in **a** Co(25Pt)/Ni, **c** Co(50Pt)/Ni, **e** Co(75Pt)/Ni diffusion couples and the corresponding calculated flux profiles are shown in **b**, **d**, and **f** [6]

can be seen that in the Co(25Pt)/Ni couple, all the components diffuse down the concentration gradient. Therefore, if the interdiffusion fluxes of Co and Pt are expressed with a positive sign, the interdiffusion flux of Ni will be expressed with a negative sign. In the Co(50Pt)/Ni couple, very minor uphill diffusion is to be observed, and in the Co(75Pt)/Ni couple, clear uphill diffusion of Co is to be seen. The Co profile in the Co(75Pt)/Ni interdiffusion zone increases first to a higher composition than the composition used (25 at.%) in the Co(75Pt) end member and then decreases in the other part of the interdiffusion zone. For this reason, the estimated interdiffusion flux of Co has a negative sign in the beginning and then changes to a positive sign. During the transition from negative to positive values, it goes through a zero value and the plane corresponding to this composition is called

the ZFP. Since the main interdiffusion coefficients are always positive, from Eq. 9.2a and 9.2b, it should be clear that the cross-interdiffusion coefficients should have a negative sign in the uphill diffusion range. Further, the flux because of cross-interdiffusion (that is, the second part of the equation) must be higher than the flux because of the main interdiffusion (that is, the first part of the equation). The profiles shown by dashed lines in Fig. 9.2 are found to have uphill diffusion. The possible occurrence of ZFP is explained by Dayananda et al. [18, 20, 21] based on their experimental evidence. According to these authors, ZFP is found when the diffusion path that is the composition profile on a Gibb's triangle crosses a constant activity line passing through a terminal alloy composition. Thompson and Morral [22, 23] have discussed different types of diffusion path and the occurrence of ZFP based on the angle of the composition vector connecting the end members. They subsequently developed an analytical model to predict the occurrence of ZFP considering constant diffusivities [24].

Diffusion paths that are plotted on a Gibb's triangle from a diffusion couple in a single phase are commonly found with an "S" shape (serpentine). In a thermodynamically ideal system, the diffusion paths are always serpentine. The authors who have considered constant diffusion constants to discuss the shape of the curve at elaborate lengths include van Loo et al. [25] and Thompson and Morral [22, 23]. As explained by Rönka et al. [26], the initial shape of the diffusion path is dependent on the relative mobilities of the components. In a diffusion couple of AB/C, if the mobilities of the components are such that $D_A > D_B > D_C$, the diffusion path will start in the B-rich side from AB and A-rich side from C. This leads to a serpentine diffusion profile. Sohn and Dayananda [14] have shown the presence of a serpentine and double serpentine profile in the β-(NiFe)Al phase. As shown in Fig. 9.5, a diffusion couple between the alloys β_3 and β_{15} shows a serpentine diffusion path, whereas a couple between β_5 and β_{17} shows the presence of a double serpentine diffusion path.

At the ZFP, if the interdiffusion flux of the component *i* is zero, it is possible to estimate the ratio of the main and cross-interdiffusion coefficients simply by measuring the composition gradient of the components at that composition since

$$\tilde{J}_i = 0 = -\tilde{D}^3_{i1}\frac{1}{v_m}\frac{\partial N_1}{\partial x} - \tilde{D}^3_{i2}\frac{1}{v_m}\frac{\partial N_2}{\partial x} \tag{9.11a}$$

$$\frac{\tilde{D}^3_{i1}}{\tilde{D}^3_{i2}} = -\frac{(\partial N_2/\partial x)}{(\partial N_1/\partial x)}\bigg|_{\text{ZFP}} \tag{9.11b}$$

Further, at the maxima or minima of a composition profile, the composition gradient of that component is zero. Therefore, the cross-interdiffusion coefficient can be estimated directly from the interdiffusion flux and the composition gradient of the other component. If the Kirkendall marker plane is found at this composition of maxima or minima, it can be understood from Eqs. 9.9a–d that three intrinsic diffusion coefficients can be estimated from a single diffusion couple. The intrinsic

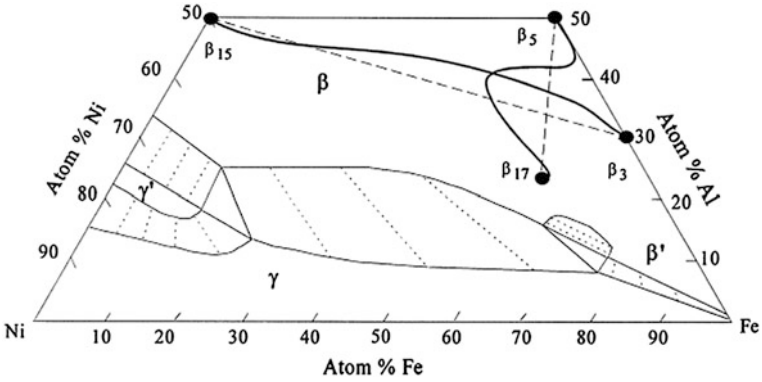

Fig. 9.5 Diffusion profiles in the Fe–Ni–Al system showing serpentine (β_{15}/β_3) and double serpentine diffusion (β_5/β_{17}) paths [14]

diffusion coefficients were estimated in this fashion by Sohn and Dayananda [14] in the Fe–Ni–Al system.

By extrapolating the interdiffusion coefficients to binary axes, we can extract the binary diffusion coefficients and the impurity diffusion coefficients [14]. For example, when the $\tilde{D}^2_{11}$ and $\tilde{D}^2_{22}$ values are extended to zero composition of 3, these values are equal to the interdiffusion coefficients in the binary 1–2 system. When the composition of component 1 approaches zero, $\tilde{D}^2_{11}$ and $\tilde{D}^3_{11}$ are equal to the impurity diffusion coefficient of 1, which is $D_1(2,3)$ in the binary 2–3 system [9].

In a quaternary system, the requirements for the estimation of the interdiffusion coefficients are even more stringent. For example, following Eq. 9.1a, the interdiffusion fluxes of the components, considering a constant molar volume, can be expressed as

$$\tilde{J}_1 = -\tilde{D}^4_{11}\frac{1}{v_m}\frac{\partial N_1}{\partial x} - \tilde{D}^4_{12}\frac{1}{v_m}\frac{\partial N_2}{\partial x} - \tilde{D}^4_{13}\frac{1}{v_m}\frac{\partial N_3}{\partial x} \tag{9.12a}$$

$$\tilde{J}_2 = -\tilde{D}^4_{21}\frac{1}{v_m}\frac{\partial N_1}{\partial x} - \tilde{D}^4_{22}\frac{1}{v_m}\frac{\partial N_2}{\partial x} - \tilde{D}^4_{23}\frac{1}{v_m}\frac{\partial N_3}{\partial x} \tag{9.12b}$$

$$\tilde{J}_3 = -\tilde{D}^4_{31}\frac{1}{v_m}\frac{\partial N_1}{\partial x} - \tilde{D}^4_{32}\frac{1}{v_m}\frac{\partial N_2}{\partial x} - \tilde{D}^4_{33}\frac{1}{v_m}\frac{\partial N_3}{\partial x} \tag{9.12c}$$

$$\tilde{J}_1 + \tilde{J}_2 + \tilde{J}_3 + \tilde{J}_4 = 0 \tag{9.12d}$$

Therefore, there are nine interdiffusion coefficients to determine and for that we need three composition profiles to intersect at one particular composition. It is almost impossible to design experiments in such a way that three diffusion couples

are able to intersect at a common point in a three-dimensional composition space [1]. This is the simple reason why there have been no previous experiments conducted to determine these nine interdiffusion coefficients in a quaternary system. Experimental studies are available in Cu–Ni–Zn–Mn [20] and Ni–Cr–Co–Mo [21] quaternary systems—the interdiffusion coefficients, however, were not estimated from three intersecting diffusion couples. In the Cu–Ni–Zn–Mn system, the interdiffusion fluxes were estimated, which can be done directly from the composition profiles measured using the relation in Eqs. 9.4a and 9.4b. In the Ni–Cr–Co–Mo system, only the major interdiffusion coefficients were estimated in a single diffusion couple in which two components did not develop the diffusion profile such that the cross-interdiffusion coefficients could be considered as zero.

There is always a special interest to develop an experimental approach for the (easy) determination of diffusion parameters in systems with three or more components. Krishtal et al. [27] first developed a treatment to estimate the diffusion parameters in a multicomponent system, considering the constant diffusion coefficients. In the following decade, Thompson and Morral [23] developed a square root diffusivity approach, again by considering the constant diffusion coefficients. This means that these treatments can be used when the composition differences of the diffusion couples are reasonably small such that the diffusion coefficients do not vary significantly over that composition range. The approach developed by Thompson and Morral was used to estimate the diffusion parameters in a few quaternary systems, keeping the composition difference of the diffusion couple end members very small such as 5 at.% [28–30]. Stalker et al. [28] have shown that in such a small composition range, they could estimate back the interdiffusion flux with a very minor error.

9.2 Average Effective and Integrated Diffusion Coefficients in Multicomponent System

As it is discussed above, in a ternary system, it is necessary to determine four interdiffusion coefficients at the point of intersection from two different diffusion couples. To circumvent this problem, Dayananda and Sohn [31] introduced the concept of the average effective interdiffusion coefficient so that this parameter could be estimated from a composition profile in a single diffusion couple. From Eq. 9.2a, we can write

$$\tilde{J}_i = -\tilde{D}_{i1}^{3} \frac{\partial C_1}{\partial x} - \tilde{D}_{i2}^{3} \frac{\partial C_2}{\partial x} \tag{9.13}$$

In terms of the effective interdiffusion coefficient

$$\tilde{J}_i = -\tilde{D}_i^{\text{eff}} \frac{\partial C_i}{\partial x} \tag{9.14}$$

Comparing Eqs. 9.13 and 9.14, we can write

$$\tilde{D}_i^{\text{eff}} = \tilde{D}_{i1}^{3}\frac{\partial C_1}{\partial C_i} - \tilde{D}_{i2}^{3}\frac{\partial C_2}{\partial C_i} \tag{9.15}$$

Therefore, the effective interdiffusion coefficients are a kind of average of the main and cross-interdiffusion coefficients and do not shed any light on the individual values. To estimate this parameter, one needs to follow the step discussed below. Suppose we are interested to estimate these parameters on either side of the initial contact plane. Integrating Eq. 9.14 from the unaffected left-hand side of the end member to the initial contact plane that is the Matano plane, we get

$$\begin{aligned} \int_{x^{-\infty}}^{x_o} \tilde{J}_i dx &= -\int_{C_i^-}^{C_i^o} \tilde{D}_i^{\text{eff}} dC_i = -\bar{\tilde{D}}_{i,L}^{\text{eff}} \int_{C_i^-}^{C_i^o} dC_i = \bar{\tilde{D}}_{i,L}^{\text{eff}}\left(C_i^- - C_i^o\right) \\ \bar{\tilde{D}}_{i,L}^{\text{eff}} &= \frac{\int_{x^{-\infty}}^{x_o} \tilde{J}_i dx}{C_i^- - C_i^o} = \frac{P}{C_i^- - C_i^o} \end{aligned} \tag{9.16a}$$

where C_i^o is the composition at the Matano plane that is the initial contact plane. $\bar{\tilde{D}}_{i,L}^{\text{eff}}$ is the average effective diffusion coefficient on the left-hand side of the Matano plane. P is the area, as shown in Fig. 9.6a.

Integrating Eq. 9.14 from the Matano plane to the unaffected right-hand side of the diffusion couple, we get

$$\begin{aligned} \int_{x_o}^{x^{+\infty}} \tilde{J}_i dx &= -\int_{C_i^o}^{C_i^+} \tilde{D}_i^{eff} dC_i = -\bar{\tilde{D}}_{i,R}^{\text{eff}} \int_{C_i^o}^{C_i^+} dC_i = \bar{\tilde{D}}_{i,R}^{\text{eff}}\left(C_i^o - C_i^+\right) \\ \bar{\tilde{D}}_{i,R}^{\text{eff}} &= \frac{\int_{x_o}^{x^{+\infty}} \tilde{J}_i dx}{C_i^o - C_i^+} = \frac{Q}{C_i^o - C_i^+} \end{aligned} \tag{9.16b}$$

$\bar{\tilde{D}}_{i,R}^{\text{eff}}$ is the average effective diffusion coefficient on the right-hand side of the Matano plane. Q is the area as shown in Fig. 9.6a. The value of $\tilde{J}_i$ can be estimated using the relation expressed in Eqs. 9.4a and 9.4b. Note here that for the composition profile considered in this figure, both the numerator and denominator of Eqs. 9.16a and 9.16b are negative in order to give positive values for the average effective interdiffusion coefficients.

Dayananda and Sohn [31] used this procedure to estimate the average effective interdiffusion coefficients on either side of the Matano plane and then estimated back the concentration profile from these estimated values to show that this is an efficient estimation procedure.

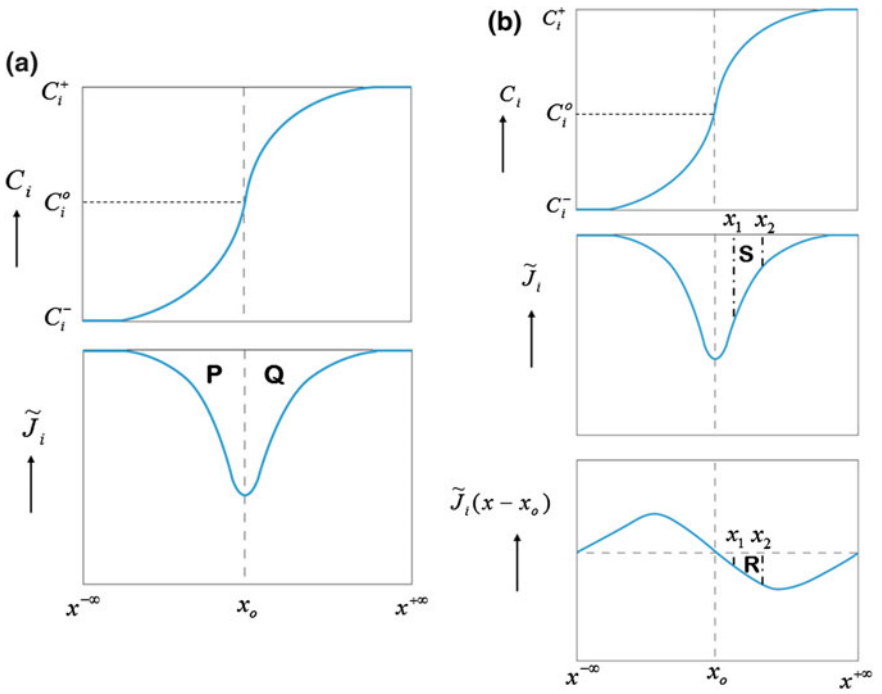

Fig. 9.6 Explanation of the **a** average effective diffusion coefficients and **b** average main and cross-interdiffusion coefficients from a single diffusion profile in a ternary system

Dayananda and Sohn [32] developed another model, following which—instead of estimating one average effective diffusion coefficient—the average values of the main and cross-interdiffusion coefficients can be estimated from only a single diffusion couple. Integrating Eq. 9.13 over the composition range of interest, we can write

$$\int_{x_1}^{x_2} \tilde{J}_i dx = -\int_{C_1(x_1)}^{C_1(x_2)} \tilde{D}_{i1}^3 dC_1 - \int_{C_2(x_1)}^{C_2(x_2)} \tilde{D}_{i2}^3 dC_2$$

$$\int_{x_1}^{x_2} \tilde{J}_i dx = -\bar{\tilde{D}}_{i1}^3 \int_{C_1(x_1)}^{C_1(x_2)} dC_1 - \bar{\tilde{D}}_{i2}^3 \int_{C_2(x_1)}^{C_2(x_2)} dC_2$$

$$\int_{x_1}^{x_2} \tilde{J}_i dx = -\bar{\tilde{D}}_{i1}^3 [C_1(x_2) - C_1(x_1)] - \bar{\tilde{D}}_{i2}^3 [C_2(x_2) - C_2(x_1)] \tag{9.17a}$$

where, $\bar{\tilde{D}}_{i1}^3$ and $\bar{\tilde{D}}_{i2}^3$ are the average interdiffusion coefficients estimated over the composition range of interest. Now, multiplying Eq. 9.13 by $(x - x_o)$ on both sides and then integrating over the same composition range of interest, we get

$$\int_{x_1}^{x_2} \tilde{J}_i(x-x_o)dx = -\int_{C_1(x_1)}^{C_1(x_2)} \tilde{D}_{i1}^3(x-x_o)dC_1 - \int_{C_2(x_1)}^{C_2(x_2)} \tilde{D}_{i2}^3(x-x_o)dC_2$$

$$\int_{x_1}^{x_2} \tilde{J}_i(x-x_o)dx = -\bar{\tilde{D}}_{i1}^3 \int_{C_1(x_1)}^{C_1(x_2)} (x-x_o)dC_1 - \bar{\tilde{D}}_{i2}^3 \int_{C_2(x_1)}^{C_2(x_2)} (x-x_o)dC_2$$

$$\int_{x_1}^{x_2} \tilde{J}_i(x-x_o)dx = -\bar{\tilde{D}}_{i1}^3 \left[\int_{C_1(x_1)}^{C_1(x^{-\infty})} (x-x_o)dC_1 + \int_{C_1(x^{-\infty})}^{C_1(x_2)} (x-x_o)dC_1 \right]$$
$$- \bar{\tilde{D}}_{i2}^3 \left[\int_{C_2(x_1)}^{C_2(x^{-\infty})} (x-x_o)dC_2 + \int_{C_2(x^{-\infty})}^{C_2(x_2)} (x-x_o)dC_2 \right]$$

$$\int_{x_1}^{x_2} \tilde{J}_i(x-x_o)dx = -\bar{\tilde{D}}_{i1}^3 \left[-\int_{C_1(x^{-\infty})}^{C_1(x_1)} (x-x_o)dC_1 + \int_{C_1(x^{-\infty})}^{C_1(x_2)} (x-x_o)dC_1 \right]$$
$$-\bar{\tilde{D}}_{i2}^3 \left[-\int_{C_2(x^{-\infty})}^{C_2(x_1)} (x-x_o)dC_2 + \int_{C_2(x^{-\infty})}^{C_2(x_2)} (x-x_o)dC_2 \right]$$

From the Matano–Boltzmann relation expressed in Eq. 6.11, we can write

$$\tilde{J}(C_i^*) = \frac{1}{2t} \int_{C_i^-}^{C_i^*} x dC_i = \frac{1}{2t} \int_{C_i^-}^{C_i^*} (x-x_o)dC_i.$$

Replacing this in the above relation, we get

$$\int_{x_1}^{x_2} \tilde{J}_i(x-x_o)\,dx = -2t\left\{ \bar{\tilde{D}}_{i1}^3 \left[-\tilde{J}_1(x_1) + \tilde{J}_1(x_2) \right] - \bar{\tilde{D}}_{i2}^3 \left[-\tilde{J}_2(x_1) + \tilde{J}_2(x_2) \right] \right\}$$

$$\int_{x_1}^{x_2} \tilde{J}_i(x-x_o)\,dx = 2t\left\{ \bar{\tilde{D}}_{i1}^3 \left[\tilde{J}_1(x_1) - \tilde{J}_1(x_2) \right] + \bar{\tilde{D}}_{i2}^3 \left[\tilde{J}_2(x_1) - \tilde{J}_2(x_2) \right] \right\} \tag{9.17b}$$

Therefore, by solving Eqs. 9.17a and 9.17b for the two components in a single diffusion profile, we can determine the four average values of the main and cross-interdiffusion coefficients from a single diffusion couple. The estimations of $\tilde{J}_i(x_1)$, $\tilde{J}_i(x_2)$, $S = \int_{x_1}^{x_2} \tilde{J}_i dx$ and $R = \int_{x_1}^{x_2} \tilde{J}_i(x-x_o)\,dx$ are explained in Fig. 9.6b.

Dayananda and Sohn [32] used this method to calculate the diffusion parameters in the Cu–Ni–Zn, Fe–Ni–Al, and Ni–Cr–Al systems. From the estimated diffusion parameters, they estimated back the composition profiles and found that the difference between the actual profiles from which these parameters were estimated and then estimated profiles is negligible.

The advantage of these two methods developed by Dayananda et al. is that it is now possible to estimate the diffusion parameters from only a single diffusion couple—compared to a need for two intersecting diffusion profiles in the conventional method previously explained in Sect. 9.1. However, the disadvantage is that we calculate a kind of average value over the composition range, where the diffusion coefficients might vary significantly. If the first method is followed, the average effective diffusion coefficients should be estimated for all the components from their composition profiles. On the other hand, in the estimation of the average main and cross-interdiffusion coefficients (explained in the second method), the compositions profiles of two components are required. Additionally, in the second case, after estimating the average main and cross-interdiffusion coefficients, the stability of the solution should be checked by validating the conditions given in Eq. (9.6a, 9.6b and 9.6c). Cermak and Rothova [33] argued that by making the interval (between x_1 and x_2) very small, the values can be estimated close to that of the actual values that were estimated at the point of intersection from the two different diffusion couples. However, much recently, Cheng et al. [34] have shown that this cannot be used to determine the composition-dependent diffusion coefficients as demanded by Cermak and Rothova.

Many times, as seen from the binary system case discussed in Chap. 6, in ternary systems, layers also grow in the interdiffusion zone with the line compounds or the phases with a narrow homogeneity range. Because of the very small composition range, it is not possible to design experiments such that composition profiles from two different diffusion couples intersect at a common composition inside the phase. Further, it is also not possible to determine the concentration gradient. Therefore, the integrated diffusion coefficients should be estimated for different components using the relation (based on Eqs. 7. 17 and 7. 19a

$$\tilde{D}^{\beta}_{\text{int,i}} = \int_{N_B^{\beta 1}}^{N_B^{\beta 2}} \tilde{D}_i^{\text{eff}} dN_B = -v_m^{\beta} \int_{x_{\beta 1}}^{x_{\beta 2}} \tilde{J}_i dx \tag{9.18a}$$

$$\tilde{J}\left(Y^*_{C,i}\right) = -\frac{\left(C_i^+ - C_i^-\right)}{2t}\left[\left(1 - Y^*_{C,i}\right)\int_{x^{-\infty}}^{x^*} Y_{C,i} dx + Y^*_{C,i}\int_{x^*}^{x^{+\infty}} \left(1 - Y_{C,i}\right) dx\right] \tag{9.18b}$$

where $Y_{C,i} = \frac{C_i - C_i^-}{C_i^+ - C_i^-}$.

Similarly, using the relations developed by Wagner [35] following Eq. 7. 19c, it can be expressed for constant molar volume as

$$\tilde{J} = -\frac{\left(N_B^+ - N_B^-\right)}{2t}\left[\left(1 - Y_B^*\right)\int_{x^{-\infty}}^{x^*}\frac{Y_B}{v_m}dx + Y_B^*\int_{x^*}^{x^{+\infty}}\frac{(1 - Y_B)}{v_m}dx\right] \tag{9.18c}$$

Note here that for the constant molar volume, Eq. 9.18b will be the same as Eq. 9.4b.

Therefore, as explained above in Chap. 7, in a ternary system also, the integrated diffusion coefficients of different components can be estimated by integrating the interdiffusion flux (determined from a composition or concentration profile) using Eq. 9.18b, 9.18c or Eq. 9.4 over the thickness $\left(\Delta x_\beta = x_{\beta_2} - x_{\beta_1}\right)$ of the phase layer of interest β. One important fact should be noted here that, in a binary case, there is only one integrated diffusion coefficient, which is the same when estimated from the composition profile of any of the components. However, in a ternary system, each component will have an integrated diffusion coefficient if these develop a diffusion profile in the interdiffusion zone.

If the composition range of the phase is narrow but known, then the average effective interdiffusion coefficient can be estimated by dividing the integrated diffusion coefficient with the composition range

$$\tilde{D}_i^{\text{eff}} = \frac{\tilde{D}_{\text{int}}^{\beta}}{\Delta N_B^{\beta}} \tag{9.19}$$

It should be noted here that the average effective interdiffusion coefficient in Eqs. 7.9 and 9.19 is the same. Further, this is called the average interdiffusion coefficient in a binary system, which is the average of the interdiffusion coefficients. In a ternary system, it is called the average effective interdiffusion coefficients—which is a kind of average of the main and cross-interdiffusion coefficients in a phase. The estimation of the average effective interdiffusion coefficient in a ternary system is the only option and very useful in many systems. For example, the diffusion paths developed in different diffusion couples in the Ni–Co–W are shown in Fig. 9.7a. It can be seen that in a few diffusion couples, μ-$(Co,Ni)_7W_6$ grows with a small composition range. The composition profile of the Co(25Ni)/W diffusion couple is shown in Fig. 9.7b [36]. It must be clear that it is not easy to design experiments such that the composition profiles from two different diffusion couples intersect in the range of phase composition. It is also difficult to calculate the concentration gradient inside the μ phase, since it does not vary enough with composition to measure with a minimum error. Therefore, the average effective diffusion coefficients were estimated to understand the interdiffusion process in this system.

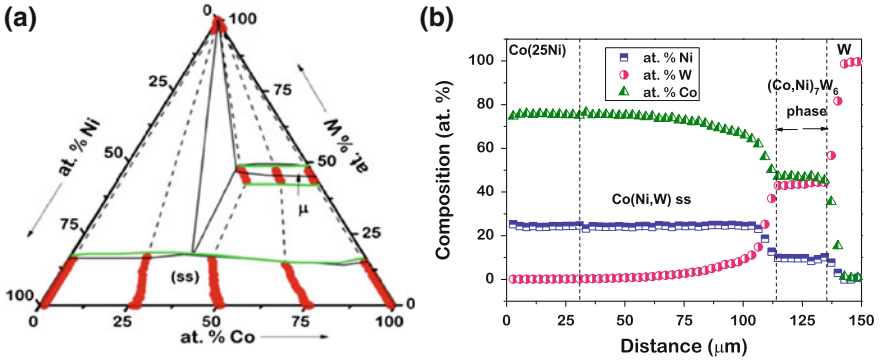

Fig. 9.7 **a** Composition profiles of different diffusion couples on a Co–Ni–W isothermal phase diagram at 1,200 °C. **b** Measured composition profile of the Co(25Ni)/W diffusion couple annealed at 1,200 °C for 25 h [36]

9.3 A Pseudobinary Approach

This approach is to estimate the interdiffusion coefficients in different systems over time, which is easier to follow compared to the approaches explained in earlier sections. Recently, Paul [37] explained added possibilities that exist—for instance, estimating the intrinsic diffusion coefficients along with the interdiffusion coefficients from a single diffusion couple. To begin with, however, we shall consider a ternary system before commenting on the multicomponent system in general, which will be similar irrespective of the number of components in the system. The main requirement to follow this approach is that the composition of the end members are selected such that only two components diffuse—i.e., to develop the diffusion profile, keeping the other components constant throughout the diffusion couple. Therefore, the composition of the two components should vary in the end members used in the diffusion couple, keeping others constant. An imaginary phase diagram is considered, as shown in Fig. 9.8. When Alloy 1 ($A_{0.15}B_{0.85}$) and Alloy 2 ($A_{0.35}B_{0.65}$) are coupled, γ grows in the interdiffusion zone, which has a composition range of $\Delta N_A^{\gamma} = 0.2 - 0.3$. This is a binary system. Now suppose, a fixed amount of 10 at.% of component C is added to both end members. Consequently, the composition of the end members of the diffusion couple is Alloy 3 ($A_{0.15}B_{0.75}C_{0.10}$) and Alloy 4 ($A_{0.35}B_{0.55}C_{0.10}$). For the ease of explanation, we consider the linear variation of the composition in the product γ phase and also consider that the molar volume is the constant. However, note here that this approach is not restricted to this condition and can be used in any real system, where the molar volume does not vary ideally. The alloying addition might replace one of the components, especially in the intermetallic compounds. In this particular case, we have considered that C replaces B. As the composition of C is the same in both end members, γ might grow with the same composition. Therefore, component C does not develop a diffusion profile but becomes mixed and the composition is fixed

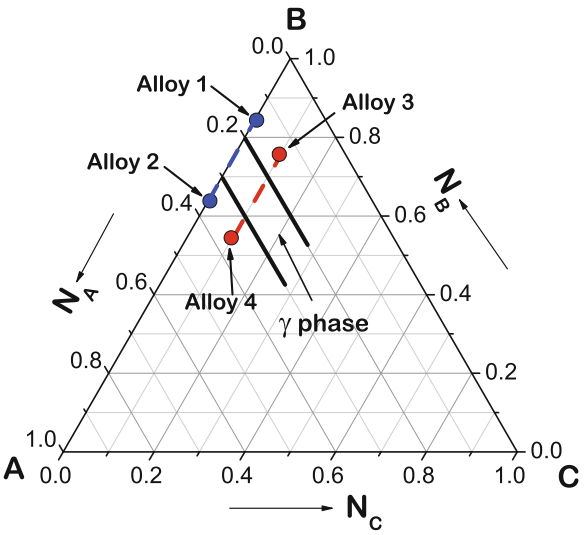

Fig. 9.8 Compositions of the alloys chosen for diffusion couples [37]

throughout the diffusion couple. Therefore, from Eqs. 9.2a, 9.2b and 9.8a–9.8d, for N_2 as fixed composition it is clear that the diffusion in this ternary system should be considered as a pseudobinary system. For example, if we consider that the composition of component 2 is fixed, from the intrinsic flux ($J_2 = 0$) the interdiffusion flux ($\tilde{J}_2 = 0$) and the concentration gradient ($dC_2/d_x = 0$), the relations are reduced to the relations in a binary system. Therefore, the estimation procedure is rather similar. To explain the steps, we first consider the couple in the binary system and then explain it for the ternary (pseudobinary) system.

9.3.1 Estimation of Diffusion Parameters in a Binary System

A diffusion couple of two blocks with compositions of, let us say, Alloy 1 ($A_{0.15}B_{0.85}$) and Alloy 2 ($A_{0.35}B_{0.65}$) as presented in Fig. 9.9a. Suppose in the middle, a single phase γ grows with a composition range of $\Delta N_A^{\gamma} = 0.2-0.3$. To simplify the explanation, we consider a linear change in the composition in the interdiffusion zone, as shown in composition profiles of A and B in Figs. 9.9b and c. Further, we consider that there is no change in the molar volume with the change in composition. These assumptions are taken such that it will be easier for the readers to calculate the diffusion parameters without the help of any software. As mentioned already, this method is applicable in any real system, where the composition profile is not linear and the molar volume deviates from ideality. For the calculation of the intrinsic diffusion coefficients, we consider the presence of the marker plane in the interdiffusion zone. Although the variation of the interdiffusion coefficients with composition can be estimated, the interdiffusion and intrinsic diffusion coefficients at the marker plane only are estimated at present so that we can validate the

results. The interdiffusion flux of a component i in a binary or multicomponent system can be estimated by Eq. 7.19c

$$\begin{aligned}\tilde{J}_i &= -\frac{\Delta N_i}{2tv_m^{\gamma}}\left[(1-Y_i)\int_{x^{-\infty}}^{x^*} Y_i dx + Y_i\int_{x^*}^{x^{+\infty}}(1-Y_i)dx\right] \\ &= -\frac{\Delta N_i}{2tv_m^{\gamma}}\left[(1-Y_i)\int_{x^{-\infty}}^{x_K} Y_i dx + Y_i\int_{x_K}^{x^{+\infty}}(1-Y_i)dx\right]\end{aligned} \tag{9.20a}$$

We can calculate the interdiffusion flux of A by

$$\tilde{J}_A = -\frac{\Delta N_A}{2tv_m^{\gamma}}\left[(1-Y_A)\int_{x^{-\infty}}^{x_K} Y_A dx + Y_A\int_{x_K}^{x^{+\infty}}(1-Y_A)dx\right]. \tag{9.20b}$$

A minus sign is there since the component A diffuses from right to left and the interdiffusion flux is negative. For the interdiffusion flux of B, a minus sign will not be there since it diffuses from left to right. The composition range of the diffusion couple is $\Delta N_A = N_A^+ - N_A^-$, where N_A^+ and N_A^- are the composition of the initial and unaffected parts of the left- and right-hand sides of the end members, x^* is the position of interest, Y_A is the composition normalized variable and is equal to $\frac{N_A - N_A^-}{N_A^+ - N_A^-}$. From Fick's first law for constant molar volume, we can write

$$\tilde{J}_A = -\tilde{D}\frac{dC_A}{dx} = -\tilde{D}\frac{1}{v_m^{\gamma}}\frac{dN_A}{dx} \tag{9.20c}$$

From Eqs. 9.20b and 9.20c, we can write the relation for the interdiffusion coefficient at the marker plane (denoted by K) as

$$\begin{aligned}\tilde{D} &= \frac{1}{2t}\left(\frac{dx}{dN_A/\Delta N_A}\right)_K\left[(1-Y_A^K)\int_{x^{-\infty}}^{x_K} Y_A dx + Y_A^K\int_{x_K}^{x^{+\infty}}(1-Y_A)dx\right] \\ &= \frac{1}{2t}\left(\frac{dx}{dY_A}\right)_K\left[(1-Y_A^K)\int_{x^{-\infty}}^{x_K} Y_A dx + Y_A^K\int_{x_K}^{x^{+\infty}}(1-Y_A)dx\right]\end{aligned} \tag{9.20d}$$

It should be noted here that the data estimated will be the same if estimated with respect to the composition profile of B instead of A. Let us consider that the markers used at the interface before annealing are shifted to 0.24 atomic fraction A (0.76 atomic fraction B) located at 40 μm from the Alloy 1/γ phase interface. The total thickness of the product γ phase grown in the interdiffusion zone is 100 μm after 25 h of annealing at one particular temperature T. The interdiffusion coefficients can be estimated at any of compositions; however, we calculate it at the

marker plane to validate our results. With the help of Eq. 9.20d and from the Y_A versus x plot, as shown in Fig. 9.9d, the interdiffusion coefficient is estimated as 2.05×10^{-14} m^2/s.

The intrinsic diffusion coefficients of components A and B can be estimated from Eqs. 6.74 and 6.76

$$\begin{aligned} D_A &= \frac{1}{2t}\left(\frac{dx}{dC_A}\right)_K \left[N_A^+ \int_{x^{-\infty}}^{x_K} \frac{Y_A}{v_m} dx - N_A^- \int_{x_K}^{x^{+\infty}} \left(\frac{1-Y_A}{v_m}\right) dx\right] \\ &= \frac{1}{2t}\left(\frac{dx}{dN_A}\right)_K \left[N_A^+ \int_{x^{-\infty}}^{x_K} Y_A dx - N_A^- \int_{x_K}^{x^{+\infty}} (1-Y_A) dx\right] \end{aligned} \tag{9.21a}$$

$$\begin{aligned} D_B &= \frac{1}{2t}\left(\frac{dx}{dC_B}\right)_K \left[N_B^+ \int_{x^{-\infty}}^{x_K} \frac{Y_A}{v_m} dx - N_B^- \int_{x_K}^{x^{+\infty}} \left(\frac{1-Y_A}{v_m}\right) dx\right] \\ &= -\frac{1}{2t}\frac{dx}{dN_A}\left[N_B^+ \int_{x^{-\infty}}^{x_K} Y_A dx - N_B^- \int_{x_K}^{x^{+\infty}} (1-Y_A) dx\right] \end{aligned} \tag{9.21b}$$

since we are considering a constant molar volume in the phase of our interest and in a binary system $N_A + N_B = 1$.

Therefore, using Fick's first law, the intrinsic fluxes can be expressed as

$$J_A = -\frac{1}{2tv_m^\gamma}\left[N_A^+ \int_{x^{-\infty}}^{x_K} Y_A dx - N_A^- \int_{x_K}^{x^{+\infty}} (1-Y_A) dx\right] \tag{9.21c}$$

$$J_B = \frac{1}{2tv_m^\gamma}\left[N_B^+ \int_{x^{-\infty}}^{x_K} Y_A dx - N_B^- \int_{x_K}^{x^{+\infty}} (1-Y_A) dx\right] \tag{9.21d}$$

Since A diffuses from right to left, $J_A = -D_A \frac{dC_A}{dx}$ and B diffuses from left to right, $J_B = D_B \frac{dC_B}{dx}$. The intrinsic diffusion coefficients are estimated at the Kirkendall marker plane as $D_A^K = 0.72 \times 10^{-14}$ and $D_B^K = 6.27 \times 10^{-14}$m^2/s. The accuracy of the estimations can be checked from the relation between the interdiffusion and intrinsic diffusion coefficients (Eq. 6.65)

$$\tilde{D}^K = N_A^K D_B^K + N_B^K D_A^K \tag{9.22}$$

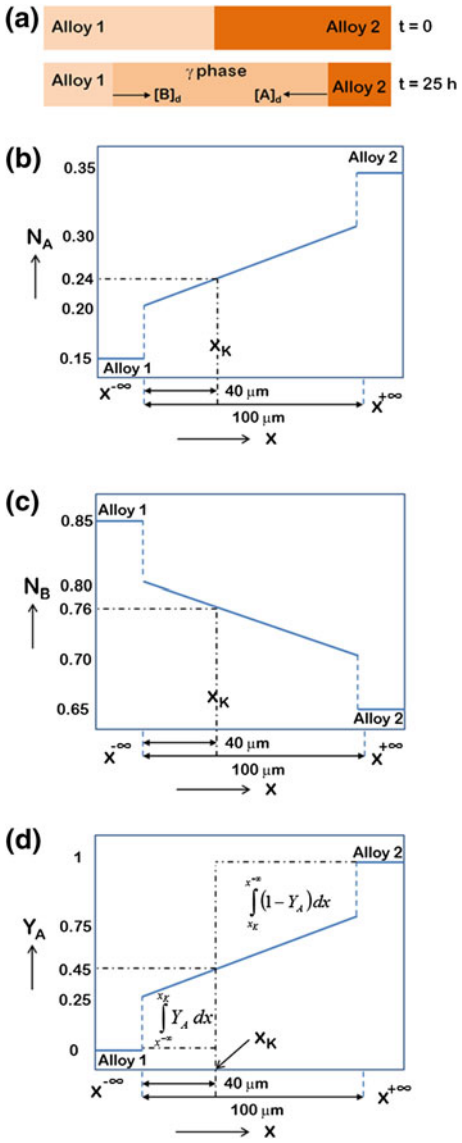

Fig. 9.9 **a** Diffusion couple of Alloys 1 and 2, **b** composition profile with respect to element *A* **c** composition profile with respect to element B and **d** composition normalized variable Y_A versus x plot [37]

9.3.2 A Pseudobinary Approach in a Ternary System

Now, consider a ternary diffusion couple of Alloy 3 and Alloy 4, as shown in Fig. 9.8. For the sake of explanation, we first consider that the homogeneity range of the γ phase does not change because of the addition of C. Furthermore, the component C replaces the component B. Now, we need to select the end-member compositions,

such that the composition range of the components A and B are the same with a fixed composition of the component C in both. To compare with the results already estimated in the binary case, we consider the same composition range of 0.2 for A and B between the end members. We choose a fixed composition C, for example, 0.1 such that the compositions of the end members are $A_{0.15}B_{0.75}C_{0.10}$ (Alloy 3) and $A_{0.35}B_{0.55}C_{0.10}$ (Alloy 4). The product phases might grow with the same fixed percentage of C. It can be seen as an interdiffusion of A and B in the presence of the other component C. The diffusion rates of the components can be affected because of the presence of other components since the concentrations of defects (thermal vacancies and structural antisites) and the thermodynamic driving forces in the γ product phase will change. As a result of the change in diffusion rates, the layer thickness of the product phase will also change. However, for the sake of explanation and to validate our estimations, we consider two cases. In one case, we assume that there is no change in layer thickness and the position of the Kirkendall marker plane is the same. This is considered first to validate the estimations. Then, we consider the change in both in layer thickness and the position of the marker plane. These are shown in Figs. 9.10a and 9.11a.

Firstly, we consider the composition range of the components to be the same as the binary system since we are seeking to validate our results. If no difference is seen in the layer thickness in the ternary system, the diffusion rates should also be the same. Since the two components A and B diffuse and the third component C does not have the concentration gradient, it can be considered as a pseudobinary system. Moreover, it should be the same when we consider either component A or B for our estimations, as can be seen immediately from the N_A versus x or Y_A versus x plots in Fig. 9.10a and c. At the location of 40 μm, the interdiffusion coefficient is estimated to be the same as that estimated in the binary system. However, note that N_B is 0.66 (since $N_A = 0.24$ and $N_C = 0.10$) in the ternary system instead of 0.76 in the binary system. As $N_A + N_B + N_C = 1$ and C replaces B in the ternary system, we would rather measure the interdiffusion coefficients at N_{B+C} (= N_B + N_C) = 0.76. For the estimation of the interdiffusion coefficients, we could consider N_B or N_{B+C}, since the composition is normalized and the composition range of the diffusion couple is the same. However, for the estimation of the intrinsic diffusion coefficients, we need to consider the total composition of B and C, that is, N_{B+C}. If we neglect C, then the total mol fraction (or the atomic fraction) will not be equal to one, making the estimation of the intrinsic diffusion coefficients incorrect. On the other hand, the composition profile for the component A is the same. Therefore, if we wish to estimate the intrinsic diffusion coefficients also, we should calculate the diffusion parameters with respect to N_A versus x or N_{B+C} versus x, as shown in Figs. 9.10a and b. Hence, we need to consider Y_A versus x or Y_{B+C} versus x. We show the estimation of the intrinsic diffusion coefficients with respect to the Y_A versus x plot, as shown in Fig. 9.10c following

$$D_A = \frac{1}{2t}\left(\frac{dx}{dN_A}\right)_K \left[N_A^+ \int_{x^{-\infty}}^{x_K} Y_A dx - N_A^- \int_{x_K}^{x^{+\infty}} (1 - Y_A) dx\right] \tag{9.23a}$$

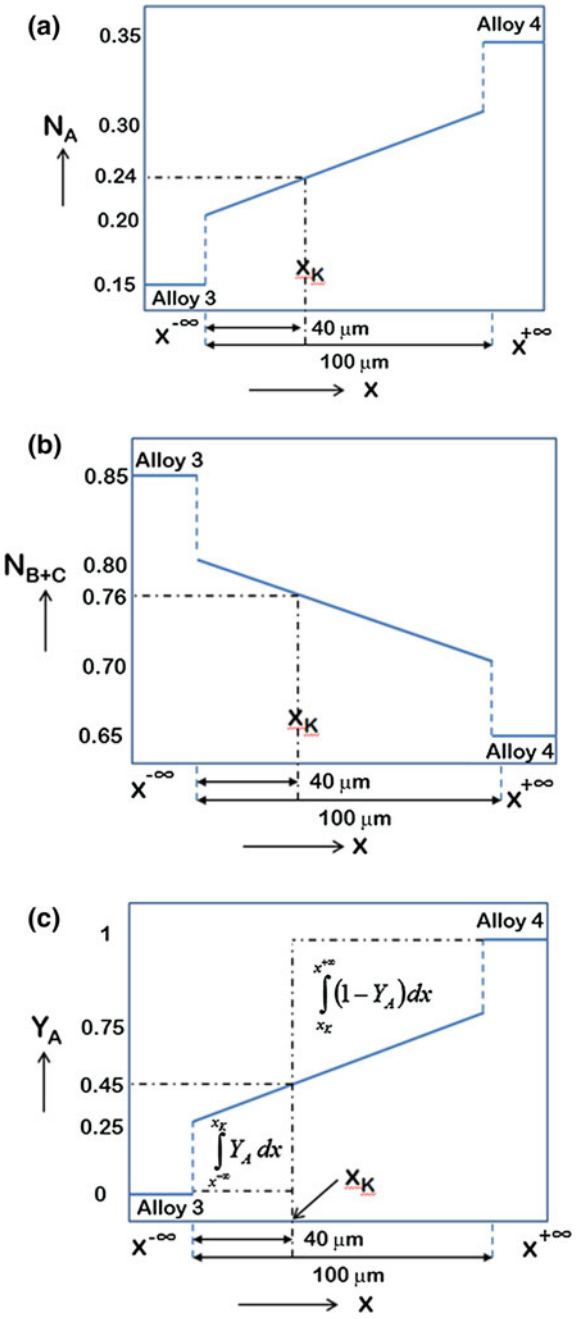

Fig. 9.10 Composition profiles of a diffusion couple in a ternary A–B–C system **a** composition profile of element *A* **b** composition profile of elements (B + C), **c** composition normalized variable Y_A versus x plot [37]

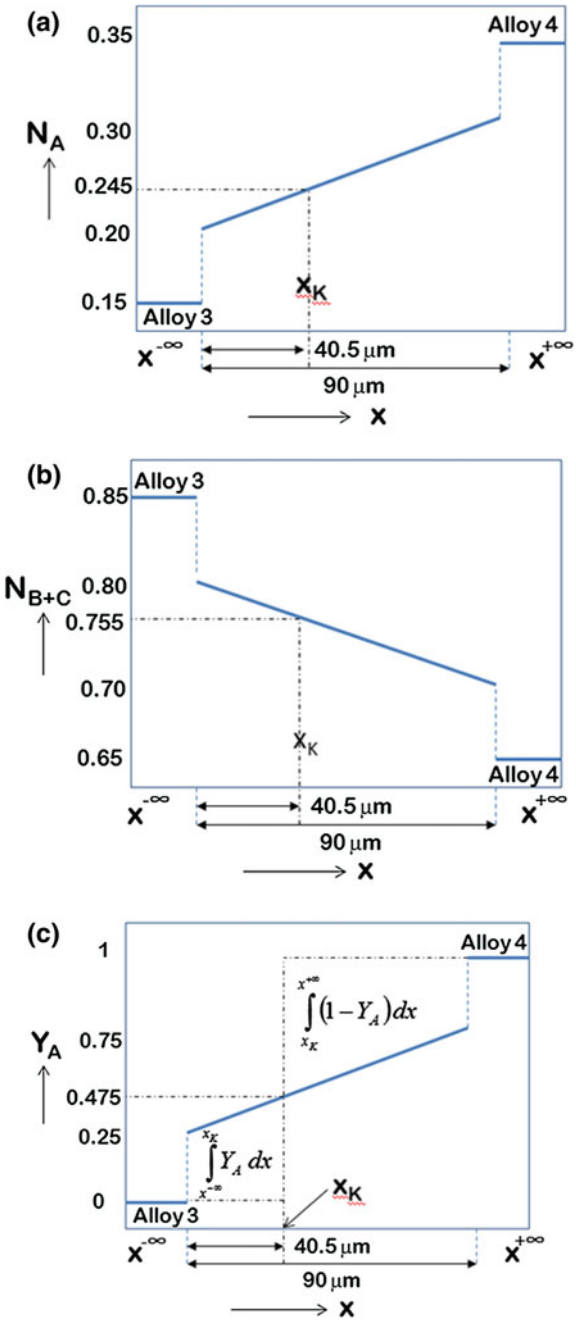

Fig. 9.11 Composition profiles of a diffusion couple in a ternary A–B–C system, where layer thickness is affected because of addition of C with A and B **a** composition profile of element A **b** composition profile of elements (B + C), **c** composition normalized variable Y_A versus x plot [37]

$$D_B = -\frac{1}{2t}\left(\frac{dx}{dN_A}\right)_K \left[N^{+}_{B+C}\int_{x^{-\infty}}^{x_K} Y_A dx - N^{-}_{B+C}\int_{x_K}^{x^{+\infty}} (1 - Y_A)dx\right] \tag{9.23b}$$

We considered exactly the same location of the marker plane and we obtain the same values of D_A and D_B as estimated in the binary system.

To validate the results, we considered the same layer thickness. However, as already mentioned, the layer thickness—and even the location of the marker plane—actually change due to the addition of another component, since it influences both defect concentrations and the thermodynamic driving force. It could increase or decrease the growth rate depending on the particular system under consideration. Let us consider that the growth rate in the presence of C is lower and the layer thickness after annealing for 25 h is 90 μm. There is also a change in the location of the marker plane, which is to be found at 0.245 of N_A, at the location of 40.5 μm from the Alloy 3/γ phase interface, as shown in Fig. 9.11a. The Y_A versus x plot is presented in Fig. 9.11c. The interdiffusion and intrinsic diffusion coefficients are estimated at the marker plane as $\tilde{D} = 1.68 \times 10^{-14}$, $D_A = 1.13 \times 10^{-14}$ and $D_B = 3.38 \times 10^{-14}$ m^2/s.

Therefore, we have seen that if the experiments are conducted in a particular way, the ternary system can be treated as a pseudobinary system and the same relations developed for the binary system can be used. We have shown the estimations at one particular composition only, however, just as in a binary system, it is possible to estimate the variation of the interdiffusion coefficients with the compositions. Any error in estimation of the data caused by the deviation in the average composition of the end member is discussed in detail [37], which indicates that we could estimate the data without much error when the average composition deviates within ±1 at.%, a task which is not very difficult to achieve.

9.3.3 A Pseudobinary Approach in a Multicomponent System

As already explained, alloy compositions are chosen such that the composition of one component is the same and then a third component is added at the cost of the second component. Similarly, we can add many components, which will replace the component B and then the estimation procedure will be the same. The interdiffusion coefficients can be estimated with respect to the composition profile of A or B. However, for the estimation of the intrinsic diffusion coefficients, we should consider the composition profile of A or the total of the other components (B + X). This approach is useful when studying the diffusion of intermetallic compounds, where, in general, one alloying component replaces another particular component. If we are interested to study interdiffusion in random solid solutions and calculate the interdiffusion at the equiatomic compositions (let us say, a five-component system), then only two components, for instance, A and B could vary in the range of 0.15–0.25. Following, 0.2 atomic fractions of all other components should be added to both the alloys that are

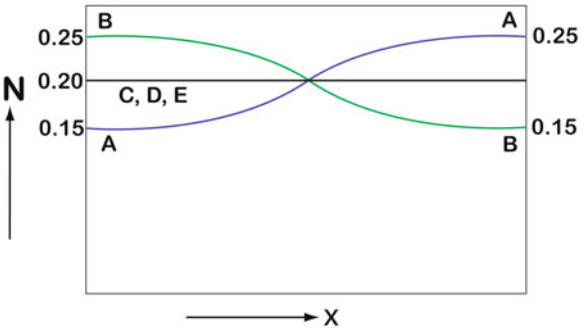

Fig. 9.12 Composition profile of multicomponent diffusion couple in random solid solution [37]

to be bonded, as shown in Fig. 9.12. Moreover, the interdiffusion coefficients can be estimated at 0.2 atomic fractions from any of the composition profiles (A or B). However, the main difficulty in this system is for the estimation of the intrinsic diffusion coefficients, since we cannot decide how to add the composition of the other components with *A* and *B*. Further, analysis is required to tackle this issue. A similar problem will be faced if one particular component replaces both of the components. In such cases, also the interdiffusion coefficient can only be estimated.

9.3.4 Estimation of Diffusion Parameters in Line Compounds Following the Pseudobinary Approach

As already explained, the integrated diffusion coefficients $\tilde{D}_{\text{int}}$ should be estimated when phases grow with a narrow homogeneity range. This is basically the interdiffusion coefficient integrated over the unknown small composition range of, for example, the phase β. This can be expressed with the help of Eq. 9.18a, 9.18b and 9.18c as

$$\widetilde{D}^{\beta}_{\text{int}} = \int_{N'_A}^{N''_A} \tilde{D}\, dN_A$$

$$\tilde{D}^{\beta}_{\text{int}} = -\int_{x_I}^{x_{II}} \tilde{J} V^{\beta}_m dx = -\tilde{J} v^{\beta}_m \Delta x^{\beta}$$

From Eq. 9.4b

$$\tilde{J} = -\frac{\left(N_A^{+} - N_A^{-}\right)}{2tv^{\beta}_m}\left[\left(1 - Y^{*}_A\right)\int_{x^{-\infty}}^{x^{*}} Y_A dx + Y^{*}_A \int_{x^{*}}^{x^{+\infty}} (1 - Y_A) dx\right] \tag{9.24}$$

Therefore,

$$\tilde{D}^{\beta}_{\text{int}} = \frac{\left(N_A^{+} - N_A^{-}\right)\Delta x^{\beta}}{2t}\left[(1 - Y_A)\int_{x^{-\infty}}^{x^{*}} Y_A dx + Y_A \int_{x^{*}}^{x^{+\infty}} (1 - Y_A) dx\right]$$

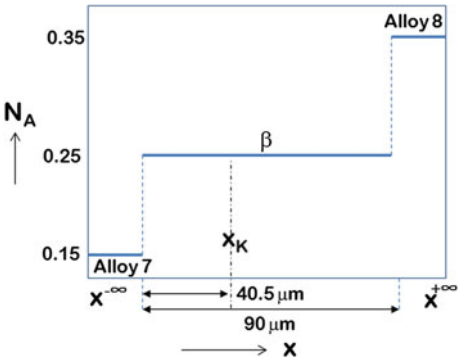

Fig. 9.13 Composition profile of element A in a multicomponent system, where a line compound grows in the interdiffusion zone [37]

As already explained in Chap. 7 [from Eq. 7.18], we can estimate the ratio of the diffusivities for a constant molar volume by

$$\frac{D_A}{D_B} = \frac{\left[N_A^+ \int_{x^{-\infty}}^{x_K} Y_A dx - N_A^- \int_{x_K}^{x^{+\infty}} (1 - Y_A) dx\right]}{\left[-N_{B+C}^+ \int_{x^{-\infty}}^{x_K} Y_A dx + N_{B+C}^- \int_{x_K}^{x^{+\infty}} (1 - Y_A) dx\right]} \tag{9.25}$$

Let us consider a diffusion couple between Alloy 7 ($A_{0.15}B_{0.75}C_{0.1}$) and Alloy 8 ($A_{0.35}B_{0.55}C_{0.1}$) where one line compound grows with the composition $A_{0.25}B_{0.65}C_{0.1}$, as shown in Fig. 9.13. Suppose the marker plane is located at a distance of 40.5 μm from the Alloy 5/β phase interface. The values are estimated as $\tilde{D}_{\text{int}} = 2.25 \times 10^{-14}\,\text{m}^2/\text{s}$ and $\frac{D_B}{D_A} = 2.33$.

The examples given above are discussed mainly based on the ternary systems; however, the same method can be followed in systems that consider more than three components as long as only two components diffuse. There are a few advantages in following this pseudobinary approach compared to the other methods explained before. For example, from a single diffusion couple, we can estimate the variation of the interdiffusion coefficients over the whole composition range in the interdiffusion zone as well as the intrinsic diffusion coefficients at the Kirkendall marker plane. This is otherwise very difficult in a ternary system and almost impossible in a quaternary system. The possibility of conducting pseudobinary experiments to examine the role of alloying additions in a more systematic approach could be understood from Fig. 9.14. Suppose, we would like to study the effect of Pt on the diffusion rate of Ni and Pt in the β-Ni(Pt)Al phase, which is used in jet engines as a bond coat for protection from oxidation. The diffusion rates of Ni and Al are very important for a proper understanding of the performance and the life of the product. To estimate the diffusion of the component and predict the defects present on different sublattices, it is necessary to conduct experiments systematically such that the data estimated at different compositions can be

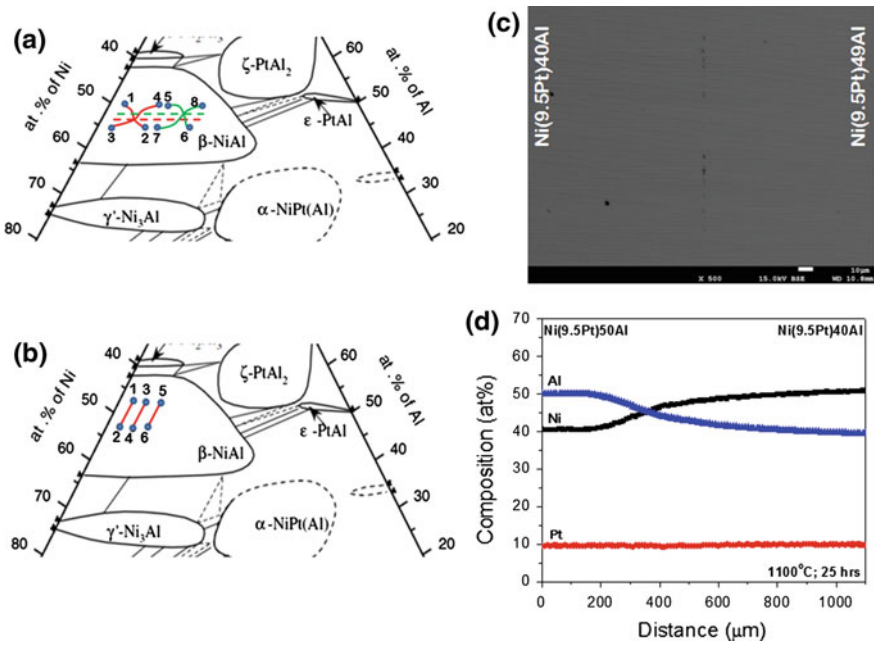

Fig. 9.14 Advantage of a pseudobinary approach explained **a** diffusion couples following conventional technique, **b** diffusion couples in a pseudobinary approach, **c** diffusion couple of Ni(9.5Pt)50Al/Ni(9.5Pt)40Al annealed at 1,100 °C for 25 h, and **d** its composition profile

compared. Since we can estimate the diffusion parameters at the point of intersection by following the conventional method, we need to prepare two couples, for example, a couple of Alloy 1/Alloy 2 and Alloy 3/Alloy 4, as shown in Fig. 9.14a. In general, diffusion profiles are S-shaped, as already discussed, and it is almost impossible to predict beforehand the point of intersection. With the aim of getting the point of intersection with the same ratio of Ni and Al (but with an increasing content of Pt), suppose another set of diffusion profiles are prepared from Alloy 5/Alloy 6 and Alloy 7/Alloy 8. In these alloys, the Pt content is increased while keeping the Ni/Al ratio the same, with the expectation of finding the point of intersection at the same Ni/Al ratio—yet with increased Pt compared to the previous case. However, these will not necessarily intersect at the desired composition and may even intersect at a different Ni/Al composition, as shown in Fig. 9.14. We are unable to compare the results from different sets of couples, which is something very commonly encountered. Therefore, the estimation in the ternary systems is mostly restricted to the data generation, without any further understanding on the complex process of diffusion. Moreover, there is rarely any chance that the markers will also be at the point of intersection to estimate the intrinsic diffusion coefficients. In this regard, pseudo-binary approach rather should be followed.

When we want to study the effect of Pt on interdiffusion of Ni and Al, we could consider the diffusion couples of Alloy 1/Alloy 2, Alloy 3/Alloy 4, and Alloy 5/Alloy 6, as shown in Fig. 9.14b. For example, an experimental diffusion profile of (Ni9.5Pt)40Al/Ni(9.5Pt)50Al is shown in Fig. 9.14c. It can be seen that Pt does not develop any diffusion profile and remains constant throughout the diffusion couple. Therefore, this approach is highly suited for understanding the diffusion mechanism by changing the Pt content systematically with the added advantage that we can estimate the intrinsic diffusion coefficients from a single diffusion couple. Additionally, we can estimate the variation of the interdiffusion coefficients over the whole composition range—unlike the other methods by which we can only estimate these parameters at the point of intersection.

9.4 Estimation of Tracer Diffusion Coefficients in a Ternary System

As we have discussed much earlier in Chap. 6, the vacancy wind effect might have an important role to play on the diffusing components. However, for the sake of simplicity, we shall neglect this contribution to show the relations for estimating the tracer diffusion coefficients directly from the interdiffusion experiments using the thermodynamic parameters. If the vacancies are at equilibrium in the system and considering that diffusion occurs by a vacancy exchange mechanism [38], the intrinsic flux of the components in terms of the phenomenological constant L_{ii} can be written (as also discussed in Chap. 6) as [2]

$$J_i = -L_{ii}\frac{\partial \mu_i}{\partial x} \tag{9.26a}$$

We have neglected the contribution from the off-diagonal terms L_{ij} by neglecting the contribution from the vacancy wind effect and the correlation effects. Furthermore, we consider the thermal equilibrium of the vacancies over the whole interdiffusion zone. Therefore, based on the analysis by Darken [39] and LeClaire [40], the phenomenological constants divided by the concentration can be related to the mobilities $M_i = D_i^*/RT$ (Eq. 6.88), where $L_{ii} = M_i C_i$ such that

$$L_{ii} = \frac{C_i D_i^*}{RT} \tag{9.26b}$$

Replacing Eq. 9.26b in Eq. 9.26a, we get

$$J_i = -\frac{C_i D_i^*}{RT}\frac{\partial \mu_i}{\partial x} = -\frac{N_i D_i^*}{RTv_m}\frac{\partial \mu_i}{\partial x} \tag{9.27}$$

Since $\mu_i = \mu_i^o + RT \ln a_i$ and $a_i = \gamma_i N_i$, as discussed in Chap. 1, Eq. 9.27 can be written as

$$J_i = -\frac{N_i D_i^*}{v_m a_i}\frac{\partial a_i}{\partial x} = -\frac{D_i^*}{v_m \gamma_i}\frac{\partial a_i}{\partial x} \tag{9.28}$$

From Eqs. 9.8a, 9.27 and 9.28 considering a constant molar volume in a ternary system, we can write

$$\begin{aligned}\widetilde{J}_1 &= -\frac{N_1 D_1^*}{RTv_m}\frac{\partial \mu_1}{\partial x} + N_1\left(\frac{N_1 D_1^*}{RTv_m}\frac{\partial \mu_1}{\partial x} + \frac{N_2 D_2^*}{RTv_m}\frac{\partial \mu_2}{\partial x} + \frac{N_3 D_3^*}{RTv_m}\frac{\partial \mu_3}{\partial x}\right) \\ &= -\frac{D_1^*}{\gamma_1 v_m}\frac{\partial a_i}{\partial x} + N_1\left(\frac{D_1^*}{\gamma_1 v_m}\frac{\partial a_1}{\partial x} + \frac{D_2^*}{\gamma_2 v_m}\frac{\partial a_2}{\partial x} + \frac{D_3^*}{\gamma_3 v_m}\frac{\partial a_3}{\partial x}\right)\end{aligned} \tag{9.29a}$$

$$\begin{aligned}\widetilde{J}_2 &= -\frac{N_2 D_2^*}{RTv_m}\frac{\partial \mu_2}{\partial x} + N_2\left(\frac{N_1 D_1^*}{RTv_m}\frac{\partial \mu_1}{\partial x} + \frac{N_2 D_2^*}{RTv_m}\frac{\partial \mu_2}{\partial x} + \frac{N_3 D_3^*}{RTv_m}\frac{\partial \mu_3}{\partial x}\right) \\ &= -\frac{D_2^*}{\gamma_2 v_m}\frac{\partial a_2}{\partial x} + N_2\left(\frac{D_1^*}{\gamma_1 v_m}\frac{\partial a_1}{\partial x} + \frac{D_2^*}{\gamma_2 v_m}\frac{\partial a_2}{\partial x} + \frac{D_3^*}{\gamma_3 v_m}\frac{\partial a_3}{\partial x}\right)\end{aligned} \tag{9.29b}$$

$$\tilde{J}_3 = -\tilde{J}_1 - \tilde{J}_2 \tag{9.29c}$$

If the thermodynamic data in a ternary system are known, using the composition in a diffusion couple, the interdiffusion fluxes are estimated at the point of interest using the relation in Eq. 9.4a. Further, from the known activities (or chemical potentials) of the components at a different composition, the composition profile can be converted to the activity or the chemical potential profile for all the components. From these profiles, the thermodynamic parameters required in Eq. 9.29a, 9.29b and 9.29c can be estimated. Subsequently, the tracer diffusion coefficients of the components can be estimated at the point of interest. Rönka et al. [26] estimated the interdiffusion and the tracer diffusion coefficients at the point of intersection from two diffusion couples in a Cu–Fe–Ni system, finding that the estimated tracer diffusion coefficients are consistent with the data available in literature in the Cu–Ni and Fe–Ni systems.

The intrinsic fluxes in the system considering the constant molar volume can be written as [26]

$$J_v = -\sum_{i=1}^{n} J_i \tag{9.30a}$$

In a ternary system, it is reduced to

$$J_v = -(J_1 + J_2 + J_3) \tag{9.30b}$$

Replacing Eq. 9.27 in Eq. 9.30b, we get

$$J_v = \frac{N_1 D_1^*}{RTv_m}\frac{\partial \mu_1}{\partial x} + \frac{N_2 D_2^*}{RTv_m}\frac{\partial \mu_2}{\partial x} + \frac{N_3 D_3^*}{RTv_m}\frac{\partial \mu_3}{\partial x} \tag{9.30c}$$

Therefore, the position of the Kirkendall marker plane can be found from the relation above, since (as discussed in Chap. 6)

$$v_m J_v = \frac{x_K}{2t} \tag{9.31}$$

By comparing the shift in the diffusion couple (and estimating the shift with the help of the estimated diffusion coefficients using the relations above), it is possible to examine the reliability of the estimation procedure.

In the above analysis, the vacancy wind effect could be neglected since we neglected the off-diagonal terms L_{ij}. In an actual case, however, these might not be negligible. As mentioned by Belova et al. [41], in some rare cases, these off-diagonal terms could dominate to change the direction of the atomic flux. Manning [42, 43] developed the relations including the vacancy wind effect. Dayananda [44] extended this theory for the determination of the vacancy wind effect experimentally in a multicomponent system, considering the non-diagonal phenomenological constants. Moleko et al. [45] also developed a model, considering the vacancy wind effect. Belova et al. [41] have reported an interesting outcome in their analysis based on the experimental data compiled by Divinski et al. [46] in the Cu–Ni–Fe system. They have shown the procedure to determine the jump frequencies, correlation factors, and the vacancy wind effects following the theory developed by Manning [43] and Dayananda [44] from the available tracer diffusion coefficients. In the process, they have shown that Darken formulism (ignoring the off-diagonal term) is reliable to express the diagonal phenomenological constants in terms of the tracer diffusion coefficients. They have also demonstrated the procedure to calculate the tracer diffusion coefficients and the vacancy wind effect from the interdiffusion coefficients following the theory developed by Darken [39], Manning [43], and Dayananda [44]

Holly and Danielewski [47] have developed an extended Darken quantitative model to describe the multicomponent interdiffusion process based on the consideration of local mass conservation and by using the expressions for drift and diffusional flux—the momentum conservation equations where the diffusivities of components vary with composition. Filipek et al. [48] used this analysis in the Fe–Co–Ni system and found good agreement between theoretically estimated and experimentally determined composition profiles developed in the diffusion couples. Divinski et al. [46] applied this model in the Cu–Fe–Ni system to show good agreement between the estimated and experimental interdiffusion concentration,

which validates the assumptions made by Holly and Danielewski in their model for the description of interdiffusion in a non-ideal system.

An important note is due here. The vacancies in a binary alloy can be considered as third component and thus, generally, even binary alloys have to be treated as multicomponent systems. Then, the off-diagonal terms cannot be neglected that results in a vacancy wind effect for the binary compositions. However, in typical situation, the vacancy concentrations are small and the resulting correction on the vacancy wind effect is about unity. In most binary couples, the corresponding contribution can safely be neglected, especially in view of the experimental uncertainties. Nevertheless, it is important to keep this fact in mind.

9.5 Determination of Phase Diagram Following Diffusion Couple Technique

Knowledge of phase diagrams is very important for developing any new material or for gaining a full understanding of the physical and mechanical behavior of materials. However, the determination of a phase diagram is a very tedious procedure. The level of complexity increases drastically in ternary system compared to simpler binary systems. Numerous samples must be prepared in order to establish a ternary phase diagram. Added complications come from the fact that the phase equilibria existing at the solid state might not be achieved by a melt route—especially if there is a peritectic reaction present. On the other hand, a diffusion couple along with the melting of selective alloys could be very handy to decrease the number of experiments (or alloys) required to establish a phase diagram. For more comprehensive treatment on this area, the readers are referred to an excellent review written by Kodentsov et al. [49] and the book on methods for phase diagram determination [50]. The use of the diffusion couple for the development of the phase diagram was, in fact, first proposed by Kirkaldy [51]. Kirkaldy and Brown [52] formulated the number of rules, which were then compiled by Clark [53] based on a hypothetical diffusion couple. Most recently, Morral [54] has compiled a few more rules developed at a later stage. At this point, we shall discuss mainly the rules described by Clark and explain the advantages and limitations of using a diffusion couple for the determination of phase diagrams.

It should be pointed out here that, unlike in a binary diffusion couple, in a ternary couple a two-phase mixture can develop when the experiment is conducted at a constant temperature. This can be understood from the Gibb's phase rule $F = C - P + 2$. At constant temperature and pressure, we can write $F = C - P$. In a ternary system, $C = 3$. Therefore, $F + P = 3$ and the two phases (that is $P = 2$) are

allowed, keeping the variation of the concentration as one degree of freedom. Previously in Chap. 4, we have seen that in a binary system, two phase mixture cannot grow in the middle of a diffusion couple since it is not allowed to develop a region of equilibrium before the whole diffusion couple reaches to an equilibrium state. Similarly, three phase mixture cannot grow in a ternary diffusion couple. A two phase mixture can grow only when the diffusion path (i.e. the composition profile) goes from one phase area to two phase area, cuts the tie-lines at a given angle and returns to one phase area. If the one phase area is named α and the two phase are is α + β, then under these circumstances the α phase contains precipitates of the β phase and thus a two phase mixture has been formed. The rules are described based on the diffusion path (that is the plot of composition profile of a diffusion couple on a Gibb's triangle) in a ternary diffusion couple between *A* and *Z* on a hypothetical phase diagram, as shown in Fig. 9.15a [49].

Note that there are many phases, such as α, β, δ, σ, π, λ, μ, and γ that are present. The two-phase equilibrium regions are shown by connected tie lines, and the three-phase regions are kept blank. When the composition profile is examined from alloy *Z*, the variation in the composition inside the δ phase should be shown by a diffusion path drawn with a solid line *ab*. Since the phases δ and σ are separated by a wavy interface, the solid-line diffusion path should intersect the tie lines as shown by *bc*. Then, the diffusion path goes through the σ phase as shown by *cd*. Following, the precipitates of the π phase appear inside this phase and again after that the σ phase is present as a single phase. This means that the diffusion path should enter the two-phase equilibrium region as shown by *def* and then returns again to the σ phase to continue up to *fg*. Phases σ and π are separated by a straight interface. Therefore, the diffusion path should run parallel to the tie lines as shown by *gh* and it should be drawn by a dotted line. *ij* shows the three-phase equilibrium region starting from phase π toward two-phase region λ and μ. *jk* shows the phase mixture of λ and μ. The location of the line in the two-phase equilibrium region depends on the relative amounts of the phases. *kl* shows the transition from one three-phase equilibrium to another three-phase equilibrium. *lm* shows the path from two-phase equilibrium λ–γ to the γ phase. Following, the diffusion path goes through the γ phase, as shown by *mn*. One important fact should be noted here, as denoted by the blue dotted line in Fig. 9.15b, the diffusion path should intersect the line connecting *Z* and *A* at least once. For any deviation in the composition profile, the diffusion path moves away from the straight line; however, because of the mass balance, it has to go in the opposite direction after intersecting the connecting line. Moreover, a two-phase mixture develops only when the diffusion path passes through a three-phase equilibrium. Let us consider another hypothetical phase diagram and the diffusion couple as explained by Kodentsov et al. [49], as shown in Fig. 9.16. Suppose two alloys *R* and *S* are coupled, so that a ternary phase develops at the interface. Therefore, the diffusion path first cuts through the tie lines between the α and the μ phases, the position of the line depending on the relative phase fractions of the phases. At the interface *I*, three phases, α, μ, and *T* are in equilibrium at specific points of contact, which is represented by a dotted line on the phase diagram. After the phase mixture, only

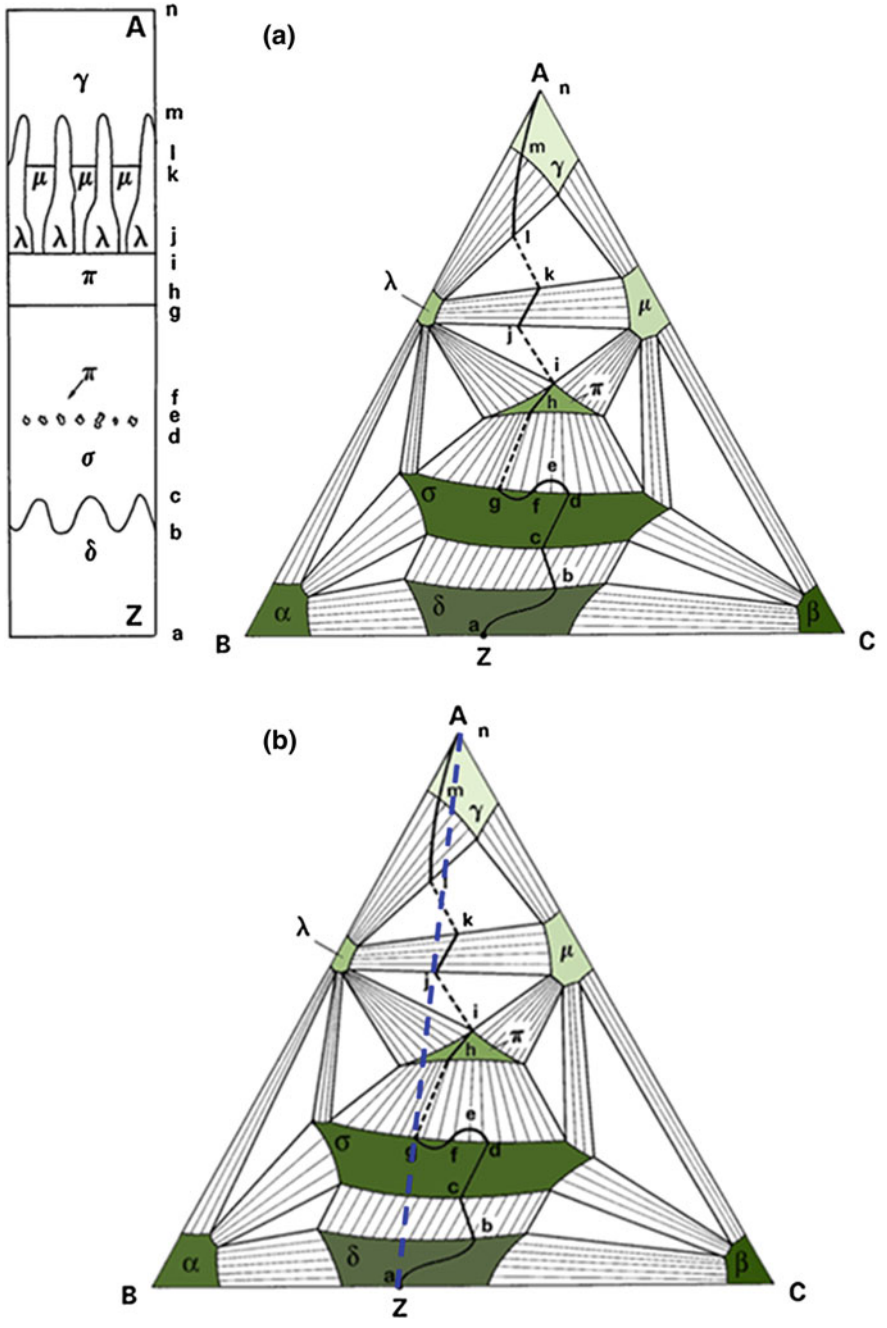

Fig. 9.15 **a** Hypothetical phase diagram showing a diffusion path in a diffusion couple between A and Z and **b** mass balance (*blue dotted*) line showing intersection with diffusion path [49]

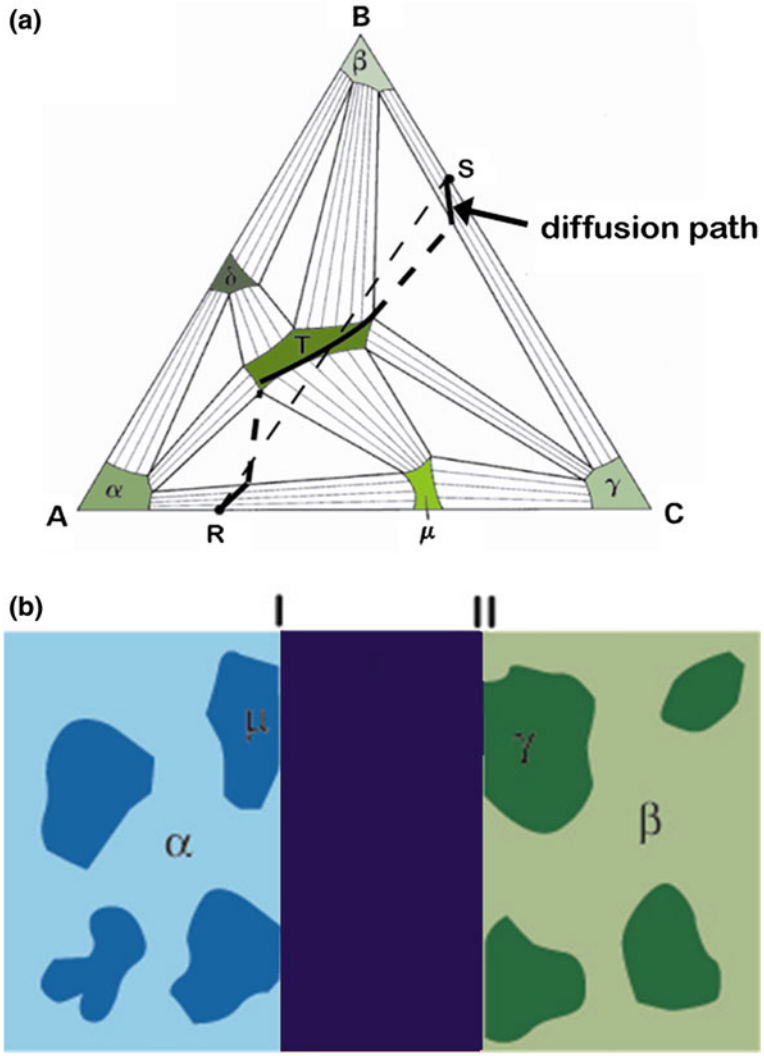

Fig. 9.16 **a** Hypothetical phase diagram and diffusion path **b** a schematic representation of the microstructure [49]

the *T* phase is developed and the diffusion path has to enter the *T* phase from the corner of the triangle representing the three-phase equilibrium. The solid line inside the *T* phase represents the composition variation in the diffusion couple. Since at the interface II, the *T*–*β*–*γ* are again in equilibrium at specific points of contact, the diffusion path shown by a dotted line enters the *β*–*γ* mixture.

Now, let us consider the phase diagram, as shown in Fig. 9.17a [49]. The experimental diffusion couples, 1 and 2 are shown in Fig. 9.17b and c. It can be

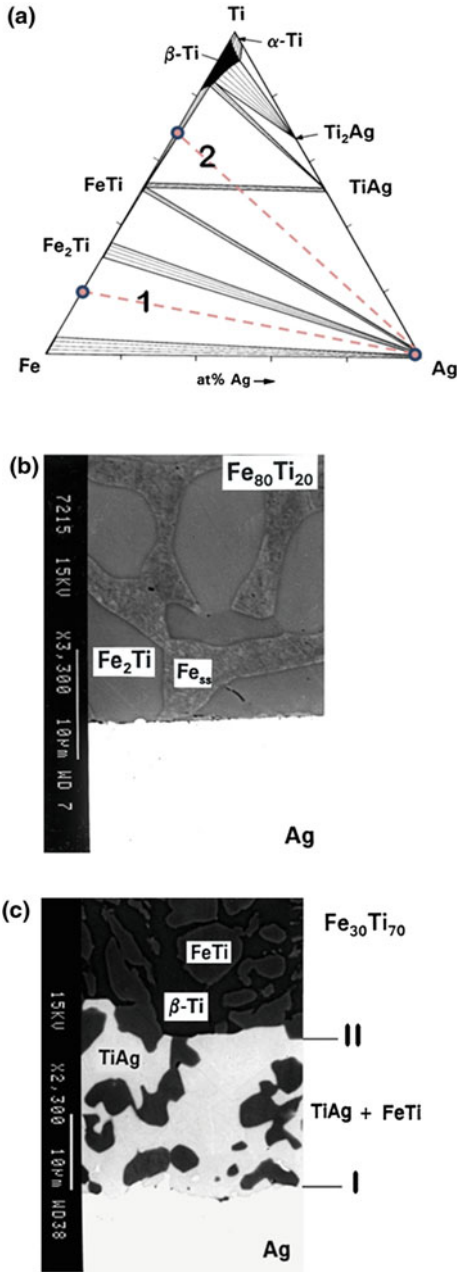

Fig. 9.17 **a** Diffusion couple composition on an isothermal Ag–Fe–Ti phase diagram, interdiffusion zone between **b** Ag/$Fe_{80}Ti_{20}$ and **c** Ag/$Fe_{30}Ti_{70}$ developed after annealing at 850 °C for 100 h [55]

seen that since Ag is in equilibrium with the Fe_{ss} solid solution and Fe_2Ti, nothing develops at the interdiffusion zone of the Ag/$Fe_{80}Ti_{20}$ diffusion couple. On the other hand, the diffusion couple Ag/$Fe_{30}Ti_{70}$ goes through two three-phase

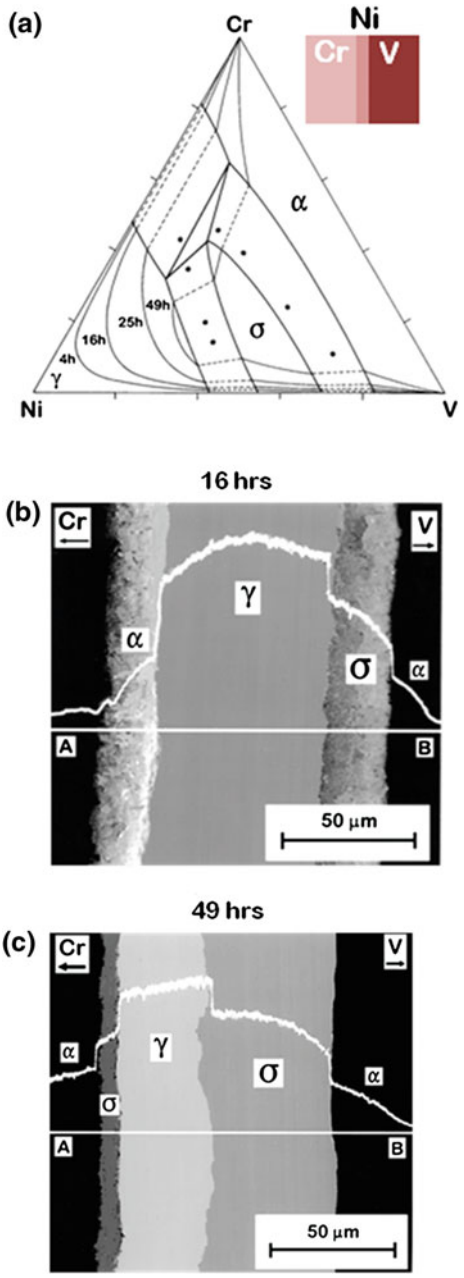

Fig. 9.18 **a** Isothermal cross section of the Ni–Cr–V phase diagram at 1,150 °C. **b** Interdiffusion zones developed after (**b**) 16 and **c** 49 h [49]

equilibriums. Therefore, at the interface I, it has the three-phase equilibrium of Ag–FeTi–TiAg. At the interface II, it has another three-phase equilibrium, that of FeTi–TiAg–β(Ti). In the interdiffusion zone, it grows as a phase mixture of FeTi and TiAg.

At times, by making a single diffusion couple, the information on the whole phase diagram can be developed by examining the interdiffusion zone of a diffusion couple at different times [49, 55], as shown in Fig. 9.18. For example, a very thin layer of Ni was sandwiched between two thick foils of Cr and V at 1,150 °C. The interdiffusion zone was examined at different time intervals for the identification of the phases evolved and measurement of the composition profiles. Using this information and with the additional help of few melted alloys as shown by dots on the phase diagram, one can define the phase boundaries much better. Many times, the diffusion couple experiments alone are not enough to establish the phase diagram. We assume local equilibrium at the interfaces in a diffusion couple, meaning that the chemical potential varies continuously over the interdiffusion zone. In a bulk diffusion couple, all the phases on a diffusion path are expected to grow. However, one or more phases might grow with a very small thickness and it could be very difficult to detect or measure the composition. Furthermore, time and time again, it is difficult to measure the exact phase boundary composition—especially if the composition varies sharply near the interface. When the composition is measured by an electron probe microanalyzer, depending on the gun (tungsten filament or field emission), the composition should be measured at least 1–3 μm inside from the edge of the phase boundary depending on the components. In the case of a sharp change in composition, the measured value could be significantly different from the actual phase boundary composition. If the composition does not change sharply, this difference could be low. Therefore, by combining the measurement of a few equilibrated alloys along with the diffusion couple experiments, we can establish a reasonably accurate phase diagram.

Often, the composition profiles measured from the diffusion couples indicate the need for further studies to establish the phase diagram correctly. For example, the composition range of the μ phase measured in the Ni–Co–W system, as shown in Fig. 9.7a, is higher than the range published in the previous phase diagrams. Similarly, issues were also found in the Co–Ta system, which was corrected by the diffusion couple experiments [58].

References

1. R.T. DeHoff and N. Kulkarni, Materials Research 5 (2002) 209
2. J.S. Kirkaldy and D.J. Young, Diffusion in the condensed state, The Institute of Metals, London 1987.
3. Diffusion in Solids: Recent Developments, Edited by M.A. Dayananda, G.E. Murch, Metallurgical Society of AIME, Warrendale, PA, 1985.
4. L. Onsager, Physical Review 37(1931) 405 and 38 (1932) 2265
5. L. Onsager, Annals of the New York Academy of Sciences 46 (1965) 241

6. V.D. Divya, U. Ramamurty and A. Paul, Philosophical Magazine 93 (2013) 2190
7. J.S. Kirkaldy, Canadian Journal of Physics 35 (1957) 435
8. J. Philibert and A.G. Guy, Comptes Rendus 257 (1963) 2281
9. T.O. Zeibold and R.E. Ogilvie, Trans TMS-AIME 239 (1967) 942-53
10. Y.H. Sohn and M.A. Dayananda, Metallurgical and Materials Transaction A 33 (2002) 3375
11. J.E. Lane and J.S. Kirkaldy, Canadian Journal of Physics 42 (1964) 1643
12. T. Heumann, Zeitschrift für Physikalische Chemie 201 (1952) 168
13. A.G. Guy and J. Philibert, Zeitschrift für Metallkunde, 50 (1965) 841
14. Y.H. Sohn and M.A. Dayananda, Acta Materialia 48 (2000) 1427
15. M.A. Dayananda, Trans TMS AIME 242 (1968) 1369
16. J.D. Whittenberger and M.A. Dayananda, Metallurgical Transactions 1 (1970) 3301
17. P.T. Carlson, M.A. Dayananda and R.E. Grace, Metallurgical Transactions A 6 (1975) 1245
18. C.W. Kim and M.A. Dayananda, Metallurgical Transactions A 14 (1983) 857
19. C.W. Kim and M.A. Dayananda, Metallurgical Transactions A 15 (1984) 649
20. K.E. Kansky and M.A. Dayananda, Metallurgical Transactions A 16 (1985) 1123
21. J.A. Heaney and M.A. Dayananda, Metallurgical Transactions A 17 (1986) 983
22. M.S. Thompson and J. E. Morral, Acta Metallurgica 34 (1986) 339.
23. M.S. Thompson and J.E. Morral, Acta Metallurgica 34 (1986) 2201
24. M.S. Thompson and J.E. Morral, Metallurgical Transactions A 28 (1987) 1565
25. F.J.J. van Loo, G.F. Bastin and J.W.G.A Vrolijk, Metallurgical Transactions A 18 (1987) 801
26. K.J. Rönka, A.A. Kodentsov, P.J.J. van Loon, J.K. Kivilahti and F.J.J. van Loo, Metallurgical and Materials Transactions A 27 (1996) 2229
27. S. Krishtal, A.P. Mokrov, A.V. Akimov, and P.N. Zakharov, Fiz Metal Metalloved 35 (1973) 1234
28. M.K. Stalker, J.E. Morral and A.D. Romig, Metallurgical Transactions A 23 (1992) 3245
29. Y. Minamino, Y. Koizumi, T. Tsuji, Y. Yamada and T. Takahashi, Materials Transactions 44 (2003) 63
30. T. Takahashi, K. Hisayuki, T. Yamane, Y. Minamino and T. Hino, Materials Transactions 44 (2003) 2252
31. M.A. Dayananda and Y.H. Sohn, Scripta Materialia 35 (1996) 683
32. M.A. Dayananda and Y.H. Sohn, Metallurgical and Materials Transactions A 30 (1999) 535
33. J. Cermak and V. Rothova, Acta Materialia 51 (2003) 4411
34. K. Cheng, W. Chen, D. Liu, L. Zhang Y. Du, Scripta Materialia 76 (2014) 5.
35. C. Wagner, Acta Metallurgica 17 (1969) 99
36. V. D. Divya, U. Ramamurty and A. Paul, Metallurgical and Materials Transactions A (2012) 1564
37. A. Paul, Philosophical Magazine 93 (2013) 2297
38. J. Bardeen and C. Herring: Atom Movements, Ed: J.H. Hollomon, ASM, Cleveland, OH, 1951 pp. 87-111
39. L.S. Darken, Atom Movements, Ed: J.H. Hollomon, ASM, Cleveland, OH, 1951 pp. 1-17
40. A.D. LeClaire: Progress in Metal Physics, Ed. B Chalmers, Pergamon, London, 4(1953) 265-332
41. I.V. Belova, G.E. Murch, R. Filipek and M. Danielewski, Acta Materialia, 53 (2005) 4613–4622.
42. J. R. Manning, Metallurgical Transactions 1970, vol. I, pp. 499
43. J.R. Manning. Physical Review B 4 (197) 1111
44. M.A. Dayananda, Metallurgical Transactions 2 (1971) 334
45. L.K. Moleko, A.R. Allnatt, E.L. Allnatt. Philosophical Magazine A 59 (1989) 141
46. S.V. Divinski, F. Hisker, Chr. Herzig, R. Filipek, M. Danielewski, Defects and Diffusion Forum 237-240 (2005) 50
47. K. Holly and M. Danielewski: Physical Review B 50 (1994) 13336
48. R. Filipek, M. Danielewski and R. Bachorczyk, Defect and Diffusion Forum 237-240 (2005) 408

49. AA. Kodentsov, G.F. Bastin and F.J.J. van Loo, Journal of alloys and compounds 320 (2001) 207
50. J.C. Zhao (Ed.), Methods of Phase diagram Determination, Elsevier, Oxford, UK, 2007
51. J.S. Kirkaldy, Canadian Journal of Physics 36 (1958) 917
52. J.S. Kirkaldy, L.C. Brown, Canadian Metallurgical Quaterly 2 (1963) 1250
53. J.B. Clark, Transactions of Metallurgical Society AIME 227 (1963) 1250
54. J.E. Morral, Metallurgical and Materials Transactions 43A (2012) 3462
55. J.A. van Beek, A.A. Kodentsov, F.J.J. van Loo, Journal of Alloys and Compounds 221 (1995) 108
56. A. Davydov, UR Kattner, Journal of Phase Equilibria 24 (2003) 209
57. H. Okamoto Journal of Phase Equilibria 28 (2007) 300
58. V. Baheti, S. Roy, R. Ravi and A. Paul, Intermetallics, 33 (2013) 87

Chapter 10
Short-Circuit Diffusion

In this chapter, we describe the basics of diffusion along short circuits in materials, especially along grain boundaries. The fundamental model of Fisher is represented and discussed in detail. Its approximate solution, which is important from a didactic point of view, is given at first. Then, the exact solutions for instantaneous and constant sources are sketched and a general approach for the analysis of experimental data is formulated. The concept of kinetic regimes of diffusion in materials with a hierarchy of short-circuit paths is introduced and discussed using original experimental data on nanocrystalline alloys. The effect of grain boundary diffusion on interdiffusion phenomena is evaluated.

Short-circuit diffusion paths in metals and alloys have attracted continuous attention because of their technological importance. Alloying, sintering, and oxidation—these are the phenomena, which demand consideration of interface- or dislocation-enhanced diffusion, just to name a couple of them. The importance of the kinetic and thermodynamic properties of interfaces grows considerably when considering the miniaturization of whole devices or the length scale of their typical structure features. The interface structure, its kinetics, stability, and possible structure transformations are strongly affected by solute segregation, both of the alloying components and residual impurities.

Typically one- and two-dimensional defects are considered as short circuits in materials, such as dislocation lines, dislocation walls, grain boundaries (i.e., interfaces between differently oriented grains), and phase boundaries (i.e., interfaces between different phases which could even be equally oriented). Furthermore, such defects are triple lines or triple junctions, i.e., lines along which three differently oriented grains meet in a polycrystalline material, and free surfaces, see Fig. 10.1, where possible short-circuit paths are sketched.

The short-circuit defects, such as dislocations and grain boundaries, could have a strong impact on the process of interdiffusion, especially since the diffusion rates of atoms are typically enhanced along these defects.

A compilation of diffusion rates in a crystalline bulk and along typical short-circuit paths in a metal is presented in Fig. 10.2 using pure silver as an example. As a rule of thumb, the reader can memorize that self-diffusion is fastest along a free surface where the activation energy Q_s constitutes 0.1–0.3 of the activation

A. Paul et al., *Thermodynamics, Diffusion and the Kirkendall Effect in Solids*,
DOI: 10.1007/978-3-319-07461-0_10, © Springer International Publishing Switzerland 2014

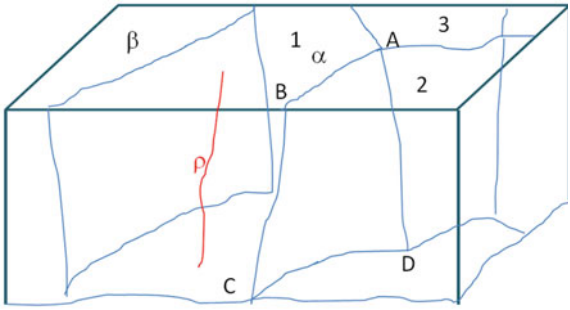

Fig. 10.1 Schematic representation of defects which may act as short-circuit paths in a polycrystalline material: dislocation line ρ; grain boundaries, e.g., *ABCD* one; triple lines as *AD* one; and phase boundaries as the interface between phases α and β

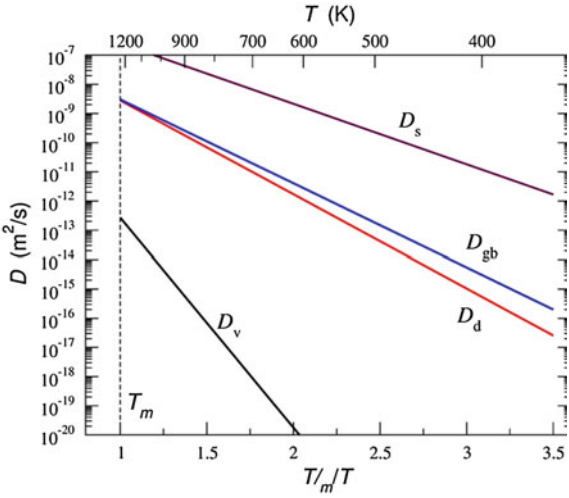

Fig. 10.2 Comparison of experimental data on diffusion rates in pure Ag in bulk, D_v [41], along dislocations, D_d [42], along grain boundaries, D_{gb} [42], and on surface in vacuum, D_s [43]. For generality, the temperature scale is normalized on the melting point of Ag, $T_m = 1{,}235\ K$

energy of the bulk diffusion Q_v. Diffusion rates along high-angle grain boundaries are slower with the activation energy Q_{gb}, which amounts typically to (0.4–0.6)Q_v. Low-angle grain boundaries and dislocation walls reveal typically slower diffusion rates, although these are scarcely studied. Again, as a rule of thumb, one may write that $D_{lb} \approx D_d$ and typically these values amount to $(0.01 \div 0.1)\ D_{gb}$; that is, the corresponding diffusion coefficients do not typically exceed 10 % of the values which correspond to the diffusivities of high-angle grain boundaries D_{gb}. Here, D_{lb} and D_d are the diffusion coefficients of the low-angle grain boundary and of individual dislocations, respectively.

Grain boundary (GB) diffusion measurements are very sensitive to the structural state of GBs. Small changes in atomic positions can result in corresponding changes of energy barriers for diffusion jumps. Since the diffusion rate depends exponentially on the energy barriers, a significant change in the GB diffusivities, both for solute and matrix atoms, can be expected.

The current GB diffusion measurements almost exclusively rely on the model which was suggested by Fisher in 1951 [1]. This is especially true for self-diffusion. Bokstein et al. [2] and later Gibbs [3] recognized that the GB diffusion problem has to be specially treated in solute diffusion cases, namely the solute segregation at grain boundaries has to be taken into account. Subsequent development of the GB diffusion theory is most completely represented by the famous handbook on the fundamentals of grain and interphase boundary diffusion [4].

10.1 Fisher Model of GB Diffusion

The commonly accepted Fisher model [1] is a model of the fast GB diffusion in which a leakage of diffusing atoms to the bulk is normal to GB (Fig. 10.3). The solid is considered as a two-dimensional (xy) object which is characterized by a unique (isotropic) diffusion coefficient D_v. The grain boundary is characterized by a (typically) enhanced diffusion coefficient D_{gb} ($D_{gb} \gg D_v$) and represents a slab of the thickness δ, oriented perpendicularly to the outer surface ($y = 0$).

The diffusion transport of atoms in material occurs then via the fast diffusion of tracer atoms from the outer surface along the grain boundaries with subsequent leakage into the crystalline bulk and further diffusion with typically a lower diffusion rate.

The diffusion problem will be formulated in the following way

$$\frac{\partial c_{gb}}{\partial t} = D_{gb}\left(\frac{\partial^2 c_{gb}}{\partial x^2} + \frac{\partial^2 c_{gb}}{\partial y^2}\right) \quad \text{when } |x| < \delta/2 \tag{10.1a}$$

$$\frac{\partial c_v}{\partial t} = D_v\left(\frac{\partial^2 c_v}{\partial x^2} + \frac{\partial^2 c_v}{\partial y^2}\right) \quad \text{when } |x| > \delta/2 \tag{10.1b}$$

The boundary condition

$$s c_v\left(\pm\delta/2, y, t\right) = c_{gb}(\pm\delta/2, y, t) \tag{10.2}$$

takes into account the GB segregation in the linear form (the so-called Henry isotherm), where s is the segregation coefficient (Fig. 10.3). The definition of s is given by Eq. 10.2 itself, i.e.,

$$s = \frac{c_{gb}(\pm\delta/2, y, t)}{c_v\left(\pm\delta/2, y, t\right)} = \frac{c_{gb}(\pm\delta/2)}{c_v\left(\pm\delta/2\right)} \tag{10.2a}$$

and is considered as a constant in the GB diffusion experiment which does not depend on the position, time, and the solute concentrations, even though the latter

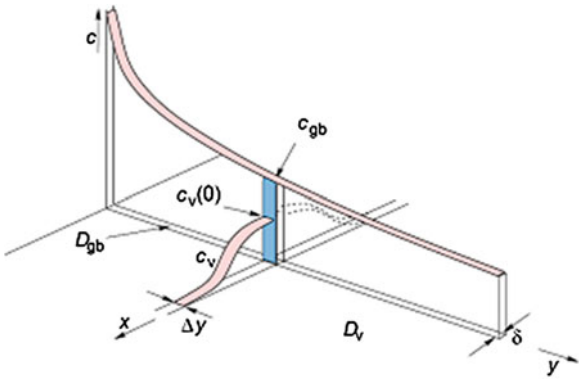

Fig. 10.3 Schematic illustration of Fisher model of GB diffusion updated including probable effect of GB segregation. The distribution of tracer atoms in the GB of the width δ and diffusion coefficient D_{gb} is sketched. Far from the outer surface ($y = 0$), the tracer atoms enter the crystallite bulk by leakage from the grain boundary and they diffuse further with the diffusion coefficient D_v

is not a necessary condition and one can go beyond the linear segregation approximation.

Additionally, we have to take into account the equality of diffusion fluxes perpendicularly to the GB at $\left(\pm\delta/2, y\right)$

$$D_v \left.\frac{\partial c_v}{\partial x}\right|_{|x|=\delta/2} = D_{gb} \left.\frac{\partial c_{gb}}{\partial x}\right|_{|x|=\delta/2} \tag{10.3}$$

Now, we may use the conditions that the GB width δ is small, several atomic distances, and $D_{gb} \gg D_v$. Then, on the same scale, the change of c_{gb} is significantly smaller than that of c_v. Thus, expanding $c_{gb}(x, y, t)$ in a Taylor series around $x = 0$, we have

$$c_{gb}(x, y, t) = c_{gb}(0, y, t) + \frac{x^2}{2} \left.\frac{\partial^2 c_{gb}(x, y, t)}{\partial x^2}\right|_{x=0} + \cdots. \tag{10.4}$$

Here, we neglected the higher-order terms and used the symmetry of the problem with respect to $x = 0$, i.e., $\left.\frac{\partial c_{gb}(x,y,t)}{\partial x}\right|_{x=0} = 0$. Denoting $c_{gb}(0) = c_{gb}(0, y, t)$ and $c''_{gb}(0) = \left.\frac{\partial^2 c_{gb}(x,y,t)}{\partial x^2}\right|_{x=0}$ and substituting Eq. 10.4 into Eq. 10.1a, we arrive at $(|x| < \delta/2)$

$$\begin{aligned}&\frac{\partial}{\partial t}\left[c_{\mathrm{gb}}(0)+\frac{x^2}{2}c''_{\mathrm{gb}}(0)\right]\\&=D_{\mathrm{gb}}\left(\frac{\partial^2}{\partial x^2}\left[c_{\mathrm{gb}}(0)+\frac{x^2}{2}c''_{\mathrm{gb}}(0)\right]+\frac{\partial^2}{\partial y^2}\left[c_{\mathrm{gb}}(0)+\frac{x^2}{2}c''_{\mathrm{gb}}(0)\right]\right)\end{aligned}\tag{10.5}$$

Since both $c_{\mathrm{gb}}(0)$ and $c''_{\mathrm{gb}}(0)$ are functions of y and t and do not depend on x by definition and limiting us by the terms linear in δ, we have

$$\frac{\partial c_{\mathrm{gb}}(0)}{\partial t}=D_{\mathrm{gb}}\left(c''_{\mathrm{gb}}(0)+\frac{\partial^2 c_{\mathrm{gb}}(0)}{\partial y^2}\right)\tag{10.6}$$

Now, we will substitute the expansion (Eq. 10.4) into the boundary conditions (Eqs. 10.2 and 10.3), and again neglecting the term of the order of δ^2 and higher, we will arrive at

$$sc\left(\pm\delta/2,y,t\right)=c_{\mathrm{gb}}(0)\tag{10.7}$$

and

$$D_{\mathrm{v}}\frac{\partial c_{\mathrm{v}}}{\partial x}\bigg|_{|x|=\delta/2}=D_{\mathrm{gb}}\left\{\frac{\partial}{\partial x}\left[c_{\mathrm{gb}}(0)+\frac{x^2}{2}c''_{\mathrm{gb}}(0)\right]\right\}\bigg|_{|x|=\delta/2}=D_{\mathrm{gb}}\frac{\delta}{2}c''_{\mathrm{gb}}(0)\tag{10.8}$$

Equation 10.8 may be rewritten as

$$D_{\mathrm{gb}}c''_{\mathrm{gb}}(0)=\frac{2}{\delta}D_{\mathrm{v}}\frac{\partial c_{\mathrm{v}}}{\partial x}\bigg|_{|x|=\delta/2}\tag{10.9}$$

After substitution of this expression into Eq. 10.6, we arrive at a final system of diffusion equations for the GB diffusion problem

$$\frac{\partial c_{\mathrm{gb}}}{\partial t}=D_{\mathrm{gb}}\frac{\partial^2 c_{\mathrm{gb}}}{\partial y^2}+\frac{2D_{\mathrm{v}}}{\delta}\frac{\partial c_{\mathrm{v}}}{\partial x}\bigg|_{|x|=\delta/2},\quad\text{when } |x|<\delta/2\tag{10.10}$$

and Eq. 10.1b for diffusion in the crystalline bulk, $|x|>\delta/2$. Here, $c_{\mathrm{gb}}\equiv c_{\mathrm{gb}}(0)\equiv c_{\mathrm{gb}}(y,\,t)$, since the GB concentration does not depend on the coordinate x under the approximations used, i.e., the small value of δ and the significant diffusion enhancement in the GB slab.

There is a straightforward interpretation of Eq. 10.10, i.e., the concentration of tracer atoms in a GB is changed due to diffusion along the GB, the first term on the on the right-hand side of the equation, and due to tracer leakage into the crystalline bulk, the rate of which is controlled by the gradient of the bulk concentration near

the GB, the second term on the right-hand side of the equation. The factor 2 in Eq. 10.10 takes into account the fact that the tracer leakage occurs in the two sides of the GB, i.e., in both crystallites.

10.1.1 Approximate Solution of the Fisher Model

An approximate solution of the GB diffusion problem, shown in Eqs. 10.10 and 10.1b, can be found for constant-source initial conditions

$$c_{\mathrm{gb}}(0,t) = s\,c_0, c_{\mathrm{v}}(x,0,t) = c_0, \tag{10.11a}$$

$$c_{\mathrm{gb}}(y,0) = c_{\mathrm{v}}(x,y,0) = 0 \quad \text{for } y > 0, \tag{10.11b}$$

$$c_{\mathrm{gb}}(\infty,t) = c_{\mathrm{v}}(x,\infty,t) = 0 \quad \text{for all } t \tag{10.11c}$$

The specific condition, given in Eq. 10.11a on the outer surface, is introduced to have a consistency with the segregation isotherm, shown in Eq. 10.2, in the bulk. Nowadays, the corresponding solutions, Eqs. 10.18 and 10.23 below, are not widely used, but they are important for didactical reasons.

The following approximations are used:

1. Tracer concentration in a sample is determined by two independent fluxes, (1) atoms diffused via the GB with subsequent outdiffusion toward the crystalline bulk, and (2) direct diffusion in the bulk from the surface with the rate D_{v}.
2. The distribution of tracer atoms that entered the crystalline bulk by the flux (1) is governed by diffusion perpendicular to the grain boundary. Diffusion along the y direction is negligible for this flux $\partial^2 c_{\mathrm{v}}/\partial y^2 \approx 0$.
3. Diffusion along the GB is very fast, and the distribution of tracer atoms along the GB is created within a very short time after the beginning of diffusion, and then, it only slowly evolves with time. Then, for longer time, it can be assumed that $\partial c_{\mathrm{gb}}/\partial t \approx 0$.

Using the second approximation, Eq. 10.1b will be transformed to

$$\frac{\partial c_{\mathrm{v}}}{\partial t} = D_{\mathrm{v}} \frac{\partial^2 c_{\mathrm{v}}}{\partial x^2} \tag{10.12}$$

According to the third approximation, diffusion in the crystal bulk proceeds from a constant source with the concentration of $c_{\mathrm{gb}}(y,t)$ and the corresponding solution of Eq. 10.12 is (see Sect. 3.2.2)

$$c_{\mathrm{v}}(x,y,t) = \frac{c_{\mathrm{gb}}(y,t)}{s} \operatorname{erfc}\left(\frac{|x| - \frac{\delta}{2}}{2\sqrt{D_{\mathrm{v}} t}}\right) \approx \frac{c_{\mathrm{gb}}(y,t)}{s} \operatorname{erfc}\left(\frac{x}{2\sqrt{D_{\mathrm{v}} t}}\right) \tag{10.13}$$

at $|x| > \delta/2$. Here erfc(u) is the complimentary error function defined as

$$\mathrm{erfc}(u) = 1 - erf(u) = \frac{2}{\sqrt{\pi}} \int_u^\infty \exp(-z^2) dz$$

Under the third approximation, Eq. 10.10 transforms to

$$\frac{\partial^2 c_{\mathrm{gb}}}{\partial y^2} = -\frac{2D_{\mathrm{v}}}{\delta D_{\mathrm{gb}}} \frac{\partial c_{\mathrm{v}}}{\partial x}\bigg|_{|x|=\delta/2} \tag{10.14}$$

Since c_{v} as a function of x for the given y and t is known (Eq. 10.13), we have to evaluate its x derivative at $|x| = \delta/2$ and substitute the resulting expression into Eq. 10.15. As a result, we have

$$\frac{\partial^2 c_{\mathrm{gb}}}{\partial y^2} = \frac{2\sqrt{D_{\mathrm{v}}/\pi t}}{s\delta D_{\mathrm{gb}}}\, c_{\mathrm{gb}} \tag{10.15}$$

This is the second-order differential equation, the solution of which in the quasi-stationary case under consideration is

$$c_{\mathrm{gb}}(y,t) = s c_0 \exp\left(-\frac{y}{L}\right) \tag{10.16}$$

where the reduced penetration depth L is defined by

$$L^2 = s\delta D_{\mathrm{gb}} \sqrt{\frac{t}{4D_{\mathrm{v}}}}\sqrt{\pi} = P\sqrt{\frac{t}{4D_{\mathrm{v}}}}\sqrt{\pi} \tag{10.17}$$

Here, the so-called triple product of GB diffusion P, $P = s\delta D_{\mathrm{gb}}$, is introduced.

The resulting distribution of tracer atoms in the crystalline bulk around a grain boundary ($|x| > \delta/2$) is then defined as

$$\begin{aligned} c_{\mathrm{v}}(x,y,t) &= c_{\mathrm{v}}^{\mathrm{I}} + c_{\mathrm{v}}^{\mathrm{II}} \\ &= c_0 \mathrm{erfc}\left(\frac{y}{2\sqrt{D_{\mathrm{v}}t}}\right) + c_0 \exp\left[-\left(\frac{4D_{\mathrm{v}}}{\pi t}\right)^{1/4} \frac{y}{\sqrt{P}}\right] \mathrm{erfc}\left(\frac{|x| - \frac{\delta}{2}}{2\sqrt{D_{\mathrm{v}}t}}\right) \end{aligned} \tag{10.18}$$

Here, the first term $c_{\mathrm{v}}^{\mathrm{I}}$ corresponds to the direct diffusion of tracer atoms from the sample surface into the crystalline bulk via bulk diffusion (see Chap. 3) and the second term $c_{\mathrm{v}}^{\mathrm{II}}$ is the Fisher solution for the GB diffusion problem and it represents the concentration of tracer atoms in the crystalline bulk which appeared there via fast GB diffusion and subsequent outdiffusion from the GB. In the GB slab ($|x| < \delta/2$), the tracer concentration follows Eq. 10.16.

In a typical GB diffusion experiment, one determines the so-called layer concentration of the tracer atoms (or a value which is proportional to it as in the case of radioactive isotopes), $\overline{c}(y,t)$, as a function of the penetration depth y for the given diffusion time t.

Let us represent our sample as a polycrystalline material with a grain size d being much larger than the diffusion length in the crystalline bulk, $d \gg \sqrt{D_v t}$ (the exact conditions for diffusion in polycrystalline material will be considered below), so that the diffusion fluxes from neighboring grain boundaries do not overlap. Following the Fisher model, the GBs are still represented as parallel slabs of the thickness δ which are perpendicular to the outer surface. Then, the tracer concentration in a thin layer perpendicular to the y-axis is determined as

$$\overline{c}(y,t) = \frac{2}{d}\left[\int_0^{\delta/2} c_{gb}(y,t)dx + \int_{\delta/2}^{d/2} \left(c_v^I(y,t) + c_v^{II}(x,y,t)\right)dx\right] \tag{10.19}$$

Here, we have used the symmetry of the GB diffusion problem and integrated only over a half of a grain and the grain boundary, i.e., from $x = 0$ to x = d/2. Since $d \gg \delta$ and c_{gb} and c_v^I do not depend on x, the first two integrals are trivial

$$\begin{aligned}\overline{c}(y,t) &= \frac{2}{d}\left[\frac{\delta}{2}c_{gb}(y,t) + \frac{d}{2}c_v^I(y,t) + \int_{\delta/2}^{d/2} c_v^{II}(x,y,t)dx\right] \\ &= \frac{\delta}{d}c_{gb}(y,t) + c_v^I(y,t) + \frac{2}{d}\int_{\delta/2}^{d/2} c_v^{II}(x,y,t)dx\end{aligned} \tag{10.20}$$

Now, we will use the condition $d \gg \sqrt{D_v t}$ that allows us to extend the upper integration bond to infinity. Performing integration (using the standard formula $\int_u^\infty \mathrm{erfc}(v)dv = \exp(-u^2)/\sqrt{\pi} - u\,\mathrm{erfc}(u)$ which is derived via integration by parts), we obtain

$$\overline{c}(y,t) = \frac{s\delta c_0}{d}\exp\left(-\frac{y}{L}\right) + c_0\mathrm{erfc}\left(\frac{y}{2\sqrt{D_v t}}\right) + 4c_0\exp\left(-\frac{y}{L}\right)\sqrt{\frac{D_v t}{\pi d^2}} \tag{10.21}$$

Or regrouping the terms

$$\overline{c}(y,t) = c_0\mathrm{erfc}\left(\frac{y}{2\sqrt{D_v t}}\right) + c_0\frac{s\delta}{d}\left[1 + \frac{2}{\sqrt{\pi}}\frac{2\sqrt{D_v t}}{s\delta}\right]\exp\left(-\frac{y}{L}\right) \tag{10.22}$$

Thus, in the case of GB diffusion from a constant source, the distribution of tracer atoms in a polycrystalline material is represented by a sum of two terms, as

given in Eq. 10.22, the first term is the result of direct diffusion via the crystalline bulk and follows a complimentary error function solution (see Chap. 2) and the second term is now a signature of the presence of GBs in the material and represents an exponential function of the depth y (for this approximate solution). Since the complimentary error function is nearly $c_0 \exp\left(-\frac{y^2}{4D_v t}\right)$ at large depths and decreases rapidly, the penetration profiles have their specific shape—rapid decrease of the tracer concentration in the near-surface region and a shallow tail which corresponds to the GB diffusion contribution. Thus, at large depths, typically, $y > 5\sqrt{D_v t}$

$$\overline{c}(y,t) \cong c_0 \frac{s\delta}{d}\left[1 + \frac{2}{\sqrt{\pi}}\frac{2\sqrt{D_v t}}{s\delta}\right]\exp\left(-\frac{y}{L}\right) \tag{10.23}$$

The term in square brackets is very important and can be written as $1 + \frac{2}{\sqrt{\pi}}\alpha^{-1}$, where α is the GB diffusion parameter

$$\alpha = \frac{s\delta}{2\sqrt{D_v t}} \tag{10.24}$$

which is the ratio of the *effective* GB diffusion width $s\delta$ and the diffusion length in the crystalline bulk $2\sqrt{D_v t}$. Equation 10.24 is simplified if $\alpha \ll 1$, and at large depths,

$$\overline{c}(y,t) \cong c_0 \frac{4\sqrt{D_v t/\pi}}{d}\exp\left(-\frac{y}{L}\right) \tag{10.25}$$

This solution of the GB diffusion problem (the Fisher solution) corresponds to the case when the amount of tracer atoms residing at the GB—the first term in the square brackets in Eq. 10.23—is negligible with respect to that in the crystalline bulk—the second term.

Equation 10.25 suggests how the GB diffusion parameter, the triple product $P = s\delta D_{gb}$, can be determined from a GB diffusion experiment. One has to plot the logarithm of the tracer concentration as a function of the depth, and having determined the slope of the curve L^{-1}, the triple product will be determined as

$$P = s\delta D_{gb} = 2\sqrt{\frac{D_v}{\pi t}}L^2 = 2\sqrt{\frac{D_v}{\pi t}}\left(-\frac{\partial \ln \overline{c}}{\partial y}\right)^{-2} \tag{10.26}$$

There exists also another way to determine the triple product experimentally. We will directly start from Eq. 10.18 and look on the isoconcentration contours for a $c_v(x, y, t)$ distribution around a GB after the given diffusion time t at large depths when the GB diffusion-related flux dominates (the second term in Eq. 10.18). The x and y derivatives of $c_v(x, y, t)$ at the GB, $|x| = \delta/2$, are (only one sign of x has to

be analyzed in view of the symmetry conditions, we will consider the positive x direction)

$$\frac{\partial c_v(x,y,t)}{\partial x} = c_0 \exp\left[-\frac{y}{L}\right] \frac{2}{\sqrt{\pi}} \exp\left(-\frac{\left(x-\frac{\delta}{2}\right)^2}{4D_v t}\right) \frac{1}{2\sqrt{D_v t}} = \frac{c_0}{\sqrt{\pi D_v t}} \exp\left[-\frac{y}{L}\right] \tag{10.27}$$

and

$$\frac{\partial c_v(x,y,t)}{\partial y} = -\frac{c_0}{L} \exp\left[-\frac{y}{L}\right] \operatorname{erfc}\left(\frac{x-\frac{\delta}{2}}{2\sqrt{D_v t}}\right) = -\frac{c_0}{L} \exp\left[-\frac{y}{L}\right] \tag{10.28}$$

The ratio of the two derivatives is equal to the cotangent of the angle ψ at which the isoconcentration line meets the GB

$$\cot\psi = \frac{\frac{\partial c_v(x,y,t)}{\partial x}}{\frac{\partial c_v(x,y,t)}{\partial y}} = \frac{L}{\sqrt{\pi D_v t}} = \pi^{-1/4} \left[\frac{P}{2D_v\sqrt{D_v t}}\right]^{1/2} = \pi^{-1/4} \left[\frac{s\delta D_{gb}}{2D_v\sqrt{D_v t}}\right]^{1/2} \tag{10.29}$$

Thus, having measured the tracer distribution around the GB after GB diffusion and having determined the angle ψ, we can determine the triple product P as

$$P = s\delta D_{gb} = 2\sqrt{\pi t} D_v^{3/2} \cot^2\psi \tag{10.30}$$

In the case of self-diffusion, the segregation effects are absent and $s = 1$. Then, the triple product P is reduced to the double product $P = \delta D_{gb}$. Thus, in a typical GB diffusion experiment, it is not the GB diffusion coefficient D_{gb} itself, but the triple product $s\delta D_{gb}$ or double product δD_{gb} which can be determined accordingly. The way of determination of s, δ, and D_{gb} individually will be described below.

10.1.2 Exact Solutions of the Fisher Model

Exact solutions of the GB diffusion problem were derived by Whipple [5] and Suzuoka [6] for constant and instantaneous source conditions and generalized by Le Claire [7]. For further details, the reader is referred to the original papers or to the textbook [4]. Here, we will present the final results.

First, the following dimensionless parameters are introduced

$$\xi = \frac{x - \delta/2}{\sqrt{D_v t}} \tag{10.31}$$

$$\eta = \frac{y}{\sqrt{D_v t}} \tag{10.32}$$

$$\beta = (\Delta - 1)\alpha = (\Delta - 1)\frac{s\delta}{2\sqrt{D_v t}} \approx \frac{s\delta D_{gb}}{2D_v\sqrt{D_v t}} \tag{10.33}$$

Here, Δ is the ratio of the GB and bulk diffusion coefficients

$$\Delta = \frac{D_{gb}}{D_v} \tag{10.34}$$

In the case of a constant source, the tracer distribution in the crystalline bulk is

$$\begin{aligned} c_v(\xi, \eta, \beta) &= c_v^I + c_v^{II} \\ &= c_0 \mathrm{erfc}(\eta) + \frac{c_0\eta}{2\sqrt{\pi}} \int_1^\Delta \frac{\exp[-\eta^2/4\sigma]}{\sigma^{3/2}} \mathrm{erfc}\left[\frac{1}{2}\left(\frac{\Delta - 1}{\Delta - \sigma}\right)^{1/2}\left(\xi + \frac{\sigma - 1}{\beta}\right)\right] d\sigma \end{aligned} \tag{10.35}$$

In the case of an instantaneous source, when the amount M of tracer atoms has been applied to the outer surface of the sample, the exact solution of the GB diffusion problem appears as

$$\begin{aligned} c_v(\xi, \eta, \beta) &= c_v^I + c_v^{II} = \frac{M}{\sqrt{\pi D_v t}} \exp\left(-\frac{\eta^2}{4}\right) \\ &+ \frac{M}{\sqrt{\pi D_v t}} \int_1^\Delta \left[\frac{\eta^2}{4\sigma} - \frac{1}{2}\right] \frac{\exp[-\eta^2/4\sigma]}{\sigma^{3/2}} \mathrm{erfc}\left[\frac{1}{2}\left(\frac{\Delta - 1}{\Delta - \sigma}\right)^{1/2}\left(\xi + \frac{\sigma - 1}{\beta}\right)\right] d\sigma \end{aligned} \tag{10.36}$$

In the case of the radiotracer diffusion experiment, when the layer concentration $\overline{c}(y)$ is determined, its distribution is governed by Eq. 10.20 with c_v^I and c_v^{II} determined by either Eq. 10.35 or 10.36. In order to derive the corresponding expressions, we again will consider only the GB diffusion-related term c_v^{II} and neglect the amount of tracer atoms within the GB; that is, $\alpha \ll 1$ is assumed (these conditions will be further classified by the B regime of GB diffusion; see below). Then, the layer tracer concentration is determined by

(*instantaneous source conditions*)

$$\overline{c}(\eta, \beta) \cong \frac{M}{d\sqrt{\pi}} \int_1^\Delta \left[\frac{\eta^2}{\sigma} - 2\right] \frac{\exp[-\eta^2/4\sigma]}{\sigma^{3/2}} \left(\frac{\Delta - \sigma}{\Delta - 1}\right)^{1/2} \left[\frac{\exp(-Y^2)}{\sqrt{\pi}} - Y\mathrm{erfc}(Y)\right] d\sigma \tag{10.37a}$$

and (*constant-source conditions*)

$$\overline{c}(\eta,\beta) \cong \frac{2c_0\eta\sqrt{D_v t}}{d\sqrt{\pi}} \int_1^{\Delta} \left[\frac{\eta^2}{\sigma} - 2\right] \frac{\exp[-\eta^2/4\sigma]}{\sigma^{3/2}} \left(\frac{\Delta-\sigma}{\Delta-1}\right)^{1/2} \left[\frac{\exp(-Y^2)}{\sqrt{\pi}} - Y\,\mathrm{erfc}(Y)\right] d\sigma \tag{10.37b}$$

Here,

$$Y = \frac{\sigma-1}{2\beta}\left(\frac{\Delta-1}{\Delta-\sigma}\right)^{1/2}$$

For the specified geometry, the grain size d has to be considered as the spacing between opposite GBs or the size of sample if a bicrystal with a single GB is considered.

Although Eq. 10.37a or 10.37b could be readily incorporated in a numerical analysis for the fitting of the experimentally determined concentration profile, Le Claire [7] has derived simplified expressions which are easy to handle, and they are commonly used in GB data processing. In this case, the GB diffusion-related tails of the penetration profiles are fitted by the following exponential function

$$\overline{c}(y) = c^* \exp\left[-\left(\frac{y}{\Lambda}\right)^{6/5}\right] \tag{10.38}$$

Here, the effective reduced penetration depth Λ was found to be a function of the GB diffusion parameters

$$\Lambda^2 = P\sqrt{\frac{t}{4D_v}} q\beta^{-p} \tag{10.39}$$

with q and p (generally small) being numerical constants. The specific values of these constants depend on the value of β and the type of initial conditions. The full set of specific constants in dependence on the value of β is given in the textbook [4]. Here, we will list the most important expressions rewriting Eq. 10.39 for the value of the triple (double) product P.

In the case of the *instantaneous source,* the diffusivity value P is determined by ($\beta > 10$)

$$P = 1.322\sqrt{\frac{D_v}{t}}\left(-\frac{\partial \ln \overline{c}}{\partial y^{6/5}}\right)^{-5/3} \tag{10.40}$$

and in the case of the *constant source,* the corresponding expression is ($\beta > 10^4$)

$$P = 1.308\sqrt{\frac{D_v}{t}}\left(-\frac{\partial \ln \overline{c}}{\partial y^{6/5}}\right)^{-5/3} \tag{10.41}$$

The main feature of GB diffusion is the linear dependence of the logarithm of the tracer concentration on the depth to the power of $1.2 = 6/5$. One has to keep in mind that the power 6/5 is only a numerical approximation of the exact solution. A general expression for the triple product P is given by the formula

$$P = q\frac{D_v^p}{t^r}\left(-\frac{\partial \ln \overline{c}}{\partial y^{6/5}}\right)^{-m} \tag{10.42}$$

Here, q, p, r, and m are numerical constants which depend on the type of initial conditions and the value of the parameter β, as seen from Table 10.1.

These solutions are valid for the case when the GBs are perpendicular to the outer surface of the sample. This situation is fulfilled in the case of diffusion in a bicrystal.

In the case of GB diffusion in a polycrystalline material with the grain size d, Levine and MacCallum have analyzed a situation [8] when the diffusion fluxes from different grains do not overlap, but the GB diffusion length Λ is significantly larger than the grain size

$$s\delta \gg d \gg \Lambda \tag{10.43}$$

Then, one has to take into account that the local positions of the GBs are typically inclined with respect to the penetration depth y that modifies the tracer distribution. In the case of instantaneous source conditions, the layer tracer concentration was shown [8] to follow Eq. 10.38 and the triple product of GB diffusion can be determined by Eq. 10.42 with the following values

$$q = 1.946; \quad p = r = 0.5; \; m = 5/3 \quad \text{if } \sqrt{D_v t} \leq 0.025d \tag{10.44}$$

and

$$q = 1.889; \; p = r = 0.5; \; m = 5/3 \quad \text{if } \sqrt{D_v t} = 0.079d \tag{10.45}$$

As a result, compared to the Le Claire approximation of the Whipple exact solution (the first row in Table 10.1), one recognizes that the same slope of the penetration profile in a polycrystalline material corresponds to the triple product P increased by a factor 1.47 with that corresponding to the bicrystalline diffusion experiment. Alternatively, we can deduce that the random orientation of GBs in a polycrystalline material reduces the effective penetration depth and this has to be taken into account in the analysis of the penetration profiles.

Table 10.1 Values of the numerical parameters in Eq. 10.42 depending on the type of initial conditions and the value of the GB diffusion parameter β

Type of initial conditions	β	q	p	r	m
Instantaneous	>10	1.322	0.5	0.5	5/3 = 1.667
	$10 < \beta < 100$	1.084	0.469	0.531	1.718
Constant	$10^2 < \beta < 10^4$	1.206	0.492	0.508	1.681
	$\beta > 10^4$	1.308	0.5	0.5	5/3

10.1.3 Comparison of the Solutions of GB Diffusion Problem

How sensitive is the result of the processing of experimental profiles to the method used? How large an error could be introduced via improper analysis? These questions will be analyzed below.

Below, the results of the radiotracer experiments on the diffusion of a ^{110m}Ag radioisotope in Cu bicrystals will be presented and different methods of analysis are compared. The Cu bicrystal was grown from two single crystalline seeds misoriented one with respect to the other by rotation around a common [001] axis on 36.3°. Correspondingly, almost each fifth atom of one crystal occupies the same positions which would correspond to the (imaginary) atomic positions of the other crystal, if it would be extended to infinity. The resulting grain boundary is termed as nearly Σ5(310)[001] where Σ5 is the inverse number of equivalent atomic positions in both crystals, (310) is the GB plane, and [001] is the rotation axis. The atomic positions near the corresponding grain boundary are shown in Fig. 10.2 as they were obtained by atomistic simulation using molecular dynamics. Such a structure indicates that the diffusion rates along the GB could be higher than those in the crystalline bulk—first of all in view of a more open structure.

For the general description of GB structures, types, and properties, the reader is referred to a number of well-known textbooks [9–12].

Diffusion of Ag along the [001] axis of the GB, the atomistic structure of which is presented in Fig. 10.4, was measured using precise parallel sectioning, and the obtained concentration profiles are plotted in Fig. 10.5. The triple product P was determined using the Fisher approximate solution plotting the profile against the depth y (Fig. 10.5a) and using Wipple (Fig. 10.5b) and Suzuoka (Fig. 10.5c) exact solutions, i.e., by plotting the tracer concentrations against the depth to the 6/5 power.

Figure 10.5 demonstrates some important points about different methods of profile processing. First, the usage of the sectioning method for measurements of GB diffusion has a great advantage in that the exact type of initial conditions is not really important—in this particular case, the difference between the application of Wipple's and Suzuoka's solutions is marginal and below 1 %—far below the typical experimental uncertainty, which amounts in total to about 10–15 % for a high-quality GB diffusion experiment. The approximate Fisher solution underestimates the diffusivity—in this particular case, the triple product is determined to be lower by about 50 % with respect to that which follows from the exact

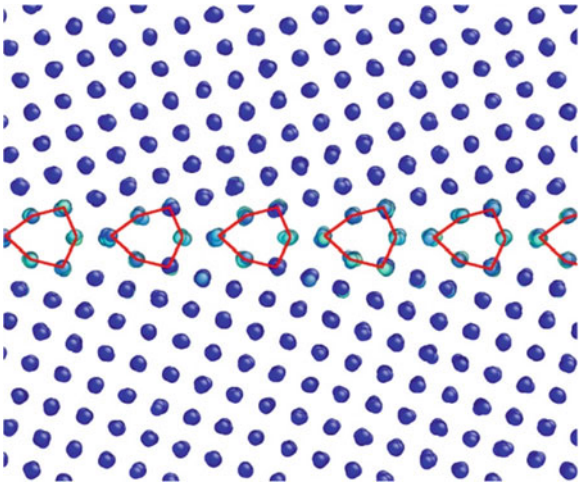

Fig. 10.4 Atomic positions corresponding to Σ5(310)[001] grain boundary as obtained by molecular dynamic simulation. Atoms are *color coded* with respect to the crystallographic symmetry of the neighborhood from *blue* (perfect FCC lattice) to *white* (random lattice)

solutions. However, it can be shown that the ratio of the deduced triple (double) products using approximate and exact solutions, $P^{\text{Fisher}}/P^{\text{Whipple}}$, is almost constant if $\beta > 10$ [7]. Thus, if GB diffusion is measured at different temperatures and uses the Fisher model for data analysis, we would underestimate the triple products at each temperature, but almost a correct value of the activation enthalpy will be determined for the temperature dependence of the deduced diffusivity.

It is hardly possible to prove the correctness of the exact solution with respect to the approximate one by the shape of the experimental profile itself—good-quality fits are obtained using both ln c versus y and ln c versus $y^{6/5}$ dependencies, as depicted in Fig. 10.5. However, if one can measure the GB diffusion-related part of the penetration profile over three or even more decades in decrease of the tracer concentration, it becomes clear that the tracer distribution does follow the ln c versus $y^{6/5}$ dependence, given in Fig. 10.6. Such a textbook example has been measured for Fe diffusion in a nanocrystalline γ-FeNi alloy with the grain size of 100 nm [13]. This example demonstrates the advantage of the serial sectioning method in determination of the GB diffusion parameters, if the penetration profiles were processed to the depths that a significant (over several orders of magnitude) decrease of the tracer concentration related to the GB diffusion contribution was followed.

10.2 Kinetic Regimes of GB Diffusion

In our derivation of the approximate and exact solutions of the GB diffusion problem in Fisher's formulation, several critical assumptions were used:

- The amount of tracer atoms within the GB itself was neglected; see for instance Eqs. 10.23 and 10.25;

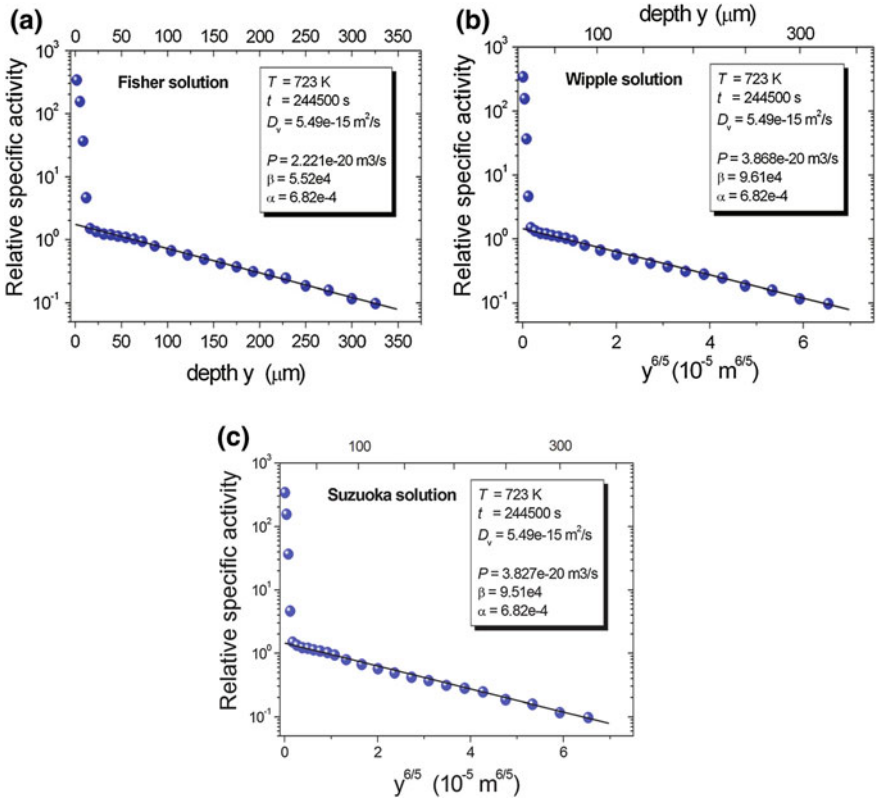

Fig. 10.5 Penetration profiles (i.e., plots of relative specific activity vs. the penetration depth y) for Ag diffusion in Cu near $\Sigma 5(310)[100]$ grain boundary when processed according to Fisher's approximate solution (**a**) and to the Whipple (**b**) and Suzuoka (**c**) exact solutions

- The diffusion fluxes from different GBs were considered as independent and not interfering with one another, as in Eq. 10.13, for instance; and
- Linear (Henry-type) segregation at the GB was assumed, as in Eq. 10.2a.

Below, we will formulate the strict conditions of the application of derived formalism (i.e., approximate Fisher or exact Whipple and Suzuoka solutions) to the GB diffusion problem and will discuss the situations when the basic assumptions above cannot be used. First, we will follow the classification of Harrison [14] who introduced the kinetic regimes of GB diffusion in a polycrystalline material with *one type of short-circuit diffusion paths* (i.e., the grain boundaries featuring the same kinetic, thermodynamic, and structural parameters—the GB diffusion coefficient, segregation factor, and GB width). Then, we will extend this common classification to real materials in which several distinct short-circuit diffusion paths may act simultaneously. The reader can easily imagine a polycrystalline material with a not negligible dislocation density in which diffusion can

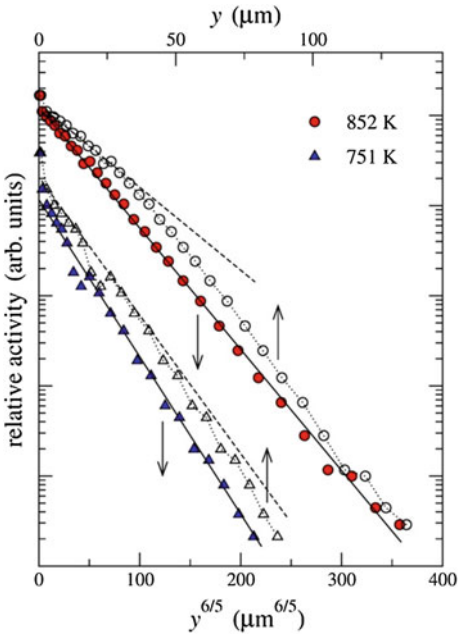

Fig. 10.6 Diffusion of Fe in γ-FeNi nanocrystalline alloy at 852 K and 751 K as analyzed using approximate Fisher solution (*open symbols*, *upper abscise axis*) and exact Suzuoka solution (*filled symbols*, *bottom abscise axis*). Perfect linearity of the profiles in the coordinates of ln c versus $y^{6/5}$ and their systematic curvature in the coordinates of ln c versus y are clearly seen

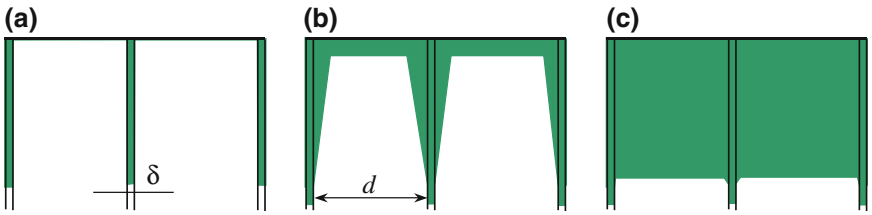

Fig. 10.7 Schematic classification of GB diffusion regimes after Harrison [16]: the C (**a**), B (**b**), and A (**c**) kinetics. The tracer distribution after a given diffusion anneal is sketched (gray regions). The grain boundaries are considered as homogeneous slabs of width δ and diffusivity D_{gb}. The grain size d is indicated

occur along the grain boundaries, dislocations, and in the crystalline bulk with fundamentally different rates.

We are starting with a parallel slab model (i.e., Fisher's model) in which three basic kinetic regimes can be distinguished, the C, B, and A regimes, as shown in Fig. 10.7.

10.2.1 C Regime of GB Diffusion

At low temperatures (short times of diffusion annealing treatment), the bulk diffusion length, $\sqrt{D_v t}$, is small with respect to the effective GB width $s{\cdot}\delta$ and the tracer atoms concentrate exclusively in the GBs (Fig. 10.7a).

Using the GB diffusion parameter α, given in Eq. 10.24—*the Le Claire parameter*—the mathematical condition for this regime corresponds to the relation

$$\alpha \equiv \frac{s\delta}{2\sqrt{D_v t}} > 1 \tag{10.46}$$

As an example, the penetration profiles measured for Ni GB diffusion in polycrystalline Cu (grain size of 400 μm) are shown in Fig. 10.8a.

If the bulk diffusion flux can be neglected, tracer atoms localize within the GBs and their distribution follows standard solutions for diffusion in homogeneous media, which is characterized by the diffusion coefficient $D_{\text{gb.}}$

An *instantaneous source* solution

$$\overline{c} = \frac{\delta M}{d\sqrt{\pi D_{\text{gb}} t}} \exp\left(-\frac{y^2}{4D_{\text{gb}} t}\right) \tag{10.47}$$

and a *constant source* solution

$$\overline{c} = \frac{\delta c_0}{d} \operatorname{erfc}\left(\frac{y}{2\sqrt{D_{\text{gb}} t}}\right) \tag{10.48}$$

Assuming the Gaussian-type solution for GB tracer diffusion, the corresponding GB diffusion coefficient can be determined as

$$D_{\text{gb}} = \frac{1}{4t}\left(-\frac{\partial \ln \overline{c}}{\partial y^2}\right)^{-1} \tag{10.49}$$

Plotting the penetration profiles in the coordinates of the logarithm of concentration against depth squared, one recognizes that the corresponding tails of the profiles do follow the Gaussian-type solution and the slopes of the fit lines allow determination of the GB diffusion coefficients directly.

The main problem of the GB diffusion measurement in the C kinetic regime is related to the extremely low signal which has to be detected from the tiny amount of tracer atoms localized in (a few) grain boundaries of a polycrystalline solid—note the factor δ/d in Eqs. 10.47 and 10.48.

However, using high-end detectors and optimizing counting facilities, it is possible to conduct reliable C-type GB diffusion measurements even for bicrystals with a single grain boundary [15]. It is not possible to overestimate the

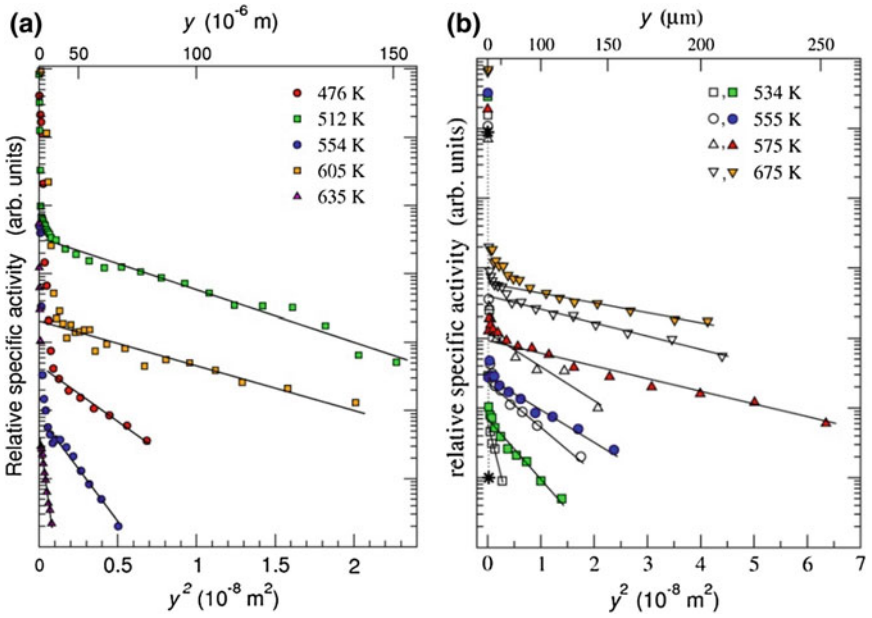

Fig. 10.8 Penetration profiles measured in the C-type kinetic regime for Ni diffusion in polycrystalline Cu [44] (**a**) and for Ag diffusion in Cu Σ5(310)[001] bicrystals [15] (**b**). In **b**, the profiles measured for Ni diffusion along (*filled symbols*) and perpendicular (*open symbols*) to the [001] tilt axis are shown

fundamental importance of such measurements, since they would provide direct information on the GB diffusion coefficient as a function of all crystallographic parameters of the specific interface under investigation. As an example, the penetration profiles for Ag diffusion in Cu Σ5(310)[001] bicrystal are presented in Fig. 10.8b. The atomic structure of the Σ5(310)[001] grain boundary, shown in Fig. 10.4, suggests an anisotropy of GB diffusion and, indeed, faster diffusion along the tilt axis (perpendicular to the image plane) was measured comparing to that perpendicular to the tilt axis (within the image plane in Fig. 10.4 along the interface).

10.2.2 B Regime of GB Diffusion

With increasing temperature, the bulk diffusion length becomes much larger than the GB width δ (for self-diffusion) or the effective GB width $s\delta$ (in the case of solute diffusion) and diffusion out of the GB into the bulk cannot be neglected. If the bulk diffusion fluxes from different GBs do not overlap (Fig. 10.7b), such

conditions correspond to the B kinetics. Formally, the following conditions have to be fulfilled

$$\alpha \equiv \frac{s\delta}{2\sqrt{D_v t}} < 0.1 \tag{10.50}$$

and

$$\Lambda^* \equiv \frac{d}{\sqrt{D_v t}} > 3 \tag{10.51}$$

As it is seen from its definition, Λ^* is the ratio of the grain size to the bulk diffusion length.

This is the regime in which the above-derived expressions, Eqs. 10.25, 10.37a, and 10.38, are valid. As the analysis has shown, the only parameter which can be determined from such a GB diffusion experiment is the triple product P of the segregation factor s, the GB width δ, and the GB diffusivity D_{gb}, $P = s{\cdot}\delta{\cdot}D_{gb}$, as presented in Eqs. 10.26 and 10.42.

Examples of the B-type penetration profiles are presented in Fig. 10.9 for Ni diffusion in polycrystalline Cu (Fig. 10.9a) and for Ag diffusion in Cu Σ5(310)[001] bicrystals (Fig. 10.9b).

The near-surface parts of the penetration profiles are caused by bulk diffusion from the outer surface, the term c_v^1 in Eq. 10.20, and they are omitted from the corresponding fit procedure. A good linearity of the GB diffusion-related parts of the profiles in the coordinates of the logarithm of the concentration against the depth to the power 6/5 is clearly to be seen.

10.2.3 A Regime of GB Diffusion

At even higher temperatures (very long diffusion times), the bulk diffusion fluxes from different GBs overlap, as in Fig. 10.7c, and diffusion proceeds in an effectively homogeneous medium. In the parallel slab model of a polycrystal, the diffusion rate is characterized by an effective diffusion coefficient, D_{eff} [16]

$$D_{eff} = gD_{gb} + (1-g)D_v \tag{10.52}$$

Here, g is the time spent by the diffused atoms within a GB,

$$g = \frac{sf}{1 - f + sf} \tag{10.53}$$

with f being the fraction of GBs in the polycrystal [4].

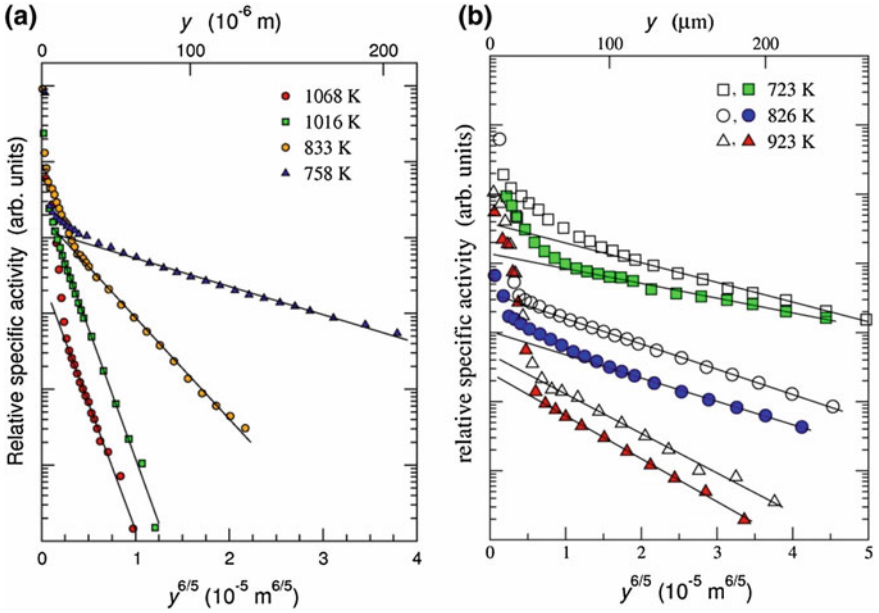

Fig. 10.9 Penetration profiles measured in the B-type kinetic regime **a** for Ni diffusion in polycrystalline Cu and **b** for Ag diffusion in Cu Σ5(310)[001] bicrystals. In **b**, the profiles measured for Ni diffusion along (*filled symbols*) and perpendicular (*open symbols*) to the [001] tilt axis are shown

In the case of a fine-grained polycrystalline material, the Maxwell–Garnet-type relation [17, 18]

$$D_{eff} = D_{\mathrm{v}} \frac{2(1-f)D_{\mathrm{v}} + (1+2f)D_{\mathrm{gb}}}{(2+f)D_{\mathrm{v}} + (1-f)D_{\mathrm{gb}}} \tag{10.54}$$

can be more appropriate. Note that Eq. 10.54 is written for the case of self-diffusion, $s = 1$.

Thus, the following solutions are applicable

$$\overline{c} = \frac{\delta M}{d\sqrt{\pi D_{\mathrm{eff}} t}} \exp\left(-\frac{y^2}{4D_{\mathrm{eff}} t}\right) \tag{10.55}$$

in the case of *instantaneous source* and

$$\overline{c} = \frac{\delta c_0}{d} \operatorname{erfc}\left(\frac{y}{2\sqrt{D_{\mathrm{eff}} t}}\right) \tag{10.56}$$

in the case of a *constant source*.

Table 10.2 Limits of GB diffusion kinetic regimes, shape of the concentration profiles, and the values which can be determined in the parallel slab model

Regime	C	Transition BC	B	Transition AB	A
GB diffusion parameters	$\alpha > 1$	$0.1 < \alpha < 1$	$\alpha < 0.1$	$\alpha < 0.1$	$\alpha < 0.1$
	–	–	$\beta > 10$	$\beta > 2$	
	–	–	$\Lambda^* > 3$	$0.4 < \Lambda^* < 3$	$\Lambda^* < 0.4$
Profile shape	$\overline{c} \sim \exp(-qy^2)$	–	$\overline{c} \sim \exp(-qy^{6/5})$	$\overline{c} \sim \exp(-qy^{3/2})$	$\overline{c} \sim \exp(-qy^2)$
	D_{gb}	D_{gb} and P	P	D_{gb}	D_{eff}

An example of penetration profile measured in the A-type kinetic regime will be presented below.

Table 10.2 gives a general overview of the GB diffusion regimes with relevant parameters and the quantities which can be measured in the case of self-diffusion ($s = 1$).

In Table 10.2, two transition regimes B–C and A–B are listed, and they will be discussed shortly below.

10.2.4 BC Transition Regime of GB Diffusion

Often, GB diffusion measurements in a coarse-grained material cannot be performed under strict C or B kinetic regime conditions and they fall into transition kinetics from the C to B regime. This is especially true for solute diffusion when the exact value of the segregation factor is not known a priori. An example of a penetration profile measured in the transition BC regime for Ni diffusion in Cu is presented in Fig. 10.10a.

Self-consistent determination of the segregation factor s for Ni in Cu allowed unambiguous analysis of the profile which was measured for the value of $\alpha = 0.66$. According to Table 10.2, this value corresponds to the transition BC regime. Figure 10.10a suggests that such a profile reveals a systematic deviation from the anticipated behavior when analyzed according to both B and C kinetic conditions.

In Fig. 10.10b, the determined GB diffusion coefficients D_{gb} are plotted as a function of inverse temperature and a very important feature of data processing is immediately seen. The filled symbols in Fig. 10.10b represent the data points measured in the true C-type conditions and determined applying Eq. 10.49, while the open square corresponds to the profile represented in Fig. 10.10a and analyzed as hypothetically measured in the C regime. Such improper processing of the GB diffusion profiles results in an underestimation of the true diffusion coefficient, in the particular case, by a factor of three.

In order to prove the diffusion regime, the diffusion experiment at 635 K was repeated with a significantly shorter diffusion time, by a factor of 20. A simple inspection of Eq. 10.46 indicates immediately that the values of α will be larger

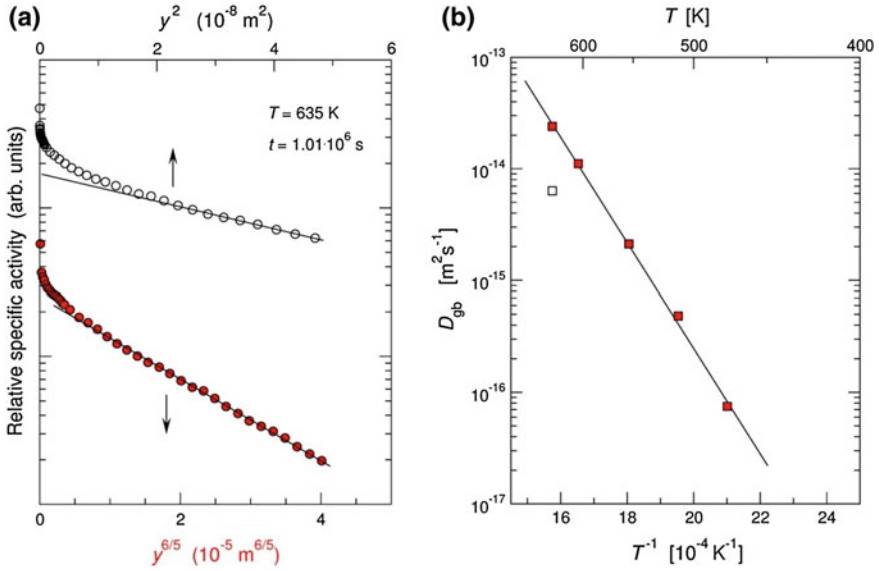

Fig. 10.10 An example of a penetration profile measured at $T = 635$ K for Ni diffusion in polycrystalline Cu and plotted according to the **a** B regime (*bottom abscise axis*) or C regime (*upper abscise axis*) of GB diffusion and **b** the Arrhenius plot for the determined D_{gb} values

and the C-type kinetic regime will be promoted with $\alpha = 13$. Indeed, the newly determined diffusion coefficient fits perfectly the Arrhenius line, denoted by the filled symbols in Fig. 10.10b.

Still, there is a possibility to process the penetration profiles measured in the transition regime introducing correction factors for the determined diffusion coefficient D_{gb} (analysis according to the C kinetics) or the triple product P (B kinetics). As a most appropriate method, one can use a modification of the approach of Szabo with co-workers [19]. The following flowchart is proposed in such cases:

1. The penetration profiles are first replotted as a function of the reduced depth $\alpha w^{4/5}$, where w is determined by

$$w = \frac{y}{\sqrt{P}}\left(\frac{4D_v}{t}\right)^{1/4} = \frac{y}{\sqrt{s\delta D_{gb}}}\left(\frac{4D_v}{t}\right)^{1/4} \tag{10.57}$$

and α is given by Eq. 10.24. The determination of α and w requires knowledge of s, δ, and D_{gb}. The self-consistent approach for determination of these parameters will be described below in more detail. Here, in order to have a first approximation of w, the profile is recommended to be analyzed as measured in the B regime, if $\alpha < 0.5$, and as measured in the C regime at $\alpha > 0.5$. In this case, the values of P or D_{gb} will be determined from the corresponding profile slope and the reduced depths w and accordingly the product $\alpha w^{4/5}$ will be estimated.

2. Using the graphical dependencies plotted in [19], the correction factor for the deduced diffusion coefficient can be determined. Pure numerical fitting reveals that the following functions reproduce the correction factors calculated in [19] to an accuracy better than 1 % in the interval of interest of $0.01 \leq \alpha w^{4/5} \leq 30$

$$G_1 \equiv \frac{(P)^{\text{exp}}}{(P)^{\text{theor}}} = \frac{(9 + 16Q) - 3}{2} + \frac{\exp(1.504 - 1.840S)}{1 + \exp(-(S - 0.873)/0.226)} \tag{10.58}$$

where

$$Q = \frac{1 - \exp(-0.700 + 0.967S)}{1 + \exp((S - 0.873)/0.226)}$$

and

$$S = \ln\left(\alpha w^{4/5}\right)$$

3. Having determined the correction factor for the apparent triple product G_1, one can use the relation

$$G_2 = (1 - G_1)(1 + G_1/4) \tag{10.59}$$

in order to determine the corresponding correction factor for the apparent GB diffusion coefficient, G_2, which is defined as

$$G_2 \equiv \frac{\left(D_{\text{gb}}\right)^{\text{exp}}}{\left(D_{\text{gb}}\right)^{\text{theor}}} \tag{10.60}$$

In these expressions, $(P)^{\text{exp}}$ and $(D_{\text{gb}})^{\text{exp}}$ stand for the apparent diffusion parameters which would be determined from the penetration profiles analyzing them according to the B or C kinetic regime, respectively. The quantities $(P)^{\text{theor}}$ and $(D_{\text{gb}})^{\text{theor}}$ denote the corresponding theoretical values. The dependencies $G_1(\alpha w^{4/5})$ and $G_2(\alpha w^{4/5})$ are represented in Fig. 10.11.

4. Then, new corrected values of P will be obtained, which allows us to give a next estimate of both, the segregation factor and the GB diffusivity, and the evaluations have to be repeated from the step #1 till convergence is reached. Typically, only several iterations are necessary.

10.2.5 AB Transition Regime of GB Diffusion

If GB diffusion is measured in a nanocrystalline or ultrafine-grained material with a small and *stable* grain size (even at moderately high temperatures), the bulk

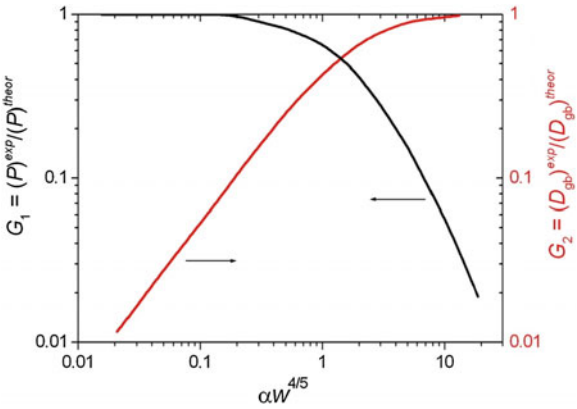

Fig. 10.11 Dependencies of the corrections factors G_1 and G_2 on the reduced depth $\alpha w^{4/5}$ as determined by approximate Eqs. 10.58 and 10.59

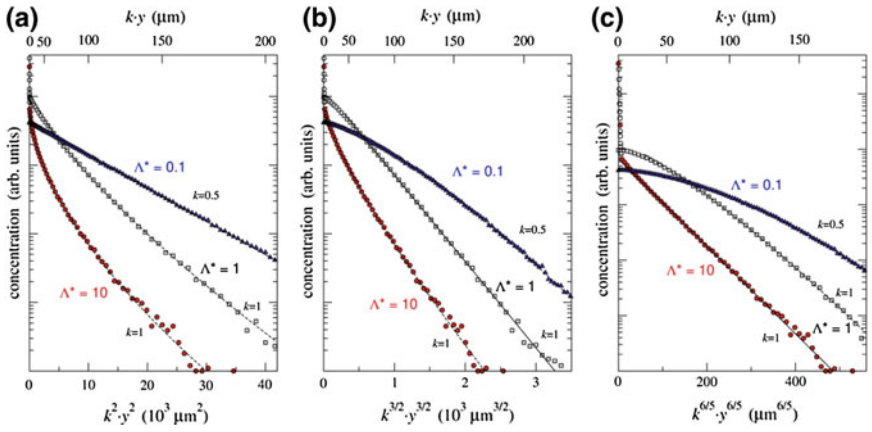

Fig. 10.12 Simulated penetration profiles at $D_v = 10^{-14}$ m^2/s, $t = 100$ s, $D_{gb} = 10^{-9}$ m^2/s, $\delta = 10^{-8}$ m, $\alpha = 0.005$, and $\beta = 500$ for grain size $d = 10^{-7}$ m, 10^{-6} m, and 10^{-5} m. The profiles are represented according to the A (**a**), AB (**b**), and B (**c**) kinetic regime conditions. The value of the parameter Λ^* is indicated. The parameter k is a scaling factor

diffusion length may become comparable to the grain size and the parameter Λ^*, taken from Eq. 10.51, would be about unity. In such a case, the penetration profiles neither follow a Gaussian solution, $\ln \overline{c} \sim y^2$ (the A kinetics), nor a Suzuoka's solution, $\ln \overline{c} \sim y^{6/5}$ (the B kinetics). In Fig. 10.12, a set of model penetration profiles are presented which are calculated with the following set of parameters: $D_v = 10^{-14}$ m^2/s, $t = 100$ s, $D_{gb} = 10^{-9}$ m^2/s, $\delta = 10^{-8}$ m, $\alpha = 0.005$, and $\beta = 500$ for grain size $d = 10^{-7}$ m, 10^{-6} m, and 10^{-5} m, thus by varying the parameter Λ^* from 10 to 1 and finally to 0.1, respectively.

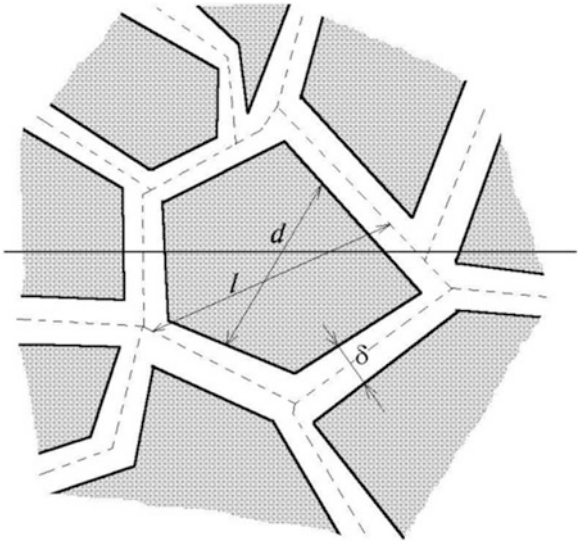

Fig. 10.13 Definition of geometric parameters for a nanocrystalline material. An arbitrary section through the body perpendicular to the diffusion direction is shown

Figure 10.12 suggests clearly (compare with Table 10.2) that if $\alpha < 0.1$ and $\beta > 10$, the conditions of the B kinetics are fulfilled at $\Lambda^* = 0.1$ and those of the A kinetics hold at $\Lambda^* = 10$ and the profiles are strictly linear when plotted against $y^{6/5}$ in the former case and against y^2 in the latter. However, if $\Lambda^* = 1$, unusual curvature of the profiles for both presentations is obvious, as seen from Fig. 10.12a, c.

This case of $\Lambda^* \approx 1$ has to be analyzed further. In the derivation, we will limit ourselves to the case of self-diffusion ($s = 1$).

Let us consider a general polyhedral polycrystalline body with an averaged grain size $\langle d \rangle$ and effective GB thickness δ. Since δ may be comparable with d (as in the case of nanocrystals), we will introduce a parameter l, $l \cong \langle d \rangle + \delta$, as shown in Fig. 10.13. This will allow us to use common geometric theorems for a polycrystalline body with an arbitrary grain size $0 \leq d \leq \infty$. Then, the volume fraction ε of the GB material will be determined by $\varepsilon = 2\delta/l \cong 2/(1 + < d >/\delta)$.

Let c_{gb} be the concentration of the diffusant in the grain boundary materials. Considering a one-dimensional problem and assuming that $c_{gb} = c_{gb}(y, t)$ depends only on the depth y and time t, the master equation for the GB diffusion in a polycrystalline body will be

$$\varepsilon \frac{\partial c_{gb}(y,t)}{\partial t} = \frac{2\varepsilon(1+\varepsilon/2)}{3} D_{gb} \frac{\partial^2 c_{gb}(y,t)}{\partial^2 y} - \sigma F \tag{10.61}$$

The following boundary conditions are valid for a *constant source*

$$c_{gb}(0,t) = 1; \quad c_{gb}(\infty,t) = 0; \quad c_{gb}(y,0) = 0, \quad y > 0 \tag{10.61a}$$

and for an *instantaneous source*

$$c_{\mathrm{gb}}(\infty, t) = 0; \quad c_{\mathrm{gb}}(y, 0) = M\delta(y), \left.\frac{\partial c_{\mathrm{gb}}}{\partial y}_{y=0}\right| = \frac{M\delta(t)}{D_{\mathrm{gb}}} \tag{10.61b}$$

Here, σ is the total GB surface area per unit volume, which may be estimated as $\sigma = 2\varepsilon(1 - \varepsilon)^2$, F is the effective flux of the tracer atoms into the grain volume from GBs, M is the amount of the tracer material for the instantaneous source, and $\delta(y)$ is the standard delta function.

The flux $F = F(y, t)$ into the grain interior is

$$F(y, t) = \int_0^t \frac{\partial c_{\mathrm{gb}}(y, \tau)}{\partial \tau} G(t - \tau) d\tau \tag{10.62}$$

where $G(t)$ is the flux into an averaged grain with the diffusivity D_{v} at zero initial diffusant concentration on its boundaries. The true form of G depends on the grain shapes. It is possible to derive their analytical formula for simple geometric forms. However, only approximate expressions can be obtained in a general case. Having introduced the reduced time $\tau = (4D_{\mathrm{v}}/\delta^2)t$, an empirical function may be used,

$$G(t) = G(\tau) = \frac{2D_{\mathrm{v}}}{\delta\sqrt{\pi\tau}} \exp\left\{-\varepsilon^2\tau\right\} \tag{10.63}$$

Let us introduce also a reduced penetration depth $\eta = \left[\frac{1}{\delta}\sqrt{\frac{6D_{\mathrm{v}}}{D_{\mathrm{gb}}(1+\varepsilon/2)}}\right] y = \left[\frac{1}{\delta}\sqrt{\frac{6}{\Delta(1+\varepsilon/2)}}\right] y$. Here, $\Delta = D_{\mathrm{gb}}/D_{\mathrm{v}}$. Then, Eq. 10.61 can be rewritten as

$$\frac{\partial c_{\mathrm{gb}}}{\partial \tau} = \frac{\partial^2 c_{\mathrm{gb}}}{\partial^2 \eta} - \frac{\delta(1 - \varepsilon)^2}{2D_{\mathrm{v}}} G(\eta, \tau) \tag{10.64}$$

The total concentration of the diffusant $\overline{c}$ averaged over a section of the polycrystalline body will be

$$\overline{c}(\eta, \tau) = \varepsilon c_{\mathrm{gb}}(\eta, \tau) + \sigma \int_0^\tau c_{\mathrm{v}}(\eta, v) G(\tau - v) dv \tag{10.65}$$

where c_{v} is the concentration inside the grains. It is convenient to use the Laplace transformation to solve Eqs. 10.61–10.64. By applying the Laplace transformation to Eq. 10.64, the general solution may be presented as (boundary conditions for a constant source being taken into account)

$$\overline{c}(\eta,\tau)=\frac{\varepsilon}{2\pi i}\int\limits_{\varsigma_0-i\infty}^{\varsigma_0+i\infty}\tilde{C}(\eta,\tau,p)dp$$
$$=\frac{\varepsilon}{2\pi i}\int\limits_{\varsigma_0-i\infty}^{\varsigma_0+i\infty}(e^{p\tau}-1)\frac{1}{p}\left[1+\frac{(1-\varepsilon)^2}{\sqrt{p+\varepsilon^2}}\right]\exp\left\{-\eta\left[p\left(1+\frac{(1-\varepsilon)^2}{\sqrt{p+\varepsilon^2}}\right)\right]^{1/2}\right\}dp \tag{10.66}$$

where the path of integration is to the right side of all singularities of the integrand $\tilde{C}$. Since the initial concentration is zero, the term $e^{p\tau}$ may be replaced by $(e^{p\tau}-1)$. We have two singularity points in the complex plane, $p=0$ and $-\varepsilon^2$ (see Fig. 10.14). Since the integrand has no singularities inside the region R, the integral along the contour L must be zero. The integrals on C_R and $C_{\rho'}$ approach zero at $R\to\infty$ and $\rho'\to 0$, respectively, and $\frac{\varepsilon}{2\pi i}\int_{C_\rho}\tilde{C}dp\to\varepsilon+(1-\varepsilon)^2$ at $\rho\to 0$. This finite value is self-extracted in the final form of the integral in Eq. 10.66. Thus, the complex integral along the line $\zeta_0\pm i\infty$ can be transformed to a sum of the integrals along four line segments (Fig. 10.13)

$$\overline{c}(\eta,\tau)=\frac{\varepsilon}{\pi}\int\limits_0^{\varepsilon^2}(1-e^{-\varsigma\tau})\frac{\Phi}{\varsigma}\sin\left(\eta\sqrt{\varsigma\Phi}\right)d\varsigma$$
$$+\frac{\varepsilon}{\pi}\int\limits_{\varepsilon^2}^{\infty}(1-e^{-\varsigma\tau})\frac{\exp\left\{-\eta\sqrt{\varsigma}A\sin\frac{\varphi}{2}\right\}}{\varsigma}\left[\frac{(1-\varepsilon)^2}{\sqrt{\varsigma-\varepsilon^2}}\cos B+\sin B\right]d\varsigma \tag{10.67}$$

Here, $\Phi=1+\frac{(1-\varepsilon)^2}{\sqrt{\varepsilon^2-\eta}}$; $A=\left[1+\frac{(1-\varepsilon)^4}{\eta-\varepsilon^2}\right]^{1/4}$; $B=\eta\sqrt{\varsigma}A\cos\frac{\varphi}{2}$; $\cos\varphi=\left[1+\frac{(1-\varepsilon)^4}{\eta-\varepsilon^2}\right]^{-1}$.

This form of solution allows performing a transition to $\varepsilon\to 1$ ($d\to 0$) limit, and the general solution for GB diffusion in a pure grain boundary material from a constant source will be obtained

$$C(\eta,\tau)=1-\frac{1}{\pi}\int\limits_0^{\infty}e^{-\varsigma\tau}\frac{\sin\left(\eta\sqrt{\varsigma}\right)}{\varsigma}d\varsigma \tag{10.68}$$

In an opposite case, a Fisher-like solution will be derived. Indeed, let us make a transition to $\varepsilon\to 0$ limit in Eq. 10.67. The first term in Eq. 10.67 gives therewith a contribution with the magnitude of only about ε^2 and can be neglected. Thus, it remains to evaluate the last term. Since $A\underset{\varepsilon\to 0}{\longrightarrow}\left(\frac{\eta+1}{\eta}\right)^{\frac{1}{4}}$, we may write

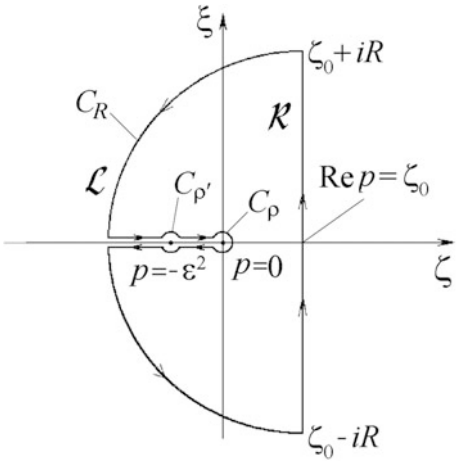

Fig. 10.14 Singularity points and the integration contour L in calculation of the integral Eq. 10.66

$$\overline{c} = \frac{\varepsilon}{\pi}\int_0^\infty (1-e^{-\varsigma\tau})\frac{\exp\left\{-\eta\left(\frac{\varsigma}{4(1+\varsigma)}\right)^{1/4}\right\}}{\varsigma} \times \left[\sin\left(\eta\left(\frac{\varsigma(1+2\varsigma)^2}{4(1+\eta)}\right)^{1/4}\right) + \frac{1}{\sqrt{\eta}}\cos\left(\eta\left(\frac{\varsigma(1+2\varsigma)^2}{4(1+\eta)}\right)^{1/4}\right)\right] d\varsigma \tag{10.69}$$

Let us evaluate the coefficient $\gamma = -\frac{d\ln C}{d\eta}\Big|_{\eta=0} = -\frac{1}{C}\frac{1}{\delta}\left(\frac{6}{\Lambda}\right)^{1/2}\frac{dC}{dy}\Big|_{y=0}$ representing the slope of the relevant curve. After simple algebraic transformations, one may find that at $\varepsilon \to 0$ $C(y=0) = 2\varepsilon\sqrt{\frac{\tau}{\pi}}$ and

$$\left.\frac{dC}{d\eta}\right|_{\substack{\eta=0\\ \varepsilon\to 0}} = \frac{\varepsilon}{\pi\sqrt{2}}\int_0^\infty \frac{1-e^{-\varsigma\tau}}{\varsigma^{5/4}(1+\varsigma)^{1/4}}\left[\sqrt{\varsigma+2\varsigma^2}-1\right]d\varsigma \cong \frac{2\sqrt{6}}{\pi^{1/4}}\sqrt{\frac{D_v}{\delta D_{gb}}}\frac{1}{(\pi D_v t)^{1/4}}\int_0^\infty \sqrt{v}\exp(-v^2)dv \tag{10.70}$$

The estimate of the integral in Eq. 10.70 suggests the slope γ in the present solution differs and distinguishes from Fisher's result only by a factor of 1.59. About the same factor (~ 1.57) was derived by Levine and McCallum for GB diffusion in a polycrystalline material [8]. The numerical analysis shows that the concentration distribution is characterized by the product $\eta \cdot \tau^{-1/4} = \eta' \cdot \beta^{-1/2}\left(\frac{3}{2+\varepsilon}\right)^{1/2}$ where $\eta' = y/\sqrt{D_v t}$ and β are conventional dimensionless parameters. Thus, Eq. 10.67 allows us to examine the GB diffusivity in the whole range of grain sizes.

In a similar way, one can derive the solution for the instantaneous source,

$$\overline{c}(\eta,\tau) \cong \int_0^{\varepsilon^2} e^{-\varsigma\tau}\frac{\Phi^{3/2}}{\sqrt{\varsigma}}\cos\left(\eta\sqrt{\varsigma\Phi}\right)d\varsigma - \int_{\varepsilon^2}^{\infty} e^{-\varsigma\tau}\frac{A\exp\left(-\eta\sqrt{\varsigma}A\sin\frac{\phi}{2}\right)}{\sqrt{\varsigma}}\left[\left(\sin\frac{\phi}{2}+\frac{(1-\varepsilon)^2}{\sqrt{\varsigma-\varepsilon^2}}\cos\frac{\phi}{2}\right)\sin B+\left(\frac{(1-\varepsilon)^2}{\sqrt{\varsigma-\varepsilon^2}}\sin\frac{\phi}{2}-\cos\frac{\phi}{2}\right)\cos B\right]d\varsigma \tag{10.71}$$

Substituting $\varepsilon = 1$, it is possible to obtain the standard Gaussian solution for diffusion in a homogeneous media from an instantaneous source,

$$\overline{c}(\eta,\tau) = \frac{M}{\sqrt{\pi D_{\mathrm{gb}}t}}\exp\left(-\frac{\eta^2}{4D_{\mathrm{gb}}t}\right) \tag{10.72}$$

Equations 10.67 and 10.69 cannot be further simplified and require a numerical evaluation. A detailed analysis in terms of stretched exponential functions such as $\ln\overline{c} \sim y^m$ demonstrates that in the case of small values of $\varepsilon^2\tau \sim \frac{4D_{\mathrm{v}}t}{l^2}$ and $\tau \sim \frac{4D_{\mathrm{v}}t}{\delta^2}$ (that corresponds to the C type of diffusion kinetics), the power $m = 2$. In the case of the B regime (large values of τ and small values of $\varepsilon^2\tau$), $m = 6/5$. The diffusion behavior in the transition regime (large values of τ and $\varepsilon^2\tau \approx 1$) is the most interesting and unusual power dependence with $m = 3/2$ being observed. In Fig. 10.12b, the simulated penetration profiles are plotted as a function of $y^{3/2}$. Almost perfect linearity of the profile with $\Lambda^* = 4(\varepsilon^2\tau)^{-1} = 1$ is clearly to be seen.

We have shown that the tracer distribution in the case of the C regime of GB diffusion allows determination of the value of D_{gb}, while the double product δD_{gb} (or the triple product $s\delta D_{\mathrm{gb}}$ for solute diffusion) is determined in the case of the B kinetic regime. Effective penetration in the B regime is described by the reduced depth $w = \eta \cdot \tau^{-1/4}$. On the other hand, the effective penetration in the transition AB regime is determined by the value

$$w^* = \eta\tau^{-0.45} = \left[\frac{1}{\delta}\sqrt{\frac{6D_{\mathrm{v}}}{D_{\mathrm{gb}}(1+\varepsilon/2)}}\left(\frac{4D_{\mathrm{v}}}{\delta^2}\right)^{-0.45}\right]yt^{-0.45} \tag{10.73}$$

This quantity is related to the standard reduced depth w via the following expression: $w^* = w\cdot\tau^{-0.2}\left(\frac{3}{2+\varepsilon}\right)^{1/2} = w\left(\frac{\Delta}{\beta}\right)^{-0.1}\left(\frac{3}{2+\varepsilon}\right)^{1/2}$. The corresponding slopes, $S = -d\ln\overline{c}/dw^{3/2}$, are a weak function of $\varepsilon^2\tau$ and $S \cong 1.128$ at $\varepsilon^2\tau \cong 1$. This fact suggests the following expression for the determination of the GB diffusion coefficient in this regime

$$D_{\mathrm{gb}} \cong \frac{5}{4}\left(\frac{4D_{\mathrm{v}}t}{\delta^2}\right)^{0.09}\frac{1}{t}\left(\frac{S}{S'_{\mathrm{exp}}}\right)^{1.33} = \frac{5}{4}\frac{\tau^{0.09}}{t}\left(\frac{S}{S'_{\mathrm{exp}}}\right)^{1.33} \tag{10.74}$$

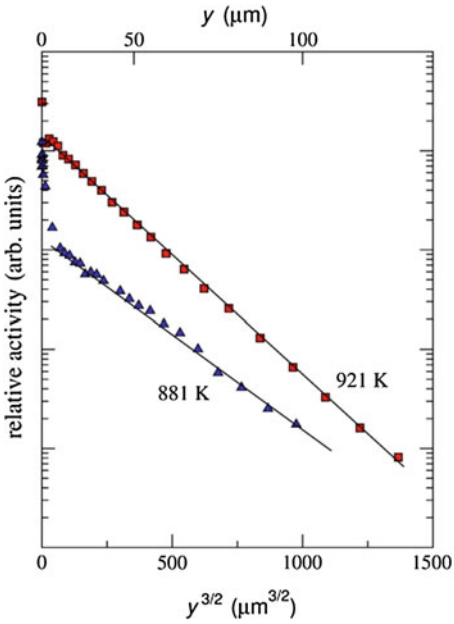

Fig. 10.15 Examples of penetration profiles measured in the AB transition regime for Fe diffusion in nanocrystalline γ-FeNi alloy [13]

Here, $S'_{\text{exp}} = -d \ln \overline{c}/dy^{3/2}$ is to be determined by fitting of the experimental profile. Inserting the numerical factors, this expression is written as

$$D_{\text{gb}} = \frac{16.65}{1+\delta/d}\frac{D_{\text{v}}^{0.1}}{\delta^{0.2}t^{0.9}}\left(-\frac{\partial \ln \overline{c}}{\partial y^{3/2}}\right)^{-4/3} \tag{10.75}$$

The value of the GB width δ enters explicitly Eq. 10.75 and has to be determined separately. However, the final result only slightly depends on the value of δ due to the power of 0.2.

Experimentally measured profiles belonging to the transition AB kinetic regime are shown in Fig. 10.15. They represent the case of Fe diffusion in a nanocrystalline (grain size of 100 nm) γ-FeNi alloy [13]. It is seen that the linearity of the profiles in the given coordinates is followed over three orders of magnitude in decrease of the tracer concentration!

10.3 Determination of the Segregation Factor *s*

The majority of GB diffusion experiments are performed under the B kinetic regime. The defined effective activation enthalpy of GB diffusion in this case

$$P = P_0 \exp\left(-\frac{Q_{gb}}{RT}\right) \tag{10.76}$$

contains the real enthalpy of GB diffusion ΔH_{gb} and the enthalpy of segregation $H_{seg} < 0$

$$Q_{gb} = \Delta H_{gb} + H_{seg} \tag{10.77}$$

Theoretically, the GB width can depend on temperature and contribute to Eq. 10.77. However, the available data are consistent with the approximation $\delta = \text{const}$, which is to be seen below. The analysis of Table 10.2 suggests a way for separate determination of GB diffusion parameters in systematic measurements on *the same* polycrystalline material. A combination of the B- and C-type experiments is crucial, since the GB diffusion coefficient D_{gb} is measured in the C kinetics (typically at lower temperatures), while the triple product P, $P = s\delta D_{gb}$, is determined at higher temperatures in the B kinetics for solute diffusion. These data can be combined, and the product $s\delta$ will be estimated

$$s\delta = \frac{(P)^{B-\text{kinetics}}}{(D_{gb})^{C-\text{kinetics}}} = \frac{(s\delta D_{gb})^{B-\text{kinetics}}}{(D_{gb})^{C-\text{kinetics}}} \tag{10.78}$$

This approach is outlined in Fig. 10.16 for selected solutes.

Figure 10.16 suggests that the values of the triple product P, being extrapolated to lower temperatures of the C-type measurements, are systematically smaller than the corresponding diffusion coefficients D_{gb} and the difference reaches orders of magnitude. This difference is exactly the product $s\delta$.

A comment is due here. The subdivision of the measured data in B and C kinetics is strongly based on the values of the segregation factor s which is typically unknown in advance. Moreover, the value of δ has also to be known. A special procedure is suggested to analyze the GB diffusion data in a self-consistent and reliable way.

The value of the GB diffusional width δ can be determined similarly to Eq. 10.78 if one performs a similar series of *self-diffusion* measurements in both B and C kinetics. Then, the corresponding segregation factor is simply unity and

$$\delta = \frac{(P)^{B-\text{kinetics}}}{(D_{gb})^{C-\text{kinetics}}} = \frac{(\delta D_{gb})^{B-\text{kinetics}}}{(D_{gb})^{C-\text{kinetics}}} \tag{10.79}$$

As an example, the GB diffusion data on high-purity polycrystalline Ni measured both in the B and C kinetic regimes are presented in Fig. 10.17.

Figure 10.17 suggests that there is a huge gap between the directly measured values of D_{gb} and the extrapolated high-temperature data for $P = \delta D_{gb}$. This is exactly the (diffusional) GB width δ. Table 10.3 lists the values reported so far

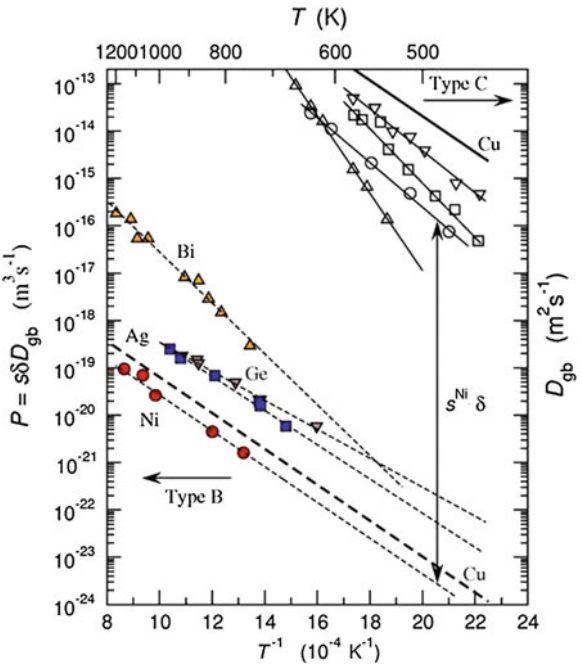

Fig. 10.16 Compilation of results on Ag [19], Ge [45], Ni [44], and Bi [46] GB diffusion in 5N8 high-purity Cu measured in both, the B-type (*solid symbols*) and C-type (*open symbols*) kinetics. The determination of the product $s\delta$ for Ni is sketched. The grain boundary self-diffusion of Cu [47] is plotted by *thick dashed* (the B kinetics) and *solid* (the C kinetics) *lines*

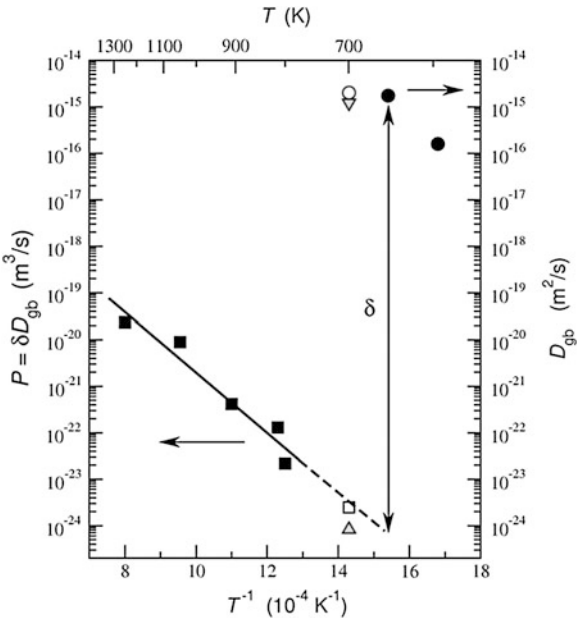

Fig. 10.17 Compilation of GB self-diffusion measurements in Ni in both, B (*squares*) and C (*circles*) kinetic regimes [30]. *Open symbols* represent the data determined in the transition BC regime. The way of determination of the GB width δ is sketched

Table 10.3 Compilation of published results on the diffusional GB width δ

Material	Tracer	δ (nm)	Reference
NiO	^{63}Ni	0.7	[48]
Ag	^{110m}Ag	0.43 ± 0.27[b]	[42]
Ag	^{110m}Ag	0.5[a]	[49]
γ-FeNi	^{59}Fe	0.5[a]	[13, 22]
γ-FeNi	^{63}Ni	0.55 ± 0.43	[50]
α-Fe	^{59}Fe	0.5[a]	[51]
Ni (99.999 wt%)	^{63}Ni	0.54 ± 0.1	[30]
Ni (99.99 wt%)	^{63}Ni	0.6 ± 0.2	[31]
α-Ti	^{44}Ti, ^{57}Co	0.5[a]	[52]

[a] The assumption $\delta = 0.5$ nm allowed to treat the results consistently
[b] Our estimate of the GB width from the data given by Sommer and Herzig [42]. The authors stated originally that assuming $\delta = 0.5$ nm, the B and C kinetic data will produce consistent results

based on the GB self-diffusion measurements. As one can see, $\delta = 0.5$ nm is a very good estimate for the GB width for the GB diffusion of matrix atoms.

The knowledge of the GB width δ allows a consistent analysis of solute GB diffusion and determination of the segregation properties. The flowchart of such analysis is as follows:

1. One starts assuming $\delta = 0.5$ nm and uses a reasonable estimate of the segregation factor s. According to the empirical relation of Hondros and Seah [20], the segregation factor s is inversely proportional to the bulk solubility of the solute c_{v0}

$$s = \frac{k_H}{c_{v0}} \tag{10.80}$$

   where the Hondros' constant is within the range $k_H = 1$ to 10 [20]. This estimate can be recommended as a good initial guess. Otherwise, one may use $s = 1$.
2. Knowing the product $s\delta$ enables us to analyze all profiles according to the given GB diffusion kinetics, as given in Table 10.2.
3. Having determined the triple products P, one should approximate them by an Arrhenius temperature dependence, $P = P^0 \exp(-Q_{gb}/RT)$. Extrapolating then the P values to lower temperatures of the D_{gb} measurements, the product $s\delta$ will be determined.
4. Again, fitting the $s\delta$ data by an Arrhenius line, $s\delta = s^0\delta \exp(-\Delta H_s/RT)$, the values of $s\delta$ can be determined for all temperatures in question. This gives new estimates of the GB diffusion parameters, (α and β) and one should repeat the loop starting from step #2.

Typically, after several iterations, a convergence is reached.

Table 10.4 Compilation of available GB diffusion and segregation data on different solutes in the same high-purity (99.9998 wt.%) Cu

Tracer	P_0 (m^3/s)	Q_{gb} (kJ/mol)	D_{gb0} (m^2/s)	ΔH_{gb} (kJ/mol)	$s_0\delta$ (m)	$-H_s$ (kJ/mol)	s_0	Refs.
Cu	3.9×10^{-16}	72.5	7.8×10^{-7}	72.5	–	–	–	[47]
Ag	1.4×10^{-15}	69.1	1.7×10^{-4}	108.6	8.0×10^{-12}	39.5	0.016	[19]
Ge	4.0×10^{-16}	58.6	2.8×10^{-6}	84.8	1.45×10^{-10}	26.2	0.29	[45]
Bi	6.6×10^{-12}	102.8	2.4×10^{-1}	156.2	2.7×10^{-11}	53.4	0.054	[46]
Ni	1.9×10^{-16}	73.8	6.9×10^{-7}	90.4	3.0×10^{-10}	16.6	0.60	[44]

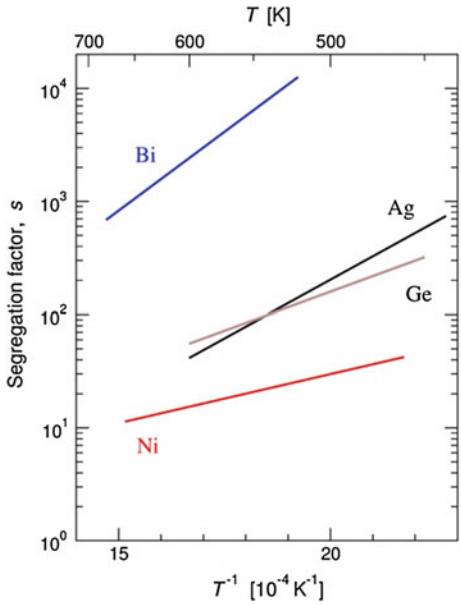

Fig. 10.18 Solute segregation in high-purity copper as determined by GB diffusion measurement. The Arrhenius parameters are listed in Table 10.4

As an example of systematic measurements of GB diffusion in the same, high-purity polycrystalline Cu, the data on different solutes are collected in Table 10.4 and shown in Fig. 10.18.

The described approach is based on the following main approximations:

- Constant and isotropic GB width δ is assumed;
- Arrhenius-type dependencies are assumed to hold for both D_{gb} and P, i.e., $D_b = D_{gb0}\exp(-\Delta H_{gb}/RT)$ and $P = P^0\exp(-Q_{gb}/RT)$, respectively;
- Linear segregation of the solute (the Henry isotherm) is supposed; that is, the segregation coefficient is not changed along the boundary, $s = \text{const}$ for the given temperature T;
- The limits of the GB diffusion regimes are strictly defined.

The next (very important) approximation is that the GB widths for self-diffusion δ_{sd} and that for solute diffusion δ_{solute} are equal: $\delta_{sd} = \delta_{solute}$. Generally speaking, this may not be the case. One may imagine that $\delta_{solute} > \delta_{sd}$ (even $\delta_{solute} \gg \delta_{sd}$) and D_{gb}^{solute} which enters the triple product P will correspond to an effective value. In such a case, the application of Eq. 10.78 would be incorrect.

There are, however, strong arguments that this is not the case, at least for such solutes as Ag and Bi in Cu in the case of true dilute solution. The segregation enthalpies derived from the application of Eq. 10.78 agree well with the independently measured data produced by Auger spectroscopy.

Several features can be highlighted:

- Fast (slow) diffusants in a bulk tend to remain identical in GB;
- Strong GB segregation tends to reduce the GB diffusivity; the stronger a segregation, the greater the retardation effect.

10.4 Nonlinear GB Segregation and GB Diffusion

The described theory of GB diffusion, contained in Eqs. 10.1–10.43, predicts linear penetration profiles in the coordinates of the logarithm of concentration against depth to the 6/5 power if GB diffusion occurs in the B kinetic regime. The solutions are derived considering (1) the constant and isotropic GB width δ, (2) the constant and isotropic GB diffusion coefficient $D_{gb} \gg D_v$, and (3) the constant value of the segregation factor s, given in Eq. 10.2. However, segregation could strongly depend on the solute concentration in the bulk that is known as nonlinear segregation [21]. In such cases, nonlinear (strongly curved) penetration profiles are expected for GB solute diffusion [4]. An example is given in Fig. 10.19a, while a perfect B-type penetration profile is measured for Ag diffusion in Cu bicrystal if a low amount of tracer material is used (0.3 kBq of radioactive ^{110m}Ag is initially deposited); strongly and characteristically curved penetration profiles are obvious if the tracer concentration is significantly increased (12 or even 120 kBq of ^{110m}Ag). The above analysis clearly demonstrates that this is not the type of boundary conditions—instantaneous versus constant source—that could introduce such a curvature of the profiles.

Using the penetration profiles presented in Fig. 10.19a, it is possible to determine the pertinent segregation isotherm, i.e., c_{gb} as a function of c_v, $c_{gb}(c_v)$. The key moment is that using radiotracer material with a known specific activity and by applying the Fisher solution, it is possible to determine the absolute bulk solute concentration just near the GB c_{v0} (in mole fractions) as a function of the penetration depth y. According to the Fisher solution for the B regime, the layer concentration of the tracer $\overline{c}(y)$ at the given depth y is fully determined by out-diffusion from the GB considered as a constant source with the concentration $c_{v0,}$ and is described by Eq. 10.13. Integrating over x, we derive

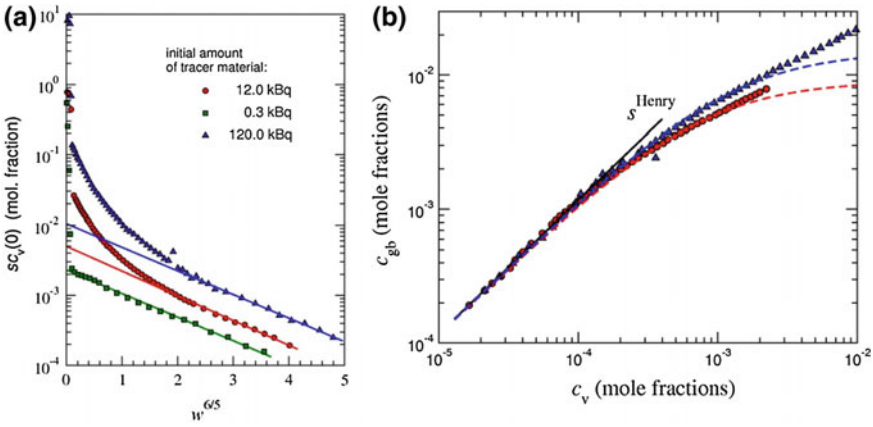

Fig. 10.19 Penetration profiles measured for Ag diffusion in Cu Σ5 bicrystal at **a** different amounts of the tracer material applied and **b** the determined segregation isotherms

$$c_{\mathrm{v}0}(y) = \frac{d}{4}\left(\frac{\pi}{D_{\mathrm{v}}t}\right)\overline{c}(y) \tag{10.81}$$

In this case, d is the diameter of the bicrystals used in the experiments presented in Fig. 10.19a.

At large depths (low tracer concentrations), a linear (Henry) segregation isotherm is valid and $c_{\mathrm{gb}}(y)$ can be determined using the value of the corresponding segregation factor s^{H}, which was found in an independent series of B- and C-type GB diffusion measurements, as shown in Table 10.4.

Let us introduce y_0 as the critic depth below which the Henry segregation is valid. Then, regrouping the term in Eq. 10.25, we have at $y > y_0$

$$\frac{d}{4}\left(\frac{\pi}{D_{\mathrm{v}}t}\right)\overline{c}(y) \equiv c_{\mathrm{v}0}(y) = c_0\exp\left(-\frac{y}{L}\right) = c_0\exp\left(-\frac{y}{L^*\sqrt{s^H}}\right) \tag{10.82}$$

and

$$c_{\mathrm{gb}}(y) = s^H c_{\mathrm{v}0} = s^H c_0\exp\left(-\frac{y}{L^*\sqrt{s^H}}\right) \tag{10.83}$$

Here, the reduced penetration depth L, seen from Eq. 10.17, is written as $L = L^*\sqrt{s^H}$ where L^* is now $L^* = \sqrt{\delta D_{\mathrm{gb}}}\left(\frac{\pi t}{4D_{\mathrm{v}}}\right)^{1/4}$

Generally, at arbitrary depth, the bulk and GB concentrations may be decomposed as

$$c_{v0}(y) = \Delta_v(y) + c_0 \exp\left(-\frac{y}{L^*\sqrt{s^H}}\right) \tag{10.84}$$

and

$$c_{gb}(y) = \Delta_{gb}(y) + s^H c_0 \exp\left(-\frac{y}{L^*\sqrt{s^H}}\right) \tag{10.85}$$

The terms $\Delta_v(y)$ and $\Delta_{gb}(y)$ represent the deviations of the measured tracer concentrations at the depth y from the Fisher solution of the GB diffusion problem in the presence of only linear segregation with $s = s^H$. The total tracer distribution obeys the standard equation of GB diffusion, Eq. 10.15, which can be presented as

$$\frac{\partial^2 c_{gb}}{\partial y^2} = L^{-2} c_{v0} \tag{10.86}$$

with the boundary condition $c_{v0} \to 0$ and $c_{gb} \to 0$ as $y \to \infty$. Combining Eqs. 10.84–10.86, the following relation is obtained

$$\frac{\partial^2 \Delta_{gb}}{\partial y^2} = L^{-2} \Delta_v \tag{10.87}$$

with a more appropriate boundary condition $\Delta_v = \Delta_{gb} = 0$ as $y \geq y_0$. This is a simple second-order differential equation which can be solved by double integration. As a result, the GB solute concentration will be found as a function of the penetration depth y

$$c_{gb}(y) = s^H c_0 \exp\left(-\frac{y}{L^*\sqrt{s^H}}\right) + L^{-2} \int_{y_0}^{y} d\tau \int_{y_0}^{\tau} \Delta_v(u) du \tag{10.88}$$

Since c_{v0} is measured as a function of the penetration depth y, as given in Eq. 10.81, the relation given in Eq. 10.88 implicitly determines the segregation isotherm $c_{gb}(c_{v0})$.

This method is applied to the two curved penetration profiles measured for GB diffusion of Ag in Cu bicrystal, as shown in Fig. 10.19a. The results, i.e., c_{gb} as function of c_{v0}, are presented in Fig. 10.19b. The resulting segregation isotherms derived from the two independent GB diffusion experiments are consistent. One realizes that using very sensitive radiotracer GB diffusion measurements with a suitable tracer on bicrystals, it is possible to reliably determine the segregation isotherm already starting from very small GB concentrations. Regarding this feature, the presented radiotracer method is superior to other experimental techniques so far applied for treating the segregation phenomena.

10.5 Microstructures with Hierarchy of Short-Circuit Diffusion Paths

Microstructure in technologically relevant materials is far more complicated as it is captured by a simple bicrystal-like model, as depicted in Fig. 10.3. Often, a hierarchic microstructure is revealed in a material as, for example, was the case of a sintered nanocrystalline γ-FeNi alloy [13, 22]—the nanocrystalline grains (with the grain size of $d \sim 100$ nm) turned out to be clustered in agglomerates with an average size d_a of 30–50 μm. This microstructure is shown in Fig. 10.20 and is sketched in Fig. 10.21a. In Fig. 10.20, the results of optical and atomic force microscopy (AFM) techniques are combined since they examine the microstructure on different scales. Individual nanograins are perfectly resolved by the AFM technique, whereas micrometer-large agglomerates are clearly seen by optical microscopy after suitable surface preparation (polishing and etching).

Thus, at least two different types of internal interfaces existed in such material—the interfaces between the nanograins and the interfaces between agglomerates (or clusters) of these grains. These interfaces are deliberately drawn as thin and thick boundaries in Fig. 10.21a since very different diffusion properties may be expected (as is the case).

On the other hand, the hierarchy of short-circuit diffusion paths in a typical polycrystalline material can be represented by the following contributions (grouped according to the corresponding diffusion rates):

- Triple junctions, i.e., line defects representing the lines along which three grains and correspondingly three GBs meet (however, so far, no direct tracer data for the dilute (Henry) limit exist, which would unambiguously confirm that the diffusion along the triple junctions is faster than along the corresponding grain boundaries, since the available data correspond to the results of microprobe analysis [23] or 3D atom-probe tomography [24], which may suffer from contaminate chemical effects);
- General (random) high-angle GBs;
- Low-angle GBs, dislocation walls, and individual dislocations.

For the effect of dislocations on GB diffusion and rigorous analysis of the corresponding kinetic regimes, the reader is referred to original papers [25, 26]. The corresponding analytical formulation (as well as the case of triple junction diffusion) are very similar to that presented below.

10.5.1 Kinetic Regimes of GB Diffusion in a Material with a Hierarchic Microstructure

In the case of a hierarchy of the microstructure (Fig. 10.21a), three potential diffusion paths should simultaneously be taken into account:

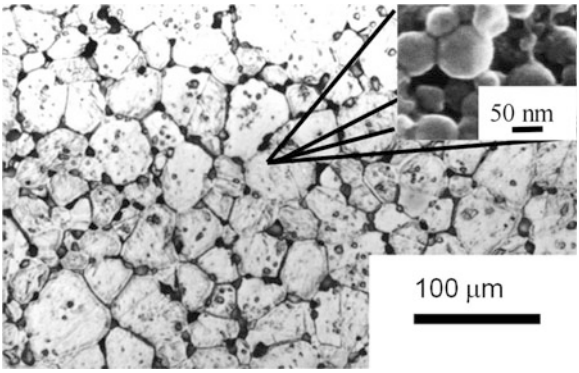

Fig. 10.20 Microstructure of nanocrystalline γ-FeNi alloy [25] as revealed by optic microscopy and atomic force microscopy (insert)—individual nanograins are clustered in micrometer-large agglomerates

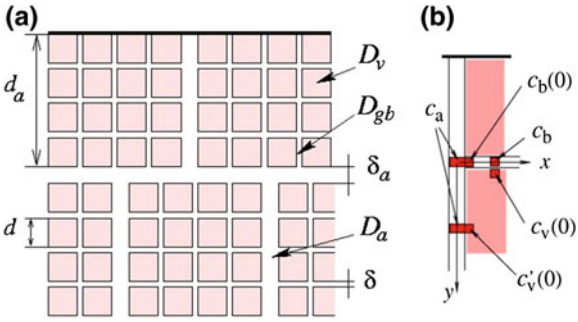

Fig. 10.21 **a** Schematic microstructure of the nanocrystalline γ-FeNi alloy with a hierarchic microstructure. Small nanograins (of the size d) are clustered in agglomerates of the size d_a. δ and δ_a are the widths of nano-GBs and inter-agglomerate boundaries, respectively; D_v, D_{gb}, and D_a are the bulk, nano-GB, and inter-agglomerate boundary diffusivities, respectively. In **b**, the concentrations, which are relevant to the definitions of the segregation factors s and s_a, are indicated

1. Short-circuit diffusion along the inter-agglomerate boundaries. Each of such interfaces is assumed to be represented by a homogeneous slab of the width δ_a and the diffusivity D_a;
2. Short-circuit diffusion along nanocrystalline GBs which are considered as homogeneous slabs of the width δ and the diffusivity D_{gb};
3. Bulk diffusion with the diffusion coefficient D_v.

It is reasonable to assume (and this was experimentally verified) that in the temperature interval of typical diffusion measurements

$$D_a \gg D_{gb} \gg D_v \tag{10.89}$$

Taking this relation into account, three different diffusion fluxes can generally be introduced:

1. Direct volume diffusion from the sample surface into the nanograins, diffusion rate D_v;
2. GB diffusion along nanocrystalline boundaries D_{gb} with subsequent outdiffusion into the grain interior, D_v; and
3. Diffusion along the inter-agglomerate boundaries D_a with subsequent outdiffusion to the nanoboundaries D_{gb} and then into the grain bulk D_v.

Thus, the regimes of interface diffusion for the processes (1) and (3) have to be specified separately in order to describe the overall diffusion kinetic. Taking this in mind, a two-letter designation was suggested [13], such as C–B. Each letter corresponds to the given Harrison kinetic regime, introduced above in Sect. 10.2, which is satisfied for the particular interface type. We first specify the regime for nano-GBs and then for inter-agglomerate boundary diffusion. Therefore, the C–B regime describes the case when the C regime of diffusion along the nanocrystalline GBs (no outdiffusion into bulk) is satisfied and when simultaneously the (quasi) B regime of diffusion along the inter-agglomerate boundaries (fast diffusion along the inter-agglomerate boundaries with subsequent outdiffusion into the adjacent nano-GBs) is fulfilled. The word "quasi" is necessary to indicate that the regime is similar to that of B, but due to the different outdiffusion kinetics (tracer leakage occurs only at places where nanocrystalline GBs cross the inter-agglomerate boundaries), the triple product is modified, see Sect. 10.5.1.2. And it does not follow it, as will be shown below.

In the case of solute diffusion, the segregation of the solute to both types of internal interfaces has to be taken into account. More than one segregation coefficient have to be introduced. The solute atoms can generally be in excess in the following (see Fig. 10.21b):

(a) Nanocrystalline GBs with respect to the adjacent bulk;
(b) Inter-agglomerate interfaces with respect to the adjacent bulk; and
(c) Inter-agglomerate interfaces with respect to the adjacent positions in the nano-GBs which intersect this inter-agglomerate interface.

In view of relation in Eq. 10.89, two segregation factors are required to describe the diffusion problem under consideration: s, which characterizes the solute excess in a nano-GB with respect to an adjacent bulk plane, and s_a, which corresponds to an excess of the solute in the inter-agglomerate boundary with respect to the adjacent position in the nanocrystalline GB

$$s = \frac{c_{gb}}{c_v(0)} \tag{10.90}$$

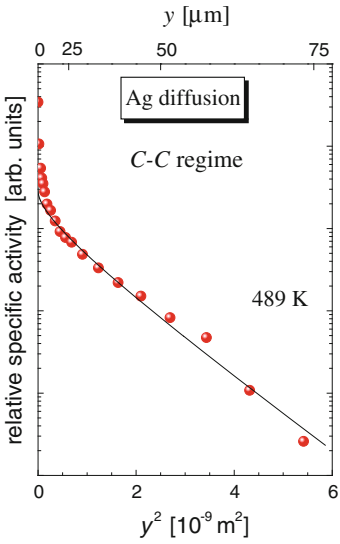

Fig. 10.22 Example of penetration profile measured in the C–C regime for Ag diffusion in nanocrystalline γ-FeNi alloy [27]

and

$$s_a = \frac{c_a}{c_{\mathrm{gb}}(0)} \tag{10.91}$$

Here, $c_{\mathrm{v}}(0)$, c_{gb}, $c_{\mathrm{gb}}(0)$, and c_{a} are the corresponding solute concentrations in the bulk just near a nanocrystalline GB, in a nano-GB, in a nano-GB just near an inter-agglomerate boundary, and in an inter-agglomerate boundary, respectively. The definition of these concentrations is illustrated more clearly in Fig. 10.21b.

The segregation factor $s_{\mathrm{av}} = c_{\mathrm{a}}/c'_{\mathrm{v}}(0)$ (the case (b) above) is not important in the present consideration as we have neglected the *direct* outdiffusion from the inter-agglomerate boundaries into the bulk (here, $c'_{\mathrm{v}}(0)$ is the bulk solute concentration just near the inter-agglomerate boundary, shown in Fig. 10.21b). Note that the excess of solute atoms in the inter-agglomerate boundaries with respect to the bulk s_{av} may be presented as $s_{\mathrm{av}} = s_{\mathrm{a}}s$, if the segregation behavior corresponds to dilute limit conditions (linear segregation). The segregation factor s is important for the flux (2), and both factors, s and s_{a}, affect the flux (3).

In dependence on the given kinetic conditions, five regimes (C–C, C–B, B–B, A–B, and A) and one subregime (AB–B) can be introduced to describe diffusion in a material with a hierarchy of kinetic properties of internal interfaces. The relevant parameters along with the diffusion characteristics, which can be determined experimentally, and the typical concentration dependencies of the penetration profiles are given in Table 10.5, and the penetration profiles are exemplified using the data for Fe, Ni, or Ag diffusion in the nanocrystalline γ-Fe–Ni alloy [13, 22].

Table 10.5 Parameters of kinetic regimes of GB diffusion in a nanocrystalline material with a hierarchical microstructure

Regime	Conditions	Measured parameters	Typical concentration dependence
C–C	$\alpha = \frac{s\delta}{2\sqrt{D_v t}} > 1; \alpha_a = \frac{s_a\delta_a}{2\lambda\sqrt{D_{gb}t}} > 1$	$D_a = \frac{1}{4t}\, q_2^{-1}$	$\overline{c} \propto \exp(-q_2 y^2)$ (Fig. 10.22)
C–B	$\alpha > 1;\ \alpha_a < 0.1,\ \beta_a = \frac{P_a}{2D_{gb}\sqrt{D_{gb}t}} \geq 2,$ $\sqrt{D_{gb}t} < d_a/4$	$D_{gb} = \frac{1}{4t}\, q_1^{-1}$ $P_a = \frac{s_a\delta_a D_a}{\lambda} = 1.31\sqrt{\frac{D_{gb}}{t}}\, q_2^{-5/3}$	$\overline{c} \propto \exp(-q_1 y^2) + \exp(-q_2 y^{6/5})$ (Fig. 10.23)
B–B	$\alpha < 0.1,\ \beta \geq 2,\ \sqrt{D_v t} < d/4;$ $\alpha'_a < 0.1,\ \beta'_a \geq 2,\ \sqrt{P}\left(\frac{\pi t}{4D_v}\right)^{1/4} < d_a/2$	$P = s\delta D_{gb} = 1.31\sqrt{\frac{D_v}{t}}\, q_1^{-5/3}$ $P_a = \frac{s_a\delta_a D_a}{\lambda} = 1.80\sqrt{\frac{D_{gb}}{s\delta}}\left(\frac{D_v}{t}\right)^{1/4} q_2^{-2}$	$\overline{c} \propto \exp(-q_1 y^{6/5}) + \exp(-q_2 y)$(Fig. 10.24)
AB–B	$d/4 < \sqrt{D_v t} < 3d;$ $\alpha''_a < 0.1, \beta''_a \geq 2,\ \sqrt{D^a_{eff}t} < d_a/4$	$sD_{gb} = 16.48\frac{D_v^{0.1}}{\delta^{0.2}t^{0.9}}\, q_1^{-4/3}$ $P'_a = s_a\delta_a D_a = 1.31\sqrt{\frac{D^a_{eff}}{t}}\, q_2^{-5/3}$	$\overline{c} \propto \exp(-q_1 y^{3/2}) + \exp(-q_2 y^{6/5})$ (Fig. 10.25)
A–B	$\sqrt{D_v t} > 3d,\ \sqrt{D^a_{eff}t} < d_a/4;$ $\alpha''_a < 0.1,\ \beta''_a \geq 2$	$D^a_{eff} \cong \frac{1}{2}\frac{sf_{gb}}{1+sf_{gb}} D_{gb} = \frac{1}{4t} q_1^{-1}$ $P'_a = s_a\delta_a D_a = 1.31\sqrt{\frac{D^a_{eff}}{t}}\, q_2^{-5/3}$	$\overline{c} \propto \exp(-q_1 y^2) + \exp(-q_2 y^{6/5})$ (Fig. 10.26)
A	$\sqrt{D^a_{eff}t} > 3d_a$	$D^M_{eff} \cong \frac{sf_{gb}/2}{1+sf_{gb}} D_{gb} + \frac{ss_a f_a/2}{1+ss_a f_a} D_a = \frac{1}{4tq_2}$	$\overline{c} \propto \exp(-q_2 y^2)$ (Fig. 10.27)

The value c is the layer concentration, y is the penetration depth, q_1 and q_2 are the numerical factors, and $\lambda = 2\delta/d$ is the density of nano-GBs intersecting an inter-agglomerate boundary. Other parameters are defined in the text

10.5.1.1 C–C Regime

This regime corresponds to very low temperatures and short diffusion times which suppress any outdiffusion from the internal interfaces in the material (Table 10.5). The condition $\alpha > 1$ means that bulk diffusion is negligible, i.e., $\sqrt{D_v t} \gg s \cdot \delta$. If the tracer enters the nanocrystalline GBs, it remains there. The diffusion length along the nanocrystalline GBs is also very small in this regime, since the next condition $\alpha_a > 1$ can approximately be rewritten as $\sqrt{D_{gb} t} < \frac{s_a \delta_a}{2\lambda} \cong s_a \cdot d$. Therefore, the diffusion length along the nanocrystalline GBs, $\sqrt{D_{gb} t}$, is very small and this flux cannot be detected by a conventional sectioning method for very small grain size, d = 10 to 100 nm. The factor λ in the expression for α_a takes into account the fact that outdiffusion from an inter-agglomerate boundary only occurs through regions where the nanocrystalline boundaries (of the width δ) intersect with the inter-agglomerate boundary. For cubic grains, $\lambda = 2\delta/d$.

Since nano-GB diffusion is almost "frozen out," the tracer is dominantly located in the inter-agglomerate boundaries. The diffusion profile corresponds to the error function or Gaussian solution of the diffusion equation in dependence on the given initial conditions. An example of such a profile, experimentally measured for Ag solute diffusion in the nanocrystalline γ-FeNi alloy [27], is shown in Fig. 10.22. Due to the small solid solubility of Ag in the FeNi alloy, the initial conditions corresponded to the thick layer solution and the error function fitting was applied to extract the diffusivity D_a of the inter-agglomerate boundaries in that case.

The segregation factors s and s_a should be known to evaluate α and α_a. Since s and s_a are not known a priori, the estimates $s = s_a = 1$ may initially be used. The self-consistent evaluation of the whole data set in all diffusion regimes, however, allows calculation of the segregation factor s and estimation of s_a, as was described above for solute diffusion in a polycrystalline material.

10.5.1.2 C–B Regime

With increasing temperature of diffusion anneals, the diffusion length along the nano-GBs increases and outdiffusion from the inter-agglomerate boundaries is becoming important, $\sqrt{D_{gb} t} \gg s_a \cdot d$. This introduces the formal B regime conditions for diffusion along the inter-agglomerate boundaries. However, since bulk diffusion is still suppressed, $\sqrt{D_v t} << s \cdot \delta$, the C kinetic conditions assert for nano-GB diffusion. These conditions define the C–B diffusion regime in the material with a bimodal interface structure (Table 10.5).

In this diffusion regime, not the values s_a, δ_a, or D_a, but only their product $P_a = s_a \delta_a D_a / \lambda$ can be determined from the penetration profiles. The specific feature of the inter-agglomerate boundaries is that outdiffusion does not proceed uniformly but only there where the nano-GBs intersect the inter-agglomerate boundary. The density of such places λ enters explicitly into the expression for the product P_a.

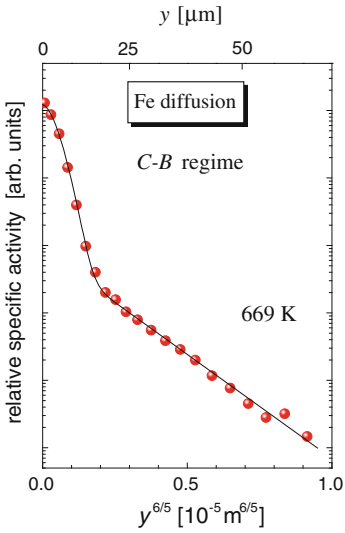

Fig. 10.23 Example of penetration profile measured in the C–B regime for Fe diffusion in nanocrystalline γ-FeNi alloy [22]

The diffusion length for diffusion along the nanocrystalline GBs, $\sqrt{D_{gb}t}$, should be smaller than the size d_a of the agglomerates in this regime. Otherwise, the diffusion fluxes from different inter-agglomerate boundaries will overlap and the formal A kinetic regime might become important. In the C–B diffusion regime, the parameter α is larger than unity and the tracer does not penetrate into the bulk. The diffusion process is thus confined to nano-GBs and inter-agglomerate boundaries only. The tracer is mainly located in the nano-GBs.

An example of such a penetration profile measured for Fe diffusion in nano-γ-FeNi [22] is presented in Fig. 10.23. A two-stage shape of the penetration profile is clearly seen. The first part, which is characterized by the $\ln \overline{c} \sim y^2$ depth dependence of the concentration profile, corresponds to the nano-GB diffusion in the C regime. As a result, the nano-GB diffusivity D_{gb} can directly be determined from this part (Table 10.5).

The second part of the penetration profile in Fig. 10.23 corresponds to the faster diffusion mode from the surface into the inter-agglomerate boundaries with subsequent outdiffusion into adjacent nanocrystalline GBs. Since formal B-type conditions are fulfilled in this diffusion mode, the Suzuoka solution, given in Eqs. 10.37a–10.38, of the interface diffusion problem has to be applied, as in Table 10.5. The solid line in Fig. 10.23 represents the relevant fit.

10.5.1.3 B–B Regime

If temperature and/or time of diffusion anneal increases further, the bulk diffusion flux becomes more significant and cannot be neglected. Then, the diffusion process will be dominated by two fluxes:

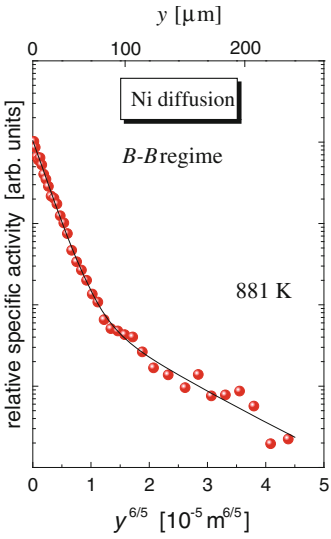

Fig. 10.24 Example of penetration profile measured in the B–B regime for Ni diffusion in nanocrystalline γ-FeNi alloy [28]

1. GB diffusion along the nanocrystalline GBs with subsequent outdiffusion into the grain interior and
2. Faster diffusion along inter-agglomerate boundaries with subsequent outdiffusion to nanoboundaries and then into the grains.

Since the bulk diffusion length $\sqrt{D_v t}$ has to be smaller than the grain size to satisfy the conditions of this B–B regime (Table 10.5), the total contribution of direct volume diffusion from the sample surface into the nanograins can be neglected. Correspondingly, two-stage penetration profiles should be observed. An example of such a profile, which was measured for Ni diffusion in nano-γ-FeNi [28], is shown in Fig. 10.24.

The B regime conditions are satisfied for the flux (1). Therefore, the Suzuoka solution to the GB diffusion problem is applied to analyze this term. As a result, the first part of the penetration profile should be linear in the coordinates of ln$c$ versus $y^{6/5}$ and only the triple product $P = s\delta D_{gb}$ can be determined, but not the nano-GB diffusivity D_{gb} itself (see Table 10.5). The parameter $\beta = P/2D_v\sqrt{D_v t}$ has to be large enough in order to observe a distinct GB diffusion-related tail. It was shown that $\beta \geq 2$ can be used as a lower limit of the B regime [22].

The diffusion flux (2) represents a fundamentally new situation. In order to describe an analytic expression for the layer tracer concentration $\overline{c}$ that entered the sample this way, we will reformulate the Fisher model for inter-agglomerate boundary diffusion from a constant source. The tracer concentrations $c_v(x, y, t)$ in the bulk, the $c_{gb}(x, y, t)$ in nanocrystalline grain boundaries, and the $c_a(x, y, t)$ in inter-agglomerate boundaries are to be considered. To derive an analytical solution, the following approximations are made (see Fig. 10.21b):

1. Diffusion in the nanocrystalline grains (bulk diffusion) occurs primarily normal to the local position of the GB, i.e., in the y direction in Fig. 10.21b, $c_v(x, y, t) = c_v(y, t)$. The direct bulk diffusion from the surface into the grain is assumed to be negligible.
2. The relationship given in Eq. 10.89 is supposed to be valid. Thus, the tracer atoms enter the GB slabs only by leaving the inter-agglomerate boundary along the x direction, while direct GB diffusion along the nanocrystalline GBs from the surface is neglected. Thus, $c_{gb}(x, y, t) = c_{gb}(x, t)$. Moreover, the condition $\partial c_{gb}(x,t)/\partial t \approx 0$ is assumed when describing bulk diffusion. The latter means that outdiffusion from the nanocrystalline GBs into the bulk occurs in nearly constant-source conditions as in the original formulation of Fisher's model.
3. With respect to GB diffusion, the tracer distribution within the inter-agglomerate boundaries is established within a very short period of time τ and the relations $c_a(x, y, t) = c_a(y, t)$ and $\partial c_a(y,t)/\partial t|_{t>\tau} \approx 0$ are assumed.

Considering the interfaces as homogeneous slabs with given diffusivities, the following equations can be written for the concentrations c_a, c_{gb}, and c_v

$$\frac{\partial c_a(y,t)}{\partial t} = D_a \frac{\partial^2 c_a(y,t)}{\partial y^2} + \lambda \frac{2}{\delta_a} J_{gb}\big|_{|x|=\delta_a/2} + \frac{2}{\delta_a} J_v|_{|x|=\delta_a/2}, \quad |x| < \delta_a/2 \tag{10.92}$$

$$\frac{\partial c_{gb}(x,t)}{\partial t} = D_{gb} \frac{\partial^2 c_{gb}(x,t)}{\partial x^2} + \frac{2D_v}{\delta} \frac{\partial c_v(y,t)}{\partial y}\bigg|_{|y|=\delta/2}, \quad |x| > \delta_a/2,\ |y| < \delta/2 \tag{10.93}$$

$$\frac{\partial c_v(x,y,t)}{\partial t} = D_v \left(\frac{\partial^2 c_v(x,y,t)}{\partial x^2} + \frac{\partial^2 c_v(x,y,t)}{\partial y^2} \right), \quad |x| > \delta_a/2, \quad |y| > \delta/2 \tag{10.94}$$

Here, J_{gb} and J_v are the fluxes of tracer atoms leaving the inter-agglomerate boundary through adjacent nanocrystalline GBs and the bulk, respectively; λ determines the density of outdiffusion paths from the inter-agglomerate boundary, as can be observed from Table 10.5.

In the present analysis, we will also neglect the amount of tracer which leaves the inter-agglomerate boundary by direct outdiffusion into the bulk, given by the last term in Eq. 10.92. Thus, $J_v|_{|x|=\delta_a/2} = 0$ and this condition decouples the concentrations c_a and c_v. Then, the tracer distribution $\tilde{c}_v$ in the volume after diffusion along an inter-agglomerate boundary and then along a given nanocrystalline GB is given by (see Eq. 10.18)

$$\tilde{c}_v = c_a \mathrm{erfc}\left(\frac{y}{2\sqrt{D_v t}} \right) \exp\left[-\left(\frac{4D_v}{\pi t} \right)^{1/4} \frac{x}{\sqrt{P}} \right] \tag{10.95}$$

Then, the total amount M_{gb} of tracer atoms entering the bulk this way is given by

$$M_{gb} = 2c_a \int_0^\infty \operatorname{erfc}\left(\frac{y}{2\sqrt{D_v t}}\right) dy \int_0^\infty \exp\left[-\left(\frac{4D_v}{\pi t}\right)^{1/4} \frac{x}{\sqrt{P}}\right] dx$$
$$= \frac{2\sqrt{2}c_a}{\pi^{3/4}} D_v^{1/4} t^{3/4} \sqrt{P} \tag{10.96}$$

Note that according to the exact solution of the GB diffusion problem with a constant source [4]

$$M_{gb} = c_a \frac{\sqrt{2P}}{\Gamma(7/4)} D_v^{1/4} t^{3/4} \tag{10.97}$$

where Γ is the Euler gamma function. We see that Eqs. 10.96 and 10.97 differ by the numerical factors only (about 1.199 and 1.539, respectively). However, in view of the approximate character of the original system of Eqs. 10.92–10.94, we will use Eq. 10.96 in the following.

The flux J_{gb} can easily be calculated as $J_{gb} = \frac{1}{\delta}\frac{\partial M_{gb}}{\partial t}$. Substituting the obtained expression for J_{gb} into Eq. 10.92 and by applying the condition $\partial c_a(y,t)/\partial t|_{t>\tau} \approx 0$, the final equation for c_a is

$$\frac{\partial^2 c_a(y,t)}{\partial y^2} = \frac{1.798\sqrt{D_{gb}/\delta}}{\delta_a D_a/\lambda} (D_v/t)^{1/4} c_a \tag{10.98}$$

This equation has the following solution under the boundary condition of $c_a \to 0$ at $y \to \infty$

$$c_a = c_0 \exp\left\{-\left(\frac{1.798}{\delta_a D_a/\lambda}\sqrt{\frac{D_{gb}}{\delta}}\left(\frac{D_v}{t}\right)^{1/4}\right)^{1/2} y\right\} \tag{10.99}$$

Thus, the plot of $\ln \bar{c}$ against y yields a straight line and its slope determines the product $P_a = \delta_a D_a/\lambda$ for inter-agglomerate boundary diffusion in the B–B kinetic regime

$$P_a = \frac{\delta_a D_a}{\lambda} = 1.798\sqrt{\frac{D_{gb}}{\delta}}\left(\frac{D_v}{t}\right)^{1/4}\left(-\frac{\partial \ln \bar{c}}{\partial y}\right)^{-2} \tag{10.100}$$

It was shown [28] that the approximate solution for P_a, as given in Eq. 10.100, is precise enough to be applied in a diffusion experiment. The parameters α'_a and β'_a, which determine the conditions of the B–B regime (Table 10.5), are defined as follows:

$$\alpha'_{\mathrm{a}} = \frac{s_{\mathrm{a}}\delta_{\mathrm{a}}}{\lambda\sqrt{s\delta D_{\mathrm{gb}}}}\left(\frac{4D_{\mathrm{v}}}{\pi t}\right)^{1/4} \tag{10.101}$$

and

$$\beta'_{\mathrm{a}} = \frac{P_{\mathrm{a}}}{D_{\mathrm{gb}}\sqrt{s\delta D_{\mathrm{gb}}}}\left(\frac{4D_{\mathrm{v}}}{\pi t}\right)^{1/4} \tag{10.102}$$

The fit in Fig. 10.24 describes the experimental points quite well over almost four decades of decrease in concentration, supplying reliable data on both nano-GB and inter-agglomerate boundary diffusion.

10.5.1.4 AB–B Regime

As it was shown, the temperature interval of the B–B regime has an upper limit by the condition that an overlap of the bulk diffusion fluxes from different nanocrystalline GBs must be avoided. With increasing temperature, this condition will be violated. For interface diffusion in a unimodal structure, it is known that the conditions of the A kinetic regime are fulfilled if the bulk diffusion length is much larger than the grain size d. In between, the transition AB regime exists, at $d/4 < \sqrt{D_{\mathrm{v}}t} < 3d$. The key feature of this subregime is the unusual depth dependence of the concentration profile: $\ln c \sim y^{3/2}$, see Sect. 10.2.5. Such profiles were indeed measured in the experiments on Fe diffusion in nano-γ-FeNi [13], observed from Fig. 10.15. The measured decrease of the logarithm of concentration with the penetration depth over more than three decades definitely allowed ruling out the B ($\ln c \sim y^{6/5}$) or A ($\ln c \sim y^2$) kinetics in the relevant cases.

In the case of a nanomaterial with a bimodal distribution of the interface characteristics, the subregime AB–B can be introduced. Examples of such profiles, which were measured for Ni diffusion in nano-γ-FeNi, are shown in Fig. 10.25. The first part of the two-stage profile measured at $T = 1{,}002$ K is linear in the coordinates of $\ln c$ versus $y^{3/2}$ (nano-GB diffusion), and the second one is linear in the coordinates of $\ln c$ versus $y^{6/5}$ (inter-agglomerate boundary diffusion). The solid line, which represents the relevant fit in Fig. 10.25, nicely reproduces the experimental data over about five orders of magnitude in concentration. The profile, which was measured at $T = 1013$ K (Fig. 10.25), reveals only a part related to nano-GB diffusion and is almost perfectly linear over three decades in the coordinates of $\ln c$ versus $y^{3/2}$. The product sD_{gb} can be determined from the first part of the profile (see Table 10.5), whereas the triple product $P''_{\mathrm{a}} = s_{\mathrm{a}}\delta_{\mathrm{a}}D_{\mathrm{a}}$ can be evaluated from the deeper part of the concentration profile. The inter-agglomerate boundary diffusion problem in such conditions is still not solved exactly. The tracer leakage from inter-agglomerate boundaries into agglomerates can approximately be described by an effective diffusivity $D^{\mathrm{a}}_{\mathrm{eff}}$ as in Eq. 10.52,

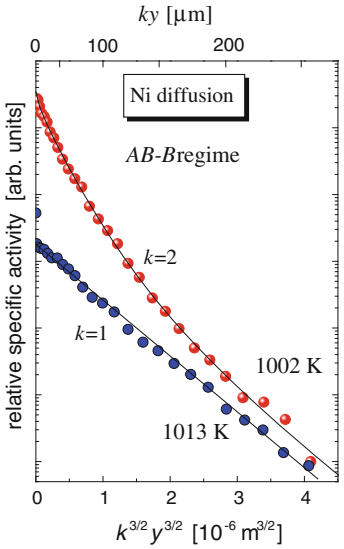

Fig. 10.25 Example of penetration profile measured in the AB–B regime for Ni diffusion in nanocrystalline γ-FeNi alloy [28]

which in the case of negligible bulk diffusion and the absence of segregation effects transforms to

$$D^{\mathrm{a}}_{\mathrm{eff}} \cong f_{\mathrm{gb}} D_{\mathrm{gb}} \tag{10.103}$$

Here, f_{gb} is the volume fraction of the nano-GBs in agglomerate. This fraction can be determined as $f_{\mathrm{gb}} = q\delta/d$ (q is a numerical factor). Then, inter-agglomerate boundary diffusion can be described by the formal Suzuoka solution with the effective diffusivity $D^{\mathrm{a}}_{\mathrm{eff}}$ instead of the GB diffusivity D_{gb} (see Table 10.5). The following parameters are important in the AB–B diffusion regime

$$\alpha''_{\mathrm{a}} = \frac{s_{\mathrm{a}}\delta_a}{2\sqrt{D^{\mathrm{a}}_{\mathrm{eff}} t}} \tag{10.104}$$

and

$$\beta''_{\mathrm{a}} = \frac{P''_{\mathrm{a}}}{2D^{a}_{\mathrm{eff}}\sqrt{D^{\mathrm{a}}_{\mathrm{eff}} t}} \tag{10.105}$$

10.5.1.5 A–B Regime

If the bulk diffusion length becomes remarkably larger than the grain size $\sqrt{D_{\mathrm{v}} t} > 3d$, the A kinetic is valid for tracer diffusion along nanocrystalline GBs. Then, the agglomerates are characterized by an effective diffusivity $D^{\mathrm{a}}_{\mathrm{eff}}$, which is

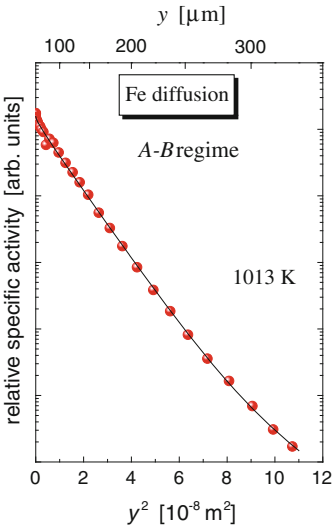

Fig. 10.26 Example of penetration profile measured in the A–B regime for Fe diffusion in nanocrystalline γ-FeNi alloy [13]

described by a modified Hart–Mottlock or Maxwell–Garnet equation in the case of solute diffusion, as shown in Eqs. 10.52 and 10.54.

Since typically $D_v \ll D_{gb}$ and $f_{gb} \ll 1$, only the nano-GB diffusion contribution becomes important (see Table 10.5).

If the resulting diffusion length inside of the agglomerates $\sqrt{D^a_{eff}t}$ is smaller than the agglomerate size $\sqrt{D^a_{eff}t} < d_a/4$, the fluxes from different inter-agglomerate boundaries do not overlap and diffusion occurs in the A–B kinetic regime in the bimodal interface microstructure under consideration. The penetration profiles generally should be composed of two parts. The first part corresponds to bulk diffusion in a homogeneous material (inner part of agglomerates) characterized by an effective diffusion coefficient D^a_{eff}. An example of such a penetration profile is presented in Fig. 10.26 for the case of Fe diffusion in nano-γ-FeNi [13]. The penetration profile turns out to be slightly curved at large depths, as seen in Fig. 10.26. However, the number of relevant experimental points is too small to be able to extract reliably the inter-agglomerate boundary diffusivity. The deviation from the linearity in this profile could only be detected due to the extremely high sensitivity of the applied radionuclide-counting facilities, which allowed an accurate detection of the penetration profile over five decades in the decrease of concentration.

10.5.1.6 A Regime

With increasing temperature, the effective diffusivity of the agglomerates D^a_{eff} in Eq. 10.94 becomes larger and the relevant diffusion length can be remarkably larger than the agglomerate size $\sqrt{D^a_{eff}t} > 3d_a$. Then, the A kinetic is valid for tracer diffusion in this material. The nanocrystalline alloy as a whole can be

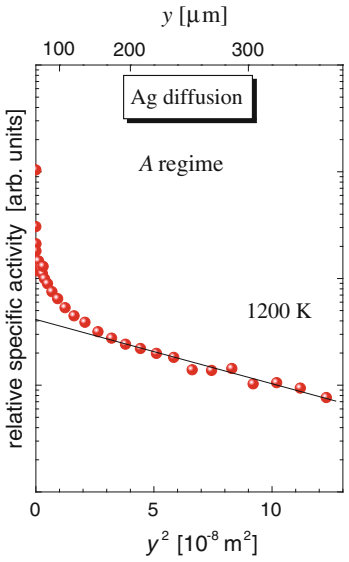

Fig. 10.27 Example of penetration profile measured in the A regime for Ag diffusion in nanocrystalline γ-FeNi alloy [27]

considered as a homogeneous material with the effective diffusivity $D_{\text{eff}}^{\text{M}}$. The penetration profile should follow the thin-layer solution of the diffusion equation, and the inclination of the fitting line in the coordinates of ln$c$ versus y^2 gives the effective diffusivity $D_{\text{eff}}^{\text{M}}$.

An example of such a profile measured for Ag diffusion in nanocrystalline FeNi alloy at $T = 1{,}200$ K [27] is shown in Fig. 10.27. The contribution of the inter-agglomerate boundary diffusivity D_{a} to the effective diffusivity $D_{\text{eff}}^{\text{M}}$ was found to be less than 10 %, and the relevant relation in Table 10.1 allows a consistent determination of the nano-GB diffusivity D_{gb}. The knowledge of the segregation factor s is imperative for such calculations, and it was determined by an iterative approach (see below).

10.5.2 Temperature Dependence of Interface Diffusion in Material with a Hierarchic Microstructure

Diffusion of Fe, Ni, and Ag in a nanocrystalline γ-FeNi alloy was intensively measured in the extended temperature interval from about 500 to 1,200 K. The penetration profiles were analyzed according to the strict mathematical conditions of the appearance of the given kinetic regime, and consistent data in the whole temperature interval were derived. For the analysis of Fe and Ni diffusion, the relevant segregation factors s_{Fe} and s_{Ni} are close to unity. Fe and Ni show complete mutual miscibility in the γ-phase, and one may expect only slight (if any) segregation of both Fe and Ni to internal interfaces in the γ-FeNi alloy. On the other

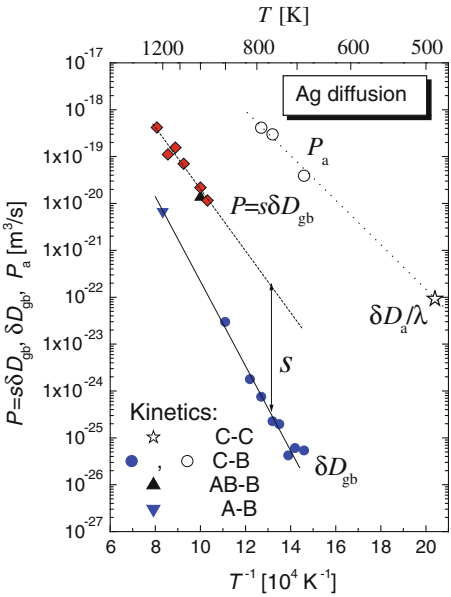

Fig. 10.28 Arrhenius diagram for Ag diffusion in nanocrystalline γ-FeNi alloy [27]. *Filled symbols* represent the diffusivity of nanocrystalline GBs, and *open symbols* correspond to inter-agglomerate boundary diffusion. The conditions $\delta = 0.5$ nm and $\delta_a = 1$ nm were used to recalculate the measured P_a and P values for the relevant diffusivities D_a and D_{gb}. The triple product P for Ag diffusion in coarse-grained FeNi alloy is also shown (*diamonds*). The method of calculation of the segregation factor s for Ag in FeNi is illustrated

hand, Ag reveals very small solubility in FeNi and a strong Ag segregation to internal interfaces is expected.

Ag diffusion in the nanocrystalline γ-FeNi was measured in various diffusion regimes, and the succession of the kinetics C–C, C–B, AB–B, and A was observed, and the diffusivities of both nano-GBs and inter-agglomerate boundaries were determined, as presented in Fig. 10.28.

The diffusivity D_{gb} of the nanocrystalline GBs was directly determined in the C–B kinetics. In order to establish the limits of relevant kinetic regimes and to analyze the experimental data, the knowledge of the segregation factor s is imperative. As it was shown above, the segregation factor s can be determined by a combination of the C- and B-type GB diffusion measurements. Whereas the B–B kinetics was observed for both Fe and Ni diffusion, it cannot be realized for Ag diffusion in the nanocrystalline FeNi alloy for formal reasons. In the case of self-diffusion, $s = 1$ and the conditions $\alpha = \delta/2\sqrt{D_v t} < 0.1$ and $2\sqrt{D_v t} < d/2$ can *simultaneously* be satisfied in the given temperature interval even for such a small grain size d as $d = 100$ nm. This is no longer the case for diffusion of such a strongly segregating solute as Ag. The above-mentioned inequalities can be rewritten as $\sqrt{D_v t} > 5s\delta$ and $\sqrt{D_v t} < d/4$, respectively. Taking into account that

$d = 100$ nm and $\delta \cong 0.5$ nm, it becomes evident that these relations *cannot simultaneously be satisfied* if $s > 10$. As the temperature increases, the C–B kinetic regime ($\sqrt{D_v t} < s\delta/2$) changes to the A–B kinetics with $\sqrt{D_v t} > 3d$.

This fundamental difficulty can be overcome by the B-type GB diffusion measurements in coarse-grained material (with a remarkably larger value of the grain size d). The key point is that the close similarity between Ni self-diffusion in the coarse-grained and nanocrystalline γ-FeNi alloy [28] suggests similar GB structures in these materials. The measurements of Ag diffusion in the coarse-grained γ-Fe–Ni alloy yielded the triple product $P = s\delta D_{gb}$ as a function of temperature (diamonds in Fig. 10.28). The data on P for Ag diffusion (determined for the coarse-grained material) can thus be combined with the direct data on D_{gb} (determined for the nanocrystalline material). As a result, the temperature dependence of the segregation factor s can be derived (Fig. 10.28).

Ag segregates strongly at GBs in the γ-FeNi alloy, for example, $s = 1{,}000$ at $T = 700$ K. Here, an iterative procedure was applied to calculate s. Having determined several values of D_{gb} (supposing that the low-temperature measurements were performed in the C kinetics), a crude estimate of s can be determined by combination of these D_{gb} values and the P values for coarse-grained material. This estimate of s allows a more precise calculation of the parameter α and thus a better evaluation of the limits of the C–B regime. This in turn allows a more justified calculation of D_{gb} until self-consistency is reached.

Having determined the segregation factor s, an Ag GB diffusion experiment in the nanocrystalline material has been designed, which satisfies the conditions of the AB–B kinetics (the B–B kinetics cannot be fulfilled for formal reasons). For this purpose, the time and temperature of the diffusion anneal have to be chosen very carefully using Table 10.5. The value determined for sD_{gb} is multiplied by the GB width δ and is plotted in Fig. 10.28 (triangle up). Almost perfect agreement with the independent data of $P = s\delta D_{gb}$ measured in coarse-grained material (diamonds) is obtained, as depicted in Fig. 10.28. This fact supports the conclusion that the diffusivities of the nanocrystalline ($d \sim 100$ nm) and coarse-grained ($d \sim 0.5$ mm) materials are very similar.

Ag diffusion along the inter-agglomerate boundaries proceeds much faster than along the nano-GBs, as portrayed in Fig. 10.28 (open symbols). Having determined $P_a = s_a\delta_a D_a/\lambda$ and D_a separately in the C–B and C–C regimes, respectively, the factor $s_a\delta_a/\lambda$ can be estimated. Taking λ as $\lambda = 2\delta/d$ with $\delta = 0.5$ nm and $d = 100$ nm, an upper estimate of the product $s_a\delta_a$ is obtained, $s_a\delta_a \sim 1$ nm. Since the inter-agglomerate boundaries present a more open structure with respect to the nano-GBs, the value of $\delta_a \approx 1$ nm seems to be a good estimate. Thus, the segregation factor s_a for Ag seems to be about unity. This means that there is practically no excess of Ag atoms in the inter-agglomerate boundaries with respect to the nanocrystalline GBs, as shown in Eq. 10.91, and the segregation behavior of these two internal interfaces with respect to the bulk is similar. In Fig. 10.28, the value of D_a measured in the C–C regime is multiplied by the factor δ_a/λ (using the estimates $\delta_a = 1$ nm and $\lambda = 0.01$) for comparison with the P_a values measured in

the C–B regime (open star and circles, respectively). Assuming $s_a = 1$, the temperature dependence of P_a can be presented by the linear Arrhenius relationship (dotted line in Fig. 10.28).

10.6 Dependence of GB Diffusion on GB Parameters

The grain boundary represents an interface between two crystals. Therefore, each GB can be characterized by the following *macroscopic* and *microscopic* parameters: matrix of rotation between the two crystalline coordinate systems, for instance, the axis $\vec{\omega}$ and angle θ of rotation (3 parameters); the inclination of the GB plane with respect to a chosen direction $\vec{n}$ (2 parameters); and the matrix of atomic translation $\vec{t} = (t_x, t_y, t_z)$. The set of parameters $(\vec{\omega}, \theta, \vec{n})$ can be chosen on demand during bicrystal preparation by setting the misorientations of the crystals and properly choosing the required position of the interface. The parameters $\vec{t}$ cannot be influenced, and thus, they are known as microscopic.

In dependence on the given set of the parameters $(\vec{\omega}, \theta, \vec{n})$, it is possible for us to distinguish the following:

- Low-angle grain boundary with $\theta \leq 15°$;
- High-angle GBs with $\theta > 15°$;
- Special (low sigma) GBs with special values of $(\vec{\omega}, \theta)$ so that the value of the inverse density of equivalent (coinciding) positions of the two lattices is small, for example, Σ5, Σ7, etc. The values of Σ1 and Σ3 correspond to the low-angle and twin boundaries, respectively;
- Pure tilt GBs with $\vec{\omega} \perp \vec{n}$, i.e., the misorientation axis lies in the GB plane;
- Pure twist GBs with $\vec{\omega} \parallel \vec{n}$, i.e., the misorientation axis is perpendicular to the GB plane;
- GB of a mixed type;
- Symmetric and asymmetric GBs.

Generally, GB diffusion and segregation depends on all these parameters.

The production and characterization of oriented bicrystals is an extremely difficult task. The desired misorientation has to be uniform along the GB with a high accuracy showing only small fluctuations of the GB plane orientation. Even nowadays, the production of top-quality-oriented bicrystals looks more like art than a technology. The state of the art in such measurements is represented by the works of Herzig with co-workers [29]. They demonstrated that the precise specification of all three misorientation angles to the accuracy of $\pm 0.1°$ (including the non-avoidable twist component) is required to rationalize the orientation dependence and to observe cusps in diffusivities at low-Σ misorientations.

In Fig. 10.29, GB diffusion of Au in Cu near Σ5 GBs [29] is presented as a function of the misorientation angle θ. The observed increase of the GB diffusivity with approaching the perfect Σ5 misorientation from large tilt angles $\theta > 36.9°$ is

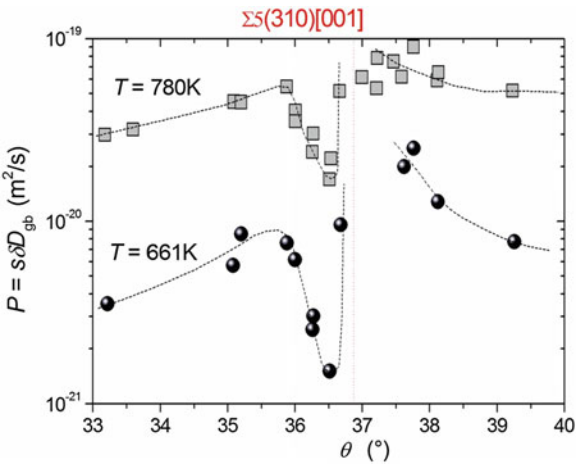

Fig. 10.29 GB diffusion of ^{195}Au in Cu Σ5(310)[001] bicrystals as a function of the tilt angle θ measured at two temperatures 661 K and 780 K after [29]. The misorientation angle corresponding to the exact Σ5(310)[001] interface is shown by dotted line. The dashed lines are drawn as guidance for eyes

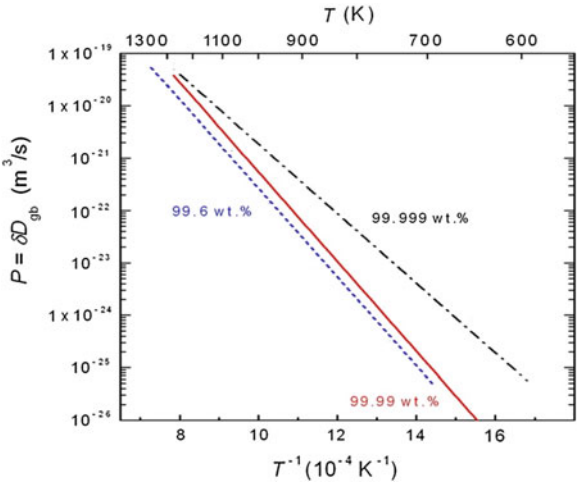

Fig. 10.30 Ni GB self-diffusion measured in 99.6 [30], 99.99 [31], and 99.999 wt.% [30] pure polycrystalline Ni materials

caused by an increase in the accompanying twist component. This effect "masks" partially the deep cusp in the GB diffusivity occurring at the perfect Σ5 misorientation.

10.7 Effect of Purity on GB Diffusion

The purity and segregation of solutes can both strongly affect the GB diffusion. In Fig. 10.30, Ni GB self-diffusion measured in coarse-grained polycrystalline Ni of different purity levels [30, 31] is compared. The GB diffusion has been measured

by the same technique and using the same equipment. As a general trend, it is seen that the higher the purity of a material, the higher the grain boundary diffusivity $P = \delta \cdot D_{gb}$ and the lower the effective activation energy for grain boundary diffusion. One has to mention that different "critical" impurities, which strongly segregate at GBs and which could affect dramatically the grain boundary diffusion, might be present in different materials.

Figure 10.30 suggests a strongly non-monotonous dependence of D_{gb} on the purity of Ni, $D_{gb}^{99.999} \gg D_{gb}^{99.99} \approx D_{gb}^{99.6}$, especially at low temperatures. The problem of the effect of impurities on GB diffusion has been analyzed in [31].

10.8 Grain Boundary Interdiffusion

So far, tracer diffusion along GBs was considered. However, as in the case of bulk diffusion, one can consider the case of chemical grain boundary diffusion just like the diffusion of A atoms along GBs of B or that of A atoms along GBs of AB, etc., occurring in corresponding couples. The predominance of GB diffusion corresponds typically to low temperatures and is especially important for thin-film or microelectronic applications. Unfortunately, this subject is even not completely understood from the theoretical point of view because of the inherent requirements to consider coupled diffusion–elasticity or diffusion–plasticity problems, just forgetting a rather small number of dedicated and well-posed experimental measurements.

Here, we will shortly consider several issues, including diffusion–strain coupling in GB interdiffusion, the manifestation of the Kirkendall effect, and morphology development under GB interdiffusion.

10.8.1 Coupling of Diffusion and Strain for GB Interdiffusion

Herring [32] has analyzed the chemical potential of atoms in a GB under assumption that the GB is a perfect sink or source of vacancies and has shown that by neglecting the higher-order contributions of the stress tensor components, the chemical potential is modified by the value of $\Delta\mu$

$$\Delta\mu = -\sigma\Omega \tag{10.106}$$

where σ is the normal tensile traction at the GB and Ω is the atomic volume.

Let us analyze a simplified GB interdiffusion problem considering a stressed bicrystal. We will follow the formulation of Klinger and Rabkin [33, 34], as seen from Fig. 10.31.

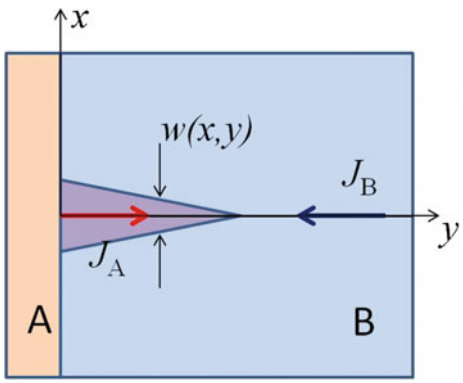

Fig. 10.31 A sample of material B, considered as a bicrystals with a single GB perpendicular to its surface, with the layer of material A deposited on its surface. The GB fluxes of A and B atoms are indicated, and an imbalance of J_A and J_A leads to formation of a wedge of extra material at the GB. The wedge thickness, $2w(x,y)$, is indicated

The atomic fluxes of the components along the GB, J_A, and J_B can be represented as the sums of two contributions associated with the gradient of concentration and the gradient of normal stress

$$J_A = -\delta D_{gb}^A \frac{\partial c_{gb}^A}{\partial y} + \frac{\delta D_{gb}^A \Omega}{kT} c_{gb}^A \frac{\partial \sigma}{\partial y} \tag{10.107a}$$

$$J_B = -\delta D_{gb}^B \frac{\partial c_{gb}^B}{\partial y} + \frac{\delta D_{gb}^B \Omega}{kT} c_{gb}^B \frac{\partial \sigma}{\partial y} \tag{10.107b}$$

Here, δ is the GB width (assumed to be the same for both components), $D_{gb}^A (D_{gb}^B)$ is the diffusion coefficient of A (B) atoms along the GB, and $c_{gb}^A (c_{gb}^B)$ is the GB concentration of A (B) atoms (in at/m^3). The atomic volume Ω is also supposed to be the same for both components, and thus,

$$c_{gb}^A + c_{gb}^B = \frac{1}{\Omega} \tag{10.108}$$

As a result of GB diffusion of A in B, the new material is plated as a wedge of the thickness w, as shown in Fig. 10.31. The conditions of mass conservation of A and B atoms are written as (for the case where the wedge is growing, $\partial w/\partial t > 0$)

$$\delta \frac{\partial c_{gb}^A}{\partial t} = \delta \frac{\partial}{\partial y}\left(D_{gb}^A \frac{\partial c_{gb}^A}{\partial y} \right) - \frac{\delta \Omega}{kT} \frac{\partial}{\partial y}\left(D_{gb}^A c_{gb}^A \frac{\partial \sigma}{\partial y} \right) - c_{gb}^A \frac{\partial w}{\partial t} \tag{10.109a}$$

$$\delta \frac{\partial c_{gb}^{B}}{\partial t} = \delta \frac{\partial}{\partial y}\left(D_{gb}^{B} \frac{\partial c_{gb}^{B}}{\partial y} \right) - \frac{\delta \Omega}{kT} \frac{\partial}{\partial y}\left(D_{gb}^{B} c_{gb}^{B} \frac{\partial \sigma}{\partial y} \right) - c_{gb}^{B} \frac{\partial w}{\partial t} \tag{10.109a}$$

In [33] the case of the same and constant GB diffusion coefficients was considered, $D_{gb}^{A} = D_{gb}^{B} = D_{gb} = \text{const}$, that Eq. 10.108 corresponds to a simplified equation

$$\frac{\partial w(y,t)}{\partial t} = -\frac{\delta \Omega D_{gb}}{kT} \frac{\partial^2 \sigma(y,t)}{\partial y^2} \tag{10.110}$$

The plated out material can be represented as a mass of edge dislocations with the Burgers vector density of $\partial w/\partial y$ [33]. Then, the diffusion of A and thickening of the wedge correspond to the climb of these dislocations toward B. The normal stresses can be written as [35]

$$\sigma(y,t) = \sigma_0 - E^* \int_0^\infty K(y,z) \frac{\partial w(z,t)}{\partial z} dz \tag{10.111}$$

Here, $E^* = E/4\pi(1 - \nu^2)$ is the equivalent elastic modulus and

$$K(y,z) = \frac{1}{y-z} + \frac{1}{y+z} - \frac{6y}{(y+z)^2} + \frac{4y^2}{(y+z)^3}$$

The solution of the system of Eqs. 10.109 and 10.111 (or a simplified solution of Eqs. 10.110 and 10.111) represents the evolution of GB concentration and normal stresses in the case of GB interdiffusion.

10.8.2 Kirkendall Effect in GB Interdiffusion

GB interdiffusion of A in B was extensively analyzed by Rabkin and Klinger [34], and we will follow their analysis. The diffusion problem is sketched in Fig. 10.31. The inequality of GB diffusion fluxes leads to plating out of additional material at the GB in the form of a wedge, as seen from Fig. 10.29. In this case, the GB concentration profiles are influenced by the normal GB stresses developing in the course of GB interdiffusion. It is important that the effective GB diffusion coefficients are weak functions of the relative difference of intrinsic GB diffusivities.

Klinger and Rabkin have shown that if $D_A > D_B$, i.e., if the solute diffuses faster than the matrix atoms, compressive GB stresses are developed in the near-surface zone, while at larger depths, the stresses are tensile. In the opposite case $D_A < D_B$, which is most probable in view of the experimental data, for instance,

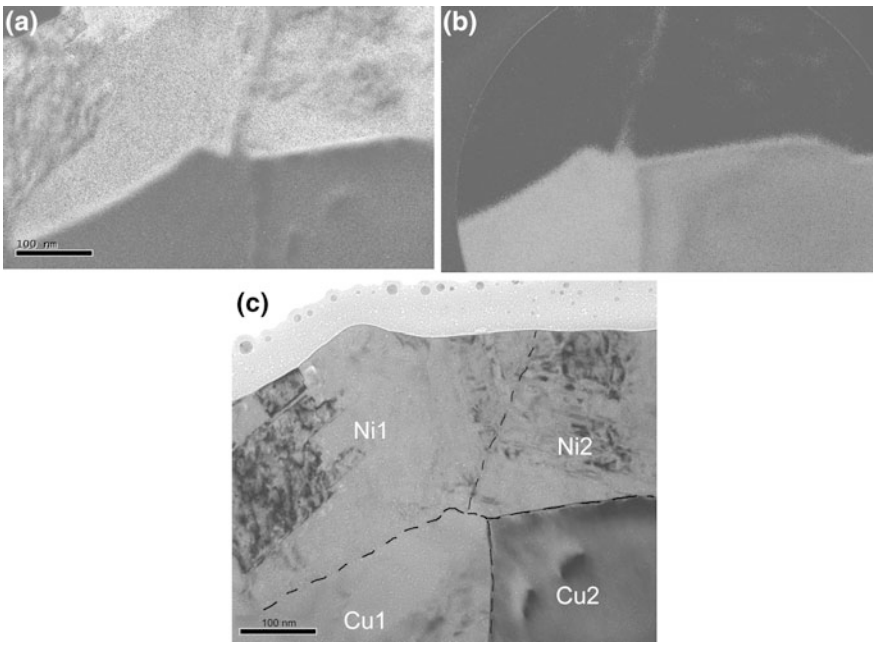

Fig. 10.32 Energy-filtered transmission electron microscopy images of the diffusion couple Ni/Cu. The distributions of Ni (**a**) and Cu (**b**) atoms are to be compared with the corresponding TEM image (**c**). The tracer of grain boundaries in Ni film and Cu substrate are sketched by dashed lines. The scale bars correspond to 100 nm

presented above for Cu, Fig. 10.16, the sequence of stressed zones along the GB is inverted.

The estimates of the maximal thickness of the wedge of extra material at a GB, which could be generated by the GB Kirkendall effect, provided values of the order of the diffusion GB thickness δ that complicates the direct experimental observations of such phenomena.

An example of GB interdiffusion in the Ni/Cu couple [36] is presented in Fig. 10.32. A thin Ni layer has been deposited in ultrafine-grained Cu (grain size of 300 nm), and the couple was annealed at $T = 450$ K for 24 h. The phenomena of Ni GB diffusion in Cu (Fig. 10.32a) and that of Cu in Ni (Fig. 10.32b) are qualitatively seen. The lines are drawn for a better understanding of the pictures. The Ni/Cu interface (thick dashed line) remains sharp after the annealing treatment. However, Cu penetrates strongly along the Ni1/Ni2 grain boundary (the bright contrast at the corresponding location in Fig. 10.32b). Marginal penetration of Ni atoms along the Cu GB can also be elucidated (see Fig. 10.32a).

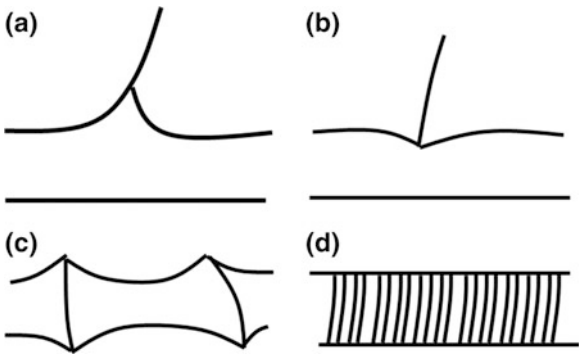

Fig. 10.33 Possible morphologies appearing in interdiffusion couples in the presence of GB diffusion: **a** formation of GB wedges toward reaction layer, **b** GB wedges toward end members with formation of solid solutions, **c** predominant growth of GB wedges due to enhanced GB diffusion, and **d** needle-like morphology of reaction layer due to the dominance of GB diffusion

10.8.3 Morphology of Growing Phases Affected by GB Diffusion

The GB interdiffusion can strongly affect the morphology of growing phases in an interdiffusion couple. The present analysis follows generally the analysis of van Loo [37]. Typical structures having been observed in different experiments are shown in Fig. 10.33.

The presence of grain boundaries in the end members can change the morphology of the reaction layer at low temperatures due to dominant GB diffusion, presented in Fig. 10.33a, b. Such cases correspond qualitatively to the model of Klinger and Rabkin considered above and given in Fig. 10.31. Experimentally, the appearance of the GB wedges was observed by Bastin [38] during the formation of β-Ti via GB diffusion of Ni into α-Ti. Tracers of iron in α-Ti were shown to play the key role in the corresponding experiments since addition of Fe stabilizes the β-Ti phase. Similar experiments on iron-free α-Ti stopped this kind of GB interdiffusion [38]. Bastin argued that the formation of a particular type of morphology, i.e., (a) or (b) in Fig. 10.33, has to depend on the position of the relevant interface with respect to the Matano plane.

If the rate of GB interdiffusion dominates over that through the crystalline bulk, morphology as in Fig. 10.33c may be formed. Such a kind of reaction layer growth has been observed for Ni_3A1 grown in the Ni/NiA1 diffusion couples [39].

At even lower temperatures, when bulk diffusion can be considered as frozen, thin needle-like crystals can often be formed, as shown in Fig. 10.33d. This case corresponds, for example, to the Cu_3Si formation in the Cu–Si couples [40]. Simultaneously, straight interphase boundaries are found. One may argue that interphase boundary diffusion is responsible for the flattering of the interface and GB interdiffusion for plating out material around grain boundaries.

References

1. J. C. Fisher, Journal of Applied Physics 22 (1951) 74.
2. B. S. Bokstein, I. A. Magidson, and I. L. Svetlov, The Physics of Metals and Metallography 6 (1958) 1040.
3. J. B. Gibbs, Physica Status Solidi 16 (1966) K27.
4. I. Kaur, Y. Mishin and W. Gust, Fundamentals of Grain and Interphase Boundary Diffusion (Chichester, John Wiley 1995).
5. R. T. P. Whipple, Philosophical Magazine 45 (1954) 1225.
6. T. J. Suzuoka, Journal of the Physical Society of Japan 19 (1964) 839.
7. A. D. Le Claire, British Journal of Applied Physics 14 (1963) 351.
8. H. S. Levine and McCallum, Journal of Appllied Physics 31 (1960) 595.
9. H. Gleiter, Microstructure, in: Physical Metallurgy, R.W. Cahn, P. Haasen (Eds.), North-Holland Physics Publishing, 1983, 649.
10. R. W. Balluffi, Grain-Boundary Diffusion Mechanisms in Metals, in: Diffusion in Crystalline Solids, G.E. Murch, A.S. Nowick (Eds.), Academic Press, Inc. (1984) 320.
11. D. Wolf and S. Yip, Materials Interfaces – Atomic-level Structure and Properties, Chapman and Hall (1992).
12. A. P. Sutton and R.W. Balluffi, Interfaces in Crystalline Materials, Clarendon Press, Oxford (1995).
13. S.V. Divinski, F. Hisker, Y.-S. Kang, J.-S. Lee and Chr. Herzig, Zeitschrift für Metallkunde 93 (2002) 256.
14. L. G. Harrison, Transactions of the Faraday Society 57 (1961) 597.
15. S.V. Divinski, H. Edelhoff and S. Prokofjev, Physical Review B 85 (2012) 144104.
16. E.W. Hart, Acta Materialia 5 (1957) 597.
17. J. C. Maxwell, A treatise on elasticity and magnetism, 3rd Ed. Clarendon press, 1892 page 435.
18. J. C. Maxwell-Garnett, Philosophical Transactions of the Royal Society A: Mathematical, Physical and Engineering Sciences 203 (1904) 385.
19. S.V. Divinski, M. Lohmann and Chr. Herzig, Acta Materialia 49 (2001) 249.
20. E. D. Hondros and M. P. Seah, Metallurgical Transactions A 8 (1977) 1363.
21. D. McLean, Grain Boundaries in Metals, Clarendon Press, Oxford (1957).
22. S.V. Divinski, F. Hisker, Y.-S. Kang, J.-S. Lee and Chr. Herzig, Zeitschrift für Metallkunde 93 (2002) 265.
23. B. Bokstein, V. Ivanov, O. Oreshina, A. Peteline and S. Peteline, Materials Science and Engineering A, 302 (2001) 151.
24. M. Reda Chellali, Z. Balogh and G. Schmitz, Ultramicroscopy 132 (2013) 164.
25. L. Klinger and E. Rabkin, Acta Materialia 47 (1999) 725.
26. S.V. Divinski, J. Geise, E. Rabkin and Chr. Herzig, Zeitschrift für Metallkunde 95 (2004) 1.
27. S.V. Divinski, Y.S. Kang, J.S. Lee and Chr. Herzig, Acta Materialia 52 (2004) 631.
28. S.V. Divinski, Y.S. Kang, J.S. Lee, F. Hisker and Chr. Herzig, Interface Science, 11 (2003) 67.
29. E. Budke, T. Surholt, S. Prokofjev, L. Shvindlerman and Chr. Herzig, Acta Materialia 47 (1999) 385.
30. S.V. Divinski, G. Reglitz and G. Wilde, Acta Materialia 58 (2010) 386.
31. D. Prokoshkina, V. Esin, G. Wilde and S.V. Divinski, Acta Materialia 61 (2013) 5188.
32. C.J. Herring, Journal of Applied Physics 21 (1950) 437.
33. L. Klinger and E. Rabkin, Acta Materialia 55 (2007) 4689.
34. L. Klinger and E. Rabkin, Acta Materialia 59 (2011) 1389.
35. H. Gao, L. Zhang, W.D. Nix, C.V. Thompson and E. Arzt, Acta Materialia 47 (1999) 2865.
36. J. Ribbe, G. Schmitz and S. V. Divinski, unpublished work (2007).
37. F. J. J. van Loo, Progress in Solid State Chemistry 21 (1990) 47.
38. G.F. Bastin and G.D. Rieck, Metallurgical Transactions 5 (1974) 1817.

39. M. M. P. Janssen and G. D. Rieck, Transactions of the Metallurgical Society of the American Institute of Mining, Metallurgical and Petroleum Engineers 239 (1967) 1372.
40. J. G. M. Becht, F. J. J. van Loo and G. Metselaar, Reactivity of Solids 6 (1988) 45.
41. S. J. Rothman, N. L. Peterson, and J. T. Robinson, Physica Status Solidi 3b (1970) 635.
42. J. Sommer and Chr. Herzig, Journal of Applied Physics 72 (1992) 2758.
43. Ya. E. Geguzin and G. N. Kovalev, Fizika Tverdogo Tela 5 (1963) 1687.
44. S.V. Divinski, J. Ribbe, G. Schmitz and Chr. Herzig, Acta Materialia 55 (2007) 3337.
45. M. Lohmann, S.V. Divinski and Chr. Herzig, Z Metallkd 94 (2003) 249.
46. S.V. Divinski, M. Lohmann and Chr. Herzig, Acta Materialia 53 (2004) 1249.
47. T. Surholt and Chr. Herzig, Acta Materialia 45 (1997) p. 3817.
48. A. Atkinson and R.I. Taylor, Philosophical Magazine A 43 (1981) 979.
49. P. Gas, D. L. Beke and J. Bernardini, Philosophical Magazine Letters 65 (1992) 133.
50. S.V. Divinski, F. Hisker, Y.-S. Kang, J.-S. Lee and Chr. Herzig, Interface Science 11 (2003) 67.
51. A. Inoue, H. Nitta and Y. Iijima. Acta Materialia 55 (2007) 5910.
52. J. Fiebig, H. Rösner, Y. Estrin and G. Wilde, Journal of Applied Physics 110 (2011) 083514.

Chapter 11
Reactive Phase Formation in Thin Films

In this chapter, we will discuss some aspects related to reactive phase formation in thin films. We try to utilize as much as possible the information accumulated during the earlier chapters and built on that. We will first have a brief look on nucleation issues, especially in solid state, before moving into effect of microstructure and impurities on the reactive phase formation. Finally, we will introduce some of the models for phase growth that have been introduced in the past and then discuss in detail about their pros and cons.

The formation of crystalline phases starts by nucleation (which is actually preceded by interdiffusion to create a driving force for the process). The nucleation stage and factors influencing it are discussed in Sect. 11.1. If the stable crystalline phases cannot form directly, metastable structures will form first, as discussed previously in Chap. 1. The formation of amorphous metastable structures is discussed in Sect. 11.2. The kinetics of phase formation is influenced by numerous factors such as impurities, interfaces, and stresses—all these are briefly discussed in Sects. 11.3, 11.4 and 11.5. Finally, growth models developed to describe reactive phase formation in thin films are critically evaluated in Sect. 11.6.

11.1 Role of Nucleation

When a new phase AB is formed at an interface between two elements A and B, the driving force for the reaction is the Gibbs energy of formation of AB from pure A and B. However, the formation of AB involves creation of two new interfaces A/AB and AB/B instead of the old A/B interface. This in general leads into increase in surface energy $\Delta\sigma$ of the system (Fig. 11.1). The classical theory of nucleation mandates that the competition between the gain in free energy ΔG and the energy loss $\Delta\sigma$ should give rise to nucleation mechanisms with an activation energy ΔG^* proportional to $\Delta\sigma^3/\Delta G^2$ (Fig. 11.2). There has been much criticism of the classical theory of nucleation. Nevertheless, it illustrates quite simply the major factors involved in the nucleation process.

A. Paul et al., *Thermodynamics, Diffusion and the Kirkendall Effect in Solids*,
DOI: 10.1007/978-3-319-07461-0_11, © Springer International Publishing Switzerland 2014

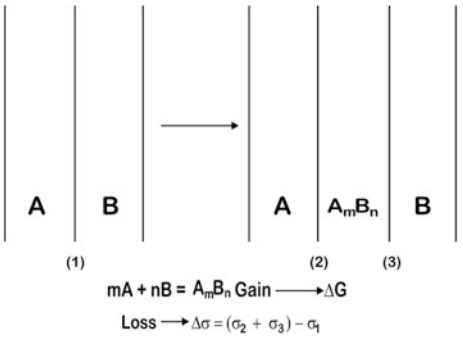

Fig. 11.1 Schematic presentation of the formation of a new phase between A and B

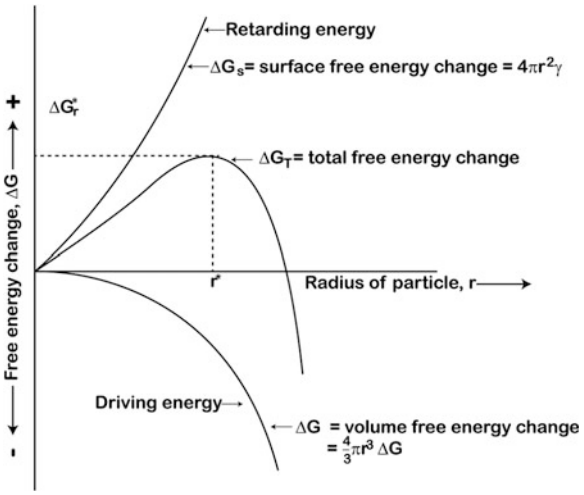

Fig. 11.2 The free energy of a nucleus as a function of its radius, showing the surface contribution (*positive*), the volume contribution (*negative*), and their sum

In its simplest form, classical nucleation theory starts with the equilibrium between two phases of a given substance at either the melting or evaporation point. At the equilibrium point T_c, the free energy change ΔG equals to zero as shown in Chap. 1

$$\Delta G = \Delta H - T_c \Delta S = 0 \tag{11.1}$$

thus leading into

$$\Delta S = \frac{\Delta H}{T_c} \tag{11.2}$$

At the transition temperature, the driving force is zero and nothing can happen. At any temperature T_1 away from the transition temperature, the phase transformation is driven by the driving force

$$\Delta G = \Delta H\left(1 - \frac{T_1}{T_c}\right) \tag{11.3}$$

as long as T_1 is not too far from T_c. This transformation is opposed by the surface energy contribution.

The total free energy of a nucleus with average radius r and free energy ΔG_1 (calculated per unit volume) is expressed generally as

$$\Delta G = br^2\sigma - ar^3\Delta G_1 \tag{11.4}$$

where a and b are geometrical terms taking into account the fact that if the nucleus is crystalline, it will generally not be spherical, because of the anisotropic characteristics of crystalline elements, but tries to adopt some definite shape with minimum surface energy. This can be determined with Wulff construction if sufficient data on surface energies of various crystal planes are available. The relation between the free energy of a nucleus and its radius is shown in Fig. 11.2. As seen, ΔG passes through a maxim that corresponds to the critical size r^* of the nucleus. The population of nuclei smaller than r^* will exist in some form of quasi-equilibrium distribution (e.g., they constantly appear and disappear maintaining some kind of "equilibrium" distribution), whereas nuclei larger than r^* will tend to grow. The value of the critical nucleus can be obtained by derivation of (11.4)

$$r^* = \frac{2b\sigma}{3a}\Delta G_1 \tag{11.5}$$

Furthermore, the free energy of the critical nuclei becomes (at any temperature T) [see, Eqs. 11.3–11.5]

$$\Delta G^* = 4b^3\sigma^3 T_c^2/27a^2\Delta H^2(T - T_c)^2 \tag{11.6}$$

At that temperature, the rate of nucleation ρ^* will be proportional to the concentration of critical nuclei and to the rate at which such nuclei can form, generally some diffusion term of the type $\exp(-Q/kT)$, so that (with a proportionality factor K)

$$\rho^* = K\exp(-\Delta G^*/kT)\exp(-Q/kT) \tag{11.7}$$

Proportionality factor can be explained briefly as follows. Under the dynamic conditions that prevail during nucleation, one expects the number of nuclei of critical size to be less than predicted by thermodynamic equilibrium. This is due to the fact that during nucleation the equilibrium population of critical nuclei is constantly being depleted by the nuclei that grow. The proportionality factor is usually estimated to be about two. It contains also the so-called the Zeldovich factor that is a measure of the probability that fluctuations will cause nuclei, even a size above the critical limit, to dissolve as long as their free energy remains within

kT of ΔG. Thus, every microcluster passing the critical size will not grow. This means also that there is a flat region with a width of δ in the free energy versus radius plot. The Zeldovich factor is the reciprocal of this width. It may assume values of the order of 10^{-2}.

In general in the formation of phases from the end elements, ΔG's are large and thus activation energy (ΔG^*) is small and the nucleation is quite easy. However, after the first phase in the formation of subsequent phases, nucleation may play a decisive role. It should be noted that ΔG^* is actually formed from two parts ΔG^*_1 and ΔG^*_2, $\Delta G^* = \Delta G^*_1 + \Delta G^*_2$, where ΔG^*_1 is related to the density of the crystalline nucleus and ΔG^*_2 to their growth, e.g., diffusion kinetics.

When a nucleus of a new phase is formed, this generally causes a volume change to take place. In solid–solid nucleation, this is accompanied by deformation energy ΔH_d (elastic energy, plus the possible plastic energy). The activation energy for nucleation becomes proportional to $\Delta\sigma^3/(\Delta G_c - \Delta H_d)^2$, where ΔG_c is the "chemical" free energy of bulk phases and the energy associated with deformation is subtracted from that value. One can derive this by first including the term for strain energy into Eq. 11.4. It is also a bit more convenient to consider the free energy per atom of the nucleus rather than the free energy per volume of the nucleus as in Eq. 11.4. The free energy associated with the formation of a nucleus of *n atoms*, Δg, may be written as

$$\Delta g = n\Delta g_C + \eta n^{\frac{2}{3}}\gamma + nh_d \tag{11.8}$$

where

n	number of atoms in nucleus
Δg_C	bulk (chemical) free energy change per atom in nucleus
η	shape factor such that $\eta n^{2/3}$ = surface area
γ	surface tension ≈ surface free energy (exactly for liquids, but only approximately with solids, because in solids there is also another factor (the surface stress) which contributes to surface energy)
h_d	strain energy per atom in nucleus

One may regroup this equation as

$$\Delta g = n(\Delta g_C + h_d) + \eta n^{\frac{2}{3}}\gamma \tag{11.9}$$

The term Δg_C will be negative below the transformation temperature, whereas h_d and γ are both positive. Hence, if $|\Delta g_C| > h_d$, then the first term is negative. The free energy required (Δg^*) to form the critical size nucleus (n^*) is found by differentiating Eq. 11.9 and assuming Δg_C, h_d, η, and γ as constants.

$$\Delta g* = \frac{4}{27}\frac{\eta^3\gamma^3}{(\Delta g_C + h_d)^2} \tag{11.10}$$

A large strain energy h_d reduces the denominator and makes Δg^* large. This means that nucleation is more difficult since the critical size nucleus has a higher energy of formation. This strain energy must be compensated by the lattice and can be done, for example, in silicides, mainly by the diffusive motion of atoms or in metals by dislocation motion. Large strains may change the energetic status of the system and lead to formation of metastable structures (e.g., amorphous phases) as will be discussed later on. It is to be noted that the strain energy is essentially irrelevant to incoherent nucleation. In the case of strained incoherent microcluster, diffusion of thermal vacancies to or from the disordered interface may completely eliminate the strain energy of the system [1]. It is the cases of coherent and semicoherent precipitates where the strain energy becomes relevant. It may be argued that all nuclei are coherent at the very first stages of nucleation. However, at the same time, it should be realized that these phenomena may be inaccessible to experimental methods in many occasions.

The most important parameters determining the phase selection during nucleation are the activation energy of nucleation, Δg^*, the interface energies σ and, the chemical driving force Δg_C, and the elastic strain energy Δh_d—although this last parameter is not relevant to incoherent precipitate cases. In order to evaluate a possible phase selection, reasonable estimates of these parameters must be obtained.

*11.1.1 Activation Energy Δg**

This term can be approximated by the activation energy of diffusion, since the formation of a critical nucleus is mainly determined by diffusional jumps. If this is not available, it can be also approximated with the activation energy of growth of the formed phase in the planar growth regime. From investigations on the later stage of growth, it has been concluded that the precipitates formed in the A/B interface first grow to coalescence within the A/B interface [2]. These results indicate that growth of the nucleus is preferred in the direction of the interface emphasizing the importance of atomic mobility of the A/B interface. Therefore, it is reasonable to assume that the activation energy of volume diffusion is only an upper estimate for the activation energy of growth.

11.1.2 Interfacial Free Energy σ

The interface free energies of crystalline phases consist of two contributions: the chemical contribution related to (chemical) atomic interaction energy, and the structural contribution that originates from the free energy of structural defects associated with semicoherent and incoherent interfaces [3]. The interface free energy terms are hardly known, and even if they are known they are usually bulk

values, and therefore, their use in early stages of phase formation is highly questionable. The interfacial free energies in the solid state are likely to vary between values approaching zero for epitaxial interfaces to maximum values of the order of few J/cm^2 for random interfaces [4]. It should be emphasized that surface free energies of crystalline solids are very much dependent on the history of the specimen, crystal orientation, defect density, impurities etc., and they may depend on the size of the microcluster. Hence, the values of surface free energies for solids are not material constants, but are specific for the sample in question.

11.1.3 (Elastic) Strain Energy Δh_d

Elastic strain energy affects the nucleation, particularly in the case of coherent or semicoherent precipitates, as can be seen from the Eq. 11.10. Here, one will consider only elastic energy, yet the deformations involved can reach proportions beyond the usual elastic limits of the materials. A complete analysis of these effects should take into account the energy stored in plastic deformation as well. The elastic energy resulting from the formation of a third phase will depend on the elastic characteristics of all three phases. In the simplified case where all three phases have the same elastic constants, the energy is given by the following relation [1, 5]

$$\Delta g_{\mathrm{el}} = [2s(1+\nu)/9(1-\nu)]\varepsilon^2 \tag{11.11}$$

where s, the shear modulus of elasticity, is also called the modulus of rigidity, ν is the Poisson ratio, and ε, the strain, is the ratio between the excess volume (under zero stress) and the volume of the hole (here the volume of the reactants) [4]. Ignoring the problems of anisotropy, the following relations from the theory of elasticity can be utilized. Young's modulus E is equal to s times $2(1 + \nu)$; some tables also give the compression or bulk modulus, which is equal to E, divided by $3(1-2\nu)$. The problems of interest here do not concern isotropic materials but three different materials at once. As a zeroth approximation, one may consider that the strain energy is given by an average of the different elastic constants.

11.1.4 The Chemical Driving Force

In order to calculate the chemical driving force for the nucleation of a new phase at the A/B interface, the free energy curves of the solid solution phases and of the formed compounds must be known. These can be determined by applying the CALPHAD method [6–10]. If there exists no information about lattice stabilities and so on in the system, these quantities can be evaluated by ab initio methods. In systems with large negative heat of compound formation, the driving force for the

nucleation of a new phase from the pure elements (with no or negligible terminal solid solubility) is large and approaches to the free energy of compound formation in the reaction temperature. However, in all systems, interdiffusion must occur first to create the necessary driving force for nucleation. Thus, as this may in some cases substantially decrease the initially available driving force for compound formation, this issue must be taken into account [11].

In Thompsons [11] treatment, it is shown that interdiffusion must precede nucleation of new phases and that only after some interdiffusion has occurred there can be a driving force for nucleation (see also Sect. 1.15 for more details). This requirement imposes a kinetic constraint to the first-phase formation. Thus, relative mobilities of diffusing components in competing phases will determine which phase will form first.

In Fig. 11.3, the Gibbs energy curves of the AB system at a given temperature are shown, where A and B have different crystal structures α and β, respectively, and they can form a stable intermediate phase η and a metastable phase M. By assuming that A diffuses into β much faster than B into α, we simplify the case so that only diffusion of A into β needs to be considered. According to the thermodynamic principle of phase equilibrium (see Sect. 1.15), as diffusion proceeds, the first phase to nucleate should be η in β when a sufficient volume of β has reached its equilibrium composition X_{eq} with η (see the tangent line between β and η in Fig. 11.3). Here, it should be remembered from the earlier discussion (Sect. 1.15) that even though η becomes stable at this point, it will not form, since there is no supersaturation, which would provide the necessary driving force for nucleation. If η cannot nucleate, it will become possible for the metastable phase M to nucleate in β when a sufficient volume of β has reached its equilibrium composition X_m with M, provided that the interdiffusion continues. Similar arguments about the required supersaturation as presented above naturally also apply here. The appearance of the metastable phase M would therefore indicate that the time required for nucleation of η is longer than the time required for interdiffusion to the point at which M can nucleate. If neither η nor M can nucleate when the composition of β passes through X_{eq} and X_m sequentially, β will polymorphically transform into M when its composition reaches X_0. This analysis leads to a conclusion that the phase selection depends on the interdiffusion rate in the parent phases as well as the nucleation rates of the product phases.

While the relative rates of nucleation are (ultimately) controlling the phase selection, which phase can nucleate (and grow) is controlled by interdiffusion. Hence, the first-phase formation depends exclusively on the kinetics. It is to be noted, however, that thermodynamics of the system influences the magnitude of the diffusion coefficients via the interaction parameters (see Chap. 1). The nucleation rates are controlled not only by the barriers to nucleation, and hence, the volume Gibbs energy ΔG_v and the energies of the interfaces σ involved, but also by the diffusion required to form critically sized clusters of the product phases. Thompson [11] further suggested that if one component diffused rapidly into the other and self-diffusion of the host was slow, polymorphic phase transitions were favored, so that phases with broad compositional ranges of stability and phases that were rich in

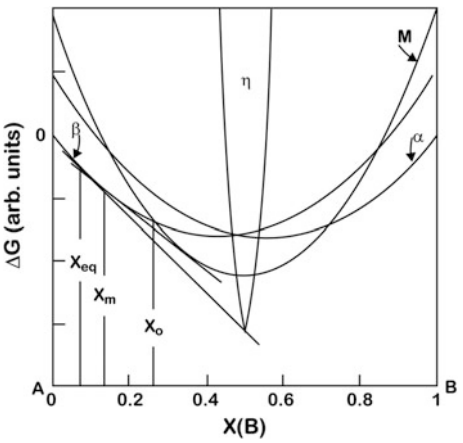

Fig. 11.3 Schematic illustration of the free energy versus composition of a system AB, where elements A and B have different equilibrium crystal structures α and β, respectively, and they can form a crystalline intermetallic phase η and a metastable intermetallic phase M [11]

the slowly moving component were preferred, and such phases with low energy interfaces with the host phase(s) would be especially favored. This points toward amorphous phase formation as will be discussed below.

It should also be emphasized that the free energies of compound formation calculated by the CALPHAD method typically refer to bulk materials. In a small nucleus, the chemical long-range order may not be fully developed due to the interfacial constraints, thus increasing its free energy with respect to the bulk value. In addition, despite the surface energy terms are important in small scales encountered during nucleation, they are typically disregarded in traditional CALPHAD calculations. Further, strain energy may also be important if incoherent interface has not yet been created between the forming nuclei and the matrix. Therefore, the free energy of an ordered chemical compound (as derived from the CALPHAD method) should be viewed as the lower limit for the free energy of the compound nucleus. Thus, the driving force for the formation of a certain compound may be considerably smaller than calculated by using bulk values.

11.1.5 Nucleation Issues in Solid-State Amorphization

The term solid-state amorphization (SSA) is used to describe manufacture of amorphous alloys by solid-state reaction of the crystalline elements. There are two important nucleation-related problems in solid-state amorphization. One is to understand how an amorphous phase forms at an interface between two crystalline elements, the other is to explain how nucleation and growth of a crystalline element is suppressed until an amorphous layer has attained a temperature- and system-dependent critical thickness. The first problem is dealt below and the second in subsequent sections.

The most studied amorphizating system is probably Ni–Zr [12, 13]. It is possible to form amorphous layer between Ni and Zr by annealing in the solid state. Once formed, the layer continues to grow until it has reached a temperature-dependent critical thickness. At this critical thickness the amorphization is terminated by nucleation of the crystalline Ni–Zr compound at the interface between the amorphous alloy and crystalline Zr. Recent experimental investigations have revealed that there is a barrier to nucleation of alloy phases at a Ni/Zr interface and that some Zr grain boundaries are sufficiently potent heterogeneous sites that they reduce this obstacle and allow reaction at a temperature sufficiently low for amorphization to be possible [14–16]. However, calculation based on classical nucleation theory suggests that no such barrier exists [17, 18]. The experimental evidence suggests that either the estimates of the volume and surface terms in the work of Johnson [17] and of Clemens [18] are incorrect or that some additional effects, not included in the classical nucleation analysis, are at work.

As has been discussed above, classical nucleation theory assumes that there is no obstacle for creating small clusters of a new phase within an existing phase. Some of these then acquire critical size and start to grow. Kelton and Greer [19] made a quantitative test based on numerical modeling of the cluster evolution for multistep annealing treatments in lithium disilicate glass. They found the classical theory of nucleation to be valid provided that the critical size was greater than 16 or 20 molecular formula units. The classical approach might not deal adequately with a situation in which the predicted critical size is of molecular dimensions or smaller for two reasons. First, the key parameters in classical theory are the volume free energy and the interfacial free energy as seen above. They may both be functions of cluster size as was discussed earlier. A second, more fundamental problem is that it may be wrong to base nucleation calculations upon clusters of the critical size while neglecting the obstacle to reaction which is presented by creating initial very small clusters of a new phase. This is related to the above treatment of Thompson showing that significant interdiffusion is required before the formation of clusters is possible in systems exhibiting extensive solid solubility.

If classical theory of nucleation is inadequate in circumstances where the predicted critical radius is small, other means of analyzing the initial reaction at, for example, Ni/Zr interface. In particular, one might examine processes, which precedes the formation of clusters of an alloy phase and which could provide a barrier to nucleation, which is larger than the one predicted by classical theory. One could examine first an unmixed interface and then calculate the likelihood of pair's exchanges. As an effect of such exchanges, two solid solutions would form, one of Ni in Zr and one of Zr in Ni. These solid solutions could act as precursors to the glassy phase. The thermodynamic quantities associated with exchange process are assumed to be the molar strain free energy g_s, the molar enthalpy of mixing h_m and the molar configurational entropy s_c [20]. If an interface contains N pairs of atoms, of which a fraction of n have exchanged, the configurational entropy is (as shown in Chap. 1)

$$s_c = -Nk[n\ln(n) + (1-n)\ln(1-n)] \tag{11.12}$$

assuming that the use of Stirling's approximation is justified. Minimizing the free energy of the interface with respect to n gives

$$n = \left[1 + \exp\left(\frac{h + g_s}{kT}\right)\right] \tag{11.13}$$

This expression predicts a barrier to reaction if $(h + g_s)$ is positive.

It is necessary to estimate the magnitudes of h_m and g_s as was done previously in the case of classical approach. Christian [21] suggests that the strain energy that results from dissolving an atom of element B in matrix of element A is

$$g_s = \frac{2s_A K_B (v_A - v_B)^2}{v_B(3K_B + 4s_A)} \tag{11.14}$$

Here, s_A and v_A are the shear modulus and atomic volume of element A, respectively, while K_B and v_B are the bulk modulus and atomic volume of element B. Substitution of atomic volumes from Barret and Massalski [22] and elastic module from Brandes [23] into Eq. 11.14 gives a free energy increase of 1.6×10^{-19} J/atom on dissolving Zr in Ni, and 2.6×10^{-19} on dissolving Ni in Zr. Thus, g_s is 128 kJ/g atom. It must be emphasized that the Eq. 11.14 is only approximate and furthermore, the Ni and Zr lattices will not strain independently of each other, and Ni is likely to dissolve in Zr also interstitially. The large value predicted by Eq. 11.14 is intrinsic to systems with propensities to form glasses by solid-state amorphization (SSA). It has been noticed that disparity between the atomic sizes of species is required in order that an amorphous phase can grow and in order to suppress the nucleation of a crystalline phase(s) as Eq. 11.14 suggests.

An attempt to estimate the enthalpy change h on exchanging a pair of atoms is more complicated because atoms at the unmixed interface already have nearest neighbors, which are not similar. For this reason, only part of the full enthalpy of mixing is available to contribute to h. It is noticeable that even the full enthalpy of mixing -43 kJ/g atom at the equiatomic composition [24] is much less than the evaluated g_s. From these values, it seems that $(h + g_s)$ may be positive and there might be a barrier to exchange atoms at the Ni/Zr interface.

Christian [21] suggests that while single dislocations cannot readily reduce stresses developed in small volumes, larger defects, such as grain boundaries, may be able to. This could explain why grain boundaries at Ni/Zr interfaces are able to act as heterogeneous sites. It does not, however, indicate why Zr, rather than Ni grain boundaries are needed. One reason might be that the free energies associated with certain Zr grain boundaries are greater than the free energies of Ni grain boundaries. A second possibility is that the strain energy associated with dissolving Ni atom in Zr is greater than that caused by dissolving Zr atom in Ni. A third possibility is that the diffusional asymmetry in Ni–Zr makes the slow-diffusing Zr the "matrix" element for SSA, and the reaction must begin in the Zr lattice.

It will be thermodynamically favorable for the precursor solid solutions to transform into an amorphous phase, since the interfacial energy increase associated with the formation of two amorphous/polycrystalline interfaces is probably less than the free energy penalty attributable to strains in the solid solutions. It should be remembered that the incoherent interface can act as a source or sink for thermal vacancies, thus enabling the relief of strains in the system. It is also possible that the stresses developed in the system may change the energetic situation in such a way that amorphous phase becomes more stable than the crystalline ones. The amorphous phase can dissolve solute atoms more easily and is also expected to be able to relax stresses more effectively than crystalline phase. The effect of stresses can be integrated into the Gibbs energy equation of a phase in question. The stress term may lift the Gibbs energy curve of the crystalline phase/phases to such high level that amorphous phase becomes the stable one (see Sect. 1.15).

11.2 Metastable Structures and Nucleation on Concentration Gradient

The types of metastability in alloys have been classified by Turnbull [25] as compositional, structural, and morphological. The degree of metastability is characterized by the free energy excess of the system over that of the equilibrium state. Turnbull [25] expressed this energy per mole as a fraction of $R\bar{T}_m$, where R is the gas constant and $\bar{T}_m$ is the average of the elemental melting points. Compositional metastability is where an equilibrium phase exists outside its normal composition range, and it is associated with large excess energies of up to about $1.0\ R\bar{T}_m$. Structural metastability is where a phase has a non-equilibrium structure, typically with excess energies of about $0.5\ R\bar{T}_m$. Morphological metastability has the lowest excess energy, about $0.1\ R\bar{T}_m$, but is perhaps the most widespread, and generally useful, type of metastability. Its excess energy arises from the abnormally large area of grain boundaries and interphase interfaces.

A system in true metastable equilibrium would not have access to any state of lower free energy by means of a continuous structural change [26]. A good example of such is a fully relaxed amorphous phase, in which any transformation to a lower free energy microstructure can commence only with a discrete nucleation stage which has an energy barrier as discussed. On the other hand, most morphologically metastable microstructures are not in metastable *equilibrium* but can evolve continuously on annealing. In this case, the energy barrier is not nucleation, but the activation energy of atoms making diffusional jumps. Such a system is thermodynamically unstable but is configurationally frozen [26]. Indeed virtually all so-called metastable microstructures, whether in fact metastable or unstable, have technologically useful lifetimes because they are at sufficiently low temperatures to be configurationally frozen. One interesting example of

morphological metastability is the room temperature annealing of either sputter or electrochemically deposited copper in IC fabrication [27–29]. After deposition, the grain size of the films increases after few hours in room temperature. The driving force is provided by the systems tendency to decrease its surface area and thereby its surface energy.

The formation of metastable structures has been observed also in many silicide forming systems [30–34]. The occurrence of these metastable structures is related to the specific features of the thin films. Among these are the very fast atomic transport and very steep concentration gradients often observed in thin-film structures. Since, amorphous films are always metastable, there always exists a crystalline phase or mixture of several crystalline phases, which are thermodynamically more stable than the amorphous phase. In other words, amorphous phases exist only due to some kind of barrier(s), which prevents the formation of equilibrium phases.

In all the above-mentioned silicide systems where the solid-state amorphous (SSA) phase formation has been observed to take place, it has been observed that in the formation temperature range only the smaller atoms are mobile (e.g., Ni in Si and Si in Ta). This can explain the absence of crystalline compound nucleation during the growth of a glassy interlayer [35]. The relative immobility of the larger atom must act as a kinetic constraint to the formation of crystalline compound nuclei. Such nucleation apparently requires the collective motion of both atomic species. Thus, glass growth seems to require diffusional asymmetry in binary diffusion couples. In higher temperatures, the formation of crystalline phases becomes possible due to the enhanced atomic transport.

The absence of compounds in SSA leads to equilibria involving much higher solute contents in the elemental solid solutions that in full equilibrium. The equilibria are also at much lower temperatures than are usual for the phases involved. Figure 11.4 shows the equilibrium phase diagram for Au–Si. This system, in which glass formation by rapid liquid quenching was first found by Klement et al. [36], is a simple eutectic. In binary eutectic systems, the chemical interaction between the elements is repulsive. As the attractive interaction between the elements is increased, compounds will start to appear in a binary system.

A good example of this is Ni–Zr (Fig. 11.5), which exhibits SSA and is indeed one of the most widely investigated systems exhibiting SSA as stated earlier. Since the compounds do not enter into the SSA reaction, the relevant metastable phase diagram is shown by the bold curves in Fig. 11.5. The curves show actually the extended liquiduses. This kind of metastable phase diagrams can be calculated with the help of CALPHAD method as already discussed. Under normal conditions of SSA in Ni–Zr system (composition of the a phase is about $Ni_{60}Zr_{40}$ annealed at 300 °C) [37], it is clear from the metastable phase diagram that there should be eutectic melting of a mixture of the elemental solid solutions. The liquid-like amorphous phase is favored with respect to the solid solutions, and it can therefore be formed by annealing, rather than by rapid quenching as in system like Au–Si. However, the SSA reaction is exothermic and not endothermic as might be expected for melting. This is because the enthalpy of mixing the two

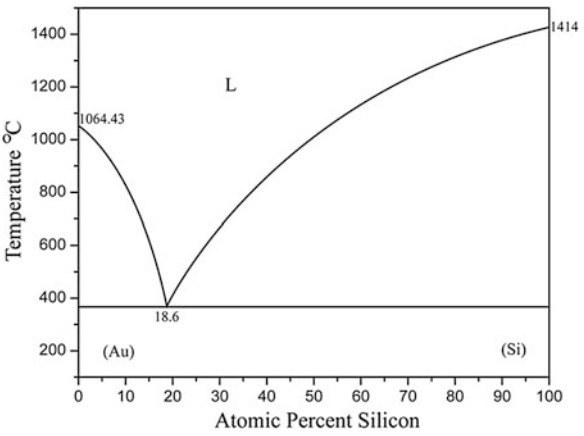

Fig. 11.4 The equilibrium phase diagram of Au–Si, a system showing glass formation by melt quenching, but not by SSA

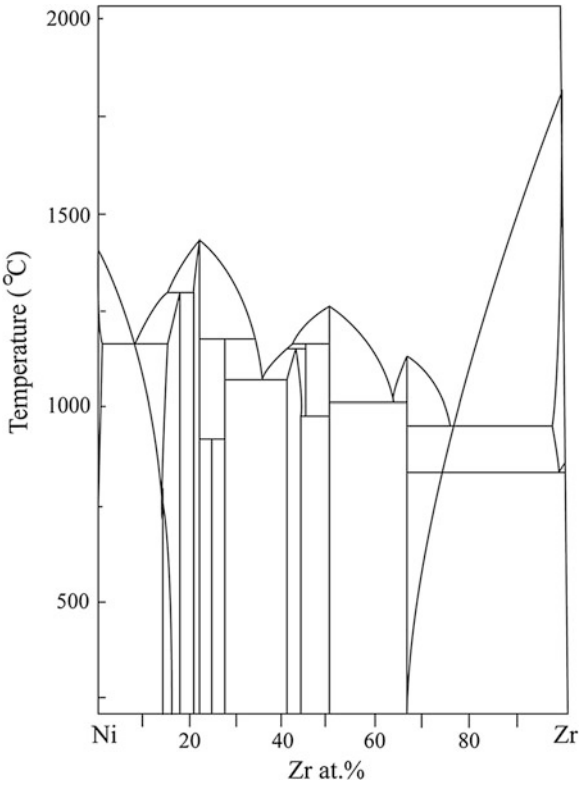

Fig. 11.5 The equilibrium phase diagram of Ni–Zr, a system exhibiting SSA. A possible metastable phase diagram in the absence of compounds is shown by *bold curves* [26]

elements in the liquid-state amorphous phase is highly negative and outweighs the average enthalpy of fusion. Such a negative enthalpy of mixing arises when the liquid alloy has a specific heat significantly higher than the solid state of the

system. In fact, substantial excess specific heats have been measured directly in good glass-forming alloys, for example, $Pd_{40}Ni_{40}P_{20}$ [38]. They are associated with ordering in the liquid state. If there were to be a eutectic melting temperature for Ni–Zr (involving only elemental phases and the liquid), the entropy of melting would have to be positive. Combined with the negative enthalpy of melting, this would imply a negative equilibrium temperature [26]. The conclusion is that for Ni–Zr, the eutectic equilibrium does not exist above absolute zero. Provided that the intermetallic compounds can be avoided, the amorphous phase in the middle of the composition range is stable down to absolute zero. The phase equilibria in systems such as Au–Si and Ni–Zr are related to each other, and an evolution from one type of eutectic system to the other is found as the ordering tendency in the liquid alloy is increased.

One example of impurity-induced amorphous phase formation can be found from the ternary Ta–C–O system. The high-resolution micrograph displayed in Fig. 11.6 reveals the presence of an amorphous layer at the TaC/Cu interface. The composition of the layer was determined to be Ta with marked amounts of oxygen and carbon from the very thin foil (tens of nanometers thick) with the X-ray energy-dispersive spectrometry (EDS) in the analytical TEM. Equally high amounts of oxygen and carbon were not detected from either side of the amorphous layer. The layer is most probably $Ta[O, C]_x$ (i.e., metastable oxide) containing some carbon released from the partly dissociated TaC layer. The formation of the amorphous layer was most likely caused by the presence of oxygen in the films and also because of the diffusion of extra oxygen to the films from the annealing environment. The structure of the Cu overlayer is strongly columnar, thus providing suitable short-circuit paths for oxygen diffusion from the atmosphere during annealing. The overall oxygen content of the as-deposited films is expected to be 1–2 at.%. In particular, the upper part of the TaC layer (i.e., near the TaC/Cu interface) should contain even higher amounts of oxygen. This is owing to the sputtering system, which is equipped with turbodrag pumps to guarantee oil-free deposition, and therefore, the pumping of water vapor from the chamber is not very efficient, although system has load lock. In the case of the Si/Ta/Cu metallization system, secondary ion mass spectrometry (SIMS) analyses revealed an amorphous oxygen-rich layer to be present already in the as-deposited films. Even though this may be the case also in this system, the major part of the incorporated oxygen is most likely present at the grain boundaries of the as-deposited TaC layer.

The isothermal section of the metastable Ta–C–O phase diagram at 600 °C is displayed in Fig. 11.7. The oxygen partial pressure used in the calculations was 0.2×10^{-4} Pa. Since no thermodynamic data for the metastable Ta oxides are available, the data for stable Ta_2O_5 phase are used [39–43]. It is evident that the metastable amorphous $Ta[O, C]_x$ will eventually transform into the stable phases (i.e., Ta_2O_5 and graphite). In fact, according to the XRD results, the formation of Ta_2O_5 took place at 725 °C (Fig. 11.8). When the formation of Ta_2O_5 takes place, TaC and graphite must also be present, since they form a three-phase field in the diagram (Fig. 11.7). TaC phase is expected to come into local equilibrium with metastable $Ta[O, C]_x$ before the formation of stable Ta_2C is possible. Therefore,

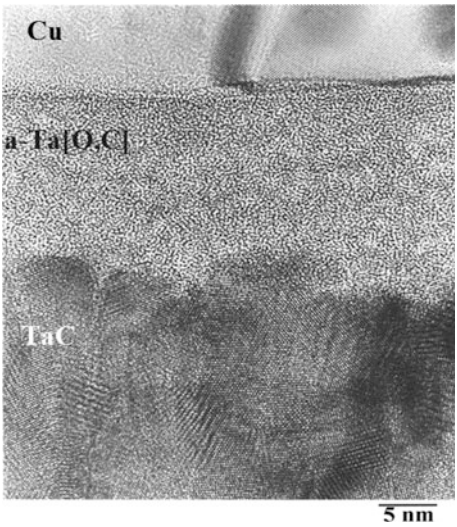

Fig. 11.6 HREM micrograph from the amorphous Ta[O, C]$_x$ phase from the sample annealed at 600 °C for 30 min

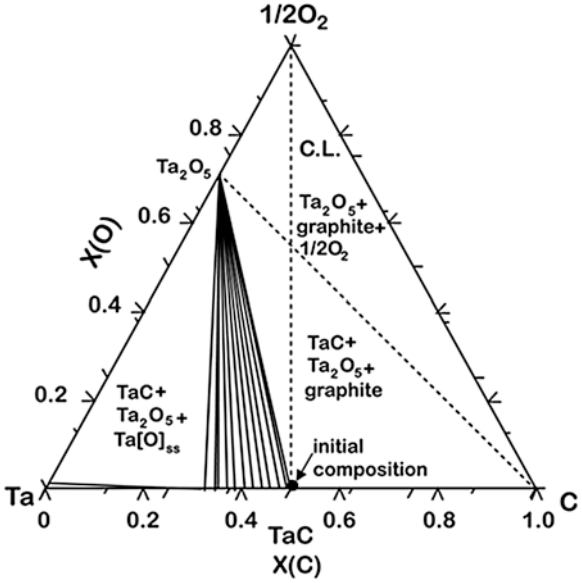

Fig. 11.7 Isothermal section from the evaluated metastable ternary Ta–C–O phase diagram at 600 °C under the external oxygen pressure of about 0.2×10^{-4} Pa. The tie-lines in the TaC–Ta_2O_5 two-phase region are shown in the diagram. The contact line (C.L.) between the TaC film and oxygen indicating the initial unstable equilibrium as well as the approximate composition of the TaC[O] are also shown

the formation of Ta_2C has been suppressed in the calculations to obtain the conditions of the actual metallization structure. The initial state of the system, where the TaC is in equilibrium with the entrapped oxygen, is marked with the contact line (C.L.) in the isothermal section, showing that the situation is highly unstable. The initial composition is located on the contact line and inside the three-phase field (TaC + Ta_2O_5 + graphite) in the isothermal section. Since the overall oxygen content is relatively low ($\sim$1–2 at.%), the composition lies close to the

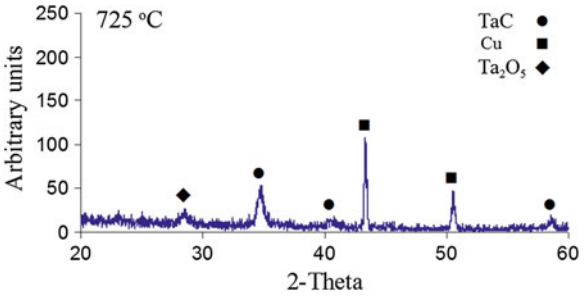

Fig. 11.8 XRD spectra from the Si/TaC(70 nm)/Cu(400 nm) sample annealed at 725 °C for 30 min

Ta–C binary system (the anticipated composition being depicted in Fig. 11.7). When the $TaC[O]_{gb}$ films are annealed at elevated temperatures, oxygen dissolves into the TaC matrix, resulting ultimately in the formation of the stable Ta_2O_5 and graphite. However, owing to the kinetic constraints, the direct formation of the stable tantalum oxide is not possible and the formation of the amorphous $Ta[O, C]_x$ layer takes place. Considering the thickness of the amorphous layer at 600 °C, it is evident that some oxygen has to be incorporated into the films also from the annealing atmosphere. Only after the temperature raises above 700 °C, the relaxation of the kinetic constraints enables the formation of the stable three-phase structure ($TaC + Ta_2O_5 +$ graphite).

The reason for the existence of the $Ta[O, C]_x$ layer in amorphous form at relatively high temperatures is not known. However, what is known, is that metalloids, such as B, C, N, Si, and P, can stabilize amorphous structure in transition metals [44]. It is expected that in this system carbon, which is released from the partially decomposed TaC layer and incorporated into the growing amorphous $Ta[O, C]_x$ layer, stabilizes the amorphous structure. The carbon inhibits the crystallization of the amorphous $Ta[O, C]_x$ up to 725 °C, where the formation of Ta_2O_5 is observed (Fig. 11.8). The reason for the absence of graphite after the crystallization of Ta oxide is the very difficult nucleation of graphite, as observed elsewhere [14]. The stabilizing effect of carbon enables the growth of the amorphous layer to about half the thickness of the original TaC layer at the temperature of crystallization.

The phenomena of SSA have lead to increased interest in interfacial reactions occurring in composition gradients. In fact, as it was stated in the beginning in thin film couples, there often occur very steep concentration gradients. Desré and Yavari attributed the formation of amorphous phase in a thin-film system to a great composition gradient [45, 46]. By using simple thermodynamic arguments, they showed that sharp composition gradients increased the stability of an amorphous phase layer by eliminating or reducing the driving force $\Delta g_{a\to c}$ for nucleation of crystalline intermetallic phases in an amorphous layer. This effect increases with increasingly negative Δh_{mix} and free energy of alloying Δg. As diffusive mixing proceeds further during growth of the amorphous layer, the composition gradient flattened out and the driving force for crystalline phase formation is gradually

restored. The energy barrier for their nucleation also diminishes toward the value of the classic theory

The existence of a composition gradient in the interfacial region has been experimentally observed in the Ni–Si system, and the width of the interfacial region was estimated to be $\leq 2 \times 10^{-3}$ μm [47]. This region can be an amorphous phase or a crystalline solution phase. Figure 11.9b shows the Gibbs energy curve of such an amorphous region (G_{am}) at the A/B interface.

According to the classic theory of homogeneous nucleation, in order for a crystalline stoichiometric phase $\beta - A_{C^*}B_{1-C^*}$ to nucleate in the amorphous region, the nucleus with radius r in Fig. 11.9a must attain a critical radius r^* and equilibrium exists at the interface between the amorphous phase and β. When composition gradient in the amorphous phase is represented by line C(X) as shown in Fig. 11.9a, since the tangents of G_{am} both at C($-r$) and C($+r$) are in touch with the Gibbs energy curve of the β phase, G_β, the nucleus can grow further, which means that the radius r has reached the critical size ($r = r^*$). If the composition gradient in the amorphous phase is greater as represented by C′(X), however, the nucleus will not attain the critical size because the tangents both from C′($-r$) and C′($+r$) miss the tip of G_β. Therefore, there exists a critical composition gradient ∇C_c for β to nucleate. As long as the composition gradient in the amorphous phase is greater than ∇C_c, the crystalline phase will not form. Note also that the orientation and shape of the nuclei with respect to composition gradient are also important as it will change the value of radius.

Following the thermodynamic approach of Cahn and Hilliard for a non-uniform system [48], the Gibbs free energy of a volume v of an amorphous layer can be written as

$$g_a(v) = \rho \int_v [g_0(C) + N_A \chi (\nabla C)^2] dv \tag{11.15}$$

where ρ is the number of moles of atoms per unit volume, g_0(C) is the Gibbs free energy per atom of an amorphous phase with uniform composition C, N_A is Avogadro's number, and χ is a constant. From this can be calculated the Gibbs free energy of formation of a nucleus for the compound $A_{C^*}B_{1-C^*}$ which includes the classic interfacial term

$$\Delta g_N = 24\sigma_{pc} r^2 + 8\rho[\Delta g_{pc}(C*) - N_A \chi (\nabla C)^2] r^3 + {}^4\!/_3 \rho \alpha (\nabla C)^2 r^5 \tag{11.16}$$

where σ_{pc} is the interfacial energy at the polymorphous crystallization front, Δg_{pc}(C*) is the Gibbs free energy of polymorphous crystallization at C*, $\alpha = \partial^2 \Delta g / \partial C^2$ is assumed to be constant in the range $C^* - r\nabla C < C < C^* + r\nabla C$.

As it can be seen from the Eq. 11.16, the concentration gradient leads to a term to the fifth power of the embryo size. As the coefficient of the r^5 is positive, this term will contribute to increase in ΔG_N.

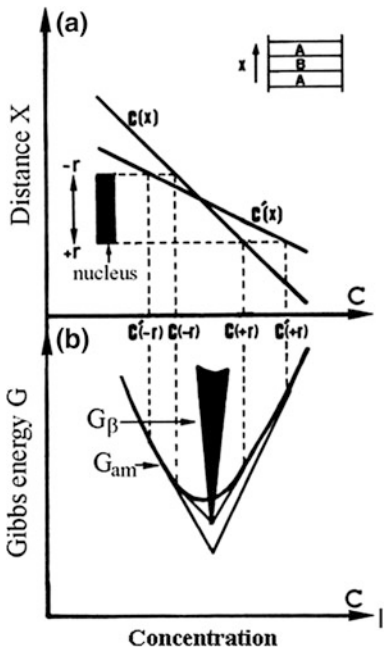

Fig. 11.9 Gibbs energy tangent constructions for compositions at the tips of the critical nucleus of intermetallic phase in an amorphous layer subject to the concentration gradient ∇C [45]

For the typical composition gradients which occur during the solid-state amorphous reaction ($\nabla C \leq 10^{+6}$/cm), the energy factor $N_A \chi (\nabla C)^2$ in Eq. 11.16 is negligible. After some algebra, an analytical expression for the critical gradient ∇C_c, at which Δg_N is both minimum and equal to zero, is obtained as

$$\nabla C_c = \frac{\rho}{9\,\sigma_{pc}} \frac{(2|\Delta g_{pc}|)^{3/2}}{\alpha^{1/2}} \tag{11.17}$$

Above this critical gradient, there is no driving force for compound nucleation.

11.3 Role of the Interfaces

The intrinsic diffusion coefficients of A and B in a given phase are generally different, thus leading into a flux of point defects equal to $J_A - J_B$. This flux changes stepwise at each interface, so that point defects must be created or annihilated at these places. If the interface is unable to perform this task, it leads to the injection of point defects into the substrate [49] (Fig. 11.10). If this injection of point defects into substrate is observed, it is always a signal of some departure from equilibrium, because then the interface is not a perfect sink for point defects as it should be in equilibrium situation. This can lead to the supersaturation or undersaturation of point defects close to interface. Hence, this means that the compound

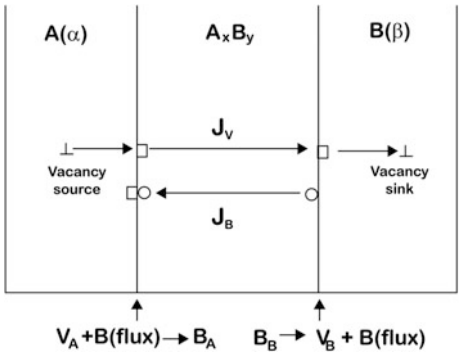

Fig. 11.10 Injection of point defects at the interfaces

will not have the expected composition (non-stoichiometry). It is to be noted that in the Darken treatment of diffusion (see from Sect. 6.7 forward) equilibrium number of point defects are assumed to be present. This means that there should be enough sources and sinks for the point defect to maintain number of vacancies at their equilibrium concentrations. This is typically the case when macroscopic diffusion phenomena are considered. However, when the nanoscale diffusion phenomena are surveyed, the distribution of vacancy sources and sinks may become an issue and the Darken analysis is not valid anymore. Then other type of analyses must be utilized, such as Nazarov-Gurov type approach (see Chap. 5 for more details).

It should also be emphasized that the "chemical constants" (see subsequent sections on the growth models), i.e., reactivity depends on the state of the interfaces and may be changed due to point defect saturation. Interfaces also offer favorable heterogeneous nucleation sites for new phases as they reduce the size of the critical nuclei (see above Sect. 11.1).

11.4 The Role of Grain Boundaries

Thin films possess usually high density of grain boundaries (Fig. 11.11), which can have effect on the growth kinetics. This is because of the enhanced atom transport via the short-circuit paths. A simple situation readily occurs in thin-film experiments: columnar grains, with their long axis along the direction of the diffusion flux. This situation can be modeled by dividing the film into two different parts: one with diffusion coefficient D_{vol} (lattice) and the other with diffusion coefficient D_{gb} (grain boundary). The number of atoms transported per unit area and unit time is given by:

$$M(t) = (A_l J_l + A_{\mathrm{gb}} J_{\mathrm{gb}}) = (A_l D_{\mathrm{vol}} + A_{\mathrm{gb}} D_{\mathrm{gb}}) \frac{dc}{dx} \tag{11.18}$$

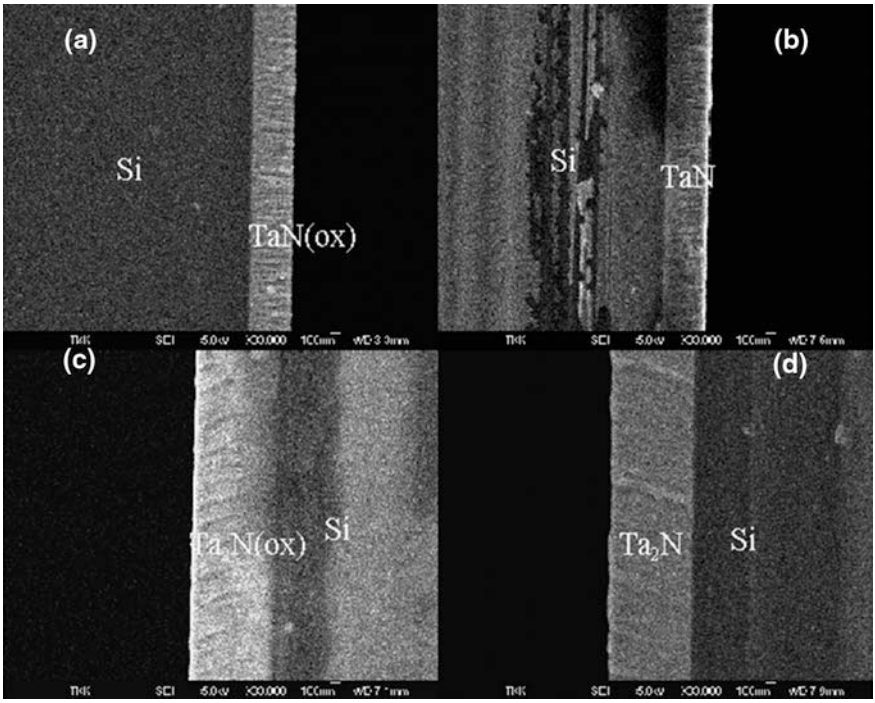

Fig. 11.11 Cross-sectional SEM micrographs of as-deposited. **a** TaN on SiO_2/Si. **b** TaN on silicon. **c** Ta_2N on SiO_2/Si, and **d** Ta_2N on silicon showing columnar microstructure. Micrographs are in the same scale, and scale bar length is 100 nm

where A_l and A_{gb} are the cross sections of the grains and the grain boundaries per unit area.

With conventional thickness δ of grain boundaries, $A_l \approx 1$ and $A_{gb} \approx 2\delta/d$, where d is the average grain diameter [50]. Instead of the lattice diffusion constant D_{vol}, the effective diffusivity D_{tot} must now be considered:

$$D_{tot} = D_{vol} + \frac{2D_{gb}\delta}{d} \tag{11.19}$$

Thus, the value of the diffusion "coefficient" has increased. This may also influence the regime of layer growth, in particular if the thickness of the film is small. Short-circuit diffusion may enhance the atom transport to such an extent that the reaction(s) at the interfaces become rate limiting. More thorough treatment of short-circuit diffusion can be found from Chap. 10.

Grain boundaries also provide favorable sizes for solid-state nucleation, for the same reasons as the interfaces (see section above). Grain boundary nuclei do not necessarily form uniformly over available grain boundary surface (e.g., two grain junction). On the contrary, as it is reasonable to assume that the energy to form a

nucleus of critical size is smaller at grain edges and grain corners (three and four grain junctions, respectively). These sites with lowest critical free energy for formation of nucleus do not necessarily contribute most to the overall nucleation rate. This is because the number of atoms which can participate in the nucleation process also decreases with the dimensionality of the site. Cahn [51] has shown that the opposing effects of lower energy barriers and fewer atoms participating in the nucleation process as the dimensionality of the site can be used to map out different nucleation conditions under which the greatest initial contribution to the nucleation rate is made by the sites of various types.

11.5 Role of the Impurities

Impurities have important effects on the formation of phases in thin film and bulk couples. Presence of some impurity may enhance the formation of a particular phase at the expense of another (see Sect. 11.2 for the case of impurity-induced amorphous phase formation). Impurities may increase or decrease reaction temperatures or influence the kinetics of a phase transformation. Impurities are also frequently responsible for the absence of phases in diffusion couples as compared to the corresponding phase diagram. One example of the increased reaction temperature is the formation of $TaSi_2$, in the reaction between thin Ta film and Si substrate, which occurs at 923 K [52]. However, if there is oxygen at the Si/Ta interface, the temperature of formation will rise well above 1,023 K [53]. Another example of bulk samples is the catalyzing effect of phosphorous on the formation of Cu_3Si in the reaction between bulk copper foil and Si substrate [54]. The effect of impurities on diffusional transport should also be considered. Impurities may segregate preferably to grain boundaries and interfaces. When they segregate to grain boundaries, they may reduce the effect of the short-circuit diffusion paths, thus affecting the mass transport in the system (see Chap. 10 for details).

The driving force for the equilibrium segregation of solute or impurity atoms to grain boundaries is systems tendency to lower its total free energy. In addition to kinetic constraints, the extent of intergranular segregation depends on impurities influence on the grain boundary energy as well as on the factors controlling their solubility, i.e., size factor and chemical interactions between dissimilar atoms. Since both the kinetics and the solubility depend on temperature, the segregation of impurities decreases with increasing temperature. By gathering large amounts of experimental data on grain boundary segregation, Hondros and Seah [55] showed that the smaller the solubility of an impurity in the solvent the higher is its segregation potential. This “rule of thumb” is frequently used when considering the segregation tendency of a given impurity.

The classical free surface adsorption models have often been used for evaluating grain boundary segregation because of the analogies between intergranular segregation and adsorption at free surfaces [56]. This approach is valid if it takes into account the specific features, which differentiate the grain interface from

surfaces. Thus, even the most dilute grain boundary can be regarded as a two-dimensional phase with the same components as in the bulk [57]. These complications imply, among other things, that one has to utilize the extended phase rule instead of the classical phase rule when evaluating the degrees of freedom for the system. A generalized phase rule has been derived for system including surfaces and interfaces by Defay and Prigogine [58]. If c is the number of components, p is the number of 3D phases, φ number of 2D surface phases, and number of degrees of freedom f can be expressed as follows:

$$f + p = (c + 2 - p) - (\varphi - s) = v - (\varphi - s) \tag{11.20}$$

where v is the classical (Gibbs) degrees of freedom (ignoring surfaces) and s is the number of "surface species." Two surfaces are of different species if they separate different couples of bulk phases. For instance, in the case of a grain boundary precipitate β in a matrix α, the interfaces α/α and α/β are of different species and $s = 2$. Also surfaces of different orientations should be considered as different species. It is to be noted that the equilibrium condition, i.e., that the chemical potential of a component i has the same value in all phases of the system, is valid also for grain boundaries and surfaces as shown in Sect. 1.15. Several treatments of intergranular segregation have been published during the past decades. Extensive reviews of the models can be found from Refs. [59, 60].

11.6 Phase Formation in Thin-Film Structures

There has been a view that phase formation in thin-film couples is sequential in comparison to simultaneous phase formation in bulk couples. In many works dealing with formation of silicides, only one or two silicide layers have been reported to grow [52, 59–69]. There have been several different approaches to explain this phenomenon [70–78], which will be summarized briefly next. It is to be noted that the method of evaluating microstructural evolution in diffusion couples introduced in Chap. 8 can be used in thin-film couples and is used as a benchmark when other treatments are discussed. As these phenomena have been thoroughly discussed in that chapter, the treatment is not repeated here for the case of thin-film couples.

11.6.1 Linear-Parabolic Treatment

This treatment has been used by many authors to describe reactive phase formation, including d'Heurle, Gas, and Philibert [49, 68, 69, 74]. The treatment was first used to describe the formation of silicon dioxide [74].

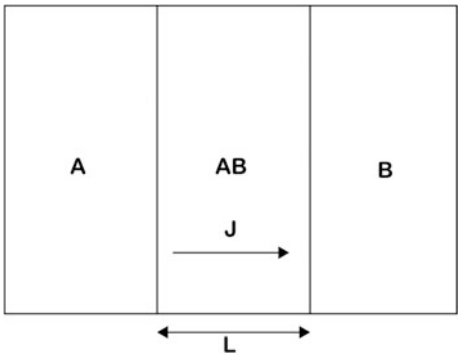

Fig. 11.12 Schematic presentation of the AB growth between the pure elements A and B

11.6.1.1 Growth of One Phase Between Pure A and B

One assumes that a compound AB grows between the pure elements A and B by the diffusion of A atoms (Fig. 11.12). If one starts from the "pure" diffusional growth, one obtains the following equation:

$$J_A = C_A \times M_A \times \frac{d\mu_A}{dL} \tag{11.21}$$

where the mobility is $M_A = \frac{D_A}{kT}$

If one assumes that the intrinsic diffusion coefficient D_A *is not* a function of concentration one obtains

$$J_A = C_A \times \frac{D_A}{kT} \times \frac{\Delta g_A}{L} \tag{11.22}$$

where Δg_A is the *Gibbs energy per A atom* of the reaction A + B = AB. More specifically, it is the required energy to move one mole of A atoms from the A/AB interface across the AB layer to the AB/B interface, i.e., the driving force for diffusion $\Delta\mu_A$. This value can again be obtained from the molar Gibbs energy plot of the system in question using common tangent construction if one has the assessed thermodynamic data of the system available as shown in Sect. 1.15 and in [79, 80]. Since

$$\frac{dL}{dt} = J_A \times v_A \tag{11.23}$$

$$c_A = \frac{1}{v_A} \tag{11.24}$$

then

$$\frac{dL}{dt} = D_A \times \frac{\Delta g_A}{kT} \times \frac{1}{L} \tag{11.25}$$

If one integrates the Eq. 11.25, one obtains the familiar parabolic growth law:

$$L^2 = Kt \tag{11.26}$$

If Eq. 11.26 is considered at very small layer thickness, one encounters a serious problem, since if the L $\approx$ 0, then

$$\frac{dL}{dt} \approx \infty \tag{11.27}$$

This means that pure parabolic kinetics seems impossible. Therefore, d'Heurle et al. [49, 68, 69] introduced the concept of linear-parabolic kinetics.

The starting point is again the Eq. 11.25, where one introduces a "kinetic parameter" to take into account reactions at the interfaces

$$\frac{dL}{dt} = D_A \times \frac{\Delta g_A}{kT} \times \frac{1}{L + K''} \tag{11.28}$$

As the thickness of the layer approaches zero $L \to 0$, then the Eq. 11.28 reaches the form

$$\frac{dL}{dt} \approx D_A \times \frac{\Delta g_A}{kT} \times \frac{1}{K''} \tag{11.29}$$

If one integrates this equation, one obtains:

$$L^2 + K'L = K(t + t_0) \tag{11.30}$$

where $K' = 2\ K''$

When layer thickness grow large and reaction time becomes long (as usually in bulk couples), one obtains the "normal" parabolic growth equation

$$L \to \infty \Rightarrow \quad L^2 \approx Kt \tag{11.31}$$

11.6.1.2 Multiphase Growth Between Pure A and B

If, instead of one phase, several phases grow between A and B, the situation is slightly different, since the growth of a specific phase depends not only its own growth kinetics but also from the growth kinetics of the adjacent phases (Fig. 11.13).Thus, the rate equations are coupled (see Chap. 8 for details). From Fig. 11.13, the following equations can be derived (A is still the only diffusing species)

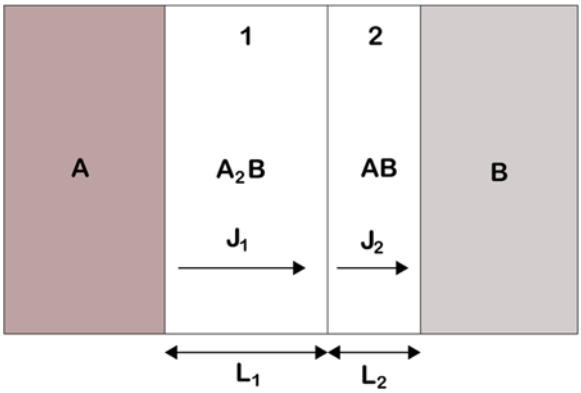

Fig. 11.13 Schematic presentation of multiphase growth between pure elements A and B

$$\frac{dL_1}{dt} \rightarrow J_1 - J_2 \tag{11.32}$$

$$\frac{dL_2}{dt} \rightarrow 2J_2 - J_1 \tag{11.33}$$

where the coefficient 2 in the Eq. 11.33 comes from the stoichiometry.

In layer 1, A atoms diffuse through the A_2B layer to react with the AB layer according to the equation:

$$1. \quad A + AB = A_2B$$

$$\Delta g_1 = \Delta g^f_{A_2B} - \Delta g^f_{AB}$$

In the other layer 2, the growth of AB takes place at two interfaces:

2a.	$A_2B - A = AB$
2b.	$A + B = AB$
total	$A_2B + B = 2AB$
	$\Delta g_2 = 2\Delta g^f_{AB} - \Delta g^f_{A_2B}$

It follows that:

$$\frac{dL_1}{dt} = 2\frac{\alpha_1}{L_1} - \frac{\Omega_1}{\Omega_2}\frac{\alpha_2}{L_2}$$
$$\alpha_1 = D_1\frac{\Delta g_1}{kT} \quad \text{and} \quad \alpha_2 = D_2\frac{\Delta g_2}{kT} \tag{11.34}$$

$$\frac{\Omega_1}{\Omega_2} = \frac{v^{A_2B}}{v^{AB}} \rightarrow \omega \tag{11.35}$$

$$\frac{dL_2}{dt} = 2\frac{\alpha_2}{L_2} - 2\frac{1}{\omega}\frac{\alpha_1}{L_1} \tag{11.36}$$

The layer thicknesses L_1, L_2 and the total thickness $L_1 + L_2$ are functions of $\sqrt{t}$.

If one investigates the growth of different layers:

L_1 grows if the inequality

$$\frac{2\alpha_1}{L_1} > \omega\frac{\alpha_2}{L_2} \tag{11.37}$$

is fulfilled.

Similarly L_2 grows if

$$\frac{\alpha_2}{L_2} > \frac{1}{\omega}\frac{\alpha_1}{L_1}, \quad \text{and} \quad 2\alpha_1 L_2 > \omega\alpha_2 L_1 > \alpha_1 L_2, \tag{11.38}$$

which leads approximately to the equation:

$$2\frac{D_1}{D_2} > \frac{L_1}{L_2} > \frac{D_1}{D_2} \tag{11.39}$$

The ratio $\frac{L_1}{L_2}$ can be solved from the following equation:

$$\frac{L_1}{L_2} = \frac{\frac{2}{\omega}\alpha_1 - \omega\alpha_2 + \sqrt{\left(\frac{2}{\omega}\alpha_1 - \omega\alpha_2\right)^2 + 8\alpha_1\alpha_2}}{4\alpha_2} \tag{11.40}$$

This ratio L_1/L_2 produces to the following diagram where there are three regimes of growth (Fig. 11.14).

At the region M, L_1 grows *and* L_2 shrinks, within the region O, L_2 grows and L_1 shrinks and at the region N, both phases can grow simultaneously. As the time increases and if it is assumed that end elements in reaction couple are not consumed, the reaction couple eventually reaches the N region and both phases can grow simultaneously.

11.6.1.3 "Pure" Diffusional Approach to Multiphase Growth

From the "pure" diffusional point of view regarding the growth of A_2B and AB layers between pure A and B, the following conclusions can be drawn:

(a) *All phases grow simultaneously*. This contradicts experimental results from thin-film experiments where sequential phase formation has been observed
(b) *Growth rate is parabolic*, e.g., $L \rightarrow \sqrt{t}$

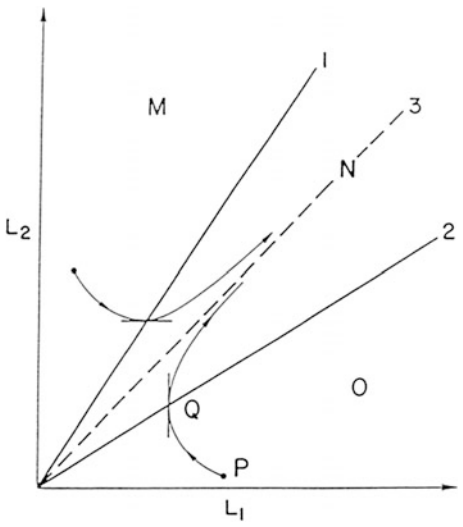

Fig. 11.14 Presentation of the different growth regions in the $A/A_2B/AB/B$ reaction couple under diffusion control [71]

(c) *Phases cannot disappear in reaction couple.* This is as a result of the fact that as the layer thickness goes to zero the growth rate should approach infinity: $L \rightarrow 0$ then $\frac{dL}{dt} \propto \infty$

(d) However, even for the pure diffusional growth of the phases, their *thickness ratio is proportional to the ratio of the diffusion coefficients in the layers* $\frac{L_1}{L_2} \rightarrow \frac{D_1}{D_2}$

For example, if the ratio of the diffusion coefficients is 10^4, which is of reasonable magnitude for real experiments, and for example, if the layer thickness of the layer 1 is $L_1 = 10^3$ Å, then the thickness of the layer 2 would be $L_2 = 10^{-1}$ Å. In this case, the layer 2 cannot be said to really exist. This shows how within the "pure" diffusional theory, without any further assumptions, one already gets into trouble with layer thicknesses that are readily used in the common thin-film technology. However, this has also been used to defend the traditional "pure" diffusion approach, since it has been stated that all the phases are present in the reaction couple as required, but the thicknesses may be so small that they are impossible to detect.

(e) One can conclude that *with small layer thicknesses with "pure" diffusional theory, mathematics of the theory, and the actual physics are contradictory*

11.6.1.4 Linear-Parabolic Approach to Multiphase Growth

As we noticed, serious problems are encountered with thin-film structures if one uses the traditional "pure" diffusion control approach. On the other hand, if one examines the problem with the help of linear-parabolic growth kinetics the

above-mentioned issues can be avoided. The equations describing the growth of the layers are the following:

$$\frac{dL_1}{dt} = 2\frac{\alpha_1}{L_1 + K_1''} - \omega\frac{\alpha_2}{L_2 + K_2''} \tag{11.41}$$

$$\frac{dL_2}{dt} = 2\frac{\alpha_2}{L_2 + K_2''} - \frac{2}{\omega}\frac{\alpha_1}{L_1 + K_1''} \tag{11.42}$$

If one assumes that the layer formation is sequential as experimentally observed in thin-film experiments, it means that $L_2 = 0$ at the beginning. The driving force for the formation of AB does, however, exist, e.g., $\frac{dL_2}{dt} > 0$, and therefore, the growth rate of AB is positive. Then, one obtains the following inequality:

$$\frac{\alpha_2}{K_2''} > \frac{1}{\omega}\frac{\alpha_1}{L_{1c} + K_1''} \tag{11.43}$$

which leads to the concept of "critical thickness":

$$L_{1c} > \frac{1}{\omega}\frac{\alpha_1}{\alpha_2}K_2'' - K_1'' \tag{11.44}$$

This means that the AB phase will not start to grow until the thickness of the A_2B layer has reached a minimal thickness, *despite the fact that the driving force for the formation of* AB *exists!* Also if the other end element is depleted (A or B) before the A_2B has reached the critical thickness, the AB phase will not occur. Furthermore, if the AB layer is present initially, it will start to shrink as the A_2B layer grows at its expense—if A_2B layer has not yet reached the critical thickness that would enable the simultaneous growth of both phases. If one plots the thickness of the phases similar to the plot as seen in Fig. 11.14, one obtains the same kind of plot—just the nodal lines are translated (Fig. 11.15). The slope of the lines remain unchanged, they are simply translated vertically by the quantity given by the "reaction" factor. There is, however, an additional important feature that can be seen from Fig. 11.15. If the conditions of the growth process lie inside the area marked as R in the figure, the phase 2 (L_2) would disappear under these conditions.

The "simultaneous" phase growth found in the bulk diffusion couples can be explained on the basis of the same critical thickness. In bulk couples, the annealing times are long and the layer thickness are large and therefore the phases "easily" reach the required critical thickness, thus enabling the observation of several phases. It should, however, be emphasized that in the bulk couples also, there are occasions where all the predicted phases are not observed.

Basically, we end up with three rules for the linear-parabolic treatment of two-phase growth

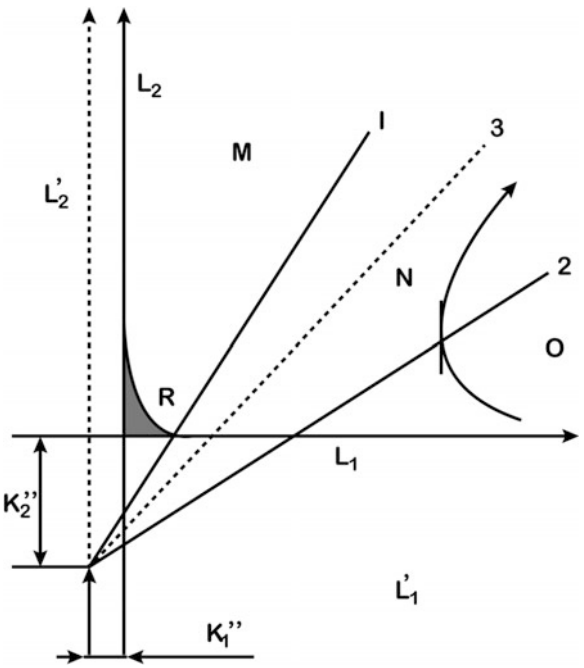

Fig. 11.15 Presentation of the different growth regions in the $A/A_2B/AB/B$ reaction couple according to linear-parabolic kinetics (see text for details) [71]

1. The criterion for the first-phase formation is a kinetic one: It is determined by the value of diffusitivity
2. The first phase grows alone until a critical thickness, which depends on the same parameters, at this point the second phase appears
3. After some transient, the both phases grow simultaneously with proportional thickness increments.

11.6.2 Interfacial Reaction Barrier Approach

The approach was introduced by Gösele and Tu [72, 77] in order to investigate the difference between thin film and bulk reaction couples. It was basically an extension of earlier work by other authors [73–75]. Interfacial reaction barrier was used to describe the energy barrier associated with changes in atomic arrangements or effects due to volume changes at the interface due to the formation of new interface at the expense of the old. In that way, it is somewhat related to interfacial energy.

They used a model system to consider the effect of the interfacial reaction barriers to multiphase growth in a reaction couple where the $A_\beta B$ and $A_\gamma B$ grow between the saturated $A_\alpha B$ and $A_\delta B$ phases ($\alpha > \beta > \gamma > \delta$). It was also assumed

that the $A_\beta B$ and $A_\gamma B$ phases are already present at the beginning with given thickness x_β and x_γ. This assumption was introduced in order to avoid the problems arising from nucleation of the phases. Intention was especially to check whether one of the layers would shrink away completely under various kinetic conditions.

Their model was characterized by the interdiffusion coefficients $\tilde{D}_\beta$ and $\tilde{D}_\gamma$. These coefficients are related to the intrinsic diffusion coefficients by the Darken equation

$$\tilde{D}_\beta = N_B D_\beta^A + N_A D_\beta^B \tag{11.45}$$

The volume of the formed compound Ω_0 per A or B atom is assumed to be constant. They also introduced β which is the ratio of A atoms to B atom in the $A_\beta B$ compound. The shift of the interfaces can be calculated from the equations

$$\frac{dx_\beta}{dt} = G_\beta J_\beta^A - G_{\beta\gamma} J_\gamma^A \tag{11.46}$$

$$\frac{dx_\gamma}{dt} = G_\gamma J_\gamma^A - G_{\gamma\beta} J_\beta^A \tag{11.47}$$

with the (positive) diffusion fluxes of A atoms in the $A_\beta B$ and $A_\gamma B$ layer

$$J_\beta^A = \Delta C_\beta^{eq} k_\beta^{eff} / (1 + x_\beta \kappa_\beta^{eff} / \tilde{D}_\beta) \tag{11.48}$$

$$J_\gamma^A = \Delta C_\gamma^{eq} \kappa_\gamma^{eff} / (1 + x_\gamma \kappa_\gamma^{eff} / \tilde{D}_\gamma) \tag{11.49}$$

where

$$\Delta C_\beta^{eq} = C_{\beta\alpha}^{eq} - C_{\beta\gamma}^{eq} \tag{11.50}$$

and

$$\frac{1}{\kappa_\beta^{eff}} = \frac{1}{\kappa_{\beta\alpha}} + \frac{1}{\kappa_{\beta\gamma}} \tag{11.51}$$

The various quantities with the subscript γ have analogous meaning for the $A_\gamma B$ layer.

The quantities G_β, $G_{\beta\gamma}$, G_γ, and $G_{\gamma\beta}$ take into account the change in composition at the interfaces

$$G_\beta = \Omega_0 (1 + \beta^2) \left(\frac{1}{\alpha - \beta} + \frac{1}{\beta - \gamma} \right) \tag{11.52}$$

$$G_\gamma = \Omega_0 (1 + \beta^2) \left(\frac{1}{\beta - \gamma} + \frac{1}{\gamma - \delta} \right) \tag{11.53}$$

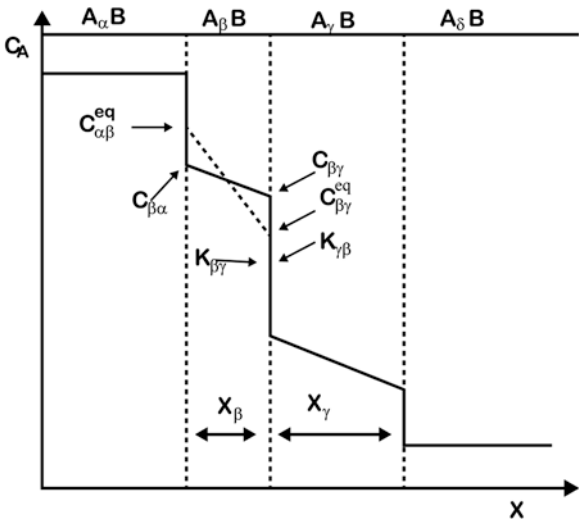

Fig. 11.16 Schematic presentation of the concentration profile of A atoms in the $A_\alpha B/A_\beta B/A_\gamma B/A_\delta B$ diffusion couple

$$G_{\beta\gamma} = G_{\gamma\beta} = \Omega_0(1+\beta)(1+\gamma)/(\beta-\gamma) \tag{11.54}$$

The fluxes described above are assumed to be independent of each other. The schematic presentation of the situation is shown in Fig. 11.16. In the figure, the different parameters are depicted only for the $A_\beta B$ layer, but they are analogous for the other interfaces and layers.

The assumption that the fluxes are independent leads into equations:

$$J_\beta{}^A = \kappa_{\beta\gamma}(C_{\beta\gamma} - C^{eq}_{\beta\gamma}), \text{ at the } A_\beta B \text{ interface} \tag{11.55}$$

and

$$J^A_\gamma = \kappa_{\gamma\beta}(C^{eq}_{\gamma\beta} - C_{\gamma\beta}), \text{ at the } A_\gamma B \text{ interface} \tag{11.56}$$

The quantity $\kappa_{\beta\gamma}$ describes the reaction barrier against the growth of $A_\beta B$ layer at the expense of the $A_\gamma B$ layer, and $\kappa_{\gamma\beta}$ characterizes the reaction barrier against the growth of the $A_\gamma B$ layer at the expense of the $A_\beta B$ layer. The basic difference between this approach and the "traditional" diffusional approach is the occurrence of the interfacial reaction barriers. If the reactions at the interfaces are fast, the reaction barriers tend to approach infinity. Hence, for fast reactions, the growth rates are as described in the "pure" diffusion theory.

The condition for growth of the $A_\beta B$ layer $\frac{dx_\beta}{dt} > 0$ may be expressed in terms of the ratio r of the diffusion fluxes

$$r = \frac{J_{\beta}^{A}}{J_{\gamma}^{A}} \tag{11.57}$$

as

$$r > \frac{G_{\gamma}}{G_{\gamma\beta}} = r_1 \tag{11.58}$$

The analogous condition for the growth of the $A_{\gamma}B$ layer is

$$r < \frac{G_{\gamma}}{G_{\gamma\beta}} = r_2 \tag{11.59}$$

with

$$r_1 = (1+\gamma)(\alpha-\beta)/(1+\beta)(\alpha-\gamma) \tag{11.60}$$

and

$$r_2 = (1+\gamma)(\beta-\delta)/(1+\beta)(\gamma-\delta) \tag{11.61}$$

where $r_2 > r_1$, holds, since $(\alpha - \beta) < (\alpha - \gamma)$ and $(\beta - \delta) > (\gamma - \delta)$

When the parameters $x_{\beta}, x_{\gamma}, D_{\beta}^{i}, D_{\gamma}^{i}, \kappa_{\beta}^{\text{eff}}$,and $\kappa_{\gamma}^{\text{eff}}$have such a values that the flux ratio r is between r_1 and r_2 both layers can grow simultaneously. However, if the flux ratio is not between them, one layer will shrink and the other will grow. Hence, situation is similar as shown already in the Fig. 11.14. This similarity also implies that there should be a critical thickness as in the other two previous treatments. It can be found also within this theory, and it is expressed as follows:

$$x_{\gamma}^{\text{crit}} = \frac{r_1 \Delta C_{\gamma}^{\text{eq}} \tilde{D}_{\gamma}}{\Delta C_{\beta}^{\text{eq}} \kappa_{\beta}^{\text{eff}}} \tag{11.62}$$

where the growth of $A_{\beta}B$ is reaction controlled and the growth of $A_{\gamma}B$ diffusion controlled, thus simulating sequential phase formation. It states that the $A_{\beta}B$ layer cannot coexist with the $A_{\gamma}B$ layer as long as the thickness of the $A_{\gamma}B$ layer is below the x_{γ}^{crit}. This means that even without any nucleation difficulties the $A_{\beta}B$ cannot form with the $A_{\gamma}B$ layer in the $A_{\alpha}B/A_{\beta}B/A_{\gamma}B/A_{\delta}B$ diffusion couple when the thickness of the x_{γ} is not large enough. This again predicts sequential phase growth.

11.6.3 Similarities Between the Growth Models

It is very interesting to compare the results obtained above and those derived in Chap. 8. Despite the differences between the approaches, all the models lead to similar results. It is also common to both approaches that they neglect the nucleation difficulties in order to avoid complications. In fact, it has been shown by d'Heurle [4] that in most cases nucleation plays a role in the very early stage of the compound formation that is at the present time beyond experimental reach. Nevertheless, nucleation still plays a decisive role with some silicides, especially after the first-phase formation.

In the above two models, reactions at the interface are taken into account with the help of a "chemical constant." This concept is common to both the above models despite the slightly different names that are used. The "chemical constant" is, however, a slightly obscure entity, because it is not clear what are its contents. In Göseles approach [72, 77], it was related to the arrangement of atoms in the interface and the volume changes due to formation of a new interface. Thus, it should contain some "nucleation" contribution also. In the other approach, the meaning of the "chemical constants" was somewhat similar. On the contrary, in the physicochemical approach outlined in Chap. 8 there is no need for *ad hoc* chemical constants as reaction related issues arise naturally from the stoichiometric considerations.

The prediction power of the two models above is quite poor, due to the nature of the "chemical constants." There is no theoretical method at the present to calculate these constants a priori. Hence, they can be determined only by experiments. Also the lack of availability to use measured or estimated thermodynamic and kinetic (diffusion constants) values reduce the use of these approaches. Again, in the physicochemical approach one can readily utilize experimental and theoretical thermodynamic and kinetic data, which makes the approach derived in detail in Chap. 8 a very strong and feasible tool to understand interfacial reaction layer growth in thin film as well as in bulk couples.

From a certain point of view, both of the above models are a posteriori in their nature, as they can explain afterward the phase formation sequence but cannot predict it. Moreover, the "chemical constants" used in all the models are very much case dependent, since they are basically depended on the conditions of the interfaces and are therefore very sensitive to impurities, additional films etc. Furthermore, these constants are not achievable by experimental methods. The approaches, however, fade away the somewhat "traditional" distinction between thin film and bulk couples, since fundamentally the behavior is more or less the same. Nevertheless, in practical situations, the contributions due to the grain boundaries, impurities etc. mentioned above (Sect. 11.5 onwards) must be taken into account in thin films. This does not change the underlying theoretical fact that even in bulk reaction couples phase formation is basically sequential.

If one compares the above treatments to the physicochemical model extensively discussed in Chap. 8, the benefits of the latter over the two approaches are

obvious. As discussed above, the physicochemical model contains only measurable quantities, and it has also predictive power. Thus, it is the opinion of the authors that the physicochemical model should be used whenever the morphological evolution of a binary diffusion zone is rationalized.

References

1. Russel, K.C. *Colloid Interface Sci*., **13**, 205, 1980.
2. Coffey K.R., Clevenger L.A., Barmak K., Rudman D.A., and Thompson C.V., *Appl. Phys. Lett.*, **55**, 852, 1989.
3. Bormann R., *Mat. Res. Soc. Symp. Proc.*, **343**, 169, 1994.
4. d' Heurle F.M., *J. Mater. Res.*, **3**, 167, 1988.
5. Eshelby J.D., *Proc. R. Soc. A London Ser. A.,* **241**, 376, 1957.
6. Saunders N. and. Miodownik A.P, *CALPHAD, Calculation of Phase Diagrams*, Pergammon Materials Series, Elsevier Science, 1998.
7. Kaufman L. and Bernstein H., *Computer Calculation of Phase Diagrams*, Academic Press, New York, 1970.
8. Ansara I., *Pure Appl. Chem.*, **62**, 71, 1990.
9. Lukas H.L., Weiss J., and Henig E.T., *CALPHAD*, **6**, 229, 1982.
10. Bormann R. and Zöltzer K., *phys. stat. sol.(a),* **131**, 691, 1992.
11. Thompson C.V., *J. Mater. Res.*, **7**, 367, 1992.
12. Newcomb S.B. and Tu K.N., *Appl. Phys. Lett.*, **48**, 1436, 1986.
13. Cotts E. J., Meng W.J., and Johnson W.L., *Phys. Rev. Lett.*, **57**, 2295, 1986.
14. Vredenberg A. M, Westendorp J.F.M., Saris F.W., van den Pers N.M., and de Keijser Th. H., *J. Mater. Res.*, **1**, 774, 1986.
15. Meng W.J., Nieh C.W., Ma E., Fultz B., and Johnson W.L., *Mater. Sci. Eng.*, **97**, 87, 1988.
16. Erhart P., Averback R., Hahn H., Yadavalli S., and Flynn C.P., *J. Mater. Res.*, **3**, 1276, 1988.
17. Johnson W.L., Dolgin B., and van Rossum M., in *Glass:Current Issues,* NATO ASI Series, eds. A.F. Wright and L. Dopuy, (Dordrecht:Martinus Nijhoff), 172, 1985.
18. Clemens B.M., *J. Appl. Phys.*, **61**, 4525, 1987.
19. Kelton K.F. and Greer A.L., *J. Phys. Rev. B*, **38**, 10089, 1988.
20. Highmore R.J., *Phil. Mag. B*, **61**, 455, 1990.
21. Christian J.W., *The Theory of Transformations in Metals and Alloys*, Part 1, (Oxford, Pergamon), 1975.
22. Barret C. and Massalski T.B., *The Structure of Metals*, (McGraw-Hill), 1966.
23. Brandes E. editor, *Smithelss Metals Reference Book*, 6th edition (London, Butterworths), 1983.
24. Saunders N. and Miodownik A.P., *J. Mater. Res.*, **1**, 38, 1986.
25. Turnbull D., *Metall. Trans. A*, **12**, 695, 1981.
26. Greer A.L., *Phil. Mag. B*, **61**, 525, 1990.
27. Barmak K., Gungor A., Cabral C., Jr., and Harper J. M. E., *J. Appl. Phys.*, **94**, 1605, 2003.
28. Harper J. M. E., Cabral C., Jr., Andricacos P. C., Gignac L., Noyan I. C., Rodbell K. P., and Hu C. K., *J. Appl. Phys.* **86**, 2516, 1999.
29. Detavernier C., Deduytsche D., Van Meirhaeghe R. L., De Baerdemaeker J., and Dauwe C., *Appl. Phys. Lett.* **82**, 1863, 2003.
30. Herd S., Tu K.N., and Ahn K.Y., *Appl. Phys. Lett.*, **42**, 597, 1983.
31. d'Heurle F.M., Petersson C.S., Baglin J.E.E., La Placa S.J., and Wong C.Y., *J. Appl. Phys*., **55**, 4208, 1984.
32. Vanderwalker D.M., *Appl. Phys. Lett.*, **48**, 707, 1986.
33. Holloway K. and Sinclair R., *J. Appl. Phys.*, **61**, 1359, 1987.

34. Meyerheim H.L., Lengeler B., and Göbel H.E., *J. Appl. Phys.*, **68**, 2694, 1990.
35. W.L. Johnson, Prog. *Mater. Sci.*, **30**, 1986, 81.
36. W. Klement, R.H. Willens, and P. Duwez, *Nature*, **187**, 1960, 869.
37. Clemens B.M., Johnson W.L., and Schwarz R.B., *J. Non-Crystal. Solids*, **61-62**, 817, 1984.
38. Evans P.V., Garcia-Escorial A., Donovan P.E., and Greer A.L., *MRS Symposium Proceedings*, **57**, 234, 1987.
39. E. Gebhardt and H. D. Sehezzi, Z. Metallkd., **50**, 521, (1952).
40. H. Jehn and E. Olzi, *J. Less-Common Met.*, **27**, 297, (1972).
41. S. Stecura, *Metall. Trans.*, **5**, 1337, (1974).
42. R. Lauf and C. Altstetter, *Scr. Metall.*, **11**, 938, (1977).
43. G. Boreau and P. Gerdanian, *J. Phys. Chem. Solids*, **42**, 749, (1981).
44. M.A. Nicolet, in: *Diffusion in Amorphous Materials,* eds. H. Jain and D. Gupta, (TMS Warrendale, 1994), pp. 225-234.
45. Desre P.J. and Yavari A.R., *Phys. Rev. Lett.*, **64**, 1533, 1990.
46. Desre P.J., *Acta Metall. Mater.*, **39**, 2309, 1991.
47. Grunthaner P. J., Grunthaner F. J., and Mayer J. W., *J. Vac. Sci. Technol*, **17**, 924, 1980.
48. Cahn W. and Hilliard J. E., *J. Chem. Phys*, **28**, 258, 1958.
49. Philibert *J., Appl. Surf. Sci.*, **53**, 74, 1991.
50. Kaur I. and Gust W., *Fundamentals of Grain and Interphase Boundary Diffusion*, Ziegler Press, 1989.
51. Cahn J.W., *Acta Metall.*, **4**, 449, (1956).
52. Ottaviani G., *Thin Solid Films*, **140**, 3, 1986.
53. Christou A. and Day H.M., *J. Electr. Mater.*, **5**, 1, 1976.
54. Becht J.G.M., "The Influence of Phosphorous on the Solid State Reaction Between Copper and Silicon or Germanium", Doctoral Thesis, Tech. University of Eindhoven Netherlands, 1987.
55. Hondros E. and Seah M., *Int. Met. Rev*, **22**, 262, 1977.
56. Hondros E. and Seah M., *Metall. Trans. A*, **8A**, 1363, 1977.
57. Guttmann M., *Metall. Trans. A*, **8A**, 1383, 1977.
58. Poate J.M. and Tisone T.S., *Appl. Phys. Lett.*, **24**, 391, 1974.
59. Lau S.S., Mayer J.W., and Tu K.N., *J. Appl. Phys.*, **49**, 4005, 1978.
60. van Gurp G.J., van der Weg W.F., and Sigurd D., *J. Appl. Phys.*, **49**, 4011, 1978.
61. Scott D.M. and Nicolet M.-A., *Phys. Stat. Solidi.*, **66**, 773, 1981.
62. Tsaur B.Y., Lau S.S., Mayer J.W., and Nicolet M.-A., *Appl. Phys. Lett.*, **38**, 922, 1981.
63. Eizenberg M. and Tu K.N., *J. Appl. Phys.*, **53**, 6885, 1982.
64. Petersson C.S., Baglin J.E.E., Dempsey J.J., d'Heurle F.M. and La Place S.S., *J. Appl. Phys.*, **53**, 4866, 1982.
65. Canali C., Catellani F., Ottaviani G. and Prudenziati M., *Appl. Phys. Lett.*, **33**, 187, 1978.
66. Coulman B. and Chen H., *J. Appl. Phys.*, **59**, 3467, 1986.
67. Lien C.-D., Nicolet M.-A., and Lau S.S., *Thin Solid Films*, **143**, 63, 1986.
68. d'Heurle F.M. and Petersson C.S., *Thin Solid Films*, **128**, 283, 1985.
69. Gas P. and d'Heurle F.M., *App. Surf. Sci.*,**73**, 153, 1993.
70. Philibert J., *Materials Science Forum*, **155-156**, 15, 1994.
71. d' Heurle F.M., "The Kinetics of Reactive Phase Formation: Silicides", in *Silicides: Fundamentals and Applications*, (Eds. L. Miglio and F. d'Heurle), World Scientific, pp. 169-186, 2001.
72. Gösele U. and Tu, K. N. *J. Appl. Phys.*, **66**, 2619, 1989.
73. Geguzin Ye Ya, Kaganovskiy Yu.S, Paritskaya L.M., and., Solunskiy V.I, *Phys. Met. Metallogr.*, **47**, 127, 1980.
74. Deal E. and Grove A.S., *J. Appl. Phys.*, **36**, 3770, 1965.
75. Farrel P., Gilmer G.H., and Suenaga M., *Thin Solid Films*, **25**, 253, 1975.
76. Taguchi O., Iijima Y., and Hirano K., *J. Japan Inst. Metals.*, **51**, 4, 292, 1987.

77. Gösele U. and Tu K.N., *J. Appl. Phys.*, **53**, 3252, 1982.
78. Wagner C., *Acta Metall.*, **17**, 99, 1969.
79. Gulpen J., "Reactive Phase Formation in the Ni-Si System", Doctoral Thesis, Technical University of Eindhoven, The Netherlands, 1995.
80. Rönkä K., "Time-Dependent Microstructural and Compositional Changes at the Interfaces between Materials in Electronics", Doctoral Thesis, Helsinki University of Technology, Finland, 2001.

Author Biography

Professor Aloke Paul is currently running an active search group working on diffusion-related problems in the Department of Materials Engineering, Indian Institute of Science, Bangalore, India. Major areas of research include development of new phenomenological models in solid-state diffusion, materials in electronic packaging, bond coat in jet engine applications, growth of A15 intermetallic superconductors, etc. He teaches a postgraduate level course on Diffusion in solids. He has guided several Ph.D. and M.E. students. At present, he has co-authored more than 80 articles in various international journals.

Professor Tomi Laurila received the D.Sc. degree (with honors) from the Helsinki University of Technology in 2001. At the moment, he is Associate Professor in the field of Microsystem technology and holds an adjunct professorship on Electronics Reliability and Manufacturing. His research involves the study of interfacial reactions between dissimilar materials used in microsystems, biocompatibility issues related to different types of materials and electrochemical measurements of neurotransmitters from the brain. He has published extensively (about 70 scientific papers, including also book chapters and a text book) on the thermodynamic–kinetic analysis of interfacial reactions, electrochemical detection of biomolecules and issues related to reliability testing of electronic devices. Prof. Laurila is also responsible for the teaching of material science, electronics reliability, and bioadaptive technology to under- and postgraduate as well as postdoctoral students.

A. Paul et al., *Thermodynamics, Diffusion and the Kirkendall Effect in Solids*,
DOI: 10.1007/978-3-319-07461-0,

Dr. Vesa Vuorinen received his M.Sc. degree in 1995 in Materials Science and Engineering and D.Sc. degree in 2006 in the Department of Electronics from the former Helsinki University of Technology, currently Aalto University. Currently, he is working as Senior University Lecturer as well as Project Manager in the research group of Electronics Integration and Reliability. His research has been focused on the interfacial reactions encountered in lead-free electronics and reliability of high-density electronics assemblies with emphasis on soldering metallurgy on physics of failure viewpoint.

Dr. Sergiy Divinski is a Privat-Docent at the Institute of Materials Physics, University of Münster, Germany, where he leads the radiotracer laboratory which represents one of the most reputed and internationally recognized diffusion schools. He teaches graduate and postgraduate courses on Diffusion in Solids, Numerical methods in Material Science and different aspects of Materials Science. He has co-authored more than 150 articles in various international journals and several book chapters in the field of Diffusion in Solids.